

The University of Nottingham

UNITED KINGDOM • CHINA • MALAYSIA

Time-Resolved Infrared Studies of Metal Carbonyl Complexes

Lingjun Wu BSc

Thesis submitted to the University of Nottingham for the degree of Doctor of Philosophy

September 2018

Declaration

I hereby declare that all the work presented in this Thesis has been undertaken by myself, unless acknowledged otherwise.



Lingjun Wu

September 2018

Abstract

Chapter 1 Introduction

A brief overview of time-resolved Infrared (TRIR) spectroscopy is given in this Chapter. This technique has been used throughout this thesis to investigate the role of transient intermediates aiding in the elucidation of reaction mechanisms.

Chapter 2 TRIR Investigations on E-H (E: Si, Ge, Sn) Bond Activation by (η^5-$C_5H_nMe_{5-n}$)$M(CO)_3$ Complexes (M= Mn, Re) – towards Time-Resolved XAFS Studies

The E-H (E: Si, Ge, Sn) bond activation of $HEBu_3$ by the (η^5-$C_5H_nMe_{5-n}$)$M(CO)_3$ complexes (M= Mn, Re) has been investigated in two solvents, *n*-heptane and perfluoromethylcyclohexane (PFMCH), in order to support future time-resolved-XAFS (TR-XAFS) investigations. In heptane upon UV photolysis, (η^5-$C_5H_nMe_{5-n}$)$M(CO)_3$ undergoes CO-loss to form the dicarbonyl species (η^5-$C_5H_nMe_{5-n}$)$M(CO)_2$, which is quickly solvated to form (η^5-$C_5H_nMe_{5-n}$)$M(CO)_2$(*n*-heptane). Triplet dicarbonyl species $^3CpMn(CO)_2$ and $^3Cp'Mn(CO)_2$ were also observed. The (η^5-$C_5H_nMe_{5-n}$)$M(CO)_2$(*n*-heptane) complex undergoes substitution by $HEBu_3$. However, this ligand exchange does not occur for $CpRe(CO)_3$ in *n*-heptane, which is attributed to the extremely strong interaction between Re and *n*-heptane. The E-H bonds were found to undergo more complete activation with the Re complexes, and it was also found that the addition of electron rich substituents onto the Cp ring can facilitate oxidative addition. The overall interaction with the metal centers follow the order: Sn > Ge > Si. While the π-backbonding interaction between Mn and E-H follows: Ge ≥ Si > Sn. In PFMCH, it is found the coordination of the E-H bond to the metal complexes is much faster than in heptane, which is attributed to the weak coordinating property of PFMCH. In PFMCH, ligand exchange within the same $HEBu_3$ molecule is observed and this mechanism is supported by the kinetics.

Chapter 3 TRIR Investigations on the Photochemistry and Photophysics of Tungsten Carbonyl Complexes

In this Chapter, the results of TRIR investigations on the photoproperties of $W(CO)_6$ and a series of its derivatives, the $W(CO)_5L$ complexes (L: pyridine, piperidine, 4-acetylpyridine) are described. Particularly the rate of E-H (E: Si, Ge, Sn) bond activation has been investigated. Upon UV photolysis, $W(CO)_6$ loses one CO to form $W(CO)_5$, which undergoes fast solvation in heptane to form $W(CO)_5$(*n*-heptane). In the presence of the dopant $HEBu_3$ (E: Si, Ge, Sn), ligand exchange occurs to form $W(CO)_5(HEBu_3)$. It is proposed that the E-H bond may coordinate to the W centre in an η^1-fashion. This is supported by TR-XAFS studies conducted by our collaborators.

Interactions with halocarbons were also investigated using TRIR. X-cyclohexane (X: Cl, Br) are found to coordinate to the W centre *via* the halogen lone pair. For benzene and F-benzene, a "ring-edge" binding mode is observed, in which the W centre coordinates to the C=C bond. For F-benzene and Cl-benzene, an unstable intermediate $W(CO)_5(CH{=}CXC_4H_4)$ (X: F, Cl) is observed, which converts to the final stable product. For F-benzene, the final product is the "ring-edge"-bound species $W(CO)_5(CH{=}CHC_4H_3F)$. The $W(CO)_5(\eta^1$-X-Ph) (X: Cl, Br, I) species were observed for Cl-benzene, Br-benzene and I-benzene as the final stable product. For Br-benzene and I-benzene, the partially oxidized product [$W(CO)_5$(X---phenyl)] (X: Br, I) was observed, in which a 3-c-2-e interaction between W and C-X is proposed.

The W-Xe interaction for the $W(CO)_5L$ (L: pyridine, piperidine, 4-acetylpyridine) complexes has also been explored using TRIR. The Xe species $W(CO)_5Xe$ forms in PFMCH in the presence of Xe upon UV photolysis. This observation is supported by TR-XAFS studies conducted by our collaborators.

Chapter 4 Photophysics Studies on Re-diimine Complexes

The photophysics of the [$Re(CO)_3$(dppz-NPh_2)Cl] complex (dppz: dipyrido[3,2-a: 2'3'-c]phenazine) in different solvents (toluene and acetone) and the

$[Re(CO)_3(Phen\text{-}TPA)X]^{n=0,1}$ (X: Cl^-, Br^- n=0; py (pyridine), dmap (4-(dimethylamino)pyridine) n=1; phen: 1,10-phenanthroline; TPA: triphenylamine) complexes in CH_2Cl_2 have been investigated using TRIR. For the $[Re(CO)_3(dppz\text{-}NPh_2)Cl]$ complex, three excited states with different lifetimes based on the dppz-NPh_2 ligand are observed, denoted as states I, II and III. Upon UV photolysis, state I and III are formed, and state I converts to state II on the ps timescale, while state III decays to the ground state. State II is observed to be stable with a lifetime of several μs. It is found that the lifetime of state III is prolonged in acetone compared to that observed in toluene, while changing the solvent has little impact on the lifetimes of state I and II. It is also found that the lifetimes of state II and III are highly dependent on the concentration of $[Re(CO)_3(dppz\text{-}NPh_2)Cl]$, while the lifetime of state I is nearly unaffected. For the Re-phen complexes $[Re(CO)_3(Phen\text{-}TPA)X]^{n=0,1}$ (X: Cl^-, Br^- n=0; py, dmap n=1), a conversion between the $^1ILCT_{TPA\rightarrow phen}$ and $^3ILCT_{TPA\rightarrow phen}$ states (ILCT: intraligand charge transfer) is observed. The lifetime of the ^{3}ILCT state for $[Re(CO)_3(Phen\text{-}TPA)L]^+$ (L: py, dmap) is *ca.* 20-30 ns, while the lifetime for the halide complexes $[Re(CO)_3(Phen\text{-}TPA)X]$ (X: Cl^-, Br^-) is much longer, for *ca.* 2.0-3.0 μs. This can be explained by the energy gap law.

Chapter 5 TRIR Investigations on the Photoproperties of MOF Materials

This Chapter details the TRIR investigations of two MOF materials, Re-MOF and Mn-MOF, as well as their linker complexes. DFT calculations have also been undertaken to aid in assignment of the mechanisms. Upon UV photolysis of the linker complex of the Re-MOF, $Re(CO)_3(bdmpzm)Cl$, a ππ* excited state and the solvated dicarbonyl species $Re(CO)_2(bdmpzm)Cl(solvent)$ are observed to form. The ππ* excited state decays in *ca*. 60 ps to the ground state, while the solvated species $Re(CO)_2(bdmpzm)Cl(solvent)$ was found to be stable and shows no decay during the experimental timescale. When incorporated into a MOF scaffold, the ππ* excited state and the solvated species $Re(CO)_2(bdmpzm)Cl(solvent)$ are also observed. However, at later timedelays, after the decay of both the ππ* excited state and $Re(CO)_2(bdmpzm)Cl(solvent)$, an excited state in the MOF scaffold is observed.

For the Mn linker complex $Mn(CO)_3(bdmpzm)Br$, upon UV photolysis, unsaturated

dicarbonyl species $Mn(CO)_2$(bdmpzm)Br in both *fac*- and *mer*-configurations are observed, which then coordinate to solvent molecules. The solvated species $Mn(CO)_2$(bdmpzm)Br(solvent) undergoes a structural isomerization to a more stable configuration. When incorporated into a MOF scaffold, similar reaction processes were apparent. Finally, different solvents in the MOF channel were investigated.

Chapter 6 Experimental

All the experimental techniques, methods and sample preparations are described in this Chapter.

Acknowledgements

First, I would like to thank my supervisor, Prof. Michael George for all his support without whom all the work presented in this Thesis would not be possible.

I would like to thank Dr. Raphael Horvath and Dr. Charlotte Clark who have taught me a lot about the research with great patience, and helped me considerably with my project. Also, I would like to thank Dr. Xue-Zhong Sun, who has given me great advice on my research, taught me about the TRIR spectroscopy and helped me with the TRIR experiments. I would also wish to thank Dr. Jie Ke, Dr. Surajit Kayal, Dr. Ashley Love, Dr. Magnus Hanson-Heine, Dr. Thomas Murphy, Dr. Jack Turner, Katherine Reynolds, and Bethany Adams for their great help.

As most of the TRIR work has been done at the Rutherford Appleton Laboratory (RAL), I would really like to thank Dr. Ian Clark, Dr. Greg Greetham, Dr. Mike Towrie and Dr. Stuart Bartlett for their assistance at RAL, and without whose help the work could not be smoothly accomplished.

Meanwhile, I would like to thank my collaborators, Prof. Keith Gordon and Dr. Georgina Shillito from University of Otago, Prof. Stephan Kupfer and Dr. Philipp Traber from Friedrich Schiller University Jena, for their great help in the Re-dppz and Re-phen complexes projects. Also, I would like to thank Prof. Christian Doonan and Prof. Christopher Sumby from University of Adelaide, as well as Prof. Neil Champness, for their great assistance on the MOF project.

I would also like to thank the School of Chemistry workshop and Mark Guyler for all their help on the equipment.

Additionally, I would like to thank all the members in the George group, whose friendliness and helpfulness has made the group a wonderful place to work. I really enjoyed the time with everyone and the time will be appreciated.

Finally, I would thank my parents and my family for their support and love.

Abbreviations

Abs	absorbance
acpy	acetylpyridine
bdmpzm	bis(3,5-dimethylpyrazol-1-yl)methane
CH_2Cl_2	dichloromethane
CH_3CN	acetonitrile
CO	carbonyl
Cp	η^5-cyclopentadienyl
Cp*	η^5-pentamethylcyclopentadienyl
Cp’	η^5-methylcyclopentadienyl
DFT	density functional theory
DMAP	dimethylaminopyridine
DMF	dimethylformamide
dppz	dipyrido[3,2-*a*:2’,3’-c]phenazine
EXAFS	extended X-ray absorption fine structure
FTIR	Fourier transform infrared
GS	ground state
$HGeBu_3$	tributylgermane
HOMO	highest occupied molecular orbital
$HSiBu_3$	tributylsilane
$HSiEt_3$	triethylsilane
$HSnBu_3$	tributylstannane
IL	intraligand
ILCT	intraligand charge transfer
λmax	wavelength at absorbance maximum
LUMO	lowest unoccupied molecular orbital
MLCT	metal to ligand charge transfer
MO	molecular orbital
ν(CO)	carbonyl stretching frequency
NMR	nuclear magnetic resonance
PFH	perfluorohexane
PFMCH	perfluoromethylcyclohexane

PFTEA	perfluorotriethylamine
phen	1,10-phenanthroline
phz	phenazine
pip	piperidine
py	pyridine
TA	transient absorption
TRIR	time-resolved infrared
$TR^{M}PS$	time-resolved multiple probe spectroscopy
TR-XAFS	time-resolved X-ray absorption fine structure
UV	ultraviolet
XANES	X-ray absorption near-edge structure
3-c-2-e	3-centre-2-electron

Contents

Declaration ii

Abstract iii

Acknowledgements vii

Abbreviations viii

Chapter 1 Introduction **1-1**

1.1 Studies of Transient Intermediates 1-1

1.2 Time-Resolved IR Spectroscopy 1-3

1.3 Point-by-Point TRIR 1-4

1.4 Ultrafast TRIR 1-5

References 1-8

Chapter 2 TRIR Investigations on E-H (E: Si, Ge, Sn) Bond Activation by (η^5-$C_5H_nMe_{5-n}$)$M(CO)_3$ Complexes (M = Mn, Re) – towards Time-Resolved XAFS Studies **2-1**

2.1 Introduction 2-1

2.1.1 X-ray Absorption Spectroscopy (XAS) 2-1

2.1.2 Investigations of E-H (E: Si, Ge, Sn) Bond Activation by Organometallic Complexes 2-6

2.2 Result and Discussion 2-16

2.2.1 TRIR Studies of E-H (E: Si, Ge, Sn) Bond Coordination to $CpMn(CO)_3$ in *n*-heptane 2-16

2.2.2 TRIR Studies of E-H (E: Si, Ge, Sn) Bond Coordination to $CpMn(CO)_3$ in Perfluoromethylcyclohexane (PFMCH) 2-27

2.2.3 TRIR Studies of E-H (E: Si, Ge, Sn) Bond Coordination to $Cp'Mn(CO)_3$ in *n*-heptane 2-37

2.2.4 TRIR Studies of E-H (E: Si, Ge, Sn) Bond Coordination to $Cp'Mn(CO)_3$ in PFMCH 2-44

2.2.5 TRIR Studies of E-H (E: Si, Ge, Sn) Bond Coordination to $CpRe(CO)_3$ in *n*-heptane 2-49

2.2.6 TRIR Studies of E-H (E: Si, Ge, Sn) Bond Coordination to $CpRe(CO)_3$ in PFMCH 2-54

2.2.7 TRIR Studies of E-H (E: Si, Ge, Sn) Bond Coordination to $Cp^*Re(CO)_3$ in *n*-heptane 2-64

2.2.8 TRIR Studies of E-H (E: Si, Ge, Sn) Bond Coordination to $Cp^*Re(CO)_3$ in PFMCH 2-69

2.3 Conclusion 2-76
References 2-77

Chapter 3 TRIR Investigations on the Photochemistry and Photophysics of Tungsten Carbonyl Complexes **3-1**
3.1 Introduction – Photochemistry Investigations of Group 6 Metal Carbonyl Complexes $M(CO)_6$ (M: Cr, Mo, W) 3-1
3.1.1 E-H Bond Activation (E: Si, Ge, Sn) by $W(CO)_6$ 3-3
3.1.2 Interactions between Halocarbons and $W(CO)_6$ 3-6
3.1.3 Photophysical and Photochemical Investigations of $W(CO)_5L$ (L: N donor) Complexes 3-24
3.2 Result and Discussion 3-44
3.2.1 E-H Bond Activation (E: Si, Ge, Sn) by $W(CO)_6$ 3-44
3.2.2 TRIR Investigations on the Interactions Between $W(CO)_6$ and Halogenated Cycloalkanes 3-56
3.2.3 TRIR Investigations on the Interactions between $W(CO)_6$ and Halogenated Benzenes 3-63
3.2.4 E-H Bond Activation of $HEBu_3$ (E: Si, Ge, Sn) by $W(CO)_5L$ Complexes (L: pyridine (py), 4-acetylpyridine (4-acpy), piperidine (pip)) in Alkane Solvent 3-83
3.2.4.1 TRIR Investigations on E-H Bond Activation of $HEBu_3$ (E: Si, Ge, Sn) by $W(CO)_5$(py) in Heptane 3-83
3.2.4.2 TRIR Investigations on E-H Bond Activation of $HEBu_3$ (E: Si, Ge, Sn) by $W(CO)_5$(4-acpy) in Heptane 3-90
3.2.4.3 TRIR Investigations on E-H bond Activation of $HEBu_3$ (E: Si, Ge, Sn) by $W(CO)_5$(pip) in Heptane 3-99
3.2.5 TRIR Investigations on the W-Xe Interaction Conducted in Perfluoronated Solvent 3-106
3.2.6 TR-XAFS Results 3-122
3.2.6.1 TR-XAFS of $W(CO)_6$ in *n*-heptane with and without $HSiBu_3$ 3-122
3.2.6.2 TR-XAFS of $W(CO)_6$ in PFMCH under He or Xe Atmosphere 3-126
3.3 Conclusion 3-129
References 3-132

Chapter 4 Photophysics Studies on Re-diimine Complexes **4-1**
4.1 Introduction 4-1
4.1.1 Photophysics of Re-dppz Carbonyl Complexes 4-1
4.1.2 Photophysics of Re-phen Complexes 4-12
4.2 Result and Discussion 4-18
4.2.1 TRIR Investigations of $[Re(CO)_3(dppz\text{-}NPh_2)Cl]$ in Toluene 4-18
4.2.2 Photophysics of $[Re(CO)_3(dppz\text{-}NPh_2)Cl]$ in Acetone 4-22
4.2.3 Photophysics of $[Re(CO)_3(Phen\text{-}TPA)L]$ (L: Cl^-, Br^-) 4-27

4.2.4 Photophysics of $[Re(CO)_3(Phen\text{-}TPA)L]^+$ (L: py, dmap)..... 4-34
4.3 Conclusion..... 4-46
References..... 4-48

Chapter 5 TRIR Investigations on the Photoproperties of MOF Materials **5-1**
5.1 Introduction..... 5-1
5.2 Result and Discussion..... 5-15
5.2.1 TRIR of the Re Linker Complex..... 5-15
5.2.2 TRIR of Re-MOF..... 5-30
5.2.3 TRIR of the Mn Linker Complex..... 5-52
5.2.4 TRIR of Mn-MOF..... 5-59
5.3 Conclusion..... 5-88
References..... 5-93

Chapter 6 Experimental **6-1**
6.1 Apparatus Information..... 6-1
6.1.1 Nottingham Ultrafast TRIR Apparatus..... 6-1
6.1.2 Ultrafast TRIR Apparatus in Rutherford Appleton Laboratory (RAL)..... 6-2
6.1.3 Time-Resolved Multiple Probe Spectroscopy (TR^MPS) Apparatus in Rutherford Appleton Laboratory (RAL)..... 6-3
6.1.4 FTIR Spectroscopy..... 6-3
6.2 Materials..... 6-4
6.2.1 Materials Used in Chapter 2..... 6-4
6.2.2 Materials Used in Chapter 3..... 6-4
6.2.3 Materials Used in Chapter 4..... 6-4
6.2.4 Materials Used in Chapter 5..... 6-5
6.3 Sample Preparations..... 6-6
6.3.1 Sample in Solution Phase..... 6-6
6.3.2 Sample in Solid Phase..... 6-6
6.4 Data Analysis..... 6-7
6.5 DFT Calculations..... 6-7
References..... 6-8

Chapter 1 Introduction

This Thesis focuses on the use of spectroscopy to detect excited states, reaction intermediates and elucidate reaction mechanisms. In particular, these studies are focused in two general areas namely: (i) probing the electron transfer and the nature of Re-diimine excited states as complexes in solution, and embedded in metal-organic frameworks (MOFs), and (ii) characterization and understanding the reactivity of organometallic alkane and noble gas complexes, with the aim to interrogate the structure and reactivity of these complexes in solution using time-resolved XAFs. In the subsequent Chapters, more detailed introductions are given relating to the specific chapter, and here is an introduction to the specialized techniques used throughout the Thesis.

1.1 Studies of Transient Intermediates

Transition organometallic complexes have shown to have significant applications in many fields such as catalysis,[1,2,3] H_2 generation,[4,5,6] solar energy capture and conversion,[7,8] and pharmaceutical applications.[9,10,11] Therefore, the detailed understanding of their mechanisms is crucial for theoretical studies and industrial processes, and as such there are a wide range of approaches that can be used to study such processes. In this work, we are especially interested in the photochemistry and photophysics of transition organometallic carbonyl complexes. In solution, it is generally observed that following UV irradiation of a transition metal carbonyl complex results in CO loss to form the 16 electron unsaturated species, which is extremely unstable and is prone to rapidly coordinate to the surrounding solvent molecule within 1 ps,[12] as shown in Figure 1.1.

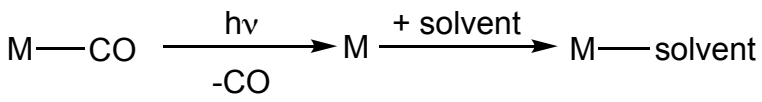


Figure 1.1 *A general scheme showing the photo-initiated solvation of transition metal carbonyl complexes.*

The formation of unsaturated intermediate can be followed by initial rapid solvation and reaction with other dopants in the system, which may occur as ligand exchange reactions, oxidative addition reactions or elimination reactions. One advantage of the photo-induced reaction is that the energy of the light can be tuned to selectively initiate the reaction of interest. For some transition metal diimine carbonyl complexes with ligands such as bypridine, irradiation does not result in photochemical reactions (no ligand dissociation), and interesting long-lived excited states can be produced such as the MLCT state (metal-to-ligand charge transfer), IL state (intraligand) and ILCT state (intraligand charge transfer).

Investigations on the photophysics of such complexes is also of significant importance, as these photophysical properties are found to have vital applications such as in dye sensitized solar cells,[13,14] CO_2 reduction[15,16] and OLED devices.[17,18,19]

However, most of these photo-induced processes occur at extremely fast timescales, some are complete on millisecond (ms), microsecond (μs), nanosecond (ns) or picosecond (ps) timescales. Therefore, in order to elucidate these extremely rapid processes and to better understand the reaction mechanism, either a particularly low-temperature environment should be created, thus the reaction process can be slowed down and conventional techniques can be used for investigations, or at room temperature where techniques that can probe ultrafast timescales need to be developed. In this work, we have exploited the use of ultrafast TRIR (time-resolve Infrared Spectroscopy) to elucidate the photochemical and photophysical properties of a series of transition metal carbonyl complexes under ambient conditions. The carbonyl group acts as a "reporting ligand" for the IR measurement. The ν(CO) is sensitive to the electron-density changes on the metal centre through the M to CO backdonation interaction. Also, ν(CO) can provide structural information regarding the complexes. In this work, Chapter 2 is about the photo-induced ligand exchange reaction between silane, germane and stannane with the solvated group 7 (M: Mn, Re) pianol-stool complexes as well as the following oxidative addition reactions. Chapter 3 is the study of tungsten carbonyl complexes, probing their photochemical and photophysical properties using TRIR. Chapter 4 is the photophysical investigations of several Re-diimine complexes with an electron

donor-acceptor system on the diimine ligands. The donor-acceptor system shows significant influence on the photophysical properties of these Re-diimine complexes studied. Chapter 5 is about the investigations of group 7 M-dipyrazole complexes (M: Mn, Re) within MOF scaffolds.

Although this work is mostly done using TRIR as the main technique, the aim of this work is to support the future TR-XAFS (time-resolved x-ray absorption fine structure) studies with which direct structural information of transient intermediates can be obtained.

1.2 Time-Resolved IR Spectroscopy

Most timed-resolved spectroscopy use a "pump-and-probe" method, which was first proposed by Norrish and Poter.[20] The concept is shown in Figure 1.2.

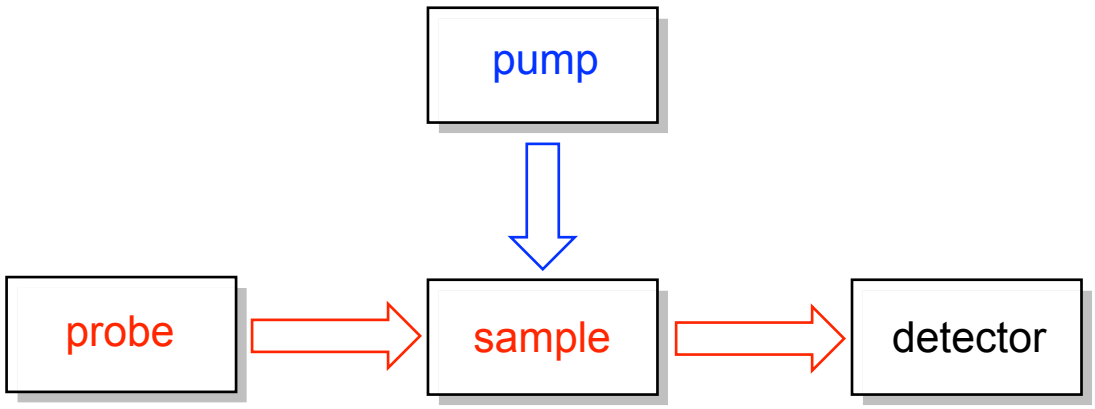


Figure 1.2 *A scheme showing the principle of the "pump-probe" concept used in flash photolysis experiments to detect short lived transients. The pump (usually a pulsed UV or visible laser) is used to initiate the reaction and then a probe (which is a continuous wave or pulsed laser) is used to monitor changes using suitable detectors and electronics.*

Flash photolysis utilizes UV pulse to initiate the reaction, then use transient spectroscopy to detect the reaction in real-time. Early time-resolved spectroscopy uses a UV pump as the initiating pump and UV-Vis spectroscopy as the probe.[21]

However, UV-Visible absorption spectroscopy has many drawbacks. UV/visible spectrum is often featureless and has broad bands in the condensed phase, which offers little information on the structure of the molecules of interest during the reaction process. Thus, IR spectroscopy has been used for detection in addition to UV-Visible absorption spectroscopy in time-resolved flash photolysis equipment. Tanner *et al.* proposed the use of dispersive IR spectroscopy as the detector in flash photolysis experiment for the first time.[22] Later FTIR (Fourier Transform Infrared Spectroscopy) replaced the dispersive IR spectroscopy. Rapid-scan FTIR can reach the time-resolution of millisecond, however, it is highly limited by the moving velocity of the mirror. For the step-scan FTIR, the mirror moves in discrete steps instead of fast-moving, and in each step, the reaction is initiated and the data is collected, allowing for the spectra to be constructed. The time-resolution can be reached down to tens of nanoseconds. However, a reversible reaction is required for step-scan FTIR measurements.[23]

1.3 Point-by-Point TRIR

Point-by-point TRIR is another time-resolved spectroscopic method using the "pump-and-probe" concept. In a point-by-point TRIR, a continuous wave IR probe is used which is tuned to a specific frequency. The spectra are built up by multiple measurements of each single IR frequency, each measurement is conducted along with time, thus kinetic information at each IR frequency can be obtained. The scheme of the point-by-point TRIR is shown in Figure 1.3.

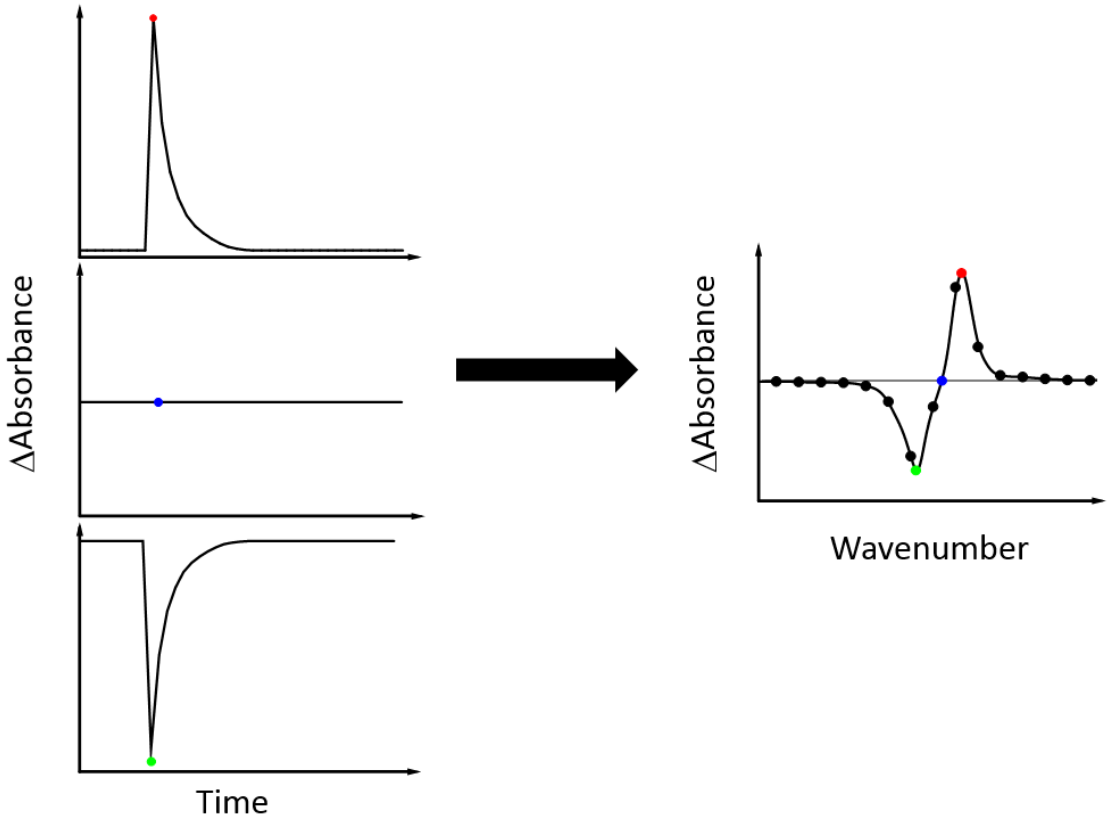


Figure 1.3 *Scheme of point-by-point TRIR measurement. The spectra are built up by measurements of discrete IR frequencies. The positive band indicates the formation of new species, while the negative band represent the depletion of the starting materials.*

Recently, development of the continuous wave mid-IR laser, known as the Quantum Cascade laser (QCL),[24] presents many advantages over the previous lead-salt diode lasers. It can operate at ambient temperature, easier to use and also generates higher energies.

However, the time-resolution of the point-by-point TRIR is limited by the rise-time of the detector. Mercury-cadmium-telluride (MCT) detectors are widely used for point-by-point TRIR, it allows for ns-timescale time-resolution.

1.4 Ultrafast TRIR

Ultrafast TRIR breaks the ns-timescale time-resolution limit of point-by-point TRIR by using optical delay lines. A sub-picosecond time-resolution can be achieved.

Figure 1.4 shows the scheme of the ultrafast TRIR spectrometer.

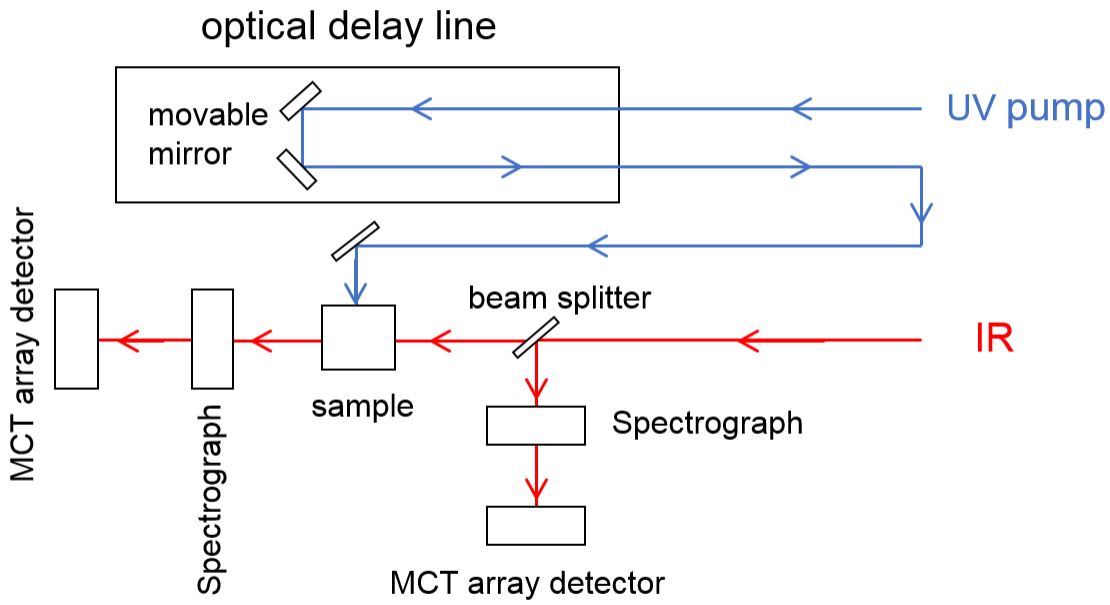


Figure 1.4 *Shows the scheme of the ultrafast TRIR spectrometer with the optical delay line. The different time-delays can be achieved by using the movable mirror, where different time-delays corresponds to different distance the light passes. In the ultrafast TRIR spectrometer, an optical delay line is used, and by tuning the difference of the path-length of the UV pump and IR probe, different time-delays can be achieved. Therefore, in theory the time-resolution of ultrafast TRIR is only limited to the pulse width of the UV pump. For most ultrafast TRIR the width of the commercial UV pump is usually in the range of 20-100 fs, therefore generally sub-ps time-resolution can be achieved. Using ultrafast TRIR, reaction process in ps-timescale can be investigated.*[25] *Another difference to the point-by-point TRIR approach is that the IR probe used in ultrafast TRIR is broad-band, therefore a full spectrum is measured at each timedelay. The measurement is operated in high repetition rates of ca. 1kHz or higher, therefore transient species of extremely weak intensities ($\Delta OD \approx 10^{-5}$) can be detected.*[26]

In recent years, an advance in ultrafast TRIR has been made namely the time-resolved multiple probe spectroscopy ($TR^{M}PS$) at the Rutherford Appleton Laboratory.[27] The UV pump and IR probe used are of different repetition rates,

therefore for each UV pump, many time-delays can be collected. The system allows for the investigation of reaction processes occurring from fs to ms timescales for a single experiment.

References

1 M. A. Ischay, M. E. Anzovino, J. Du and T. P. Yoon, *J. Am. Chem. Soc.*, 2008, **130**, 12886–12887.

2 D. A. Nicewicz and D. W. C. MacMillan, *Science*, 2008, **322**, 77–80.

3 C. K. Prier, D. A. Rankic and D. W. C. MacMillan, *Chem. Rev.*, 2013, **113**, 5322–5363.

4 M. Graetzel, *Acc. Chem. Res.*, 1981, **14**, 376–384.

5 R. E. Rodríguez-Lugo, M. Trincado, M. Vogt, F. Tewes, G. Santiso-Quinones and H. Grützmacher, *Nat. Chem.*, 2013, **5**, 342–347.

6 V. Balzani, L. Moggi, M. F. Manfrin, F. Bolletta and M. Gleria, *Science*, 1975, **189**, 852–856.

7 M. K. Nazeeruddin, A. Kay, I. Rodicio, R. Humphry-Baker, E. Mueller, P. Liska, N. Vlachopoulos and M. Graetzel, *J. Am. Chem. Soc.*, 1993, **115**, 6382–6390.

8 T. J. Whittemore, H. J. Sayre, C. Xue, T. A. White, J. C. Gallucci and C. Turro, *J. Am. Chem. Soc.*, 2017, **139**, 14724–14732.

9 M. J. Clarke, *Coord. Chem. Rev.*, 2002, **232**, 69–93.

10 A. B. Becceneri, C. P. Popolin, A. M. Plutin, E. L. Maistro, E. E. Castellano, A. A. Batista and M. R. Cominetti, *J. Inorg. Biochem.*, 2018, **186**, 70–84.

11 Z. Tavsan, P. K. Yaman, E. Subasi and H. A. Kayali, *JBIC J. Biol. Inorg. Chem.*, 2018, **23**, 425–435.

12 J. D. Simon and X. Xie, *J. Phys. Chem.*, 1986, **90**, 6751–6753.

13 A. S. Polo, M. K. Itokazu and N. Y. Murakami Iha, *Coord. Chem. Rev.*, 2004, **248**, 1343–1361.

14 N. Robertson, *Angew. Chem. Int. Ed.*, **45**, 2338–2345.

15 H. Hori, F. P. A. Johnson, K. Koike, K. Takeuchi, T. Ibusuki and O. Ishitani, *J. Chem. Soc. Dalton Trans.*, 1997, 1019–1024.

16 A. Rosas-Hernández, P. G. Alsabeh, E. Barsch, H. Junge, R. Ludwig and M. Beller, *Chem. Commun.*, 2016, **52**, 8393–8396.

17 H. Yersin, A. F. Rausch, R. Czerwieniec, T. Hofbeck and T. Fischer, *Coord. Chem. Rev.*, 2011, **255**, 2622–2652.

18 R. C. Evans, P. Douglas and C. J. Winscom, *Coord. Chem. Rev.*, 2006, **250**,

2093–2126.

19 J. A. Gareth Williams, S. Develay, D. L. Rochester and L. Murphy, *Coord. Chem. Rev.*, 2008, **252**, 2596–2611.

20 R. G. W. Norrish and G. Porter, *Nature*, 1949, **164**, 658.

21 R. G. W. Norrish and G. Porter, *Prog. React. Kinet. Mech.*, 1952, **27**.

22 K. N. Tanner and R. L. King, *Nature*, 1958, **181**, 963.

23 X. Z. Sun, S. M. Nikiforov, J. Yang, C. S. Colley and M. W. George, *Appl. Spectrosc.*, 2002, **56**, 31–39.

24 J. Faist, F. Capasso, D. L. Sivco, C. Sirtori, A. L. Hutchinson and A. Y. Cho, *Science*, 1994, **264**, 553–556.

25 J. B. Asbury, H. N. Ghosh, J. S. Yeston, R. G. Bergman and T. Lian, *Organometallics*, 1998, **17**, 3417–3419.

26 M. Towrie, D. C. Grills, J. Dyer, J. A. Weinstein, P. Matousek, R. Barton, P. D. Bailey, N. Subramaniam, W. M. Kwok, C. Ma, D. Phillips, A. W. Parker and M. W. George, *Appl. Spectrosc.*, 2003, **57**, 367–380.

27 G. M. Greetham, D. Sole, I. P. Clark, A. W. Parker, M. R. Pollard and M. Towrie, *Rev. Sci. Instrum.*, 2012, **83**, 103107.

Chapter 2 - TRIR Investigations on E-H (E: Si, Ge, Sn) Bond Activation by (η^5-$C_5H_nMe_{5-n}$)$M(CO)_3$ Complexes (M = Mn, Re) – towards Time-Resolved XAFS Studies

2.1 Introduction

Bond activation is a significant step in many industrial processes, and transition metal complexes are known as effective catalysts in such reactions. As a result, studies on the mechanism of such reactions have attracted much attention during the last few decades. Many studies have been focused on C-H and H-H bond activations,[1,2,3,4] but activations of the Si-H, Ge-H and Sn-H bonds of Group 14 are also important in many industrial processes such as hydrosilylation,[5,6,7] hydrogermylation[8,9,10] and hydrostannation.[11,12,13] Time-resolved spectroscopy has proved to be an important technique for studying reaction mechanisms with timescales ranging from femtoseconds to hours. This approach can be used with techniques including NMR, ESR, IR, UV/visible and Raman spectroscopy to allow insight into the mechanism. This Thesis focuses on the use of time resolved infrared (TRIR) to study possible mechanisms, and there have been several reported studies elucidating the coordination and activation of C-H,[14,15,16,17] H-H,[4,18] Si-H,[19,20,21] Ge-H[22,23] and Sn-H[24,25,26] bonds.

This Chapter aims at developing approaches to investigate the bond activation of tertiary silane, germane and stannane with the formula HER_3 (E: Si, Ge, Sn), by transition metal carbonyl complexes of group 7 with the piano-stool structure (η^5-$C_5H_nMe_{5-n}$)$M(CO)_3$ (M = Mn, Re), using a combination of TRIR spectroscopy and time-resolved X-ray absorption fine structure (TR-XAFS).

2.1.1 X-ray Absorption Spectroscopy (XAS)

X-ray absorption spectroscopy (XAS) is a powerful technique in exploring the local structure of a specific atom, such as the chemical bonding with other atoms, the

bond length, bond angles, identity and the number of coordinating atoms. Compared to conventional XRD, XAS does not require samples with highly organized crystal structure, either amorphous or crystalized samples can be analyzed for short-range local structures of a specific atom.[27,28] Therefore, even samples in the solution phase and gas phase can be analyzed. The principle of XAS is that, by using intensive X-ray beams, specific atoms can be excited by the core electrons. The high selectivity of XAS is based on the fact that the binding energy of the core shell differs for different elements, thus by choosing the energy of the X-ray photons, the atoms to be investigated can be stimulated specifically. The XAS spectrum can be divided into two parts, one is the X-ray absorption near-edge structure (XANES), and the other is the extended X-ray absorption fine structure (EXAFS), as shown in Figure 2.1.

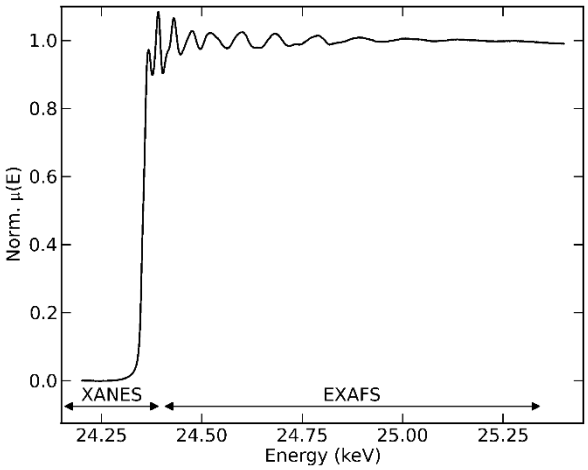


Figure 2.1 *A typical XAS spectrum of Pd foil showing both the XANES and EXAFS regions.*[29]

The XAS measures the absorption coefficient μ(E) versus the incident energy of the X-ray photons. The X-ray absorbance follows the equation (1):

$$I_t = I_0 e^{-\mu l} \quad (1)$$

I_t is the intensity of the X-ray transmitted through the sample (the intensity can also be regarded as the number of photons); I_0 is the intensity of the initial X-ray before reaching the sample; μ: absorption coefficient; l: sample thickness. Therefore, the absorption coefficient μ(E) can be presented as in equation (2):

$$\mu = \frac{-\ln\left(\frac{I_t}{I_0}\right)}{l} \quad (2)$$

The large step in the XANES region as shown in Figure 2.1 is usually known as the "rising edge". This is caused when the intensive X-ray beam irradiates the core electron of the specific atom, when the photon energy reaches the binding energy of the electron shell, the core electron can be ejected from the specific electron shell and the I_t is dramatically decreased. Based on which specific electron shell the electron is photo-initiated from, according to the principal quantum numbers n= 1, 2, 3, …, the rising edge are denoted as K-edge, L-edge, M-edge, *etc.* When a specific core electron is photo-ejected by the intensive X-ray beam, the photoelectron is proposed to be ejected to the final states where the energy is 50-100 eV higher than the ionization energy level (the energy range of EXAFS).

Following the photo-ejection of the core electron, two phenomena are proposed to occur. The electron at higher energy level than the vacant "core hole" can move down to fill the "core hole", while the excess energy is released by either emission of fluorescent photon or ejection of Auger electron, as shown in Figure 2.2.

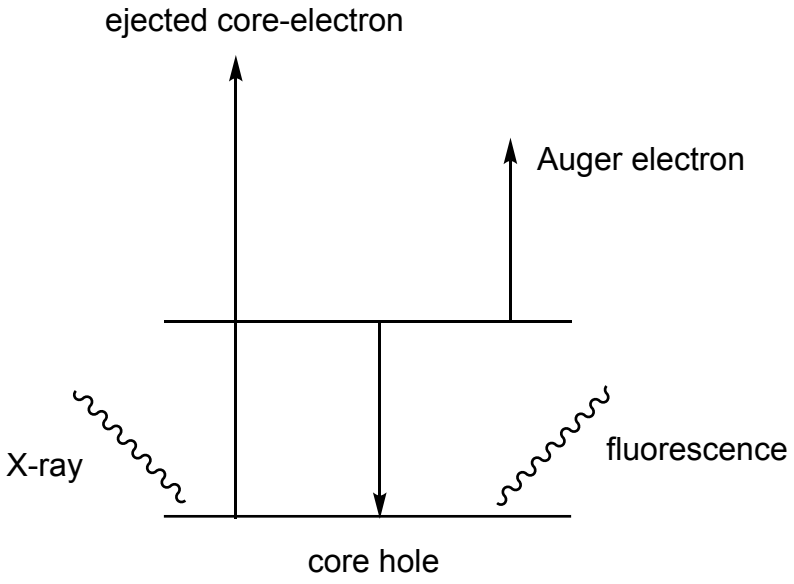


Figure 2.2 *Generation of the fluorescence and Auger electron after X-ray irradiation.*

For dilute samples, measuring the fluorescent emission instead of the X-ray absorption is a good alternative, as fluorescent emission measurement does not require background measurement.[30] The measurement of Auger electron emission also does not require background measurement, however the measurement of Auger electron emission is limited to surface investigations due to limitation of the mean free path of the Auger electrons (of the order of 1 nm). Meanwhile the Auger electron measurements require high vacuum environment, which also limits its applications.[31]

The energy of the X-ray beam is sufficiently high that the ejected photoelectron is proposed to be free electron with wave characteristics. In the EXAFS region, the wiggly oscillations correspond to the modulations of interference by the scattering from the surrounding atoms with the outgoing wave of the ejected photoelectrons with different energies. The oscillation in the EXAFS region is only observed when the sample is in a condensed phase. For an individual atom, the EXAFS spectrum is observed to be smooth. The peak in the EXAFS spectrum corresponds to the constructive interference while the valley corresponds to the destructive interference. By Fourier transform, the contributions of different shells surrounding the atom can be distinguished, thus information regarding the local structure of the atom can be obtained.[32,33]

Recently, there have been reports of studies that have combined XAFS with time-resolved techniques.[34,35,36,37] Time-resolved techniques combining NMR, ESR, IR, UV/visible and Raman spectroscopy have been proved to be powerful techniques in studies of reaction mechanism, as it allows detection of reaction intermediates. Time-resolved IR (TRIR) spectroscopy, using a time-resolution of picosecond is especially useful for complexes containing the "reporting ligands" CO and CN, which have intense IR signals, and relatively narrow IR peaks that can be used for detailed analysis of the reaction mechanism. However, a comprehensive exploration of the structure is unsuccessful using only TRIR. XAFS can provide direct surrounding structural information of an atom. When combined with time-resolved technique, the real-time direct analysis of the structure of transient intermediates can be achieved, which could be a powerful complementary technique for TRIR. The

concept of TR-XAFS was first proposed by Dent *et al.* that both structural and kinetic information of a reaction process can be obtained using EXAFS spectra. Although in their work, the reaction process is relatively slow (~ 12 h).[38] In the TR-XAF approach, the "pump-and-probe" concept has also been used similar to other TR-techniques. In this approach, the sample is first initiated by a short pump laser pulse, followed by a probe pulse. In early decades, several strategies have been proposed for achieving fast time-resolutions for TR-XAFS — the quick-EXAFS (QEXAFS),[39] energy-dispersive-EXAFS (EDE or DEXAFS),[40,41] and the Turbo EXAFS.[42,43] For the QEXAFS, time-resolution is generally in the order of tens of seconds, and for the Turbo EXAFS, the time-resolution can achieve a few seconds. While the best time-resolution is achieved by the DEXAFS down to sub-millisecond. Recently, the development of third-generation synchrotron radiation sources has brought about the improvement of the time-resolution down to the ps-scale (most third generation synchrotron sources can provide X-ray pulse with width of *ca.* 100 ps).[44] This improvement of time-resolution has significantly facilitated the application of TR-XAFS in in-situ measurements of reaction processes. There are many examples using TR-XAFS to investigate the reaction mechanisms and transient intermediates in real-time, such as the investigation of structure changes after photo-induced excited states,[45,46] reaction mechanisms of biochemical systems,[47,48] and geometry changes during charge transfer.[49] In combination with other ultrafast time-resolved techniques such as TRIR, TR-XAFS can provide complementary direct information on the structure of transient intermediates which significantly contributes to the comprehensive understanding of the mechanisms on the ultrafast-timescale. In this Chapter, we examine the photochemistry of metal carbonyls using TRIR in order to see if suitable systems can be produced to be studied by XAFS to obtain more detailed information about bonding in such transient species.

2.1.2 Investigations of E-H (E: Si, Ge, Sn) Bond Activation by Organometallic Complexes

One of the main targets for the characterization of organometallic mechanisms that I have focused upon is the reactions to form organometallic silane complexes. There has been considerable research work reported on the bond activation reaction of silanes by transition metal organometallic complexes. For trialkyl silane with the formula $HSiR_3$, the most common binding mode to metal centre is recognized to be an η^2-mode, where the Si-H bond coordinates to the metal "edge-on", as shown in Figure 2.3.

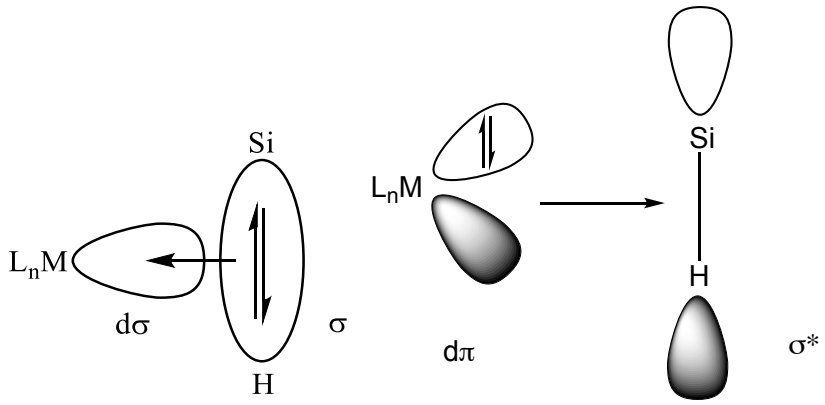


Figure 2.3 *η^2-interaction between a silane and a metal centre.*

The η^2-interaction is considered to compose of two consecutive steps. First, the σ bond of Si-H donates into a vacant d orbital of the transition metal centre, then if the transition metal has a d orbital of π-symmetry that can interact with the σ^* orbital of Si-H, then the σ^* orbital of Si-H can act as an electron acceptor and M can donate electrons into the σ^* orbital, and this interaction is denoted as π-backbonding. If the π-backbonding is efficient, full oxidative addition can occur, *i.e.* the complete cleavage of Si-H bond to form the 2c-2e (2-centre-2-electron) M-Si and M-H bonds, also known as the "classical interaction". Otherwise, a "non-classical interaction" is formed, also known as "arrested addition". The formation of the "classical interaction" and "non-classical interaction" of Si-M-H is shown in Figure 2.4.

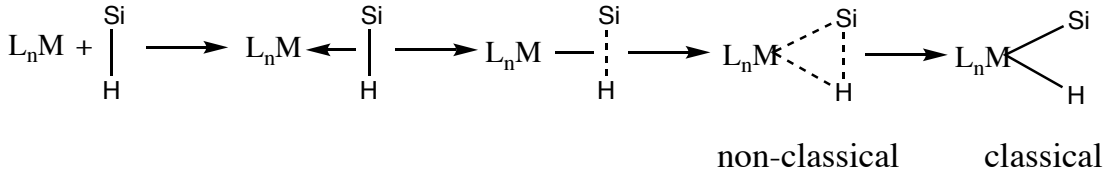


Figure 2.4 *Steps in the Si-H bond activation by a transition metal complex.*

The "nonclassical interaction" is described as the 3c-2e (3-centre-2-electron) interaction between the M centre and Si-H (the complex is denoted as the "σ-complex"). However, it has been proposed for other possible interactions such as a η^1-mode in which the Si-H coordinates to the metal centre *via* the H atom, while Si has little interaction with the metal centre, and forms a "M-H-Si" bridge, in which the angle of M-H-Si can reach up to *ca.* 160°, as shown in Figure 2.5.

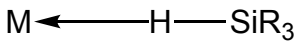


Figure 2.5 *η^1-interaction involved in coordinating to a metal centre.*

An early example of η^1-bonding between a metal centre and silane was reported by Yang *et al*.[50] They found that for the $[(POCOP)Ir(H)(acetone)]^+$ complex (POCOP: 2,6-$[OP(tBu)_2]_2C_6H_3$), when treated with excess $HSiEt_3$, a silane-bound complex in the η^1-fashion is formed, supported by XRD measurements and DFT calculations. The reaction process is shown in Figure 2.6.

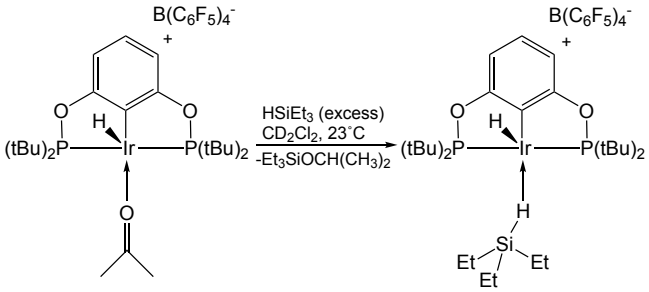


Figure 2.6 *Reaction scheme of the formation of the silane-bound species in an η^1-fashion. Reproduced from Ref 50.*

XRD analysis of the product shown in Figure 2.6 reveals that the distance between Ir and Si is 3.346 Å, which is 0.97 Å greater than the sum of the radii of Ir and Si atoms, and the angle of Ir-H-Si is 157°, which both indicate an η^1-bonding mode. DFT calculations on the analogue $HSiMe_3$ complex agree well with the XRD results (the Ir-Si distance is calculated to be 3.38 Å, and the Ir-H-Si angle to be 161°). However, it is also found that for the "trimmed" complexes, in which all the butyl ligands are replaced by methyl ligands, the Ir-Si distance is reduced to *ca.* 2.62 Å, and the Ir-H-Si angle is reduced to *ca.* 101°, which suggests an η^2-bonding mode between Ir and H-Si. This demonstrates how steric factors can affect the interactions between Si-H and the metal centre. There are also η^1-mode silane examples for main group metals and non-metals. Houghton *et al.* investigated the metal-free bond activation of silanes by boranes, and found that the coordination mode of Si-H to the B centre is consistent with the η^1-fashion.[51] Similar examples are also found for $Al(C_6F_5)_3$,[52] and carboranes.[53]

The interactions shown in Figure 2.3 have also been observed for Ge-H ligands binding to the metal centre. Lichtenberger *et. al.*[54] has analyzed the nature of the coordination of Ge-H to metal centres for the $CpMn(CO)_2(HGePh_3)$, $Cp'Mn(CO)_2(HGePh_3)$ and $Cp^*Mn(CO)_2(HGePh_3)$ complexes (Cp': η^1-methylcyclophentadienyl; Cp*:η^5-pentamethylcyclopentadienyl), and confirmed the interactions of σ and σ^* orbitals of Ge-H with the metal centre. The nature of the Ge-H-M interaction is considered to be similar to Si-H-M, and the σ-donations are of similar magnitude. However, the σ^* interaction of Ge-H is considered to be slightly greater than Si-H. There have been relatively few studies comparing the interactions of Si-H and Ge-H to metal centres. Vincent *et al.*[55] investigated the oxidative addition of $EH_{4-n}Ph_n$ (E: Si, Ge; n=0-3) with Mo(CO)(diphosphine)$_2$. They found that oxidative addition of Ge-H is much easier than for Si-H.

There have also been some reports of Sn-H bond activation. Schubert *et al.*[56] prepared $Cp'Mn(CO)_2(HSnPh_3)$ by photolysis of $Cp'Mn(CO)_3$ with $HSnPh_3$, and the interaction between Sn-H and the metal is considered to be 3-centre-2-electron. However, the Sn-H interaction in the σ-complex $Cp'Mn(CO)_2(HSnPh_3)$ is found to be weaker than the silyl analogue $CpMn(CO)_2(HSiR_3)$, indicating that the Sn, Mn,

H 3-c-2-e interaction is in a later stage of the oxidative addition than the Si, Mn, H 3-c-2-e interaction in $Cp'(CO)_2Mn(HSiR_3)$.

There are many factors that can affect the interaction between the metal centre and the E-H bond (E: Si, Ge, Sn), such as changing the nature of the metal centre and E-H. Also, steric factors can affect the interaction, too. Research[55,57,58,59] has suggested that electron rich metals or strong electron withdrawing groups on silane, germane or stannane ligands will facilitate the interaction between the metal and E-H, and also may lead to complete oxidative addition. This is explained by the π-backbonding interaction, as increasing electron density on the metal centre or decreasing electron density on the E-H bond can strengthen the π-backbonding interaction. Steric factors are also important in the interaction between the transition metal and E-H bonds. Vincent *et. al.*[55] found that the addition of either H_2SiPh_2 or H_2GePh_2 to $Mo(CO)(dppe)_2$ in toluene is unsuccessful, possibly because of steric crowding, as addition of SiH_4, H_3SiPh, GeH_4, H_3GePh was observed.

Many techniques have been used in determine the extent of oxidative addition of silanes, such as X-ray structural analysis,[60,61,62] NMR,[23,63] PES,[54] IR[58,59] and also DFT.[64,65] X-ray structure analysis is useful to directly determine the structure of the crystal. The bond length is an important indication of the interaction extent. It is found that a shorter M-Si bond is achieved when silane is substituted with stronger electron withdrawing groups, which facilitates the π-backbonding from the metal centre to the Si-H σ*-orbital. For instance, it is found that for the $Co(CO)_4(SiX_3)$ complexes (X: H[66], Cl[67], F[68]), the Si-X bond can accept π-back-donation from the Co centre, and the bond lengths of Co-Si were found to follow the trend: F < Cl < H. This has also been observed for other transition metal complexes. Wright and co-workers[59] examined the M-Si bonding of the $Os(SiR_3)Cl(CO)(PPh_3)_2$ complexes (R = F, Cl, OH, Me), and it was found that the Os-Si bond length is affected by the substituent R group with the trend F < Cl < OH < Me. The actual specific bond distance of Si-H can also be an indicator of the interaction extent. Schubert proposed that the bond distance of 2.00 Å is the upper limit of any interaction existing between Si and H.[69] Thus if the Si-H distance found in an Si-TM-H

interaction is longer than 2.00 Å, then it is considered to be a full oxidative addition. The bond distance for free silane is *ca.* 1.48 Å, thus bond distances between 1.48 Å – 2-00 Å are considered to be a 3-centre-2-electron interaction. However, it has to be noted that, the bond distance can only be used to roughly compare the extent of interactions, as changes on metal or silane, germane, stannane will all result in changes on the bond distance range.

NMR spectroscopy is also an important technique for comparing the extent of the oxidative addition. Much work[70,71] has proposed that the coupling constant $J_{E\text{-}H}$ can reveal the interactions between E and H (E: Si, Ge, Sn). Smaller $J_{E\text{-}H}$ values reflect weaker interaction between E and H, thus a more complete oxidative addition. However, similar to the X-ray structural analysis, no exact standard for the coupling constant $J_{E\text{-}H}$ has been set to determine the interactions. Conventional IR can also be useful in determining the extent of oxidative addition, especially for metal complexes with the *"reporting ligand"*, such as CN and CO. The wavenumber shift of ν(CO) can reflect the extent of π-backbonding from the metal to E-H (E: Si, Ge, Sn). As when more electron density from the metal is donated into the $\sigma*$ orbital of E-H, there is less π–backbonding into the $\pi*$ orbitals of CO, and ν(CO) band positions will blue-shift. Wright and co-workers have investigated the effect of R (R: F, Cl, OH, Me) on the $Os(SiMe_nR_{3-n})Cl(CO)(PPh_3)_2$ complexes (R = F, Cl, OH; n=0-3) using IR.[59] The results show that the ν(CO) band positions blue-shift further when the electronegativity of the R substituents is increased. These results are tabulated in Table 2.1.

Table 2.1 *The ν(CO) band positions of $Os(SiMe_nR_{3-n})Cl(CO)(PPh_3)_2$ (R = F, Cl, OH; n=0-3), reproduced from Ref. 59.*

R	F	Cl	OH
$SiMe_3$	1895	1895	1895
$SiMe_2R$	1917	1917	1910
$SiMeR_2$	1933	1928	1917
SiR_3	1946	1944	1919

As shown in Table 2.1, the highest ν(CO) position is 1946 cm^{-1}, when all R groups

are substituted by F. While the lowest ν(CO) band position is for the $Os(SiMe_3)Cl(CO)(PPh_3)_2$ complex. Higher ν(CO) band positions reflect less electron density on the metal centre.

However, all these techniques cannot provide real-time information on the oxidative addition reaction process, only information on the final product can be obtained. More detailed studies on the reaction mechanism are required for catalysis of hydrosilation, hydrogermation and hydrostannation reactions. The Harris group has done several studies investigating the reaction mechanism of oxidative addition of silane to metal complexes using TRIR.[72,73,74] They reported the first investigation on the activation of Si-H bond by $CpM(CO)_3$ (M: Mn, Re) using femtosecond to nanosecond IR spectroscopy. They found that for the Mn and Re complexes, although both belong to group 7, have very different mechanisms in activation of triethylsilane. The proposed mechanism for $CpMn(CO)_3$ is shown in Figure 2.7.

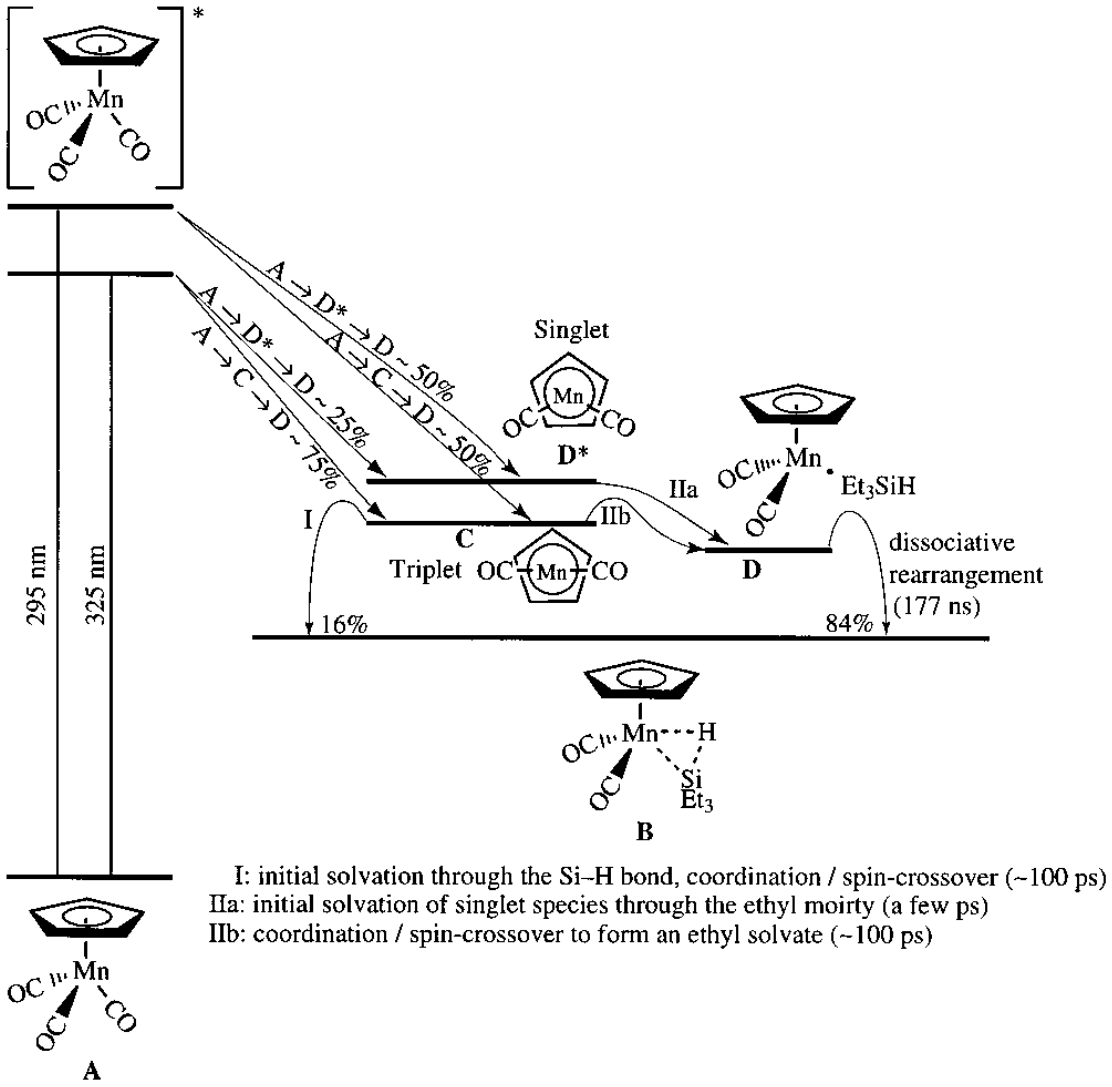


Figure 2.7 *Reaction mechanism of the Si-H activation by $CpMn(CO)_3$ in neat $HSiEt_3$, by Yang et. al.*[73]

It is found that upon UV photolysis, in neat $HSiEt_3$ the activated species $CpMn(CO)_2(HSiEt_3)$ is generated *via* two routes. After UV irradiation, two dicarbonyl species are formed, one is the singlet dicarbonyl species which is too unstable to be detected and instantly coordinates to the ethyl group of $HSiEt_3$ in a few ps. The other dicarbonyl species is in triplet state (lifetime: ~100 ps). 16% of this triplet dicarbonyl species directly coordinates to Si-H of $HSiEt_3$ and forms the final activated species $CpMn(CO)_2(HSiEt_3)$, while 84% of the triplet dicarbonyl species coordinates to the ethyl group of $HSiEt_3$, and then the ethyl group is replaced by Si-H in a dissociative way. It is also found that UV light of lower energy will result in more formation of the triplet dicarbonyl species. For the Re analogue, no triplet

dicarbonyl species but only singlet dicarbonyl species was observed upon UV photolysis. There was also no direct observation of the unsaturated $CpRe(CO)_2$. Some of the dicarbonyl (~25%) directly coordinates to Si-H to form the final activated species $CpRe(CO)_2(HSiEt_3)$ (in a few ps), while 75% coordinates to the ethyl group of $HSiEt_3$ (in a few ps), and then this group is replaced by Si-H in a dissociative way on the μs timescale, to form the final activated species $CpRe(CO)_2(HSiEt_3)$. The extent of oxidative addition in the activated species $CpM(CO)_2(HSiEt_3)$ (M: Mn, Re) was examined using *ab initio* calculations. The calculation results suggest that in $CpMn(CO)_2(HSiEt_3)$, a 3-c-2-e interaction exists among Si-Mn-H, while for $CpRe(CO)_2(HSiEt_3)$, a full oxidative addition is achieved. This is expected as Re is more electron rich compared to Mn, and the π-backbonding to Si-H is expected to be more sufficient.

TRIR has also been used to investigate how the substituents on silanes will affect the oxidative addition. George *et al.* investigated the activation of $HSiEt_nCl_{3-n}$ (n: 0, 1 and 3) by $CpV(CO)_4$ using TRIR.[57] They found that for $HSiCl_3$ and $HSiEtCl_2$, complete activation of the Si-H bonds is achieved. The ν(CO) band positions of the final activated species $CpVH(CO)_3Si(Et_nCl_{3-n})$ (n: 0 or 1) all moved to higher wavenumber compared to the parent bands, indicating an oxidation of the V centre. While for $HSiEt_3$, a σ-complex $CpV(CO)_3(\eta^2\text{-}HSiEt_3)$ is obtained, of which the ν(CO) band positions all red-shifted compared to the parent bands.

There are also reports of TRIR investigations on Sn-H bond activation. Harris and co-workers[75] investigated the Sn-H bond activation by three transition metal complexes which are known to form triplet dicarbonyls after UV photolysis, $Fe(CO)_5$, $CpCo(CO)_2$ and $CpV(CO)_4$. It is found that for $Fe(CO)_5$ and $CpCo(CO)_2$, the formation of the Sn-H activated species is exclusively *via* the coordination of Sn-H to the triplet dicarbonyl species $^3Fe(CO)_4$ and $^3CpCo(CO)$. While for $CpV(CO)_4$, the Sn-H activated species $CpV(CO)_3(HSnBu_3)$ is formed either from the triplet dicarbonyl speices $^3CpV(CO)_3$ or the solvated singlet dicarbonyl species $^1CpV(CO)_3(BuHSnBu_2)$, as shown in Figure 2.8.

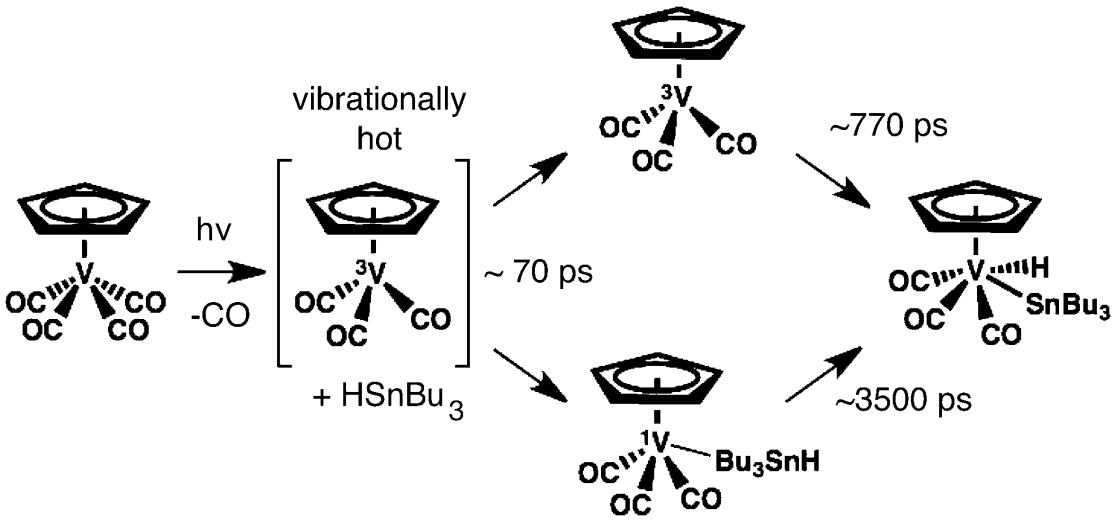


Figure 2.8 Reaction mechanism of Sn-H bond activation by $CpV(CO)_4$.[75]

The results are consistent with previous work on Si-H activation, which reveals that the triplet state dicarbonyls activate the E-H (E: Si, Sn) bond faster than the singlet dicarbonyls. This is attributed to the weak spin-forbidden solvent interaction for the triplet state, therefore it is expected to be easier for the triplet dicarbonyl species to diffuse in the solution compared to the alkyl-bound singlet dicarbonyl species, thus when the triplet dicarbonyl species encounters a stronger coordinating ligand Sn-H, it readily undergoes spin-crossover and forms the final Sn-H activated species, known as the concerted spin-crossover/solvate process.

The singlet dicarbonyls, first coordinate to the alkyl-group of HER_3 (E: Si, Sn; R: Et, Bu), then the alkyl-group is replaced by a E-H bond to form the final activated species. Many mechanisms have been proposed for the ligand rearrangement between the alkyl-group and E-H bonds. One is the "chain walk" mechanism, which suggests that the metal centre moves along the molecule chain. Simon and co-workers[76] investigated the coordination of a series of alcohols with chains of different lengths to $Cr(CO)_5$ using transient absorption spectroscopy, and found that the coordination between these alcohols and $Cr(CO)_5$ is consistent with the "chain walk" mechanism.

However, many research works have raised doubts on this theory. Zhang *et al*.[77,78,79] investigated the ligand rearrangement reaction using PAC and UV-Vis flash

photolysis, and they found that these ligand rearrangement reactions were intermolecular. Harris and co-workers investigated the Si-H bond activation by many transition metal complexes such as group 6[74] and group 7[72,73] metal complexes, and found that the rearrangement of C-H by Si-H was best explained by a dissociative mechanism, as the reaction rate (ns to μs timescale) is too long for the reported chain walk reaction rate (*ca.* 100 ps). They also used silane with a long carbon chain, *n*-Pr_3SiH, compared to $HSiEt_3$, to examine the chain walk theory, as if the chain walk mechanism is correct for silane, the ligand rearrangement rate for *n*-Pr_3SiH is expected to be longer than for $HSiEt_3$. However, the results suggested that the rates of silanes with different carbon chain lengths are similar. Therefore, a dissociative mechanism was proposed to be the most reasonable mechanism for the ligand rearrangement reactions.

In this Chapter, we are going to investigate the E-H (E: Si, Ge, Sn) bond activation by the $(\eta^5\text{-}C_5H_nMe_{5-n})M(CO)_3$ (M = Mn, Re) complexes in both alkane and perfluoroalkane solvents, using TRIR which are then used to inform future possible XAFS research.

2.2 Result and Discussion

In this work, we report our investigations on the photo-coordination of E-H (E: Si, Ge, Sn) bond in $HEBu_3$ to the $(\eta^5\text{-}C_5H_nMe_{5-n})M(CO)_3$ (M = Mn, Re) complexes in alkane or perfluoroalkane solvents using TRIR spectroscopy. It is the first time that real-time reaction processes of all of the substrates E-H (E: Si, Ge, Sn) bond coordination to transition metal complexes are investigated using time-resolved IR spectroscopy, and the influence of different metal centres, dopant concentration, solvents and substituents on the metal complexes are also investigated.

2.2.1 TRIR Studies of E-H (E: Si, Ge, Sn) Bond Coordination to $CpMn(CO)_3$ in *n*-heptane

It is generally recognized that the coordination of E-H (E: H, C, Si, Ge, Sn, *etc.*) bond to the metal centre requires a vacant coordinating site, which can be obtained by thermal or photochemical methods. Many reports[72,73] on the photochemistry of $CpMn(CO)_3$ reveal that in solution, photolysis results in the ejection of one CO ligand, leaving a vacant coordination site. Thus, we chose $CpMn(CO)_3$ to investigate the E-H bond coordination reaction and use TRIR to probe the photoproducts.

Although Harris and co-workers have reported the Si-H bond activation by $CpMn(CO)_3$ in neat triethylsilane, no work so far has been reported on Si-H bond activation by $CpMn(CO)_3$ in alkane solvents. We chose *n*-heptane as the solvent for the following reasons. The complexes of interest typically have high solubility in heptane and the infrared spectrum of heptane has low IR absorbance enabling a wide IR detection range. This should allow the feasibility to study this reaction as a model system by XAFS as $CpMn(CO)_2$(heptane) and $CpMn(CO)_2$(silane) should have different spectra. Figure 2.9 shows the TRIR spectra of $CpMn(CO)_3$ in heptane doped with tributylsilane (0.25 M) following photolysis at different time delays.

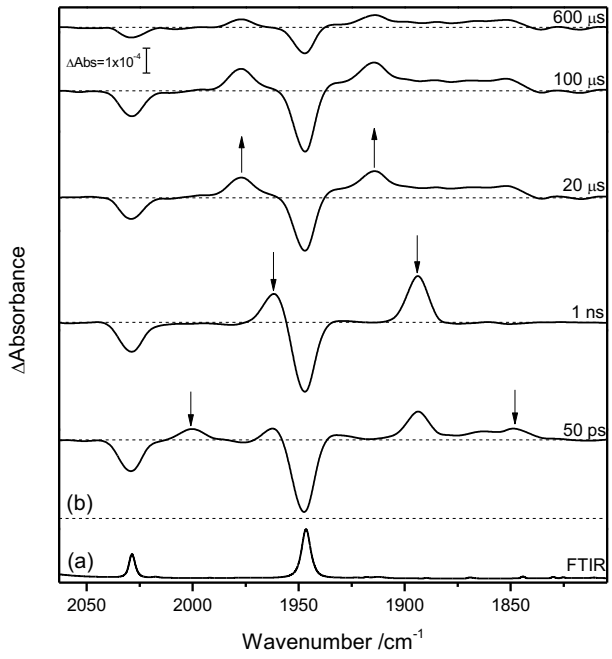


Figure 2.9 *(a) FTIR spectrum and (b) TRIR spectra obtained at specific time delays following photolysis (266 nm) of $CpMn(CO)_3$ in heptane doped with 0.25 M $HSiBu_3$.*

Upon UV photolysis, four broad vibrationally hot features were formed which then narrowed and blue-shifted to four bands at 2001, 1961, 1893 and 1848 cm^{-1} within 50 ps. Similar results were observed with four bands at similar band positions according to previous TRIR research on $CpMn(CO)_3$ in neat triethylsilane.[73,80] Thus the bands at 2001 and 1848 cm^{-1} can be assigned to the triplet dicarbonyl species $^3CpMn(CO)_2$ by comparison to the bands from the reported study in neat triethylsilane[73] (2001 and 1840 cm^{-1}) and in neat heptane (2004 and 1849 cm^{-1}).[80] Also, the lifetime of the transient with bands at 2001 and 1848 cm^{-1} (110 ±20 ps, Figure 2.10) is similar to the reported lifetime of $^3CpMn(CO)_2$ in neat triethylsilane[73] (100 ps) and in neat heptane (110 ps).[80] The bands assigned to the triplet dicarbonyl species were observed to decay as the intensity of the bands at 1961 and 1893 cm^{-1} increased (Figure 2.10). The bands at 1961 and 1893 cm^{-1} are assigned to the heptane complex, $CpMn(CO)_2$(*n*-heptane), by comparison to the band position of $CpMn(CO)_2$(*n*-heptane) in neat heptane (1960 and 1897 cm^{-1}),[80] and also compared to the ethyl-bound species in neat triethylsilane

$CpMn(CO)_2(EtHSiEt_2)$[73] (1960 and 1892 cm^{-1}). We observe no apparent evidence for a butyl-bound species $CpMn(CO)_2(BuHSiBu_2)$, and this is not surprising given the vast excess of heptane compared to $HSiBu_3$ in these experiments. On the microsecond-timescale, two bands at 1976 and 1915 cm^{-1} were observed to form.

The bands at 1976 and 1915 cm^{-1} are assigned to the silane species $CpMn(CO)_2(HSiBu_3)$, in comparison with the work of Harris and co-workers who reported ν(CO) positions of 1979 and 1915 cm^{-1} for $CpMn(CO)_2(H\text{---}SiEt_3)$ in neat triethylsilane[73]. This work is similar to the results reported in neat triethylsilane (Figure 2.7), with the decay of $^3CpMn(CO)_2$, both $CpMn(CO)_2$(heptane) and $CpMn(CO)_2(HSiBu_3)$ are formed, see Figure 2.10.

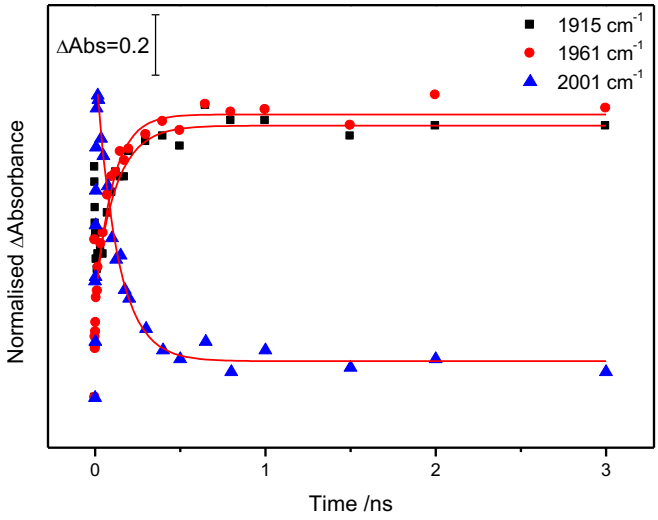


Figure 2.10 *Kinetic traces of different species observed following photolysis of $CpMn(CO)_3$ in heptane in the presence of tributylsilane. 2001 cm^{-1}: $^3CpMn(CO)_2$; 1961 cm^{-1}: $CpMn(CO)_2$(n-heptane); 1915 cm^{-1}: $CpMn(CO)_2(HSiBu_3)$.*

From analysis of the kinetic data, it is concluded that $^3CpMn(CO)_2$ decays and forms both the heptane-bound species $CpMn(CO)_2$(*n*-heptane) as well as the silane species $CpMn(CO)_2(HSiBu_3)$. The bands assigned to the $CpMn(CO)_2$(*n*-heptane) species show a two-stage growth as this transient is visible at the early time delays (Figure 2.9). The instantaneous formation of $CpMn(CO)_2$(*n*-heptane) is reported to occur *via* the singlet dicarbonyl $^1CpMn(CO)_2$ intermediate which instantly coordinates to the surrounding heptane molecules.[73] The detection of the formation

rate is limited due to equipment risetime. $CpMn(CO)_2(HSiBu_3)$ is also formed *via* two-stage process and is formed in early time as $^3CpMn(CO)_2$ decays, while the rest is formed later from reaction of $CpMn(CO)_2$(*n*-heptane) with silane, which occurs on the microsecond timescale (*ca*. 4.5 μs), Figure 2.11.

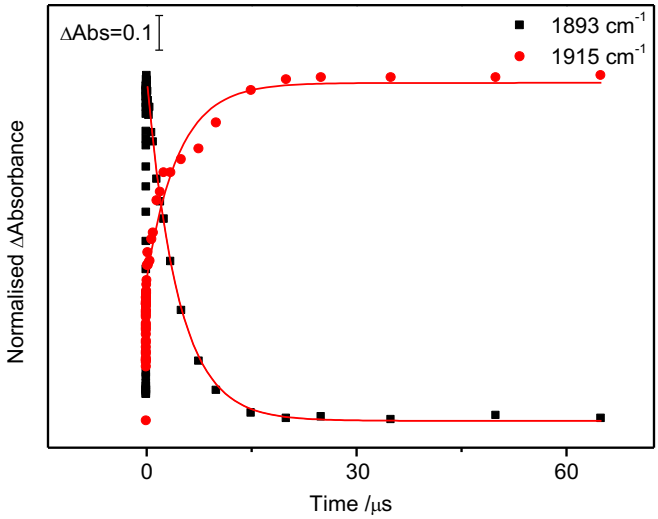


Figure 2.11 *TRIR kinetic traces obtained at 1915 and 1893 cm^{-1} corresponding to $CpMn(CO)_2(HSiBu_3)$ and $CpMn(CO)_2$(heptane).*

The silane species $CpMn(CO)_2(HSiBu_3)$ is observed to be very stable and shows no decay during the experimental timescale (up to ~1 ms). Upon UV photolysis, $CpMn(CO)_2$(*n*-heptane) is formed instantly, together with the formation of $^3CpMn(CO)_2$, which has a lifetime of *ca.* 100 ps, similar to that in neat triethylsilane and in neat *n*-heptane. And the triplet dicarbonyl species decays and undergoes spin crossover to form $CpMn(CO)_2$(*n*-heptane) or directly forms the final silane species $CpMn(CO)_2(HSiBu_3)$. The reaction mechanism is shown in Figure 2.12.

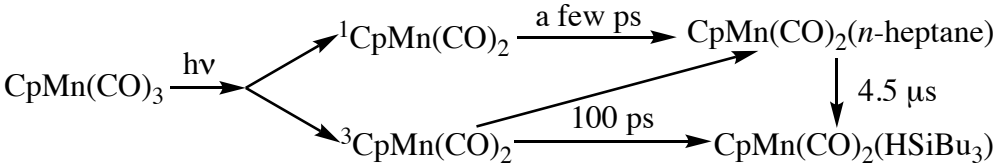


Figure 2.12 *Key summary result for the photochemical reaction of $CpMn(CO)_3$ in heptane in the presence of $HSiBu_3$.*

As shown in Figure 2.12, the reaction mechanism is similar to the photo-reaction of $CpMn(CO)_3$ reported in neat triethylsilane (Figure 2.7).[73] However, in neat triethylsilane the $CpMn(CO)_2$ coordinates to the ethyl group of triethylsilane. It was also observed that there are significant differences in the kinetics. In neat triethylsilane, the ligand exchange rate between $CpMn(CO)_2(EtHSiEt_2)$ and $CpMn(CO)_2(HSiEt_3)$ is *ca.* 177 ns, while in heptane the rate is much slower, at *ca.* 4.5 μs. It is also found that the ligand exchange rate between $CpMn(CO)_2$(*n*-heptane) and $CpMn(CO)_2(HSiBu_3)$ is dependent on the dopant concentration of $HSiBu_3$ (Table 2.2). The ligand exchange rate decreases with increasing dopant concentration.

Table 2.2 *Effects of the dopant ($HSiBu_3$) concentration on the Ligand exchange rate between $CpMn(CO)_2$(n-heptane) and $CpMn(CO)_2(HSiBu_3)$, and the observed rate constant k_{obs}.*

Dopant concentration /M	ligand exchange rate /μs	$K_{obs}x10^5$ /s^{-1}
0.05	9.3 ± 0.4	1.1
0.1	5.0 ± 0.1	2.0
0.25	4.5 ± 0.3	2.2

For the potential future XAFS experiments to monitor transient reactions, we are not only interested in the bond activation of Si-H, but also in the related Ge-H and Sn-H activations. Thus, similar TRIR investigations have been conducted on the photoreaction of $CpMn(CO)_3$ with $HGeBu_3$ and $HSnBu_3$.

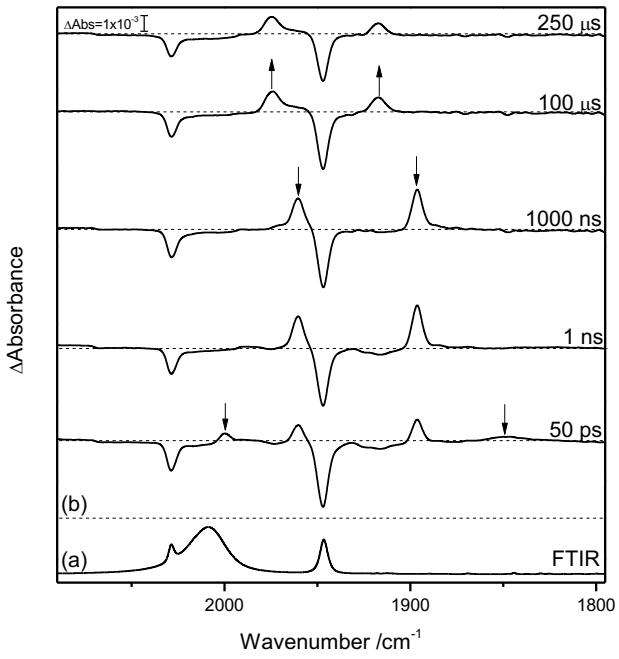


Figure 2.13 *(a) FTIR spectrum and (b) TRIR spectra obtained following photolysis (266 nm) of $CpMn(CO)_3$ in heptane doped with 0.05 M $HGeBu_3$.*

Similar results have been observed in heptane doped with $HGeBu_3$ (Figure 2.13). Upon UV photolysis, four bands are formed at *ca.* 2001, 1961, 1896 and 1848 cm^{-1}, and the bands at *ca.* 2001 and 1848 cm^{-1} are assigned to $^3CpMn(CO)_2$ compared to the experiment with $HSiBu_3$ (2001 and 1848 cm^{-1}). $^3CpMn(CO)_2$ also has a similar lifetime (106 ±2 ps) to that observed with $HSiBu_3$. The bands at 1961 and 1896 cm^{-1} are readily assigned to $CpMn(CO)_2$(*n*-heptane). Similar to the experiment with $HSiBu_3$, the activated species $CpMn(CO)_2(HGeBu_3)$ are observed at 1975 and 1918 cm^{-1}. The transformations from $^3CpMn(CO)_2$ to $CpMn(CO)_2$(*n*-heptane) and $CpMn(CO)_2(HGeBu_3)$ have also been observed. The ligand exchange rate between $CpMn(CO)_2$(*n*-heptane) and $CpMn(CO)_2(HGeBu_3)$ is found also to be related to the dopant concentration, and faster (*ca.* 7.9 μs) than $HSiBu_3$ (*ca.* 9.3 μs) under the same dopant concentration (0.05 M). The rate is observed to decrease to *ca.* 4.1 μs when the concentration of $HGeBu_3$ is doubled to 0.1 M.

Figure 2.14 shows the TRIR spectra of experiment with $HSnBu_3$.

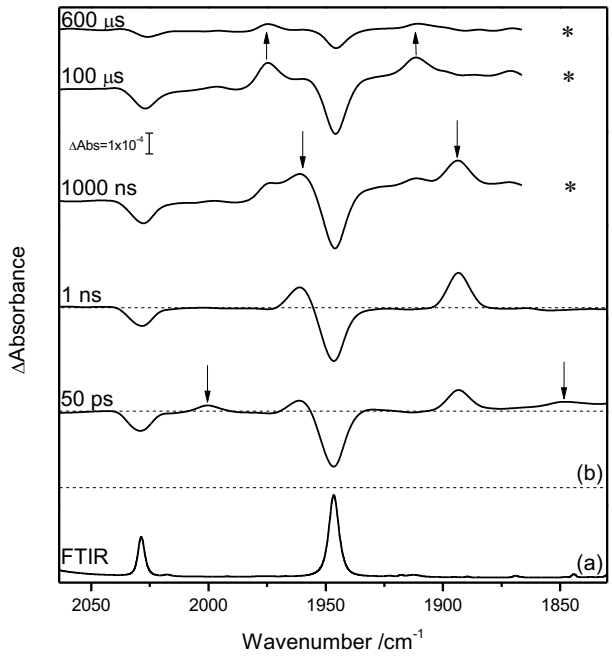


Figure 2.14 *(a) FTIR spectrum and (b) TRIR spectra obtained following photolysis (266 nm) of $CpMn(CO)_3$ in heptane doped with 0.17 M $HSnBu_3$. * indicates region obscured by noise created by shockwave at later time delays.*

For $HSnBu_3$, similar results were observed to $HSiBu_3$ and $HGeBu_3$. The lifetime of the $^3CpMn(CO)_2$ species was measured to be *ca.* 110 (±7) ps, similar to that in heptane doped with $HSiBu_3$ and $HGeBu_3$. Thus, it can be concluded that, the lifetime of $^3CpMn(CO)_2$ in heptane is not significantly affected by the dopants $HSiBu_3$, $HGeBu_3$ and $HSnBu_3$. Transformation from $^3CpMn(CO)_2$ to $CpMn(CO)_2$(*n*-heptane) and direct formation of $CpMn(CO)_2(HSnBu_3)$ (1976, 1912 cm^{-1}) were also observed, while the ligand exchange reaction between $CpMn(CO)_2$(*n*-heptane) (1961, 1893 cm^{-1}) and the stannane species $CpMn(CO)_2(HSnBu_3)$ was determined to be faster than $HSiBu_3$ and $HGeBu_3$, and is also dependent on the dopant concentration, as summarized in Table 2.3.

Table 2.3 *Effects of the dopant ($HSnBu_3$) concentration on the Ligand exchange rate between $CpMn(CO)_2$(n-heptane) and $CpMn(CO)_2(HSnBu_3)$, and the observed rate constant k_{obs}.*

Dopant concentration /M	ligand exchange rate /μs	$K_{obs}x10^5$ /s^{-1}
0.05	5.1 ± 0.3	2.0
0.1	2.9 ± 0.1	3.4
0.17	2.2 ± 0.2	4.5

The ligand exchange reaction between $CpMn(CO)_2$(*n*-heptane) and $CpMn(CO)_2(HSnBu_3)$ is first order for the $HSnBu_3$ concentration, revealed by the linear relation between K_{obs} and the $HSnBu_3$ concentration, as shown in Figure 2.15.

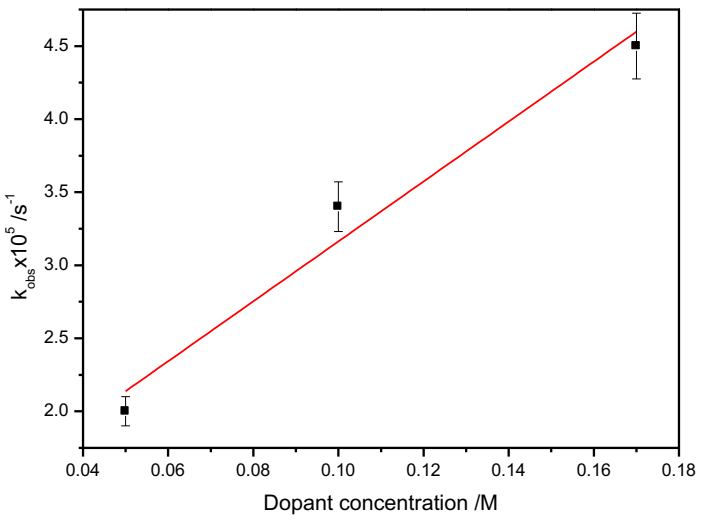


Figure 2.15 *Relation between the concentration of $HSnBu_3$ (M) and the observed rate constant k_{obs} for the ligand exchange reaction between $CpMn(CO)_2$(n-heptane) and $CpMn(CO)_2(HSnBu_3)$*

The second order rate constant calculated is k_2= 2.1(±0.3) x 10^6 dm^3 mol^{-1} s^{-1}.

Therefore, the ligand exchange rates are observed to be dependent on the dopant concentration for all three dopants, $HSiBu_3$, $HGeBu_3$ and $HSnBu_3$. For $HSiBu_3$, the k_{obs} is found not to be in a linear relation with the concentration of $HSiBu_3$, different to $HSnBu_3$. This is possibly due to the solubility of $HSiBu_3$ in heptane, therefore the actual $HSiBu_3$ concentration in heptane may be lower than 0.25 M.

The extent of E-H (E: Si, Ge, Sn) bond activation by $CpMn(CO)_3$ is also an interesting topic for discussion. Previous work on Si-H activation of $HSiEt_3$ by $CpMn(CO)_3$ has suggested that there exists a "non-classical" 3-c-2-e interaction among Si-Mn-H,[73] *i.e.* the Si-H bond is not fully activated by $CpMn(CO)_3$ in neat triethylsilane. Here the IR bands of $CpMn(CO)_2(HSiBu_3)$ and $CpMn(CO)_2(HSiEt_3)$ are compared with their parent bands, as shown in Table 2.4.

Table 2.4 *IR frequency comparison of activated species $CpMn(CO)_2(HSiR_3)$ (R: Et, Bu).*

species	ν(CO) / cm^{-1}	ν(CO) of $CpMn(CO)_3$ / cm^{-1}	Ref.
$CpMn(CO)_2(HSiEt_3)$	1979, 1915	2029, 1946	73
$CpMn(CO)_2(HSiBu_3)$	1976, 1915	2028, 1947	This work

From Table 2.4 it can be observed that, the $\Delta\nu$(CO) of $CpMn(CO)_2(HSiBu_3)$ compared to the parent bands are similar to that of $CpMn(CO)_2(HSiEt_3)$. As the ν(CO) band position reflects the π-backbonding between Mn and CO, which in turn can reflect the extent of the interaction between Mn and Si-H, and hence the extent of Si-H bond activation. The movement to lower wavenumber compared to the parent bands for both $CpMn(CO)_2(HSiBu_3)$ and $CpMn(CO)_2(HSiEt_3)$ suggests that in both species the σ-donation from Si-H to Mn dominates the interaction. Meanwhile, the similarity between $CpMn(CO)_2(HSiBu_3)$ and $CpMn(CO)_2(HSiEt_3)$ suggests that the extent of Si-H bond activation in these two complexes are similar. Thus, we assign the interaction between Mn and Si-H in $CpMn(CO)_2(HSiBu_3)$ to be 3-c-2-e in nature, and that the Si-H bond in $CpMn(CO)_2(HSiBu_3)$ is not fully activated. This is also consistent with expectation. As for $HSiBu_3$, compared to $HSiEt_3$, the butyl group is similar in electron donation ability. Also, the bulkier butyl groups may sterically hinder the interaction between Mn and Si-H. One may raise the question that the η^1-coordination mode may also be possible considering the larger size of the butyl ligands which may hinder the η^2-coordination as previous work suggests.[50] However, as shown in Figure 2.9, for $CpMn(CO)_2(HSiBu_3)$, the ν(CO) band positions are blue-shifted compared to the heptane species $CpMn(CO)_2$(*n*-heptane), which indicates a stronger electron density donation from the Mn centre to the Si-H moiety than to the C-H moiety of heptane, while this supports the η^2-coordination mode instead

of the η^1-mode.

We are also interested in the bond activation of $HGeBu_3$ and $HSnBu_3$. Table 2.5 summarizes the ν(CO) band positions of the three activated species and the ligand exchange rates at a dopant concentration of 0.05 M.

Table 2.5 *Comparison of the ligand exchange rates between C-H and E-H of activated species $CpMn(CO)_2(HEBu_3)$ (E: Si, Ge, Sn) in heptane with the dopant concentration of 0.05 M.*

Species	ν(CO) /cm^{-1}	Ligand exchange rate /μs
$CpMn(CO)_2(HSiBu_3)$	1976, 1915	9.3 ± 0.4
$CpMn(CO)_2(HGeBu_3)$	1974, 1918	7.9 ± 0.8
$CpMn(CO)_2(HSnBu_3)$	1975, 1912	5.1 ± 0.3

From Table 2.5 it can be observed that, there are no significant differences in ν(CO) positions among the three complexes. The dominant interaction between Mn and E-H (E: Si, Ge, Sn) is a σ-interaction. Compared to $CpMn(CO)_2$(*n*-heptane) (1960, 1897 cm^{-1}), all the activated species have moved to higher energies (Δ(CO) of $CpMn(CO)_2(HSiBu_3)$: 18, 16 cm^{-1}; $CpMn(CO)_2(HGeBu_3)$: 21, 14 cm^{-1}; $CpMn(CO)_2(HSnBu_3)$: 15, 15 cm^{-1}), reflecting stronger bonding between Mn and E-H (E: Si, Ge, Sn) compared to C-H. Thus, it can be concluded that the Germane species $CpMn(CO)_2(HGeBu_3)$ may have the strongest Mn to E-H π-backbonding. There is not much difference between the Si- and Sn-species. This may indicate that the activation extent for all dopants may be in the following sequence: Ge > Si ≈ Sn. This is consistent with previous research[54] which reported that for the Ge-H activation by transition metal complexes, the σ-donation still dominates the interaction between the metal centre and Ge-H, while the π-backbonding from M to Ge-H is slightly higher than Si-H, which results in fuller Ge-H bond activation compared to Si-H. Previous work[56] has also suggested that the Sn-H bond activation of $HSnPh_3$ by Cp'$Mn(CO)_3$ (Cp' = methylcyclopentadiene) is not complete and forms a 3-c-2-e interaction. The rate of the C-H/E-H ligand exchange shows the trend Si < Ge < Sn, which may indicate an increasing interaction between Mn and E-H (E: Si, Ge, Sn). As this interaction is dominated by a σ-interaction, the

more electron rich Sn-bond is expected to have a stronger σ-interaction with the Mn centre.

In conclusion, based on the ν(CO) shift comparison of the activated species $CpMn(CO)_2(HSiBu_3)$, $CpMn(CO)_2(HGeBu_3)$ and $CpMn(CO)_2(HSnBu_3)$, the E-H (E: Si, Ge, Sn) bond activation is observed to be incomplete for all three dopants, all forming a 3-c-2-e interaction with the Mn centre. For all three dopants, the dominant interaction with the Mn centre is the σ-donation interaction, reflected by the red-shift of the ν(CO) band positions compared to the parent bands. The ligand exchange rate Si < Ge < Sn may indicate an increasing interaction between E-H (E: Si, Ge, Sn) bond and the Mn centre, due to richer electron density located on Sn-H bond compared to the other two dopants, which facilitates the σ-interaction. The Δν(CO) band shift to higher wavenumbers for the activated species $CpMn(CO)_2(HEBu_3)$ compared to the solvated species $CpMn(CO)_2$(*n*-heptane) indicates the π-backbonding between Mn and E-H. From the result, the activation extent is proposed to follow this sequence: Ge > Si ≈ Sn.

2.2.2 TRIR Studies of E-H (E: Si, Ge, Sn) Bond Coordination to $CpMn(CO)_3$ in Perfluoromethylcyclohexane (PFMCH)

As detailed above, the ultimate aim is to examine transient species by XAFS. There are several reasons for extending the studies above in perfluorinated solvents. Firstly, the solvated intermediates are expected to have different XAFS spectra depending upon whether a perfluorinated or aliphatic alkane is bound to the metal. Secondly, the use of the perfluorinated alkane solvent may allow the coordination of dissolved gases such as Xe to be examined as the noble gas is expected to bind more strongly to the metal centre. Thirdly, the high solubility of gases in this perfluorinated solvent allow measurements with dissolved gases to be undertaken at room temperature and low pressures. Previously in our research group, TRIR of $CpMn(CO)_3$ in neat PFMCH and in triethylsilane-doped PFMCH have been conducted.[80]

As previous work suggested, the heptane species $CpMn(CO)_2$(*n*-heptane) undergoes ligand exchange to the activated species $CpMn(CO)_2(HEBu_3)$ (E: Si, Ge, Sn) on the μs-timescale. As we wish to decrease the binding interaction between $^3CpMn(CO)_2$ with solvent, we chose perfluoromethylcyclohexane (PFMCH) as our solvent for investigation. We have conducted TRIR experiments of $CpMn(CO)_3$ in PFMCH doped with 0.25M $HSiBu_3$, and the results are described below.

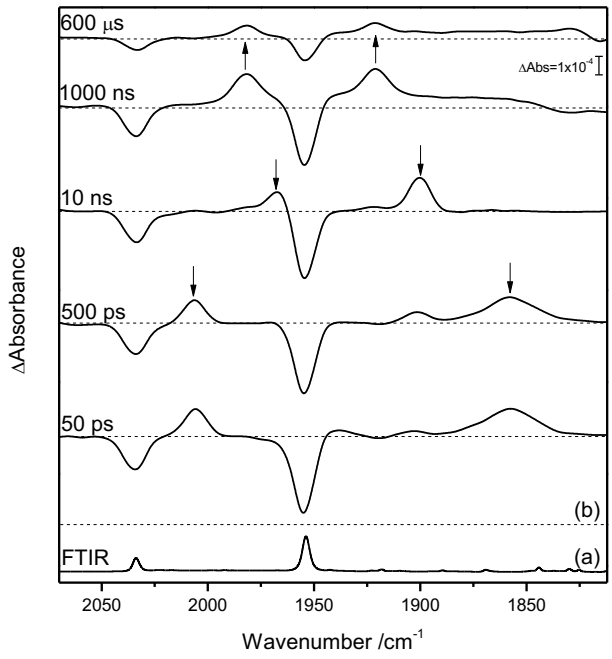
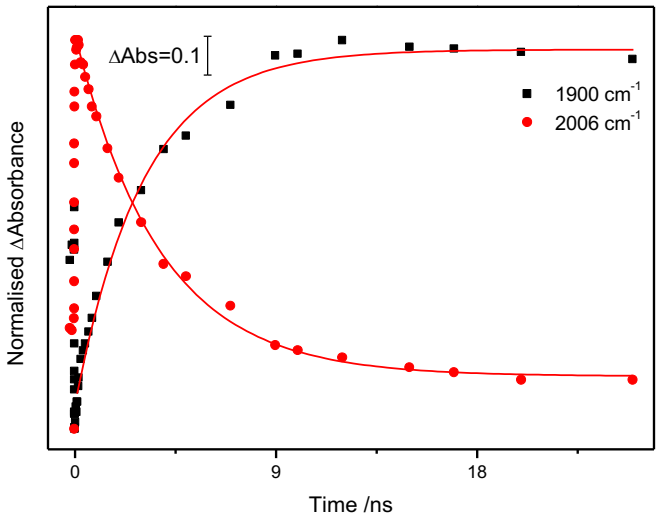


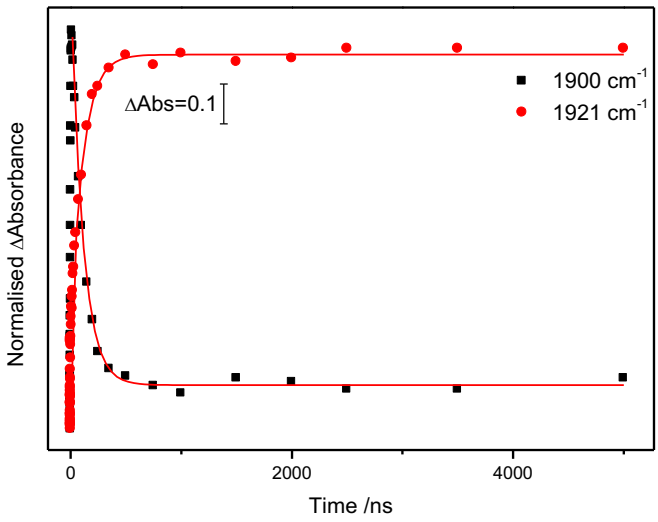
Figure 2.16 *(a) FTIR spectrum and (b) TRIR spectra obtained following photolysis (266 nm) of $CpMn(CO)_3$ in PFMCH doped with 0.25 M $HSiBu_3$.*

These experiments in PFMCH can be compared with TRIR results in heptane. Upon UV photolysis, four broad vibrational hot features are formed initially (Figure 2.16), which then narrowed and blue-shifted giving four bands at 2006, 1968 (w), 1900 and 1858 cm^{-1}. The bands at 2006 and 1858 cm^{-1} are assigned to $^3CpMn(CO)_2$ based on previous work,[80] while the bands at 1968 and 1900 cm^{-1} are assigned to the butyl-bound species $CpMn(CO)_2(BuHSiBu_2)$ in comparison with previous work in PFMCH doped with $HSiEt_3$ (1966 and 1897 cm^{-1}), in which the Mn centre is proposed to coordinate to the butyl ligand *via* C-H bond in a 3-c-2-e mode.[80] The lifetime of $^3CpMn(CO)_2$ in PFMCH is much longer compared in heptane, for *ca.* 4 ns (Figure 2.17), consistent with that reported previously.[80] As $^3CpMn(CO)_2$ decays, the bands of $CpMn(CO)_2(BuHSiBu_2)$ are formed at the same rate (Figure 2.17). The formation of the butyl-bound species $CpMn(CO)_2(BuHSiBu_2)$ in PFMCH confirms the stronger coordination ability of the butyl-group compared to PFMCH. Then these bands decay and at later time delays, two bands at 1982 and 1921 cm^{-1} are observed. These bands (1982 and 1921 cm^{-1}) are assigned to the silane species $CpMn(CO)_2(HSiBu_3)$. The formation rate of $CpMn(CO)_2(HSiBu_3)$ is found to be bi-

exponential, with a determined growth rate of τ =4.0 ±0.4 ns and 90 ±20 ns (Figure 2.17). The decay of the CpMn($BuHSiBu_2$) species is also on a similar timescale to the slower component (*ca.* 100 (±10) ns, Figure 2.17). Thus, it can be concluded that the final silane species $CpMn(CO)_2(HSiBu_3)$ is formed both from $^3CpMn(CO)_2$ and the butyl-bound species $CpMn(CO)_2(BuHSiBu_2)$, as shown in Figure 2.17. The silane species is observed to be stable and shows no decay on the experimental timescale (up to ~1 ms).



(a)



(b)

Figure 2.17 *Kinetic traces of (a) bands at 2006 and 1900 cm^{-1} corresponding to $^3CpMn(CO)_2$ and $CpMn(CO)_2(BuHSiBu_2)$, respectively, and (b) decay of $CpMn(CO)_2(BuHSiBu_2)$ and formation of the band at 1921 cm^{-1}: $CpMn(CO)_2(HSiBu_3)$, in PFMCH in the presence of 0.25 M $HSiBu_3$.*

The reaction proceeds with a similar mechanism to that described before in heptane and that reported in neat triethylsilane.[73,80] However, the kinetic analysis shows that the lifetime of $^3CpMn(CO)_2$ is prolonged to *ca.* 4 ns compared to 100 ps in either neat triethylsilane or in heptane. Also, in this solvent the ligand exchange

rate between $CpMn(CO)_2(BuHSiBu_3)$ and $CpMn(CO)_2(HSiBu_3)$ is *ca.* 100 ns, similar to that reported in PFMCH doped with $HSiEt_3$ (*ca.* 145 ns) and in neat $HSiEt_3$ (*ca.* 177 ns), which is significantly faster compared to that measured in heptane (*ca.* 4.5 μs).

Following this, TRIR experiments were conducted on $CpMn(CO)_3$ in PFMCH doped with $HGeBu_3$. The spectra are shown in Figure 2.18.

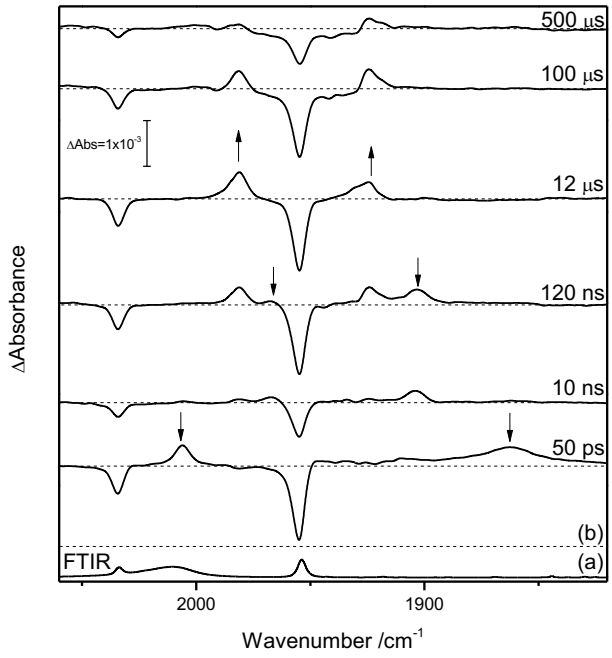


Figure 2.18 *(a) FTIR spectrum and (b) TRIR spectra obtained following photolysis (266 nm) of $CpMn(CO)_3$ in PFMCH doped with 0.078 M $HGeBu_3$.*

In this experiment, the lifetime of the $^3CpMn(CO)_3$ species was determined to be 3.7 (±0.7) ns. Decay of this species results in the growth of the bands at *ca.* 1966 and 1904 cm^{-1} (5.3 ±3.0 ns), which are assigned to the alkyl-bound species $CpMn(CO)_2(BuHGeBu_2)$, and the initial growth of the bands at 1981 and 1924 cm^{-1} (3.5 ±1.8 ns), which are assigned to the activated species $CpMn(CO)_2(HGeBu_3)$. However, unlike the experiments described above, the initial formation of the $CpMn(CO)_2(BuHGeBu_2)$ species upon UV photolysis is not apparent in the early time delays of the TRIR spectra, perhaps due to the low concentration of $HGeBu_3$ (0.078 M) compared to $HSiBu_3$ (0.25M). The formation rate of

$CpMn(CO)_2(HGeBu_3)$ (133 ±15 ns) is similar to the decay of $CpMn(CO)_2(BuHGeBu_2)$ (118 ±21 ns).

Finally, the presence of $HSnBu_3$ on the ligand exchange of $CpMn(CO)_3$ in PFMCH was investigated. The spectra are shown in Figure 2.19.

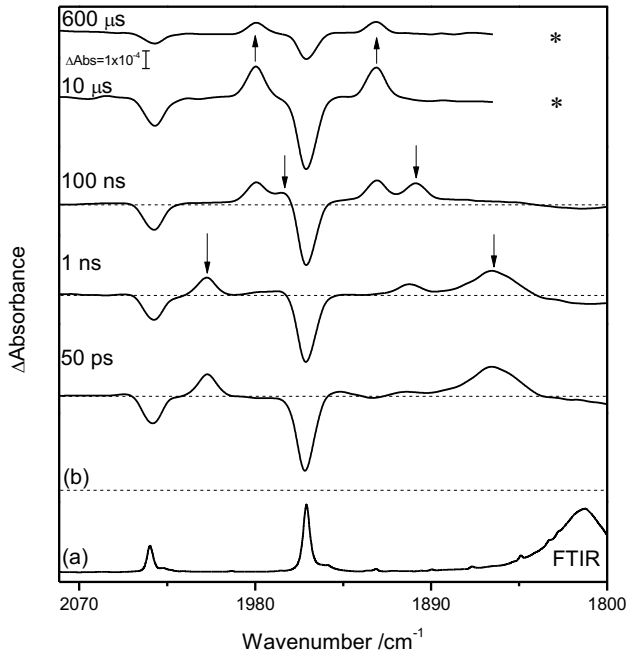


Figure 2.19 *(a) FTIR spectrum and (b) TRIR spectra obtained following photolysis (266 nm) of $CpMn(CO)_3$ in PFMCH doped with 0.17M $HSnBu_3$. * indicates region obscured by noise created by shockwave at later time delays.*

Similar to experiments with $HSiBu_3$ and $HGeBu_3$, the parent bands bleach instantly upon UV photolysis, along with the formation of $^3CpMn(CO)_2$ (2004 and 1859 cm^{-1}). Similar to $HGeBu_3$, the early formation of the alkyl-bound species $CpMn(CO)_2(BuHSnBu_2)$ is not apparent and only a weak broad band at *ca.* 1901 cm^{-1} was observed. And then two bands at *ca.* 1965 and 1899 cm^{-1} are formed, and are assigned to the alkyl-bound species $CpMn(CO)_2(BuHSnBu_2)$. The formation of the activated species $CpMn(CO)_2(HSnBu_3)$ was also observed at 1980 and 1917 cm^{-1}. The former formation of the band at 1901 cm^{-1} (there is also a band at *ca.* 1970 cm^{-1} of very weak intensity) before the formation of the bands at 1965 and 1899 cm^{-1} raises the question as whether there is a set of bands at higher

wavenumber before the formation of the alkyl-bound species. Although previous work[80] has suggested that the red-shift of ν(CO) has not been observed for $CpMn(CO)_3$ while has been observed for $CpRe(CO)_3$ in PFMCH,[80] it is still possible that before the formation of $CpMn(CO)_2(BuHSnBu_2)$, another dicarbonyl species might already has been formed. There are many possible candidates, such as the PFMCH species $CpMn(CO)_2$(PFMCH), as the coordination ability of butyl-group is considered to be much better than PFMCH while PFMCH is in vast excess than $HSnBu_3$, thus $CpMn(CO)_2$(PFMCH) is formed first and then converts into the $CpMn(CO)_2(BuHSnBu_2)$ species. This is also supported by previous DFT research on $CpRe(CO)_2$ dicarbonyls, which reveals that the ν(CO) positions of the C-H bound species $CpRe(CO)_2(C_5H_{10})$ (DFT result: 2038, 1988 cm^{-1}, actual ν(CO): 1952, 1887 cm^{-1}) is red-shifted compared to the C-F bound species $CpRe(CO)_2(C_7F_{14})$ (DFT result: 2044, 1991 cm^{-1}, actual ν(CO): 1958, 1889 cm^{-1}) by *ca.* 3~6 cm^{-1}.[80] However, other possibilities cannot be excluded, such as the unsaturated singlet dicarbonyl species $CpMn(CO)_2$.

Similar reaction kinetics have been observed to the experiments with $HSiBu_3$ and $HGeBu_3$. The lifetime of $^3CpMn(CO)_2$ is 4.4 (± 0.2) ns, which decays at a similar rate to the formation rate of $CpMn(CO)_2(BuHSnBu_2)$ (4.3 ±0.7 ns), as well as the initial formation of the activated species $CpMn(CO)_2(HSnBu_3)$ (4.4 ±0.3 ns, 200 ±12 ns). The second component of the growth of $CpMn(CO)_2(HSnBu_3)$ (200 ±12 ns) fits the decay of $CpMn(CO)_2(BuHSnBu_2)$ (198 ±6 ns). This rate is similar to the ligand exchange reaction in neat $HSiEt_3$ and in PFMCH doped with $HSiBu_3$ and $HGeBu_3$.

From the results above, it can be concluded that for all three dopants ($HSiBu_3$, $HGeBu_3$, $HSnBu_3$), the reaction mechanism and kinetics in PFMCH are similar. The proposed mechanism is shown in Figure 2.20.

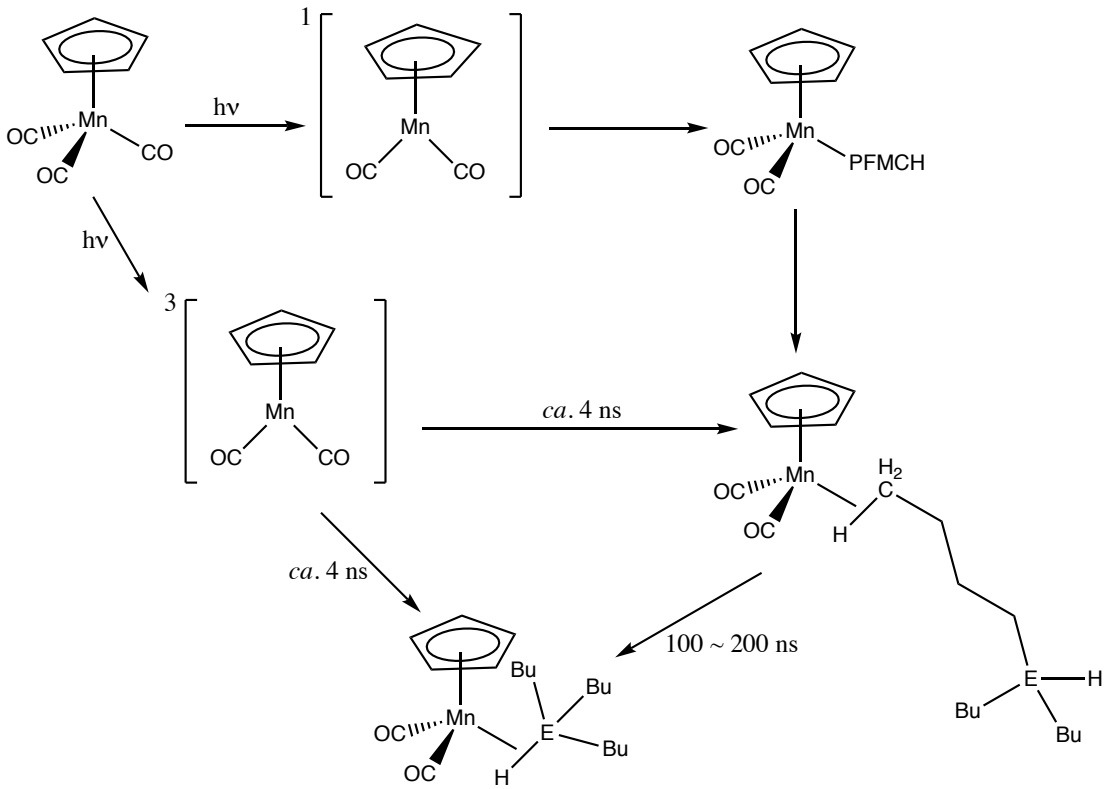


Figure 2.20 *Proposed reaction mechanism of $CpMn(CO)_3$ in PFMCH in the presence of $HEBu_3$ (E: Si, Ge, Sn).*

The lifetime of $^3CpMn(CO)_2$ is *ca.* 4 ns in PFMCH regardless of dopant. This lifetime is prolonged compared with that observed in *n*-heptane and in neat $HSiEt_3$ (*ca.* 100 ps). Thus, it can be concluded that the lifetime of $^3CpMn(CO)_2$ is affected by the solvent, and as PFMCH is a weak-coordinating solvent, it may stabilize $^3CpMn(CO)_2$ and slow down the rate of spin crossover. For the ligand exchange reaction between $CpMn(CO)_2(BuHEBu_2)$ and $CpMn(CO)_2(HEBu_3)$ (E: Si, Ge, Sn) in PFMCH, the rate at *ca.* 100~200 ns is comparable to the reported ligand exchange rates in neat $HSiEt_3$ (*ca.* 177 ns)[73] and in PFMCH doped with $HSiEt_3$ (*ca*. 150 ns).[80] The ν(CO) band positions of the activated species $CpMn(CO)_2(HEBu_3)$ and ligand exchange rates are summarized and compared in Table 2.6.

Table 2.6 *Summary of the ν(CO) band positions obtained from the TRIR spectra for specific species and the ligand exchange rates of the activated species $CpMn(CO)_2(HEBu_3)$ (E: Si, Ge, Sn) in PFMCH with different dopant concentrations.*

Species	ν(CO) /cm^{-1}	Dopant concentration /M	Ligand exchange rate /ns
$CpMn(CO)_2(HSiBu_3)$	1981, 1922	0.25	110 ± 4
$CpMn(CO)_2(HGeBu_3)$	1981, 1924	0.078	126 ± 18
$CpMn(CO)_2(HSnBu_3)$	1980, 1917	0.17	199 ± 9

For all three dopants, consistent with our results in heptane discussed before, the interaction for all three dopants with the Mn centre is considered to be the non-classical 3-c-2-e interaction. Different to reactions in heptane, the ligand exchange lifetime shows no apparent difference when changing the dopants. However, different experiments may bring a system error. For instance, the photoreaction of $CpMn(CO)_3$ in neat $HSiEt_3$ has been both reported by Yang *et al.*[73] and Murphy,[80] and the ligand exchange rate is slightly different. According to Yang, the lifetime is *ca.* 177 ns, while by Murphy it is *ca.* 150 ns in neat $HSiEt_3$ or in PFMCH doped with 0.5 M $HSiEt_3$. The rate would be expected to be also related to the concentration of dopant and $CpMn(CO)_3$, and this could be investigated in future research.

Based on the results obtained, and previous research it is proposed that the ligand exchange reaction between C-H and Si-H is dissociative, and it is also proposed that the ligand rearrangement is dissociative while within the same silane molecule in PFMCH, *i.e.* in PFMCH, for $CpMn(CO)_2(RHER_2)$ (E: Si, Ge, Sn), the HER_3 ligand is first dissociated and then the unsaturated $CpMn(CO)_2$ is coordinated to the Si-H moiety of the same HER_3 molecule, rather than coordinated to another HER_3 molecule, as shown in Figure 2.21.

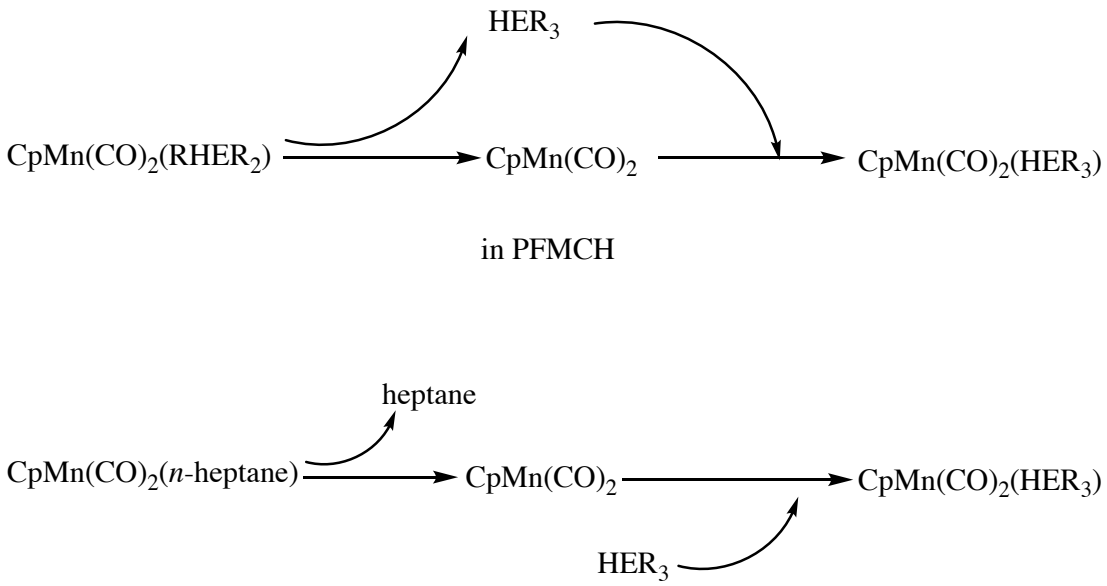


Figure 2.21 *Proposed reaction scheme of $CpMn(CO)_3$ with HER_3 (E: Si, Ge, Sn) in different solvents.*

This assumption is rationalized by the similar ligand exchange rate between C-H and E-H in neat triethylsilane (where ligand-exchange within same molecule or between different molecules may be identical) and in PFMCH. In heptane, as the heptane molecule is in vast excess compared to the butyl group of $HEBu_3$, and also, the coordination ability of heptane is much stronger than PFMCH, thus $^1CpMn(CO)_2$ coordinates to heptane rather than the butyl group of $HEBu_3$. $CpMn(CO)_2$(*n*-heptane) first dissociates the heptane molecule, and then coordinates to another HER_3 molecule, herein the ligand exchange rate is significantly prolonged to several μs compared to *ca.* 100-200 ns in PFMCH. Therefore, the ligand exchange rate is expected to be dependent on the concentration of $HEBu_3$ in heptane, and this is consistent with the results discussed.

However, the reason for the faster exchange rate observed with $HSiBu_3$ (0.25 M) in PFMCH (*ca.* 100 ns) compared to in neat $HSiEt_3$ (*ca.* 177 ns) is still uncertain and will need further investigation.

2.2.3 TRIR Studies of E-H (E: Si, Ge, Sn) Bond Coordination to $Cp'Mn(CO)_3$ in *n*-heptane

As discussed before, the extent of the E-H bond activation depends on how intense the π-backbonding from the metal centre to the E-H (E: Si, Ge, Sn) σ^* orbital is. Thus, increasing the electron density on the metal centre can facilitate the π-backbonding interaction between M and E-H which may lead to more complete cleavage of the E-H bond.

Therefore, we have conducted TRIR experiments on $Cp'Mn(CO)_3$, in which the Cp ring is substituted by an electron rich methyl group. This increase in electron density is in an attempt to increase the π-backbonding and obtain more activated products. The results from these experiments are discussed below.

The TRIR spectra obtained following photolysis of $Cp'Mn(CO)_3$ in heptane doped with $HSiBu_3$ (0.25 M) are shown in Figure 2.22.

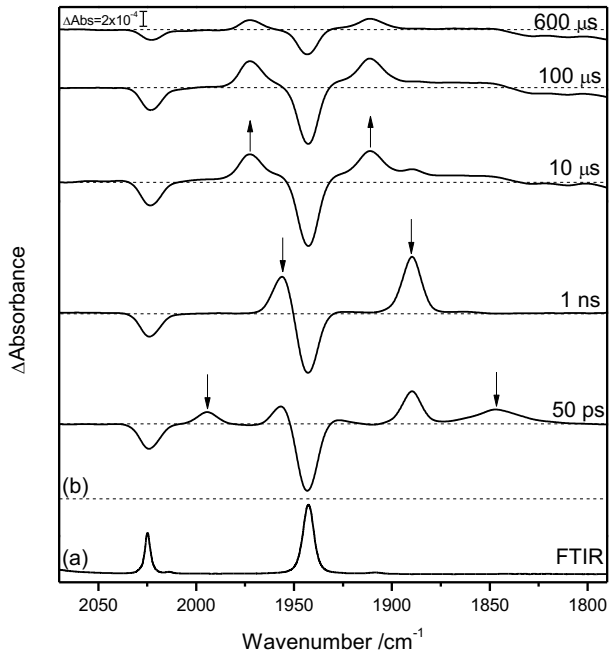
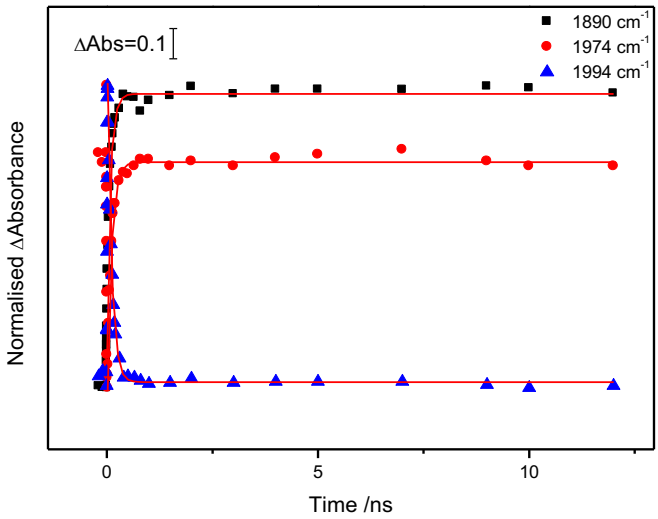


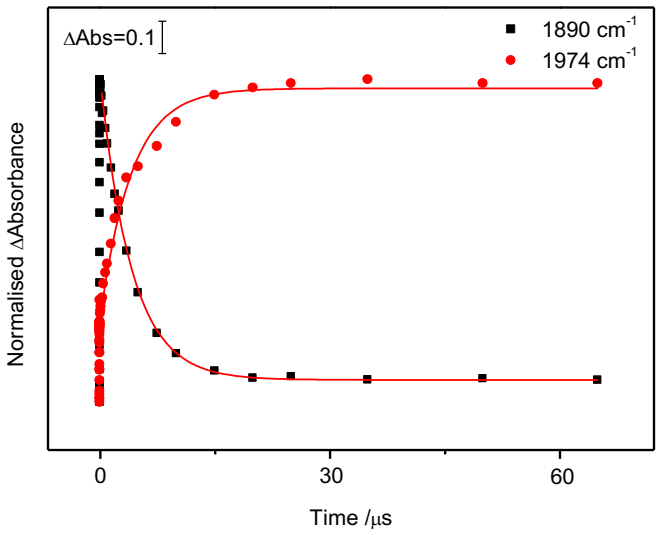
Figure 2.22 *(a) FTIR spectrum and (b) TRIR spectra obtained following photolysis (266 nm) of $Cp'Mn(CO)_3$ in heptane doped with 0.25 M $HSiBu_3$.*

Similar to $CpMn(CO)_3$ in *n*-heptane, upon UV photolysis, along with the bleach of the parent bands (2025, 1943 cm^{-1}), four ν(CO) bands at 1994, 1955, 1890 and 1846 cm^{-1} are formed. Considering the increase of electron density on the Mn centre by introducing an inductive methyl group onto the Cp ring, it is expected that the ν(CO) positions of the analogue species should be slightly red-shifted compared to $CpMn(CO)_3$. From this, the bands at 1994 and 1846 cm^{-1} are assigned as the triplet dicarbonyl species $^3Cp'Mn(CO)_2$. The lifetime of $^3Cp'Mn(CO)_2$ is 105 (±6) ps (Figure 2.23), similar to the lifetime of $^3CpMn(CO)_2$ (*ca.* 100 ps) in *n*-heptane as discussed in Section 2.2.1. Similarly, the bands at 1955 and 1890 cm^{-1} are assigned as the heptane species $Cp'Mn(CO)_2$(heptane). At later time delays, two bands at 1974 and 1912 cm^{-1} are observed, and assigned as the silane species $Cp'Mn(CO)_2(HSiBu_3)$. It was observed that all the ν(CO) positions compared to $CpMn(CO)_3$ are slightly red-shifted, reflecting the increasing electron density on the Mn centre.

However, what we found interesting is that, although one electron rich methyl group has been substituted into the Cp ring, the kinetics are very similar to $CpMn(CO)_3$. The decay of $^3Cp'Mn(CO)_2$ is accompanied by growth of the heptane species $Cp'Mn(CO)_2$(heptane) and part of the activated species $Cp'Mn(CO)_2(HSiBu_3)$ (105 ±5 ps, 4.1 ±0.2 μs, Figure 2.23), similar to $CpMn(CO)_2(HSiBu_3)$ at same silane concentration (103 ±10 ps, 4.5 ±0.5 μs). Also, the ligand exchange rate between $Cp'Mn(CO)_2$(*n*-heptane) and $Cp'Mn(CO)_2(HSiBu_3)$ has been observed to be *ca.* 4.1 (±0.1) μs (Figure 2.23), similar to $CpMn(CO)_3$ (*ca.* 4.5 μs). The kinetics are shown in Figure 2.23.



(a)



(b)

Figure 2.23 *TRIR kinetic traces of (a) bands at 1994, 1974 and 1890 cm^{-1} corresponding to ^{3}Cp'Mn(CO)$_2$, Cp'Mn(CO)$_2$(HSiBu$_3$) and Cp'Mn(CO)$_2$(n-heptane), respectively, and (b) decay of species Cp'Mn(CO)$_2$(n-heptane) and formation of Cp'Mn(CO)$_2$(HSiBu$_3$), in heptane in the presence of HSiBu$_3$.*

From the kinetics, it can be concluded that a similar reaction mechanism to CpMn(CO)$_3$ in heptane has been observed for Cp'Mn(CO)$_3$. Upon UV photolysis, ^{1}Cp'Mn(CO)$_2$ and ^{3}Cp'Mn(CO)$_2$ are generated, and ^{1}Cp'Mn(CO)$_2$ is not stable which quickly coordinates to the solvent to form Cp'Mn(CO)$_2$(*n*-heptane) within a few ps.

Lifetime of the $^3Cp'Mn(CO)_2$ species is *ca.* 100 ps, similar to $^3CpMn(CO)_2$ in heptane. $^3Cp'Mn(CO)_2$ then decays and undergoes spin crossover to form both $Cp'Mn(CO)_2$(*n*-heptane) and the activated species $Cp'Mn(CO)_2(HSiBu_3)$. The formation rate of $Cp'Mn(CO)_2(HSiBu_3)$ is bi-exponential (105 ±5 ps, 4.1 ±0.2 μs), for which t_1 fits the decay of $^3Cp'Mn(CO)_2$, while t_2 fits the decay of the heptane species $Cp'Mn(CO)_2$(*n*-heptane). Following on from these results, similar TRIR studies with $HGeBu_3$ were also conducted.

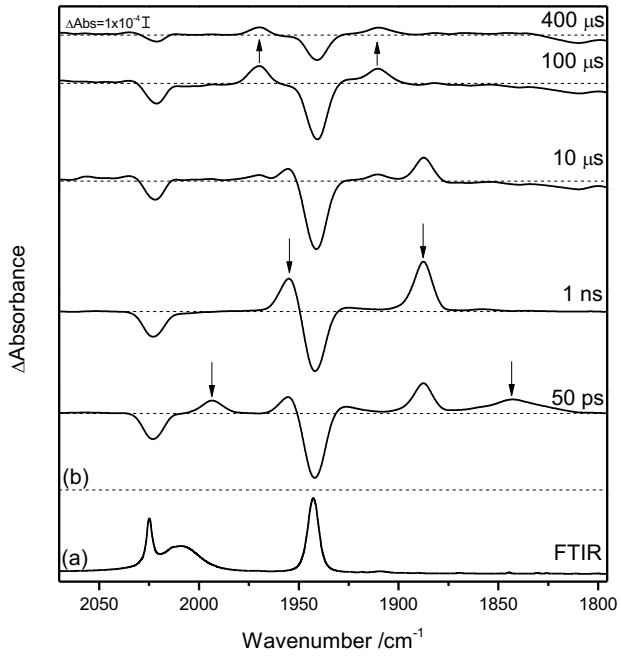


Figure 2.24 *(a) FTIR spectrum and (b) TRIR spectra obtained following photolysis (266 nm) of $Cp'Mn(CO)_3$ in heptane doped with 0.078 M $HGeBu_3$.*

Similar to the previous experiment with $HSiBu_3$, $^3Cp'Mn(CO)_2$ (1994, 1843 cm^{-1}) and $Cp'Mn(CO)_2$(*n*-heptane) (1954, 1888 cm^{-1}) are formed after photolysis. The activated species $Cp'Mn(CO)_2(HGeBu_3)$ were also observed (1969, 1911 cm^{-1}).

Kinetic analysis suggests that the reaction processes are similar to the experiment with $HSiBu_3$. Both $^1Cp'Mn(CO)_2$ and $^3Cp'Mn(CO)_2$ are formed after UV irradiation, while the species $^1Cp'Mn(CO)_2$ coordinates to the solvent to form $Cp'Mn(CO)_2$(*n*-heptane) in a few ps. The lifetime of $^3Cp'Mn(CO)_2$ was determined to be 106 (±9) ps, which on decay undergoes spin crossover to form $Cp'Mn(CO)_2$(*n*-heptane) (105

±12 ps) and $Cp'Mn(CO)_2(HGeBu_3)$ (99 ±6 ps, 12.8 ±1.2 μs). The second component of the growth of $Cp'Mn(CO)_2(HGeBu_3)$ matches the decay of $Cp'Mn(CO)_2$(*n*-heptane) (13.8 ±0.4 μs), which indicates the formation of $Cp'Mn(CO)_2(HGeBu_3)$ from $Cp'Mn(CO)_2$(*n*-heptane).

The ligand exchange rate between $Cp'Mn(CO)_2$(*n*-heptane) and $Cp'Mn(CO)_2(HGeBu_3)$ (*ca.* 13 μs) is slower than the former experiment with $HSiBu_3$ (*ca.* 4 μs). However, the concentration of the dopants ($HSiBu_3$: 0.25 M; $HGeBu_3$: 0.078 M) should be taken into consideration. The results suggest that the reaction mechanism of $Cp'Mn(CO)_3$ is similar to $CpMn(CO)_3$, and thus the ligand rearrangement rate is related to concentration of the dopants. Finally, to complete the scene, TRIR experiments with $HSnBu_3$ as a dopant have also been conducted, as shown in Figure 2.25.

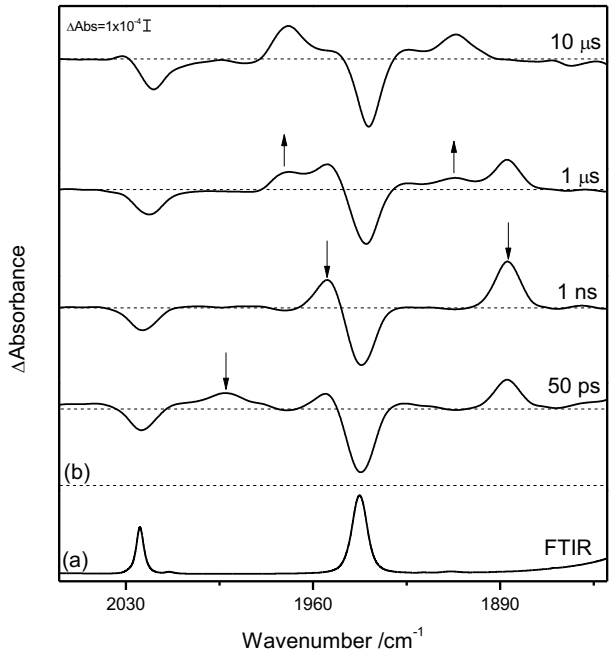


Figure 2.25 *(a) FTIR spectrum and (b) TRIR spectra obtained following photolysis (266 nm) of $Cp'Mn(CO)_3$ in heptane doped with 0.17 M $HSnBu_3$.*

Similar to the experiments with $HSiBu_3$ and $HGeBu_3$, upon UV photolysis $^3Cp'Mn(CO)_2$ and $Cp'Mn(CO)_2$(*n*-heptane) are formed. The stannane species $Cp'Mn(CO)_2(HSnBu_3)$ is also observed at *ca.* 1969 and 1906 cm^{-1}.

The ligand exchange rate between Cp'Mn(CO)$_2$(*n*-heptane) and Cp'Mn(CO)$_2$(HSnBu$_3$) is found to be *ca.* 3.4 μs. It can be concluded that the reaction mechanism for Cp'Mn(CO)$_3$ in heptane with HSiBu$_3$, HGeBu$_3$ and HSnBu$_3$ are very similar to CpMn(CO)$_3$. The ν(CO) positions of the corresponding species compared to the CpMn(CO)$_3$ analogues have been red-shifted, as shown in Table 2.7.

Table 2.7 *Summary of ν(CO) band positions of (η^5-$C_5H_{5-n}Me_n$)Mn(CO)$_3$ and (η^5-$C_5H_{5-n}Me_n$)Mn(CO)$_2$L species (n: 0, 1).*

Species	ν(CO) /cm^{-1}
Cp'Mn(CO)$_3$	2025, 1943
CpMn(CO)$_3$	2028, 1947
^{3}Cp'Mn(CO)$_2$	1994, 1844
^{3}CpMn(CO)$_2$	2000, 1848
Cp'Mn(CO)$_2$(*n*-heptane)	1954, 1889
CpMn(CO)$_2$(*n*-heptane)	1961, 1894
Cp'Mn(CO)$_2$(HSiBu$_3$)	1974, 1912
CpMn(CO)$_2$(HSiBu$_3$)	1976, 1915
Cp'Mn(CO)$_2$(HGeBu$_3$)	1969, 1911
CpMn(CO)$_2$(HGeBu$_3$)	1975, 1918
Cp'Mn(CO)$_2$(HSnBu$_3$)	1969, 1906
CpMn(CO)$_2$(HSnBu$_3$)	1976, 1912

For the activated species Cp'Mn(CO)$_2$(HEBu$_3$) (E: Si, Ge, Sn), the ν(CO) positions are red-shifted compared to the parent bands, indicating that the predominate interaction between Mn and the E-H bonds in Cp'Mn(CO)$_2$(HEBu$_3$) is still a σ-donation, similar to CpMn(CO)$_2$(HEBu$_3$) (E: Si, Ge, Sn). When comparing the Δν(CO) positions of the activated species Cp'Mn(CO)$_2$(HEBu$_3$) to the parent complex Cp'Mn(CO)$_3$, it can be noticed that the differences Δν(CO) are similar to the analogues of CpMn(CO)$_3$, which indicates that in Cp'Mn(CO)$_2$(HEBu$_3$), the π-back-donation from Mn to E-H has not been apparently increased by the substitution of the methyl group. Therefore, in Cp'Mn(CO)$_2$(HEBu$_3$) the coordination mode is assumed to be 3-c-2-e, similar to CpMn(CO)$_2$(HEBu$_3$).

For the kinetics, the lifetime of $^3Cp'Mn(CO)_2$ is similar to $^3CpMn(CO)_2$ (*ca.* 100 ps). The ligand exchange rate between $Cp'Mn(CO)_2$(*n*-heptane) and $Cp'Mn(CO)_2(HEBu_3)$ is also observed to be related to the types of dopant. For $Cp'Mn(CO)_3$, the ligand exchange rate is *ca.* 4.1 μs with the $HSiBu_3$ concentration of 0.25 M, similar to that of $CpMn(CO)_3$ (*ca.* 4.5 μs).

However, what is interesting is that the ligand exchange rates for $Cp'Mn(CO)_2(HGeBu_3)$ and $Cp'Mn(CO)_2(HSnBu_3)$ are slower than the $CpMn(CO)_2(HEBu_3)$ analogues. The ligand exchange rate for $Cp'Mn(CO)_2(HGeBu_3)$ is *ca.* 13 μs with a $HGeBu_3$ concentration of 0.078 M. In our previous discussion on $CpMn(CO)_3$, the rate of exchange with a $HGeBu_3$ concentration of 0.05 M is *ca.* 7.9 μs, while the lifetime at a concentration of 0.1 M is *ca.* 4.1 μs. From this it would be expected that for a $HGeBu_3$ concentration of 0.078 M, the lifetime of exchange should fall between 4.1 and 7.9 μs, thus the ligand exchange rate with this dopant for the $Cp'Mn(CO)_3$ species appears to be much slower than the $CpMn(CO)_3$ species. The ligand exchange rate between C-H/Sn-H for $Cp'Mn(CO)_3$ (*ca.* 3.4 μs) is also slower than the $CpMn(CO)_3$ species (*ca.* 2.2 μs) under the same $HSnBu_3$ concentration of 0.17 M.

The reason for this can be ascribed to the size of both $Cp'Mn(CO)_3$ and the dopants $HEBu_3$ (E: Si, Ge, Sn). As methyl is substituted onto the Cp ring, this increases the size of the complex compared to $CpMn(CO)_3$, and steric factors could be important in the reaction process. As the size of $HEBu_3$ (E: Si, Ge, Sn) increases with the trend Si < Ge < Sn, the influence of the sizes of $HGeBu_3$ and $HSnBu_3$ may be more important compared to $HSiBu_3$. Thus, the larger sizes of both $Cp'Mn(CO)_3$ and $HGeBu_3$ or $HSnBu_3$ could hinder the coordination between the Mn centre and the dopants.

2.2.4 TRIR Studies of E-H (E: Si, Ge, Sn) Bond Coordination to $Cp'Mn(CO)_3$ in PFMCH

TRIR experiments in PFMCH with three dopants $HEBu_3$ (E: Si, Ge, Sn) have also been conducted, and are discussed in the following sections.

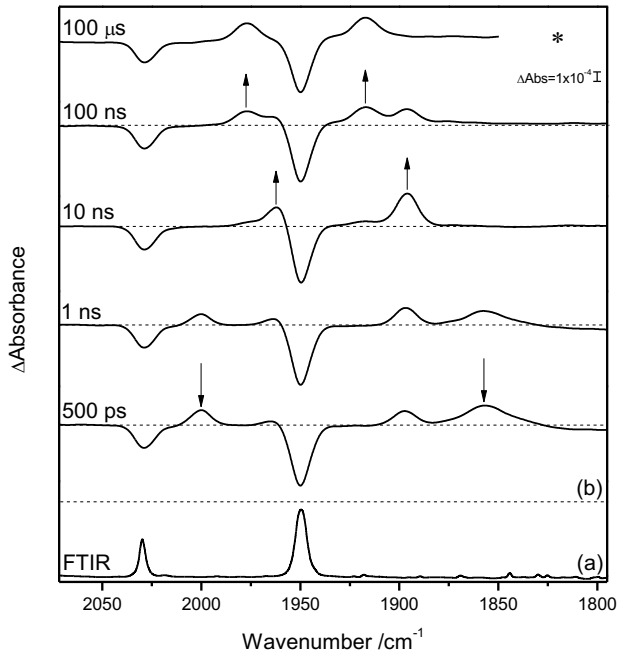
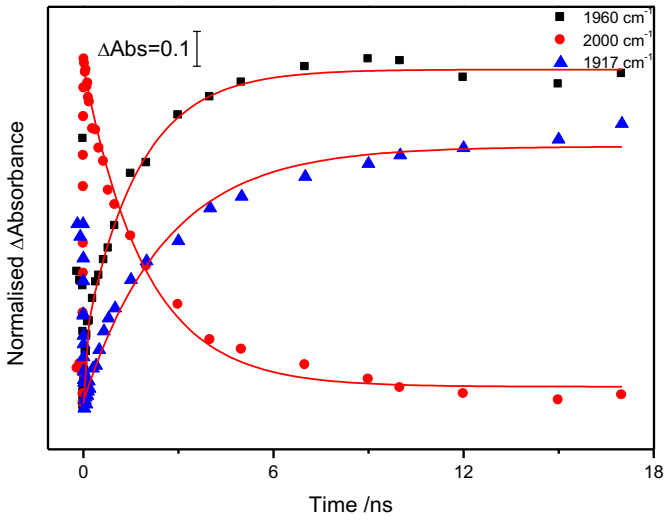


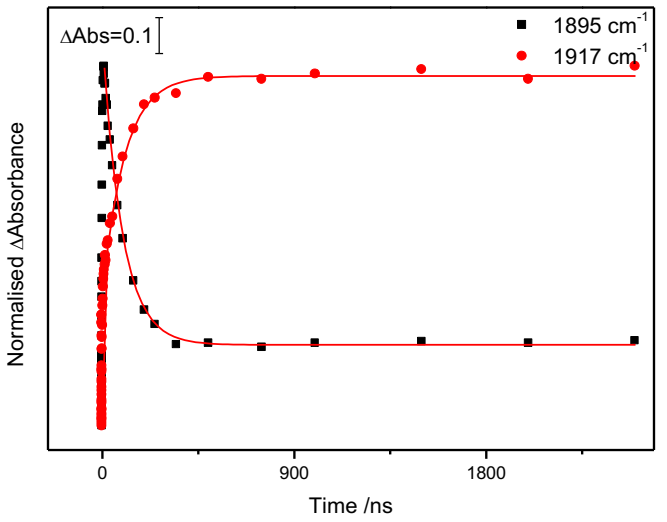
Figure 2.26 *(a) FTIR spectrum and (b) TRIR spectra obtained following photolysis (266 nm) of $Cp'Mn(CO)_3$ in PFMCH doped with 0.25 M $HSiBu_3$. * indicates region obscured by noise created by shockwave at later time delays.*

Similar to $CpMn(CO)_3$ in PFMCH, four bands at *ca.* 2000, 1960, 1895(weak), and 1856 cm^{-1} are formed, along with the bleach of the parent bands upon UV photolysis. The bands at 2000 and 1856 cm^{-1} are assigned to $^3Cp'Mn(CO)_2$, and the bands at 1960 and 1895 cm^{-1} are assigned to the butyl-bound species $Cp'Mn(CO)_2(BuHSiBu_2)$, in comparison with the analogue species in previous work. The silane species $Cp'Mn(CO)_2(HSiBu_3)$ was also observed at *ca.* 1977 and 1917 cm^{-1}.

Kinetic analysis suggests similar reaction mechanism to $CpMn(CO)_3$ in PFMCH (Figure 2.27).



(a)



(b)

Figure 2.27. *TRIR kinetic traces of (a) bands at 2000, 1917 and 1960 cm^{-1} corresponding to ^{3}Cp'Mn(CO)$_2$, Cp'Mn(CO)$_2$(HSiBu$_3$) and Cp'Mn(CO)$_2$(BuHSiBu$_2$), respectively, and (b) decay of the band at 1895 cm^{-1}: Cp'Mn(CO)$_2$(BuHSiBu$_2$) and formation of Cp'Mn(CO)$_2$(HSiBu$_3$), in PFMCH in the presence of HSiBu$_3$.*

Upon UV irradiation, ^{1}Cp'Mn(CO)$_2$ and ^{3}Cp'Mn(CO)$_2$ are formed, and ^{1}Cp'Mn(CO)$_2$ is not stable and coordinates to the butyl group of HSiBu$_3$ in *ca.* 63 ps. However, when compared to the same species in *n*-heptane as discussed before, which coordinates to the solvent within a few ps, the non-coordinating solvent PFMCH

prolongs the lifetime of $^1Cp'Mn(CO)_2$. The lifetime of $^3Cp'Mn(CO)_2$ (*ca.* 2 ns) is much longer than the same species in heptane (*ca.* 100 ps), while is shorter than $^3CpMn(CO)_2$ in PFMCH (*ca.* 4 ns) as discussed before in Section 2.2.2.

Similar to previous studies, $^3Cp'Mn(CO)_2$ decays and spin crossover occurs to form the $Cp'Mn(CO)_2(BuHSiBu_2)$ species and the silane species $Cp'Mn(CO)_2(HSiBu_3)$. The formation of $Cp'Mn(CO)_2(HSiBu_3)$ is bi-exponential and fits the decay of $^3Cp'Mn(CO)_2$ (*ca.* 2 ns) and $Cp'(CO)_2(BuHSiBu_2)$ (*ca.* 98 ns). The ligand exchange rate between $Cp'Mn(CO)_2(BuHSiBu_2)$ and $Cp'Mn(CO)_2(HSiBu_3)$ (*ca.* 98 ns) is similar to the previous study of $CpMn(CO)_3$ (*ca.* 110 ns).

TRIR with $HGeBu_3$ has also been investigated, as shown in Figure 2.28.

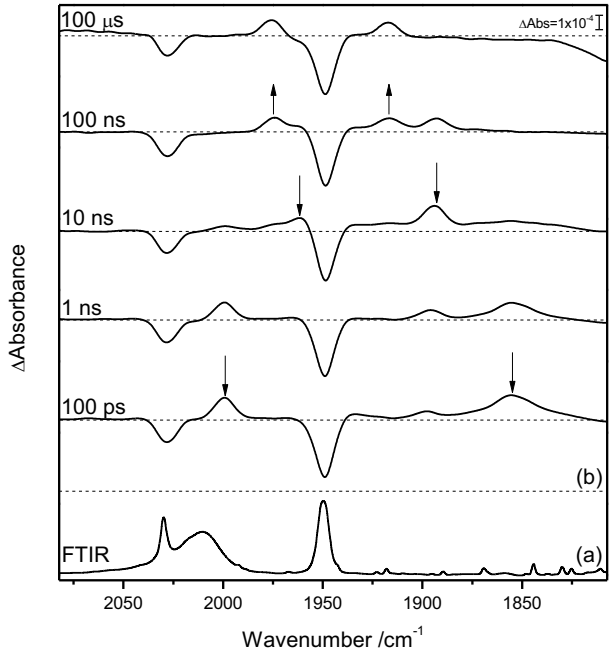


Figure 2.28 *(a) FTIR spectrum and (b) TRIR spectra obtained following photolysis (266 nm) of $Cp'Mn(CO)_3$ in PFMCH doped with 0.078 M $HGeBu_3$.*

Similar to the experiment with $HSiBu_3$, the bands at 1999 and 1856 cm^{-1} are formed and assigned to $^3Cp'Mn(CO)_2$. The bands at 1961 and 1894 cm^{-1} are formed and assigned to $Cp'Mn(CO)_2(BuHGeBu_2)$, and the bands at 1974 and 1916 cm^{-1} are assigned to the $Cp'Mn(CO)_2(HGeBu_3)$ species. Similar to previous studies, before

the formation of the bands at 1894 and 1961 cm^{-1}, there is a band at slightly higher wavenumber at *ca.* 1898 cm^{-1}. Also, this might be other species with weaker coordination such as the PFMCH species $Cp'Mn(CO)_2$(PFMCH), or the unsaturated species $^1Cp'Mn(CO)_2$, as discussed before.

Kinetic analysis has suggested similar reaction mechanism to previous studies. The lifetime of $^3Cp'Mn(CO)_2$ is *ca.* 6.4 (±0.8) ns, which decays and forms $Cp'Mn(CO)_2(BuHGeBu_2)$ (4.9 ± 0.3 ns) and $Cp'Mn(CO)_2(HGeBu_3)$ (4.7 ± 0.6 ns). $Cp'Mn(CO)_2(HGeBu_3)$ is also formed from $Cp'Mn(CO)_2(BuHGeBu_2)$, as its formation rate (113 ± 5 ns) fits the decay of $Cp'Mn(CO)_2(BuHGeBu_2)$ (106 ±4 ns).

TRIR experiments probing the ligand exchange with $HSnBu_3$ as a dopant have also been undertaken, as shown in Figure 2.29.

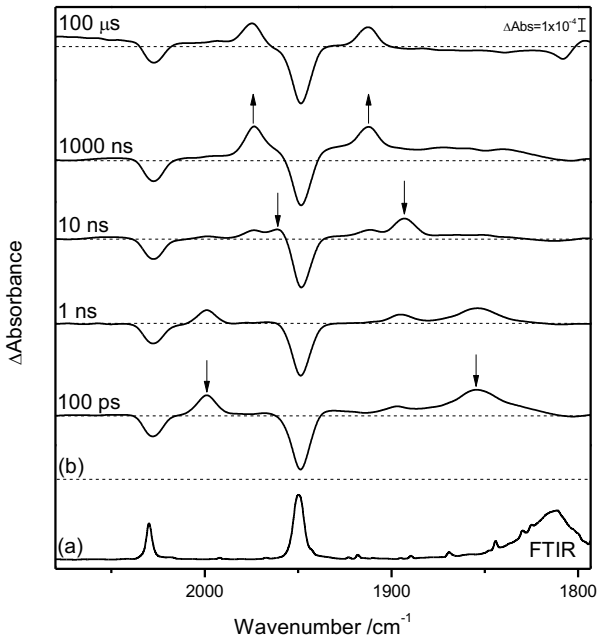


Figure 2.29 *(a) FTIR spectrum and (b) TRIR spectra obtained following photolysis (266 nm) of $Cp'Mn(CO)_3$ in PFMCH doped with 0.068 M $HSnBu_3$.*

The transformation from $^3Cp'Mn(CO)_2$ (1999 and 1854 cm^{-1}, lifetime 3.4 ±0.5 ns) to $Cp'Mn(CO)_2(BuHSnBu_2)$ (1961 and 1893 cm^{-1}, formation rate: 3.1 ±0.2 ns) and $Cp'Mn(CO)_2(HSnBu_3)$ (1974 and 1912 cm^{-1}, formation rate 3.3 ±0.3 ns, 170 ±8 ns)

is observed, and the formation of $Cp'Mn(CO)_2(HSnBu_3)$ also fits the decay of $Cp'Mn(CO)_2(BuHSnBu_2)$ (156 ±5 ns).

Based on the results, it can be concluded that the reaction mechanism of $Cp'Mn(CO)_3$ in PFMCH is very similar to $CpMn(CO)_3$. However, the kinetics suggest that the lifetime of the triplet dicarbonyl $^3Cp'Mn(CO)_2$ is affected by the dopants. The reason for this is unclear. The lifetime of $^3Cp'Mn(CO)_2$ may also be affected by dopant concentration, which may need further investigations.

The rate of ligand exchange between C-H and E-H (E: Si, Ge, Sn), similar to the $CpMn(CO)_3$ analogue species, is also in the range of *ca.* 100~200 ns. Meanwhile, similar to $CpMn(CO)_3$, the ligand exchange rate for Sn-H is slower than Si-H and Ge-H. The reason is attributed to the fact that for both $Cp'Mn(CO)_3$ and $CpMn(CO)_3$, the ligand exchange reaction in PFMCH is a dissociative mechanism, and is occurring within the same $HEBu_3$ molecule. Thus, the steric factors are important. And as $HSnBu_3$ is bulkier than $HSiBu_3$ and $HGeBu_3$, as a result, it may take slightly longer for the ligand exchange reaction to complete.

2.2.5 TRIR Studies of E-H (E: Si, Ge, Sn) Bond Coordination to $CpRe(CO)_3$ in *n*-heptane

The results of $CpMn(CO)_3$ and $Cp'Mn(CO)_3$ indicate that the E-H bond activation by the Mn complexes may not be complete, and only σ-complexes have been generated. Previous research has suggested that unlike $CpMn(CO)_3$, the Si-H bond of $HSiEt_3$ can be fully activated by the electron rich $CpRe(CO)_3$ complex.[73] Thus, we also wish to investigate the E-H bond activation of $HEBu_3$ (E: Si, Ge, Sn) by $CpRe(CO)_3$, as a comparison to the $CpMn(CO)_3$ complexes.

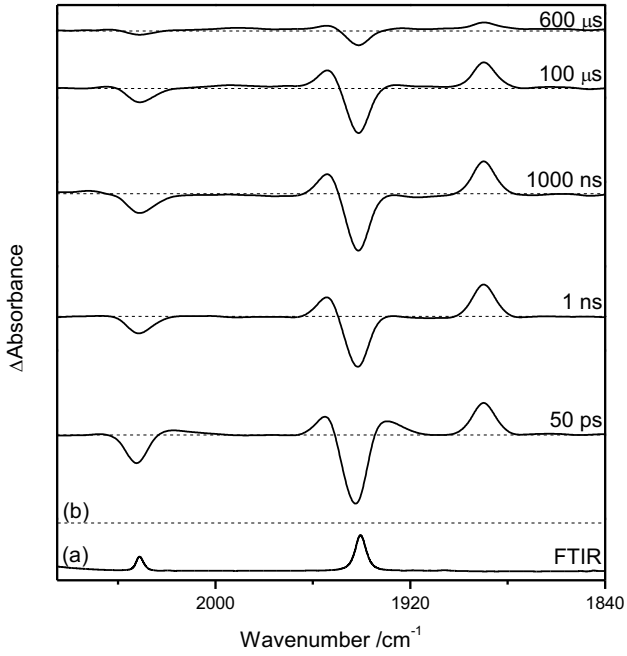


Figure 2.30 *(a) FTIR spectrum and (b) TRIR spectra obtained following photolysis (266 nm) of $CpRe(CO)_3$ in heptane doped with 0.25 M $HSiBu_3$.*

Figure 2.30 shows the TRIR spectra recorded of $CpRe(CO)_3$ in heptane with 0.25 M $HSiBu_3$. It can be observed from the spectra that, UV photolysis results in bleaching of the parent bands at 2031 and 1941 cm^{-1}, and the formation of two bands at *ca.* 1953 and 1890 cm^{-1}, together with two broad features at *ca.* 2019 and 1929 cm^{-1}. For the two broad features, kinetic analysis shows that the decay of these two bands (2019 cm^{-1}: 40 ±5 ps; 1929 cm^{-1}: 45 ± 4 ps) fits the recovery of the parent bands at 2031 (48 ± 3 ps) and 1941 cm^{-1} (30 ± 1 ps). According to previous studies,

the vibrational hot parent complex can be formed upon UV photolysis and decays on the ps-timescale[1,2], which is consistent with the kinetic behaviour observed with the bands at 2019 and 1929 cm^{-1}. Therefore, here we assign these bands to the vibrational hot $CpRe(CO)_3$*.

The bands at 1890 and 1953 cm^{-1} are formed immediately after photolysis, and show no apparent decay on the experimental timescale (up to 1 ms). These ν(CO) positions are in accordance with $CpRe(CO)_2$(*n*-heptane),[3] which is recognized as one of the most stable organometallic-alkane complexes reported up to date.[81] Thus, it can be concluded from the observations that, tributylsilane is incapable of replacing the heptane, at least on the timescale in our experiment, as no silane species has been observed during the experimental timescale.

Experiments utilizing TRIR with $HGeBu_3$ have also been conducted. The spectra are shown in Figure 2.31.

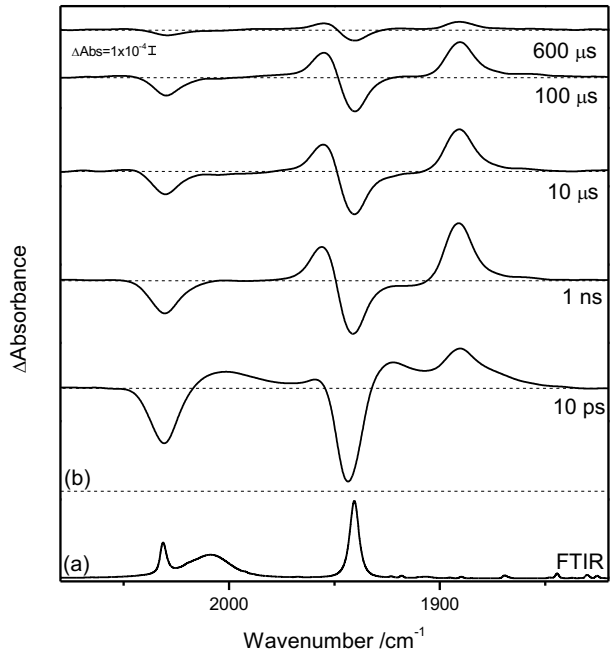


Figure 2.31 *(a) FTIR spectrum and (b) TRIR spectra obtained following photolysis (266 nm) of $CpRe(CO)_3$ in heptane doped with 0.078 M $HGeBu_3$.*

As can be observed from Figure 2.31, upon UV photolysis, along with the depletion of the parent bands, two bands at 1954 and 1889 cm^{-1} are formed instantly and remain until the end of the experiment, and are assigned to the heptane species $CpRe(CO)_2$(*n*-heptane). Also formed are the vibrational hot bands as discussed before. Similar to $HSiBu_3$, no germane species has been observed on the experimental timescale (up to 1 ms).

TRIR experiments with $HSnBu_3$ have also been conducted, and similar results to silane and germane are obtained. Also, no bond activated species were observed in heptane even after raising the concentration of tributylstannane. The spectra are shown in Figure 2.32. However, there is a band at *ca.* 1923 cm^{-1} in later time delays. Another band of similar intensity compared to 1923 cm^{-1} is expected in the region of *ca.* 1990~1970 cm^{-1} if 1923 cm^{-1} is one of the bands of the activated species $CpRe(CO)_2(HSnBu_3)$. However, no such band at this region was observed.

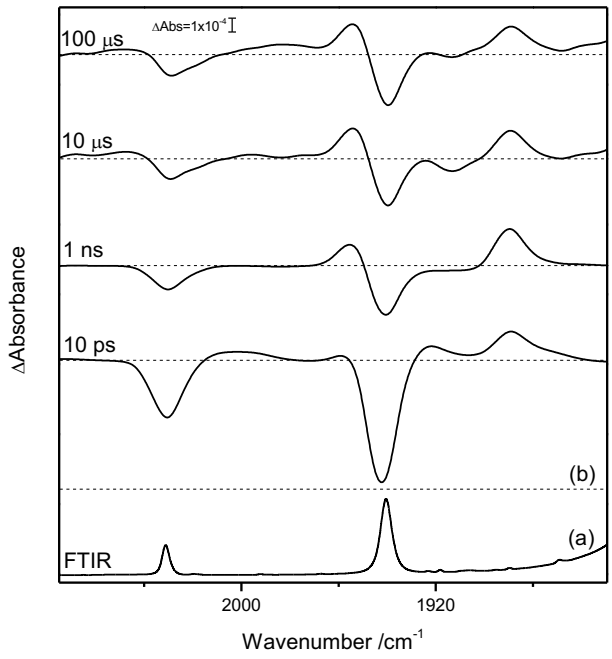


Figure 2.32 *(a) FTIR spectrum and (b) TRIR spectra obtained following photolysis (266 nm) of $CpRe(CO)_3$ in heptane doped with saturated $HSnBu_3$.*

It is interesting to note that although much work has suggested that Re complexes tend to activate the E-H bond (E: Si, Ge, Sn) more completely than the Mn analogue complexes, however, the results we obtain suggests that in alkane solvent, no E-H bond activated species are formed for $CpRe(CO)_3$, at least on the experimental timescale (up to 1 ms). While for $CpMn(CO)_3$, all three activated species have been observed. This is in agreement with work previously done using TRIR of $CpRe(CO)_3$ in *n*-heptane doped with $HSiEt_3$, similarly, no activated species were observed.[80] This was explained by the author that the binding to *n*-heptane is much stronger than the binding to $HSiEt_3$. As has been discussed before, the ligand exchange between C-H and E-H is proposed to be dissociative, thus the reaction not only includes the coordination of the E-H bond to the metal centre, but also involves the dissociation of the C-H bond. Thus, the interaction between C-H and the metal centre could also be important in determining the reaction rate. Ligand exchange may still occur but beyond the experimental timescale (up to 1 ms).

Systematic investigation of the reactivity of organometallic alkane complexes of

group V, VI and VII has been done,[57,82,83,84] and it is found that the stability of these alkane complexes increases along and down the groups. Re alkane complexes are found to be the most stable complexes in the study. $CpRe(CO)_2$(cyclopentane) has been found to be *ca.* 50,000 times more stable than $CpV(CO)_3$(*n*-heptane). Previous research has suggested that $CpRe(CO)_2$(*n*-heptane) is *ca.* 400 times more stable than $CpMn(CO)_2$(*n*-heptane). Thus, here the absence of the activated species for $CpRe(CO)_3$ is attributed to the strong interaction with heptane.

2.2.6 TRIR Studies of E-H (E: Si, Ge, Sn) Bond Coordination to $CpRe(CO)_3$ in PFMCH

Considering the strong coordination ability of heptane which may have caused the unsuccessful coordination of Si, Ge or Sn, PFMCH was chosen as a solvent in an attempt to observe the activated species.

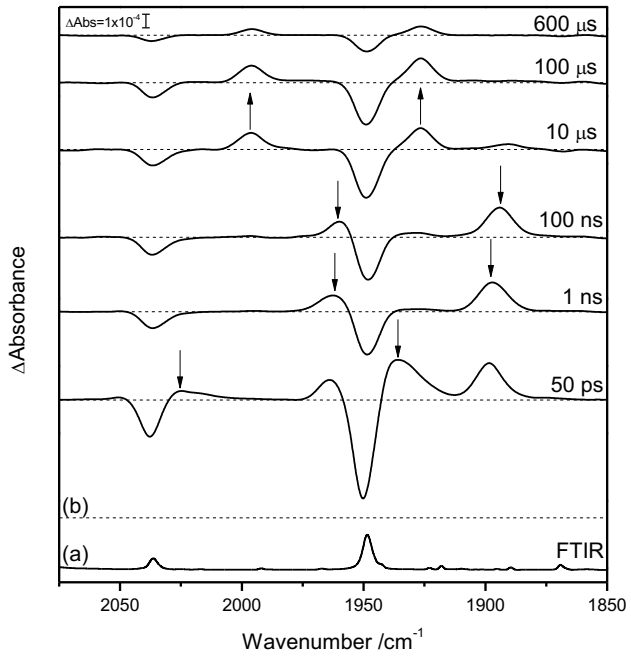


Figure 2.33 *(a) FTIR spectrum and (b) TRIR spectra obtained following photolysis (266 nm) of $CpRe(CO)_3$ in PFMCH doped with 0.25 M $HSiBu_3$.*

The TRIR spectra recorded for this experiment are shown in Figure 2.33. Similar to the reaction in heptane, upon UV photolysis, the vibrational hot $CpRe(CO)_3$* species are formed together with two bands at 1965 and 1898 cm^{-1}. However, on the ns-timescale it shows a significant difference compared to the reaction in *n*-heptane. The two bands at 1965 and 1898 cm^{-1} decay with the growth of another set of bands to lower wavenumber at 1960 and 1894 cm^{-1}.

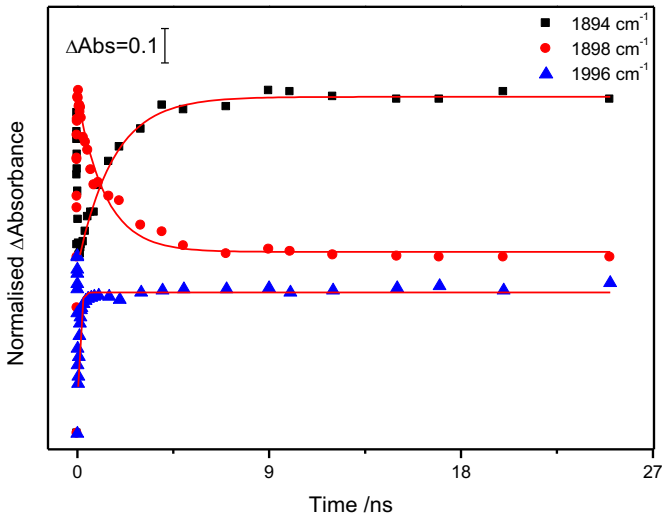


Figure 2.34 *TRIR kinetic traces of different species observed following photolysis of $CpRe(CO)_3$ in PFMCH in the presence of $HSiBu_3$. 1996 cm^{-1}: $CpRe(HSiBu_3)$; 1898 cm^{-1}: the first dicarbonyl species; 1894 cm^{-1}: the second dicarbonyl species.*

This interchange between two dicarbonyls has also been observed in our research group previously,[80] using TRIR to investigate the photo-induced reactions of $CpRe(CO)_3$ in neat PFMCH and in PFMCH doped with 0.5 M $HSiEt_3$. The coordination ability of the butyl group of $HSiBu_3$ is much stronger than PFMCH, thus the bands at lower wavenumber, 1960 and 1894 cm^{-1} are assigned to the butyl-bound species $CpRe(CO)_2(BuHSiBu_2)$, which occur at similar positions to $CpRe(CO)_2(EtHSiEt_2)$ in PFMCH (1958, 1889 cm^{-1}), according to our previous research. While for the short-lived first dicarbonyl species with ν(CO) bands at 1965 and 1898 cm^{-1}, many assumptions have been proposed:[80]

1. The first transient is the $CpRe(CO)_2Ar$ species. The $CpRe(CO)_2Ar$ species has been observed in photolysis of $CpRe(CO)_3$ in scAr (supercritical Ar).[87] However, considering the presence of CO in the system, as well as the vast excess of PFMCH with similar weak coordination ability as demonstrated by previous matrix studies,[85] the formation of an argon species $CpRe(CO)_2Ar$ in PFMCH with a lifetime of *ca.* 1.5 ns is not a likely possibility.

2. Another possibility is that the first transient is a coordinatively unsaturated

species, $CpRe(CO)_2$. The weak coordination of PFMCH may stabilize the uncoordinated 16 electron dicarbonyl species $CpRe(CO)_2$, which is normally solvated in alkane solvents within a few ps at room temperature. The $CpRe(CO)_2$ species has been observed in Nujol at 77K.[86] The IR band positions in Nujol were at 1947 and 1879 cm^{-1}, with parent bands at 2029 and 1934 cm^{-1} (band shifts: 82 and 55 cm^{-1} respectively). When compare the relative shift $\Delta\nu$(CO) of the first species at 1965 and 1898 cm^{-1} to the parent bands at 2038 and 1949 cm^{-1} (band shifts: 73 and 51 cm^{-1} respectively), the band at lower energy shows good agreement while the band at higher energy shows less agreement. From this the possibility of the existence of a coordinatively unsaturated $CpRe(CO)_2$ cannot be excluded.

3. Finally the possible identity of the first dicarbonyl species might be the PFMCH species $CpRe(CO)_2$(PFMCH). Although PFMCH is a non-coordinating solvent, the significantly unstable 16 electron species $CpRe(CO)_2$ could still weakly coordinates to PFMCH first before coordinating to the butyl group of $HSiBu_3$, due to the vast excess of PFMCH. DFT calculations[80] on the IR frequency of different $CpRe(CO)_3$ species in comparison with the experimental results have previously been reported.[81] According to the TRIR results, the relative shifts $\Delta\nu$(CO) of $CpRe(CO)_2(C_7F_{14})$ (1958, 1889 cm^{-1}) compared to $CpRe(CO)_2(C_5H_{10})$ (1952, 1887 cm^{-1}) is *ca.* 6 and 2 cm^{-1}, respectively, compared to the DFT result of 6 and 3 cm^{-1}. This is also consistent with the shifts of the ν(CO) positions at 1965, 1898 cm^{-1} to 1960, 1894 cm^{-1}, with shifts of *ca.* 5 and 4 cm^{-1}, respectively.

Along with the decay of the bands at 1960 and 1894 cm^{-1}, which have been assigned to the butyl species $CpRe(CO)_2(BuHSiBu_2)$, two bands at higher wavenumber at *ca.* 1996 and 1926 cm^{-1} are formed at the same rate of *ca.* 4.5 μs on the later timescale, as shown in Figure 2.35.

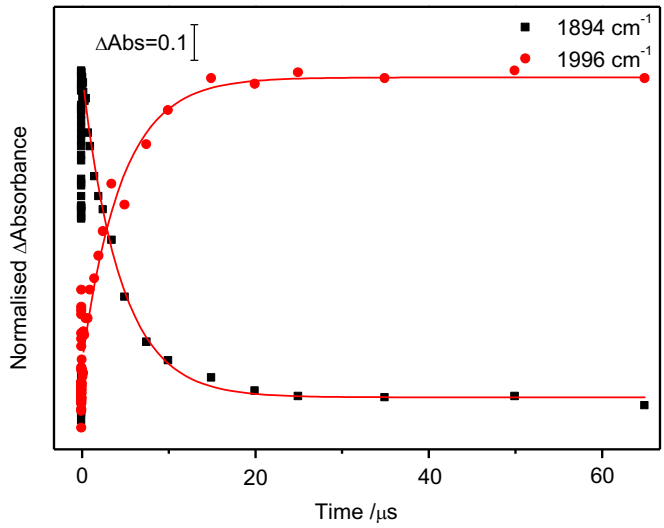


Figure 2.35 *TRIR kinetic traces obtained at 1996 and 1894 cm^{-1} corresponding to $CpRe(CO)_2(HSiBu_3)$ and $CpRe(CO)_2(BuHSiBu_2)$.*

By comparing to analogue species $CpRe(CO)_2(HSiEt_3)$ (1999, 1926 cm^{-1}) in PFMCH, the bands at 1996 and 1926 cm^{-1} are assigned to the silane species $CpRe(CO)_2(HSiBu_3)$. From Figure 2.34 and 2.35, it can be observed that the silane species $CpRe(CO)_2(HSiBu_3)$ either forms directly from the first dicarbonyl species at 1965 and 1898 cm^{-1}, or transformed from the butyl-bound species $CpRe(CO)_2(BuHSiBu_2)$. The silane species $CpRe(CO)_2(HSiBu_3)$ is very stable and was observed to remain during the experimental timescale (up to 1 ms). The possible mechanism is shown in Figure 2.36.

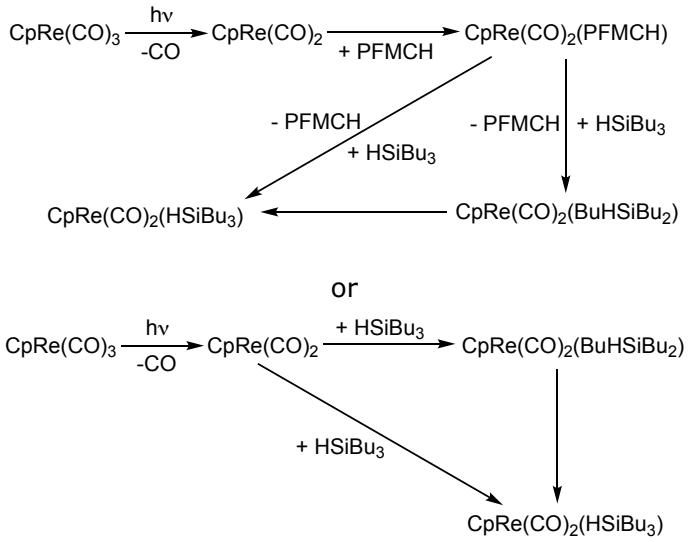


Figure 2.36 *Proposed reaction mechanism of $CpRe(CO)_3$ in PFMCH with $HSiBu_3$.*

The reaction mechanism shown in Figure 2.36 is similar to the work of Harris' group on the photoreaction of $CpRe(CO)_3$ in neat triethylsilane, as shown in Figure 2.37.

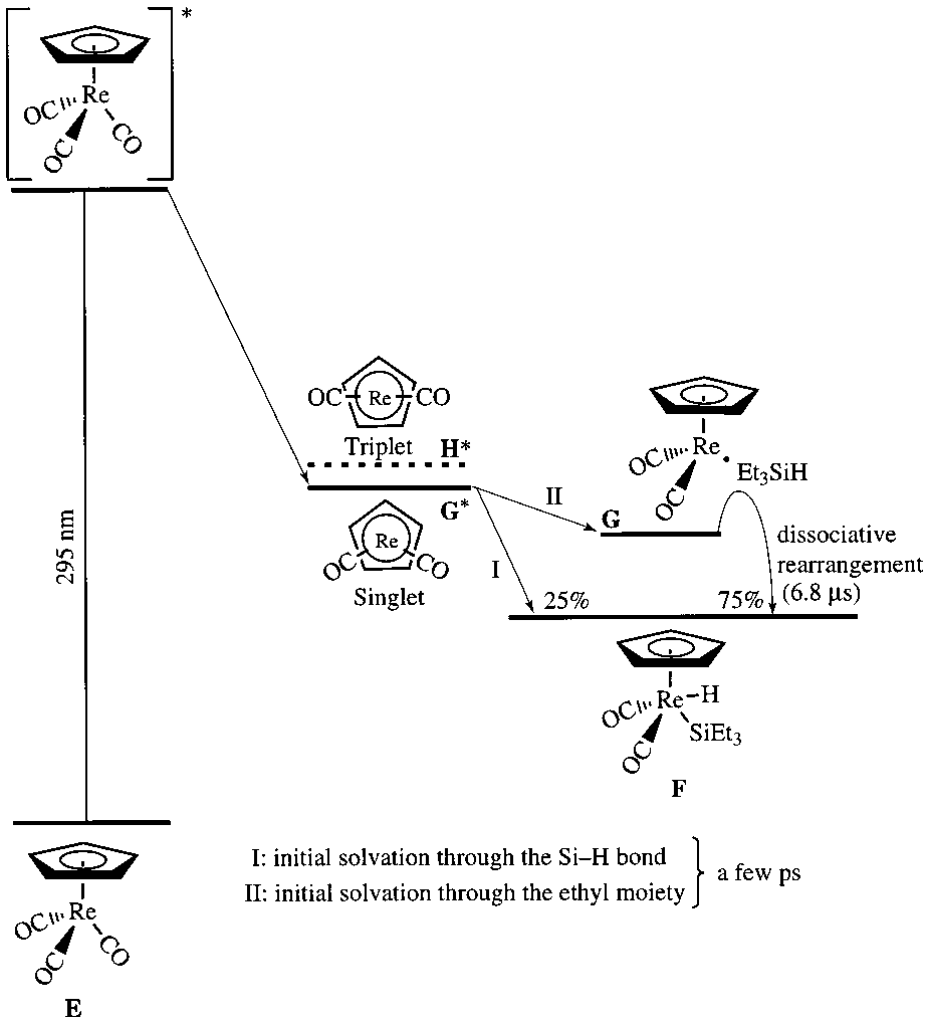


Figure 2.37 *Reaction mechanism of $CpRe(CO)_3$ in neat $HSiEt_3$, irradiated by 295 nm.*[73]

Similar to Harris' work, the final silane species $CpRe(CO)_2(HSiR_3)$ (R: Et, Bu) is converted both from the initial dicarbonyl species and the alkyl-bound species $CpRe(CO)_2(RHSiR_2)$. Kinetics shows that the conversion rate from $CpRe(CO)_2$ to $CpRe(CO)_2(HSiEt_3)$ occurs in a few ps, while in our work the conversion rate is slower (*ca.* 1 ns). If the first dicarbonyl species in our work is $CpRe(CO)_2$, then this may be attributed to the stabilization by PFMCH. Compared to the experiments in neat $HSiEt_3$, the concentration of $HSiR_3$ in PFMCH is much lower, which may also slow down the collision between $CpRe(CO)_2$ and $HSiBu_3$. While if the first dicarbonyl

is $CpRe(CO)_2$(PFMCH), this slow rate may be an evidence of the coordination to $CpRe(CO)_2$. The conversion rate between $CpRe(CO)_2(BuHSiBu_2)$ and $CpRe(CO)_2(HSiBu_3)$ (*ca.* 4.5 μs) is slightly faster than in neat $HSiEt_3$ (*ca.* 6.8 μs). This is surprising as according to previous work, the conversion rate between $CpRe(CO)_2(EtHSiEt_2)$ and $CpRe(CO)_2(HSiEt_3)$ in neat $HSiEt_3$ (*ca.* 6.8 μs) is faster than in $HSiEt_3$-doped PFMCH (*ca.* 14 μs), which is attributed to interactions with the solvent PFMCH.[80] Considering the steric factor that butyl is larger in size than ethyl, the faster rate in PFMCH compared to in neat $HSiEt_3$ may suggest that in $CpRe(CO)_2(HSiBu_3)$ and in $CpRe(CO)_2(HSiEt_3)$, the binding modes between the Re centre and Si-H may differ. According to previous work,[73] in $CpRe(CO)_2(HSiEt_3)$ it is stated that the Si-H bond is cleaved, and $CpRe(CO)_2(HSiEt_3)$ should be more accurately written as $CpReH(CO)_2(SiEt_3)$. However, considering the faster conversion rate for $CpRe(CO)_2(HSiBu_3)$ and also the steric factors, in $CpRe(CO)_2(HSiBu_3)$, the Si-H bond may not have been cleaved, the coordination mode may instead be the η^2-mode. The η^1-mode may not be very likely, as the ν(CO) band positions of $CpRe(CO)_2(HSiBu_3)$ are blue-shifted compared to $CpRe(CO)_2(BuHSiBu_2)$, reflecting a stronger π-back-donation from the Re centre to Si-H than to C-H of the butyl ligand.

The rate of ligand substitution with $HGeBu_3$ has also been investigated using TRIR, as shown in Figure 2.38.

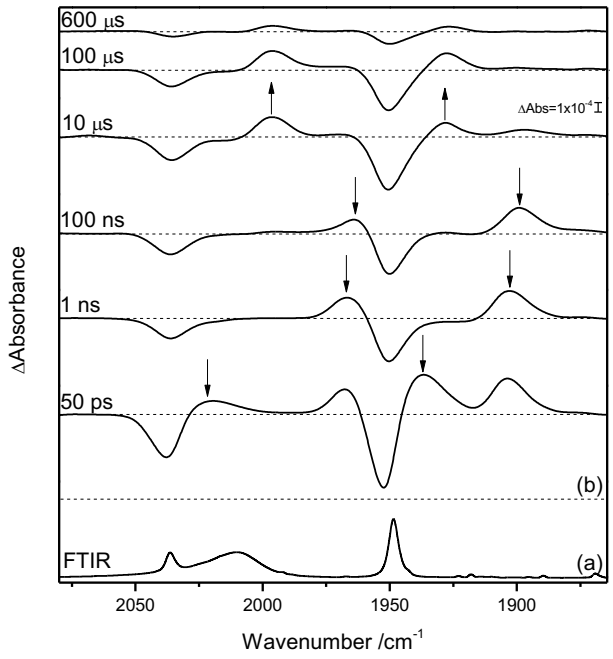


Figure 2.38 *(a) FTIR spectrum and (b) TRIR spectra obtained following photolysis (266 nm) of $CpRe(CO)_3$ in PFMCH doped with 0.078 M $HGeBu_3$.*

Similar to the experiment with $HSiBu_3$, the interchange between two dicarbonyl species was observed (1965, 1901 cm^{-1} to 1959, 1896 cm^{-1}), with an exchange rate of 3.1 (±0.5) ns. The germane species $CpRe(CO)_2(HGeBu_3)$ was also observed at *ca.* 1994 and 1924 cm^{-1}. $CpRe(CO)_2(HGeBu_3)$ was observed to have formed from the butyl-bound species $CpRe(CO)_2(BuHGeBu_2)$ at a rate of *ca.* 3.9 (±0.4) μs. However, no direct formation of the germane species $CpRe(CO)_2(HGeBu_3)$ from the first dicarbonyl (1965 and 1901 cm^{-1}) was observed. The reason for this might be attributed to the low concentration of $HGeBu_3$ (0.078 M) in PFMCH, thus $CpRe(CO)_2(HGeBu_3)$ cannot be formed directly from the first dicarbonyl species.

Finally, the rate of ligand substitution with the dopant $HSnBu_3$ was explored using TRIR, as shown in Figure 2.39.

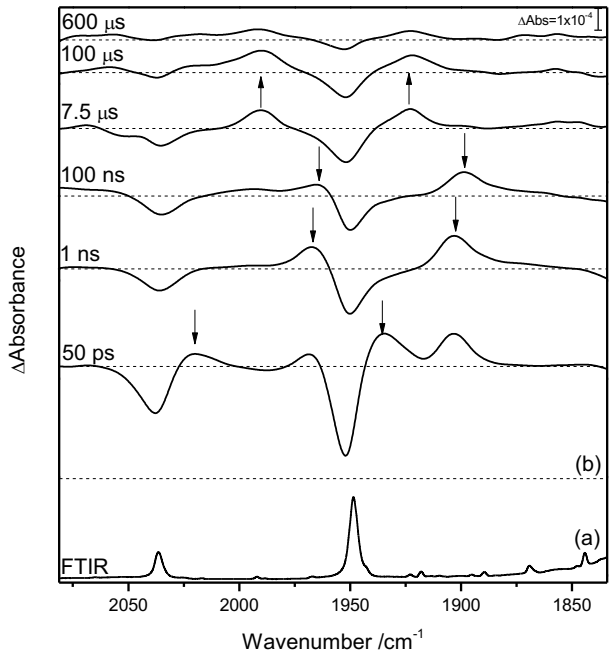


Figure 2.39 *(a) FTIR spectrum and (b) TRIR spectra obtained following photolysis (266 nm) of $CpRe(CO)_3$ in PFMCH doped with 0.068 M $HSnBu_3$.*

For experiments with $HSnBu_3$ as shown in Figure 2.39, the stannane species $CpRe(CO)_2(HSnBu_3)$ (1988, 1919 cm^{-1}) was observed as expected, and the conversion from the first dicarbonyl species to $CpRe(CO)_2(BuHSnBu_2)$ was observed with an exchange rate of *ca.* 4.0 (±0.8) ns. The ligand exchange rate between $CpRe(CO)_2(BuSnHBu_2)$ and $CpRe(CO)_2(HSnBu_3)$ is 1.4 (±0.1) μs. No direct formation of $CpRe(CO)_2(HSnBu_3)$ from the first dicarbonyl species was observed, which may also be attributed to the low concentration of $HSnBu_3$ (0.068 M).

Based on the results, it can be noted that the ν(CO) band positions of the final activated species of $CpRe(CO)_3$ are still at lower wavenumbers compared to the parent bands, which indicates that σ-donation may still dominate the interaction between the metal centre and E-H bond (E: Si, Ge, Sn). In previous research, the ν(CO) of $CpRe(CO)_2H(SiEt_3)$ is also at lower wavenumber than the parent bleaches, and the Si-H bond is reported to be completely cleaved, according to Ab Initio calculations. However, as discussed before, here for $CpRe(CO)_2(HSiBu_3)$, it is proposed that the Si-H bond may not be fully cleaved from the kinetic results. But

when compared to $CpMn(CO)_3$, the ν(CO) positions of the activated species $CpRe(CO)_2(HEBu_3)$ move further to higher energies compared to the alkyl-bound species $CpRe(CO)_2(BuHEBu_2)$, which may indicate a more complete activation of the E-H bond, as shown in Table 2.8.

Table 2.8 *Comparison of $\Delta\nu$(CO) of different activated CpMn- and CpRe-species to their corresponding butyl-bound species.*

Species	ν(CO) /cm^{-1}	$\Delta\nu$(CO) /cm^{-1}	solvent	Ref.
$CpMn(CO)_2(BuHSiBu_2)$	1966, 1901	15, 21	PFMCH	This work
$CpMn(CO)_2(HSiBu_3)$	1981, 1922			
$CpMn(CO)_2(BuHGeBu_2)$	1966, 1904	15, 20	PFMCH	This work
$CpMn(CO)_2(HGeBu_3)$	1981, 1924			
$CpMn(CO)_2(BuHSnBu_2)$	1965, 1899	15, 18	PFMCH	This work
$CpMn(CO)_2(HSnBu_3)$	1980, 1917			
$CpRe(CO)_2(BuHSiBu_2)$	1960, 1894	36, 32	PFMCH	This work
$CpRe(CO)_2(HSiBu_3)$	1996, 1926			
$CpRe(CO)_2(BuHGeBu_2)$	1959, 1896	35, 28	PFMCH	This work
$CpRe(CO)_2(HGeBu_3)$	1994, 1924			
$CpRe(CO)_2(BuHSnBu_2)$	1959, 1895	29, 24	PFMCH	This work
$CpRe(CO)_2(HSnBu_3)$	1988, 1919			
$CpMn(CO)_2(EtHSiEt_2)$	1960, 1892	19, 23	Neat $HSiEt_3$	73
$CpMn(CO)_2(HSiEt_3)$	1979, 1915			
$CpRe(CO)_2(EtHSiEt_2)$	1948, 1887	42, 31	Neat $HSiEt_3$	73
$CpReH(CO)_2(SiEt_3)$	1990, 1918			
$CpMn(CO)_2(EtHSiEt_2)$	1966, 1897	19, 22	PFMCH	80
$CpMn(CO)_2(HSiEt_3)$	1985, 1919			
$CpRe(CO)_2(EtHSiEt_2)$	1958, 1889	41, 37	PFMCH	80
$CpReH(CO)_2(SiEt_3)$	1999, 1926			

Thus based on the data it can be concluded that, $CpRe(CO)_3$ tends to activate the E-H bond more completely than $CpMn(CO)_3$, consistent with previous work.[73] The extent of the oxidative addition for all three activated species $CpRe(CO)_2(HEBu_3)$ follows the trend as the Δ(CO) indicates: Si > Ge > Sn.

The kinetics show significant differences compared to previous work on $CpMn(CO)_3$. The ligand exchange rate between C-H and E-H is extremely long occurring on the μs-timescale, compared to *ca.* 100~200 ns for $CpMn(CO)_3$ in PFMCH. This can be attributed to the stability of the butyl-bound species $CpRe(CO)_2(BuHEBu_2)$, which is considered to have similar stability to $CpRe(CO)_2$(*n*-heptane). As $CpRe(CO)_2(BuHEBu_2)$ may be much more stable than $CpMn(CO)_2(BuHEBu_2)$, thus the dissociation of the butyl group may take longer time for $CpRe(CO)_2(BuHEBu_2)$.

The ligand exchange rate between C-H and E-H is found to be faster for $HSnBu_3$ than $HSiBu_3$ and $HGeBu_3$, which is in contrary with $CpMn(CO)_3$ (Table 2.9). This can be attributed to the fact that as the interaction between the Re centre and the E-H bond is dominated by σ-donation, the more electron-rich Sn-H bond tends to coordinate to the metal centre more easily than Si-H and Ge-H. However, for $CpMn(CO)_3$, as the interaction between the metal centre and E-H bond is weaker, the steric factors become dominant and the bulkier Sn-H bond coordinates to the Mn centre at a slightly slower rate than Si-H and Ge-H.

Table 2.9 *Summary of the C-H/E-H (E: Si, Ge, Sn) ligand exchange rates of CpMn- and CpRe-complexes under different conditions (solvent, dopant concentration).*

Species	solvent	Dopant	Dopant concentration /M	Ligand exchange lifetime	Ref
$CpMn(CO)_3$	PFMCH	$HSiBu_3$	0.25	110 ± 4 ns	This work
	PFMCH	$HGeBu_3$	0.078	126 ± 18 ns	This work
	PFMCH	$HSnBu_3$	0.17	199 ± 9 ns	This work
$CpRe(CO)_3$	PFMCH	$HSiBu_3$	0.25	4.5 ± 0.3 μs	This work
	PFMCH	$HGeBu_3$	0.078	3.9 ± 0.4 μs	This work
	PFMCH	$HSnBu_3$	0.068	1.4 ± 0.1 μs	This work
$CpMn(CO)_3$	$HSiEt_3$	-	-	177 ns	73
$CpRe(CO)_3$	$HSiEt_3$	-	-	6.8 μs	73
$CpMn(CO)_3$	PFMCH	$HSiEt_3$	0.5	145 ± 18 ns	80
$CpRe(CO)_3$	PFMCH	$HSiEt_3$	0.5	1.1 ± 0.1 μs, 14 ± 1.5 μs	80

2.2.7 TRIR Studies of E-H (E: Si, Ge, Sn) Bond Coordination to $Cp^*Re(CO)_3$ in *n*-heptane

As no activated species were observed for $CpRe(CO)_3$ in heptane, we chose to increase the electron density on the Re centre in an attempt to obtain E-H (E: Si, Ge, Sn) activated species in the alkane solvent. we chose $Cp^*Re(CO)_3$ as our target complex in which five H on the Cp ring have been substituted by five electron rich methyl groups. The results are discussed in the following sections.

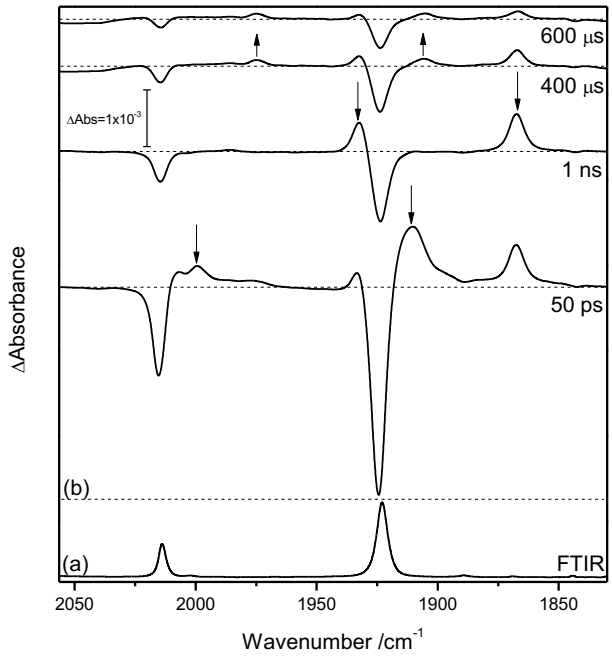


Figure 2.40 *(a) FTIR spectrum and (b) TRIR spectra obtained following photolysis (266 nm) of $Cp^*Re(CO)_3$ in n-heptane doped with 0.1 M $HSiBu_3$.*

The TRIR spectra of $Cp^*Re(CO)_3$ in heptane doped with 0.1 M $HSiBu_3$ are shown in Figure 2.40. Similar to the TRIR spectra of $CpRe(CO)_3$ in heptane, upon UV photolysis, along with the bleach of the parent bands at *ca.* 2014 and 1924 cm^{-1}, two broad vibrational hot bands at *ca.* 2000 and 1911 cm^{-1} are formed, along with two other bands at *ca.* 1932 and 1868 cm^{-1}. The lifetime of the bands at 1932 and 1868 cm^{-1} is very long and these two bands can even be observed after 600 μs. Also, the $\Delta\nu$(CO) of these two band positions compared to the parent bands (56, 82 cm^{-1}, respectively) are similar to the $\Delta\nu$(CO) of $CpRe(CO)_2$(*n*-heptane) compared

to $CpRe(CO)_3$ (51, 78 cm^{-1}, respectively). As a result, the bands at 1932 and 1868 cm^{-1} are assigned to the Cp*Re(CO)$_2$(*n*-heptane) species.

However, different to $CpRe(CO)_3$, on the μs-timescale the decay of the Cp*Re(CO)$_2$(*n*-heptane) species and another two bands at *ca.* 1975 and 1906 cm^{-1} were observed. However, the decay of Cp*Re(CO)$_2$(*n*-heptane) and the formation of the final product after *ca.* 100 μs is out of the timescale in which we can conduct accurate kinetic analysis. The bands at *ca.* 1975 and 1906 cm^{-1} are likely to be the silane species $Cp*Re(HSiBu_3)$. From analysis of the kinetics, it was found that the initial vibrational hot complex decays along with the recovery of the parent complex (*ca.* 45 ps). From this the growth of the bands at *ca.* 1975 and 1906 cm^{-1} is proposed to be related to the decay of the Cp*Re(CO)$_2$(*n*-heptane) species. Also, when compare the $\Delta\nu$(CO) of the bands at 1975 and 1906 cm^{-1} to Cp*Re(CO)$_2$(*n*-heptane) (38, 43 cm^{-1}, respectively) and the $\Delta\nu$(CO) of $CpRe(CO)_2(HSiBu_3)$ to $CpRe(CO)_2(BuHSiBu_2)$ in PFMCH (32, 36 cm^{-1} respectively), it is reasonable to assign the bands at 1975 and 1906 cm^{-1} to the $Cp*Re(HSiBu_3)$ species.

TRIR experiments with $HGeBu_3$ have also been conducted.

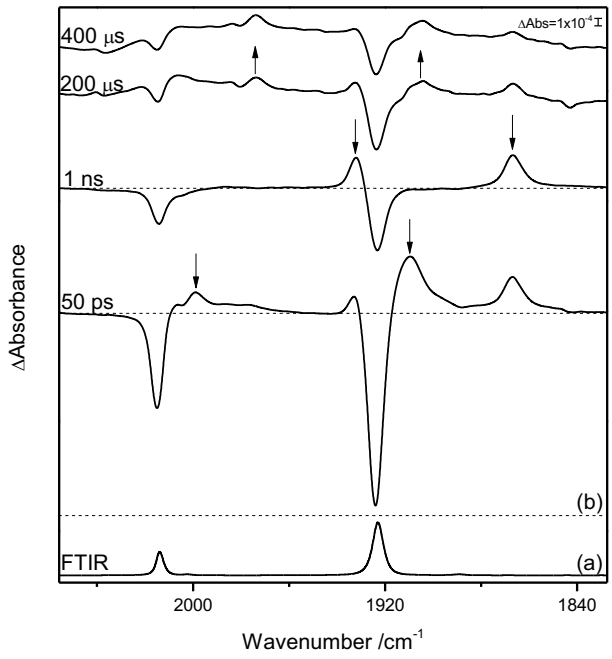


Figure 2.41 *(a) FTIR spectrum and (b) TRIR spectra obtained following photolysis (266 nm) of Cp*Re(CO)$_3$ in n-heptane doped with 0.1 M HGeBu$_3$.*

From the TRIR spectra shown in Figure 2.41, it can be observed that the reaction process with the dopant $HGeBu_3$ behaves similarly to $HSiBu_3$. The bands at 1932 and 1866 cm^{-1} are assigned to the heptane species $Cp^*Re(CO)_2$(*n*-heptane), while the bands at *ca.* 1974 and 1904 cm^{-1} are assigned to the germane species $Cp^*Re(CO)_2(HGeBu_3)$.

Finally, TRIR experiments with $HSnBu_3$ were also conducted. The spectra are shown in Figure 2.42.

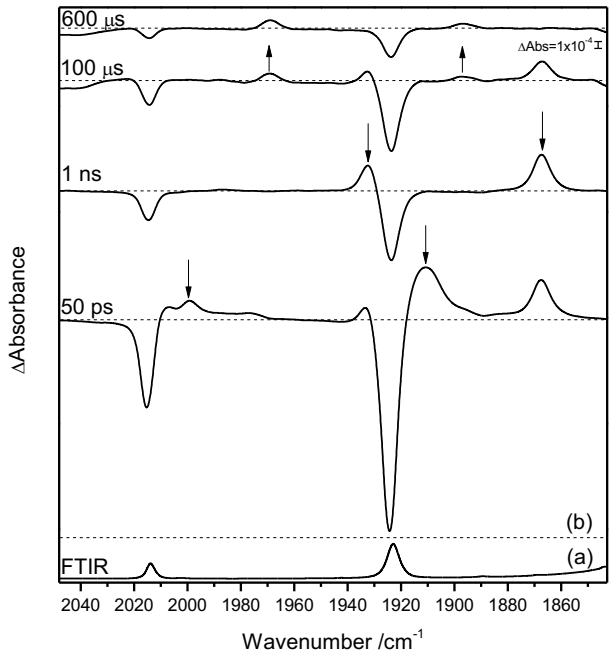


Figure 2.42 *(a) FTIR spectrum and (b) TRIR spectra obtained following photolysis (266 nm) of Cp*Re(CO)$_3$ in n-heptane doped with 0.1 M HSnBu$_3$.*

Similar to TRIR with $HSiBu_3$ and $HGeBu_3$, the bands at 1932 and 1867 cm^{-1} are assigned to Cp*Re(CO)$_2$(*n*-heptane), while the bands formed on the μs-timescale at *ca.* 1970 and 1896 cm^{-1} are assigned to Cp*Re(CO)$_2$($HSnBu_3$). Analogously, the accurate ligand exchange rate between Cp*Re(CO)$_2$(*n*-heptane) and Cp*Re(CO)$_2$($HSnBu_3$) cannot be obtained. However, at the 600 μs time delay, from the spectra it can be observed that Cp*Re(CO)$_2$(*n*-heptane) has almost completely decayed, which is different to the experiments with $HSiBu_3$ and $HGeBu_3$. From this, it can be proposed that the ligand exchange rate between Cp*Re(CO)$_2$(*n*-heptane) and Cp*Re(CO)$_2$($HSnBu_3$) may be faster than Cp*Re(CO)$_2$($HSiBu_3$) and Cp*Re(CO)$_2$($HGeBu_3$).

Based on the results, it can be concluded that by increasing the electron density on the Re centre *via* adding electron-donating groups onto the Cp ring, the interaction between the Re centre and E-H (E: Si, Ge, Sn) has been facilitated as all three bond activated species Cp*Re(CO)$_2$($HEBu_3$) (E: Si, Ge, Sn) have been observed for Cp*Re(CO)$_3$.

The $\Delta\nu$(CO) of Cp*Re(CO)$_2$(HEBu$_3$) compared to Cp*Re(CO)$_2$(*n*-heptane) is summarized in Table 2.10.

Table 2.10 *Comparison of $\Delta\nu$(CO) of the activated species Cp*Re(CO)$_2$(HEBu$_3$) (E: Si, Ge, Sn) compared to the solvated species Cp*Re(CO)$_2$(n-heptane).*

Species	ν(CO) /cm^{-1}	Δ(CO) /cm^{-1}
Cp*Re(CO)$_2$(HSiBu$_3$)	1975, 1906	43, 38
Cp*Re(CO)$_2$(HGeBu$_3$)	1974, 1904	42, 38
Cp*Re(CO)$_2$(HSnBu$_3$)	1970, 1896	38, 29

The $\Delta\nu$(CO) of Cp*Re(CO)$_2$(HSiBu$_3$) and Cp*Re(CO)$_2$(HGeBu$_3$) are slightly larger than CpReH(CO)$_2$(SiEt$_3$) in neat HSiEt$_3$ (31, 42 cm^{-1}) and in PFMCH (37, 41 cm^{-1}), which has been assigned to be the complete activation of the Si-H bond.[73,80] The Si-H and Ge-H bonds in Cp*Re(CO)$_2$(HSiBu$_3$) and Cp*Re(CO)$_2$(HGeBu$_3$) are thus proposed to be fully activated, and should be denoted as Cp*ReH(CO)$_2$(SiBu$_3$) and Cp*ReH(CO)$_2$(GeBu$_3$), respectively. Compared to the CpRe-analogue species, for which the binding mode between the Re centre and the E-H bond of HEBu$_3$ is *via* a η^2-mode as discussed before, this is evidence of how increasing the electron density on the metal centre can facilitate the oxidative addition of the E-H bonds. Also, as has been discussed above, previous work suggested that steric factors will also affect the binding modes between the metal centre and the E-H bond. Bulky ligands attached to the metal centre or dopants will hinder the η^2-coordination preferring to the η^1-mode.[50] Here the results suggest that the effects of the electron density increase on the metal centre overtake the effects of the size enlargement brought by introducing the five methyl groups onto the Cp ring. The $\Delta\nu$(CO) of Cp*Re(CO)$_2$(HSnBu$_3$) is also large but smaller compared to Cp*Re (CO)$_2$(HSiBu$_3$) and Cp*Re(CO)$_2$(HGeBu$_3$), thus it is still unclear whether the Sn-H bond has been fully activated in Cp*Re(CO)$_2$(HSnBu$_3$) to the same extent (this may be ascribed to the fact that the Sn-H bond is more electron rich), and this needs further investigation.

2.2.8 TRIR Studies of E-H (E: Si, Ge, Sn) Bond Coordination to $Cp^*Re(CO)_3$ in PFMCH

TRIR investigations in PFMCH were conducted as shown in Figure 2.43.

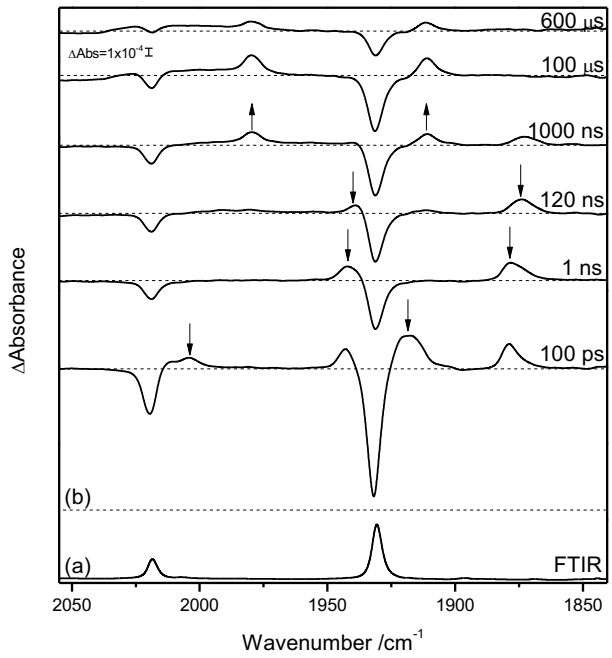


Figure 2.43 *(a) FTIR spectrum and (b) TRIR spectra obtained following photolysis (266 nm) of $Cp^*Re(CO)_3$ in PFMCH doped with saturated tributylsilane.*

At early time delays, similar processes to $CpRe(CO)_3$ in PFMCH were observed. Upon UV photolysis, along with the bleach of the parent bands (2019, 1931 cm^{-1}), the vibrational hot bands are formed (2004, 1919 cm^{-1}), together with the formation of the first dicarbonyl species (1943, 1879 cm^{-1}), which then transforms into the alkyl-bound species $Cp^*Re(CO)_2(BuSiHBu_2)$ (1939, 1874 cm^{-1}). The alkyl species decays and is replaced by Si-H to form the activated species $Cp^*ReH(CO)_2(SiBu_3)$ (1980, 1911 cm^{-1}). The identity of the first dicarbonyl species, as has been suggested before, could have several candidates such as the unsaturated $Cp^*Re(CO)_2$ or the PFMCH species $Cp^*Re(CO)_2(PFMCH)$.

The exchange rate between the first dicarbonyl species and $Cp^*Re(CO)_2(BuHSiBu_2)$ is *ca.* 2.1 (±0.4) ns. The rate is similar to the exchange rate observed for $CpRe(CO)_3$

in PFMCH doped with 0.25 M tributylsilane (0.25 M). The ligand exchange rate between $Cp^*Re(CO)_2(BuHSiBu_2)$ and $Cp^*ReH(CO)_2(SiBu_3)$ is *ca.* 1.3 (±0.1) μs, which is significantly faster than $CpRe(CO)_3$ (4.5 μs) under 0.25 M dopant concentration, as shown in Figure 2.44.

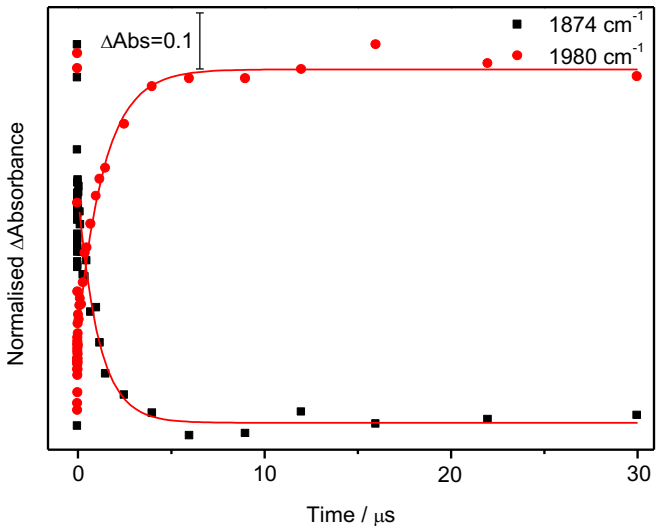


Figure 2.44 *TRIR kinetic traces obtained at 1980 and 1874 cm^{-1} corresponding to $Cp^*ReH(CO)_2(SiBu_3)$ and $Cp^*Re(CO)_2(BuSiHBu_2)$.*

Different to $CpRe(CO)_3$ in PFMCH, the direct formation of $Cp^*ReH(CO)_2(SiBu_3)$ from the first dicarbonyl species (1879, 1943 cm^{-1}) was not observed. We also repeated the measurements with $HGeBu_3$ as a dopant in this solvent.

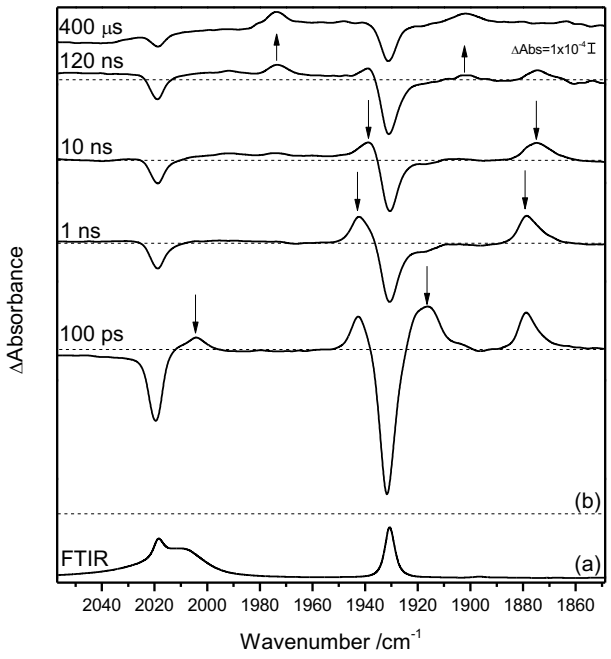


Figure 2.45 *(a) FTIR spectrum and (b) TRIR spectra obtained following photolysis (266 nm) of Cp*Re(CO)$_3$ in PFMCH doped with saturated HGeBu$_3$.*

From Figure 2.45 it was observed that, similar to experiments with $HSiBu_3$, there exist the exchange between two dicarbonyl species, with bands at 1943 and 1879 cm^{-1} undergoing a slight red-shift to 1939 and 1874 cm^{-1}. The bands at 1939 and 1874 cm^{-1} are assigned to the alkyl-bound species $Cp^*Re(CO)_2(BuGeHBu_2)$, compared to the silane analogue $Cp^*Re(CO)_2(BuSiHBu_2)$ in PFMCH (1939 and 1874 cm^{-1}). Following the decay of $Cp^*Re(CO)_2(BuGeHBu_2)$, two bands at *ca.* 1974 and 1902 cm^{-1} are formed and assigned to the germane species $Cp^*ReH(CO)_2(GeBu_3)$.

The kinetic analysis shows that the lifetime of the first dicarbonyl species (1943 and 1879 cm^{-1}) is *ca.* 2.7 ns. The decay of the $Cp^*Re(CO)_2(BuGeHBu_2)$ species fits the growth rate of the activated species $Cp^*ReH(CO)_2(GeBu_3)$ with a lifetime of *ca.* 0.8 μs, as shown in Figure 2.46.

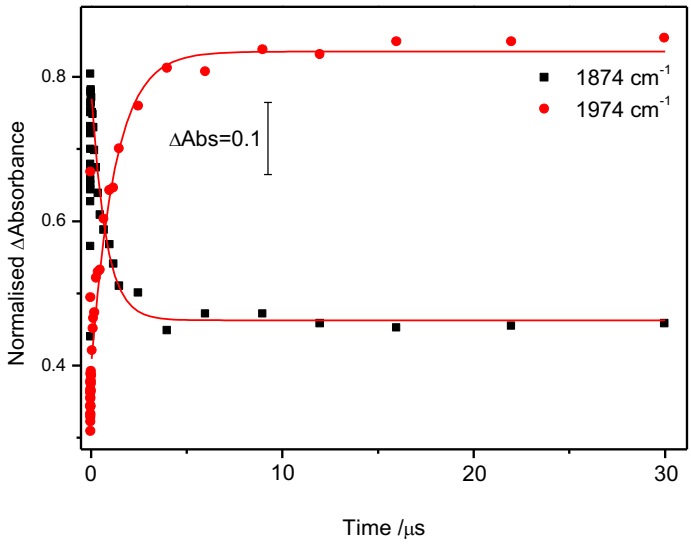


Figure 2.46 *TRIR kinetic traces obtained at 1974 and 1874 cm^{-1} corresponding to $Cp^*ReH(CO)_2(GeBu_3)$ and $Cp^*Re(CO)_2(BuHGeBu_2)$.*

Similar to the experiment with $HSiBu_3$, no formation of the activated species from the first dicarbonyl were apparent according to the kinetic analysis. The ligand exchange rate between $Cp^*Re(CO)_2(BuHGeBu_2)$ and $Cp^*ReH(CO)_2(GeBu_3)$ is slightly faster than that of the silane analogue. Similar processes were also observed for tributylstannane (Figure 2.47).

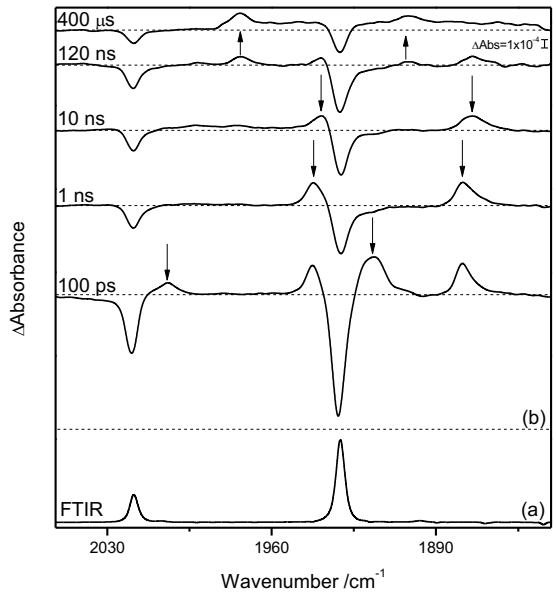


Figure 2.47 *(a) FTIR spectrum and (b) TRIR spectra obtained following photolysis (266 nm) of Cp*Re(CO)$_3$ in PFMCH doped with saturated HSnBu$_3$.*

The exchange of two dicarbonyl species (1943, 1879 cm^{-1} to 1939, 1875 cm^{-1}) and the final formation of the stannane species Cp*Re(CO)$_2$(HSnBu$_3$) is apparent. By kinetic analysis, it is found that, similar to HGeBu$_3$, the decay rate of the second dicarbonyl species Cp*Re(CO)$_2$(BuHSnBu$_2$) fits one component of the bi-exponential growth of the final stannane product Cp*Re(CO)$_2$(HSnBu$_3$) (*ca.* 0.4 μs), as shown in Figure 2.48.

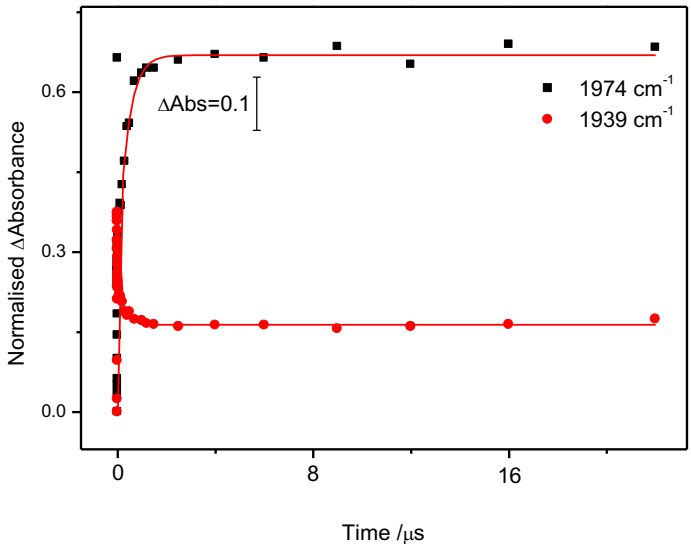


Figure 2.48 *TRIR kinetic traces obtained at 1974 and 1939 cm^{-1} corresponding to $Cp^*ReH(CO)_2(SnBu_3)$ and $Cp^*Re(CO)_2(BuHSnBu_2)$.*

The formation of the stannane species $Cp^*Re(CO)_2(HSnBu_3)$ is bi-exponential. The τ_1 (~ 1 ns) component fits the lifetime of the first dicarbonyl species (*ca.* 2 ns). And therefore, the activated species $Cp^*ReH(CO)_2(SnBu_3)$ is proposed to form both from the first dicarbonyl species and from $Cp^*Re(CO)_2(BuHSnBu_2)$.

Comparing the TRIR results of the three dopants, it can be concluded that the ligand exchange rate between $Cp^*Re(CO)_2(BuHEBu_2)$ and $Cp^*ReH(CO)_2(EBu_3)$ (E: Si, Ge, Sn) in saturated PFMCH follows the sequence: Si < Ge < Sn. This may be attributed to the increasing electron donation ability of Si < Ge < Sn, which facilitates the coordination to the Re centre. This is similar to the results obtained with $CpRe(CO)_3$ while different to the $CpMn(CO)_3$ and $Cp'Mn(CO)_3$ complexes, for which the ligand exchange rate for $HSnBu_3$ is the slowest, which is ascribed to steric factors. Compared to the exchange rate in heptane, the rate in PFMCH is significantly accelerated.

From these TRIR studies, we have learnt a large amount about the reactivity of these transient intermediates, and these species were ideal candidates to be studied by time-resolved XAFS. These complexes and ligand exchanges were attempted to be studied by XAFS (in collaboration with Dr R. Horvath and S. Bartlett)

at the APS synchrotron facility. Unfortunately, the signals obtained in these experiments were difficult to be resolved from the noise in these measurements. These results indicated that for the time-resolved XAFs measurements, the complexes should have not only a long lifetime but also high quantum yield. Preliminary studies towards these goals are the subject of the next Chapter.

2.3 Conclusion

Investigations on the E-H bond photo-activation (E: Si, Ge, Sn) by (η^5-$C_5H_nMe_{5-n}$)$M(CO)_3$ (M = Mn, Re) in alkane solvent (*n*-heptane) and perfluorinated solvent (PFMCH) have been conducted using TRIR. These results show that, in summary, the E-H bond activation by Re is more complete than by Mn in these complexes. Adding electron rich substituents onto the Cp ring was found to facilitate the oxidative addition as it increased the π–backbonding from the metal centre to the E-H σ* orbital.

The reaction was observed to be highly dependent on the solvent, and the reactions in both solvents were observed to be dissociative. While in heptane, it was observed that the solvated species dissociates the heptane molecule first before coordinating to the $HEBu_3$. In PFMCH dissociation within the same $HEBu_3$ molecule was observed, that the butyl-bound species first dissociates the butyl group, then re-coordinated by the E-H bond of the same $HEBu_3$ molecule. This mechanism is supported by the observed kinetics, as in heptane the ligand exchange rate between C-H and E-H is observed to be dependent on the dopant concentration while in PFMCH, the effect of the dopant concentration is small. This is the result of the weak coordination ability of PFMCH compared to heptane. Also, heptane was observed to react with the triplet dicarbonyl species faster than PFMCH. The C-H/E-H ligand exchange rate in heptane is also observed to be much slower than in PFMCH owing to the stability of the $CpM(CO)_2$(heptane) species. For the three dopants $HEBu_3$ (E: Si, Ge, Sn), the interaction with the metal centre is dependent on many factors, such as the nature of the metal centre, dopant, solvent, steric factors, *etc.* For all activated species (η^5-$C_5H_nMe_{5-n}$)$M(CO)_2(HEBu_3)$ [or (η^5-$C_5H_nMe_{5-n}$)$MH(CO)_2(EBu_3)$] (M: Mn, Re), the dominant interaction with the dopants $HEBu_3$ is found to be a σ-interaction. It was found that the overall interaction with the metal centre follows: Sn > Ge > Si, due to larger electron density on the Sn-H bond, thus facilitating the σ-interaction. While the π-backbonding interaction between Mn and E-H follows the order: Ge ≥ Si > Sn, which is reflected by the $\Delta\nu$(CO) of the activated species compared to the alkyl-bound species. Larger blue-shift of $\Delta\nu$(CO) indicates greater π-backbonding from the metal centre to the σ* orbital of the E-H bond.

References

1 A. E. Shilov and G. B. Shul'pin, *Chem. Rev.*, 1997, **97**, 2879–2932.

2 W. D. Jones, *Acc. Chem. Res.*, 2003, **36**, 140–146.

3 C.-H. Jun, *Chem. Soc. Rev.*, 2004, **33**, 610–618.

4 D. G. Musaev and K. Morokuma, *J. Am. Chem. Soc.*, 1995, **117**, 799–805.

5 J. Sun and L. Deng, *ACS Catal.*, 2016, **6**, 290–300.

6 Y. Nakajima and S. Shimada, *RSC Adv.*, 2015, **5**, 20603–20616.

7 X. Du and Z. Huang, *ACS Catal.*, 2017, **7**, 1227–1243.

8 K. Choi and J. M. Buriak, *Langmuir*, 2000, **16**, 7737–7741.

9 M. Itazaki, M. Kamitani and H. Nakazawa, *Chem. Commun.*, 2011, **47**, 7854–7856.

10 T. Nakamura, S. Tanaka, H. Yorimitsu, H. Shinokubo and K. Oshima, *Comptes Rendus Académie Sci. - Ser. IIC - Chem.*, 2001, **4**, 461–470.

11 M. Cai, Y. Wang and W. Hao, *Eur. J. Org. Chem.*, 2008, **2008**, 2983–2988.

12 N. D. Smith, J. Mancuso and M. Lautens, *Chem. Rev.*, 2000, **100**, 3257–3282.

13 Rummelt Stephan M. and Fürstner Alois, *Angew. Chem. Int. Ed.*, 2014, **53**, 3626–3630.

14 J. A. Labinger and J. E. Bercaw, *Nature*, 2002, **417**, 507–514.

15 A. D. Ryabov, *Chem. Rev.*, 1990, **90**, 403–424.

16 I. P. Rothwell, *Polyhedron*, 1985, **4**, 177–200.

17 McKeown Bradley A., Lee John P., Mei Jiajun, Cundari Thomas R. and Gunnoe T. Brent, *Eur. J. Inorg. Chem.*, 2016, **2016**, 2296–2311.

18 G. J. Kubas, C. J. Unkefer, B. I. Swanson and Eiichi. Fukushima, *J. Am. Chem. Soc.*, 1986, **108**, 7000–7009.

19 J. Y. Corey and J. Braddock-Wilking, *Chem. Rev.*, 1999, **99**, 175–292.

20 J. Y. Corey, *Chem. Rev.*, 2016, **116**, 11291–11435.

21 J. Y. Corey, *Chem. Rev.*, 2011, **111**, 863–1071.

22 A. Takaoka, A. Mendiratta and J. C. Peters, *Organometallics*, 2009, **28**, 3744–3753.

23 M. Zyder and T. Szymańska-Buzar, *J. Organomet. Chem.*, 2009, **694**, 2110–2113.

24 Sindlinger Christian P., Aicher Frederik S. W., Schubert Hartmut and Wesemann Lars, *Angew. Chem. Int. Ed.*, 2017, **56**, 2198–2202.

25 L. Carlton and J. J. Molapisi, *J. Organomet. Chem.*, 2000, **609**, 60–65.

26 A. Bihlmeier, T. M. Greene and H.-J. Himmel, *Organometallics*, 2004, **23**, 2350–2361.

27 S. N. Ehrlich, J. C. Hanson, A. Lopez Camara, L. Barrio, M. Estrella, G. Zhou, R. Si, S. Khalid and Q. Wang, *Nucl. Instrum. Methods Phys. Res. Sect. Accel. Spectrometers Detect. Assoc. Equip.*, 2011, **649**, 213–215.

28 E. D. Crozier, *Nucl. Instrum. Methods Phys. Res. Sect. B Beam Interact. Mater. At.*, 1997, **133**, 134–144.

29 R. C. Nelson and J. T. Miller, *Catal. Sci. Technol.*, 2012, **2**, 461–470.

30 E. A. Stern, *Contemp. Phys.*, 1978, **19**, 289–310.

31 A. Bianconi, *Appl. Surf. Sci.*, 1980, **6**, 392–418.

32 P. Eisenberger and B. M. Kincaid, *Science*, 1978, **200**, 1441–1447.

33 D. E. Sayers, E. A. Stern and F. W. Lytle, *Phys. Rev. Lett.*, 1971, **27**, 1204–1207.

34 M. A. Newton, A. J. Dent and J. Evans, *Chem. Soc. Rev.*, 2002, **31**, 83–95.

35 L. X. Chen, X. Zhang and M. L. Shelby, *Chem. Sci.*, 2014, **5**, 4136–4152.

36 S. A. Bartlett, M. L. Hamilton and J. Evans, *Dalton Trans.*, 2015, **44**, 6313–6319.

37 M. Chergui and E. Collet, *Chem. Rev.*, 2017, **117**, 11025–11065.

38 A. J. Dent, L. J. Farrugia, A. G. Orpen and S. E. Stratford, *J. Chem. Soc. Chem. Commun.*, 1992, 1456–1457.

39 J.-D. Grunwaldt, D. Lützenkirchen-Hecht, M. Richwin, S. Grundmann, B. S. Clausen and R. Frahm, *J. Phys. Chem. B*, 2001, **105**, 5161–5168.

40 T. Matsushita and R. P. Phizackerley, *Jpn. J. Appl. Phys.*, 1981, **20**, 2223.

41 D. Lützenkirchen-Hecht, S. Grundmann and R. Frahm, *J. Synchrotron Radiat.*, 2001, **8**, 6–9.

42 S. Pascarelli, T. Neisius and S. De Panfilis, *J. Synchrotron Radiat.*, 1999, **6**, 1044–1050.

43 S. Pascarelli, S. De Panfilis and T. Neisius, *Phys. Rev. B*, 2000, **62**, 3717–3721.

44 J. Evans, *Phys. Chem. Chem. Phys.*, 2006, **8**, 3045–3058.

45 L. X. Chen, G. B. Shaw, I. Novozhilova, T. Liu, G. Jennings, K. Attenkofer, G. J. Meyer and P. Coppens, *J. Am. Chem. Soc.*, 2003, **125**, 7022–7034.

46 L. X. Chen, P. L. Lee, D. Gosztola, W. A. Svec, P. A. Montano and M. R. Wasielewski, *J. Phys. Chem. B*, 1999, **103**, 3270–3274.

47 A. B. Stickrath, M. W. Mara, J. V. Lockard, M. R. Harpham, J. Huang, X. Zhang, K. Attenkofer and L. X. Chen, *J. Phys. Chem. B*, 2013, **117**, 4705–4712.

48 M. L. Shelby, M. W. Mara and L. X. Chen, *Coord. Chem. Rev.*, 2014, **277–278**, 291–299.

49 X. Zhang, G. Smolentsev, J. Guo, K. Attenkofer, C. Kurtz, G. Jennings, J. V. Lockard, A. B. Stickrath and L. X. Chen, *J. Phys. Chem. Lett.*, 2011, **2**, 628–632.

50 Yang Jian, White Peter S., Schauer Cynthia K. and Brookhart Maurice, *Angew. Chem. Int. Ed.*, 2008, **47**, 4141–4143.

51 A. Y. Houghton, J. Hurmalainen, A. Mansikkamäki, W. E. Piers and H. M. Tuononen, *Nat. Chem.*, 2014, **6**, 983–988.

52 Chen Jiawei and Chen Eugene Y.-X., *Angew. Chem. Int. Ed.*, 2015, **54**, 6842–6846.

53 S. P. Hoffmann, T. Kato, F. S. Tham and C. A. Reed, *Chem. Commun.*, 2006, 767–769.

54 D. L. Lichtenberger and A. Rai-Chaudhuri, *J. Chem. Soc. Dalton Trans.*, 1990, 2161–2166.

55 J. L. Vincent, S. Luo, B. L. Scott, R. Butcher, C. J. Unkefer, C. J. Burns, G. J. Kubas, A. Lledós, F. Maseras and J. Tomàs, *Organometallics*, 2003, **22**, 5307–5323.

56 U. Schubert, E. Kunz, B. Harkers, J. Willnecker and J. Meyer, *J. Am. Chem. Soc.*, 1989, **111**, 2572–2574.

57 M. W. George, M. T. Haward, P. A. Hamley, C. Hughes, F. P. A. Johnson, V. K. Popov and M. Poliakoff, *J. Am. Chem. Soc.*, 1993, **115**, 2286–2299.

58 R. H. Hill and M. S. Wrighton, *Organometallics*, 1987, **6**, 632–638.

59 K. Hübler, P. A. Hunt, S. M. Maddock, C. E. F. Rickard, W. R. Roper, D. M. Salter, P. Schwerdtfeger and L. J. Wright, *Organometallics*, 1997, **16**, 5076–5083.

60 F. Carre, E. Colomer, R. J. P. Corriu and A. Vioux, *Organometallics*, 1984, **3**, 1272–1278.

61 A. A. Zuzek and G. Parkin, *Dalton Trans.*, 2015, **44**, 2801–2808.

62 Martin. Cowie and M. J. Bennett, *Inorg. Chem.*, 1977, **16**, 2325–2329.

63 A. Shinohara, J. McBee and T. D. Tilley, *Inorg. Chem.*, 2009, **48**, 8081–8083.

64 J. Handzlik and T. Szymańska-Buzar, *J. Organomet. Chem.*, 2014, **769**, 136–143.

65 M. Zyder, A. Kochel, J. Handzlik and T. Szymańska-Buzar, *Organometallics*, 2009, **28**, 5857–5865.

66 A. G. Robiette, G. M. Sheldrick, R. N. F. Simpson, B. J. Aylett and J. A. Campbell, *J. Organomet. Chem.*, 1968, **14**, 279–283.

67 W. T. Robinson and J. A. Ibers, *Inorg. Chem.*, 1967, **6**, 1208–1213.

68 K. Emerson, P. R. Ireland and W. T. Robinson, *Inorg. Chem.*, 1970, **9**, 436–440.

69 U. Schubert, in *Advances in Organometallic Chemistry*, eds. F. G. A. Stone and R. West, Academic Press, 1990, vol. 30, pp. 151–187.

70 U. Schubert and H. Gilges, *Organometallics*, 1996, **15**, 2373–2375.

71 F. Delpech, S. Sabo-Etienne, B. Chaudret and J.-C. Daran, *J. Am. Chem. Soc.*, 1997, **119**, 3167–3168.

72 H. Yang, K. T. Kotz, M. C. Asplund and C. B. Harris, *J. Am. Chem. Soc.*, 1997, **119**, 9564–9565.

73 H. Yang, M. C. Asplund, K. T. Kotz, M. J. Wilkens, H. Frei and C. B. Harris, *J. Am. Chem. Soc.*, 1998, **120**, 10154–10165.

74 K. T. Kotz, H. Yang, P. T. Snee, C. K. Payne and C. B. Harris, *J. Organomet. Chem.*, 2000, **596**, 183–192.

75 J. P. Lomont, S. C. Nguyen and C. B. Harris, *Organometallics*, 2012, **31**, 3947–3957.

76 X. Xie and J. D. Simon, *J. Am. Chem. Soc.*, 1990, **112**, 1130–1136.

77 S. Zhang, G. R. Dobson and T. L. Brown, *J. Am. Chem. Soc.*, 1991, **113**, 6908–6916.

78 S. Zhang, V. Zang, H. C. Bajaj, G. R. Dobson and R. van Eldik, *J. Organomet. Chem.*, 1990, **397**, 279–289.

79 G. R. Dobson and S. Zhang, *J. Coord. Chem.*, 1999, **47**, 409–416.

80 T. S. Murphy, *Ph.D. thesis,* University of Nottingham, 2015.

81 X.-Z. Sun, D. C. Grills, S. M. Nikiforov, M. Poliakoff and M. W. George, *J. Am.*

Chem. Soc., 1997, **119**, 7521–7525.

82 J. A. Calladine, K. Q. Vuong, X. Z. Sun and M. W. George, *Pure Appl. Chem.*, 2009, **81**, 1667–1675.

83 G. I. Childs, D. C. Grills, X. Z. Sun and M. W. George, *Pure Appl. Chem.*, 2001, **73**, 443–447.

84 C. J. Breheny, J. M. Kelly, C. Long, S. O'Keeffe, M. T. Pryce, G. Russell and M. M. Walsh, *Organometallics*, 1998, **17**, 3690–3695.

85 R. N. Perutz and J. J. Turner, *J. Am. Chem. Soc.*, 1975, **97**, 4791–4800.

86 T. E. Bitterwolf, K. A. Lott, A. J. Rest and J. Mascetti, *J. Organomet. Chem.*, 1991, **419**, 113–126.

87 D. C. Grills, *Ph.D. thesis*, University of Nottingham, 1999.

Chapter 3 - TRIR Investigations on the Photochemistry and Photophysics of Tungsten Carbonyl Complexes

3.1 Introduction – Photochemistry Investigations of Group 6 Metal Carbonyl Complexes $M(CO)_6$ (M: Cr, Mo, W)

The group 6 metal carbonyl complexes, $M(CO)_6$ (M: Cr, Mo, W), have been used as prototype complexes for photochemical investigations of transition metal complexes for decades. The primary work was done by Perutz *et al.* in 1970s,[1] with the photochemical investigation of $M(CO)_6$ in numerous low-temperature matrices (Ne, Ar, Kr, Xe, CF_4, SF_6, CH_4, *etc.*). It was found that in low-temperature matrices, upon UV photolysis, group 6 metal carbonyl $M(CO)_6$ undergoes CO loss to form the pentacarbonyl species $M(CO)_5$, which then forms a weak interaction with the surrounding matrix molecule X to form $M(CO)_5X$. Since then, much work has been done on the photochemical investigations of the group 6 metal carbonyl complexes and its derivatives.

Apart from matrix studies, many investigations of the photochemical properties of group 6 metal carbonyls $M(CO)_6$ have been carried out in the solution phase. In the solution phase, at ambient temperature, the reaction rate is significantly accelerated compared to that in low-temperature matrices, thus transient experimental techniques are often required. Therefore, transient UV-Vis and TRIR are often utilised in the solution phase investigations.[2,3] After decades of research, the photochemistry of group 6 metal carbonyls $M(CO)_6$ in the solution phase is well understood. It is found that in solution after UV photolysis, similar to that in low temperature matrices, one CO ligand will be ejected and form the pentacarbonyl species $M(CO)_5$, within hundreds of femtoseconds.[4,5] Compared to the experiments in gas phase, where UV photolysis of metal complexes can result in multiple CO loss, the only formation of the pentacarbonyl species $M(CO)_5$ is attributed to the energy relaxation by energy diffusion into the condensed phase.[6,7,8] It is found that the unsaturated pentacarbonyl $M(CO)_5$ will be solvated by surrounding solvent

molecules to form a $M(CO)_5$(sol) species within 1~2 ps, such as in pentanol,[9] methanol,[5,10] and cyclohexane.[10] The formation of the unsaturated 16 electron species $M(CO)_5$, endows group 6 metal carbonyls with significant photochemical reactivity. Many reactions have been investigated for the $M(CO)_6$ complexes.[2,3,11] In most alkane solvents, it is recognised that alkane molecules can form weak interactions with the $M(CO)_5$ species *via* a C-H in a 3-c-2-e (3-centre-2-electron) agostic fashion.[12] When there exists ligands with stronger coordinating abilities than alkane molecules, then the ligand exchange reaction between $M(CO)_5$(alkane) and $M(CO)_5$(dopant) will take place.

In this work, we are especially interested in investigating the photochemistry of $W(CO)_6$ and its derivative complexes using TRIR, which will support the future TR-XAFS investigations. Different types of reactions are divided into different sections, and will be introduced in detail in the corresponding sections.

3.1.1 E-H Bond Activation (E: Si, Ge, Sn) by $W(CO)_6$

As has been discussed in the Introduction Section of Chapter 2, E-H bond (E: Si, Ge, Sn) activation is essential in industrial catalytic processes, and has attracted much attention during the recent decades. Group 6 metal carbonyl complexes are also discovered to act as catalysts in the hydrosilylation process of alkenes.[13,14,15] Therefore, much research work has been focused on exploring the mechanism of Si-H bond activation by Group 6 metal carbonyl complexes. Zhang and co-workers conducted flash photolysis experiments of $Cr(CO)_6$ in hexane with silanes.[16] $Cr(CO)_5(HSiEt_3)$ was generated after photolysis, the Si-H bond was found to coordinate to the Cr centre in an η^2-fashion. It is also found that opposite to $CpMn(CO)_2$, $(\eta^6\text{-}C_6H_6)Cr(CO)_2$ and related fragments, for the $Cr(CO)_5$-silane species, the stability of $Cr(CO)_5$-silane decreases when the Si is attached with more electron-withdrawing groups. For $CpMn(CO)_2(HSiR_3)$ and $(\eta^6\text{-}C_6H_6)Cr(CO)_2(HSiR_3)$ complexes, the stabilities increase when the Si is substituted by more electron withdrawing groups, as electron withdrawing groups on silane can facilitate the π-backbonding from the metal centre d-orbital to the Si-H σ^*-orbital. As discussed in Chapter 2, the interaction between the metal centre and the Si-H composes of two interactions, the σ-donation from Si-H to the metal centre, as well as the π-back-donation from the metal d-orbital to the σ^*-orbital of Si-H, when the coordination mode between the metal centre and the Si-H is in an η^2-fashion. As for the $CpMn(CO)_3$ and $CpRe(CO)_3$ complexes discussed in Chapter 2, increasing the electron density on the metal centre *via* electron rich alkyl groups on the Cp ring facilitates the interaction between the metal centre and Si-H through strengthening the π-back-donation. In the author's view, for $Cr(CO)_5(HSiR_3)$, the energy level of the Cr d-orbital is much lower compared to that of $CpMn(CO)_2(HSiR_3)$ and $(\eta^6\text{-}C_6H_6)Cr(CO)_2(HSiR_3)$ complexes. The Cr is also strongly electrophilic, therefore the π-backbonding is less important, and the predominant interaction between Cr and Si-H is σ-donation from Si-H to Cr centre. Also, compared to the $CpMn(CO)_2(HSiR_3)$ and $(\eta^6\text{-}C_6H_6)Cr(CO)_2(HSiR_3)$ complexes, the interaction is found to be weaker between Cr and Si-H in $Cr(CO)_5$-silane complexes.

Investigations on Mo and W carbonyl complexes have also been conducted.

Matthews *et al.* investigated the coordination modes between the metal centre and Si-H of $M(CO)_5$-silane complexes (M: Cr, Mo, W) using NMR spectroscopy.[17] The η^2-fashion of the bond between the metal centre and Si-H of $HSiEt_3$ for $M(CO)_5(HSiEt_3)$ complexes is supported by NMR spectroscopy. For comparison, the $[Re(CO)_5(\eta^2\text{-}HSiEt_3)]^+$ complex shows much lower J_{SiH} than the $M(CO)_5(HSiEt_3)$ complexes (M: Cr, Mo, W), which further supported that σ-donation dominates the interaction between the group 6 metal centres and Si-H. $M(CO)_5(HSiPh_3)$ complexes have also been investigated. NMR shows higher J_{SiH} for $M(CO)_5(HSiPh_3)$ than $M(CO)_5(HSiEt_3)$, while $Mo(CO)_5(HSiPh_3)$ was not observed, which both may reflect that steric factors could influence the interaction between the metal centre and Si-H. For both $HSiEt_3$ and $HSiPh_3$, it is found that Si-H is more activated by W than by Cr. The ligand exchange reaction between C-H and Si-H of group 6 metal carbonyl complexes has also been investigated in terms of bond energies. Burkey and co-workers have conducted photoacoustic calorimetry studies on the C-H/Si-H ligand exchange reaction of $M(CO)_6$ (M: Cr, Mo, W) in alkane solvents.[18] It is found that the enthalpies for CO substitution by triethylsilane and alkanes are both positive, suggesting that M-C-H and M-Si-H bondings are weaker than M-CO. The ethalpies are summarised in Table 3.1.

Table 3.1 *Enthalpies of CO substitution by $HSiEt_3$ (ΔH_1) and alkanes (ΔH_2). Reproduced from Ref 18.*

Compounds	ΔH_1 / kcal mol^{-1}	ΔH_2 / kcal mol^{-1}
$Cr(CO)_6$	15.7 ± 1.1	27.2 ± 1.2
$Mo(CO)_6$	18.5 ± 0.5	31.8 ± 1.3
$W(CO)_6$	18.2 ± 0.5	32.6 ± 0.4
$PhCr(CO)_3$	17.1 ± 2.5	32.8 ± 0.3
$CpMn(CO)_3$	30.9 ± 1.0	44.7 ± 1.4

The enthalpies by $HSiEt_3$ for all complexes are lower than that by alkanes, as shown in Table 3.1, suggesting that the M-Si-H bonding is more stable than M-C-H. The IR spectroscopy also indicates that the $W(CO)_5(HSiEt_3)$ complex is more stable than the $Cr(CO)_5(HSiEt_3)$ complex.

However, little is known about the transient reaction mechanisms on the ultrafast timecale. TRIR is a powerful technique in reaction mechanism investigation on the ultrafast timescale. Kotz *et al.* investigated the Si-H bond activation of trialkylsilanes by group 6 carbonyls $M(CO)_6$ using ultrafast TRIR,[19] and it is found that in neat trialkylsilanes ($HSiEt_3$, $HSiPr_3$), the photo-initiated CO-loss species $M(CO)_5$ is quickly solvated by coordinating to the alkyl-group of the silane within a few ps, and then the C-H is replaced by the Si-H of silane in few nanoseconds, *i.e.* coordination to the Si-H bond to form the 3-c-2-e σ-complex. The ligand exchange reaction is found to be of dissociative mechanism.

In this work, we are especially interested in the investigation of reaction mechanism of the activations of tributylsilane ($HSiBu_3$), tributylgermane ($HGeBu_3$) and tributylstannane ($HSnBu_3$) by $W(CO)_6$ in alkane solutions using TRIR, with which ultrafast reaction process can be revealed and hopefully the results are supportive for future TR-XAFS investigations.

3.1.2 Interactions between Halocarbons and $W(CO)_6$

Halocarbons are useful not only as intermediates in synthesis, but also as solvents in many reaction processes. Therefore, significant amount of research has focused on exploring the properties of halocarbons during the recent decades. In this work, we are especially interested in the C-X (X: F, Cl, Br, I) bond activation of haloalkanes and halobenzenes by $W(CO)_6$, using TRIR to explore the ultrafast reaction process.

Properties of C-X (X: F, Cl, Br, I) bonds vary significantly due to different properties of the halogens. Some of the physical properties of halogens and the halocarbon, MeX, are shown in Table 3.2 and Table 3.3, respectively.

Table 3.2 *Physical property parameters of halogens. Reproduced from Ref. 20.*[20]

Halogen atom (X)	F	Cl	Br	I
Pauling electronegativity (χ)	3.98	3.16	2.96	2.66
$\Delta\chi$ (C-X)	1.43	0.61	0.41	0.11
Covalent radius (Å)	0.64	0.99	1.14	1.33
Ionic radius of X^- (Å)	1.33	1.81	1.96	2.20
Van der Waals radius (Å)	1.47	1.75	1.85	1.96
Ionization energy (eV)	-17.42	-12.97	-11.81	-10.45
Electron affinity (eV)	+3.448	+3.613	+3.363	+3.063

Table 3.3 *Physical property parameters of the halocarbon MeX (X: F, Cl, Br, I). Reproduced from Ref. 20.*

MeX	MeF	MeCl	MeBr	MeI
Dipole moment (D)	1.85	1.87	1.81	1.62
C-X bond distance (Å)	1.831	1.767	1.937	2.135
C-X bond dissociation energy (kcal mol^{-1})	108	83.5	70	56
Ionization energy (eV)	13.04	11.3	10.65	9.85
Bond polarizability ($x10^{-24}$ cm^3)	0.96	3.67	5.04	8.09
Ionization energy of C_6H_5X (eV)	13.85	11.7	11.25	10.55

As shown in Table 3.2 and Table 3.3, down the group from F to I, the electronegativity decreases, and the relative electronegativity to carbon in C-X bond ΔX decreases drastically from F to I. The C-X bond dissociation energy also decreases drastically from F to I. For C-F the dissociation energy is nearly double than that of C-I. F is considered to be highly electron withdrawing and also much smaller in size compared to the other halogens. Due to its high electronegativity, the C-F bond is extremely stable. In fact, the C-F is known to be the strongest bond with carbon, with a dissociation enthalpy of *ca.* 500 kJ mol^{-1}.[21] Therefore, perfluoroalkanes are used as inert solvents in many reactions due to the extremely strong bonding between C and F. While Br and especially I are considered to have "softer" properties compared to F, with weaker oxidation abilities for Br_2 and I_2 and stronger reducibilities for Br^- and I^- anions.

In this work, we are especially interested in C-X (X: F, Cl, Br, I) bond activations by the low valent W (0) complex $W(CO)_6$.

Most of the C-X bond activations by transition metals reported are by the electron rich transition metal centres d^n ($n \geq 6$), *via* oxidative addition.[22] Oxidative addition mechanisms generally can be classified into 3 types. Firstly, the concerted mechanism, is the most common oxidative addition mechanism for most nonpolar substrates such as H_2 and substrates with weak polarity such as C-H and Si-H, and also common for unsaturated halocarbons, such as haloarenes, haloalkynes and haloalkenes. The substrate first coordinates to the transition metal centre in a 3-c-2-e fashion to form the σ-comlex, which is then followed by the bond cleavage due to strong back-donation from the metal centre to the σ^* orbital of the X-Y bond, as shown in Figure 3.1.

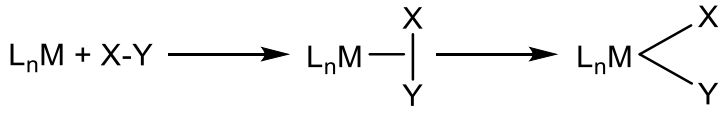


Figure 3.1 *Scheme of the concerted mechanism. Substrate first coordinates to the metal centre to form the 3-c-2-e interaction, which may be followed with the cleavage of the X-Y bond.*

The second is the S_N2-type mechanism. For some substrates of higher polarities, the S_N2 mechanism is more often observed, such as the carbon-halide bond activation in saturated haloalkanes. In the reaction process, the less electronegative atom in the bond is first attacked by the nucleophilic transition metal centre, which results in the cleavage of the bond. Then this step is quickly followed by coordination with the anion moiety, as shown in Figure 3.2.

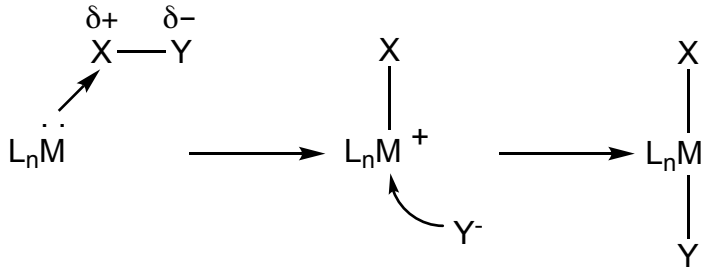


Figure 3.2 *Scheme of the S_N2 mechanism. For substrate with high polarity, the electron-positive end of the bond first coordinates to the electron rich metal centre and then the bond is cleaved, which is then followed by the quick coordination of the anion moiety.*

The third is the radical mechanism, which is also commonly observed for the activation of unsaturated halocarbons. The radical mechanism can be divided into two categories, the chain and the non-chain mechanisms. Their main difference is that the chain mechanism usually requires an initiator for the reaction, as shown in Figure 3.3.

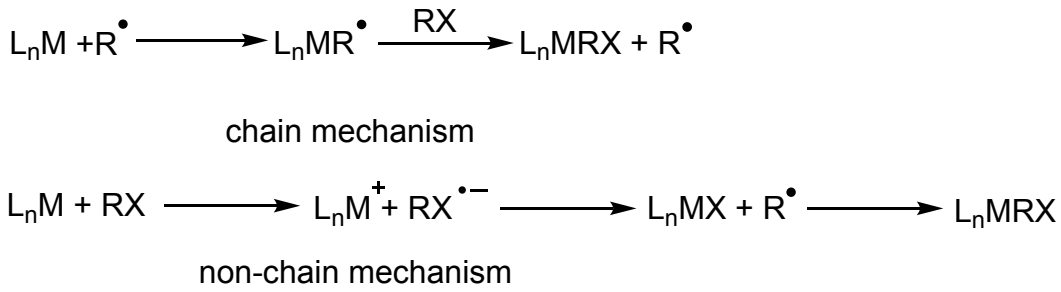


Figure 3.3 *Scheme of the radical mechanism. The radical mechanism is also typical for many substrates with high polarities. For the chain mechanism, a radical initiator is needed which coordinates to the metal centre first, and followed by the coordination of the substrate, the radical is then released. For the non-chain mechanism, the electron is first transferred from the metal centre to the substrate, and then the metal centre coordinates to the substrate and releases one radical,*

which is then followed by the coordination to the radical.

The carbon-halogen bond activation in many unsaturated halocarbons are found to follow the concerted and the radical mechanisms, while for the saturated halocarbons, the S_N2 mechanism is more commonly observed.

Therefore, either for the concerted or the radical mechanism, an electron rich metal centre and a weak carbon-halogen bond is desired for the oxidative addition of C-X. For the transition metals, the tendency for oxidative addition generally increases in the transition metal section of the periodic table from right to left, and down the groups. Metal centres of low valent state are considered to have larger tendency for oxidative addition. For instance, it was discovered by Crabtree and co-workers that for the Ir complex $[IrH_2(IMe)_2(PPh_3)_2]SbF_6$, the IMe ligands coordinate to the Ir (III) centre *via* the lone pair of I, while when the H_2 ligand is removed and Ir(III) is reduced to Ir(I), oxidative addition of I-C occurs and leads to the formation of $[MeIr(\mu\text{-}I)(PPh_3)_2]_2$.[23] Metal anion fragments are reported to initiate difficult oxidative additions. For instance, $[CpFe(CO)_2]^-$, $[Re(CO)_5]^-$ are known to be able to initiate C-F bond activation.[24,25] Ligands in the metal complexes can alter the electron density of the metal centre, thus influence the oxidative addition. For instance, triphenylphosphine (PPh_3) is considered to be a σ-donor (*via* the lone-pair) that can increase the electron density on the metal centres. While carbonyl CO is considered to be a π-acceptor due to the π-backbonding from the metal centre to the CO π-orbital, therefore CO is expected to reduce the electron density on the metal centres to some extent.[26]

As C-Cl, C-Br, and C-I are more reactive compared to C-F due to the properties discussed before, thus here transition metal interactions with C-Cl, C-Br, and C-I bonds are discussed first.

For the Cl-, Br- and I-halocarbons RX (R: alkyl, aryl; X: Cl, Br, I), as shown in Table 3.2 and Table 3.3, compared to F, the C-X bonds are much weaker, and the C-X polarizability increases significantly down the group. These factors make the oxidative addition of RX (X: Cl, Br, I) much easier than C-F. Meanwhile, the

increasing basicity of Cl, Br and I makes them also good electron-donating ligands. Therefore, for C-X (X: Cl, Br, I), when coordinating to transition metal centres, apart from oxidative addition, coordination *via* the lone pair of X has also been observed.

It is found that C-Cl, C-Br and C-I may have different coordination modes to transition metal centres compared to C-F. Research by Zhang *et al.* reveals that the ligand exchange rate between $Cr(CO)_5$(sol) and $Cr(CO)_5$(1-hexane) (sol: C_6H_5X. X: H, F, Cl, Br) is highly related to the solvent types.[27,28] For Cl-benzene and Br-benzene, the ligand exchange rates are much slower than benzene and F-benzene, but all follow the dissociative mechanism. The reason is the differences in binding modes. The coordination from benzene and F-benzene to the $Cr(CO)_5$ fragment is *via* the "CH=CH ring edge", while for Cl-benzene and Br-benzene, the coordination is more possibly *via* the lone pairs of Cl and Br. The bindings of Cl-benzene and Br-benzene to the $M(CO)_5$ fragment (M: Cr, Mo, W) are also revealed to be stronger than F-benzene.[29] Kulawiec *et al.* investigated the interactions beween a series of ruthenium (II) and iron (II) cyclopentadienyl complexes with iodoalkanes, p-iodotoluene, and chelating (P, X) (*o*-halophenyl) diphenylphosphine (X=Cl, Br) ligands.[30] For these halocarbons, it is found that they coordinate to the ruthenium (II) and iron (II) complexes *via* the σ-donation of the lone pair of the X atoms and the C-X bond is retained.

As expected, according to the properties of Cl, Br, I, the electron-donation ability increases as Cl <Br <I. It was discovered by Crabtree *et al.* that for the Ir (III) complex $[IrH_2S_2L_2]BF_4$ (S=Me_2CO; L=PPh_3), under certain circumstances it will lose the S group and expose two cis-binding sites.[31] Interactions with a series of X_2-benzenes (X: Cl, Br, I) have been investigated. It is found that the most stable X_2-benzene bound complex is $[IrH_2(C_6H_4I_2)(PPh_3)_2]BF_4$, which is the product of $[IrH_2S_2L_2]BF_4$ complex with $C_6H_4I_2$ in CH_2Cl_2 at room temperature. NMR and XRD results suggested that in $[IrH_2(C_6H_4I_2)(PPh_3)_2]BF_4$, $C_6H_4I_2$ coordinates to the Ir centre *via* the two I atoms. It is found that only MeCN and bipyridyl can displace the $C_6H_4I_2$ in $[IrH_2(C_6H_4I_2)(PPh_3)_2]BF_4$. Neither Me_2CO or THF can displace $C_6H_4I_2$, while EtOH is found to be competitive with $C_6H_4I_2$ in solution. The mutual

displacement of ligands is in the sequence: THF <Me_2CO <EtOH <MeCN <bpy. For C_6H_4BrI, it is also found to be able to react with $[IrH_2S_2L_2]BF_4$ to form $[IrH_2(C_6H_4BrI)(PPh_3)_2]BF_4$, while in $[IrH_2(C_6H_4BrI)(PPh_3)_2]BF_4$, C_6H_4BrI is proposed to bind to the Ir centre *via* Br and I atoms, and Me_2CO is found to be competitive with C_6H_4BrI, while for $C_6H_4I_2$, Me_2CO is unable to displace $C_6H_4I_2$. For $C_6H_4Br_2$, $C_6H_4Cl_2$ and C_6H_5I, direct reaction with $[IrH_2S_2L_2]BF_4$ is unsuccessful, $[IrH_2(L)_2(PPh_3)_2]BF_4$ (L: $C_6H_4Br_2$, $C_6H_4Cl_2$, C_6H_5I) is formed by hydrogenation of $[Ir(cod)(PPh_3)_2]^+$ in $CDCl_3$ in the presence of L (cod: 1,5-cyclooctadiene). L can be completely displaced by EtOH. For MeI, reaction with $[IrH_2S_2L_2]BF_4$ to form $[IrH_2(MeI)_2(PPh_3)_2]BF_4$ is successful, while MeI cannot be completely displaced by EtOH. The overall stability constants according to the author is in the order: $C_6H_4I_2$>C_6H_4BrI>RI (R: Me, Et, i-Pr) >C_6H_5I >$C_6H_4Br_2$ >$C_6H_4Cl_2$. Steric factors also seem to play a significant role in the reaction process. For all halocarbons studied, no binding *via* the aromatic ring was observed, which may reflect better electron donation of halogens compared to the arene rings.

Burk *et al.* also discovered that $[Ir(cod)Cl]_2$ complex (cod: 1,5-cyclooctadiene) can reacts with *o*-$BrC_6H_4PPh_2$ in CH_2Cl_2 under 20 °C for 1 day and generates $[Ir(cod)(\eta^1\text{-}PPh_2C_6H_4Br)Cl]$ in which Ir coordinates to *o*-$BrC_6H_4PPh_2$ in an η^1-fashion *via* the P atom. Treatment of $[Ir(cod)(\eta^1\text{-}PPh_2C_6H_4Br)Cl]$ in the presence of $AgSbF_6$ leads to the formation of $[Ir(cod)(\eta^2\text{-}PPh_2C_6H_4Br)Cl]$, in which Ir coordinates to *o*-$BrC_6H_4PPh_2$ *via* both the P and Br atoms. The strong resistance to oxidative addition of $[Ir(cod)Cl]_2$ complex is attributed to the electron withdrawing nature of the cod ligand according to the author. The rhodium analogues have been prepared in the same way, and reactions with *o*-$ClC_6H_4PPh_2$ lead to similar results.[32]

For the oxidative addition of C-X, much research work has suggested that the easiness of oxidative addition of the C-X bond follows the order: C-I >C-Br >C-Cl. Fitton and co-workers investigated the C-X oxidative addition by $Pd(PPh_3)_4$ in benzene solution, and found that $Pd(PPh_3)_4$ can react with a series of halocarbons XR at room temperature, including MeI and PhI, to form the oxidative addition product $PdX(PPh_3)_2R$ in a *trans*-configuration,[33] as shown in Figure 3.4.

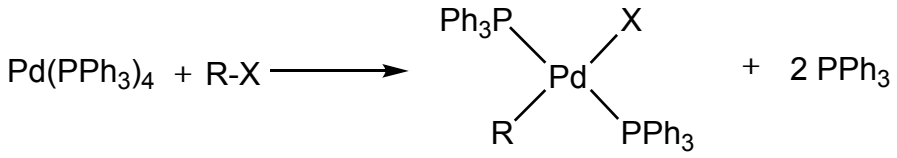


Figure 3.4 *Reaction process proposed for $Pd(PPh_3)_4$ with halocarbon XR. Reproduced from Ref. 33.*

Then Fitton and co-workers continued to investigate the oxidative addition of $Pd(PPh_3)_4$ with other haloarenes,[34] and discovered that the order of the reactivity of oxidative addition with $Pd(PPh_3)_4$ for haloarenes PhX (X: Cl, Br, I) is PhI >PhBr >PhCl. PhI can react with $Pd(PPh_3)_4$ forming the *trans*-$PdI(PPh_3)_2R$ as shown in Figure 3.4 at room temperature, for PhBr the temperature needs to be raised to 80 °C to generate the analogue *trans*-$PdBr(PPh_3)_2R$ complex, while for PhCl, even when the temperature is as high as 135 °C, the reaction is unsuccessful, while raising the temperature higher than 135 °C is unachievable as $Pd(PPh_3)_4$ would undergo thermal decomposition. It is also found that when PhCl is substituted with electron donating groups, it is unreactive, while when substituted with electron withdrawing groups, its reactivity increases, as in the order: 4-$NO_2C_6H_4Cl$ >4-CN-C_6H_4Cl >4-$PhCOC_6H_4Cl$ >PhCl. For the flouroarenes, it is found that whether for flourobenzene, or flouroarenes with electron donating groups or electron withdrawing groups, no analogue reaction was successful at temperature of 135 °C.

Hartwig and co-workers investigated the mechanism of oxidative addition of PhX (X: Cl, Br, I) to Pd (0) complex [Pd(Q-phos-tol)$_2$] (denoted as complex 2 in Figure 3.5).[35] The potential reaction paths and results are shown in Figure 3.5.

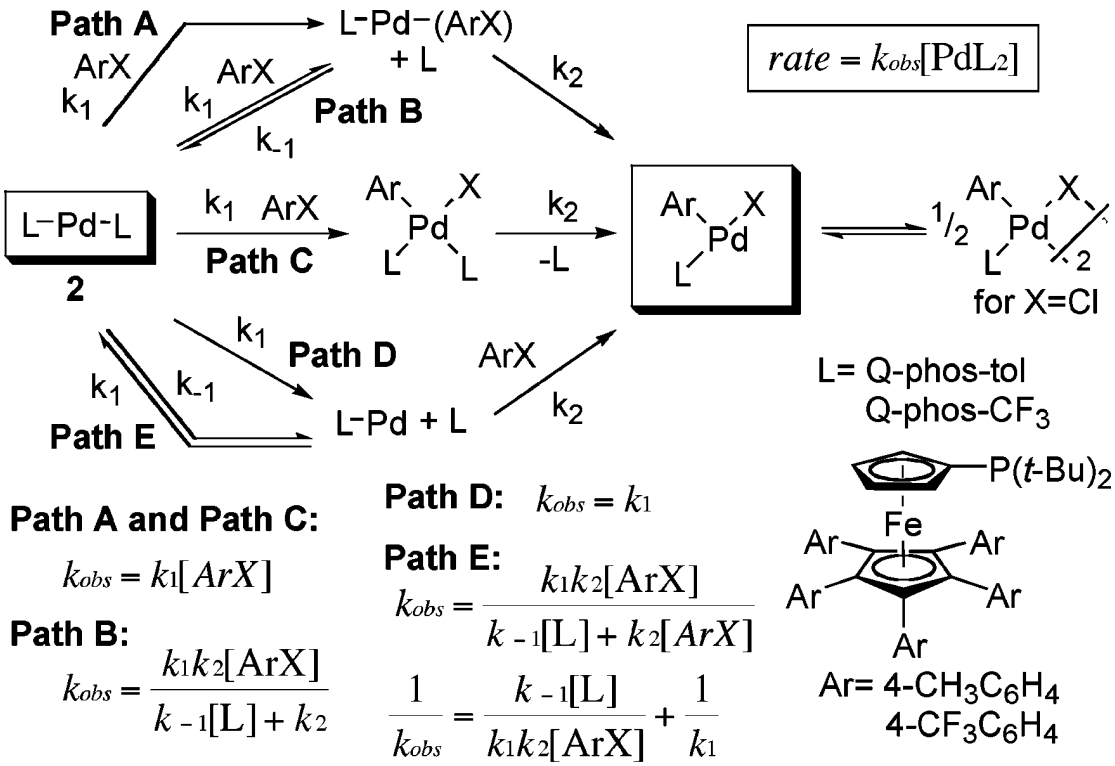


Figure 3.5 *Potential reaction paths and investigation results of the oxidative addition of PhX (X: Cl, Br, I) by the Pd (0) complex [Pd(Q-phos-tol)$_2$] in neat PhX solvents at 30-65 ºC.*[35]

Several reaction paths of oxidative addition have been discovered. It is found that PhCl, PhBr, PhI take different reaction mechanisms. For PhI, it takes the path A as shown in Figure 3.5. At 30 ºC in neat PhI, [Pd(Q-phos-tol)$_2$] complex first loss one phosphine ligand in an associative way with ArX to form the intermediate L-Pd-(ArX), in which Pd is considered to coordinate to ArX either in an η^1- fashion to I or in an η^2-fashion to the benzene ring. This is followed by the C-I bond cleavage and formation of the oxidative addition product [Pd(Q-phos-tol)(Ar)I]. For PhBr, it is observed to follow the path D, for which an irreversible dissociative ligand loss is suggested before oxidative addition, while for PhCl the ligand loss is reversible.

Bond activation of C-X (Cl, Br, I) in halocarbons by group 6 metal complexes has also been investigated. Richmond and co-workers have investigated the C-X (Cl, Br, I) bond activation by the chelated W complexes.[36] It is reported that for ligand A with structure shown in Figure 3.6, one C-X (X: Cl, Br, I) bond can be cleaved upon

reaction with the W (0) complex $W(CO)_3(NCR)_3$ to form the 7-coordinated W (II) species (Figure 3.6).

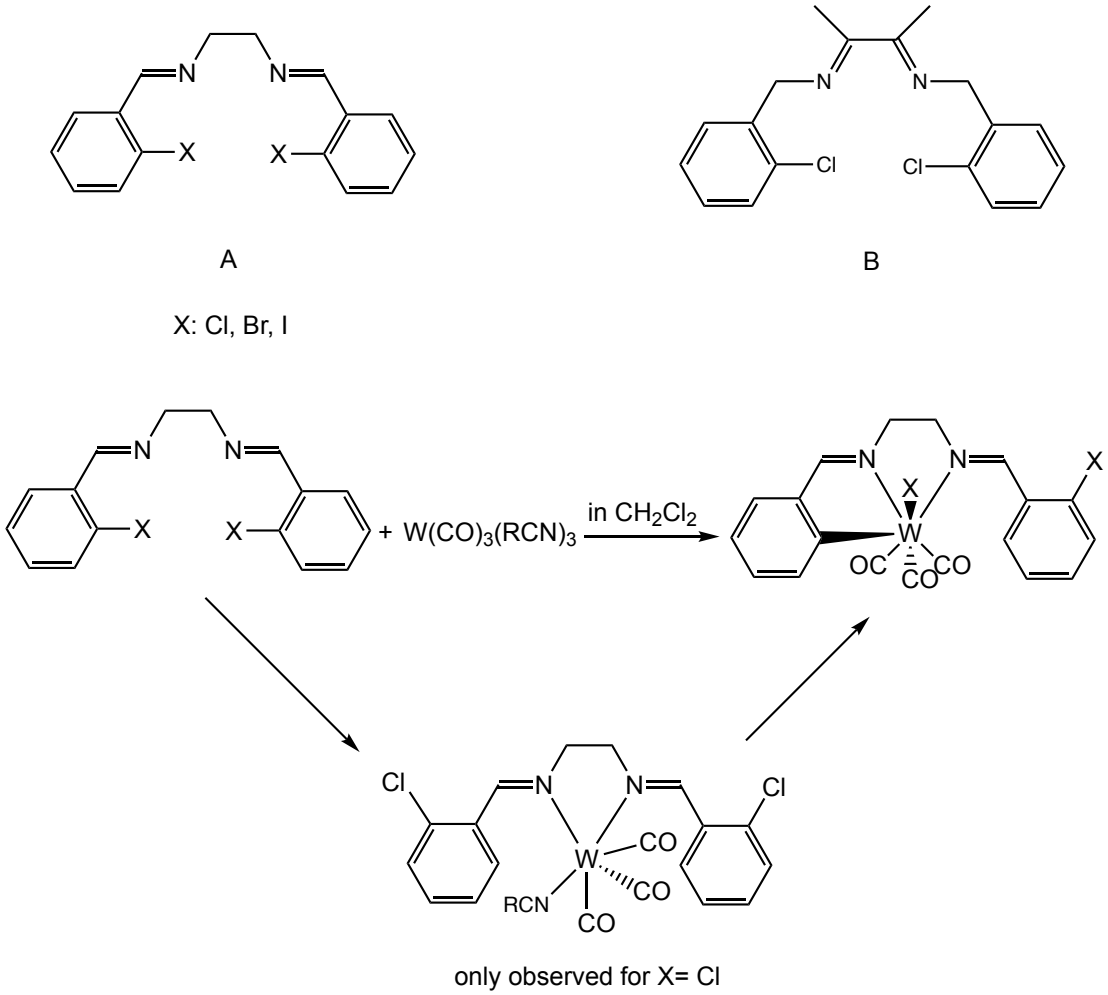


Figure 3.6 *C-X (X: Cl, Br, I) bond activation by the W (0) complex $W(CO)_3(NCR)_3$ at room temperature in CH_2Cl_2.*[36]

For X=Cl, an intermediate in which W coordinates to two N donors with one NCR ligand left is observed. IR frequencies of different species are summarised in Table 3.4.

Interestingly, it is found that for ligand B as shown in Figure 3.6, no oxidative addition was observed under the same conditions with ligand A. Under the same conditions, ligand B is observed to react with $W(CO)_3(NCR)_3$ to form $W(CO)_3(NCR)(B)$, which combines with CO when exposed to atmosphere to form $W(CO)_4(B)$. The IR frequencies of related species are summarised in Table 3.4.

Table 3.4 *IR frequency of different species observed in oxidative addition shown in Figure 3.6. Reproduced from Ref. 36.*

species	ν(CO) /cm^{-1}
$W(CO)_3(NCR)_3$	1914, 1793
$W(CO)_3$(A-Cl)	2016, 1941, 1911
$W(CO)_3$(A-Br)	2014, 1936, 1905
$W(CO)_3$(A-I)	2010, 1939, 1909
$W(CO)_3$(NCR)(A-Cl)	1906, 1790
$W(CO)_3$(NCR)(B)	1918, 1814
$W(CO)_4$(B)	2009, 1905, 1852

Comparing the IR frequencies of species $W(CO)_3$(NCR)(A-Cl) and $W(CO)_3$(NCR)(B) may lead to the assumption that for $W(CO)_3$(NCR)(A-Cl), the imine in the metallacycle can promote the C-Cl bond activation *via* conjugation with the phenyl ring. However, according to the author, the steric factors are more important, as in ligand B, the framework is more likely to be tortured during oxidative addition than ligand A. And most importantly, as will be discussed later for the C-F bond activation, the chelation effect plays a significant role in the C-X bond activation.

Interestingly, a "ring walk" mechanism has been discovered by Strawser *et al.*[37] The C-Br activation of 4-[*trans*-2-(4-bromophenyl)vinyl]pyridine by $Pt(PEt_3)_4$ is *via* a "ring walk" by Pt through the conjugated ring. The reaction process is shown in Figure 3.7.

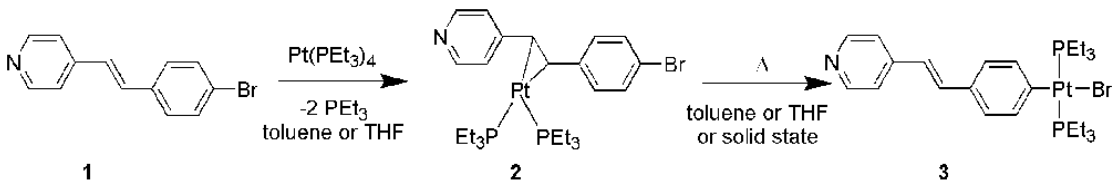


Figure 3.7 *Oxidative addition of [2-(4-bromophenyl)vinyl]pyridine to $Pt(PEt_3)_4$.*[37]

Complex 1 is found to react with $Pt(PEt_3)_4$ in THF to form complex 2 at room temperature for 2 days. In complex 2, the Pt metal centre coordinates to the C=C

double bond of the bridge part. Complex 2 is stable and can be isolated as a yellow solid. Thermolysis of complex 2 in solution or in solid state at 65 °C leads to the formation of complex 3. It is also found that reaction of complex 1 with $Pt(PEt_3)_4$ in toluene or THF in a sealed pressure vessel at 65 °C for 1 day leads to the formation of complex 3. Complex 3 is also stable and can be isolated as a white solid. Therefore, it is concluded that the formation of complex 2 is kinetically favored while formation of 3 is thermodynamically favoured. Interestingly, it was discoved that, for the conversion from complex 2 to complex 3, many phenomena have suggested an intramolecular "ring walk" mechanism rather than dissociative mechanism as expected. Kinetics reveal that conversion from complex 2 to complex 3 follows first-order kinetic, and no intermediate has been observed, indicating a unimolecular reaction. Also, the conversion rate from complex 2 to complex 3 is independent of concentration of complex 2, and is not affected by excess PEt_3 in presence. According to the results, Strawser *et al.* has proposed the "ring walk" mechanism, that the Pt centre is moving through the conjugated ring progressively until the final oxidative addition of the C-Br bond. This theory is also supported by DFT calculations. Reactions of the I analogue complexes have also been investigated, and it is found that for the I analogue complex with same structure to complex 2, it can convert completely to the oxidative addition product, the C-I activated complex with same structure to complex 3 in THF within 2 days just at room temperature, while complex 2 requires thermolysis.

Lucassen *et al.* has extended the work by investigating the oxidative addition of the fluorinated complex 4'-bromo-2',3',5',6'-tetrafluorostilbazole (1, Figure 3.8) by stoichiometric amount of $Pt(PEt_3)_4$ in toluene or THF under atmosphere of N_2 at room temperature. The rapid direct oxidative addition of Ar_f-Br (2, Figure 3.8) was observed, while the intermediate in which Pt coordinates to the C=C bond in the "bridge" between two rings (3, Figure 3.8) was not observed,[38] as shown in Figure 3.8.

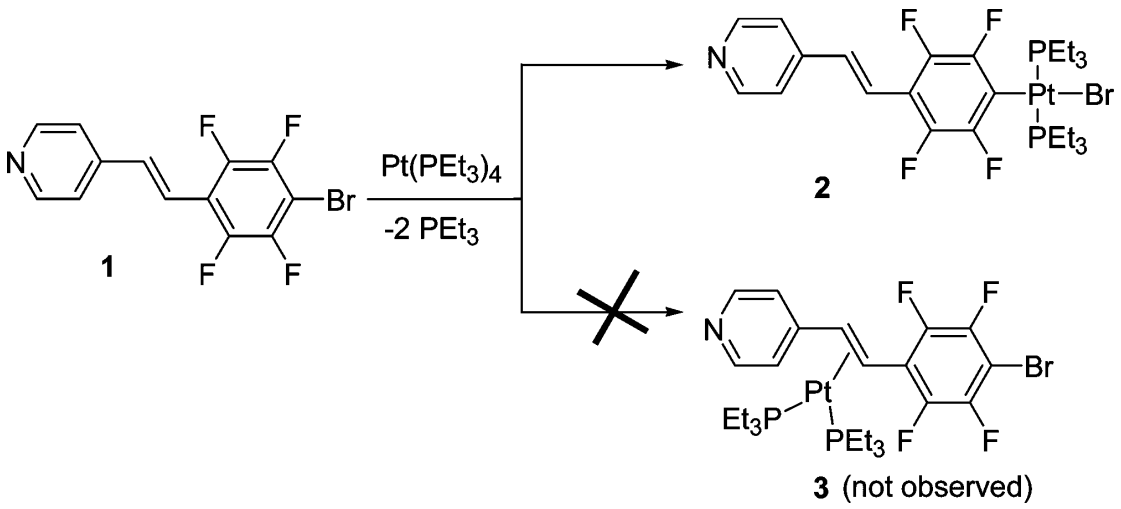


Figure 3.8 *Reaction scheme of the direct oxidative addition of 4'-bromo-2',3',5',6'-tetrafluorostilbazole to stoichiometric amount of $Pt(PEt_3)_4$.*[38]

Interestingly, when complex 1 reacts with twice the stoichiometric amount of $Pt(PEt_3)_4$, Pt coordination to C=C and the oxidative addition of Ar_f-Br are both observed, as shown in Figure 3.9.

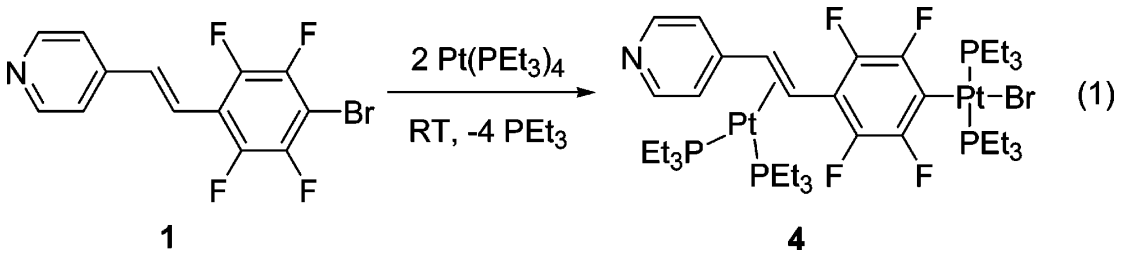


Figure 3.9 *Reaction scheme of the oxidative addition of 4'-bromo-2',3',5',6'-tetrafluorostilbazole to double stoichiometric amount of $Pt(PEt_3)_4$.*[38]

However, for pentafluorostilbazole, reaction with stoichiometric amount of $Pt(PEt_3)_4$ results in the exclusive formation of the C=C bound complex, as shown in Figure 3.10.

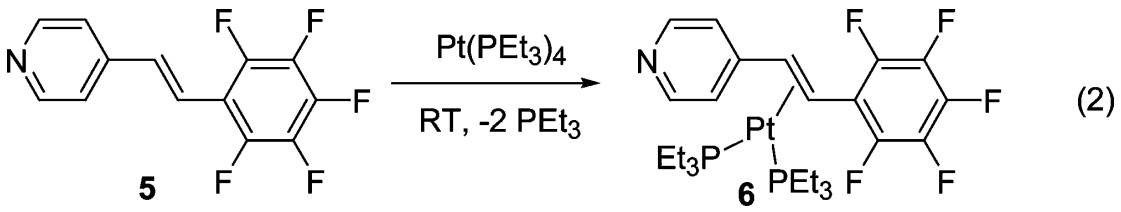


Figure 3.10 *Reaction scheme of pentafluorostilbazole to stoichiometric amount of $Pt(PEt_3)_4$.*[38]

As the result shows, for complex 1, the oxidative addition of Ar_f-Br to Pt is both kinetically and thermodynamically preferred, direct oxidative addition of Ar_f-Br is observed without the C=C bound intermediate, unlike the un-fluoronated stilbasole as discussed before. Therefore, it shows how the strong electron withdrawing fluorine atoms can affect the chemical properties of the haloarenes. As the metal centre tends to coordinate to more electron rich C=C moieties, the extremely electronegative fluorine atoms may significantly decrease the electron density on the C=C bond, thus no "ring-walk" is observed for the fluorinated stilbazoles.

For fluorocarbons, situations are more complicated due to the unique properties of F. The interaction between C-F bond with transition metal is relatively weak due to the extremely low polarizability of C-F bond, therefore perfluoronated alkanes are often used as inert solvents for many reactions. Interactions between group 6 metal centres and C-F have long been discovered. Perutz *et al.* observed interaction between photo-initiated $Cr(CO)_5$ with CF_4 in low-temperature matrix.[1] It was observed that the visible band maximum of $Cr(CO)_5(CF_4)$ (547 nm) is similar to that with Ar, $Cr(CO)_5(Ar)$ (533 nm), indicating that the interaction between $Cr(CO)_5$ and CF_4 is extremely weak ($Cr(CO)_5(Ne)$: 624 nm, $Cr(CO)_5(CH_4)$: 489 nm, for comparison). Brown *et al.* investigated the interaction of a series of fluoroalkanes with $W(CO)_6$ in gas-phase.[39] It is found that the interaction of fluoroalkanes with $W(CO)_6$ is dependent on the extent of fluorination and substitution position of the F atoms. For fluoroalkanes CF_4, CF_3H and CH_3CF_3, no interactions with $W(CO)_5$ were observed. While the interactions with $W(CO)_5$ were observed for CH_3F, CH_3CH_2F and CH_2F_2 with lower fluorination extents. According to the author, the lack of interaction of $W(CO)_5$ with perfluorinated alkane CF_4 reflected that there is little or no interaction between C-F or the F lone pair with $W(CO)_5$. The interactions of CH_3F, CH_3CH_2F and CH_2F_2 with $W(CO)_5$ fragment are considered *via* the 3-c-2-e C-W-H interaction. Higher fluorination extent is expected to reduce the σ-donation from C-H to the W centre.

However, there are examples reported for intramolecular F coordination to transition metal centres. Uson *et al.* reported the first examples of fluorocarbons coordinating to transition metal complexes.[40] Crabtree and co-workers reported the

first spectroscopic evidence of fluorocarbon 8-fluoroquinoline coordinating to transition metal iridium using NMR.[41] Brookhart *et al.* reported that photolysis of (η^2-dfepe)$Cr(CO)_4$ (dfepe: $(C_2F_5)_2PCH_2CH_2P(C_2F_5)_2$) in low temperature matrices of Ar, CH_4, and Xe at 12 K leads to the formation of both (η^2-dfepe)$Cr(CO)_3$(S) (S= matrix Ar, CH_4 and Xe) and (η^1-F-$F_4C_2C_2F_5PCH_2CH_2P$-$(C_2F_5)_2$)$Cr(CO)_3$, demonstrated by IR and UV-Vis.[42] The reaction scheme is shown in Figure 3.11.

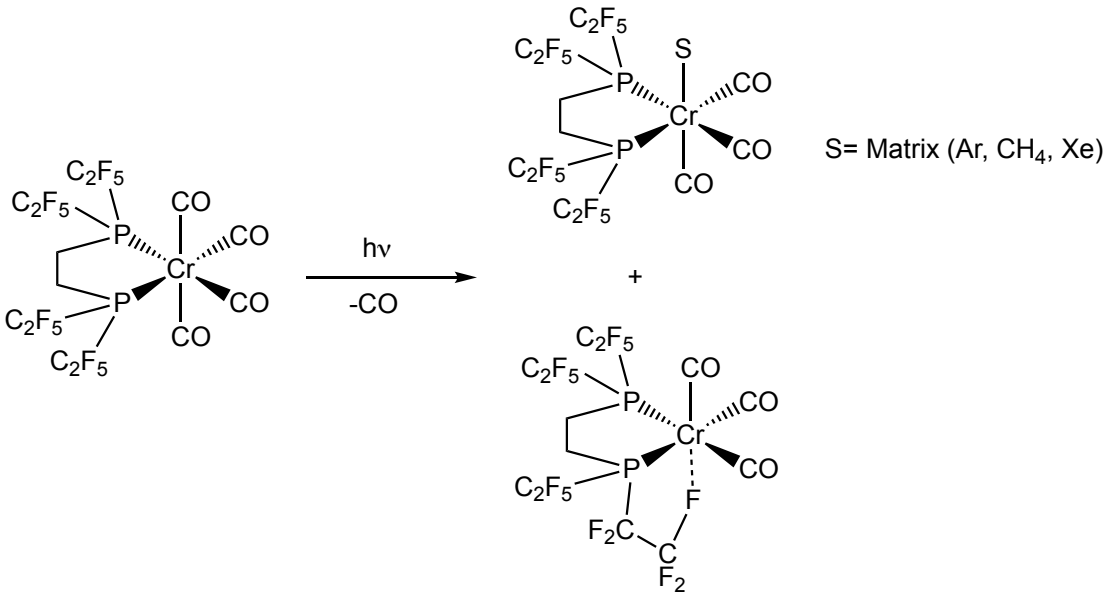


Figure 3.11 *Intramolecular interaction between F and the Cr centre upon UV photolysis in inert matrices Ar, CH_4 and Xe at low temperature (12 K). Reproduced from Ref. 42.*

The assignment of (η^1-F-$F_4C_2C_2F_5PCH_2CH_2P(C_2F_5)_2$)$Cr(CO)_3$ is based on the fact that the UV-Vis of this species is almost independent of the matrice, also because of the similarity with the UV-Vis result of $Cr(CO)_5(CF_4)$ by Perutz *et al.*[1] However, all the η^1-F coordination observed so far was intramolecular, *i.e.*, the coordination may have been facilitated by the chelation effects. The chelation effects not only affect the η^1-F coordination but also can promote the C-F bond activation, as discussed in the following.

Although C-F bond activation may be difficult due to strong bonding strength, numerous cases have been reported. C-F bond activation requires several significant factors. First, unsaturated fluorocarbon is required, such as fluoroalkenes and fluoroarenes. Compared to saturated fluoroalkanes, fluoro-

alkenes and arenes are more reactive towards oxidative addition. As F has significantly high electronegativity, it prefers to form bonds with carbon orbitals of lower electronegativity, *i.e.*, carbon orbitals with less s character. Also, the orbitals of the lone pair on F match the p-orbitals of the adjacent carbon. Thus, apart from its σ-withdrawing interaction with carbon, the π-donation from F to C also exists. Therefore, with these two factors combined, F prefers to reside on sp^3 rather than sp^2 or sp carbon centres, which caused the increased reactivities of fluoroalkenes and fluoroarenes.[43] Actually, most studies of the C-F bond activation reported are on unsaturated fluorocarbons. Higher fluorination extent is proposed to activate the C-F bond while stabilize the C-H bond. Meanwhile, similar to bond activation of C-Cl, C-Br and C-I, electron rich low oxidation state metal centres are preferred. Chelation effects also play significant roles in the C-F bond activation.

Richmond *et al.* extended the work of C-X bond activation by chelated W complexes as discussed before to C-F bond activation, and they reported the first facile oxidative addition of C-F to the metal centre of a tungsten complexes under mild conditions.[44] The fuoroarene ligand 1 (Figure 3.12) is found to react with $W(CO)_3(NCEt)_3$ in THF to form the C-F bond activated product 3 in 10 mins at room temperature, as shown in Figure 3.12.

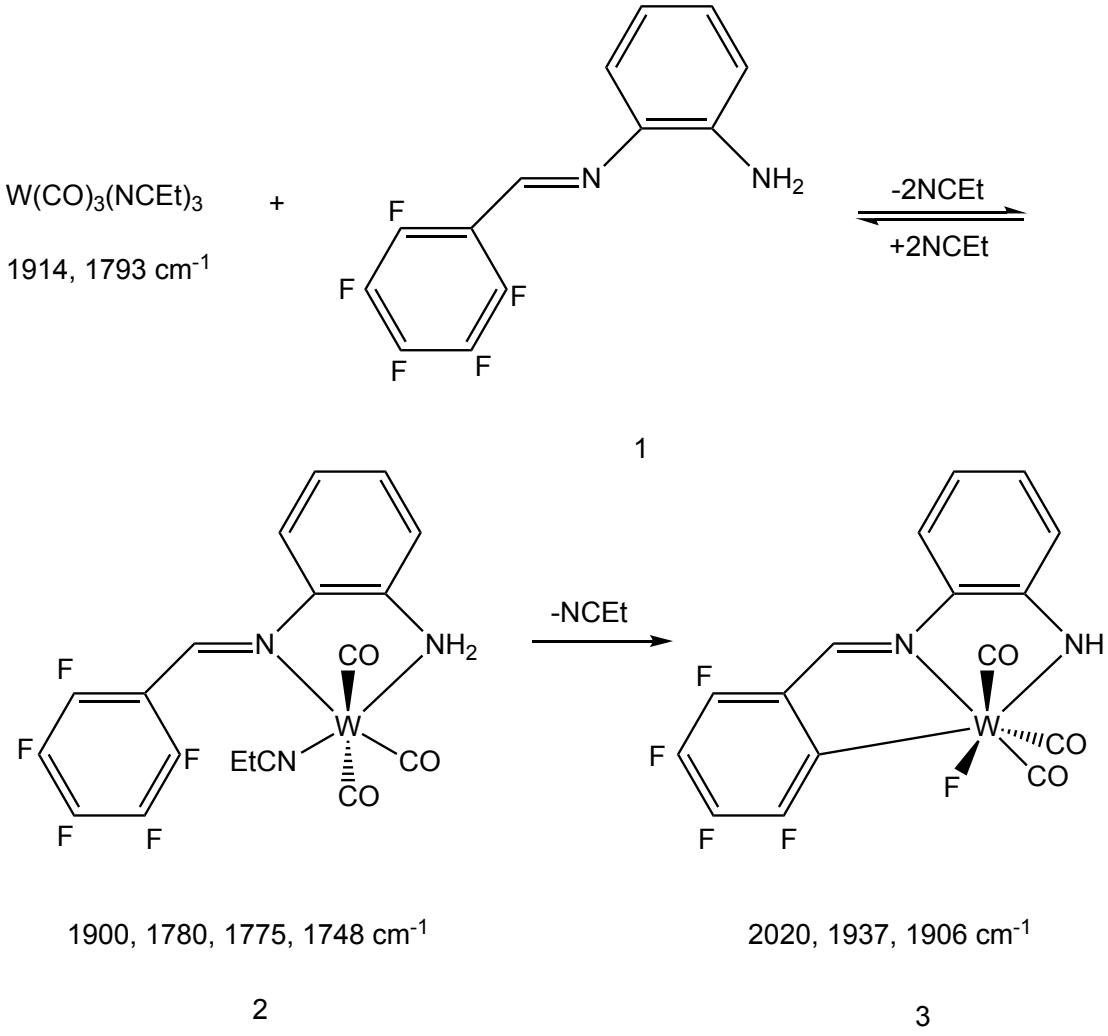


Figure 3.12 *Reaction scheme of fast (≤ 10 min) C-F bond activation by $W(CO)_3(NCEt)_3$ under mild conditions (room temperature) with high yield (69%). Reproduced from Ref. 44.*

The chelation of the ligand to W is discovered to be important for the C-F bond activation. No C-F bond activation for C_6F_6 by $W(CO)_3(NCR)_3$ has been observed. The chelation is considered to assist the C-F bond activation as not only the two N coordinated to W increase the electron density on W thus can facilitate the oxidative addition, also chelation places W and C-F close to each other and can reduce the entropic barrier for the C-F activation by W. Finally, the conjugation of the imine in the metallacycle also promotes the C-F bond activation. The chelation effect significantly facilitates the C-F bond activation, as even C-F activations of mono- or difluoro-substitued arenes have been reported for the chelation-assisted W (0) complexes.[45]

Without the chelation effect, compared to highly fluoronated arenes, monofluoro-arenes are inert towards bond activation, as reflected by the lack of reactivity of fluorobenzene with the metal anion $[CpFe(CO)_2]^-$. For partially fluorinated arenes, activation of C-H, C-F and mere coordination to the arene rings have all been reported. Research on the photo-reactions of the $Cp^*Re(CO)_2$ fragment (Cp^*:pentamethylcyclopentadienyl) with $C_6H_nF_{6-n}$ (n: 0-6) shows that, when the number of electron-withdrawing groups (*i.e.* F atoms) decreases, the η^2-complex will overtake the C-H bond activated complex to be the preferred product. Examples are shown in Table 3.5.

Table 3.5 *Reaction trend of the $Cp^*Re(CO)_2$ fragments with fluorinated benzenes.*

Fluorinated benzene	Reaction type	Ref.
C_6F_6	C-F and C-H activations	47, 48
C_6HF_5	C-H activation	49
1,2,4,5-$C_6H_2F_4$	C-H activation	49
1,4-$C_6H_4F_2$	C-H activation and η^2-coordination	46
C_6H_6	η^2-coordination	51

Photoreaction of $Cp^*Re(CO)_3$ with C_6F_6 results in the formation of $[(\eta^5\text{-}C_5Me_4CH_2)Re(CO)_2(C_6F_5)]$ where the Re centre inserts into both a C-F bond of C_6F_6 and a C-H bond on the Cp^* ring.[46] While for the $[(\eta^5\text{-}C_5H_4R)Re(CO)_3]$ complexes (R: H, Me), reaction with C_6F_6 only yields the η^2-coordination complex $[CpRe(CO)_2(\eta^2\text{-}C_6F_6)]$ in which Re centre coordinates to the ring-edge CF=CF.[47]

However, when reacting with C_6HF_5 or 1,2,4,5-$C_6H_2F_4$, for both $CpRe(CO)_3$ and $Cp^*Re(CO)_3$, the final products are observed to be the C-H bond activated complexes $[(\eta^5\text{-}C_5R_5)Re(CO)_2(Ar)H]$ (R: H, Me; Ar: C_6F_5, 2,3,5,6-C_6F_4H).[48] Therefore, it can be noted that, in the presence of C-H bond, in highly fluoronated arenes the C-H bond activation is preferred over C-F bond activation.

However, when more than two H atoms are in the F-arene, reaction with the $Cp^*Re(CO)_2$ fragment results in the yield of a mixture of both the C-H bond activated procduct $[Cp^*Re(CO)_2(2,5\text{-}C_6H_3F_2)H]$ and the η^2-coordinated product

[Cp*Re(CO)$_2$(2,3-η^2-1,4-$C_6H_4F_2$)].[49] The η^2-coordinated products [Cp*Re(CO)$_2$-(2,3-η^2-1,4-$C_6H_4F_2$)] is proved to be more stable than the hydride complex [Cp*Re(CO)$_2$(2,5-$C_6H_3F_2$)H]. It is postulated by the author that the hydride complex is formed photochemically from the more stable η^2-complex. This view is supported by other similar research work on Rh-complexes that the C-F bond activated complex [Cp*Rh(PMe_3)(C_6F_5)F] is formed from the photolysis of the initially formed η^2-complex [Cp*Rh(PMe_3)(η^2-C_6F_6)].[50] Meanwhile, NMR result shows that the η^2-coordination *via* the C=C bond is preferred over the more electron-deficient C=F bond, which is also supported by DFT calculations. For benzene C_6H_6, only stable η^2-coordinated product is observed in reaction with Cp*Re(CO)$_3$.[51] While for the more electron rich Cp*Re(CO)(PMe_3) fragment, the C-H bond-activated product [Cp*Re(CO)(PMe_3)(C_6H_5)H] is observed.[52] Therefore, a trend is clearly revealed that, for an organometallic complex with a given electron density, in the reaction with fluoroarenes, the η^2-coordination mode is preferred over the C-H bond activation when the number of the F atoms in the arene decreases.

Apart from binding *via* the arenes, coordination *via* the F atoms has also been reported for several early transition metal complexes such as Sc, Ti, V.[53]

For fluoroalkanes, it is recognized that bond activation is much more difficult due to the more stable α-carbon. Therefore it is generally thought that for the fluoroalkanes, coordination to the metal centre of organometallic complexes is *via* two binding modes, one is *via* the lone pair of the F atom, the other is by forming a 3-c-2-e binding mode C-M-H between the metal centre and the C-H bond of fluoroalkanes. The interaction between fluoroalkanes and organometallic complexes has been investigated by Dobson *et al.*[54] It is found that for fluorohexane the preferred binding mode to W(CO)$_5$ fragment is *via* F atom rather than the C-H agostic interaction. The intramolecular C-Cr-H to Cr-F isomerization is suggested.

3.1.3 Photophysical and Photochemical Investigations of $W(CO)_5L$ (L: N donor) Complexes

For $M(CO)_6$ (M: Cr, Mo, W) complexes, the one-electron energy level diagram is shown in Figure 3.13 (a).[55]

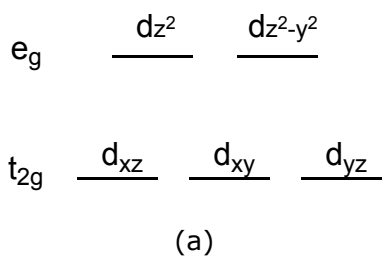


Figure 3.13 *one-electron energy level diagram of (a) $M(CO)_6$ complexes; (b) $M(CO)_5L$ complexes with C_{4v} symmetry (M: Cr, Mo, W). Reproduced form Ref. 55.*

It is generally believed that when the O_h symmetry of $M(CO)_6$ is reduced to C_{4v} (*e.g.* for derivative complexes $M(CO)_5L$), the one-electron energy levels will change to scheme (b) (Figure 3.13). Thus, the transition of lowest energy for the $M(CO)_5L$ complexes is believed to be LF $^1A_1(e^4b_2^2)\rightarrow{}^{1,3}E(e^3b_2^2a_1^1)$. The transitions of higher energies are believed to be related to MLCT states.

For $W(CO)_5L$ (L: nitrogen donor, such as pyridine, piperidine, *etc.*) complexes, much research work has proposed that the L ligand tends to be more labile than CO upon UV photolysis. Although the photo dissociation of the L ligand and CO are found to

be dependent on the irradiation wavelength, L ligand dissociation is always predominant. Wrighton *et al.* investigated the dependency of photo-induced ligand loss of $M(CO)_5L$ (M: Mo, W; L: NH_3, n-$PrNH_2$, piperidine) under different irradiation wavelengths (366, 405, 436 nm).[56] Two photoreactions have been investigated, one is photolysis of $M(CO)_5L$ in the presence of L. Formation of $M(CO)_4L_2$ has been observed, while ligand exchange between L and L cannot be detected. The quantum yields of $M(CO)_4L_2$ are summarised in Table 3.6.

Table 3.6 *Quantum yields of the ligand substitution reactions of the $M(CO)_5L$ (M: Mo, W; L: NH_3, n-$PrNH_2$, piperidine) complexes.*

M	L	X	Product	Φ 366 nm[a]	Φ 405 nm[a]	Φ 436 nm[a]
Mo	piperidine	piperidine	$Mo(CO)_4L_2$	0.13	0.11	0.048
Mo	n-$PrNH_2$	n-$PrNH_2$	$Mo(CO)_4L_2$	0.24	0.20	0.057
W	piperidine	piperidine	$W(CO)_4L_2$	0.034	0.0081	0.0061
W	n-$PrNH_2$	n-$PrNH_2$	$W(CO)_4L_2$	0.057	0.022	0.016
Mo	NH_3	CO	$Mo(CO)_6$	-	0.64	0.58
Mo	NH_3	1-pentene	$Mo(CO)_5X$[b]	0.74	0.84	0.71
W	NH_3	1-pentene	$W(CO)_5X$[c]	0.49	0.66	0.56
W	n-$PrNH_2$	1-pentene	$W(CO)_5X$[c]	0.60	0.65	0.73
W	piperidine	1-pentene	$W(CO)_5X$[c]	0.45	0.51	0.49
W	piperidine	CO	$W(CO)_6$	-	0.65	-

[a] *All quantum yields are ± 10%;* [b] *Constitutes > 70% of primary photoproducts;* [c] *Constitutes > 90% of primary photoproducts.*

From Table 3.6 it can be noted that for both the Mo and W complexes, the quantum yield of $M(CO)_4L_2$ is relatively low, and the quantum yield also increases with shorter irradiation wavelength. Also, generally the quantum yields for Mo complexes are higher than the W analogues. For different ligands, quantum yields for n-$PrNH_2$ is in general higher than piperidine.

Photosubstitution reaction with entering ligand X has also been investigated. Two X groups have been used, CO and 1-pentene. It is found that for CO the only product observed is $M(CO)_5X$ (CO-CO exchange cannot be detected), while for 1-

pentene, the $W(CO)_5$(1-pentene) is the predominant product. No formation of $M(CO)_4(L)$(1-pentene) has been observed. however, it is still expected as one of the photoproducts. From the data in Table 3.6 it can be noted that, for both the Mo and W complexes, the L dissociation predominates the photoreaction, while highest quantum yield reaches at irradiation wavelength of 405 nm.

It is established that the LF state as shown in Figure 3.13 is reactive towards the photo-initiated L dissociation, while MLCT is virtually unreactive.[57] Therefore, it is not difficult to understand the result that under 405 nm the quantum yields reach the maximum, as the irradiation is in the LF regions of these complexes. However, it is also discovered that the relative energy levels of the MLCT and LF states can be tuned by altering the L ligand. Wrighton *et al.* have conducted investigations on the photochemistry of a series of $W(CO)_5L$ (L: pyridyl ligands) complexes.[57] It is found that for $W(CO)_5$(pyridine), by adding an electron withdrawing group onto the pyridine ligand, such as cyano, acetyl, benzoyl and formyl groups, the LF state is almost unaffected, while the energy level of the W→L MLCT state is decreased, and MLCT can replace the LF state to become the lowest-lying state. As shown in Figure 3.14.

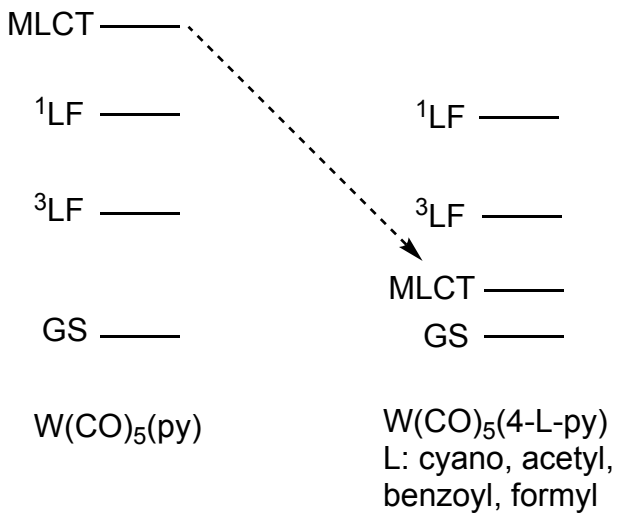


Figure 3.14 *Energy level scheme of the $W(CO)_5$(py) and $W(CO)_5$(4-L-py) complexes where L is an electron withdrawing group (L: cyano, acetyl, benzoyl, formyl). Reproduced from Ref. 57.*

For the L substitution reaction, it is found that for complexes with LF as the lowest-lying state, the quantum yields are usually >0.5 at 436 nm. However, when the L ligand in $W(CO)_5L$ complexes are substituted with strong electron withdrawing ligands such as cyano, acetyl and benzoyl, the quantum yield at 436 nm dramatically drops to *ca.* 0.1. For the formyl substituted L ligand, the quantum yield is as low as 0.05. Moreover, when under irradiation at 514 nm, the quantum yields are even lower. For cyano, acetyl and benzoyl substituted L ligands, the quantum yields are *ca.* 0.02, while for the formyl substituted L ligand it is 0.002. It is interesting to note that the binding site for electron withdrawing groups is important in determine the photo-properties of the $W(CO)_5L$ complexes. For $W(CO)_5$(3-acetylpyridine), $W(CO)_5$(3-benzoylpyridine), $W(CO)_5$(4-acetylpyridine) and $W(CO)_5$(4-benzoylpyridine) complexes, the lowest-lying states for the 3-substituted complexes are the LF states, while for the 4-substituted complexes are the W→L MLCT states. The L substitution quantum yields for $W(CO)_5$(3-acetylpyridine) and $W(CO)_5$(3-benzoylpyridine) at 436 nm are 0.75 nm and 0.73 nm, respectively, while for $W(CO)_5$(4-acetylpyridine) and $W(CO)_5$(4-benzoylpyridine) the yields are 0.15 and 0.12, respectively. This may be due to the fact that different binding sites may affect the electron withdrawing efficiency of the groups on pyridine, thus can result in absolute different photo-properties of the two isomers.

Moralejo *et al.* further investigated the influence of irradiation wavelength on the quantum yields of complexes $W(CO)_5L$ as extension of Wrighton's work.[58] The range of irradiation wavelength is extended from 313 to 488 nm (313, 365, 436, 457.9, 488 nm). The absorption spectra of $W(CO)_5$(pyridine) and $W(CO)_5$(piperidine) in isooctane at room temperature show that, for $W(CO)_5$(pyridine), there is an intensive band at *ca.* 382 nm, while for $W(CO)_5$(piperidine) there is an intensive band at *ca.* 404 nm. These bands are assigned to the $^1LF\ ^1A_1 \rightarrow {}^1E$ transitions for $W(CO)_5$(pyridine) and $W(CO)_5$(piperidine), respectively. For both complexes, there is a relatively weak band at lower energy at *ca.* 442 nm, shown as a shoulder band of the ^1LF transition bands of $W(CO)_5$(pyridine) and $W(CO)_5$(piperidine), and is assigned to the $^3LF\ ^1A_1 \rightarrow {}^3E$ transition. Also for both complexes, there is an intense band at *ca.* 270 nm. Based on the spectra of $W(CO)_6$,[59] this band is assigned to the

W→CO transition. For $W(CO)_5$(pyridine), there is a hidden band at *ca.* 350 nm overlaps with the ^{1}LF transition band, and is observed to be resolved in more polar solvents, and is assigned to the W→pyridine transition. The MLCT transition has not been observed for $W(CO)_5$(piperidine).[58]

Photolysis of $W(CO)_5$(pyridine) and $W(CO)_5$(piperidine) in isooctane at different irradiation energies in the LF transition regions leads to the only observation of $W(CO)_5$(1-hexene), which evidenced that the pyridine and piperidine dissociation dominate the photo-initiated dissociation reactions. In agreement with Wrighton's work, the quantum yields for both complexes are dependent on the irradiation energies. Irradiation into the triplet ^{3}LF region at lower energy leads to lower quantum yields compared to irradiation at the ^{1}LF region. The quantum yields of $W(CO)_5$(pyridine) is generally higher than that of $W(CO)_5$(piperidine). Although MLCT state is recognised as unreactive,[57] experiments are also conducted in two other solvents with different polarities, benzene and dichloromethane, in order to investigate the contribution of MLCT transition in the quantum yields. In benzene and dichloromethane, the W→pyridine CT transition blue-shifted and is resolved from the ^{1}LF band compared to that in isooctane. Similar to that observed in isooctane, the quantum yields at 313 nm is slightly lower than at 365 nm. According to the author, this is due to the internal conversion from MLCT to the lower LF states.

Investigations of the photo initiated L substitution on the ultrafast timescale using TRIR have also been conducted. Johnson *et al.*[60] investigated the photophysics of the $W(CO)_5L$ (L: pyridine, piperidine) complexes using TRIR in low temperature glasses. Interestingly, for both compounds, the TRIR spectra show downward movements of the ν(CO) positions of the excited states compared to the parent bleaches. According to the author, this result suggests that in the ^{3}LF state, the C-O bond length is elongated, while the W-C bond length is shortened, and can be explained by the fact that the LUMO d* orbital of W may have mixed with the π* orbital of CO.

However, the traditional LF/MLCT model has been questioned and challenged in

recent years. Recent theory calculations on group 6 compounds $M(CO)_6$ have suggested that the photo dissociation occurs *via* the M→CO MLCT excited state. The M→CO MLCT state is proposed to be the lowest-lying excited state instead of the LF state. And the LF state lies at much higher energy level than expected.[61] This also explains for the TRIR results of Johnson *et al.* as discussed before. The observation of the ν(CO) positions of the excited state red-shifted compared to the parent bleaches might be indicative of the M→CO MLCT excited state.[60,62,63] For many $W(CO)_4L$ complexes (L : electron accepting diimine ligands), similar mechanism has been suggested by theoretical calculations, such as for $W(CO)_4$(bpy),[64] $M(CO)_4$(phen), $M(CO)_4$(tmp) (M: Cr, W),[65] of which the energy levels are revealed by CASSCF/CASPT2 calculations, that the lowest-lying MLCT (M→L) is followed by M→CO states, while LF d-d transitions are at much higher energy levels. Zális *et al.* has combined theoretical calculations and experimental techniques to investigate the photophysics of $W(CO)_4$(1,2-ethylenediamine) using TDDFT, Raman spectroscopy and ps-TRIR.[66] DFT calculations show that the lowest-lying excited state for $W(CO)_4$(1,2-ethylenediamine) is MLCT (W→CO). The TDDFT results matches the absorption spectrum of $W(CO)_4$(1,2-ethylenediamine), and is also supported by the Raman results. Ps-TRIR spectra show that upon UV photolysis, along with the parent bleaches, several bands at lower wavenumbers are formed, which all decay at similar rate. The red-shift of ν(CO) positions of this exited state is consistent with the assignment of a $MLCT_{W\rightarrow CO}$ state, where the C=O bond is expected to be elongated. This is the first time that the existence of a $MLCT_{W\rightarrow CO}$ state is observed using ps-TRIR, as shown in Figure 3.15.

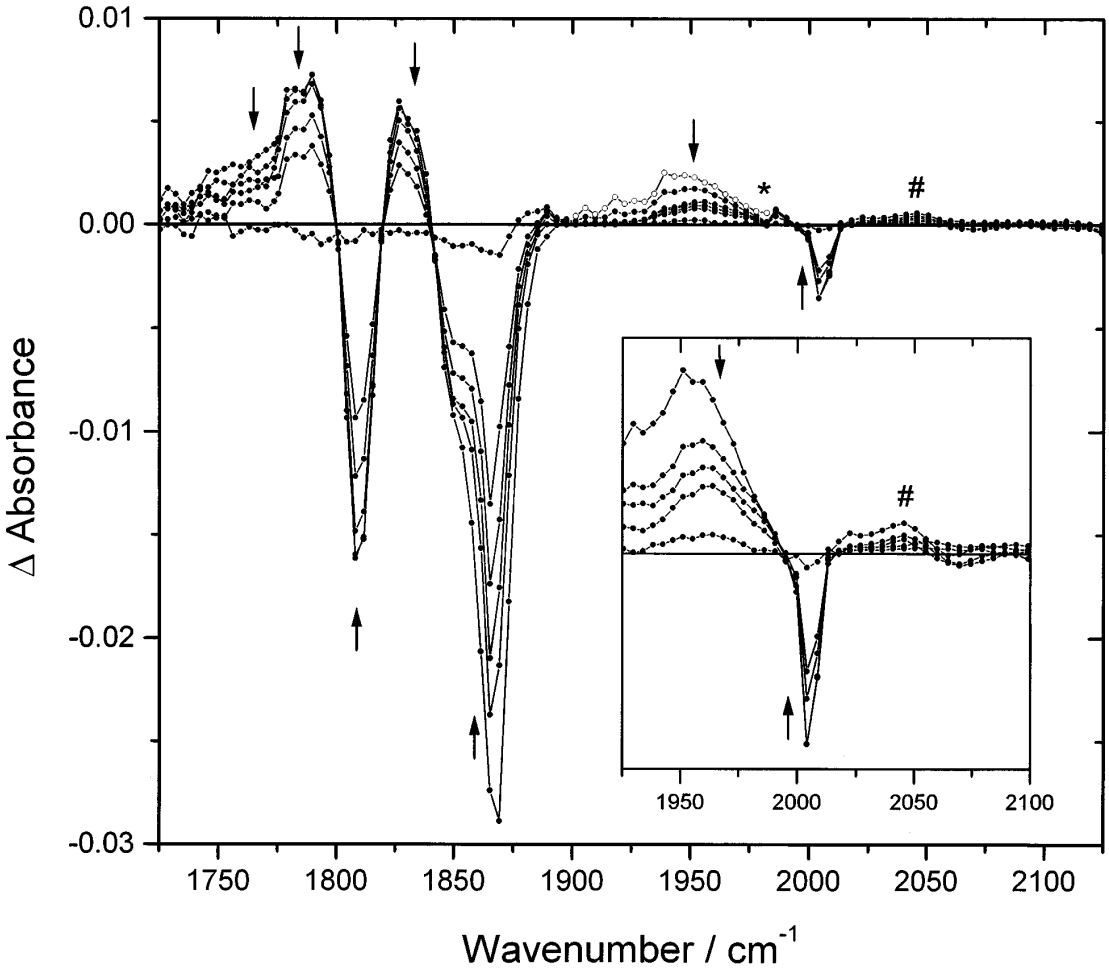


Figure 3.15 *ps-TRIR of* $W(CO)_4$(1,2-ethylenediamine) *in* CH_3CN *at room temperature. o: spectrum measured at 1 ps. Only 1982~1900* cm^{-1} *is shown for clarity. •: spectra measured at time delays of 2, 8, 20, 50, 100, 1000 ps. *: noise caused by joint windows. #: the signal in the 2080~2030* cm^{-1} *range appears to be noisy.*[66]

Zális *et al.* also investigated the photophysics of $W(CO)_5$(pyridine), $W(CO)_5$(4-cyanopyridine) and $W(CO)_5$(piperidine) using ps-TRIR, Raman spectroscopy and DFT calculations.[67] DFT calculations show that for all three compounds, the HOMO composition is very similar, all contains *ca.* 60% d_W orbital, while the cis and trans π^*_{CO} orbitals contribute 25% and 15% of the HOMO, respectively. For both $W(CO)_5$(pyridine) and $W(CO)_5$(4-cyanopyridine), almost 96% of the LUMOs are $\pi^*_{(py)}$ or $\pi^*_{(CN\text{-}py)}$, while for $W(CO)_5$(piperidine), the composition of the LUMO is 86% π^*_{CO}, 10% d^*_W and only 3% $\pi^*_{(pip)}$. The LUMO+n closely follow the LUMO, which are a series of MO orbitals based mainly on π^*_{CO} for all three compounds, while the

LF states based on the d-d transitions are too high in energy to be considered.

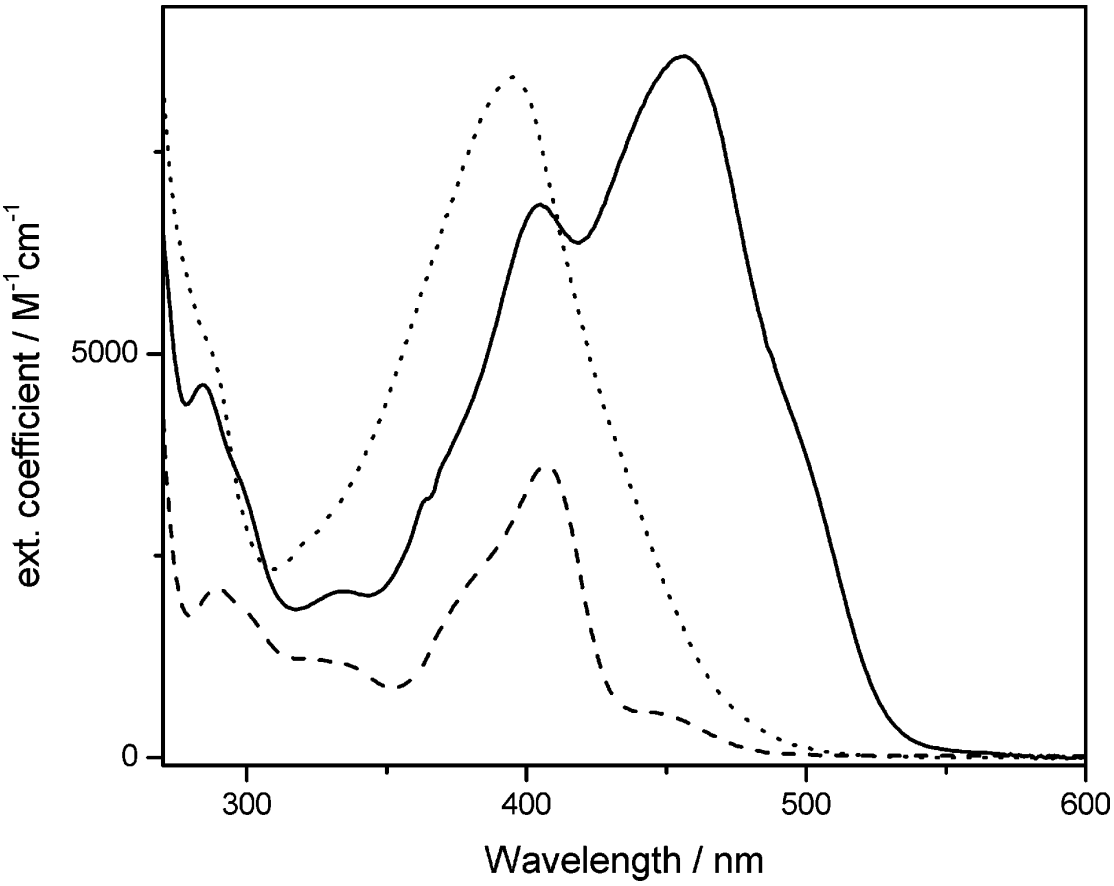
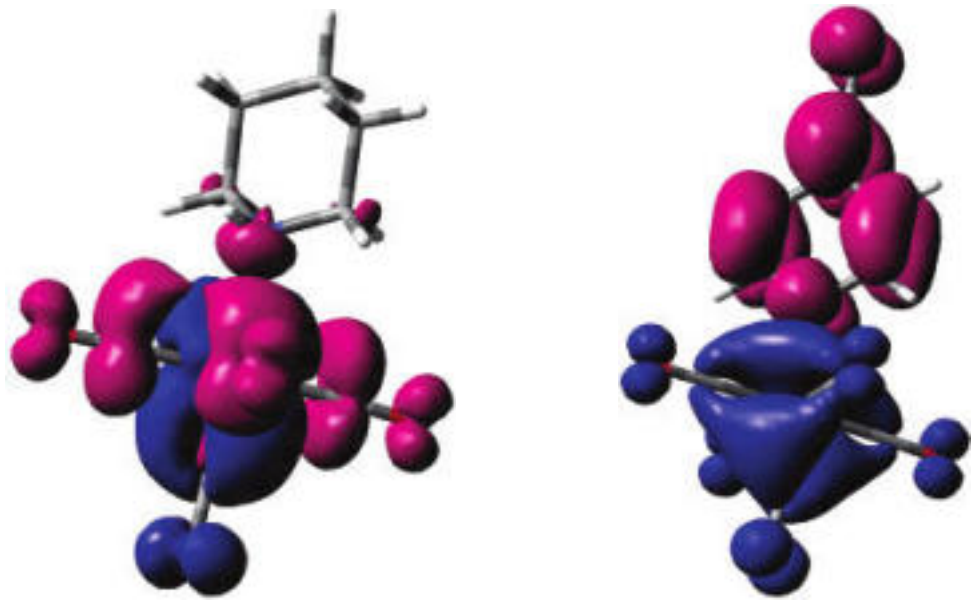


Figure 3.16 *Electronic absorption spectra of $W(CO)_5$(4-cyanopyridine) in methylcyclohexane (solid line); $W(CO)_5$(4-cyanopyridine) in MeCN (dotted line); $W(CO)_5$(pip) in methylcyclohexane (dashed line).*[67]

According to Zális *et al.*, the two lower absorptions of $W(CO)_5$(pip) (Figure 3.16) are both assigned to the $MLCT_{W\rightarrow CO}$ transitions rather than the conventional assignment of the LF states as discussed before. Electron density distribution calculation of the lowest electron transition has also been conducted, as shown in Figure 3.17.



(a) (b)

Figure 3.17 *Electron density distribution calculation of the lowest electron transition of (a) $W(CO)_5$(pip) and (b) $W(CO)_5$(4-cyanopyridine). Blue and purple represent the decrease and increase of electron density, respectively.*[67]

As shown in Figure 3.17, for $W(CO)_5$(pip), the electron is transferred from the W centre and CO_{ax} to CO_{eq}, while the pip ligand is nearly unaffected. The peak at *ca.* 407 nm in the absorption spectra in Figure 3.16 is responsible for the lowest $MLCT_{W\rightarrow CO}$ transition, while the peak at *ca.* 443 nm is responsible for the spin-forbidden triplet $^3MLCT_{W\rightarrow CO}$ transition. The emissions of $W(CO)_5$(pip) are attributed to emissions from these two $MLCT_{W\rightarrow CO}$ states.

For $W(CO)_5$(4-cyanopyridine), the strong electron withdrawing ligand cyano on the pyridine gives rise to 96% of the LUMO is on the 4-CNpy ligand (Figure 3.17). For the HOMO-LUMO transition of $W(CO)_5$(4-cyanopyridine), the electron is transformed from the $W(CO)_5$ fragment to the 4-CNpy ligand. $MLCT_{W\rightarrow 4\text{-}CNpy}$ is responsible for the peak at *ca.* 454 nm in methylcyclohexane in Figure 3.16, and *ca.* 395 nm in MeCN, which shows strong solvatochromic effects, blue-shifted when the solvent polarity is increased. The peak at *ca.* 400 nm in methylcyclohexane is attributed to the $MLCT_{W\rightarrow CO}$ state. The assignment of the lowest transition to $MLCT_{W\rightarrow 4\text{-}CNpy}$ is supported by the Raman spectroscopy results. For $W(CO)_5$(py), although TD-DFT suggests that the lowest transition is $MLCT_{W\rightarrow py}$, however,

absorption spectra show that the lowest transition is unsolvatochromic and has high py-substitution photo quantum yield. Meanwhile $MLCT_{W\rightarrow py}$ and $MLCT_{W\rightarrow CO}$ is close in energy, thus it is very likely that the lowest transition for $W(CO)_5(py)$ is $MLCT_{W\rightarrow CO}$.

Figure 3.18 shows the ps-TRIR of $W(CO)_5(pip)$ in methylcyclohexane and CH_3CN.

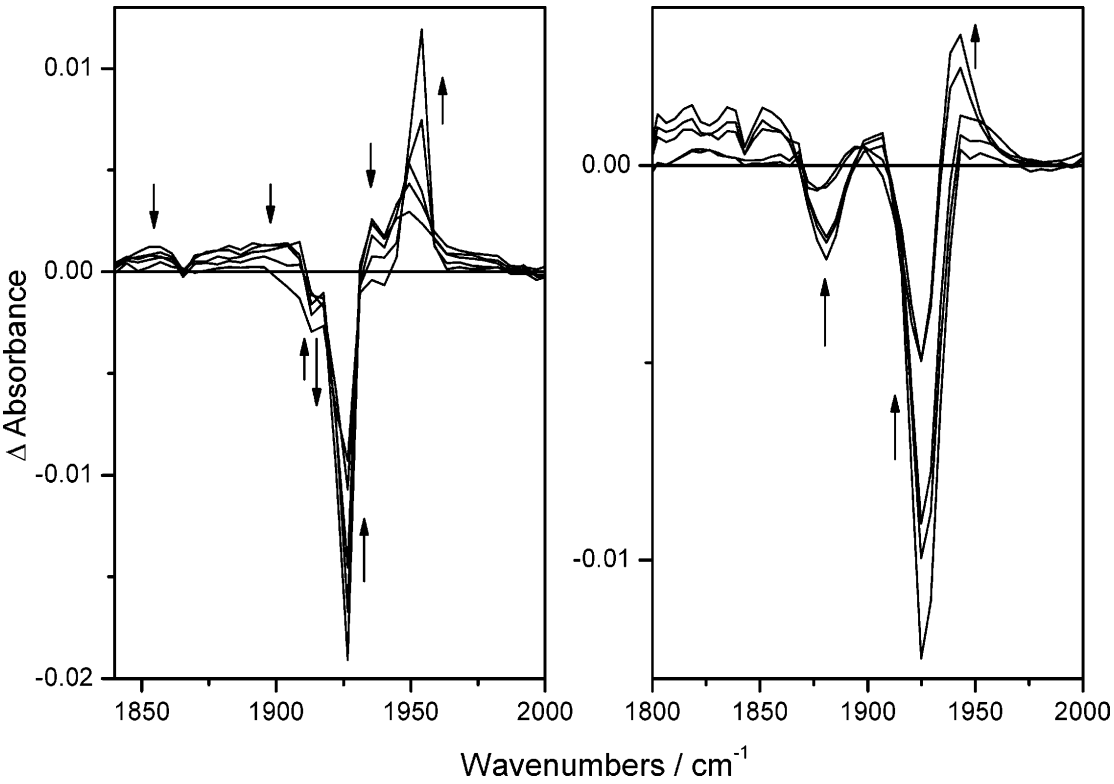


Figure 3.18 *Ps-TRIR of $W(CO)_5(pip)$ in left: methylcyclohexane; right: CH_3CN. Both spectra evolve in time delays of 2, 3, 7, 40 and 1000 ps. Irradiated by 400 nm UV pulse.*[67]

In MCH (methylcyclohexane), the spectra and dynamics of $W(CO)_5(pip)$ are found to be similar to that of $W(CO)_6$ in hexane. No $MLCT_{W\rightarrow CO}$ state was observed. Simiar reaction has been observed in CH_3CN. It is considered that the pip is dissociated *via* the MLCT (W→CO) state and undergoes solvation to form $W(CO)_5(sol)$ within 1 ps, which cannot be detected due to the limit of the equipment rise-time.

For $W(CO)_5(4\text{-}CNpy)$, different irradiation energies have been investigated. The spectra are shown in Figure 3.19.

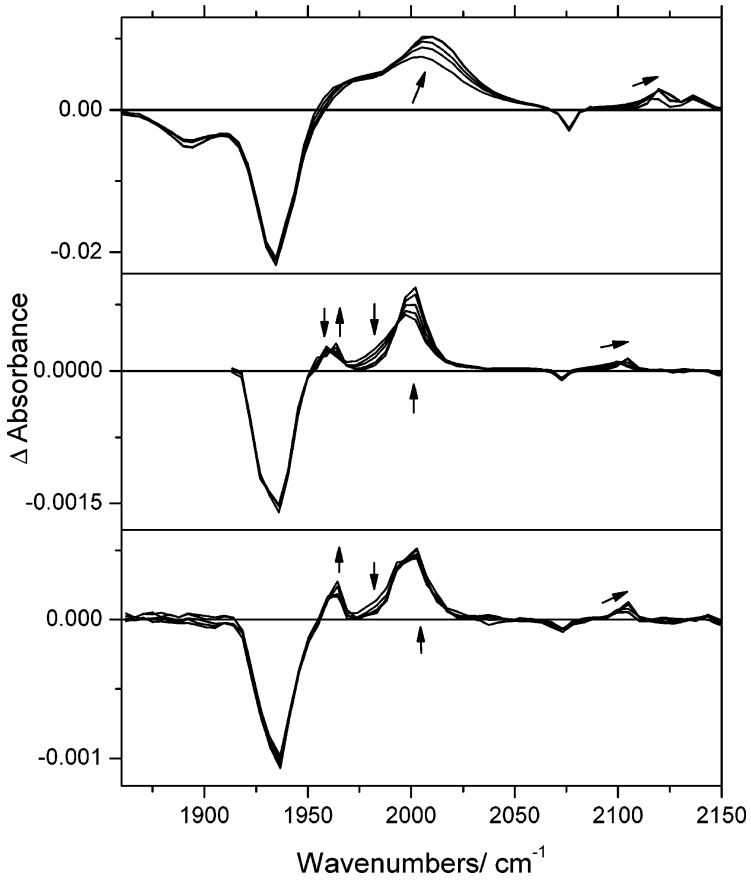


Figure 3.19 *Ps-TRIR of $W(CO)_5$(4-CNpy). Top: in CH_3CN, time delays: 2, 4, 7, 40, 200 ps, irradiated by 400 nm; middle: in MCH, time delays: 2, 4, 8, 20, 300 ps, irradiated by 400 nm; bottom: in MCH, time delays: 2, 4, 8, 30, 300 ps, irradiated by 500 nm.*[67]

As shown in Figure 3.19, in MCH the excitation of $W(CO)_5$(4-CNpy) at 500 nm is directed into $MLCT_{W\rightarrow 4CN\text{-}py}$, while excitation at 400 nm is directed into $MLCT_{W\rightarrow CO}$. For $W(CO)_5$(4-CN-py), ps-TRIR shows that upon UV photolysis, in MCH by 400 nm, only $MLCT_{W\rightarrow CN\text{-}py}$ and weak $W(CO)_5$(MCH) have been observed, which indicate ultrafast interconversion between $MLCT_{W\rightarrow CN\text{-}py}$ and $MLCT_{W\rightarrow CO}$. The low quantum yield of $W(CO)_5$(MCH) is due to the low reactivity of the $MLCT_{W\rightarrow CN\text{-}py}$ state. However, it must be point out that the formation of the $W(CO)_5$(MCH) complex has only been observed when irradiated by 400 nm. When irradiated by 500 nm, this species is not observed. Therefore, the formation of the solvated species $W(CO)_5$(MCH) is thought to be related to the $MLCT_{W\rightarrow CO}$ state. The sequential growth of $W(CO)_5$(MCH) is attributed to the vibrational cooling process. Nevertheless, it has to be pointed out that in Zális' work, the TRIR has only been conducted on the ps-timescale. Glyn

et al. has conducted TRIR of $W(CO)_5$(4-CNpy) complex in methylcyclohexane at room temperature, and the reaction process occurring on the μs-timescale was investigated.[68] It was revealed by TRIR that similar to the ps-TRIR results of Zális *et al*., when $W(CO)_5$(4-CNpy) is irradiated by UV pulse that can only initiate the $MLCT_{4\text{-}CNpy}$ state, the $MLCT_{4\text{-}CNpy}$ state was observed as expected, however on the μs-timescale, along with the decay of the $MLCT_{4\text{-}CNpy}$ state, the solvated species $W(CO)_5$(MCH) was observed to form, along with the recovery of the parent bands. It was found that the decay of the $MLCT_{4\text{-}CNpy}$ state is consistent with the formation rate of the solvated species $W(CO)_5$(MCH) and the recovery of the parent bands, which indicates the conversion from the $MLCT_{4\text{-}CNpy}$ state to speices $W(CO)_5$(MCH) and parent complex. In Glyn's work, the photo-dissociation reactivity of the $MLCT_{4\text{-}CNpy}$ state is attributed to the rapid equilibrium with the reactive LF state. However, as discussed before here the reactivity of the $MLCT_{4\text{-}CNpy}$ state can be attributed to the equilibrium with the reactive $MLCT_{W\rightarrow CO}$ state, rather than the LF state which is expected to lie at much higher energy level. Therefore, the traditional $MLCT_{W\rightarrow L}$/LF model is questioned and may be replaced by the $MLCT_{W\rightarrow L}$/$MLCT_{W\rightarrow CO}$ model.

In this work, we are especially interested in the E-H bond (Si, Sn, Ge) activation by the $W(CO)_5L$ (L: pyridyl) complexes. Though rare investigations have been conducted, numerous investigations on $W(CO)_6$ have been reported, which has been discussed in Section 3.1.1 and thus will not be discussed here. As has been mentioned, the L dissociation of $W(CO)_5L$ complexes dominates the photo-initiated ligand dissociation reactions, which leads to the formation of the $W(CO)_5$ species. Thus, the photo substitution reactions in solvents for $W(CO)_5L$ complexes are expected to be similar to $W(CO)_6$, except for some $W(CO)_5L$ complexes the photochemically inert $MLCT_{W\rightarrow L}$ state may be observed.

Apart form E-H bond activation, we are also interested in the interactions of $W(CO)_5L$ (L: pyridyl) complexes with inert gases.

Noble gases are extremely inert due to their closed electron shells. However, there are numerous reports on the reactions of noble gases. Generally, the reactivity of noble gases increases down the group. The first noble gas complex was discovered

by Bartlett in 1962.[69] Xenon was reported to react with PtF_6 to form a complex originally believed to have the formula $XePtF_6$. Since then, numerous research on the reactivity of noble gases has followed.

Noble gases have long been discovered that they can act as ligands coordinating to unsaturated transition metal centres. Perutz *et al.* investigated the photo-intitialed interactions of noble gases with group 6 hexacarbonyls using low-temperature matrices.[1] It is found that the visible absorption maximum bands of the metal pentacarbonyls are extremely sensitive to the matrices. The results are shown in Table 3.7.

Table 3.7 *Visible absorption maximum bands of $M(CO)_5$ (M: Cr, Mo, W) in different matrices. Reproduced from Ref. 1*

	Visible absorption maximum band		
	$Cr(CO)_5$	$Mo(CO)_5$	$W(CO)_5$
matrices	nm	nm	nm
Ne	624		
SF_6	560	450	461
CF_4	547		
Ar	533	429	437
Kr	518		
Xe	492	413	417
CH_4	489	411	413

It is also found that for saturated $Cr(CO)_6$ and $Cr(CO)_5(NH_3)$ complexes, the relative shifts in different matrices under same conditions are pretty small, within 5 nm. Therefore, the sensitivity to different matrices of $M(CO)_5$ is attributed to the interactions with the matrices. In the experiment with $Cr(CO)_6$ in mixed matrices, Ne with 2% Xe at 4K, two bands are observed at 628 and 487 nm (*cf.* in pure Ne: 624 nm; in pure Xe: 492 nm). It is found that irradiation into either band, the corresponding band will decay while the other band will grow. The band at 628 nm is assigned to $Cr(CO)_5Ne$, while the band at 487 nm is assigned to $Cr(CO)_5Xe$. This evidenced the interactions between the noble gases and the unsaturated metal

complexes.

IR measurements have also been conducted in mixed matrices. The results are summarised in Table 3.8.

Table 3.8 *IR frequencies and visible band positions of $Cr(CO)_5$ in different mixed matrices. Reproduced from Ref. 1.*

matrices	ν(CO) /cm^{-1}	Visible band/ nm	assignment
Ne(2% Xe)	1971, 1933	628	$Cr(CO)_5Ne$
	1966, 1943	487	$Cr(CO)_5Xe$
Ne(2% Ar)		630 (shoulder)	$Cr(CO)_5Ne$
	1972, 1941	533	$Cr(CO)_5Ar$
Ar(2% Xe)	2092,4, 1964.5, 1936.3	525	$Cr(CO)_5Ar$
	2088.6, 1962.9, 1939.1	490	$Cr(CO)_5Xe$
Ar(2% CH_4)	1964.9, 1934.8	525	$Cr(CO)_5Ar$
	1964.3, 1937.7	490	$Cr(CO)_5CH_4$
CH_4(10% Ar)	1961, 1933	491	$Cr(CO)_5CH_4$

Other transition metal noble gas complexes have also been observed using matrix isolation. It was discovered by Poliakoff *et al.* that in Xe matrice at 20K, $Fe(CO)_5$ can react with Xe to form $Fe(CO)_4Xe$.[70] The formation of $Mn(CO)_5Kr$ and $Fe(CO)_5Kr^+$ in krypton matrice at low temperatures under irradiation have been reported by Fairhurst *et al*.[71]

The first observation of a transition metal noble gas complex in solution phase was reported by Simpson *et al.*[72] In liquefied Xenon, or in liquefied Krypton doped with 5% Xe at -100 °C, upon UV photolysis, $Cr(CO)_5Xe$ can be observed using FTIR, with an extremely long lifetime of *ca.* 2 s.

The Xe-bound species is discovered to be much more stable than the Ar and Kr-bound species, the reactivity of the noble gas bound species follows: Ar >Kr >Xe.[73,74,75] Weiller and co-workers have investigated the photo-initiated interactions between Kr, Xe and $M(CO)_5$ (M: Cr, W) in liquefied noble gases using

laser photolysis and rapid-scan FTIR.[76] Both $M(CO)_5Kr$ and $M(CO)_5Xe$ have been observed in liquefied noble gases at low temperatures. The lifetime of $M(CO)_5Kr$ is much shorter than $M(CO)_5Xe$. *e.g.,* for $W(CO)_5Kr$ at 150 K in liquid Kr, its lifetime is *ca.* 0.1 s, while for $W(CO)_5Xe$ the lifetime is *ca.* 1.5 min at 170 K in liquid Xe. The bond dissociation energy of W-Xe has been determined to be *ca.* 35 kJ mol^{-1}, which is much lower than the W-heptane bond dissociation energy (65 kJ mol^{-1}).

Wells *et al.* investigated the photochemistry of $M(CO)_6$ (M: Cr, Mo, W) with noble gases Ar, Kr Xe in the gas phase at ambient temperature, with irradiation of 355 nm using transient IR spectroscopy. The bond dissociation energies for Cr-Xe, Mo-Xe and W-Xe in $M(CO)_5Xe$ are determined to be 9.0 ± (0.9) kcal mol^{-1}, 8.0 ± (1.0) kcal mol^{-1} and 8.2 ± (1.0) kcal mol^{-1}, respectively. The upper limit for W-Kr bond dissociation energy in $W(CO)_5Kr$ is estimated to be *ca.* 6 kcal mol^{-1}, while for W-Ar in $W(CO)_5Ar$ it is estimated to be only *ca.* 3 kcal mol^{-1}.[77]

Arai and co-workers investigated the photochemistry of $W(CO)_6$ in the gas phase (*ca.* 10 mTorr) in the presence of 6.0 Torr Xe with total pressure of 10 Torr (the rest is Ar) by irradiation of 355 nm at ambient temperature using TRIR.[78] The $W(CO)_5Xe$ was observed, and it was propsed that the Xe is acting as a weak σ-donor to the W centre in $W(CO)_5Xe$. It was suggested by the authors that there is an electron donation from Xe to the a_1 orbital of $W(CO)_5$, which involves the π^* orbitals of the equatorial COs. The orbital interactions is shown in Figure 3.20.

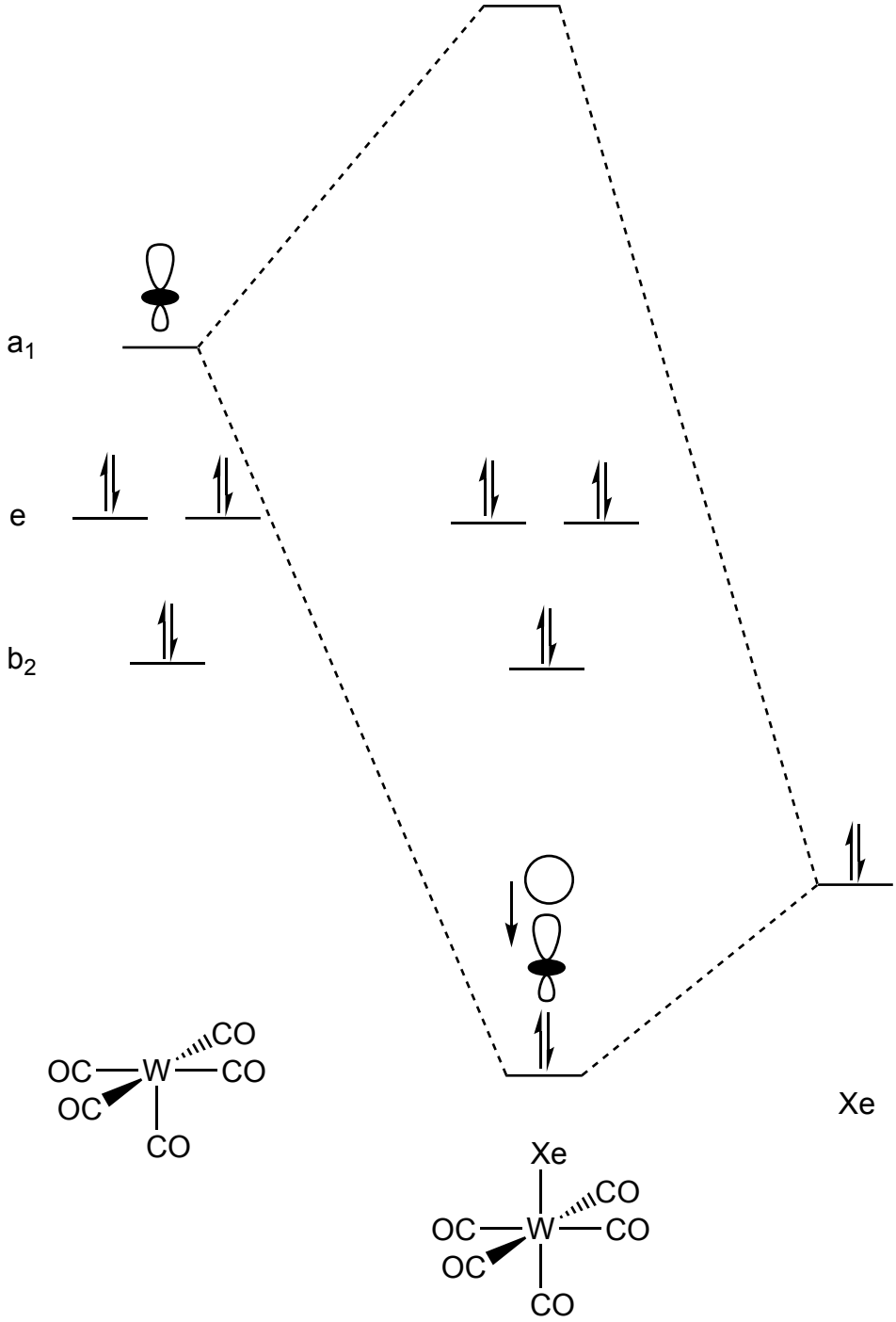


Figure 3.20 *Proposed orbital interactions between $W(CO)_5$ and Xe in $W(CO)_5Xe$ by Arai and co-workers, reproduced from Ref. 78.*

For the above studies, the investigation of noble gase complexes is either conducted in gas phase or in liquefied noble gases at low temperatures. Nevertheless, for the studies in the gas phase, it is often limited to metal complexes with high vapour pressure such as group 6 hexacarbonyl complexes $M(CO)_6$ (M: Cr, Mo, W), while for studies in liquefied noble gases, usually extremely low

temperature is required.[79] Supercritical fluid (Sc fluid) provides a better solution. A supercritical fluid has the hybrid properties of both gas and liquid; it shows great solvation abilities towards not only a wide range of gases but also various metal complexes. Moreover, it allows investigations at ambient temperature which normally cannot be achieved in liquefied gases. Sun *et al.* investigated the photochemistry of $M(CO)_6$ (M: Cr, Mo, W) in a series of supercritical noble gases (Ar(W only), Kr, Xe) using TRIR and UV-Vis spectroscopy.[80] It is found that for $M(CO)_5L$ (M: Cr, Mo, W; L: Kr, Xe), the general reactivity follows the order: Cr ≈ Mo > W.

However, although supercritical fluids allow investigations to be conducted at ambient temperature, it usually requires extremely high pressure of the system. Perfluoroalkane solvents have been proposed as ideal alternatives for investigations on gas interactions. Perfluoroalkane solvents, compared to other conventional solvents, have several distinct advantages due to the extremely strong C-F bond. First of all, they are highly inert towards chemical reactions, nontoxic and nonflammable. The intermolecular interactions are extremely weak, and their boiling points are low, more volatile compared to the alkane solvents, thus can be easily recycled. Furthermore, they are extremely nonpolar, with high solubility of gases. Therefore, perfluoroalkanes are great media for investigations on reactions involving gases.

In this work, we are extremely interested in the W-Xe interaction in $W(CO)_5Xe$ formed from photolysis of $W(CO)_5L$ (L: py, pip, 4-acpy) in the presence of Xe, also in an attempt to support our future TR-XAFS investigations. Therefore perfluoromethylcyclohexane (PFMCH) has been used as the solvent. The investigation is conducted at ambient temperature, and does not require high pressure of the system. Interaction between M and Xe of $M(CO)_6$ (M: Cr, Mo, W) in PFMCH has been investigated previously by our group members.[21] For $W(CO)_6$ in PFMCH under argon, within 1 ps the parent band (1989 cm^{-1}) was observed to have bleached, with formation of broad new features, which narrowed and blue-shifted to form two bands at 1966 and 1930 cm^{-1} after *ca.* 100 ps, indicating the formation of a $W(CO)_5L$ species. The species at 1966 and 1930 cm^{-1} was not stable, which

decayed in *ca*. 6 ns to form another pentacarbonyl species at 1961 and 1935 cm^{-1}. The second W pentacarbonyl species was observed to decay in *ca*. 12 μs to form the water species $W(CO)_5(H_2O)$, as trace amount of H_2O still exists in the system. The first pentacarbonyl → second pentacarbonyl → $M(CO)_5(H_2O)$ reaction process has also been observed for $Cr(CO)_6$ and $Mo(CO)_6$. the second pentacarbonyl is assigned to the solvated species $M(CO)_5$(PFMCH).

Then 1.5 bar Xe was added into the system. It was observed that after the addition of Xe, similar to the experiment in neat PFMCH, the first pentacarbonyl → second pentacarbonyl → $W(CO)_5(H_2O)$ reaction process has also been observed. However, it was found that the ν(CO) positions of the second pentacarbonyl was different to that in neat PFMCH. The ν(CO) band positions of the second pentacarbonyl slightly blue-shifted (1963, 1937 cm^{-1}) compared to that in pure PFMCH (1961, 1935 cm^{-1}). Meanwhile, the reaction rates in each step in the first pentacarbonyl → second pentacarbonyl → $W(CO)_5(H_2O)$ reaction process were observed to have changed. The formation rate of the second pentacarbonyl from the first pentacarbonyl was accelerated, while the conversion rate from the second pentacarbonyl to $W(CO)_5(H_2O)$ was slowed down. This applies to all metal complexes $M(CO)_6$ (M: Cr, Mo, W). This phenomenon, according to the author, indicates the formation of a Xe complex $M(CO)_5Xe$ (the second pentacarbonyl).

What is interesting is the observation of two pentacarbonyl species and their conversion in neat PFMCH, which normally cannot be observed in alkane solvents. This phenomenon has also been observed for $CpRe(CO)_3$ and $Cp^*Re(CO)_3$ in neat PFMCH.[21] Similar to $CpRe(CO)_3$, the addition of a small amount of cyclopentane into the W system eliminated the conversion between the two pentacarbonyls, that only one pentacarbonyl species at 1959 and 1934 cm^{-1} was observed, which was assigned to $W(CO)_5$(cyclopentane).

For the first W pentacarbonyl species, several candidates have been proposed. First is the unsaturated $W(CO)_5$. Second is a solvated species which coordinates weakly to PFMCH. Transient Absorption spectroscopy (TA) investigations have been conducted for further understanding. The results are summarised in Table 3.9.

Table 3.9 *Summaries of IR frequencies and TA λ_{max} of $M(CO)_6$ (M: Cr, Mo, W) photolysed in PFMCH. Reproduced from Ref. 21 and 81.*

species	condition	ν(CO) /cm^{-1}	TA λ_{max} /nm	Ref.
$Cr(CO)_6$	PFMCH	1993	-	21
	PFMCH+Xe			21
$Mo(CO)_6$	PFMCH	1995	-	21
	PFMCH+Xe			21
$W(CO)_6$	PFMCH	1989	-	21
	PFMCH+Xe			21
1^{st} $Cr(CO)_5$(?)	PFMCH	1967, 1936	610	21
			620	81
	PFMCH+Xe		-	21
1^{st} $Mo(CO)_5$(?)	PFMCH	1975, 1930	470	21
			460	81
	PFMCH+Xe	1975, 1931	-	21
1^{st} $W(CO)_5$(?)	PFMCH	1966, 1930	475	21
			475	81
	PFMCH+Xe		-	21
$Cr(CO)_5$(PFMCH)	PFMCH	1962, 1937	490	21
$Cr(CO)_5$(Xe)	PFMCH+Xe	1966, 1939	500	21
$Mo(CO)_5$(PFMCH)	PFMCH	1971, 1935	435	21
$Mo(CO)_5$(Xe)	PFMCH+Xe	1973, 1937	-	21
$W(CO)_5$(PFMCH)	PFMCH	1961, 1935	420	21
$W(CO)_5$(Xe)	PFMCH+Xe	1963, 1937	-	21

The TA results suggest that for $Cr(CO)_6$ in neat PFMCH, upon UV photolysis of 266 nm, a broad absorption band centred at *ca.* 610 nm was initially formed, which on the ns-timescale decayed in similar rate of the first Cr pentacarbonyl species observed by TRIR, and a new band at *ca.* 490 nm was formed later. Therefore, the band at 610 nm was considered to be the same species as the first Cr pentacarbonyl observed by TRIR, and the band at 490 nm was the solvated species $Cr(CO)_5$(PFMCH). Similar TA results have been observed for $Mo(CO)_6$ and $W(CO)_6$, as shown in Table 3.9.

Observation of the band at 610 nm is consistent with work of Kelly *et al.*[81] (Table 3.9). In Kelly's work, the initial absorption bands observed were assigned to the unsaturated $M(CO)_5$ species in PFMCH. However, Kelly also suggested that there may be weak interactions between $M(CO)_5$ and PFMCH.

Meanwhile, the similarity of the λ_{max} between $Cr(CO)_5$(PFMCH) (490 nm) and $Cr(CO)_5Xe$ (500 nm) may indicate that the M-Xe interaction is weak.

In this work, we are seeking suitable systems for XAFS investigations using TRIR as the main technique. In the following sections, the TRIR investigations of the E-H (E: Si, Ge, Sn) bond activation by $W(CO)_6$ and $W(CO)_5$(L) (L: pyridine, piperidine, 4-acetylpyridine), the activation of halocarbons by $W(CO)_6$, the interaction with noble gas Xe of $W(CO)_5$(L) (L: pyridine, piperidine, 4-acetylpyridine) will be presented and discussed seperately in each sections. $W(CO)_6$ and its derivative complexes shows satisfying photo quantum yields, and the XAFS studies on activations of E-H(E: Si, Ge, Sn) and the interaction with Xe of $W(CO)_6$ have been conducted by our collaborators and show excellent results, and the results are presented in the end of this Chapter.

3.2 Result and Discussion

3.2.1 E-H Bond Activation (E: Si, Ge, Sn) by $W(CO)_6$

The E-H bond activation by $(\eta^5\text{-}C_5H_nMe_{5-n})M(CO)_3$ (M: Mn, Re) have been discussed in Chapter 2, but we are also interested in the E-H activation by tungsten carbonyl complexes. We'll start with the simplest W carbonyl complex, $W(CO)_6$, with *n*-heptane used as the solvent as heptane has been proved to be ideal for many previous TRIR experiments for its excellent solvation ability of transition metal complexes and its wide IR detection window. Figure 3.21 shows the TRIR spectra of photo-initiated $W(CO)_6$ in neat *n*-heptane.

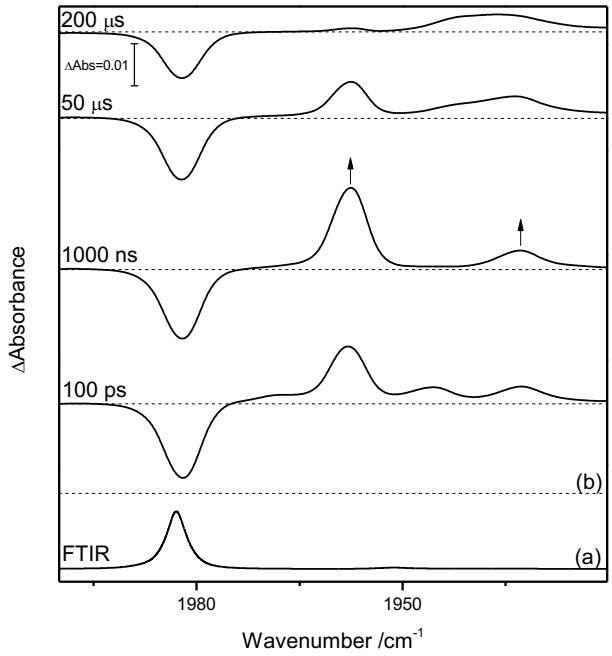


Figure 3.21 *(a) FTIR spectrum and (b) TRIR spectra obtained following photolysis (266 nm) of 0.5 mM $W(CO)_6$ in neat heptane.*

Upon UV photolysis, three bands at *ca.* 1958, 1945 and 1932 cm^{-1} are formed, along with the depletion of the parent band at 1983 cm^{-1}. According to previous research, the band at 1945 cm^{-1} is assigned to the hot $\nu_1 \rightarrow \nu_2$ transition of $W(CO)_5$(*n*-heptane) which quickly decays after 105 (±7) ps.[19] The bands at 1958 and 1932 cm^{-1} are assigned to the solvated heptane species $W(CO)_5$(*n*-heptane), based on

previous work (1959, 1929 cm^{-1}).[82] On the late μs-timescale, as shown in time delay of 200 μs (Figure 3.21), the band at 1958 cm^{-1} decays while a broad band from *ca.* 1942 cm^{-1} to 1930 cm^{-1} is formed, which might be the decomposition of $W(CO)_5$(*n*-heptane), or the reaction with impurities in the solvent.

Three dopants $HSiBu_3$ (tributylsilane), $HGeBu_3$ (tributylgermane) and $HGeBu_3$ (tributylstannane), have been investigated.

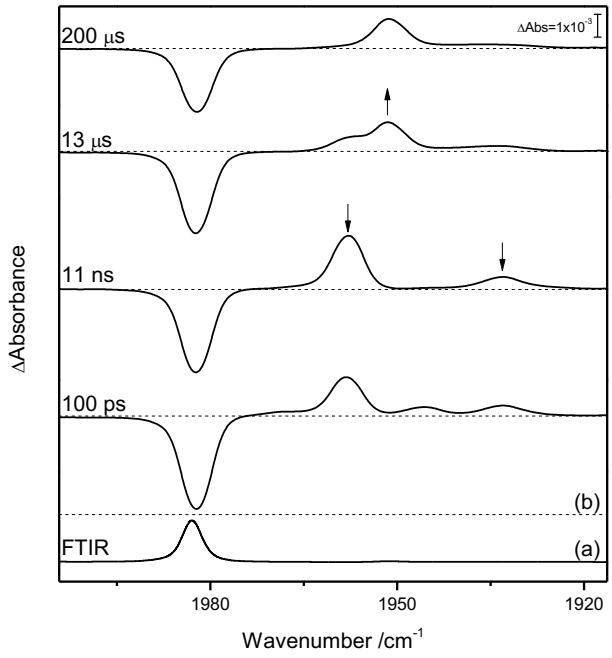


Figure 3.22 *(a) FTIR spectrum and (b) TRIR spectra obtained following photolysis (266 nm) of 0.2 mM $W(CO)_6$ in heptane doped with 0.05 M $HSiBu_3$.*

As shown in Figure 3.22, upon UV photolysis, similar to the experiment in neat heptane, three bands at *ca.* 1958, 1945 and 1932 cm^{-1} are formed immediately. The bands at 1958 and 1932 cm^{-1} are assigned to the solvated species $W(CO)_5$(*n*-heptane). Also, it can be observed that on later timescales the bands for $W(CO)_5$(*n*-heptane) decay along with the formation of a new band at *ca.* 1952 cm^{-1}, which is observed to be very stable and shows no decay during the experimental timescale (up to ~ 1 ms). The band at 1952 cm^{-1} is assigned to the silane species $W(CO)_5(HSiBu_3)$, based on previous work.[19] Another band at lower wavenumber is expected for $W(CO)_5(HSiBu_3)$, however it may be too weak to be observed

according to previous studies.[19] It is interesting to note the differences with $CpMn(CO)_2(HSiBu_3)$ and $CpRe(CO)_2(HSiBu_3)$, as discussed in Chapter 2, that for $W(CO)_5(HSiBu_3)$, the ν(CO) band position is red-shifted compared to $W(CO)_5$(*n*-heptane). As discussed in Chapter 2, it is recognised that between the metal centre and Si-H of trialkylsilanes, there exists three modes of interactions, the oxidative addition mode, in which the Si-H bond is fully cleaved; the η^2-mode, in which the Si-H coordinates to the metal centre forming a 3-c-2-e interaction, or the η^1-interaction in which the Si-H coordinates to the metal centre *via* the hydrogen atom. In the η^2-mode, there exists two interactions, the σ-donation from Si-H to the metal centre, as well as the π-back-donation from the metal d-orbital to the Si-H σ^*-orbital. When the π-back-donation is strong enough, then full cleavage of the Si-H bond can be achieved, *i.e.*, the oxidative addition mode. For $CpMn(CO)_2(HSiBu_3)$ and $CpRe(CO)_2(HSiBu_3)$, the ν(CO) positions are blue-shifted compared to $W(CO)_5$(*n*-heptane), reflecting stronger π-back-donation from the metal centre to Si-H compared to C-H of heptane. Here the red-shift of ν(CO) for $W(CO)_5(HSiBu_3)$ compared to $W(CO)_5$(*n*-heptane) suggests that the π-back-donation in $W(CO)_5(HSiBu_3)$ is extremely weak. Our collaborators from Rutherford Appleton Laboratory have done XAFS measurements, and according to their result, a η^1-mode is suggested between W and Si-H in $W(CO)_5(HSiBu_3)$, and this is consistent with our result. Although previous work has suggested that in $W(CO)_5(HSiEt_3)$, the W is coordinated to Si-H in a 3-c-2-e mode. [16,17,19] However, as previous research has suggested, the steric factors can play a significant role in determining the interaction mode.[83] Increasing the size of the silane can hinder the formation of the σ-complex. Therefore, an η^1-coordination *via* H is suggested for $W(CO)_5(HSiBu_3)$.

Kinetic analysis indicates that the silane species $W(CO)_5(\eta^1\text{-}HSiBu_3)$ (7.6 $\pm$0.1 μs) is converted from the solvated species $W(CO)_5$(*n*-heptane) (7.5 $\pm$0.3 μs), as shown in Figure 3.23.

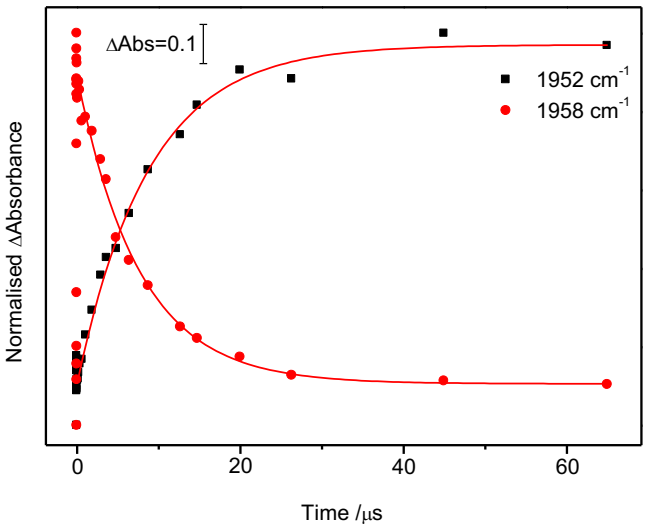


Figure 3.23 *TRIR kinetic traces obtained at 1958 and 1952 cm^{-1} corresponding to W(CO)$_5$(n-heptane) and W(CO)$_5$(η^1-HSiBu$_3$) (HSiBu$_3$ concentration: 0.05 M).*

The ligand exchange rate is in excellent agreement with the EXAFS data collected by our collaborators, which shows a rate of *ca.* 7.8 μs, under the same $HSiBu_3$ concentration (0.05 M). However, compared to the ligand exchange rate in neat triethylsilane (*ca.* 2 ns),[19,21] the rate in *n*-heptane is significantly slowed down. According to previous work,[19] the ligand exchange between C-H and Si-H follows the dissociative mechanism. This may indicate that the ligand exchange rate is related to the reagent concentration.

Therefore, investigations on the influence of concentration of both $W(CO)_6$ and $HSiBu_3$ on the C-H/Si-H ligand exchange rate were conducted, the results are summarised in Table 3.10.

As shown in Table 3.10, change of $W(CO)_6$ concentration has little influence on the C-H/Si-H exchange rate, while when the dopant concentration doubles, the exchange rate is halved. Thus, it may indicate that according to the reaction rate equation:

$$R=K[A]^a[B]^b$$

Where R refers to the reaction rate, while A, B refer to the reagent concentrations, and a, b are the kinetic orders of A and B respectively. K is the rate constant.

Therefore, the kinetic order of $W(CO)_6$ in the C-H/Si-H ligand exchange reaction is 0, while for the dopant $HSiBu_3$ it is 1, shown as follow:

$$R=K[W(CO)_6]^0[HSiBu_3]^1$$

Table 3.10 *Influence of the concentration of $W(CO)_6$ and $HSiBu_3$ on the C-H/Si-H ligand exchange rate.*

$W(CO)_6$ concentration /mM	$HSiBu_3$ concentration /M	C-H/Si-H exchange rate /μs
0.05	0.05	7.7±0.4
0.1	0.05	7.1±0.5
0.2	0.05	7.5±0.3
0.5	0.05	7.8±0.2
1	0.05	8.5±0.5
0.2	0.05	7.9±0.1
0.2	0.1	3.7±0.05

TRIR investigation in neat $HSiBu_3$ has also been conducted, the spectra are shown in Figure 3.24. A very similar reaction process to that in heptane doped with $HSiBu_3$ (Figure 3.22) was observed in neat $HSiBu_3$. The band position of $W(CO)_6$ in neat $HSiBu_3$ is the same to that in heptane at 1983 cm^{-1}. Upon irradiation, two bands at 1959 and 1932 cm^{-1} are observed, and are assigned to the alkyl-bound species $W(CO)_5(BuHSiBu_2)$ as analogue to the heptane species $W(CO)_5$(*n*-heptane) (1958, 1932 cm^{-1}). The alkyl-bound species $W(CO)_5(BuHSiBu_2)$ decays, and on later timescales a new band at 1952 cm^{-1} forms, which is quite stable and the band position is similar to $W(CO)_5(\eta^1\text{-}HSiBu_3)$ in heptane, and thus is assigned to the silane species $W(CO)_5(\eta^1\text{-}HSiBu_3)$.

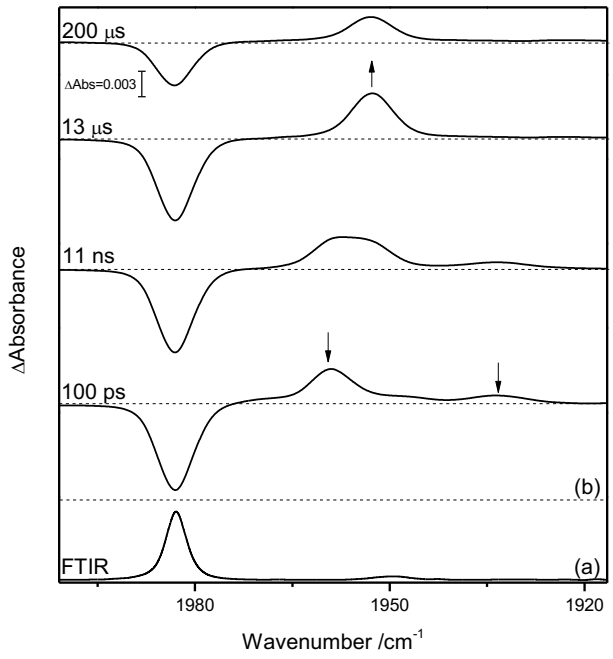


Figure 3.24 *(a) FTIR spectrum and (b) TRIR spectra obtained following photolysis (266 nm) of $W(CO)_6$ in neat $HSiBu_3$.*

The conversion from $W(CO)_5(BuHSiBu_2)$ to $W(CO)_5(\eta^1\text{-}HSiBu_3)$ was also observed, and the exchange rate in neat $HSiBu_3$ is found to be *ca.* 19 ns (Figure 3.25), much faster than in heptane doped with $HSiBu_3$, but slightly slower compared to that in neat $HSiEt_3$ (*ca.* 2 ns).[19]

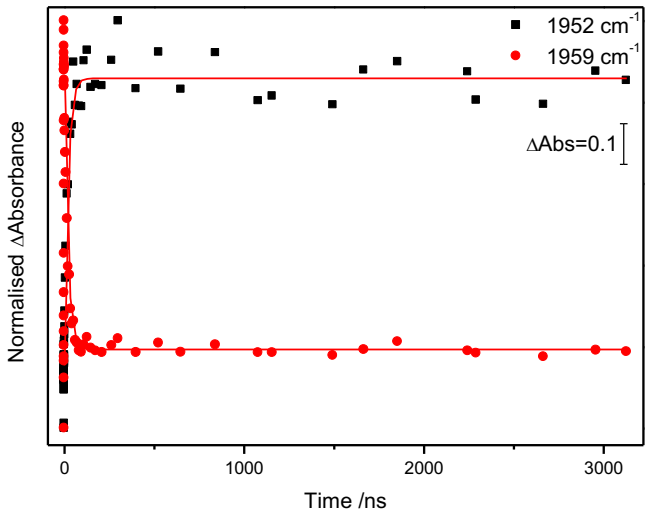


Figure 3.25 *TRIR kinetic traces obtained at 1959 and 1952 cm^{-1} corresponding to $W(CO)_5(BuHSiBu_2)$ and $W(CO)_5(\eta^1\text{-}HSiBu_3)$.*

The faster ligand substitution rate in neat $HSiBu_3$ compared to in heptane could be explained by the higher concentration of $HSiBu_3$ in neat $HSiBu_3$. Also, it could be due to the fact that in neat $HSiBu_3$, the C-H/Si/H exchange reaction occurs within the same molecule, as shown in Figure 3.26.

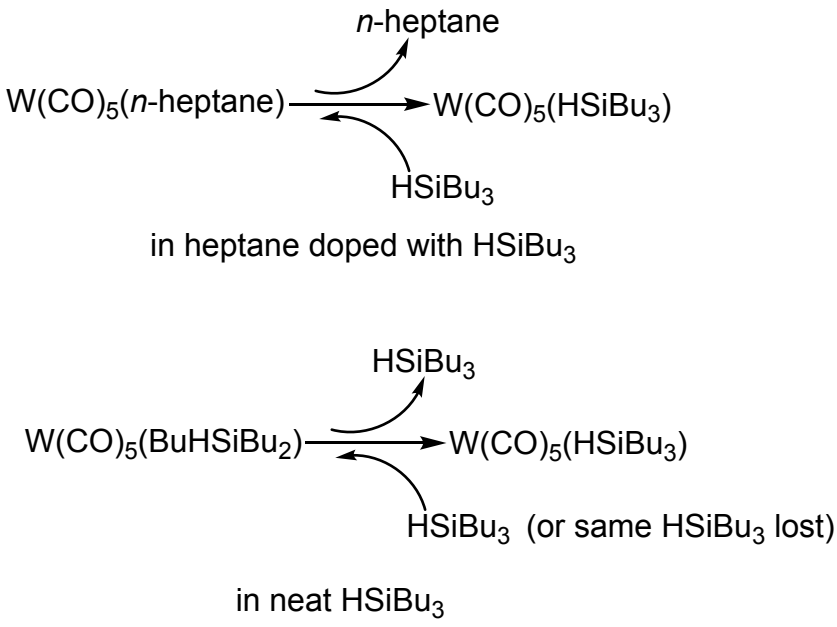


Figure 3.26 *Proposed reaction mechanism of $W(CO)_6$ in n-heptane doped with $HSiBu_3$ and in neat $HSiBu_3$.*

From the comparison with the ligand exchange rate in neat $HSiEt_3$ (*ca.* 2 ns), it can be concluded that the steric factors may also play an important role. Compared to $HSiEt_3$, $HSiBu_3$ has bigger alkyl ligands, which may hinder the quick coordination of H-Si to the W centre.

Similar reaction processes have also been observed for dopants $HGeBu_3$ and $HSnBu_3$.

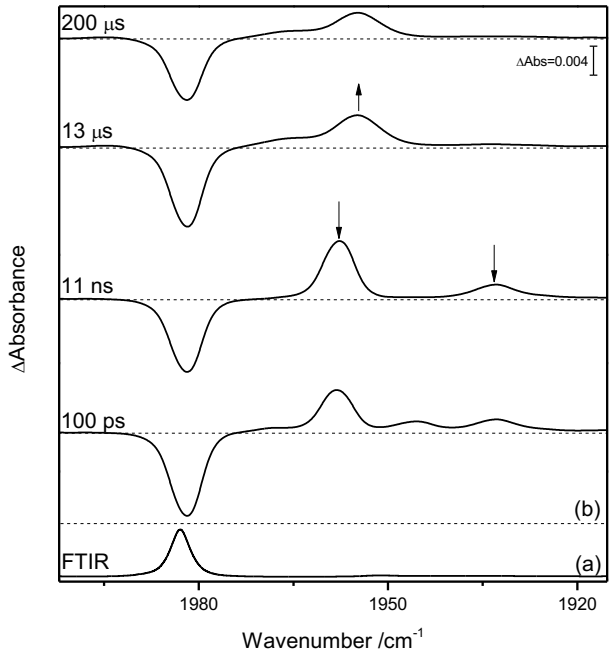


Figure 3.27 *(a) FTIR spectrum and (b) TRIR spectra obtained following photolysis (266 nm) of 0.2 mM $W(CO)_6$ in heptane doped with 0.05 M $HSnBu_3$.*

Figure 3.27 shows the TRIR spectra of $W(CO)_6$ in heptane with dopant $HSnBu_3$. Similar to the experiment with dopant $HSiBu_3$, upon UV photolysis, the solvated species $W(CO)_5$(*n*-heptane) is formed, which then decays and a new species at *ca.* 1955 cm^{-1} is formed, which is assigned to the stannane species $W(CO)_5(HSnBu_3)$, analogue to $W(CO)_5(HSiBu_3)$ (1952 cm^{-1}). Interestingly, it should be noted that the ν(CO) band positon of $W(CO)_5(HSnBu_3)$ (1955 cm^{-1}) is slightly blue-shifted compared to $W(CO)_5(\eta^1\text{-}HSiBu_3)$ (1952 cm^{-1}). As Sn-H is supposed to be more electron rich than Si-H, this phenomenon may indicate that in $W(CO)_5(HSnBu_3)$, there may exist the π-backbonding from W to Sn-H. Therefore, whether in

$W(CO)_5(HSnBu_3)$ the coordination of Sn-H to the W centre is *via* an η^1- or η^2-mode is still in question and may need further investigations.

Kinetics show that $W(CO)_5(HSnBu_3)$ (2.9 ±0.06 μs) is converted from $W(CO)_5$(*n*-heptane) (3.0 ±0.1 μs), as shown in Figure 3.28.

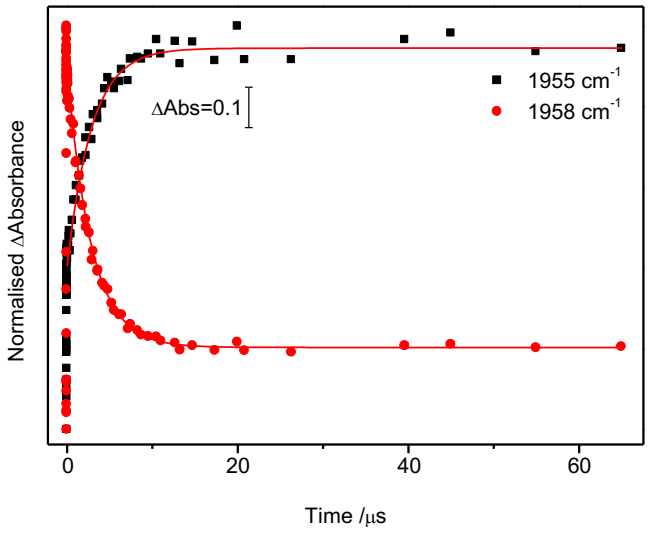


Figure 3.28 *TRIR kinetic traces obtained at 1958 and 1955 cm^{-1} corresponding to $W(CO)_5$(n-heptane) and $W(CO)_5(HSnBu_3)$ ($HSnBu_3$ concentration: 0.05 M).*

Comparing the ligand exchange rate with that of $HSiBu_3$ under the same concentration, the C-H/Sn-H ligand exchange rate is much faster. This may be due to the better electron donation ability of Sn-H.

Investigations on the influence of concentration of $W(CO)_6$ and $HSnBu_3$ on the C-H/Sn-H exchange rate have also been conducted, the results are summarised in Table 3.11.

Table 3.11 *Influence of the concentration of $W(CO)_6$ and $HSnBu_3$ on the C-H/Sn-H ligand exchange rate.*

$W(CO)_6$ concentration /mM	$HSnBu_3$ concentration /M	C-H/Sn-H exchange rate /μs
0.01	0.05	4.2±0.3
0.05	0.05	3.4±0.2
0.2	0.05	2.9±0.08
0.5	0.05	3.1±0.3
1	0.05	3.6±0.1
0.2	0.05	3.4±0.1
0.2	0.1	1.9±0.06

From the data in Table 3.11, it can be noted that, similar to $HSiBu_3$, the ligand exchange rate is unaffected by the concentration of $W(CO)_6$, while the rate is halved when doubling the concentration of $HSnBu_3$. Thus, the kinetic order of $HSnBu_3$ is proposed to be 1 in the C-H/Sn-H ligand exchange reaction.

Figure 3.29 shows the TRIR spectra in presence of $HGeBu_3$.

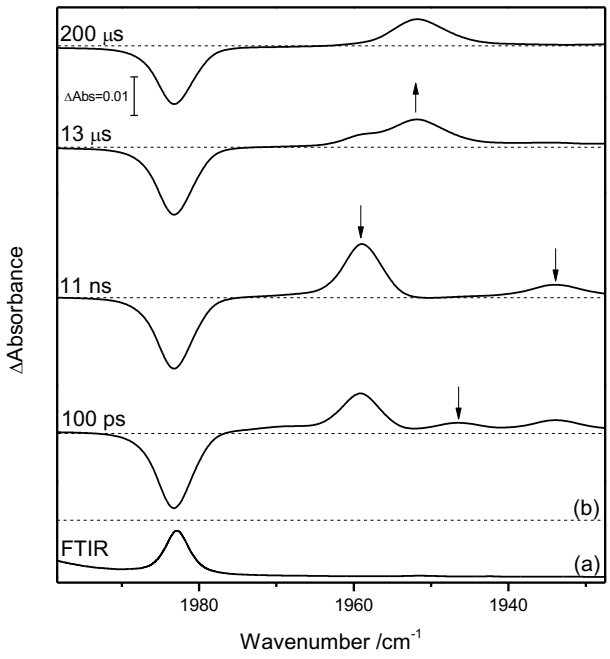


Figure 3.29 *(a) FTIR spectrum and (b) TRIR spectra obtained following photolysis (266 nm) of 0.2 mM $W(CO)_6$ in heptane doped with 0.04 M $HGeBu_3$.*

A similar reaction process to $HSiBu_3$ and $HSnBu_3$ was observed. The heptane species $W(CO)_5$(*n*-heptane) decays and converts to the germane species $W(CO)_5(HGeBu_3)$ (1952 cm^{-1}). Similar ν(CO) positions to $W(CO)_5(HSiBu_3)$ indicates a similar η^1-coordination interaction with the W centre. Influence of the dopant concentration on the C-H/Ge-H ligand exchange rate has been investigated and the results are shown in Table 3.12.

Table 3.12 *Influence of the concentration of $HGeBu_3$ on the C-H/Ge-H ligand exchange rate.*

$W(CO)_6$ concentration /mM	$HGeBu_3$ concentration /M	C-H/Ge-H exchange rate /μs
0.2	0.04	7.0 ±0.2
0.2	0.08	3.4 ±0.06

As shown in Table 3.12, for $HGeBu_3$ the kinetic order is 1. When comparing the data in Table 3.10, 3.11 and 3.12, it can be noted that the reaction rate follows the

sequence Sn > Ge > Si, which is consistent with their electron donating abilities. The coordination to the W centre is facilitated with more electron rich E-H.

3.2.2 TRIR Investigations on the Interactions between $W(CO)_6$ and Halogenated Cycloalkanes

ns-TRIR of $W(CO)_6$ in heptane doped with Cl-cyclohexane or Br-cyclohexane has been conducted, the effect of dopant concentration has also been investigated.

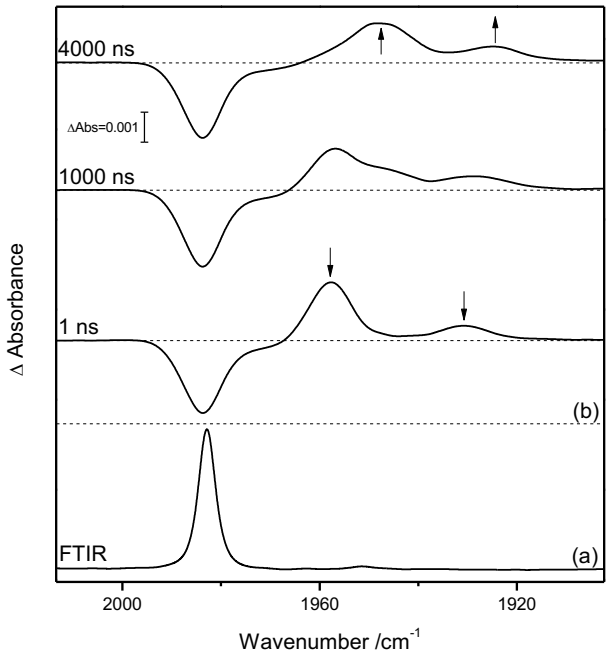


Figure 3.30 *(a) FTIR spectrum and (b) ns-TRIR spectra obtained following photolysis (266 nm) of 0.2 mM $W(CO)_6$ in n-heptane doped with 0.02 M Cl-cyclohexane.*

Figure 3.30 shows the ns-TRIR spectra of $W(CO)_6$ in *n*-heptane doped with Cl-cyclohexane. Upon UV photolysis, two bands at lower wavenumber than the parent bleach (1983 cm^{-1}) at *ca.* 1957 and 1931 cm^{-1} are formed, which is assigned to $W(CO)_5$(*n*-heptane) based on previous results in heptane (1959, 1929 cm^{-1}).[82] At later time delays, $W(CO)_5$(*n*-heptane) decays and two new bands are formed at lower wavenumber at *ca.* 1947 and 1924 cm^{-1}. This indicates that a more electron rich ligand has replaced *n*-heptane. These bands are assigned to $W(CO)_5$(Cl-cyclohexane). According to previous research, the ν(CO) band positions of $W(CO)_5$(cyclohexane) in neat cyclohexane, where W coordinates to the C-H bond of cyclohexane in a 3-c-2-e agostic mode are at 1960 and 1934 cm^{-1}.[11] Therefore,

here the final species (1947 and 1924 cm^{-1}) is not considered to be the C-H bound species in which the W centre coordinates to the C-H of Cl-cyclohexane in an agostic mode. As suggested by Dobson *et al.*,[54] for $W(CO)_5$(F-hexane), the preferred binding mode of F-hexane to W is *via* the F atom lone pair rather than the C-H agostic mode, the ν(CO) band positon of $W(CO)_5$(F-hexane) in F-hexane is at 1952 cm^{-1}. As Cl is recognised as less electronagtive and has a larger polarizability than F, therefore it is proposed that in $W(CO)_5$(Cl-cyclohexane), the W may have coordinated to the lone pair of Cl.

Kinetic analysis shows that $W(CO)_5(\eta^1$-Cl-cyclohexane) (2.2 ±0.1 μs) is converted from $W(CO)_5$(*n*-heptane) (2.1 ±0.04 μs), as shown in Figure 3.31.

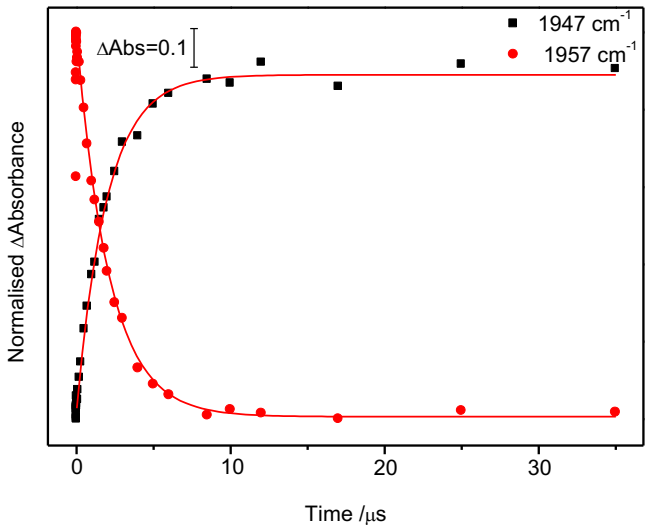


Figure 3.31 *TRIR kinetic traces obtained at 1957 and 1947 cm^{-1}, corresponding to $W(CO)_5$(n-heptane) and $W(CO)_5(\eta^1$-Cl-cyclohexane).*

$W(CO)_5(\eta^1$-Cl-cyclohexane) is stable and shows no decay during the experimental timescale (200 μs).

The ligand exchange rate is accelerated when increasing the concentration of Cl-cyclohexane, as shown in Table 3.13.

Table 3.13 *Effects of the dopant (Cl-cyclohexane) concentration on the rate of ligand exchange between W(CO)$_5$(n-heptane) and W(CO)$_5$(η^1-Cl-cyclohexane).*

Dopant concentration /M	Ligand exchange rate/μs	$K_{obs}x10^5$ /s^{-1}
0.02	2.2±0.1	4.6
0.04	1.1±0.04	9.1
0.08	0.7±0.02	14.3
0.12	0.5±0.02	20.0

The relation between the dopant concentration and the observed rate constant is shown in Figure 3.32.

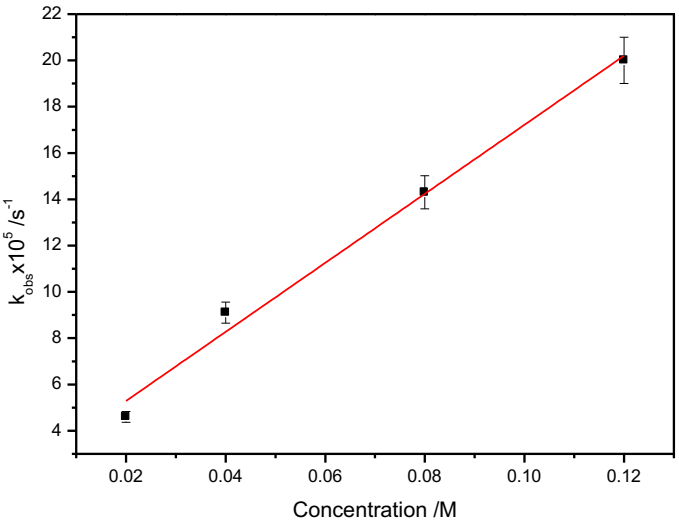


Figure 3.32 *Relation between the concentration of Cl-cyclohexane (M) and the observed rate constant k_{obs} for the ligand exchange reaction between W(CO)$_5$(n-heptane) and W(CO)$_5$(η^1-Cl-cyclohexane).*

As shown in Figure 3.32, the observed rate constant K_{obs} is in a linear relation with the concentration of the dopant Cl-cyclohexane, which indicates that the ligand exchange reaction between W(CO)$_5$(*n*-heptane) and W(CO)$_5$(η^1-Cl-cyclohexane) is first order for the concentration of the dopant Cl-cyclohexane. The second order rate constant calculated is k_2 = 1.5(±0.1)x10^7 dm^3 mol^{-1} s^{-1}. A similar reaction process has been observed for the dopant Br-cyclohexane.

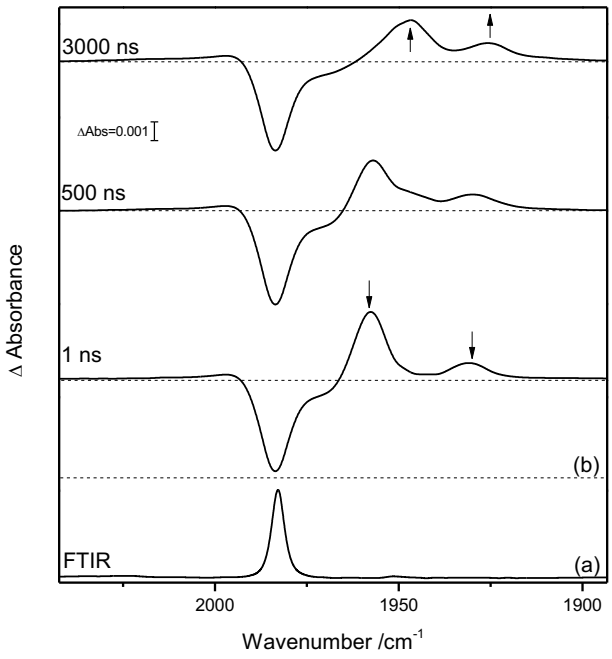


Figure 3.33 *(a) FTIR spectrum and (b) ns-TRIR spectra obtained following photolysis (266 nm) of 0.2 mM $W(CO)_6$ in n-heptane doped with 0.02 M Br-cyclohexane.*

As shown in Figure 3.33, similar to TRIR of Cl-cyclohexane, the decay of $W(CO)_5$(*n*-heptane) and the formation of $W(CO)_5$(Br-cyclohexane) have been observed in the TRIR spectra. The ν(CO) positions of $W(CO)_5$(Br-cyclohexane) (1946, 1925 cm^{-1}) is similar to that of $W(CO)_5$(Cl-cyclohexane) (1947, 1924 cm^{-1}). For $W(CO)_5$(Br-cyclohexane), it is also proposed that the W centre is coordinated to the Br atom *via* the lone pair, as Br is considered to be more electron rich than Cl.

DFT calculations have been conducted to support the band assignment. The results are shown in Table 3.14.

Table 3.14. *DFT calculation results of IR frequencies of different species (B3LYP, 6-31G(d), gas phase).*

Species	ν(CO) /cm^{-1} (DFT)	ν(CO) /cm^{-1} (experimental)
$W(CO)_6$	2076	1983
$W(CO)_5$(*n*-heptane)	2052, 2036	1957, 1931
$W(CO)_5(\eta^1$-Cl-cyclohexane)	2041, 2037, 2029	1947, 1924
$W(CO)_5(\eta^1$-Br-cyclohexane)	2040, 2035, 2028	1946, 1925

According to the DFT results, for both $W(CO)_5(\eta^1$-Cl-cyclohexane) and $W(CO)_5(\eta^1$-Br-cyclohexane), a broad band composed of two close bands at higher wavenumber is expected. For $W(CO)_5(\eta^1$-Cl-cyclohexane) at 2041 and 2037 cm^{-1}, while for $W(CO)_5(\eta^1$-Br-cyclohexane) the bands are at 2040 and 2035 cm^{-1}. As shown in Figure 3.30 and Figure 3.33, the corresponding bands centred at *ca.* 1947 and 1946 cm^{-1} are actually quite broad, consistent with the DFT results. The $\Delta\nu$(CO) between $W(CO)_5(\eta^1$-Cl-cyclohexane) and the band of $W(CO)_5$(*n*-heptane) at higher wavenumber is *ca.* 13 cm^{-1}, while between $W(CO)_5(\eta^1$-Br-cyclohexane) and $W(CO)_5$(*n*-heptane) is *ca.* 14 cm^{-1}, similar to the experimental results of 10 and 11 cm^{-1}, respectively. The $\Delta\nu$(CO) between the two bands of $W(CO)_5(\eta^1$-Cl-cyclohexane) and $W(CO)_5(\eta^1$-Br-cyclohexane) are both *ca.* 10 cm^{-1}, which is smaller than the experimental results (*ca.* 22 cm^{-1}). This may indicate that DFT has overestimated the wavenumber of the lower bands of $W(CO)_5(\eta^1$-Cl-cyclohexane) and $W(CO)_5(\eta^1$-Br-cyclohexane), which is also the case for $W(CO)_5$(*n*-heptane). However, the $\Delta\nu$(CO) between the two lower bands of complexes $W(CO)_5(\eta^1$-Cl-cyclohexane) (2029 cm^{-1}) and $W(CO)_5$(*n*-heptane) (2036 cm^{-1}) is 7 cm^{-1}, similar to the experimental result of 7 cm^{-1}. Also the $\Delta\nu$(CO) between the two lower bands of $W(CO)_5(\eta^1$-Br-cyclohexane) (2028 cm^{-1}) and $W(CO)_5$(*n*-heptane) (2036 cm^{-1}) is 8 cm^{-1}, similar to the experimental result of 6 cm^{-1}. Therefore, the DFT results support the assignments of the new bands to the $W(CO)_5(\eta^1$-X-cyclohexane) (X: Cl, Br) complexes, in which the W centre coordinates to the lone pair of the halogen atoms Cl and Br.

Kinetic analysis reveals the ligand exchange reaction between $W(CO)_5$(*n*-heptane) (1.6 ±0.03 μs) and $W(CO)_5(\eta^1$-Br-cyclohexane) (1.6 ±0.03 μs), as shown in Figure 3.34.

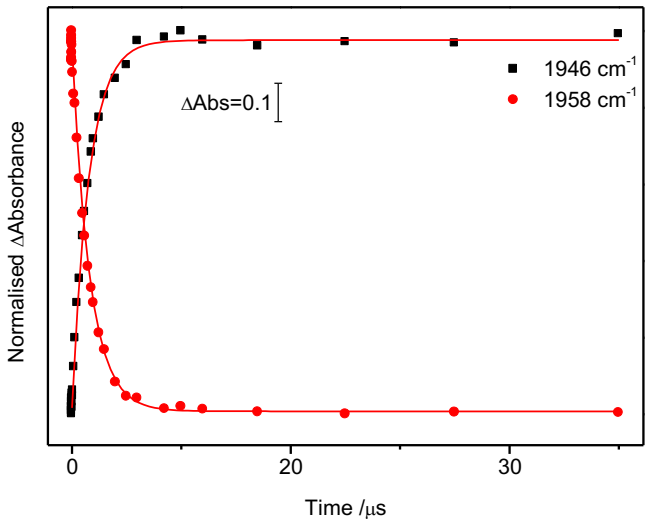


Figure 3.34 *TRIR kinetic traces obtained at 1958 and 1946 cm^{-1}, corresponding to $W(CO)_5$(n-heptane) and $W(CO)_5(\eta^1$-Br-cyclohexane).*

Investigations on the effects of the dopant concentration on the ligand exchange rate have been conducted, the results are summarised in Table 3.15.

Table 3.15 *Effects of the dopant (Br-cyclohexane) concentration on the rate of ligand exchange between $W(CO)_5$(n-heptane) and $W(CO)_5(\eta^1$-Br-cyclohexane).*

Dopant concentration /M	Ligand exchange rate /μs	$K_{obs}x10^5$ /s^{-1}
0.02	1.6±0.03	6.3
0.04	0.9±0.03	11.1
0.08	0.5±0.02	20.0
0.12	0.4±0.02	25.0

The relation between the dopant concentration and the observed rate constant K_{obs} is shown in Figure 3.35.

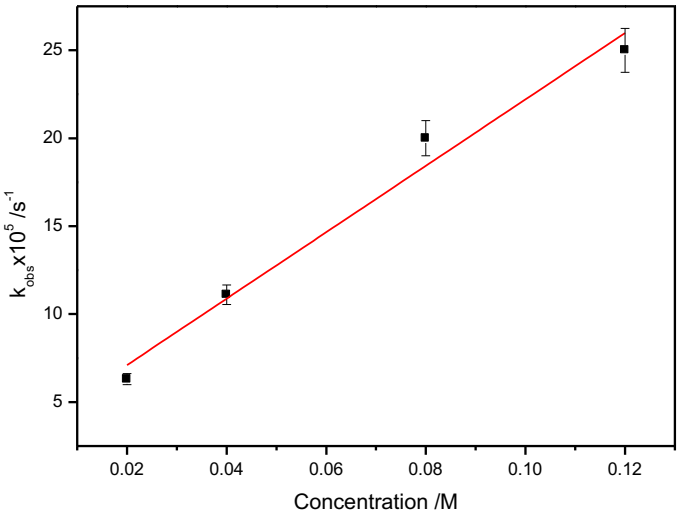


Figure 3.35 *Relation between the concentration of Br-cyclohexane (M) and the observed rate constant k_{obs} for the ligand exchange reaction between W(CO)$_5$(n-heptane) and W(CO)$_5$(η^1-Br-cyclohexane).*

Similar to the experiment with Cl-cyclohexane, the observed rate constant K_{obs} is in a linear relation with the concentration of the dopant Br-cyclohexane, indicating that the ligand exchange reaction between W(CO)$_5$(*n*-heptane) and W(CO)$_5$(η^1-Br-cyclohexane) is first order for the concentration of the dopant Br-cyclohexane. The second order rate constant calculated is k_2 = 1.9(±0.2)x10^7 dm^3 mol^{-1} s^{-1}.

When comparing the ligand exchange rates of Cl-cyclohexane and Br-cyclohexane, it can be observed that for Br-cyclohexane, the exchange rate is faster compared to Cl-cyclohexane at the same dopant concentration, and the second order rate constant for Br-cyclohexane is larger than Cl-cyclohexane, which reflects that in the presence of Br-cyclohexane, the W(CO)$_5$(*n*-heptane) species is more reactive. The results may be explained by the fact that the Br atom in Br-cyclohexane is more electron rich than Cl in Cl-cyclohexane, thus facilitated the coordination to the W centre.

3.2.3 TRIR Investigations on the Interactions between $W(CO)_6$ and Halogenated Benzenes

As mentioned throughout the previous two Chapters, the main drive was to find systems that are suitable for performing time-resolved XAFs measurements. The investigations here were aimed at coordinating heavy halogens to the metal centre such that they could be potentially distinguished from the other M-CO bonds during the XAFs measurement. TRIR investigations on the interactions between $W(CO)_6$ and a series of halogenated benzenes X-benzene (X:H, F, Cl, Br, I) have been conducted.

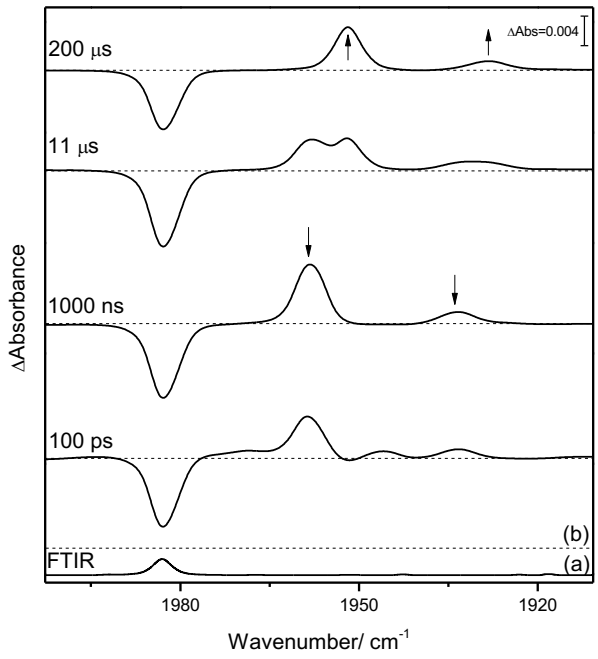


Figure 3.36 *(a) FTIR spectrum and (b) TRIR spectra obtained following photolysis (266 nm) of 0.4 mM $W(CO)_6$ in heptane doped with 0.15 M benzene.*

As shown in Figure 3.36, upon UV photolysis, the formation of $W(CO)_5$(*n*-heptane) is observed (1959, 1946, 1932 cm^{-1}), which decays and at later time delays two new bands at *ca.* 1952 and 1927 cm^{-1} formed. Considering the addition of the dopant benzene, the bands at 1952 and 1927 cm^{-1} are assigned to the $W(CO)_5$(benzene) species, in which the W centre is coordinated to CH=CH of benzene in an η^2-manner, therefore is denoted as $W(CO)_5(\eta^2\text{-}CH{=}CHC_4H_4)$. The

"ring-edge" binding mode is well-recognised by many previous studies in M-benzene interactions where benzene is acting as a two electron donor.[85,28,86]

The kinetics show that $W(CO)_5(\eta^2\text{-}CH{=}CHC_4H_4)$ is transformed from $W(CO)_5$(*n*-heptane), as shown in Figure 3.37.

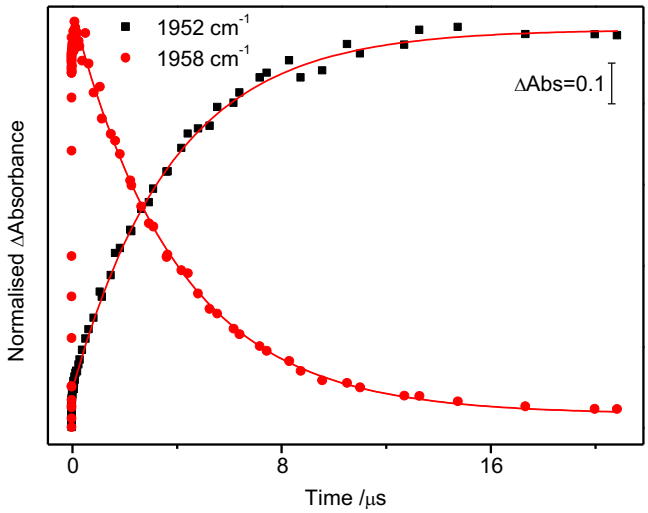


Figure 3.37 *TRIR kinetic traces obtained at 1958 and 1952 cm^{-1} corresponding to $W(CO)_5$(n-heptane) and $W(CO)_5(\eta^2\text{-}CH{=}CHC_4H_4)$, in the presence of 0.15 M benzene.*

Investigations on the effects of the dopant concentration on the ligand exchange rate have been conducted, the results are summarized in Table 3.16.

Table 3.16 *Effects of the dopant (benzene) concentration on the rate of ligand exchange between $W(CO)_5$(n-heptane) and $W(CO)_5(\eta^2\text{-}CH{=}CHC_4H_4)$.*

Dopant concentration /M	Ligand exchange rate /μs	$K_{obs}x10^5$ /s^{-1}
0.05	12.5±0.3	0.8
0.1	10.7±1.3	0.9
0.15	3.8±0.07	2.6

As shown in Table 3.16, the ligand exchange rate is accelerated by increasing the concentration of benzene.

TRIR investigations on halogenated X-benzene (X: F, Cl, Br, I) have also been conducted.

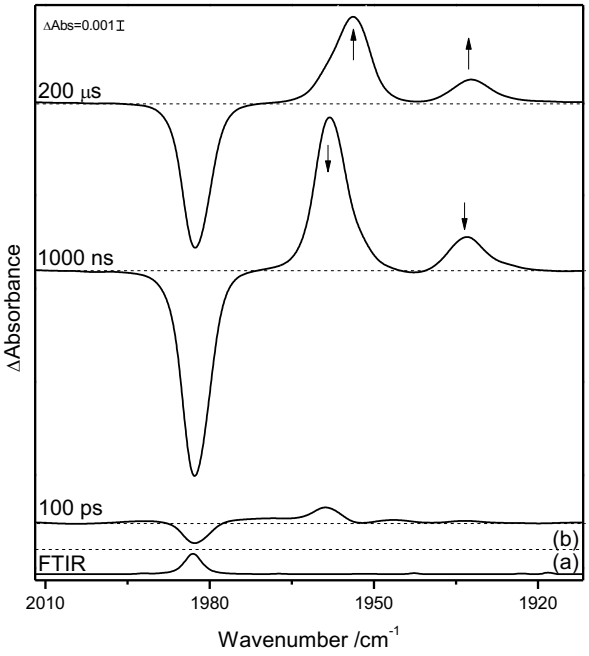


Figure 3.38 *(a) FTIR spectrum and (b) TRIR spectra obtained following photolysis (266 nm) of 0.4 mM $W(CO)_6$ in heptane doped with 0.15 M F-benzene.*

As shown in the spectra, the bands at 1958 and 1932 cm^{-1} [$W(CO)_5$(*n*-heptane)] are formed after UV photolysis, which then decay and a new band at *ca.* 1954 cm^{-1} is formed. However, the band at 1932 cm^{-1} shows no decay when the band at 1958 cm^{-1} decays, therefore, the band at 1932 cm^{-1} may consist of two species, one is the heptane species $W(CO)_5$(*n*-heptane), while the band at 1932 cm^{-1} may also be the other band of the W pentacarbonyl species formed later (1954 cm^{-1}). The bands at 1954 and 1932 cm^{-1} are assigned to the $W(CO)_5$(F-benzene) species. Due to the strong electronegativity of F, the CH=CF is expected to be more electron deficient than CH=CH, therefore W is expected to avoid the F atom. Also the ν(CO) is similar to $W(CO)_5(\eta^2\text{-}CH{=}CHC_4H_4)$ (1952, 1927 cm^{-1}). Therefore in $W(CO)_5$(F-benzene), the W centre is expected to coordinate to the CH=CH edge of the benzene ring, and is denoted as $W(CO)_5(\eta^2\text{-}CH{=}CHC_4H_3F)$. This is consistent with previous work.[29,86] The slightly higher ν(CO) of $W(CO)_5(\eta^2\text{-}CH{=}CHC_4H_3F)$ (1954 and 1932 cm^{-1}) compared to $W(CO)_5(\eta^2\text{-}CH{=}CHC_4H_4)$ (1952 and 1927 cm^{-1}) may be

the indication of how electron withdrawing F reduces the π electron donating ability of the benzene ring. DFT calculations have been conducted in an attempt to assist the assignment, the results are summarised in Table 3.17.

Table 3.17 *Result of DFT calculations on IR frequencices (Method: B3LYP, Basis-set: 6-31G(d), gas phase).*

Species	IR freq. /cm^{-1}	IR intensity /x10^3 Km mol^{-1}	Exp. ν(CO) /cm^{-1}
$W(CO)_6$	2076	1.93	1983
$W(CO)_5$(*n*-heptane)	2052, 2036	1.97, 0.945	1958, 1932
$W(CO)_5(\eta^2$-CH=$CHC_4H_3F)$	2044, 2032	1.82, 0.970	1954, 1932

Calculation of $W(CO)_5(\eta^2$-CH=$CFC_4H_4)$ was unsuccessful, as the geometry of $W(CO)_5(\eta^2$-CH=$CFC_4H_4)$ changes to $W(CO)_5(\eta^2$-CH=$CHC_4H_3F)$ after optimization, indicating the high energy and instability of the $W(CO)_5(\eta^2$-CH=$CFC_4H_4)$ species.

As shown in Table 3.17, the DFT calculations highly overestimated the IR frequencies, Nevertheless, the relative $\Delta\nu$(CO) is still indicative. The $\Delta\nu$(CO) between $W(CO)_6$ (2076 cm^{-1}) and the band at 2052 cm^{-1} for $W(CO)_5$(*n*-heptane) by DFT is 24 cm^{-1}, which is in good agreement with the experimental data (25 cm^{-1}). The $\Delta\nu$(CO) between the two bands of $W(CO)_5$(*n*-heptane) by DFT (2052, 2036 cm^{-1}) is 16 cm^{-1}, while by experiment it is 26 cm^{-1}, which may indicate the band at 2036 cm^{-1} by DFT may not be very reliable. The $\Delta\nu$(CO) between 2052 cm^{-1} of $W(CO)_5$(*n*-heptane) and 2044 cm^{-1} of $W(CO)_5(\eta^2$-CH=$CHC_4H_3F)$ by DFT is 8 cm^{-1}, while by experiment it is 4 cm^{-1}, which is considered to be in reasonable error. Therefore, the assignment of the final species at 1954 and 1932 cm^{-1} to $W(CO)_5(\eta^2$-CH=$CHC_4H_3F)$ is not only consistent with previous work,[29,86] but also supported by the DFT calculations.

Kinetics show that the decay rate of the band at 1958 cm^{-1} (growth rate: 54 ± 5 ns; decay rate: 3.4 ± 0.4 μs) fits the second component of the growth rate of the band at 1954 cm^{-1} (53 ± 8 ns; 2.9 ± 0.1 μs), which suggests an conversion between the two species, as shown in Figure 3.39.

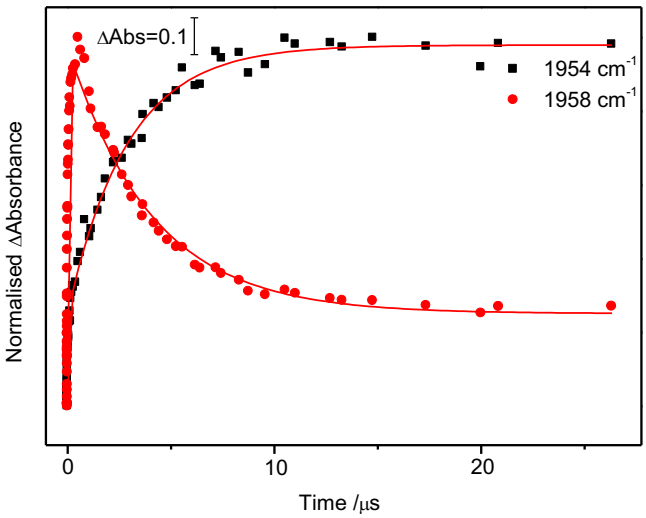


Figure 3.39 *TRIR kinetic traces obtained at 1958 and 1954 cm^{-1} corresponding to W(CO)$_5$(η^2-CH=CFC$_4$H$_4$) and W(CO)$_5$(η^2-CH=CHC$_4$H$_3$F), in the presence of 0.15 M F-benzene.*

The growth of the band at 1954 cm^{-1} is bi-exponential. And as shown in the TRIR spectra (Figure 3.38) the growth of the band at 1958 cm^{-1} is slow, at *ca.* 55 ns according to kinetic analysis. This is inconsistent with the solvation rate of W(CO)$_5$ in alkane solutions according to many previous studies that suggest the solvation of W(CO)$_5$ by alkane should occur within a few picoseconds. Thus, as there are potentially many binding modes between arene and W(CO)$_5$, it is proposed that the band at 1958 cm^{-1} may not only consist of the solvated species W(CO)$_5$(*n*-heptane), but also another F-benzene bound species which forms at the rate for tens of ns. Kinetic analysis also reveals that the formation rate of the band at 1932 cm^{-1} is 60 (±5) ns, consistent with the formation rate of the band at 1958 cm^{-1}. It also needs to be noted that the parent bleach shows further decay on the ns-timescale with similar rate compared to the formation rate of bands at 1958 and 1932 cm^{-1} as well as the formation rate of the final species W(CO)$_5$(η^2-CH=CHC$_4$H$_3$F) on the ns-timescale. This rate is found to be related to the dopant concentration (Table 3.18). This may suggest that the species at 1958 and 1932 cm^{-1} as well as part of W(CO)$_5$(η^2-CH=CHC$_4$H$_3$F) may be directly formed from the parent complex. There is an assumption for the band at 1958 cm^{-1} with the formation rate of *ca.* 55 ns (and 1932 cm^{-1} with the formation rate of *ca.* 60 ns) to be the W(CO)$_5$(η^2-

$CH{=}CFC_4H_4$) species, in which the W centre coordinates to the CF=CH bond. The electron deficient $W(CO)_5(\eta^2\text{-}CH{=}CFC_4H_4)$ species converts to the electron sufficient species $W(CO)_5(\eta^2\text{-}CH{=}CHC_4H_3F)$ on the μs-timescale (Figure 3.39).

Investigations on the effects of dopant concentration on the formation rates of $W(CO)_5(\eta^2\text{-}CH{=}CFC_4H_4)$ and $W(CO)_5(\eta^2\text{-}CH{=}CHC_4H_3F)$, as well as their exchange rate have been conducted. Results are summarised in Table 3.18.

Table 3.18 *Effects of the dopant (F-benzene) concentration on the ligand exchange rate between $W(CO)_5(\eta^2\text{-}CH{=}CFC_4H_4)$ and $W(CO)_5(\eta^2\text{-}CH{=}CHC_4H_3F)$, and the formation rates of $W(CO)_5(\eta^2\text{-}CH{=}CHC_4H_3F)$ and $W(CO)_5(\eta^2\text{-}CH{=}CFC_4H_4)$, and the decay rate of the parent complex $W(CO)_6$.*

Dopant concentration /M	Ligand exchange rate/ μs	Observed rate constant $k_{obs}x10^5$ /s^{-1}	Formation rate of $W(CO)_5(\eta^2\text{-}CH{=}CHC_4H_3F)$	Formation rate of $W(CO)_5(\eta^2\text{-}CH{=}CFC_4H_4)$ /ns	Decay rate of the parent band /ns
0.05	10.1±0.9	0.99	140±19 ns, 10.3±0.6 μs	110±11	149±12
0.1	5.2±0.5	1.92	145±22 ns, 5.3±0.4 μs	101±12	128±10
0.15	3.2±0.3	3.13	58±8 ns, 2.9±0.1 μs	58±6	89±5

The observed rate constant K_{obs} for the ligand exchange rate between $W(CO)_5(\eta^2\text{-}CH{=}CFC_4H_4)$ and $W(CO)_5(\eta^2\text{-}CH{=}CHC_4H_3F)$ is in linear relation with the concentration of F-benzene, which reflects the reaction order of F-benzene is 1, as shown in Figure 3.40.

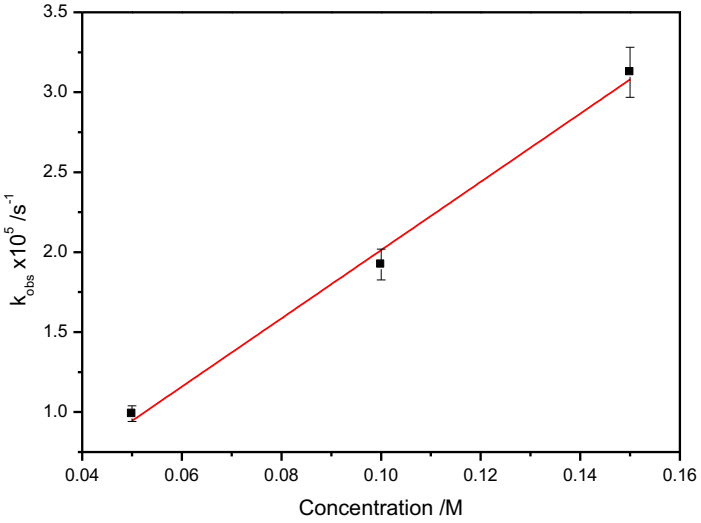


Figure 3.40 *Relation between the concentration of F-benzene (M) and the observed rate constant k_{obs} for the ligand exchange reaction between $W(CO)_5(\eta^2$-$CH{=}CFC_4H_4)$ and $W(CO)_5(\eta^2$-$CH{=}CHC_4H_3F)$.*

Therefore, the mechanism of $W(CO)_6$ in heptane doped with fluorobenzene can be shown in Figure 3.41.

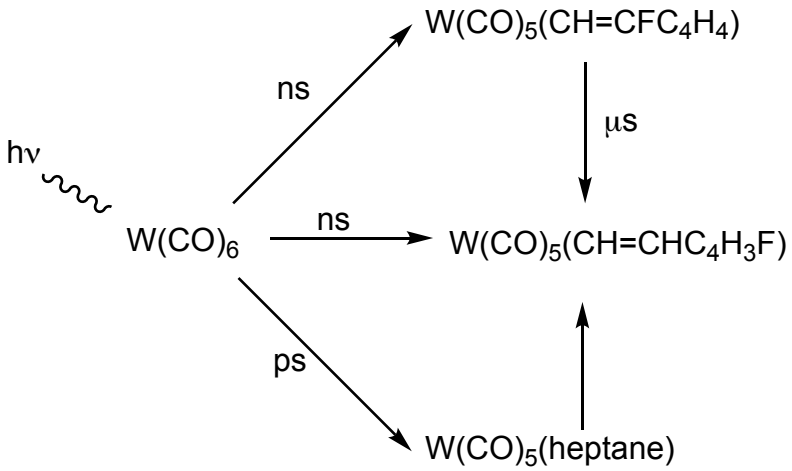


Figure 3.41 *Proposed mechanism of $W(CO)_6$ in heptane doped with fluorobenzene upon UV photolysis.*

The $\nu1\rightarrow2$ band of vibrationally hot $W(CO)_5$(*n*-heptane)* at 1946 cm^{-1} confirms the formation of the heptane species $W(CO)_5$(*n*-heptane). However, as can be observed from the TRIR spectra (Figure 3.38), the IR intensity of the $W(CO)_5$(*n*-heptane) species is significantly weaker than $W(CO)_5(\eta^2$-$CH{=}CFC_4H_4)$, and meanwhile these

two species overlap with each other. Therefore, kinetic analysis of $W(CO)_5$(*n*-heptane) becomes extremely difficult, and how the solvent species $W(CO)_5$(heptane) evolves at later time delays is unknown.

Figure 3.42 shows the TRIR spectra of $W(CO)_6$ in heptane doped with Cl-benzene.

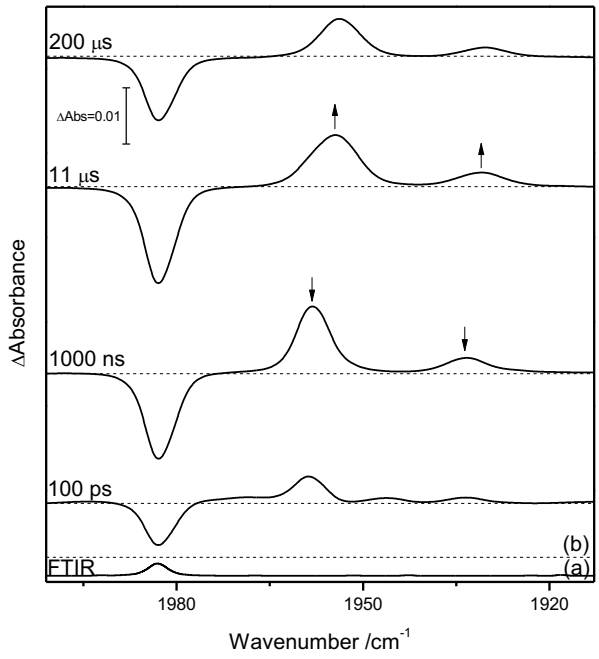


Figure 3.42 *(a) FTIR spectrum and (b) TRIR spectra obtained following photolysis (266 nm) of 0.4 mM $W(CO)_6$ in n-heptane doped with 0.15 M Cl-benzene.*

Similar to TRIR with F-benzene, upon UV photolysis, three bands at *ca.* 1958, 1946 and 1933 cm^{-1} are formed. The band at 1946 cm^{-1} is short-lived which decays within 100 ps. This is consistent with previous work assigned as the solvated species $W(CO)_5$(*n*-heptane). However, similar to TRIR with F-benzene, the bands at 1958 and 1933 cm^{-1} are observed to form relatively slow (*ca.* 290 ns) compared to the commonly quick solvation process of $W(CO)_5$ in alkane solvents within a few ps. Thus, the bands at 1958 and 1933 cm^{-1} are considered to compose of both the solvated species $W(CO)_5$(*n*-heptane) and another species, possibly the $W(CO)_5(\eta^2$-$CH{=}CClC_4H_4)$ species, in which W coordinates to CH=CCl of Cl-benzene.

Similar to the experiment with F-benzene, after the decay of the bands at 1958 and 1933 cm^{-1}, two new bands at *ca.* 1954 and 1930 cm^{-1} are formed. Considering the red shift compared to the bands at 1958 and1933 cm^{-1}, the bands at 1954 and 1930 cm^{-1} are assigned to $W(CO)_5(\eta^1$-Cl-benzene), in which the W centre coordinates to the lone pair of Cl. According to previous research that for the interactions between the metal centre and X-benzene (X: Cl, Br), the metal centre coordinates to the lone pair of the X atom, rather than coordinate to the CH=CH ring-edge as observed for benzene or F-benzene.[29,86] In this binding mode, more electron donation to the W centre are expected compared to $W(CO)_5(\eta^2$-$CH{=}CClC_4H_4)$ (1958, 1933 cm^{-1}). The bands at 1954 and 1930 cm^{-1} are quite stable and shows no decay during the experimental timescale (~200 μs).

DFT calculations have been conducted to assist the assignment, as summarised in Table 3.19.

Table 3.19 *Results of the DFT calculations on IR frequencies (method: B3LYP; Basis-set: 6-31G(d); gas phase).*

Species	DFT ν(CO) /cm^{-1}	IR intensity /x10^3 Km mol^{-1}	Exp.ν(CO) /cm^{-1}
$W(CO)_6$	2076	1.93	1983
$W(CO)_5$(heptane)	2052, 2036	1.97, 0.945	1958, 1933
$W(CO)_5(\eta^2$-$CH{=}CHC_4H_3Cl)$	2044, 2033	1.78, 0.975	-
$W(CO)_5(\eta^1$-Cl-$C_6H_5)$	2045, 2031	1.92, 0.985	1954, 1930

Calculation of the $W(CO)_5(\eta^2$-$CH{=}CClC_4H_4)$ species is unsuccessful, as the geometry of $W(CO)_5(\eta^2$-$CH{=}CClC_4H_4)$ changes to $W(CO)_5(\eta^2$-$CH{=}CHC_4H_3Cl)$ after optimization, indicating the high energy and instability of the $W(CO)_5(\eta^2$-$CH{=}CClC_4H_4)$ species.

As the DFT results in Table 3.19 suggest, the $\Delta\nu$(CO) between $W(CO)_5(\eta^1$-Cl-$C_6H_5)$ and $W(CO)_5$(heptane) is 7 cm^{-1} (the band at 2036 cm^{-1} may not be reliable as discussed before, thus only the bands at 2052 and 2045 cm^{-1} are used for comparison), similar to the experimental value (4 cm^{-1}). As the $W(CO)_5(\eta^2$-

$CH{=}CHC_4H_3Cl$) species is expected to red shift to lower energy than 1954 and 1932 cm^{-1}, the $\nu(CO)$ positions of the $W(CO)_5(\eta^2\text{-}CH{=}CHC_4H_3F)$ species as discussed before, therefore the species at 1958 and 1933 cm^{-1} is still considered to be the $W(CO)_5(\eta^2\text{-}CH{=}CClC_4H_4)$ species.

The conversion from $W(CO)_5(\eta^2\text{-}CH{=}CClC_4H_4)$ (growth rate: 290 ± 65 ns; decay rate: 2.6 ± 0.5 μs) to $W(CO)_5(\eta^1\text{-Cl-benzene})$ (growth rate: 236 ± 74 ns; 2.1 ± 0.09 μs) is revealed by kinetic analysis, as shown in Figure 3.43.

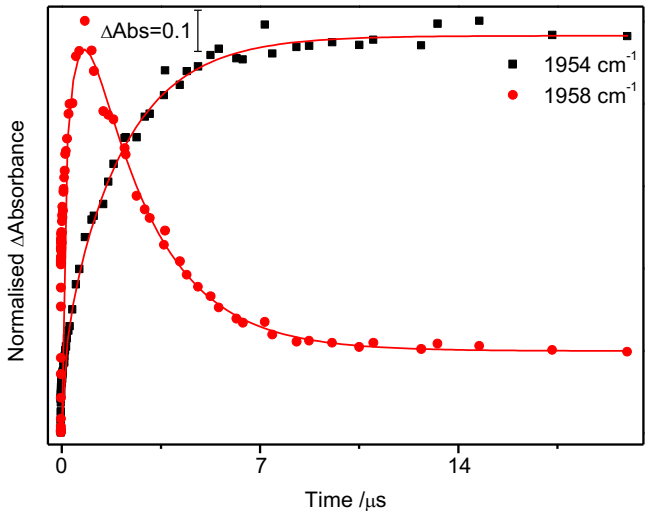


Figure 3.43 *TRIR kinetic traces obtained at 1958 and 1954 cm^{-1} corresponding to $W(CO)_5(\eta^2\text{-}CH{=}CClC_4H_4)$ and $W(CO)_5(\eta^1\text{-}Cl\text{-}C_6H_5)$, in the presence of 0.15 M Cl-benzene.*

As shown in Figure 3.43, the decay of the band at 1958 cm^{-1} fits the growth of the band at 1954 cm^{-1}. Kinetic analyisis of the band at 1933 cm^{-1} reveals similar kinetics with the band at 1958 cm^{-1}, which grows in at 311 (±23) ns, and decays at 3.0 (±0.3) μs. While the band at 1930 cm^{-1} shows similar kinetics to the band at 1954 cm^{-1}. Thus, here $W(CO)_5(\eta^2\text{-}CH{=}CClC_4H_4)$ converts into $W(CO)_5(\eta^1\text{-Cl-benzene})$, indicating the replacement by another more stable binding mode which increases the electron density on the W centre.

Meanwhile, the parent band at 1983 cm^{-1} decays further on the ns-timescale, similar to the experiment with fluorobenzene. The decay rate of the parent band is

consistent with the formation rate of $W(CO)_5(\eta^2\text{-}CH{=}CClC_4H_4)$ as well as the initial formation rate of $W(CO)_5(\eta^1$-Cl-benzene) (Table 3.20). This indicates that $W(CO)_5(\eta^2\text{-}CH{=}CClC_4H_4)$ and part of $W(CO)_5(\eta^1$-Cl-benzene) are formed directly from the parent complex, similar to the experiment with F-benzene.

Investigations on the effects of dopant concentration on the ligand exchange rate have been conducted, results are summarised in Table 3.20.

Table 3.20 *Effects of the dopant (Cl-benzene) concentration on the ligand exchange rate between $W(CO)_5(\eta^2\text{-}CH{=}CClC_4H_4)$ and $W(CO)_5(\eta^1$-Cl-benzene), and the formation rates of $W(CO)_5(\eta^2\text{-}CH{=}CClC_4H_4)$ and $W(CO)_5(\eta^1$-Cl-benzene), and the decay rate of the parent complex $W(CO)_6$.*

Dopant concentration /M	Ligand exchange rate /μs	Observed rate constant $k_{obs}x10^5$ /s^{-1}	Formation rate of $W(CO)_5(\eta^1$-Cl-benzene)	Formation rate of $W(CO)_5(\eta^2\text{-}CH{=}CClC_4H_4)$ /ns	Decay rate of the parent band /ns
0.05	6.3±0.3	1.59	543±138 ns, 6.4±0.4 μs	520±35	559±38
0.1	3.3±0.1	3.03	502±323 ns, 2.8±0.2 μs	518±23	532±25
0.15	2.4±0.3	4.17	236±74 ns, 2.1±0.09 μs	280±60	445±25

It is also found that the observed rate constant k_{obs} and the concentration of Cl-benzene is in linear relation, which suggests that the reaction order of Cl-benzene in the ligand exchange reaction between $W(CO)_5(\eta^2\text{-}CH{=}CClC_4H_4)$ and $W(CO)_5(\eta^1$-Cl-benzene) is one, as shown in Figure 3.44.

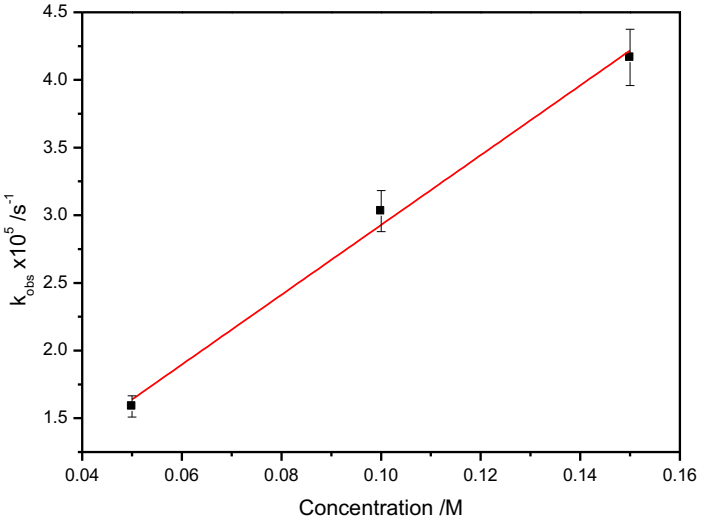


Figure 3.44 *Relation between the concentration of Cl-benzene (M) and the observed rate constant k_{obs} for the ligand exchange reaction between $W(CO)_5(\eta^2$-$CH{=}CClC_4H_4)$ and $W(CO)_5(\eta^1$-Cl-benzene).*

The second order rate constant for Cl-benzene is 2.58(±0.2)x10^6 dm^3 mol^{-1} s^{-1}, while for F-benzene is 2.13(±0.2)x10^6 dm^3 mol^{-1} s^{-1}, which reflects that in the presence of the more electron rich dopant Cl-benzene, the ligand exchange reaction is significantly faciliated.

The reaction mechanism for chlorobenzene might be very similar to that of fluorobenzene, except that the final most stable product is $W(CO)_5(\eta^1$-Cl-benzene) in which the W centre coordinates to the lone pair of Cl. Upon UV photolysis, $W(CO)_6$ dissociates one CO and forms the solvated species $W(CO)_5$(*n*-heptane) in a few ps. Meanwhile $W(CO)_5$ directly combines with chlorobenzene to form both $W(CO)_5(\eta^2$-$CH{=}CClC_4H_4)$ and $W(CO)_5(\eta^1$-Cl-Phenyl) on the ns-timescale. $W(CO)_5(\eta^1$-Cl-Phenyl) is more stable, and $W(CO)_5(\eta^2$-$CH{=}CClC_4H_4)$ converts to $W(CO)_5(\eta^1$-Cl-Phenyl) on the μs-timescale. The ligand exchange rate is dependent on the concentration of chlorobenzene.

However, the TRIR results reveal that the reaction processes for Br-benzene and I-benzene are very different.

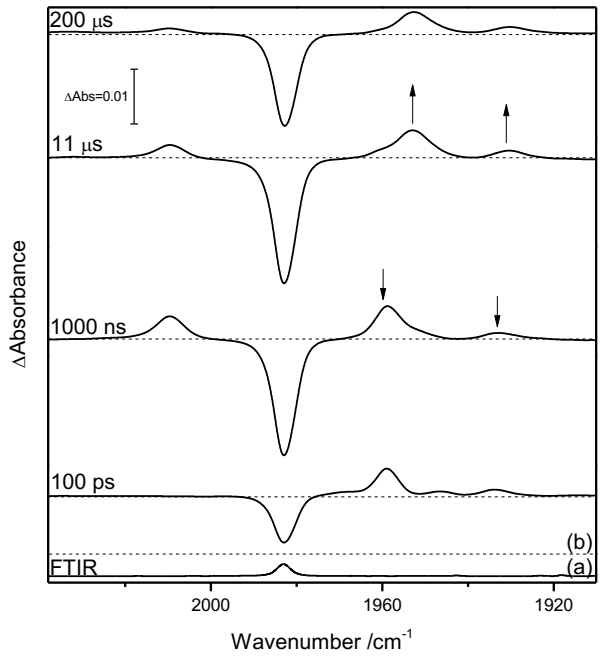


Figure 3.45 *(a) FTIR spectrum and (b) TRIR spectra obtained following photolysis (266 nm) of 0.4 mM $W(CO)_6$ in heptane doped with 0.05 M Br-benzene.*

As shown in Figure 3.45, upon UV photolysis, three bands typical of the solvated species $W(CO)_5$(*n*-heptane) are formed at *ca.* 1958, 1946 and 1932 cm^{-1}. While at later time delays, the bands at 1958 and 1932 cm^{-1} remain when a new band at higher wavenumber than the parent bleach is formed at *ca.* 2010 cm^{-1}. On the μs-timescale, the bands at 1958 and 1932 cm^{-1} decay and two new bands at lower wavenumber at *ca.* 1953 and 1930 cm^{-1} are formed.

The formation of a band at higher wavenumber than the parent bleach has not been observed for F-benzene and Cl-benzene. Kinetic analysis shows that the band at 2010 cm^{-1} forms after 96 (±4) ns, which is consistent with the decay rate of the parent band at 1983 cm^{-1} for 129 ± (17) ns, indicating the species at 2010 cm^{-1} may have been directly formed from the parent complex. The blue shift of the band compared to the parent band may indicate the oxidation of the metal centre.

Different to the F-benzene and Cl-benzene, the bands at 1958 and 1932 cm^{-1} show no further growth on the ns-timescale, similar to $W(CO)_6$ in neat heptane. The

kinetics show that the formation rate of the band at 1958 cm^{-1} is 88 (±7) ps, similar to that in neat heptane (85 ±13 ps, including vibrational cooling). Therefore, the bands at 1958 and 1932 cm^{-1} are thought to be merely the solvated species $W(CO)_5$(*n*-heptane).

DFT calculations have been conducted to assist the assignment, as summarised in Table 3.21.

Table 3.21 *Results of the DFT calculations on IR frequencies (method: B3LYP; Basis-set: 6-31G(d); gas phase).*

Species	IR freq. /cm^{-1}	IR intensity /x10^3 Km mol^{-1}	Energy /a.u.
$W(CO)_6$	2076	1.93	-747.9234
$W(CO)_5$(heptane)	2052, 2036	1.97, 0.945	-910.8082
$W(CO)_5(\eta^2$-$CH{=}CHC_4H_3Br)$	2045, 2033	1.79, 0.978	-879.3701
$W(CO)_5(\eta^2$-$CBr{=}CHC_4H_4)$	2046, 2033	1.77, 0.976	-879.3691
$W(CO)_5(\eta^1$-Br-$C_6H_5)$	2044, 2031	1.91, 0.979	-879.3582
$W(CO)_5$(phenyl)Br	2139, 2069, 2064	1.14, 1.65, 0.634	-879.3743

For the species (2010 cm^{-1}) at higher wavenumber than the parent bleach, as discussed in the Introduction Section in 3.1.2, it is likely that the reaction may follow a concerted mechanism (Figure 3.1). In $W(CO)_6$, the CO is considered to be an electron-acceptor, which will reduce the electron density on the W centre to some extent, therefore the non-chain mechanism which requires electron transfer from W to Br-benzene may not be very likely (Figure 3.3). The IR frequency calculation of the complete oxidative addition species $W(CO)_5$(phenyl)Br has been conducted (Table 3.21). However, as shown in Table 3.21, the experimental value does not match well with the DFT results. the $\Delta\nu$(CO) between the experimental value of $W(CO)_6$ and its DFT result is 93 cm^{-1}, while the $\Delta\nu$(CO) for the species at 2010 cm^{-1} is 129 cm^{-1}. The large red-shift of 2010 cm^{-1} compared to the calculated ν(CO) of $W(CO)_5$(Phenyl)Br may indicate that the C-Br is not completely cleaved. Therefore, the band at 2010 cm^{-1} is tentatively assigned as [$W(CO)_5$(Br---phenyl)], in which the C-Br bond forms a 3-c-2-e interaction with the W centre.

Kinetic analysis shows the decay of the band at 1958 cm^{-1} (5.0 ± 0.2 μs) fits the formation of the band at 1953 cm^{-1} (4.9 ± 0.2 μs), indicating a conversion between these two species, as shown in Figure 3.46.

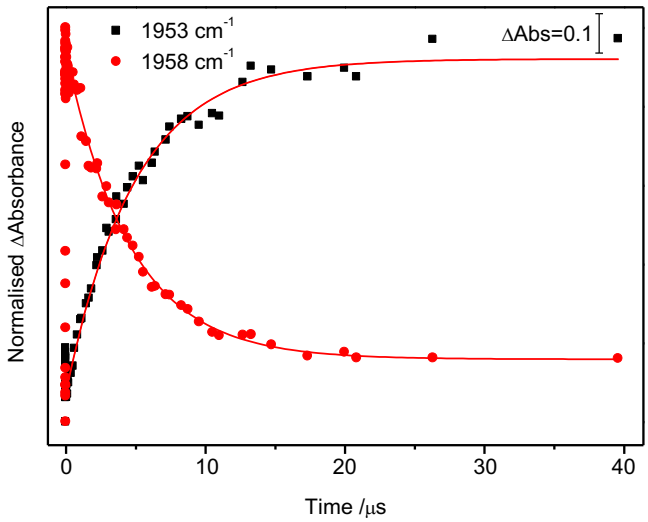


Figure 3.46 *TRIR kinetic traces obtained at 1958 and 1953 cm^{-1} corresponding to $W(CO)_5$(heptane) and $W(CO)_5(\eta^1\text{-Br-}C_6H_5)$ (dopant concentration: 0.05 M).*

Kinetic analysis shows the growth of the band at 1930 cm^{-1} is similar to the band at 1953 cm^{-1}, at 4.5 (±0.5) μs. Thus the bands at 1953 and 1930 cm^{-1} belong to the same species. The bands at 1953 and 1930 cm^{-1} are observed to be stable and show no decay during the experimental timescale (~200 μs). According to previous research, it is proposed that the metal centre coordinates to the lone pair of Br in the interaction between the metal centre and Br-benzene, similar to Cl-benzene.[29] Thus, here the bands at 1953 and 1930 cm^{-1} are assigned to $W(CO)_5(\eta^1$-Br-benzene).

Investigations on the influence of the dopant concentrations on the ligand exchange rate between $W(CO)_5$(heptane) and $W(CO)_5(\eta^1\text{-Br-}C_6H_5)$, and the formation rate of the [$W(CO)_5$(Br---phenyl)] species have been conducted. Results are summarised in Table 3.22.

Table 3.22 *Effects of the dopant (Br-benzene) concentration on the ligand exchange rate between W(CO)$_5$(heptane) and W(CO)$_5$(η^1-Br-C$_6$H$_5$), and the formation rate of the [W(CO)$_5$(Br---phenyl)] species.*

Dopant concentration /M	Ligand exchange rate /μs	Observed rate constant k_{obs}x10^5 /s^{-1}	Formation rate of [W(CO)$_5$(Br---phenyl)] /ns	Decay rate of the parent band /ns
0.05	5.0±0.2	2	96±4	129±17
0.1	2.7±0.1	3.70	97±2	168±15
0.15	2.2±0.2	4.55	102±4	126±17

It was also found that the observed rate constant k_{obs} and the concentration of Br-Benzene is in linear relation for the interchange reaction between W(CO)$_5$(*n*-heptane) and W(CO)$_5$(η^1-Br-C$_6$H$_5$), suggesting a reaction order of 1 for Br-Benzene, and the second order rate constant is calculated to be 2.55(±0.5)x10^6 dm^3 mol^{-1} s^{-1}, as shown in Figure 3.47.

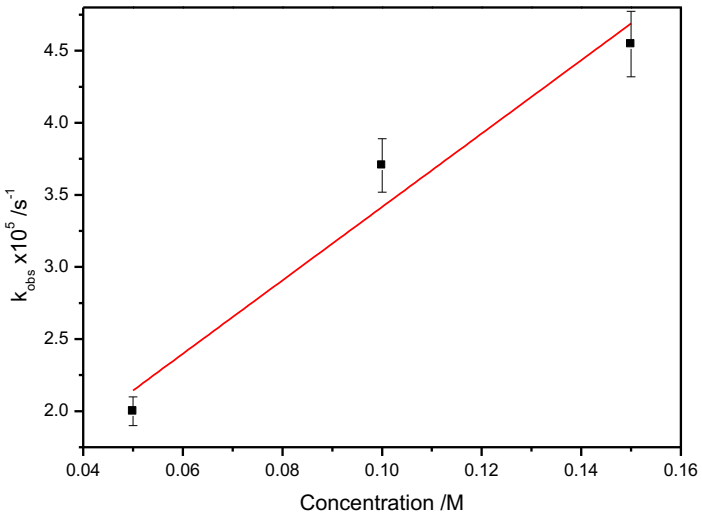


Figure 3.47 *Relation between the concentration of Br-benzene (M) and the observed rate constant k_{obs} for the ligand exchange reaction between W(CO)$_5$(heptane) and W(CO)$_5$(η^1-Br-C$_6$H$_5$).*

Different to chlorobenzene, there is no evidence for the direct conversion from the parent complex W(CO)$_6$ to the W(CO)$_5$(η^1-Br-benzene) species. However, as the

kinetics shown in Table 3.22 indicate, the oxidative addition complex [$W(CO)_5$(Br---phenyl)] may be directly formed from the parent complex $W(CO)_6$.

Therefore, the mechanism for the br-benzene can be shown in Figure 3.48.

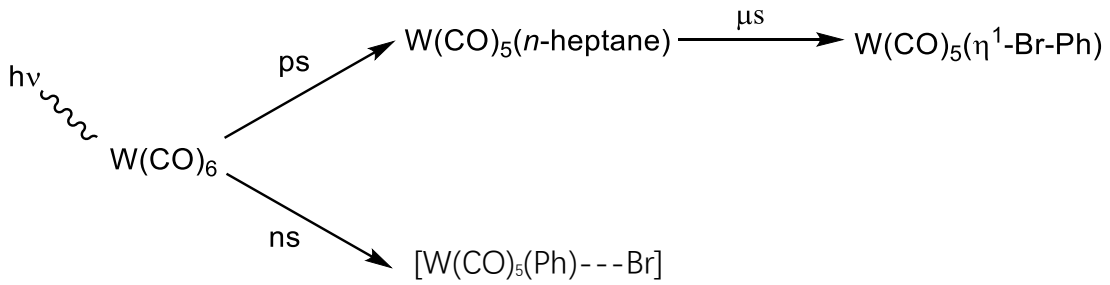


Figure 3.48 *Proposed mechanism of $W(CO)_6$ in heptane doped with bromobenzene.*

For I-benzene, similar reaction process to Br-benzene has been observed.

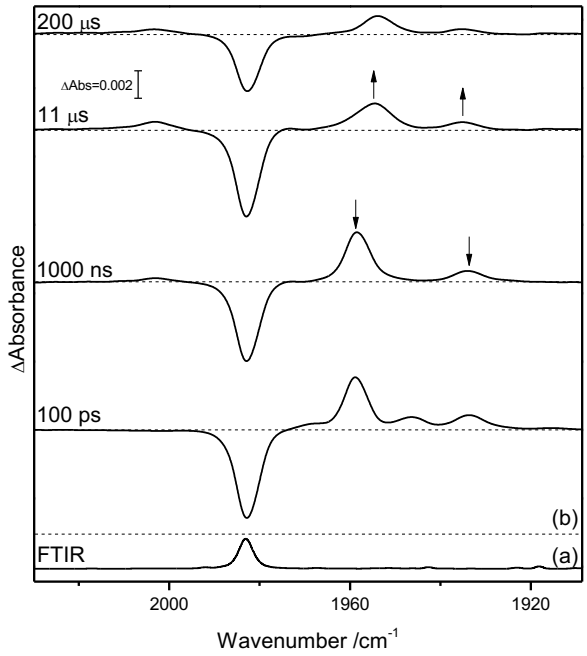


Figure 3.49 *(a) FTIR spectrum and (b) TRIR spectra obtained following photolysis (266 nm) of 0.4 mM $W(CO)_6$ in heptane doped with 0.05 M I-benzene.*

It can be observed from Figure 3.49 that, similar to Br-benzene, upon UV photolysis, three of the typical $W(CO)_5$(*n*-heptane) bands are formed at *ca.* 1958, 1946 and

1932 cm^{-1}. At later time delays, a band at higher wavenumber to the parent bleach at *ca.* 2003 cm^{-1} is formed. After the decay of the bands at 1958, 1946 and 1932 cm^{-1}, two bands at 1954 and 1935 cm^{-1} are formed on the μs-timescale.

Kinetic analysis shows the formation rate for the band at 1958 cm^{-1} is 82 (±3) ps, consistent with the formation rate of $W(CO)_5$(*n*-heptane) in neat heptane. And the decay rate of the band at 1946 cm^{-1} is 88 (±7) ps, also consistent with the decay rate of the $\nu_1 \rightarrow \nu_2$ transition hot band at *ca.* 1945 cm^{-1} in neat heptane. Thus, the bands at 1958, 1946 and 1933 cm^{-1} are assigned to the solvated species $W(CO)_5$(*n*-heptane).

DFT calculations have also been conducted for the I-benzene complexes, as shown in Table 3.23.

Table 3.23 *Results of the DFT calculations on IR frequencies of I-benzene complexes (method: B3LYP; Basis-set: 6-31G(d); gas phase).*

Species	IR frequencies /cm^{-1}	IR intensity /x10^3 Km mol^{-1}	Energy /a.u.
$W(CO)_6$	2076	1.932	-747.9234
$W(CO)_5$(heptane)	2052, 2036	1.97, 0.945	-910.8082
$W(CO)_5(\eta^2$-$CH{=}CHC_4H_3I)$	2044, 2033	1.79, 0.980	-877.5898
$W(CO)_5(\eta^2$-$CI{=}CHC_4H_4)$	2045, 2032	1.77, 0.975	-877.5864
$W(CO)_5(\eta^1$-I-$C_6H_5)$	2044, 2033	1.91, 0.958	-877.5986
$W(CO)_5$(phenyl)I	2131, 2068	1.13, 1.63	-877.5943

As indicated by the data in Table 3.23, the band at 2003 cm^{-1} is tentatively assigned as [$W(CO)_5$(I---phenyl)]. The relative lower wavenumber of [$W(CO)_5$(I---phenyl)] compared to [$W(CO)_5$(Br---phenyl)] (2010 cm^{-1}) is attributed to the greater electron donation of I. Kinetic analysis shows that the formation rate of [$W(CO)_5$(I---phenyl)] is 1.9 (±0.2 μs), much slower than [$W(CO)_5$(Br---phenyl)]. The bands at 1954 and 1935 cm^{-1} are observed to be quite stable during the experimental timescale (~200 μs), and are assigned to $W(CO)_5(\eta^1$-I-benzene).

The conversion between $W(CO)_5$(*n*-heptane) (2.5 ±0.1 μs) and $W(CO)_5(\eta^1$-I-Phenyl) (2.6 ±0.1 μs) is revealed by kinetic analysis, as shown in Figure 3.50.

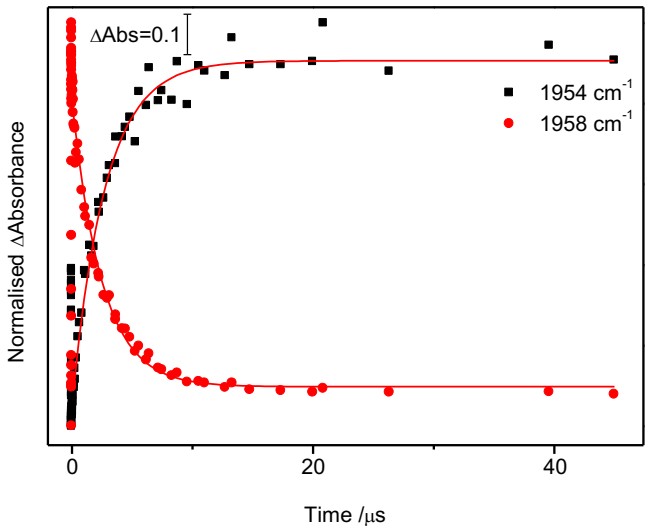


Figure 3.50 *TRIR kinetic traces obtained at 1958 and 1954 cm^{-1}corresponding to $W(CO)_5$(n-heptane) and $W(CO)_5(\eta^1$-I-benzene) (dopant concentration: 0.05 M).*

Investigations on the influence of the dopant concentration on the ligand exchange rate between $W(CO)_5$(*n*-heptane) and $W(CO)_5(\eta^1$-I-benzene), and the formation rate of [$W(CO)_5$(I---phenyl)] have been conducted, results are summarised in Table 3.24.

Table 3.24 *Effects of the dopant (I-benzene) concentration on the ligand exchange rate between $W(CO)_5$(n-heptane) and $W(CO)_5(\eta^1$-I-benzene), and the formation rate of [$W(CO)_5$(I---phenyl)].*

Dopant concentration /M	Ligand exchange rate /μs	Observed rate constant $k_{obs}x10^5$ $/s^{-1}$	Formation rate of [$W(CO)_5$(I---phenyl)]
0.05	2.6±0.1	3.8	123±26 ns, 1.9±0.2 μs
0.1	4.0±0.2	2.5	96±15 ns, 1.8±0.1 μs
0.15	0.9±0.6	11.2	18±4 ns, 1.0±0.08 μs

The abnormal slow rate observed for the dopant concentration of 0.1 M may be caused by wrongly-controlled dopant concentration.

Different to F-benzene, Cl-benzene, and Br-benzene, there was no further decay of the parent band at 1983 cm^{-1}, only the recovery from the vibrational hot state within 100 ps was observed.

It also needs to be noted that, different to bromobenzene, the oxidative addition species [$W(CO)_5$(I---phenyl)] is converted from the heptane species $W(CO)_5$(*n*-heptane), as suggested by kinetics [the formation rate of [$W(CO)_5$(I---phenyl)] (1.9±0.2 μs) matches the decay rate of $W(CO)_5$(*n*-heptane) (2.5 ±0.1 μs)].

Therefore, in conclusion, for benzene, F-benzene and Cl-benzene, no oxidative addition has been observed. Upon UV photolysis, the CO-loss pentacarbonyl species $W(CO)_5$ is quickly solvated to form $W(CO)_5$(*n*-heptane), as well as coordinating to the CX=CH bond of F-benzene and Cl-benzene. On the μs-timescale, $W(CO)_5$(*n*-heptane) undergoes ligand exchange reaction with benzene, and F-benzene to form $W(CO)_5(\eta^2$-CH=CHC_4H_3L) (L: H, F). For Cl-benzene, $W(CO)_5$(*n*-heptane) and $W(CO)_5(\eta^2$-CH=CClC_4H_4) are observed to convert to the lone-pair coordinated species $W(CO)_5(\eta^1$-Cl-Ph). For Br-benzene and I-benzene, along with the formation of $W(CO)_5$(*n*-heptane), the oxidative addition complex [$W(CO)_5$(X---phenyl)] (X: Br, I) is observed to form (no formation of the ring-edge bound species is observed). Also on the μs-timescale, $W(CO)_5$(*n*-heptane) is observed to convert to the lone-pair coordinated species $W(CO)_5(\eta^1$-X-Ph).

3.2.4 E-H Bond Activation of $HEBu_3$ (E: Si, Ge, Sn) by $W(CO)_5L$ Complexes (L: pyridine (py), 4-acetylpyridine (4-acpy), piperidine (pip)) in Alkane Solvent

As will become apparent at the end of this Chapter, the success in time-resolved XAFs came from a system with a high-quantum yield namely $W(CO)_6$. However, chronologically the investigations into systems related to $W(CO)_6$, particularly the activation of E-H bond of $HEBu_3$ (E: Si, Ge, Sn) by a series of W pentacarbonyl complexes of the formula $W(CO)_5L$ (L: py, 4-acpy, pip) in heptane have been investigated using TRIR.

3.2.4.1 TRIR Investigations on E-H Bond Activation of $HEBu_3$ (E: Si, Ge, Sn) by $W(CO)_5$(py) in Heptane

First, the TRIR of $W(CO)_5$(py) in neat heptane was conducted.

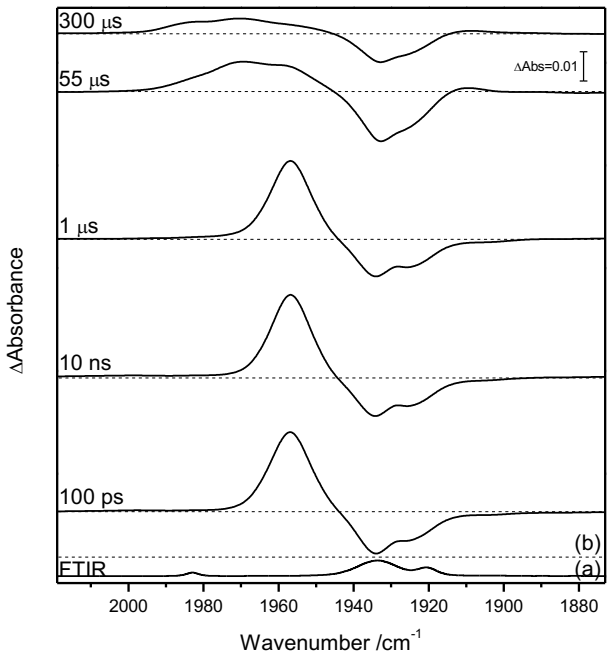


Figure 3.51 *(a) FTIR spectrum and (b) TRIR spectra obtained following photolysis (400 nm) of $W(CO)_5$(py) in neat heptane.*

Figure 3.51 shows the TRIR spectra of $W(CO)_5(py)$ in neat heptane, from which it can be observed that a band at 1957 cm^{-1} is instantly formed upon UV photolysis, and is very stable till μs-timescale. On the microsecond timescale a broad feature from *ca.* 1980 to 1950 cm^{-1} is formed. As discussed in the Introduction Section, upon UV photolysis, the L loss in the $W(CO)_5L$ complex (L: n-donor) is predominant, thus here it is expected that after UV irradiation, the W pentacarbonyl speices $W(CO)_5$ should form, which is unstable and should rapidly coordinate to the surrounding solvent molecules. Compared to the analogue species $W(CO)_5$(*n*-heptane) (1959, 1929 cm^{-1}) observed in neat *n*-heptane according to previous work,[82] the band at 1957 cm^{-1} is assigned to the solvated species $W(CO)_5$(*n*-heptane). The band expected at *ca.* 1929 cm^{-1} may be obscured by overlap with the parent bleaches (1934, 1921 cm^{-1}). While the broad feature formed at later time delays is proposed to be caused by the impurities in the solvent, such as trace amount of water or O_2.

Figure 3.52 shows the TRIR spectra of $W(CO)_5(py)$ in heptane doped with $HSiBu_3$.

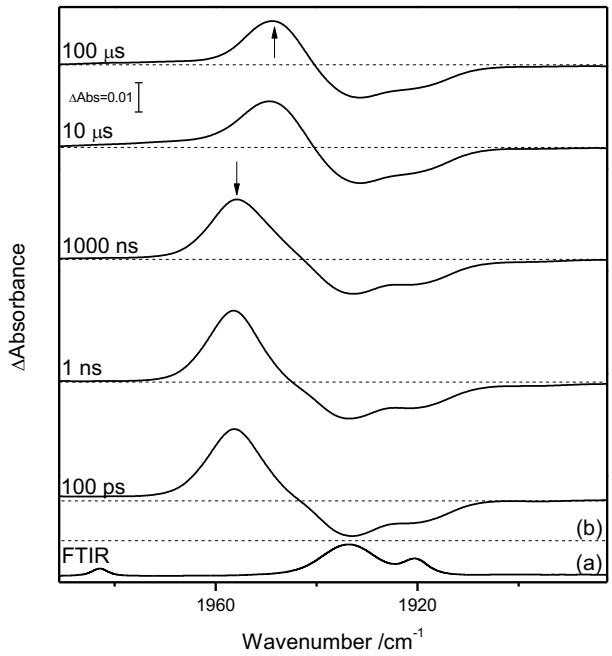


Figure 3.52 *(a) FTIR spectrum and (b) TRIR spectra obtained following photolysis (400 nm) of $W(CO)_5(py)$ in heptane doped with 0.1 M $HSiBu_3$.*

As shown in Figure 3.52, similar to that in neat *n*-heptane (Figure 3.51), $W(CO)_5(py)$ first dissociates the py ligand and generates $W(CO)_5$, which quickly coordinates to the surrounding heptane molecule to form $W(CO)_5$(*n*-heptane), as shown by the formation of a band at 1957 cm^{-1}.

The solvated species $W(CO)_5$(*n*-heptane) then decays and a new band at *ca.* 1951 cm^{-1} is formed. This is consistent with the silane species $W(CO)_5(\eta^1\text{-}HSiBu_3)$ (1952 cm^{-1}) as discussed before in Section 3.2.1. Thus, the band at 1951 cm^{-1} is assigned to $W(CO)_5(\eta^1\text{-}HSiBu_3)$.

Kinetic analysis reveals the conversion between $W(CO)_5$(*n*-heptane) (3.9 ±0.06 μs) and $W(CO)_5(\eta^1\text{-}HSiBu_3)$ (3.7 ±0.08 μs), as shown in Figure 3.53.

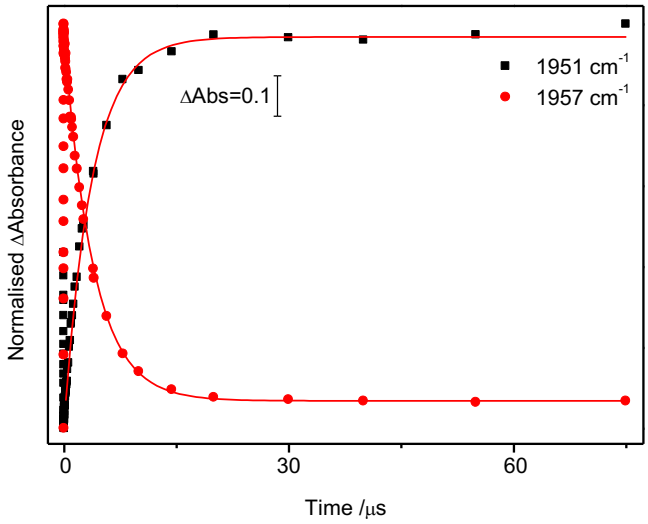


Figure 3.53 *TRIR kinetic traces obtained at 1957 and 1951 cm^{-1} corresponding to $W(CO)_5$(n-heptane) and $W(CO)_5(\eta^1\text{-}HSiBu_3)$ ($HSiBu_3$ concentration: 0.1 M).*

As previous work suggests, the lowest-lying excited state of $W(CO)_5(py)$ is either the ^3LF state or the $^3MLCT_{W\rightarrow CO}$ state. Both these states are considered to be highly reactive, and *via* which the ligand L dissociation with high quantum yield can occur. However, as both the ^3LF and the $^3MLCT_{W\rightarrow CO}$ states are very short-lived at room temperature, which undergo rapid L dissociation, therefore direct observation of either the ^3LF or the ^3MLCT (W→CO) state was not achieved.

The ligand exchange rate between $W(CO)_5$(*n*-heptane) and $W(CO)_5(\eta^1\text{-}HSiBu_3)$ is similar to that of $W(CO)_6$ (3.7 ±0.05 μs) at the same dopant concentration (0.1 M), as discussed in Section 3.2.1.

When decreasing the concentration of $HSiBu_3$ to 0.05 M, it is found that the ligand exchange rate is also slowed down to 6.6 (±0.1) μs. The result is very similar to $W(CO)_6$ in heptane doped with $HSiBu_3$ (*ca*. 7.5 μs) at the same dopant concentration, which indicates that the kinetic order of the dopant $HSiBu_3$ in the C-H/Si-H ligand exchange reaction in *n*-heptane for both $W(CO)_5$(py) and $W(CO)_6$ is 1. This is also evidence of similar photo-reaction mechanism for $W(CO)_5$(py) and $W(CO)_6$.

TRIR investigation on Ge-H bond activation of $HGeBu_3$ has been conducted, as shown in Figure 3.54.

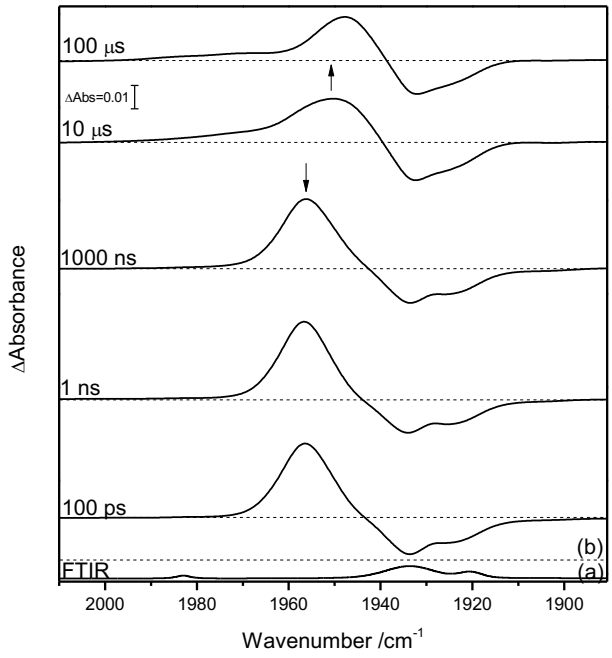


Figure 3.54 *(a) FTIR spectrum and (b) TRIR spectra obtained following photolysis (400 nm) of $W(CO)_5$(py) in heptane doped with 0.05 M $HGeBu_3$.*

Similar to $HSiBu_3$, after UV photolysis, the parent bands are bleached, while a new band at *ca.* 1957 cm^{-1} is formed, and can be assigned to $W(CO)_5$(*n*-heptane). On

the μs-timescale, $W(CO)_5$(*n*-heptane) decays and a new band at *ca.* 1951 cm^{-1} is formed, which can be assigned to $W(CO)_5(\eta^1\text{-}HGeBu_3)$ based on similar previous work of Ge-H activation by $W(CO)_6$ in *n*-heptane ($W(CO)_5(\eta^1\text{-}HGeBu_3)$:1952 cm^{-1}).

The conversion from $W(CO)_5$(*n*-heptane) (7.0 ±0.1 μs) to $W(CO)_5(\eta^1\text{-}HGeBu_3)$ (6.9 ±0.1 μs) has also been revealed by kinetic analysis, as shown in Figure 3.55.

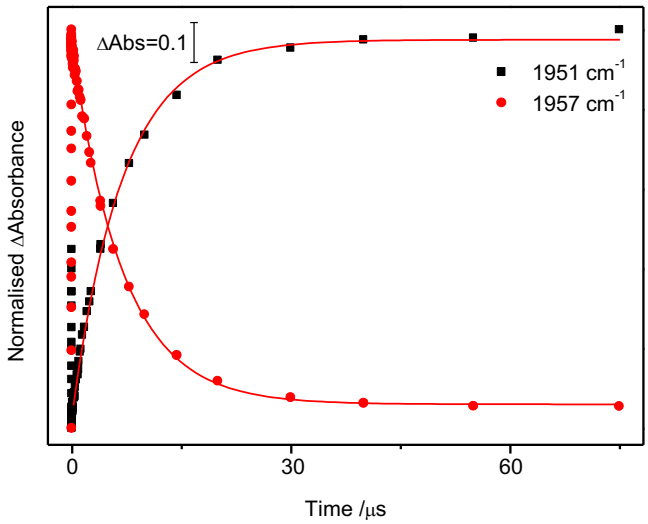


Figure 3.55 *TRIR kinetic traces obtained at 1957 and 1951 cm^{-1} corresponding to $W(CO)_5$(n-heptane) and $W(CO)_5(\eta^1\text{-}HGeBu_3)$ ($HGeBu_3$ concentration: 0.05 M).*

The C-H/Ge-H ligand exchange rate for $W(CO)_5$(py) is similar to that of $W(CO)_6$ ($HGeBu_3$: 0.04 M; τ: 7.0 ±0.2 μs).

TRIR investigation on Sn-H bond activation of $HSnBu_3$ by $W(CO)_5$(py) has also been conducted, as shown in Figure 3.56.

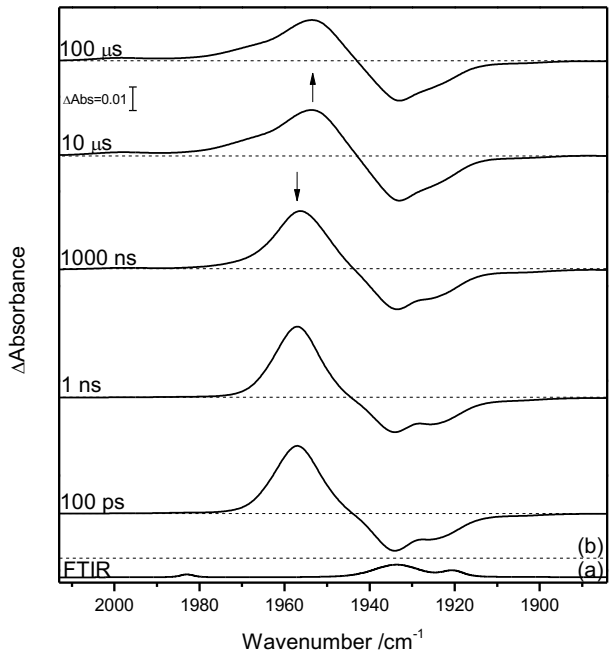


Figure 3.56 *(a) FTIR spectrum and (b) TRIR spectra obtained following photolysis (400 nm) of $W(CO)_5$(py) in heptane doped with 0.1 M $HSnBu_3$.*

Similar to $HSiBu_3$ and $HGeBu_3$, after UV irradiation, along with the parent bleaches, the solvated species $W(CO)_5$(*n*-heptane) is formed, which then decays and a new band at *ca.* 1954 cm^{-1} is formed, and is assigned to the stannane species $W(CO)_5(HSnBu_3)$ compared to the $W(CO)_5(HSnBu_3)$ species (1955 cm^{-1}) formed *via* photoreaction of $W(CO)_6$ in heptane with dopant $HSnBu_3$, as discussed in Section 3.2.1.

Kinetic analysis reveals that compared to $HSiBu_3$ and $HGeBu_3$, the ligand exchange rate between $W(CO)_5$(*n*-heptane) and the stannane species $W(CO)_5(HSnBu_3)$ (1.65 ±0.045 μs) is faster under the same dopant concentration (0.1 M), as shown in Figure 3.57.

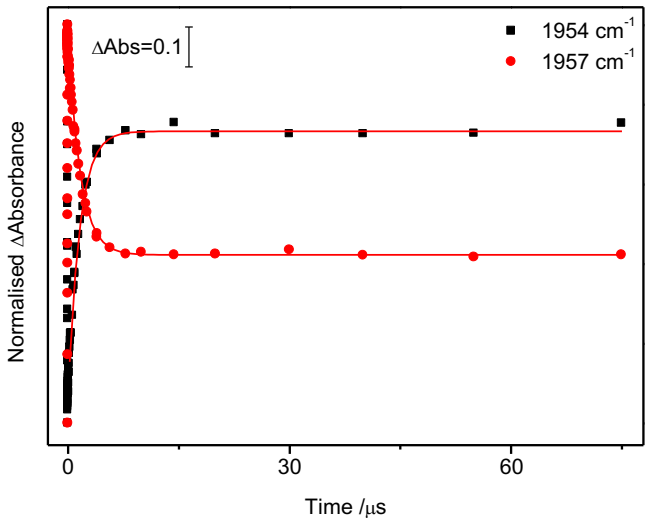


Figure 3.57 *TRIR kinetic traces obtained at 1957 and 1954 cm^{-1} corresponding to $W(CO)_5$(n-heptane) and $W(CO)_5(HSnBu_3)$ ($HSnBu_3$ concentration: 0.1 M).*

This is similar to $W(CO)_6$ under the same $HSnBu_3$ concentration (1.9 ±0.06 μs). Kinetic analysis shows that the C-H/Sn-H ligand exchange rate is dependent on the dopant concentration. When the $HSnBu_3$ concentration is reduced to 0.05 M, the ligand exchange rate is slowed down to 3.1 (±0.1) μs. Therefore, the kinetic order of $HSnBu_3$, similar to $HSiBu_3$, is 1 in the C-H/Sn-H ligand exchange reaction, same to that observed for $W(CO)_6$.

Hence, it can be concluded that the reaction mechanism of $W(CO)_5$(py) with $HEBu_3$ (E: Si, Ge, Sn) is similar to that of $W(CO)_6$. The pyridine ligand is first dissociated after photolysis, forming the pentacarbonyl species $W(CO)_5$, which is quickly solvated and undergoes ligand exchange with dopants $HEBu_3$ (E: Si, Ge, Sn).

3.2.4.2 TRIR Investigations on E-H Bond Activation of $HEBu_3$ (E: Si, Ge, Sn) by $W(CO)_5$(4-acpy) in Heptane

E-H bond activation of $HEBu_3$ (E: Si, Ge, Sn) by $W(CO)_5$(4-acpy) has been investigated using TRIR. TRIR in neat heptane has also been conducted as comparison, as shown in Figure 3.58.

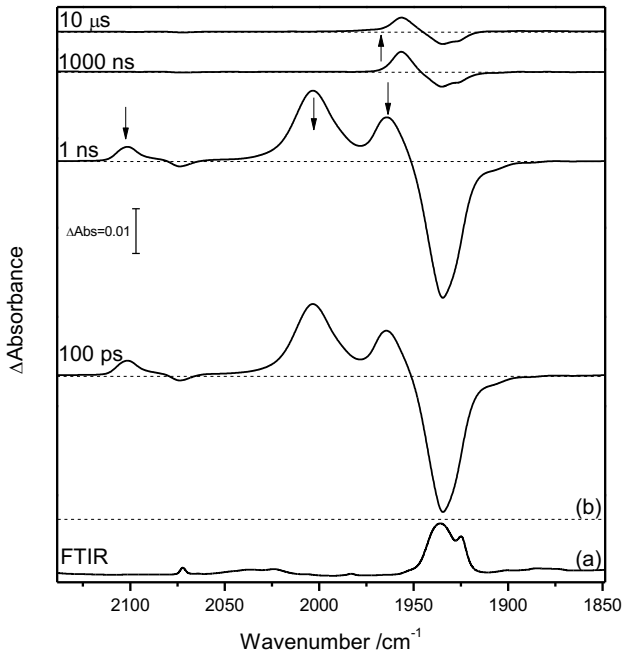


Figure 3.58 *(a) FTIR spectrum and (b) TRIR spectra obtained following photolysis (400 nm) of $W(CO)_5$(4-acpy) in neat heptane.*

As shown in Figure 3.58, different to $W(CO)_5$(py), after UV phtolysis, rather than the direct formation of $W(CO)_5$(*n*-heptane), three bands at higher wavenumber than the parent bleaches (2072, 1936 and 1925 cm^{-1}) at *ca.* 2101, 2004 and 1964 cm^{-1} are formed, which are typical of a $MLCT_{W\rightarrow L}$ state. This is consistent with previous work that the addition of an electron withdrawing group on the *para* positon of the pyridine ring lowers the energy level of the $MLCT_{W\rightarrow L}$ state, which replaces the ^3LF or $MLCT_{W\rightarrow CO}$ state to become the lowest-lying excited state.

Kinetic analysis shows that the decay rates of the three bands at 2101, 2004 and 1964 cm^{-1} are 146 (±3) ns, 161 (±1) ns and 149 (±3) ns, respectively, which are

consistent with the initial recovery rate of the parent bands (169 ±1 ns). The $MLCT_{W\rightarrow L}$ state is usually considered to be photochemically unreactive. After the decay of the $MLCT_{W\rightarrow L}$ state, a new band at 1957 cm^{-1} is observed, and is assigned to the solvated species $W(CO)_5$(*n*-heptane). Another band of $W(CO)_5$(*n*-heptane) at *ca.* 1931 cm^{-1} might be obscured by the overlap with the parent bleaches. At later μs-timescales not shown in the spectra, the $W(CO)_5$(*n*-heptane) species also decays and broad features similar to that observed for $W(CO)_5$(py) in neat heptane are observed, and this is thought to be the decomposition of the $W(CO)_5$(*n*-heptane) species, or reaction of $W(CO)_5$(*n*-heptane) with impurities such as water in the solvent.

Unfortunately the band of the solvated species $W(CO)_5$(*n*-heptane) overlaps with the band at 1964 cm^{-1} for the $MLCT_{W\rightarrow L}$ state. Therefore, one is unable to analyse the early time kinetics of the band at 1957 cm^{-1}. However, according to previous research which has been discussed in the Introduction Section, it is generally recognised that the photo-initiated CO-loss occurs due to rapid equilibrium between the lowest $MLCT_{W\rightarrow L}$ state and the photo-active ^{3}LF state or $MLCT_{W\rightarrow CO}$ state.

$HEBu_3$ (E: Si, Ge, Sn) is added into the system to investigate the E-H bond activation by $W(CO)_5$(4-acpy).

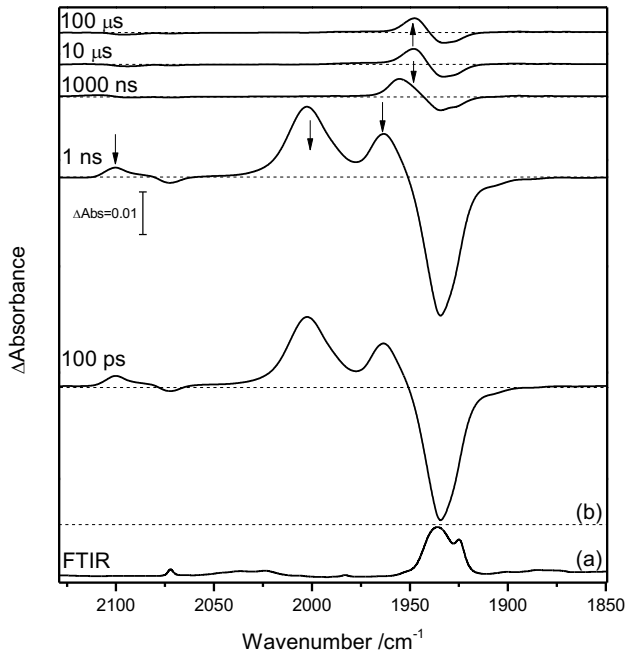


Figure 3.59 *(a) FTIR spectrum and (b) TRIR spectra obtained following photolysis (400 nm) of W(CO)$_5$(4-acpy) in neat heptane doped with 0.1 M HSiBu$_3$.*

As shown in Figure 3.59, similar to that in neat heptane, the $MLCT_{W\rightarrow L}$ state is observed to form instantly upon UV photolysis. Then the solvated species W(CO)$_5$(*n*-heptane) is observed (1957 cm^{-1}) after the $MLCT_{W\rightarrow L}$ state decays. On the μs-timescale, a new band at *ca.* 1951 cm^{-1} is observed to form after the decay of W(CO)$_5$(*n*-heptane). This can be assigned to W(CO)$_5$(η^1-HSiBu$_3$) compared to the work in previous sections.

The lifetime of the $MLCT_{W\rightarrow L}$ state is 160 (±5) ns, consistent with the parent recovery (185 ±3 ns), seemly unaffected by the dopant.

Kinetic analysis reveals the conversion between W(CO)$_5$(*n*-heptane) (2.9 ±0.08 μs) and W(CO)$_5$(η^1-HSiBu$_3$) (176 ±6 ns, 2.7 ±0.2 μs), as shown in Figure 3.60.

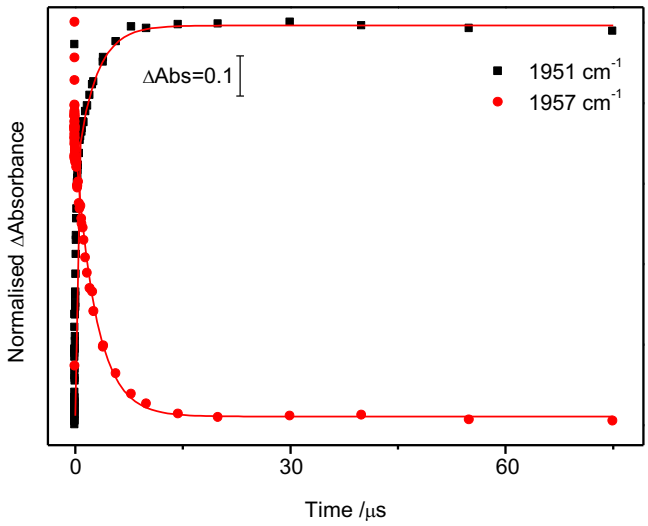


Figure 3.60 *TRIR kinetic traces obtained at 1957 and 1951 cm^{-1} corresponding to W(CO)$_5$(n-heptane) and W(CO)$_5$(η^1-HSiBu$_3$) (HSiBu$_3$ concentration: 0.1 M).*

W(CO)$_5$(η^1-HSiBu$_3$) is formed bi-exponentially. The second component fits the decay rate of W(CO)$_5$(*n*-heptane), while the first component fits the decay rate of the MLCT$_{W\rightarrow L}$ state. Thus, it can be assumed that the W(CO)$_5$(η^1-HSiBu) species is formed both from the rapid equilibrium of MLCT$_{W\rightarrow L}$ state with the reactive ^{3}LF or MLCT$_{W\rightarrow CO}$ state, and also from W(CO)$_5$(*n*-heptane).

When the concentration of HSiBu$_3$ is halved to 0.05 M, the ligand exchange rate between W(CO)$_5$(*n*-heptane) and W(CO)$_5$(η^1-HSiBu$_3$) is slowed down to 4.4 (±0.2) μs, while the first growth rate of W(CO)$_5$(η^1-HSiBu$_3$) is still 173 (±4) ns, which fits the lifetime of the MLCT$_{W\rightarrow L}$ state (149 ±4 ns). This suggests that the kinetic order of HSiBu$_3$ is 1 for the C-H/Si-H ligand exchange reaction, while the lifetime of the MLCT$_{W\rightarrow L}$ state is unaffected by the dopant HSiBu$_3$. However, it needs to be noted that, the ligand exchange rate between W(CO)$_5$(*n*-heptane) and W(CO)$_5$(η^1-HSiBu$_3$) is significantly shortened compared to the reactions for W(CO)$_6$ (ca. 7.5 μs) and W(CO)$_5$(py) (*ca.* 6.6 μs) under same dopant concentration (0.05 M). This is confusing as although the initial parent compounds are different, the C-H/Si-H ligand exchange is between W(CO)$_5$(*n*-heptane) and W(CO)$_5$(η^1-HSiBu$_3$), under same HSiBu$_3$ concentration. This phenomenon may need to be further investigated. TRIR spectra of experiment with HGeBu$_3$ are shown in Figure 3.61.

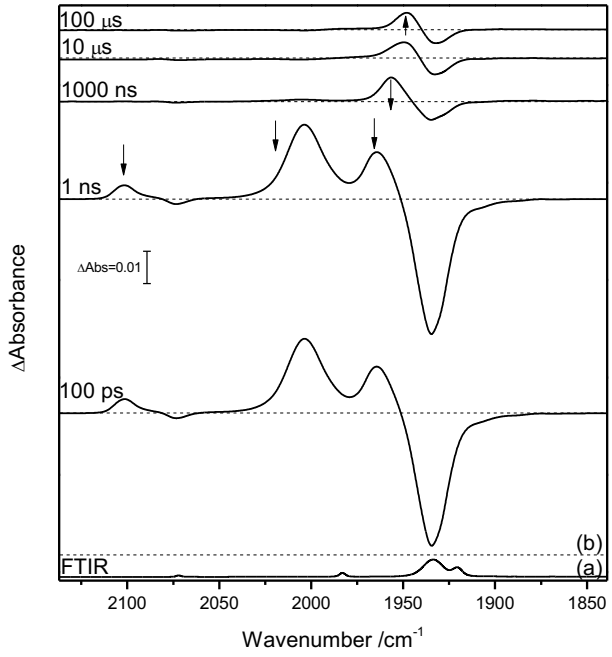


Figure 3.61 *(a) FTIR spectrum and (b) TRIR spectra obtained following photolysis (400 nm) of $W(CO)_5$(4-acpy) in heptane doped with 0.05 M $HGeBu_3$.*

As shown in Figure 3.61, similar to $HSiBu_3$, the $MLCT_{W\rightarrow L}$ state is formed initially after UV photolysis, and $W(CO)_5$(*n*-heptane) is observed after the MLCT state decays. The new band formed on the μs-timescale at *ca.* 1951 cm^{-1} is assigned to the germane species $W(CO)_5(\eta^1\text{-}HGeBu_3)$ compared to previous work.

Kinetic analysis shows that the lifetime of the $MLCT_{W\rightarrow L}$ state is slightly longer than when doped with $HSiBu_3$ or in neat heptane. The lifetimes of the bands at 2100, 2004 and 1964 cm^{-1} are 216 (±8) ns, 239 (±3) ns and 239 (±3) ns, respectively, which are consistent with the recovery rate of the parent bands for 250 (±3) ns.

The formation rate of $W(CO)_5(\eta^1\text{-}HGeBu_3)$ is bi-exponential (254 ±7 ns, 5.4 ±0.3 μs), formed from both the $MLCT_{W\rightarrow L}$ state and $W(CO)_5$(*n*-heptane) (6.7 ±0.1 μs), as shown in Figure 3.62.

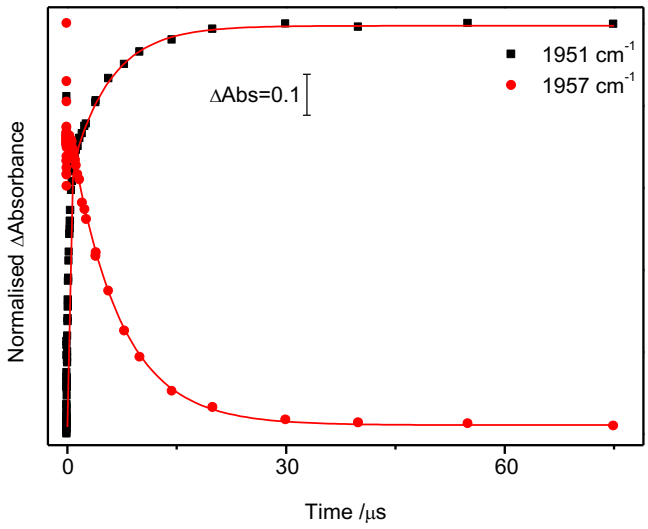


Figure 3.62 *TRIR kinetic traces obtained at 1957 and 1951 cm^{-1} corresponding to $W(CO)_5$(n-heptane) and $W(CO)_5(\eta^1$-$HGeBu_3)$ ($HGeBu_3$ concentration: 0.05 M).*

Compared to $HSiBu_3$ under the same dopant concentration (0.05 M), the C-H/ Ge-H ligand exchange rate is slightly slower. This is confusing when one consider the electron donation ability of Ge-H is greater than Si-H. This could be due to experimental error as the dopant concentration in the experiment may be wrongly controlled, and further investigation is required.

TRIR has also been conducted for $HSnBu_3$, as shown in Figure 3.63.

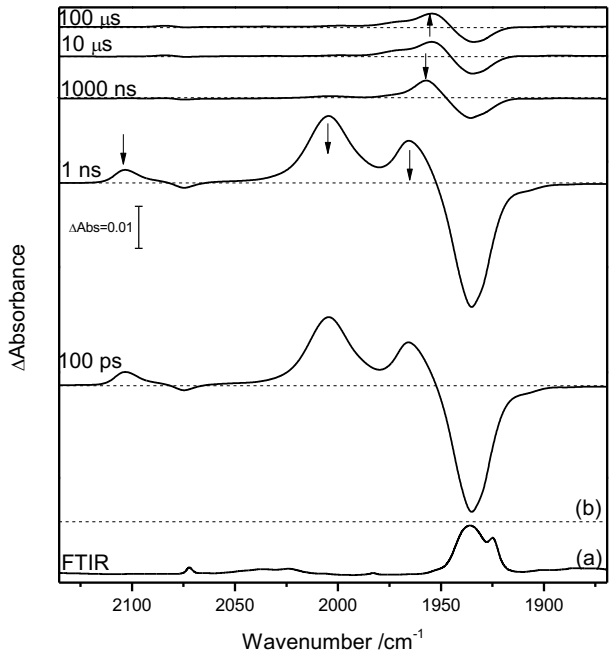


Figure 3.63 *(a) FTIR spectrum and (b) TRIR spectra obtained following photolysis (400 nm) of $W(CO)_5$(4-acpy) in heptane doped with 0.1 M $HSnBu_3$.*

A similar reaction process to $HSiBu_3$ and $HGeBu_3$ has been observed for $HSnBu_3$. The band for $W(CO)_5(HSnBu_3)$ is observed at *ca.* 1954 cm^{-1}. The lifetime of $MLCT_{W\rightarrow L}$ state is similar to the experiment with $HGeBu_3$, at 237 (±4) ns. The C-H/Sn-H ligand exchange rate (*ca.* 1.7 μs, Figure 3.64) between $W(CO)_5$(*n*-heptane) and $W(CO)_5(HSnBu_3)$ is faster compared to $HSiBu_3$ and $HGeBu_3$ as expected. The ligand exchange rate is similar compared to that of $W(CO)_6$ and $W(CO)_5$(py) under the same dopant concentration (0.1 M).

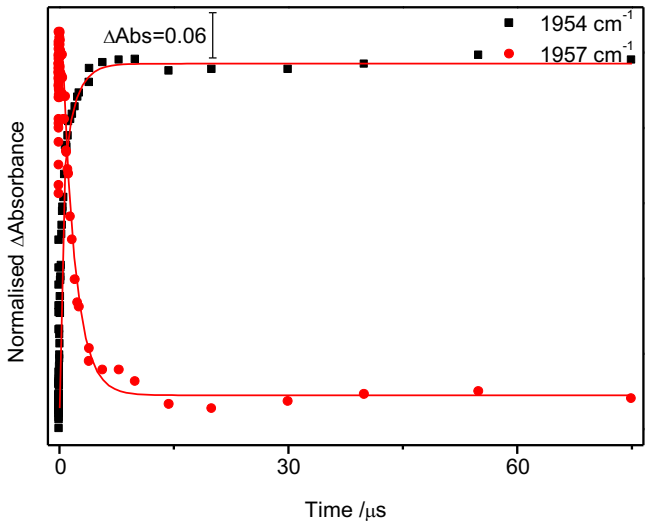


Figure 3.64 *TRIR kinetic traces obtained at 1957 and 1954 cm^{-1} corresponding to $W(CO)_5$(n-heptane) and $W(CO)_5(HSnBu_3)$ ($HSnBu_3$ concentration: 0.1 M).*

The $W(CO)_5(HSnBu_3)$ species (269 ±29 ns, 1.6 ±0.2 μs) is formed from both the $MLCT_{W\rightarrow L}$ state and $W(CO)_5$(*n*-heptane) (1.7 ±0.1 μs). When the concentration of $HSnBu_3$ is halved to 0.05 M, the lifetime of the $MLCT_{W\rightarrow L}$ state is unaffected, while the C-H/Sn-H ligand exchange rate is slowed down to 3.4 (±0.5) μs. This indicates that the kinetic order of $HSnBu_3$ in the ligand exchange reaction between $W(CO)_5$(*n*-heptane) and $W(CO)_5(HSnBu_3)$ is 1, similar to $W(CO)_6$ and $W(CO)_5$(py).

Therefore, it can be concluded from the above TRIR results that, compared to $W(CO)_6$ and $W(CO)_5$(py), $W(CO)_5$(4-acpy) has similar but also different photoproperties in solution. Upon UV photolysis, unlike $W(CO)_6$ and $W(CO)_5$(py), a $MLCT_{W\rightarrow L}$ state is observed, which reflects how the strong electron withdrawing group acetyl on the pyridine ring lowers the energy of the $MLCT_{W\rightarrow L}$ state. The solvated species $W(CO)_5$(*n*-heptane) has been observed, and the dopant species $W(CO)_5(HEBu_3)$ (E: Si, Ge, Sn) is observed to form both from $W(CO)_5$(*n*-heptane) and surprisingly, the $MLCT_{W\rightarrow L}$ state. This is explained by the rapid equilibrium with either the photo-reactive ^3LF or $^3MLCT_{W\rightarrow CO}$ state at a slightly higher energy level.

However, interestingly it is found that the ligand exchange rate for the C-H/E-H exchange between $W(CO)_5$(*n*-heptane) and $W(CO)_5(HEBu_3)$ (E: Si, Ge) is faster

than that of $W(CO)_6$ and $W(CO)_5(py)$, and the C-H/Ge-H ligand exchange is slower than that of C-H/Si-H, which is unexpected. However, for the C-H/Sn-H exchange the rate is similar to that of $W(CO)_6$ and $W(CO)_5(py)$, and is faster than C-H/Si-H and C-H/Ge-H as expected. The ν(CO) band positions of the dopant complexes $W(CO)_5(HEBu_3)$ (E: Si, Ge, Sn) follow the trend Si ≈ Ge < Sn, same with that of $W(CO)_6$ and $W(CO)_5(py)$, which is expected.

3.2.4.3 TRIR Investigations on E-H Bond Activation of $HEBu_3$ (E: Si, Ge, Sn) by $W(CO)_5$(pip) in Heptane

Compared to $W(CO)_5$(py) and $W(CO)_5$(4-acpy), in $W(CO)_5$(pip) the W is coordinated to the piperidine (pip) ligand, which doesn't possess the huge conjugation configuration as the pyridine groups does, and is a non-planar structure. Thus, the electron accepting ability of the pip ligand is considered to be much weaker than the pyridine ligands.

Figure 3.65 shows the TRIR spectra of $W(CO)_5$(pip) in neat heptane.

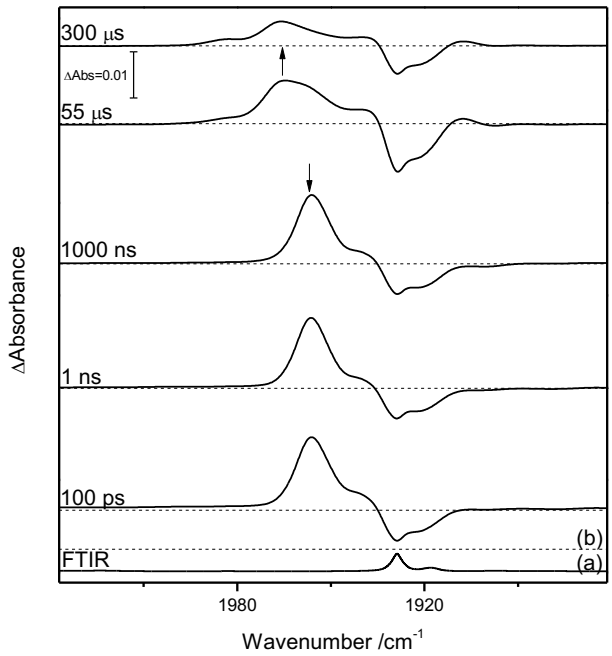


Figure 3.65 *(a) FTIR spectrum and (b) TRIR spectra obtained following photolysis (400 nm) of $W(CO)_5$(pip) in neat heptane.*

As shown in Figure 3.65, after UV photolysis, no MLCT state is observed, which is different to $W(CO)_5$(4-acpy) while similar to what was observed for $W(CP)_5$(py). Only $W(CO)_5$(*n*-heptane) (1957 cm^{-1}) was observed to form. On the μs-timescale, a broad feature centred at *ca.* 1967 cm^{-1} is observed, which is considered to be due to the decomposition of $W(CO)_5$(*n*-heptane) or reactions with impurities in the solvent such as water, similar to $W(CO)_5$(py) and $W(CO)_5$(4-acpy).

When doped with $HEBu_3$, the activated species $W(CO)_5(HEBu_3)$ (E: Si, Ge, Sn) has been observed as expected. Following are the discussions.

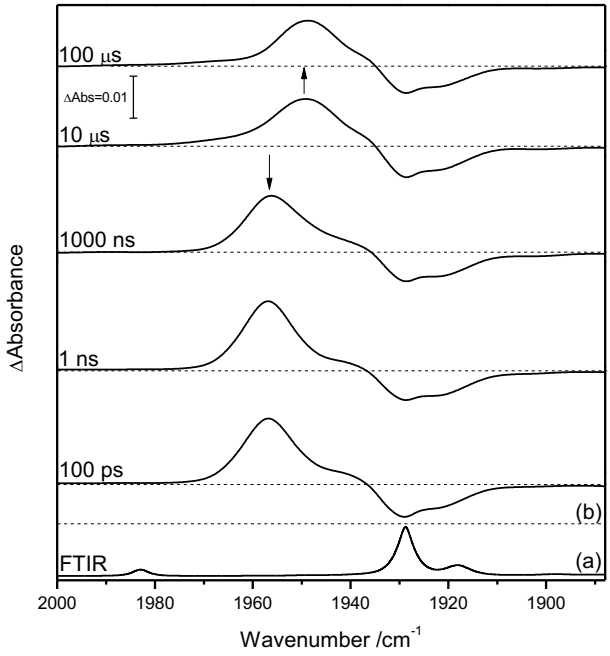


Figure 3.66 *(a) FTIR spectrum and (b) TRIR spectra obtained following photolysis (400 nm) of $W(CO)_5$(pip) in heptane doped with 0.1 M $HSiBu_3$.*

Figure 3.66 shows the TRIR in presence of the dopant $HSiBu_3$. As shown in the spectra, the solvated species $W(CO)_5$(*n*-heptane) is formed directly after irradiation, similar to that in neat *n*-heptane. The silane speices $W(CO)_5(\eta^1\text{-}HSiBu_3)$ is observed to form on the μs-timescale (1951 cm^{-1}). Kinetic analysis is shown in Figure 3.67 which reveals the conversion between $W(CO)_5$(*n*-heptane) (4.2 ±0.07 μs) and $W(CO)_5(\eta^1\text{-}HSiBu_3)$ (4.3 ±0.09 μs).

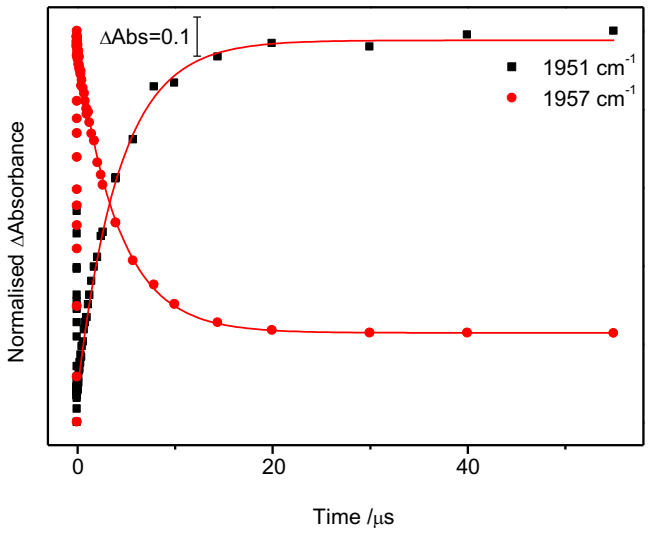


Figure 3.67 *TRIR kinetic traces obtained at 1957 and 1951 cm^{-1} corresponding to $W(CO)_5$(n-heptane) and $W(CO)_5(\eta^1$-$HSiBu_3)$ ($HSiBu_3$ concentration: 0.1 M).*

When the concentration of $HSiBu_3$ is lowered to 0.05 M, the ligand exchange rate is slowed down to 6.8 (±0.2) μs, similar to $W(CO)_6$ and $W(CO)_5$(py), as expected.

Figure 3.68 shows the TRIR spectra with the dopant $HGeBu_3$.

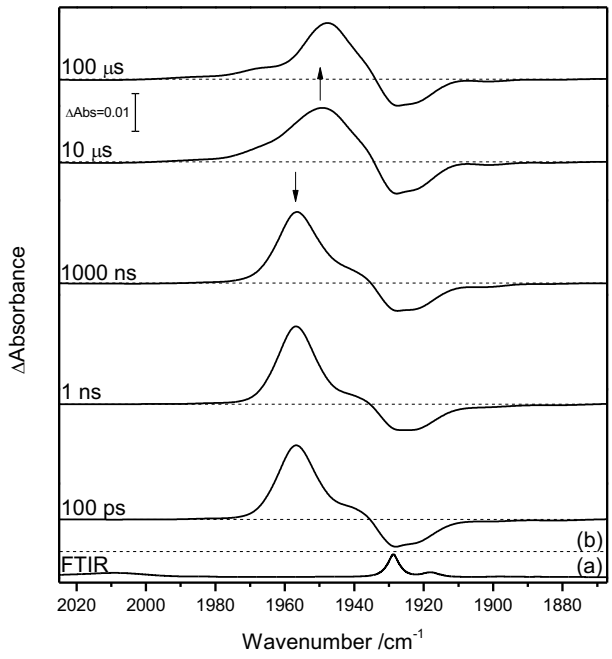


Figure 3.68 *(a) FTIR spectrum and (b) TRIR spectra obtained following photolysis (400 nm) of $W(CO)_5$(pip) in heptane doped with 0.05 M $HGeBu_3$.*

Similar to $HSiBu_3$, the germane species $W(CO)_5(\eta^1\text{-}HGeBu_3)$ (1951 cm^{-1}) has been observed after the decay of $W(CO)_5$(*n*-heptane). The conversion between $W(CO)_5$(n-heptane) (6.7 ±0.1 μs) and $W(CO)_5(\eta^1\text{-}HGeBu_3)$ (6.2 ±0.08 μs) is shown in Figure 3.69.

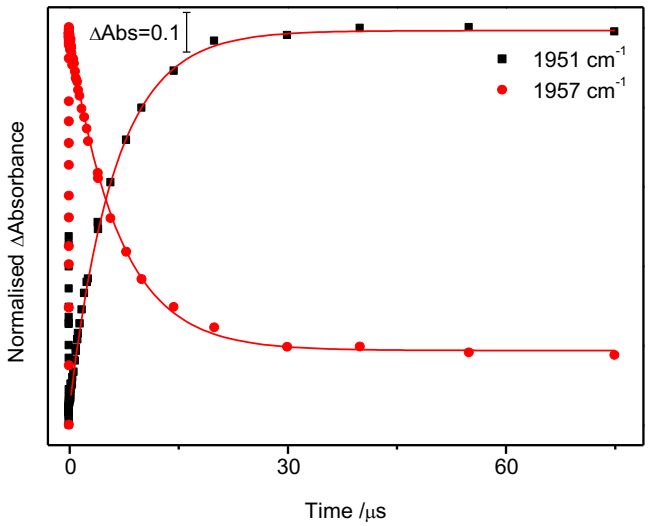


Figure 3.69 *TRIR kinetic traces obtained at 1957 and 1951 cm^{-1} corresponding to $W(CO)_5$(n-heptane) and $W(CO)_5(\eta^1$-$HGeBu_3)$ ($HGeBu_3$ concentration: 0.05 M).*

This ligand exchange rate is similar to that of C-H/Si-H exchange under the same dopant concentration (0.05 M), and also similar to that of $W(CO)_6$ and $W(CO)_5$(py) as expected.

Figure 3.70 shows the TRIR spectra with dopant $HSnBu_3$.

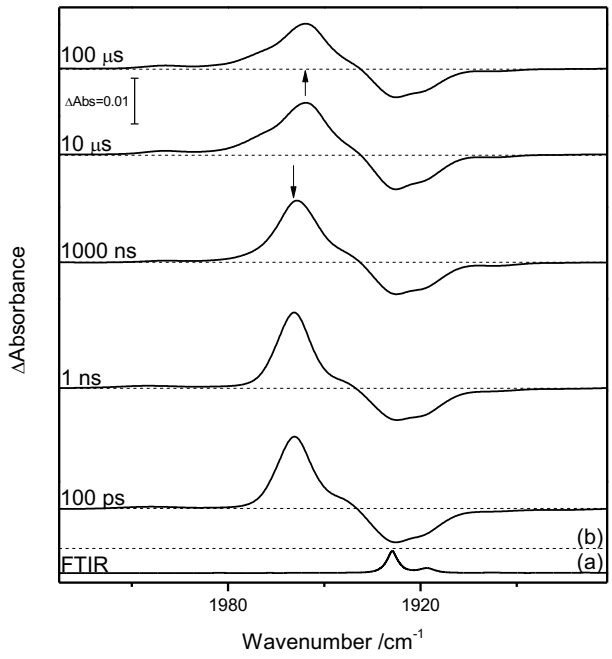


Figure 3.70 *(a) FTIR spectrum and (b) TRIR spectra obtained following photolysis (400 nm) of $W(CO)_5$(pip) in heptane doped with 0.1 M $HGeBu_3$.*

As shown in Figure 3.70, similar to $HSiBu_3$ and $HGeBu_3$, the stannane species $W(CO)_5(HSnBu_3)$ (1954 cm^{-1}) is observed after the decay of $W(CO)_5$(*n*-heptane). The ligand exchange between $W(CO)_5$(*n*-heptane) (1.5 ±0.06 μs) and $W(CO)_5(HSnBu_3)$ (1.3 ±0.1 μs) is shown in Figure 3.71.

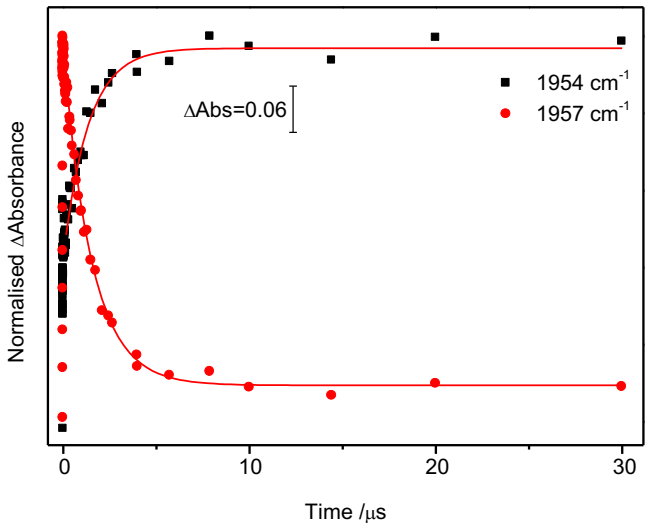


Figure 3.71 *TRIR kinetic traces obtained at 1957 and 1954 cm^{-1} corresponding to $W(CO)_5$(n-heptane) and $W(CO)_5(HSnBu_3)$ ($HSnBu_3$ conentration: 0.1 M).*

Similar ν(CO) band position for $W(CO)_5(HSnBu_3)$ and C-H/Sn-H ligand exchange rate to $W(CO)_6$, $W(CO)_5$(py) and $W(CO)_5$(4-acpy) under the same dopant concentration (0.1 M) have been observed as expected.

When the concentration of $HSnBu_3$ is halved to 0.05 M, the ligand exchange rate is also observed to slow down to 2.4 (±0.1) μs. This is slightly faster than expected, as for $W(CO)_6$, $W(CO)_5$(py) and $W(CO)_5$(4-acpy), the rate under the same concentration (0.05 M) is *ca.* 3.3 μs. This might be due to the wrong control of the dopant concentration.

To conclude, for $W(CO)_5$(pip), the photoproperties are observed to be very similar to $W(CO)_6$ and $W(CO)_5$(py), that upon UV photolysis the pip ligand is ejected, then the solvated speices $W(CO)_5$(*n*-heptane) undergoes ligand exchange with dopants $HEBu_3$ (E: Si, Ge, Sn).

3.2.5 TRIR Investigations on the W-Xe Interaction Conducted in Perfluoronated Solvent

TRIR investigations on the W-Xe interaction of $W(CO)_5L$ (L: py, 4-acpy, pip) have been conducted in perfluoromethylcyclohexane (PFMCH), a perfluorinated solvent. PFMCH, as discussed before, is a weak-coordinating and non-polar solvent, thus can provide an excellent environment for mechanism studies on the ultrafast timescale, due to its stabilization of unstable transient intermediates, as well as its excellent solubility of gases.

First, TRIR of $W(CO)_5(py)$ in neat PFMCH has been conducted, as shown in Figure 3.72.

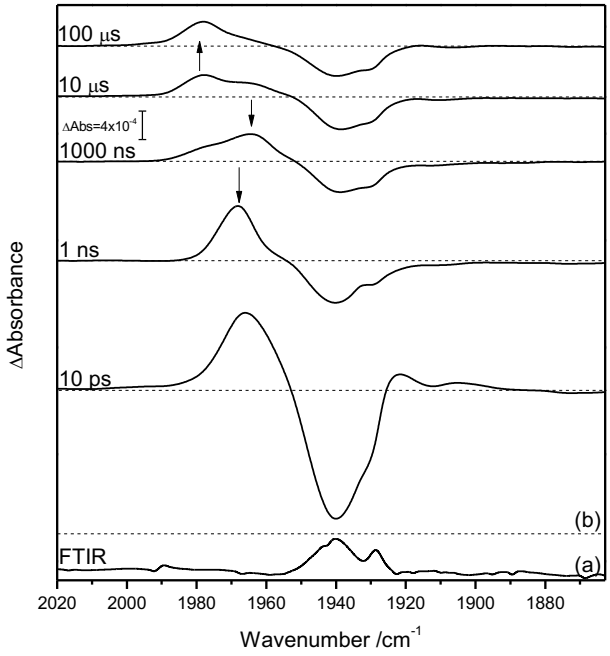


Figure 3.72 *(a) FTIR spectrum and (b) TRIR spectra obtained following photolysis (400 nm) of $W(CO)_5(py)$ in neat PFMCH.*

As shown in Figure 3.72, in PFMCH, upon UV photolysis, several bands at *ca.* 1967, 1921 cm^{-1}, and a broad feature at *ca.* 1905 cm^{-1} are formed. The bands at 1921 and 1905 cm^{-1} are not stable, and are observed to decay with a rate of *ca.* 30 ps, which is consistent with the vibrational cooling rate (<100 ps).

It can be observed from the spectra that in 1000 ns time delay, a new band at *ca.* 1962 cm^{-1} is formed. This is similar to the previous research conducted by our group of $W(CO)_6$ in PFMCH, that upon UV photolysis, the first W pentacarbonyl species at 1966 and 1930 cm^{-1} is formed (lifetime: 6.4 ±0.4 ns) initially, which then decays and converts to the second W pentacarbonyl species at 1961 and 1935 cm^{-1}.[21] Therefore, comparing to the previous work, here the band at 1967 cm^{-1} is assigned to the first W pentacarbonyl species, while the band at 1962 cm^{-1} is assigned to the second W pentacarbonyl species.

In our results, the bands at *ca.* 1930 cm^{-1} may be obscured due to overlap with the parent bleaches. However, the conversion between the first W pentacarbonyl species (1967 cm^{-1}) and the second W pentacarbonyl species (1962 cm^{-1}) has been revealed by kinetic analysis. The lifetime of the band at 1967 cm^{-1} is bi-exponential (0.4 ±0.06 ns, 60 ±6 ns), while the growth rate of the band at 1962 cm^{-1} is 60 (±12) ns, as shown in Figure 3.73. The exchange rate is much slower than that reported by our previous research (*ca.* 6 ns).[21]

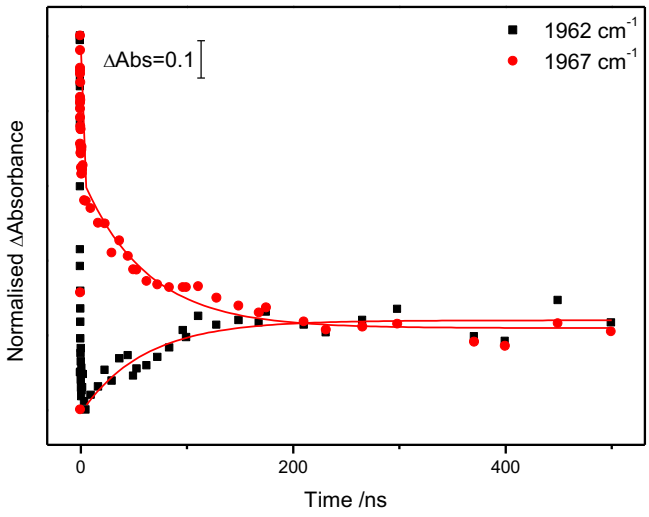


Figure 3.73 *TRIR kinetic traces obtained at 1967 and 1962 cm^{-1} corresponding to the first W pentacarbonyl species and the second W pentacarbonyl species.*

On the μs-timescale, a band at *ca.* 1977 cm^{-1} is observed to form. According to our previous research,[21] this band is assigned to the water species $W(CO)_5(H_2O)$. Although a purifying process has been conducted for the PFMCH solvent, small trace

amount of water is inevitable. In our work, the conversion from the second W pentacarbonyl speices (1962 cm^{-1}, 6.5 ±0.4 μs) to the water species $W(CO)_5(H_2O)$ (1977 cm^{-1}, 8.1 ±0.4 μs) has been observed, supported by the kinetics as shown in Figure 3.74.

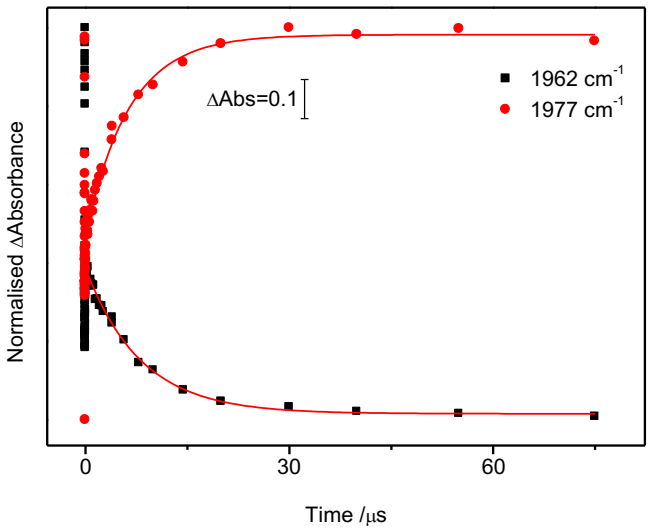


Figure 3.74 *TRIR kinetic traces obtained at 1977 and 1962 cm^{-1} corresponding to the water species $W(CO)_5(H_2O)$ and the second W pentacarbonyl species.*

In conclusion, an A → B → C mechanism has also been observed in our results, similar to the previous work (A: the first W pentacarbonyl species; B: the second W pentacarbonyl species; C: $W(CO)_5(H_2O)$).[21] In their work, the first W pentacarbonyl species A is assigned to the unsaturated W pentacarobnyl species $W(CO)_5$, and the second W pentacarbonyl species B is assigned to the solvated species $W(CO)_5$(PFMCH). However, it has to be pointed out that, the lifetime of the first W pentacarbonyl species in their work is *ca.* 6 ns, while in our work it is *ca.* 60 ns, which might be too long for an unsaturated pentacarbonyl species at room temperature. Actually, the conversion between two CO-loss metal carbonyl species in PFMCH has been observed for other complexes, such as $CpRe(CO)_3$ and $Cp^*Re(CO)_3$.[21] According to the author, several assumptions have been made for the assignment for the two dicarbonyl species. The first assumption is that the first Re dicarbonyl species is the unsaturated $CpRe(CO)_2$ species, while the second Re dicarbonyl species is the solvated species $CpRe(CO)_2$(PFMCH). The second assumption is that the first Re dicarbonyl species is a weakly-bound PFMCH species,

which then undergoes isomerization to the second Re dicarbonyl species in a more stable binding mode, as PFMCH provides more than one binding site, such as the CF_3, CF_2 and CF binding sites. The third assumption is that this might be the isomerization between the η^1-F and the η^2-CF binding modes. TRIR of $CpRe(CO)_3$ has also been conducted in perfluorohexane (PFH), similar reaction process has been observed. The conversion rate is slower than that observed in PFMCH. This indicate that the conversion between the two dicarbonyl species is related to the nature of the solvents.

Therefore, question is raised on the first assumption that whether the first W pentacarbonyl species is the unsaturated $W(CO)_5$. As in our work, the lifetime of the first W pentacarbonyl is as long as *ca.* 60 ns. Nevertheless, the second W pentacarbonyl species can be tentatively assigned to the PFMCH species $W(CO)_5$(PFMCH).

TRIR in PFMCH doped with Xe has also been conducted, as shown in Figure 3.75.

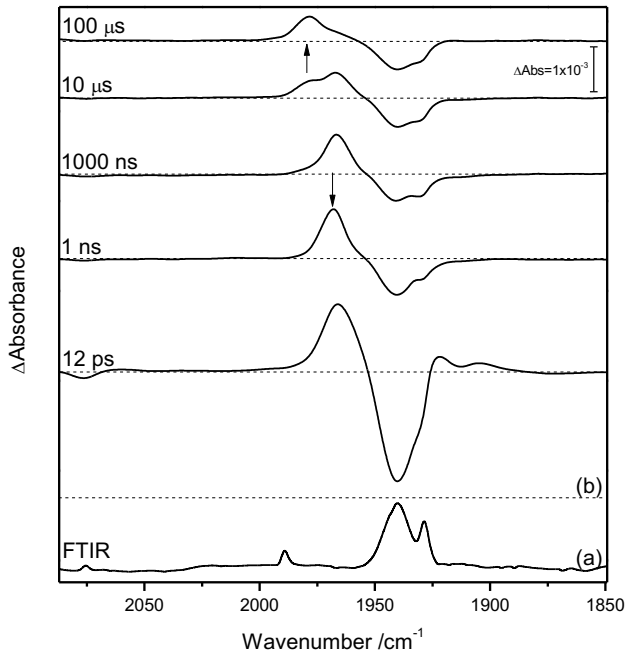


Figure 3.75 *(a) FTIR spectrum and (b) TRIR spectra obtained following photolysis (400 nm) of $W(CO)_5$(py) in PFMCH doped with 1.5 bar of Xe.*

As shown in Figure 3.75, upon UV photolysis, the parent bands are bleached, along with the formation of new bands at *ca.* 1967, 1921 and 1905 cm^{-1}, similar to that observed in neat PFMCH (Figure 3.72). On the μs-timescale, the band at 1967 cm^{-1} decays and the band at *ca*. 1978 cm^{-1} is formed, which is stable and shows no decay during the experimental timescale (~1 ms). One difference with the TRIR results in neat PFMCH has to be noted is that no band at lower wavenumber than 1967 cm^{-1} has been observed upon adding Xe. The conversion between the two bands at 1967 (753 ±53 ps, 11.4 ±0.7 μs) and 1978 cm^{-1} (12.7 ±0.5 μs) is revealed by kinetic analysis, as shown in Figure 3.76.

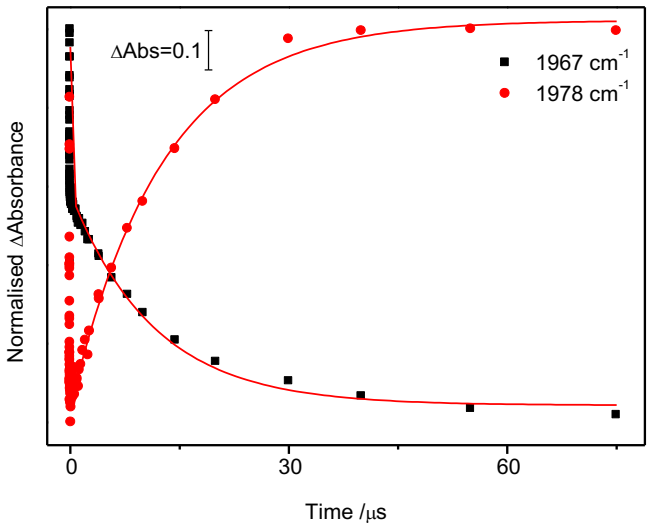


Figure 3.76 *TRIR kinetic traces obtained at 1978 ($W(CO)_5(H_2O)$) and 1967 cm^{-1}.*

The band at 1978 cm^{-1} can be assigned to the water species $W(CO)_5(H_2O)$ as discussed before. The reaction process observed is quite different to that observed in the previous research of $W(CO)_6$ in PFMCH doped with Xe.[21] In theory, the reaction process of $W(CO)_5(py)$ should be similar to $W(CO)_6$, as they both loss one CO ligand and generate $W(CO)_5$ after UV photolysis. In the previous research, what has been observed is that upon UV photolysis, a set of bands at 1966 and 1930 cm^{-1} are formed, which is assigned to the unsaturated $W(CO)_5$, then it decays to form the Xe species $W(CO)_5Xe$ (1963, 1937 cm^{-1}). The conversion from $W(CO)_5Xe$ to the water species $W(CO)_5(H_2O)$ has been observed, but the PFMCH species $W(CO)_5$(PFMCH) observed in neat PFMCH is not observed in the presence of Xe.

The $W(CO)_5Xe$ species is formed directly from $W(CO)_5$. The absent of the solvated species in PFMCH in the presence of Xe has also been observed for other complexes, such as $CpRe(CO)_3$ and $Cp^*Re(CO)_3$.[21]

However, in our work, no bands at 1961 ($W(CO)_5$(PFMCH))[21] or 1963 cm^{-1} ($W(CO)_5Xe$)[21] have been observed. It can be observed that the water species $W(CO)_5(H_2O)$ is directly formed from the species at 1967 cm^{-1} (Figure 3.76).

Therefore, it raises the question whether in our work the Xe species $W(CO)_5Xe$ has been generated or not. In the previous work,[21] it is found that the formation rate of $W(CO)_5Xe$ compared to $W(CO)_5$(PFMCH) in neat PFMCH is faster, while the formation of the final water species $W(CO)_5(H_2O)$ is slowed down in the presence of Xe. Thus, we have examined these rates. Compared to the experiment conducted in neat PFMCH, the formation rate of $W(CO)_5(H_2O)$ is definitely slowed down (*ca.* 12 μs compared to *ca.* 7 μs in neat PFMCH). As the ν(CO) band positon of the band at 1967 cm^{-1} is not consistent with $W(CO)_5$(PFMCH) (1961 cm^{-1}) and $W(CO)_5Xe$ (1963 cm^{-1}),[21] the assignment of the band at 1967 cm^{-1} is unclear. However, the lifetime of the band at 1967 cm^{-1} (*ca.* 12 μs) is much prolonged compared to the lifetime observed in neat PFMCH (*ca.* 60 ns), which may indicate different species.

Therefore, there is an assumption that the band at 1967 cm^{-1} may consists of two species, the first W pentacarbonyl species as well as the Xe species $W(CO)_5Xe$. The similarity of electron donation abilities between Xe and perfluorinated alkanes has been observed for many organometallic complexes, including $CpM(CO)_3$ (M: Mn, Re) and $M(CO)_6$ (M: Cr, Mo, W), also suppored by DFT calculations according to our previous research.[21] Therefore, the ν(CO) positions of the two species may not be well resolved in the IR spectra. And this may be the reason why when doped with Xe, the band at 1967 cm^{-1} is much more stable than that in pure PFMCH.

Figure 3.77 shows the TRIR spectra of $W(CO)_5$(pip) in neat PFMCH.

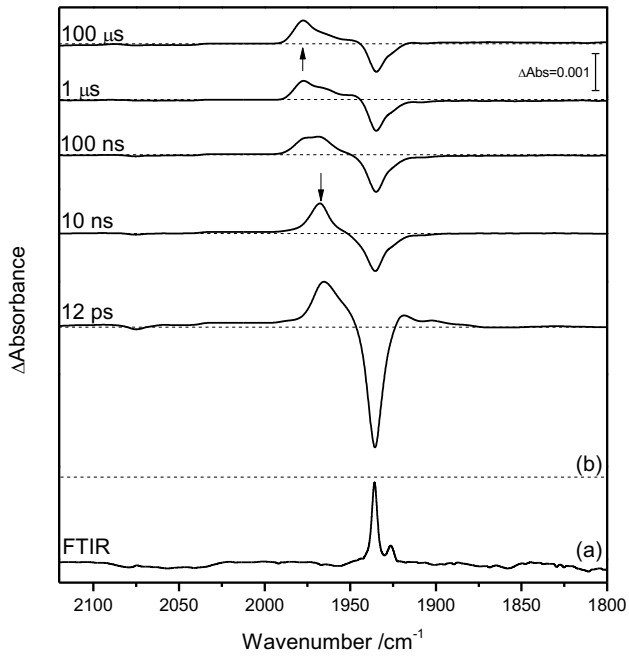


Figure 3.77 *(a) FTIR spectrum and (b) TRIR spectra obtained following photolysis (400 nm) of $W(CO)_5$(pip) in neat PFMCH.*

Similar to $W(CO)_5$(py), upon UV photolysis, along with the bleach of the parent bands, a band at *ca.* 1967 cm^{-1}, the first W pentacarbonyl species is formed, which then decays on the ns-timescale, and the water species $W(CO)_5(H_2O)$ at *ca.* 1978 cm^{-1} is formed. Kinetic shows that the formation of the water species $W(CO)_5(H_2O)$ is bi-exponential. The first component is similar to the decay rate of the first W pentacarbonyl species, for *ca.* 50 ~ 100 ns, while the second component is *ca.* 4.5 μs. The recovery of the parent band at 1936 cm^{-1} is also bi-exponential (71 ± 4 ps, 111 ± 18 ns). The rate at 71 ± 4 ps fits the vibrational cooling, and the rate at 111 ± 18 ns may be due to parts of the first W pentacarbonyl species recombines with CO. Therefore, the later formation of the water species $W(CO)_5(H_2O)$ for *ca.* 4.5 μs should not be either from the parent complex or the first W pentacarbonyl species. The kinetic analysis for the bands at 1978, 1967 cm^{-1}, and the parent band at 1936 cm^{-1} is shown in Figure 3.78.

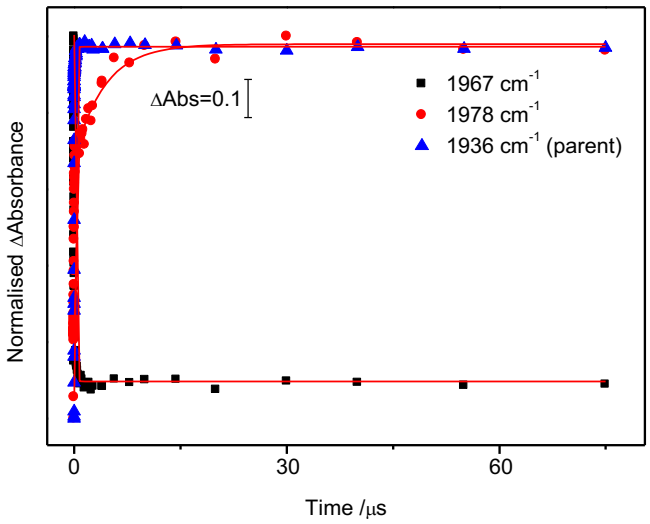


Figure 3.78 *TRIR kinetic traces obtained at 1978, 1967 cm^{-1} and the parent band at 1936 cm^{-1}. Decay rate of 1967 cm^{-1}: t_1 = 0.3 ± 0.07 ns, t_2 = 11 ± 2 ns, t_3 = 118 ± 9 ns; formation rate of 1978 cm^{-1}: t_1 = 51 ± 3 ns, t_2 = 4.2 ± 0.5 μs; Recovery rate of the parent band at 1936 cm^{-1}: t_1 = 71 ± 4 ps, t_2 = 111 ± 18 ns.*

Therefore, considering that in our previous work,[21] for the $W(CO)_6$, $CpRe(CO)_3$ and $Cp^*Re(CO)_3$ complexes, the TRIR in neat PFMCH all shows the A → B → C process (A: the first CO-loss species; B: the second CO-loss species; C: the water species), here it is also proposed that a second W pentacarbonyl species with ν(CO) positions moving to lower wavenumber to the first W pentacarbonyl species (1967 cm^{-1}) should have formed. However, the IR intensity of the second W pentacarbonyl species might be too weak, also may have overlapped with the intense band for the first W pentacarbonyl species (1967 cm^{-1}). Insufficient IR resolution may be another problem. Therefore, the second W pentacarbonyl species is not observed in the TRIR spectra. As shown in Figure 3.72, the intensity of the second W pentacarbonyl species at 1962 cm^{-1} is weaker than the first W pentacarbonyl species. However, this phenomenon is not observed for $W(CO)_6$ in neat PFMCH according to our previous research.[21] This is thought to be affected by the water concentration in the PFMCH solvent. It is proposed that in our PFMCH solvent, the water concentration is higher than that used in our previous research. Therefore, the direct formation of the water species $W(CO)_5(H_2O)$ from the first W pentacarbonyl species is observed in our work, while is not observed in our previous

research.[21] Meanwhile, the conversion rate from the second W pentacarbonyl species to $W(CO)_5(H_2O)$ is much faster in our work (for $W(CO)_5$(py): *ca.* 7 μs, for $W(CO)_5$(pip): *ca.* 4.5 μs, for $W(CO)_6$[21]: 12 μs). Therefore, the weak IR intensity of the second W pentacarbonyl species may be caused by the higher water concentration in our solvent, as the water species $W(CO)_5(H_2O)$ is competing with the second W pentacarbonyl species to be converted from the first W pentacarbonyl species.

Figure 3.79 shows the TRIR spectra of $W(CO)_5$(pip) in PFMCH doped with 1.5 bar of Xe.

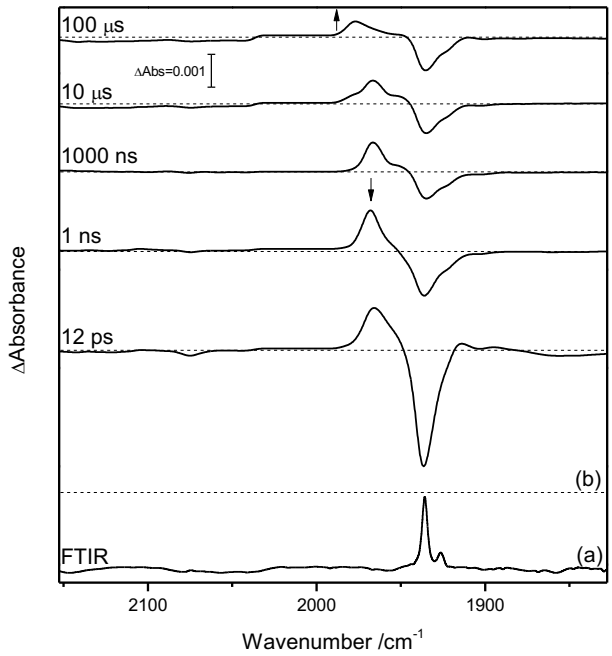


Figure 3.79 *(a) FTIR spectrum and (b) TRIR spectra obtained following photolysis (400 nm) of $W(CO)_5$(pip) in PFMCH doped with 1.5 bar of Xe.*

Similar to the TRIR in neat PFMCH (Figure 3.77), upon UV photolysis, only a band at *ca.* 1967 cm^{-1} is formed, which decays on the μs-timescale, and the water species at *ca.* 1978 cm^{-1} is generated. Similar to $W(CO)_5$(py), when doped with Xe, the lifetime of the band at 1967 cm^{-1} is significantly prolonged (*ca.* 16 μs, Figure 3.80), and no band at lower wavenumber to 1967 cm^{-1} has been observed at later time

delays. The decay rate of the band at 1967 cm^{-1} fits the growth rate of the water species at *ca.* 1978 cm^{-1}, for *ca.* 16 μs, as shown in Figure 3.80.

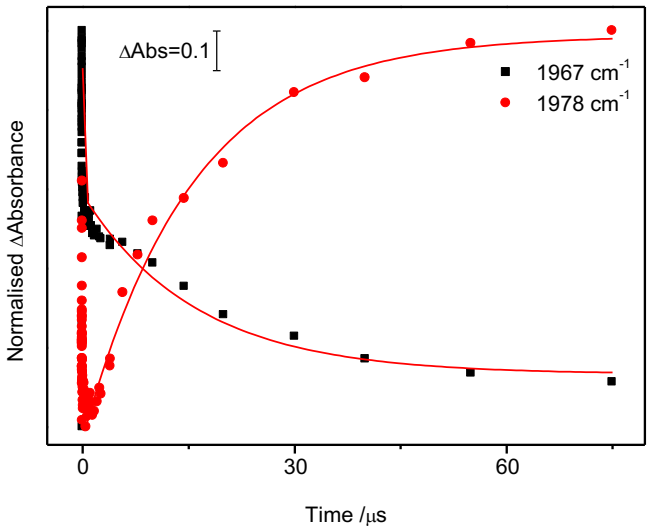


Figure 3.80 *TRIR kinetic traces obtained at 1978 and 1967 cm^{-1}.*

Different to the TRIR in neat PFMCH, the final water species $W(CO)_5(H_2O)$ is proposed to be converted from the species at 1967 cm^{-1}, as suggested by the kinetics (Figure 3.80). Also, the formation rate of $W(CO)_5(H_2O)$ is significantly prolonged compared to that observed in neat PFMCH (*ca.* 4.2 μs). Therefore, similar to $W(CO)_5(py)$, it is proposed that the band at 1967 cm^{-1} may consists of two species, one being the first W pentacarbonyl species, the other one might be the Xe species $W(CO)_5(Xe)$.

Figure 3.81 shows the TRIR spectra of $W(CO)_5(4\text{-acpy})$ in neat PFMCH.

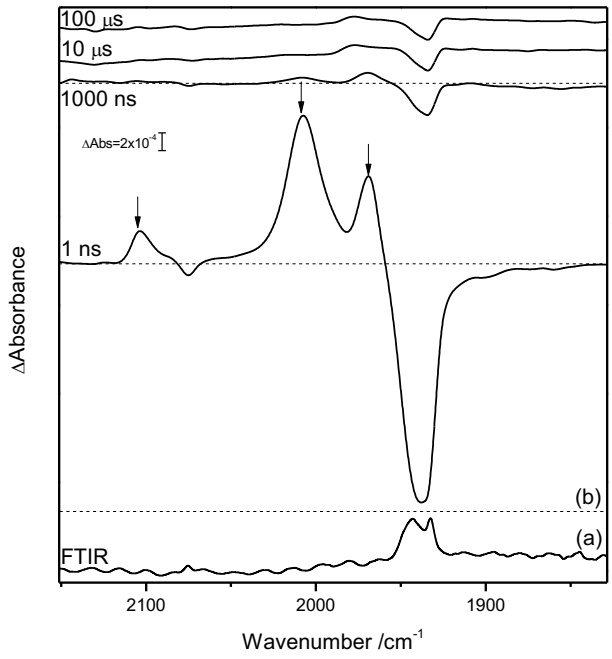


Figure 3.81 *(a) FTIR spectrum and (b) TRIR spectra obtained following photolysis (400 nm) of $W(CO)_5$(4-acpy) in neat PFMCH.*

As shown in Figure 3.81, upon UV photolysis, the MLCT state (2104, 2009, 1967 cm^{-1}) is observed, with a lifetime of 308 (±12) ns, slightly longer than that observed in heptane (*ca.* 150~250 ns). It can be observed that the ν(CO) positions of the MLCT state overlap with the expected first W pentacarbonyl species (*ca.* 1967 cm^{-1}). Also, the lifetime of the MLCT state is longer than the expected lifetime of the first W pentacarbonyl species (60~100 ns). And the IR bands of the MLCT state is extremely intense. All these factors increase the difficulties in kinetic analysis of the band at 1967 cm^{-1}. After the decay of the MLCT state, a band at *ca.* 1972 cm^{-1} is observed before the formation of the water species $W(CO)_5(H_2O)$ (1978 cm^{-1}). The MLCT state is too intense as shown in Figure 3.81, the spectra on the μs-timecale is more clearly shown in Figure 3.82.

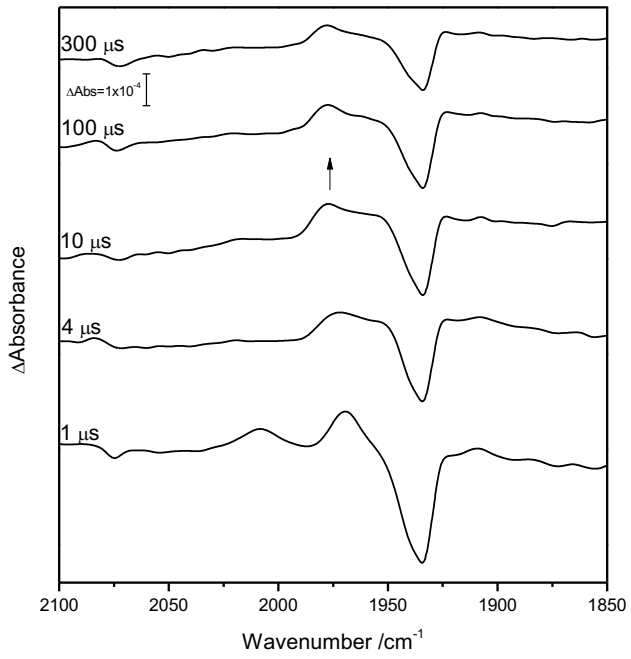


Figure 3.82 *μs-timescale TRIR spectra of $W(CO)_5$(4-acpy) in neat PFMCH.*

Kinetic analysis shows that the formation rate of $W(CO)_5(H_2O)$ (1978 cm^{-1}) is 3.9 (±1.3) μs, which does not fit the lifetime of the MLCT state. The recovery rate of the parent bands is discovered to be tri-exponential (t_1= 179 ± 67 ps, t_2= 299 ± 14 ns, and t_3= 3.3 ± 2.6 μs). The lifetime for t_1 fits the decay of the initial vibrational cooling process, t_2 fits the decay of the MLCT state, and t_3 fits the formation rate of $W(CO)_5(H_2O)$, suggesting that there may be another species that decays for *ca.* 3~4 μs, which converts to $W(CO)_5(H_2O)$ as well as recovers to the parent complex. According to previous research,[21] the ν(CO) of the second W pentacarbonyl species is proposed to be at *ca.* 1961 cm^{-1}. However, the kinetic analysis of both bands at 1972 and 1961 cm^{-1} are similar to the band at 1978 cm^{-1}. The observation of the band at 1972 cm^{-1} may be the combination of the band at 1978 cm^{-1} as well as the species at *ca.* 1962 cm^{-1}, which is weak in intensity.

Figure 3.83 shows the TRIR spectra of $W(CO)_5$(4-acpy) in PFMCH doped with Xe.

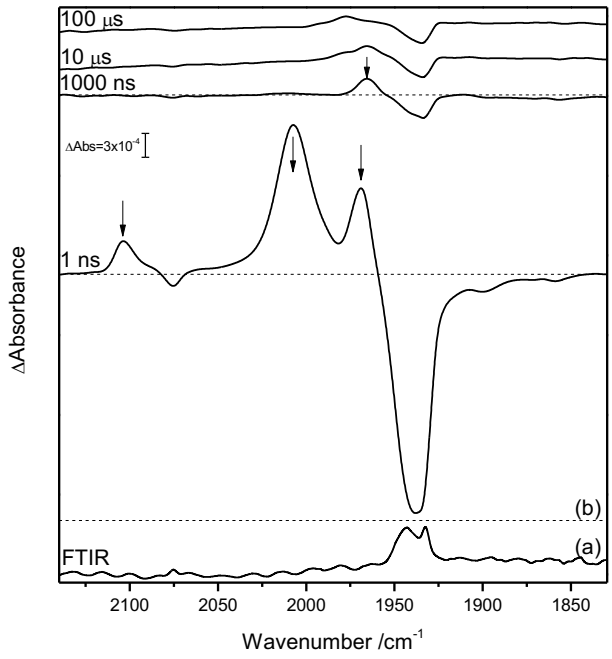


Figure 3.83 *(a) FTIR spectrum and (b) TRIR spectra obtained following photolysis (400 nm) of $W(CO)_5$(4-acpy) in PFMCH doped with 1.5 bar of Xe.*

As can be observed from Figure 3.83, similar to that in neat PFMCH, upon UV photolysis the MLCT state is formed. Kinetic analysis also shows a similar lifetime for the MLCT state to that observed in neat PFMCH (214 ±7 ns). Different to that observed in neat PFMCH, after the decay of the MLCT state, a band at 1967 cm^{-1} is observed in early μs-timescales, as shown in Figure 3.84.

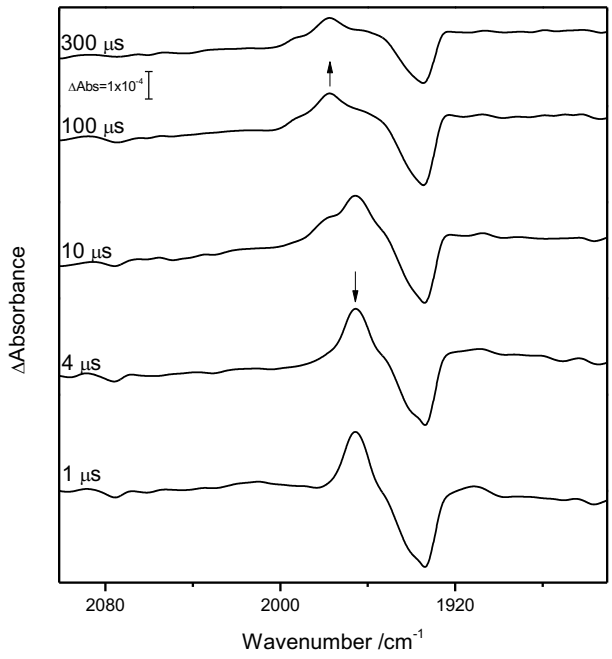


Figure 3.84 *μs-timescale TRIR spectra of $W(CO)_5$(4-acpy) in PFMCH doped with 1.5 bar of Xe.*

As shown in Figure 3.84, a band at 1967 cm^{-1} is formed on the early μs-timescales, which then decays, and the water species $W(CO)_5(H_2O)$ (1978 cm^{-1}) is formed at later μs-timescales. Kinetic analysis shows similar kinetics to that in neat PFMCH. The decay rate of the MLCT state fits the recovery rate of the parent bands. Kinetic analysis also reveals that the water species $W(CO)_5(H_2O)$ (13.5 ±4.7 μs) is converted from the species at 1967 cm^{-1} (210 ±7 ns, 13.5 ±4.7 μs), as shown in Figure 3.85.

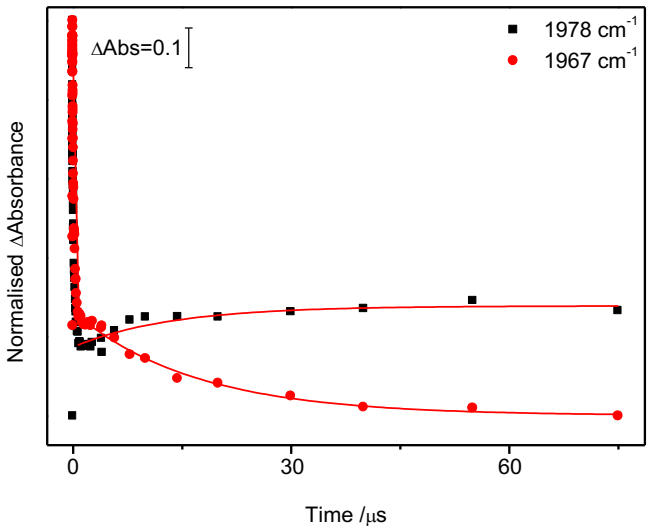


Figure 3.85 *TRIR kinetic traces obtained at 1978 ($W(CO)_5(H_2O)$) and 1967 cm^{-1}.*

As shown in Figure 3.85, similar to $W(CO)_5(py)$ and $W(CO)_5(pip)$, the lifetime of the band at 1967 cm^{-1} is extremely prolonged upon addition of Xe. Also, different to that in neat PFMCH, the water species $W(CO)_5(H_2O)$ is proposed to be converted from the species at 1967 cm^{-1}. Therefore, similar to previous studies on $W(CO)_5(py)$ and $W(CO)_5(pip)$, it is suspicious that the band at 1967 cm^{-1} may be the Xe species $W(CO)_5Xe$ or a combination of the first W pentacarbonyl species and $W(CO)_5Xe$.

In conclusion, for all three complexes $W(CO)_5(py)$, $W(CO)_5(pip)$ and $W(CO)_5(4\text{-}acpy)$, in PFMCH, upon photolysis the formation of the first W pentacarbonyl species is observed consistent with the previous work.[21] The assignment of the first W pentacarbonyl species to the unsaturated $W(CO)_5$ species is questioned as the lifetime in this work is prolonged to 60~100 ns compared to the previous work (*ca.* 6 ns).[21] The water concentration in the PFMCH solution is considered to be an important factor in affecting the reaction process, which may explain the weak IR intensity of the second W pentacarbonyl species observed or the absent observation of the second W pentacarbonyl species in neat PFMCH. However, the existence of the second W pentacarbonyl species is supported by the formation of the water species $W(CO)_5(H_2O)$.

When Xe is added into the system, different to the results observed in neat PFMCH, the lifetime of the band at 1967 cm^{-1} is significantly prolonged, and fits the formation rate of the final water species $W(CO)_5(H_2O)$. The band at 1967 cm^{-1} is considered to consists of two species, the first W pentacarbonyl species as well as the Xe species $W(CO)_5(Xe)$. This is different to our previous work, in which it is reported the ν(CO) positions of the Xe species $W(CO)_5(Xe)$ move to lower wavenumber (1963, 1937 cm^{-1}) compared to the first W pentacarbonyl species (1966, 1930 cm^{-1}).[21] This could be due to the insufficient IR resolution in our TRIR experiments, as 1 pixel in the IR spectra corresponds to $\Delta\nu$(CO) of *ca.* 5-6 cm^{-1}, which may be the reason of the absent of observation.

The $W(CO)_5$(4-acpy) is different to the other two complexes $W(CO)_5$(py) and $W(CO)_5$(pip), as an intensive and photochemically unreactive MLCT state has been observed upon UV photolysis. The lifetime of the MLCT state is similar or slightly longer than that in *n*-heptane, which may indicate that the inert PFMCH solvent may be able to stabilize the MLCT state of $W(CO)_5$(4-acpy).

3.2.6 TR-XAFS Results

In this section, we are going to present the time-resolved XAFS carried out by Drs Raphael Horvath and Stewart Bartlett on the photochemistry of $W(CO)_6$ in solutions.

3.2.6.1 TR-XAFS of $W(CO)_6$ in *n*-heptane with and without $HSiBu_3$

First, TR-XAFS of $W(CO)_6$ in *n*-heptane with and without the dopant $HSiBu_3$, has been carried out. The difference XANES spectra are shown in Figure 3.86.

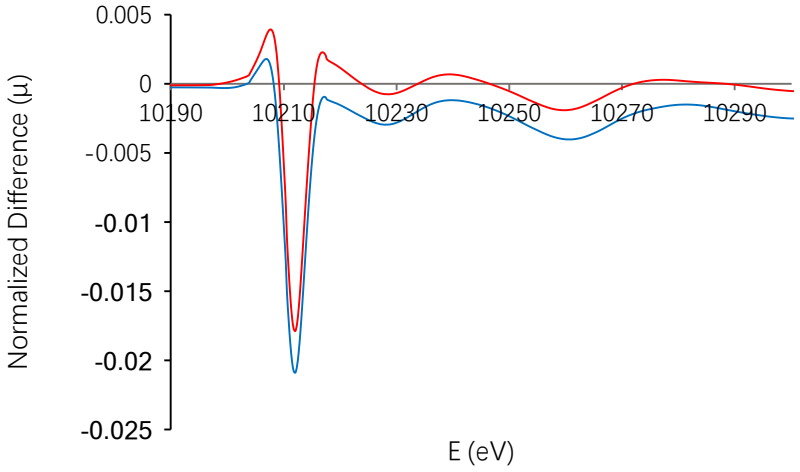


Figure 3.86 *W L_{III} Edge XAS and difference spectra after 30 μs of $W(CO)_6$ in neat heptane (blue) and in the presence of dopant $HSiBu_3$ (red).*

As shown in Figure 3.86, the negative band indicates the bleach of the original absorption edge, while the formation of a positive band at 10209 eV indicates the shift of the absorption edge to lower energy.

By analysing the EXAFS region, structural information can be obtained from the osillations as shown in Figure 3.87. The results are summarised in Table 3.25.

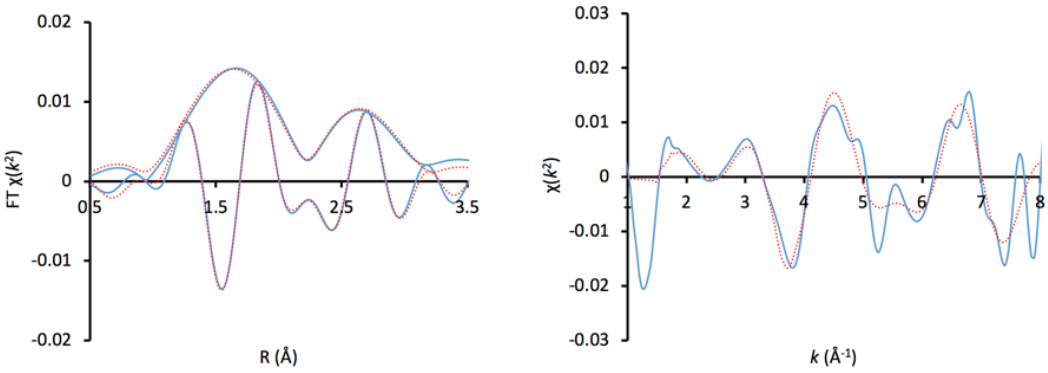


Figure 3.87 *W L_{III} Edge EXAFS difference data of $W(CO)_6$ in n-heptane after 30 μs: EXAFS of background subtracted experimental (blue solid) and fit model of $W(CO)_5$(n-heptane) (red dashed). Left: Modulus and imaginary part of Fourier transform; right: k^2 weighted EXAFS.*

Table 3.25 *EXAFS and DFT results of $W(CO)_5$(n-heptane) from the photolysis of $W(CO)_6$ in n-heptane after 30 μs. [a]DFT results from coordination via the primary C-H bond to W; [b]DFT results from coordination via the secondary C-H bond to W; [c]DFT results from coordination via the statistical average of primary and secondary C-H bonds to W.*

Ligand	Paths	EXAFS R (Å)	DFT R(Å)[a]	DFT R(Å)[b]	DFT R(Å)[c]
trans W-CO	W-C	1.94	1.96	1.96	1.96
	W-O	3.13	3.11	3.11	3.11
4 *cis* W-CO	W-C	2.03	2.06	2.06	2.06
	W-O	3.21	3.20	3.20	3.20
W-heptane	W-C	3.07	2.86	3.11	3.06

The fit of the EXAFS data indicates three shells, as shown in Table 3.25. The first shell consists of W-C from W-CO, the second shell consists of W-O, and the third shell consists of W-C from W-heptane. The fitting of EXAFS for $W(CO)_6$ was obtained from the laser-off spectrum, which reveals that the W-C is at a distance of 2.07Å, similar to the *cis* W-CO distance in $W(CO)_5$(*n*-heptane) (Table 3.25).

DFT calculations have also been conducted, and the results are summarised in Table 3.25. As shown in Table 3.25, the DFT results of the W-CO distances are in good agreement with the EXAFS data. For the W-heptane distances, two values of 2.86 and 3.11 Å are obtained for the bindings with the primary and secondary C-H, respectively. However, in solution, it is proposed that the W centre should coordinate both to the primary and secondary C-H, and the $W(CO)_5$ moeity is in a dynamic process walking along the alkane, therefore an average of the primary and secondary C-H coordinations is expected. The averaged binding given by DFT is satisfying, as shown in Table 3.25.

For the photolysis of $W(CO)_6$ in *n*-heptane in presence of the dopant $HSiBu_3$, as shown in Figure 3.86, the XANES spectra are similar to the undoped one, while the signal is observed to be stronger than the undoped one.

The analysis of the EXAFS of $W(CO)_6$ in *n*-heptane in presence of $HSiBu_3$ after 50-75 μs has revealed the formation of the silane species $W(CO)_5(HSiBu_3)$, as well as the structural information. The results are summarised in Table 3.26.

Table 3.26 *EXAFS and DFT results of $W(CO)_5(HSiBu_3)$ from the photolysis of $W(CO)_6$ in n-heptane in presence of $HSiBu_3$ after 50-75 μs.*

Ligand	Paths	EXAFS R (Å)	DFT R (Å)
trans W-CO	W-C	2.01	1.99
	W-O	3.18	3.14
4 cis W-CO	W-C	2.06	2.06
	W-O	3.23	3.20
$W\text{-}HSiBu_3$	W-Si	3.20	3.13

As shown in Table 3.26, the W-Si distance is 3.20 Å according to EXAFS, and the DFT results are in good agreement with the experimental results. The EXAFS results indicate the η^1-binding of $HSiBu_3$ to the W centre, consistent with the TRIR results as discussed.

The ligand exchange between $W(CO)_5$(*n*-heptane) and $W(CO)_5(HSiBu_3)$ has been monitored using TR-XANES, as shown in Figure 3.88.

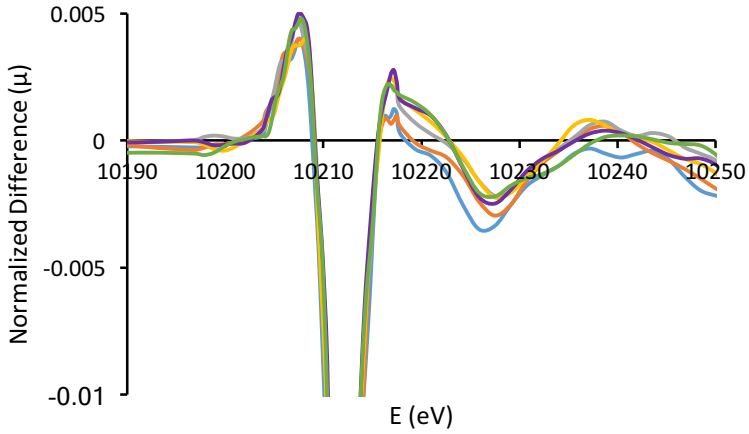


Figure 3.88 *Difference spectra of $W(CO)_6$ in n-heptane in presence of dopant $HSiBu_3$. Blue: 0-2 μs; orange: 2-4 μs; grey: 4-6 μs; yellow: 6-8 μs; purple: 8-10 μs; green: 10-12 μs.*

Using linear combination analyses (LCA), kinetic information can be obtained from the XANES results, which show similar kinetics to the TRIR results that the exchange reaction between $W(CO)_5$(*n*-heptane) and $W(CO)_5(HSiBu_3)$ occurs within the first 20 μs after photolysis in presence of 0.05 M $HSiBu_3$.

3.2.6.2 TR-XAFS of $W(CO)_6$ in PFMCH under He or Xe Atmosphere

The TR-XAFS measurements of $W(CO)_6$ in PFMCH with and without Xe have been carried out.

Figure 3.89 shows the XAFS spectra of $W(CO)_6$ in PFMCH under a helium or xenon atmosphere, which show marked changes. The absorption signal at 10.220 KeV under Xe is stronger than that observed under He, indicating that under different atmospheres, two different products may have formed.

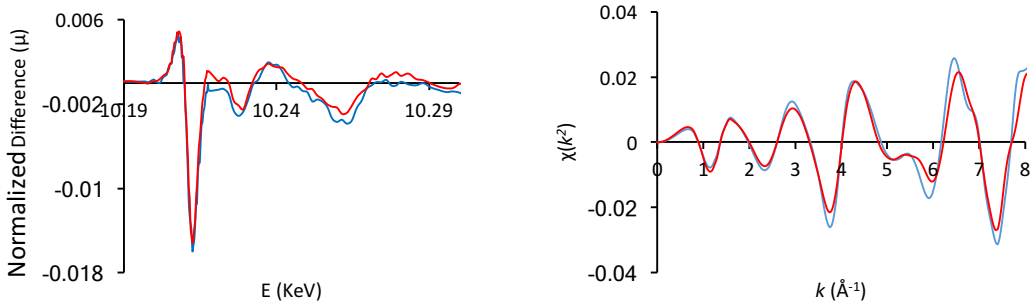


Figure 3.89 *W L_{III} Edge XAS and difference spectra after 4 μs (left) and extracted EXAFS after 8 μs of $W(CO)_6$ in PFMCH under He (blue) and Xe(red).*

Figure 3.90 shows the time interval difference spectra under He and Xe.

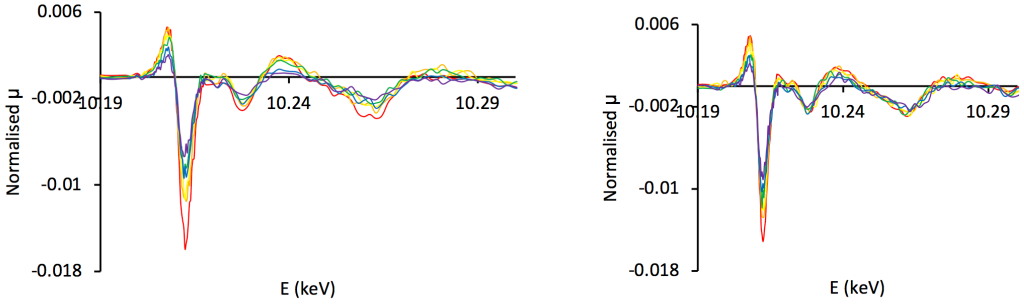


Figure 3.90 *Time interval difference spectra under He (left) and Xe (right). Red: 0-4 μs; orange: 4-8 μs; yellow: 8-12 μs; green: 12-16 μs; blue: 16-20 μs; purple: 20-30 μs,*

Comparison of these two conditions reveals that the photoproduct under He has a slightly shorter lifetime than that formed under Xe.

The W L_{III} Edge EXAFS difference spectra of $W(CO)_6$ in PFMCH under He and Xe are shown in Figure 3.91, and the results are summarised in Table 3.27 and Table 3.28.

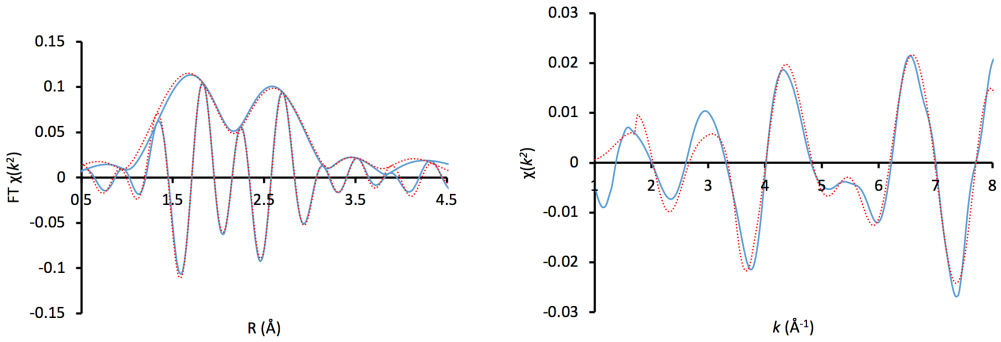


Figure 3.91 *W L_{III} Edge EXAFS difference spectra of $W(CO)_6$ in PFMCH under Xe over the first 8 μs: EXAFS of background subtracted experimental (blue solid) and fit model of $W(CO)_5(Xe)$ (red dashed). Left: Modulus and imaginary part of Fourier transform; right: k^2 weighted EXAFS.*

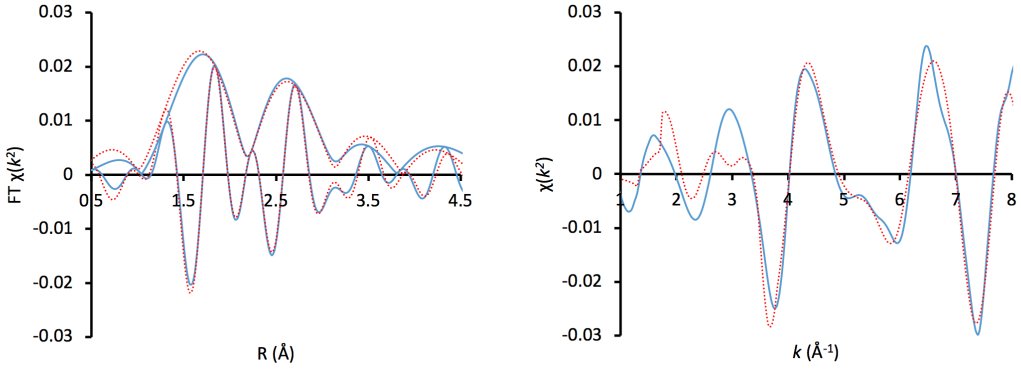


Figure 3.92 *W L_{III} Edge EXAFS difference spectra of $W(CO)_6$ in PFMCH under He over the first 8 μs: EXAFS of background subtracted experimental (blue solid) and fit model of $W(CO)_5(PFMCH)$ (red dashed). Left: Modulus and imaginary part of Fourier transform; right: k^2 weighted EXAFS.*

Table 3.27 *EXAFS and DFT results of $W(CO)_5(Xe)$ from the photolysis of $W(CO)_6$ in PFMCH under Xe over the first 8 μs.*

Ligand	Paths	EXAFS R (Å)	DFT R (Å)
trans W-CO	W-C	1.90	1.96
	W-O	3.06	3.11
4 *cis* W-CO	W-C	1.96	2.06
	W-O	3.13	3.20
W-Xe	W-Xe	3.56	3.07

Table 3.28 *EXAFS and DFT results of $W(CO)_5(PFMCH)$ from the photolysis of $W(CO)_6$ in PFMCH under He over the first 8 μs.*

Ligand	Paths	EXAFS R (Å)	DFT R (Å)
trans W-CO	W-C	1.97	2.02
	W-O	3.12	3.15
4 *cis* W-CO	W-C	2.05	2.10
	W-O	3.19	3.22
W-PFMCH	W-F	2.65	2.58

It can be observed from the data that the W-CO distances under He atmosphere are significantly longer than that under Xe, and the EXAFS results are in good agreement with the DFT calculations. The fit of W-Xe reaches a R-factor of 0.008, while when the contribution of the W-Xe bond is excluded, the R-factor increases dramatically to 0.08. This is a strong evidence for the presence of the W-Xe bond.

3.3 Conclusion

For the E-H bond activation of $HEBu_3$ (E: Si, Ge, Sn) by $W(CO)_6$ in alkane solvent - heptane, the E-H bound species $W(CO)_5(HEBu_3)$ is observed for all dopants $HEBu_3$. The photo-initiated $W(CO)_5$ fragment first coordinates to the solvent molecule *n*-heptane, in which the W centre is coordinated to the C-H bond. Then C-H is replaced by the more electron rich E-H bond of the dopants $HEBu_3$. For $HSiBu_3$ and $HGeBu_3$, the extent of the E-H bond activation is similar. The interaction between W and H-E is proposed to be in an η^1-mode *via* H. While for $HSnBu_3$, the extent of the Sn-H bond activation is proposed to be greater than Si-H and Ge-H, comparing the relavent ν(CO) positions of the $W(CO)_5(HEBu_3)$ complexes. Also, as for all $W(CO)_5(HEBu_3)$ complexes the ν(CO) positions are red-shifted compared to the parent bands, which suggests that in all $W(CO)_5(HEBu_3)$ complexes, the predominant interaction between W and E-H is still the electron donation from E-H to the W centre.

The C-H/Si-H ligand exchange rate for $HSiBu_3$ is much slower in *n*-heptane compared to previous work done in neat $HSiEt_3$. Investigations on the effects of reagent concentrations on the ligand exchange rate show that the kinetic order of $W(CO)_6$ in the C-H/E-H ligand exchange reaction is 0, while for the dopants $HEBu_3$ the kinetic orders are one, which reflects that the ligand exchange rate is highly dependent on the dopant concentration. The C-H/Si-H ligand exchange rate in neat $HSiBu_3$ is slower than that observed in neat $HSiEt_3$, which suggests that steric factors could also play an important role in the ligand exchange reaction.

The ligand exchange rates for the three dopants follows: Sn-H > Ge-H ≥ Si-H, which is consistent with their electron donation abilities. Electron rich E-H can facilitate the coordination to the W centre.

For the interaction with halogenated cyclohexanes (X-cyclohexane; X: Cl, Br), for both Cl-cyclohexane and Br-cyclohexane, the binding to the $W(CO)_5$ fragment is likely *via* the lone pair of the halogen atom, as suggested by Dobson *et al.*[54] The ligand exchange rate between $W(CO)_5$(*n*-heptane) and $W(CO)_5$(X-cyclohexane) is

found to be related to the dopant concentration. The kinetic orders of both X-cyclohexanes are found to be one, while the second order rate constants reveal that Br-cyclohexane is more reactive regard the ligand exchange between $W(CO)_5$(*n*-heptane) and $W(CO)_5$(X-cyclohexane).

For interactions with X-benzene (X: F, Cl, Br, I) as well as benzene, TRIR and DFT results show that for benzene and F-benzene, the most stable interaction with the photo-generated CO-loss $W(CO)_5$ is *via* the double bond edge of the benzene ring. For both F-benzene and Cl-benzene, the formation of the CX=CH bound species is observed. For Br-benzene and I-benzene, no ring edge bound species is observed. The W centre coordinates to Br-benzene and I-benzene *via* the lone pair of Br and I. Meanwhile, the oxidative addition species [$W(CO)_5$(X---phenyl)] (X: Br, I) is observed, in which a 3-c-2-e interaction is formed between W and C-X.

For the E-H bond activation of $HEBu_3$ [E: Si, Ge, Sn) by $W(CO)_5L$ (L: pyridine (py), 4-acetylpyridine (4-acpy), piperidine (pip)] in heptane, similar reaction mechanism to $W(CO)_6$ discussed in Section 3.2.1 has been observed. As for $W(CO)_5L$ (L: py, pip, 4-acpy), the predominant photochemical reaction upon UV photolysis is the L-dissociation instead of CO-loss, which generates the W pentacarbonyl species $W(CO)_5$, and quickly coordinates to the surrounding solvent molecule *n*-heptane, similar to $W(CO)_6$. Upon addition of the dopant $HEBu_3$ (E: Si, Ge, Sn), ligand exchange reaction between $W(CO)_5$(*n*-heptane) and the dopant species $W(CO)_5(HEBu_3)$ is also observed. However, for $W(CO)_5$(4-acpy), a strong and inert $MLCT_{W\rightarrow L}$ state has been observed upon UV photolysis. The final dopant species $W(CO)_5(HEBu_3)$ is found to be formed both from the $MLCT_{W\rightarrow L}$ state and $W(CO)_5$(*n*-heptane). The reactivity of the $MLCT_{W\rightarrow L}$ state is attributed to the quick equilibrium with the reactive LF or $MLCT_{W\rightarrow CO}$ state.

For all $W(CO)_5L$ complexes (L: py, pip, 4-acpy), the general trend of the ν(CO) positions of $W(CO)_5(HEBu_3)$ is found to be Si ≈ Ge < Sn, and for $W(CO)_5$(py) and $W(CO)_5$(pip), the C-H/E-H ligand exchange rate is found to follow: Si ≈ Ge < Sn, which is consistent with the results of $W(CO)_6$ discussed in Section 3.2.1. This is expected as for all complexes $W(CO)_5$(py), $W(CO)_5$(pip) and $W(CO)_6$, the C-H/E-H

ligand exchange reaction is the same, between $W(CO)_5$(*n*-heptane) and $W(CO)_5(HEBu_3)$. However, for $W(CO)_5$(4-acpy), the C-H/Si-H exchange rate is found to be faster than expected, while the C-H/Ge-H exchange rate is found to be slower than C-H/Si-H.

The W-Xe interaction has been investigated using TRIR. UV irradiation of the $W(CO)_5L$ complexes (L: py, pip, 4-acpy) in PFMCH in presence of Xe results in the formation of $W(CO)_5(Xe)$, similar to the previous work of $W(CO)_6$,[21] which is also supported by TR-XAFS results by our collaborators.

The aim of the TRIR is to support the TR-XAFS experiments. TR-XAFS results by our collaborators show consistent conclusions to our TRIR work, that in $W(CO)_5(HSiBu_3)$ the $HSiBu_3$ coordinates to the W centre *via* H in an η^1-fashion. The XAFS results also provide evidence for the formation of $W(CO)_5(Xe)$ when $W(CO)_6$ is irradiated in PFMCH under a Xe atmosphere, consistent with our TRIR results. Besides, XAFS also provides structural information which TRIR cannot provide. Bond distances have been obtained and are in excellent agreement with the DFT results. Kinetics obtained from XAFS are also shown to be consistent with the TRIR results.

References

1 R. N. Perutz and J. J. Turner, *J. Am. Chem. Soc.*, 1975, **97**, 4791–4800.

2 R. Paur-Afshari, J. Lin and R. H. Schultz, *Organometallics*, 2000, **19**, 1682–1691.

3 A. Lugovskoy, R. Paur-Afshari and R. H. Schultz, *J. Phys. Chem. A*, 2000, **104**, 10587–10593.

4 T. Lian, S. E. Bromberg, M. C. Asplund, H. Yang and C. B. Harris, *J. Phys. Chem.*, 1996, **100**, 11994–12001.

5 A. G. Joly and K. A. Nelson, *Chem. Phys.*, 1991, **152**, 69–82.

6 J. D. Simon and K. S. Peters, *Chem. Phys. Lett.*, 1983, **98**, 53–56.

7 L. J. Rothberg, N. J. Cooper, K. S. Peters and V. Vaida, *J. Am. Chem. Soc.*, 1982, **104**, 3536–3537.

8 J. A. Welch, K. S. Peters and V. Vaida, *J. Phys. Chem.*, 1982, **86**, 1941–1947.

9 J. D. Simon and Xiaoliang. Xie, *J. Phys. Chem.*, 1987, **91**, 5538–5540.

10 J. D. Simon and X. Xie, *J. Phys. Chem.*, 1986, **90**, 6751–6753.

11 H. Hermann, F. W. Grevels, A. Henne and K. Schaffner, *J. Phys. Chem.*, 1982, **86**, 5151–5154.

12 R. D. Young, D. J. Lawes, A. F. Hill and G. E. Ball, *J. Am. Chem. Soc.*, 2012, **134**, 8294–8297.

13 M. S. Wrighton and M. A. Schroeder, *J. Am. Chem. Soc.*, 1974, **96**, 6235–6237.

14 W. Abdelqader, D. Chmielewski, F.-W. Grevels, S. Özkar and N. B. Peynircioglu, *Organometallics*, 1996, **15**, 604–614.

15 S. Asako, S. Ishikawa and K. Takai, *ACS Catal.*, 2016, **6**, 3387–3395.

16 S. Zhang, G. R. Dobson and T. L. Brown, *J. Am. Chem. Soc.*, 1991, **113**, 6908–6916.

17 S. L. Matthews, V. Pons and D. M. Heinekey, *Inorg. Chem.*, 2006, **45**, 6453–6459.

18 T. J. Burkey, *J. Am. Chem. Soc.*, 1990, **112**, 8329–8333.

19 K. T. Kotz, H. Yang, P. T. Snee, C. K. Payne and C. B. Harris, *J. Organomet. Chem.*, 2000, **596**, 183–192.

20 R. J. Kulawiec and R. H. Crabtree, *Coord. Chem. Rev.*, 1990, **99**, 89–115.

21 T. S. Murphy, *Ph.D. thesis,* University of Nottingham, 2015.

22 J. L. Kiplinger, T. G. Richmond and C. E. Osterberg, *Chem. Rev.*, 1994, **94**, 373–431.

23 M. J. Burk, Brigitte. Segmuller and R. H. Crabtree, *Organometallics*, 1987, **6**, 2241–2246.

24 R. B. King and M. B. Bisnette, *J. Organomet. Chem.*, 1964, **2**, 38–43.

25 M. I. Bruce, P. W. Jolly and F. G. A. Stone, *J. Chem. Soc. Inorg. Phys. Theor.*, 1966, 1602–1606.

26 J. K. Stille and K. S. Y. Lau, *Acc. Chem. Res.*, 1977, **10**, 434–442.

27 S. Zhang and G. R. Dobson, *Polyhedron*, 1990, **9**, 2511–2516.

28 S. Zhang, G. R. Dobson, V. Zang, H. C. Bajaj and R. Van Eldik, *Inorg. Chem.*, 1990, **29**, 3477–3482.

29 S. Ladogana, G. R. Dobson and J. P. Smit, *Inorganica Chim. Acta*, 1998, **278**, 202–208.

30 R. J. Kulawiec, J. W. Faller and R. H. Crabtree, *Organometallics*, 1990, **9**, 745–755.

31 R. H. Crabtree, J. W. Faller, M. F. Mellea and J. M. Quirk, *Organometallics*, 1982, **1**, 1361–1366.

32 M. J. Burk, R. H. Crabtree and E. M. Holt, *Organometallics*, 1984, **3**, 638–640.

33 P. Fitton, M. P. Johnson and J. E. McKeon, *Chem. Commun. Lond.*, 1968, 6–7.

34 P. Fitton and E. A. Rick, *J. Organomet. Chem.*, 1971, **28**, 287–291.

35 F. Barrios-Landeros and J. F. Hartwig, *J. Am. Chem. Soc.*, 2005, **127**, 6944–6945.

36 T. G. Richmond, M. A. King, E. P. Kelson and A. M. Arif, *Organometallics*, 1987, **6**, 1995–1996.

37 D. Strawser, A. Karton, O. V. Zenkina, M. A. Iron, L. J. W. Shimon, J. M. L. Martin and M. E. van der Boom, *J. Am. Chem. Soc.*, 2005, **127**, 9322–9323.

38 A. C. B. Lucassen, L. J. W. Shimon and M. E. van der Boom, *Organometallics*, 2006, **25**, 3308–3310.

39 C. E. Brown, Y. Ishikawa, P. A. Hackett and D. M. Rayner, *J. Am. Chem. Soc.*, 1990, **112**, 2530–2536.

40 R. Uson, J. Fornies, M. Tomas, F. A. Cotton and L. R. Falvello, *J. Am. Chem. Soc.*, 1984, **106**, 2482–2483.

41 R. J. Kulawiec, E. M. Holt, M. Lavin and R. H. Crabtree, *Inorg. Chem.*, 1987, **26**, 2559–2561.

42 M. Brookhart, W. Chandler, R. J. Kessler, Y. Liu, N. J. Pienta, C. C. Santini, C. Hall, R. N. Perutz and J. A. Timney, *J. Am. Chem. Soc.*, 1992, **114**, 3802–3815.

43 R. P. Hughes, in *Advances in Organometallic Chemistry*, eds. F. G. A. Stone and R. West, Academic Press, 1990, vol. 31, pp. 183–267.

44 T. G. Richmond, C. E. Osterberg and A. M. Arif, *J. Am. Chem. Soc.*, 1987, **109**, 8091–8092.

45 B. L. Lucht, M. J. Poss, M. A. King and T. G. Richmond, *J. Chem. Soc. Chem. Commun.*, 1991, 400–401.

46 A. H. Klahn, M. H. Moore and R. N. Perutz, *J. Chem. Soc. Chem. Commun.*, 1992, 1699–1701.

47 C. L. Higgitt, A. H. Klahn, M. H. Moore, B. Oelckers, M. G. Partridge and R. N. Perutz, *J. Chem. Soc. Dalton Trans.*, 1997, 1269–1280.

48 F. Godoy, C. L. Higgitt, A. H. Klahn, B. Oelckers, S. Parsons and R. N. Perutz, *J. Chem. Soc. Dalton Trans.*, 1999, 2039–2048.

49 J. J. Carbó, O. Eisenstein, C. L. Higgitt, A. Hugo Klahn, F. Maseras, B. Oelckers and R. N. Perutz, *J. Chem. Soc. Dalton Trans.*, 2001, 1452–1461.

50 S. T. Belt, M. Helliwell, W. D. Jones, M. G. Partridge and R. N. Perutz, *J. Am. Chem. Soc.*, 1993, **115**, 1429–1440.

51 H. van der Heijden, A. G. Orpen and P. Pasman, *J. Chem. Soc. Chem. Commun.*, 1985, 1576–1578.

52 A. Hugo. Klahn-Oliva, R. D. Singer and Derek. Sutton, *J. Am. Chem. Soc.*, 1986, **108**, 3107–3108.

53 M. W. Bouwkamp, P. H. M. Budzelaar, J. Gercama, I. Del Hierro Morales, J. de Wolf, A. Meetsma, S. I. Troyanov, J. H. Teuben and B. Hessen, *J. Am. Chem. Soc.*, 2005, **127**, 14310–14319.

54 G. R. Dobson, J. P. Smit, S. Ladogana and W. B. Walton, *Organometallics*, 1997, **16**, 2858–2861.

55 M. Wrighton, *Chem. Rev.*, 1974, **74**, 401–430.

56 Mark. Wrighton, *Inorg. Chem.*, 1974, **13**, 905–909.

57 M. S. Wrighton, H. B. Abrahamson and D. L. Morse, *J. Am. Chem. Soc.*, 1976, **98**, 4105–4109.

58 C. Moralejo, C. H. Langford and D. K. Sharma, *Inorg. Chem.*, 1989, **28**, 2205–2209.

59 N. A. Beach and H. B. Gray, *J. Am. Chem. Soc.*, 1968, **90**, 5713–5721.

60 F. P. A. Johnson, M. W. George, S. L. Morrison and J. J. Turner, *J. Chem. Soc. Chem. Commun.*, 1995, 391–393.

61 C. Pollak, A. Rosa and E. J. Baerends, *J. Am. Chem. Soc.*, 1997, **119**, 7324–7329.

62 A. Rosa, E. J. Baerends, S. J. A. van Gisbergen, E. van Lenthe, J. A. Groeneveld and J. G. Snijders, *J. Am. Chem. Soc.*, 1999, **121**, 10356–10365.

63 E. J. Baerends and A. Rosa, *Coord. Chem. Rev.*, 1998, **177**, 97–125.

64 D. Guillaumont, Vlček Antonin and C. Daniel, *J. Phys. Chem. A*, 2001, **105**, 1107–1114.

65 I. R. Farrell, F. Hartl, S. Záliš, T. Mahabiersing and J. Antonín Vlček, *J. Chem. Soc. Dalton Trans.*, 2000, 4323–4331.

66 S. Záliš, I. R. Farrell and A. Vlček, *J. Am. Chem. Soc.*, 2003, **125**, 4580–4592.

67 S. Záliš, M. Busby, T. Kotrba, P. Matousek, M. Towrie and A. Vlček, *Inorg. Chem.*, 2004, **43**, 1723–1734.

68 Paul. Glyn, F. P. A. Johnson, M. W. George, A. J. Lees and J. J. Turner, *Inorg. Chem.*, 1991, **30**, 3543–3546.

69 *Proc. Chem. Soc.*, 1962, 197–236.

70 M. Poliakoff and J. J. Turner, *J. Chem. Soc. Dalton Trans.*, 1974, 2276–2285.

71 S. A. Fairhurst, J. R. Morton, R. N. Perutz and K. F. Preston, *Organometallics*, 1984, **3**, 1389–1391.

72 M. B. Simpson, M. Poliakoff, J. J. Turner, W. B. Maier and J. G. McLaughlin, *J. Chem. Soc. Chem. Commun.*, 1983, 1355–1357.

73 B. H. Weiller, E. P. Wasserman, R. G. Bergman, C. B. Moore and G. C. Pimentel, *J. Am. Chem. Soc.*, 1989, **111**, 8288–8290.

74 R. H. Schultz, A. A. Bengali, M. J. Tauber, B. H. Weiller, E. P. Wasserman, K. R. Kyle, C. B. Moore and R. G. Bergman, *J. Am. Chem. Soc.*, 1994, **116**, 7369–7377.

75 A. A. Bengali, R. H. Schultz, C. B. Moore and R. G. Bergman, *J. Am. Chem. Soc.*, 1994, **116**, 9585–9589.

76 B. H. Weiller, *J. Am. Chem. Soc.*, 1992, **114**, 10910–10915.

77 J. R. Wells and E. Weitz, *J. Am. Chem. Soc.*, 1992, **114**, 2783–2787.

78 M. Jyo-o, H. Takeda, K. Omiya, Y. Ishikawa and S. Arai, *Bull. Chem. Soc. Jpn.*, 1993, **66**, 3618–3626.

79 G. I. Childs, C. S. Colley, J. Dyer, D. C. Grills, X.-Z. Sun, J. Yang and M. W. George, *J. Chem. Soc. Dalton Trans.*, 2000, 1901–1906.

80 X.-Z. Sun, M. W. George, S. G. Kazarian, S. M. Nikiforov and M. Poliakoff, *J. Am. Chem. Soc.*, 1996, **118**, 10525–10532.

81 J. M. Kelly, C. Long and R. Bonneau, *J. Phys. Chem.*, 1983, **87**, 3344–3349.

82 G. R. Dobson, P. M. Hodges, M. A. Healy, M. Poliakoff, J. J. Turner, S. Firth and K. J. Asali, *J. Am. Chem. Soc.*, 1987, **109**, 4218–4224.

83 Yang Jian, White Peter S., Schauer Cynthia K. and Brookhart Maurice, *Angew. Chem. Int. Ed.*, 2008, **47**, 4141–4143.

84 P. M. Hodges, S. A. Jackson, J. Jacke, M. Poliakoff, J. J. Turner and F. W. Grevels, *J. Am. Chem. Soc.*, 1990, **112**, 1234–1244.

85 Z. Shulin and G. R. Dobson, *Inorganica Chim. Acta*, 1991, **181**, 103–109.

86 S. Zhang, V. Zang, H. C. Bajaj, G. R. Dobson and R. van Eldik, *J. Organomet. Chem.*, 1990, **397**, 279–289.

Chapter 4 Photophysics Studies on Re-diimine Complexes

4.1 Introduction

4.1.1 Photophysics of Re-dppz Carbonyl Complexes

Metal-dppz complexes have been the focus of research for decades due to their interesting photoproperties. The dppz ligand (dipyrido[3,2-a: 2'3'-c]phenazine) possesses two close lying lowest unoccupied π^* orbitals based on two sections of the ligand, the phenazine part and the phenanthroline part, both can act as electron-acceptors in the CT (charge transfer) process. This behavior has been confirmed by various spectroscopic and electrochemical studies.[1,2,3,4] The dppz ligand thus can be viewed as the combination of the phen (1,10-phenanthroline) and the phz (phenazine) moieties. The structures of these and the ligand as a whole are shown in Figure 4.1.

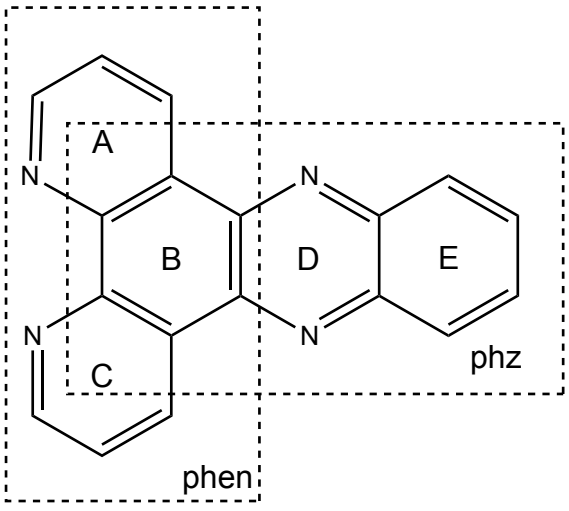


Figure 4.1 *The structure of dppz (dipyrido[3,2-a: 2'3'-c]phenazine). Rings A, B and C compose the phen (1,10-phenanthroline) moiety. Rings B, D and E compose of the phz (phenazine) moiety.*

Therefore, when complexed with metal centre, two MLCT processes based on the phz and phen moieties can be observed. One example is the famous "light switch

effect" phenomenon which has been observed for the Ru-dppz complexes $[Ru(dppz)(bpy)_2]^+$.[5] It is found that the emission of $[Ru(dppz)(bpy)_2]^+$ is solvent-dependent. In aprotic solvents, $[Ru(dppz)(bpy)_2]^+$ are found to be emissive, while in aqueous or protic solvents, the emission can be quenched. Nevertheless, the emission is observed in aqueous solvents containing DNA. This effect is explained by the two different MLCT states based on different moieties of the dppz ligand. The LUMO is phz-based, while the LUMO+1 is phen-based. The phen MLCT is recognized as emissive while the phz MLCT is non-emissive, known as the dark state. The solvent will influence the relative energy level of the two MLCT states. In aprotic solvents, the lowest state is $MLCT_{phen}$. While in protic solvents, the energy levels reverses, $MLCT_{phz}$ in turn becomes the lowest-lying state, and thus the emission is quenched. H-bonding with the phz moiety stabilizes the $MLCT_{phz}$ state, and when intercalating to DNA or in non-protic solvents, this stabilization cannot be achieved. However, this theory is disproved by Brennaman *et al.*[6,7] They investigated the photophysics of $[Ru(dppz)(bpy)_2]^{2+}$ in both protic and aprotic solvents, and they found that the emission of the Ru complex is temperature-dependent. When increasing the temperature in both solvents, the population of the emissive $MLCT_{phen}$ is facilitated, while the dark state $MLCT_{phz}$ is better populated at low temperatures. This is attributed to the fact that the $MLCT_{phz}$ state is enthalpically favoured, while the $MLCT_{phen}$ state is entropically favoured, and the "light switch effect" is due to the equilibrium of these two states. In other words, the energy reversal of these two states does not occur.

Although for many metal-dppz complexes, the predominate photo-induced lowest-lying excited states are MLCT states, such as the Ru- and Os-dppz complexes. However, for the Re-dppz complexes, the photophysics is more complicated. The intensity of the MLCT state is dependent on how much the $d\pi$ orbital of the metal overlaps with the π-orbital of the dppz ligand. For the Os and Ru complexes, the overlap is considered to be larger than Re. Thus, the MLCT excited state is more often observed for the Os-dppz and Ru-dppz complexes upon UV photolysis. While for the Re-dppz complexes, the photophysics can be more easily tuned by changing substituents on the dppz ligand or by changing the Re-moiety.[8]

Previous experimental and theoretical work proposed that for the Re-dppz complexes, LUMOs are usually located in the dppz ligand.[2,9] The LUMO is usually phz-based, while LUMO+1 and LUMO+2 are phen-based. Normally the MLCT and intraligand states are close-lying in energy for many Re-dppz complexes.[3,8] The energy levels of the dppz-based MO orbitals can be tuned by changing the substituents on the dppz ligand. As the LUMO is based on phz in most cases, substituents on the phz-moeity has been investigated the most. Previous TRIR investigations on the photophysics of the $[Re(CO)_3(dppz\text{-}11, 12\text{-}X_2)Cl]$ complexes (X:CH_3, H, Br, Cl, F)[10,11] show that, with increasing electron withdrawing effects (CH_3 < H < Br < Cl < F), the LUMO phz-orbital gets stabilized, and the $MLCT_{phz}$ state can be promoted. However, when substituted with ligands with greater electron donating abilities, the intraligand states are facilitated. For X=Br, Cl and F, only Re-to-dppz MLCT state can be observed, while for X=H and CH_3, both IL $\pi\pi^*$ and $MLCT_{phen}$ state have been observed. This is also supported by the DFT calculations. It is also discovered that the introduction of strong electron-donor ligands such as TPA (triphenylamine) into the dppz ligand can facilitate the intraligand charge transfer (ILCT) from the electron-donor ligands to the dppz LUMO orbital (often phz-based), and normally the ILCT is the lowest-lying transition.[12,13,14,15,16]

Changing the axial ligand L in the metal moiety $[Re(CO)_3L]$ can affect the $d\pi$ orbital of the metal centre, thus influence the overall photophysics. For many Re-dppz complexes with an electron withdrawing ancillary ligand, IL $\pi\pi^*$ states are often observed rather than the MLCT state. While the electron donating L ligand can increase the electron density on the metal centre and destabilize the $d\pi$ orbital of the metal centre, therefore facilitate the Re-to-dppz MLCT process. This view has been supported by many studies. Investigations on the photophysics of $[Re(CO)_3(dppz)(py)]^+$, $[Re(CO)_3(dppz)(PPh_3)]^+$, $[Re(CO)_3(dppz)(py\text{-}PTZ)]^+$ (py-PTZ: 10-(4-picolyl)-phenothiazine) and $[Re(CO)_3(4\text{-}Me\text{-}py)(dppz)]^+$ show that, compared with $[Re(CO)_3(dppz)Cl]$ with an electron rich Cl^- ligand, these complexes exhibit merely the IL_{dppz} states, except for $[Re(CO)_3(dppz)(py)]^+$, the $MLCT_{phz}$ state has been observed.[3,17,18,19] Other research work on $[Re(CO)_3(dppz\text{-}COOEt)L]^{n=0,1}$ (L: Cl^-, n=0; py, n=1; DMAP (4-(dimethylamino)pyridine), n=1), $[Re(CO)_3(dppz\text{-}$

Me_2)L]$^+$ (L: py, 4-etpy, py-PTZ), [Re(CO)$_3$(dppz-Cl$_2$)L]$^+$ (L: py, DMAP), [Re(CO)$_3$(dppz-PhNPh$_2$)L]$^{n=0,1}$ (L: Cl$^-$, n=0; py, n=1; DMAP, n=1) have also shown similar results.[18,20,21,22,23,24]

The photophysics of the Re-dppz complexes has been discovered to be also affected by the solvent. As discussed before, protic solvent can quench the emission of the Ru-dppz complexes. While for the Re-dppz complexes, solvents of different polarities are discovered to influence the photophysics. Kuimova's research on the photophysics of a series of Re-dppz complexes reveals that, the solvent polarity has more impact on the MLCT states, while the $\pi\pi^*$ states are unaffected.[10] Increasing the solvent polarity can shorten the lifetime of the MLCT state, although instance exists that the lifetime of the IL $\pi\pi^*$ state is shortened in polar solvents for [Re(CO)$_3$(dppz)(4-mepy)]$^+$. However, the MLCT state of [Re(CO)$_3$(dppz)(4-mepy)]$^+$ is considered to be close-lying to the lowest-lying IL $\pi\pi^*$ state, thus the interconversion between the ^{3}IL and ^{3}MLCT states deactivates the ^{3}IL state in more polar solvents. The hydrogen-bonding is also observed to shorten the lifetime of the excited states.

Many research techniques have been used to explore the photophysics of metal-dppz complexes, such as UV-Vis absorption and emission spectroscopy, Raman spectroscopy, EPR, transient vibrational spectroscopy, TRIR and quantum chemical calculations.[24] Among these techniques, TRIR is excellent in revealing ultrafast reaction processes down to even ps-timescale.[25] Especially for complexes with the reporting ligand CO, such as the [Re(CO)$_3$(dppz)L] complexes. For metal carbonyl complexes, TRIR can be used to distinguish between the MLCT states and the intraligand states. In a MLCT state, the electron density on the metal centre is decreased, resulting in the weakening of the π-backbonding from the metal centre to carbonyl, therefore ν(CO) of the MLCT states is expected to occur at higher energies than the parent complex. While for the intraligand states, the electron density on the metal centre is increased, thus, the ν(CO) of the intraligand state is expected to occur at lower wavenumber. As a MLCT state is a direct charge transfer of an electron from the metal centre to the ligand, the extent of the electron density change of MLCT is much larger than the intraligand state. Therefore, the $\Delta\nu$(CO)

compared to the parent complex for the MLCT state is usually much larger than the intraligand state. TRIR can also be used to identify different CT states based on the same ligand but with different moieties. For example, the $MLCT_{phen}$ (CT ends on the phen moiety of dppz) and the $MLCT_{phz}$ (CT ends on phz) states can be distinguished as accepting moieties with different overlap extents with the metal centre will result in different electron density changes on the metal, thus the backbonding to CO will be diagnostic. $MLCT_{phen}$ is usually recognized to cause a $\Delta\nu$(CO) of *ca.* 40 cm^{-1} compared to the parent bands, while for $MLCT_{phz}$ the $\Delta\nu$(CO) is usually expected to be larger, for *ca.* 60 cm^{-1}. The fingerprint region of the IR spectrum at *ca.* 1300 — 1600 cm^{-1} is also diagnostic for distinguishing different states. Larsen *et al.*[24] used TRIR to investigate the photophysics of a series of the $[Re(CO)_3(dppz\text{-}PhNPh_2)L]$ complexes. It is found that in the carbonyl region of the IR, two IL states are difficult to distinguish from each other. However this problem is solved by the corresponding peaks in the fingerprint region.

In this work, we used TRIR to investigate the photophysics of $[Re(CO)_3(dppz\text{-}NPh_2)Cl]$ in different solvents, in order to explore how the solvent polarities can affect the photophysics of $[Re(CO)_3(dppz\text{-}NPh_2)Cl]$. The structure of $[Re(CO)_3(dppz\text{-}NPh_2)Cl]$ is shown in Figure 4.2.

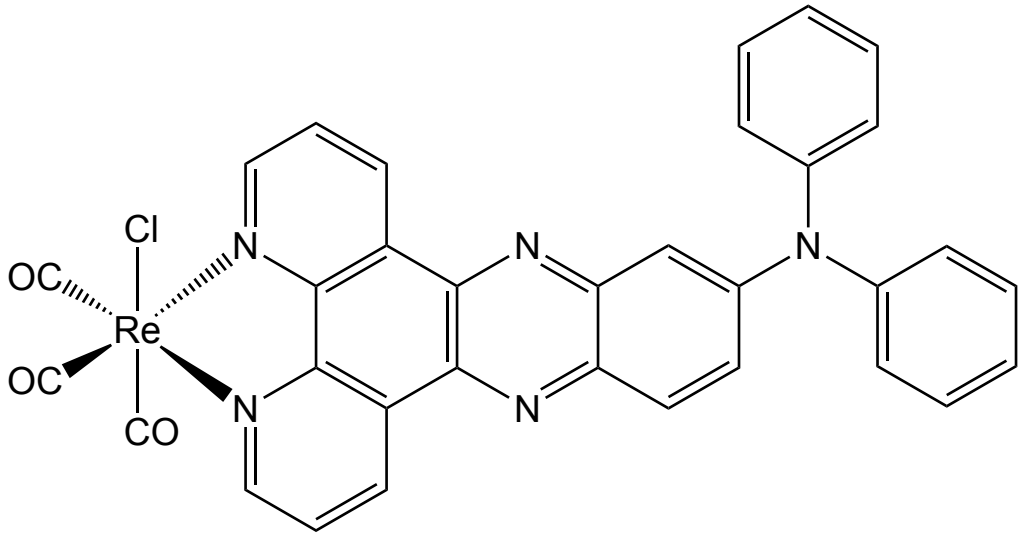


Figure 4.2 *Structure of the $[Re(CO)_3(dppz\text{-}NPh_2)Cl]$ complex.*

The $[Re(CO)_3(dppz\text{-}NPh_2)Cl]$ complex is a typical "D-A" structure, where the dppz ligand is acting as the electron-accepting end, while the electron rich NPh_2 ligand

is acting as the electron donor.

Previous TRIR investigations on the photophysics of $[Re(CO)_3(dppz\text{-}NPh_2)Cl]$ have been conducted by Adams *et al.*[26] It was found that upon UV photolysis, two excited states are generated, denoted as state I and state III. State I is observed to convert to state II in *ca.* 30 ps, while state II and state III are observed to decay independently into the ground state for *ca.* 2 μs and 2 ns, respectively, as shown in Figure 4.3.

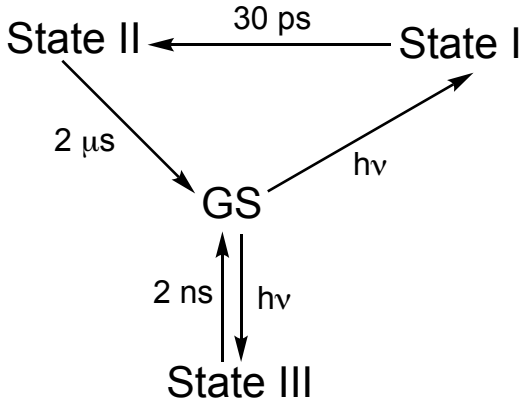


Figure 4.3 *Reaction mechanism of $[Re(CO)_3(dppz\text{-}NPh_2)Cl]$ in CH_2Cl_2 after UV irradiation according to Adams' work.*[26]

There are different views on the assignment of the excited states. According to Adams *et al.*, state I and state II are assigned to the singlet $^1IL\pi\pi^*$ and the triplet $^3IL\pi\pi^*$, respectively, while state III is assigned to the ILCT state in which the electron density is transferred from the electron rich donor NPh_2 to the phz moiety. The reasons are as following:

1. As the DFT results suggest the $IL\pi\pi^*$ transition is possible. Therefore, state I is tentatively assigned as the singlet $^1IL\pi\pi^*$. The red-shift of ν(CO) to state II with extremely long lifetime indicates the formation of the triplet $^3IL\pi\pi^*$.

2. The fingerprint regions show that for state III, there is a band at *ca.* 1560-1583 cm^{-1}, which according to previous work is tentatively assigned as the oxidized TPA. This may suggest that state III is a charge-transfer state, and thus is assigned as an ILCT state.

While Gordon and co-workers have contrasting views. They have proposed that state I and state II are singlet ^{1}ILCT and triplet ^{3}ILCT states respectively, while state III is the $\pi\pi^*$ excited state.[26] Their reasons are as following:

1. Electronic absorption and emission spectroscopy for a series of Re-dppz complexes [$Re(CO)_3$(dppz-NPh_2)Cl], [$Re(CO)_3$(dppz-TPA)Cl] (TPA: triphenylamine), [$Re(CO)_3$(dppz-$(TPA)_2$)Cl], [$Re(CO)_3$(dppz-$(OMe)_2$TPA)Cl] as well as the discrete ligands [dppz-L ligands (L: NPh_2, TPA, $(TPA)_2$, $(OMe)_2$TPA)] have been conducted. The results are summarized in Table 4.1.

Table 4.1 *Electronic absorption and emission spectroscopy results and TD-DFT results of a series of Re-dppz complexes. Reproduced from Ref. 26.*

	experimental			TDDFT	
	λ_{abs}/ nm	λ_{em}/ nm	$\Delta\mu$/ D	λ_{DFT}/ nm	MO
dppz-NPh_2	476	620	10±2	401	H→L (90%)
dppz-TPA	451	653	20±3	384	H→L (70%)
dppz-(OMe_2)-TPA	430	652	19±5	360	H→L (66%), H-2→L(22%)
dppz-$(TPA)_2$	457	666	22±4	366	H→L (64%), H-3→L (17%)
[$Re(CO)_3$(dppz-NPh_2)Cl]	499	670	12±2	412	H→L (87%)
[$Re(CO)_3$(dppz-TPA)Cl]	488	740	26±4	390	H→L (75%), H-3→L (13%)
[$Re(CO)_3$(dppz-(OMe_2)TPA)Cl]	470	701	22±8	386	H→L (70%), H-4→L (15%)
[$Re(CO)_3$(dppz-$(TPA)_2$)Cl]	491	685	25±4	398	H→L (76%), H-4→L (10%)

The Stokes shift ($\tilde{\nu}_{St}$) is the wavenumber difference between λ_{abs} and λ_{em}. The dipole difference $\Delta\mu$ between the ground state (μ_g) and the emitting excited state (μ_e) can be estimated using the following equation, known as the Lippert-Mataga equation.

$$\tilde{\nu}_{St} = \frac{2(\mu_e - \mu_g)^2}{4\pi\varepsilon_0}\frac{\Delta f}{hca^3} + c \qquad (1)$$

Δf: solvent polarity parameter; a (m): Onsager radius of the fluorophores of interest; fundamental constants: h (Js); ε_0 (C^2/Jm); c (cm/s).

The results of $\Delta\mu$ are summarized in Table 4.1. As shown in Table 4.1, significant Stokes shifts have been observed for all complexes and ligands, which is indicative of large changes in the dipole ($\Delta\mu$) due to the electronic transitions. This is most indicative of a charge-transfer (CT) state. It is noted that the $\Delta\mu$ for the complexes and the corresponding ligands are similar, indicating that the complexation of the dppz-L ligands to the [$Re(CO)_3Cl$] moiety has little effect on the CT state, which may indicate that the electronic transition is based on the dppz-L ligand.

Also, it needs to be noted that the dppz-NPh_2 ligand, as well as the [$Re(CO)_3$(dppz-NPh_2)Cl] complex, when compared to other ligands and the corresponding complexes, have much smaller values of $\Delta\mu$. This is attributed to the lack of a complete TPA electron donor. Also as the estimated Onsager radius is smaller. However, as TDDFT calculations suggest, for all complexes, the lowest-lying excited states are the ligand-based donor-acceptor transitions, as shown in Figure 4.4.

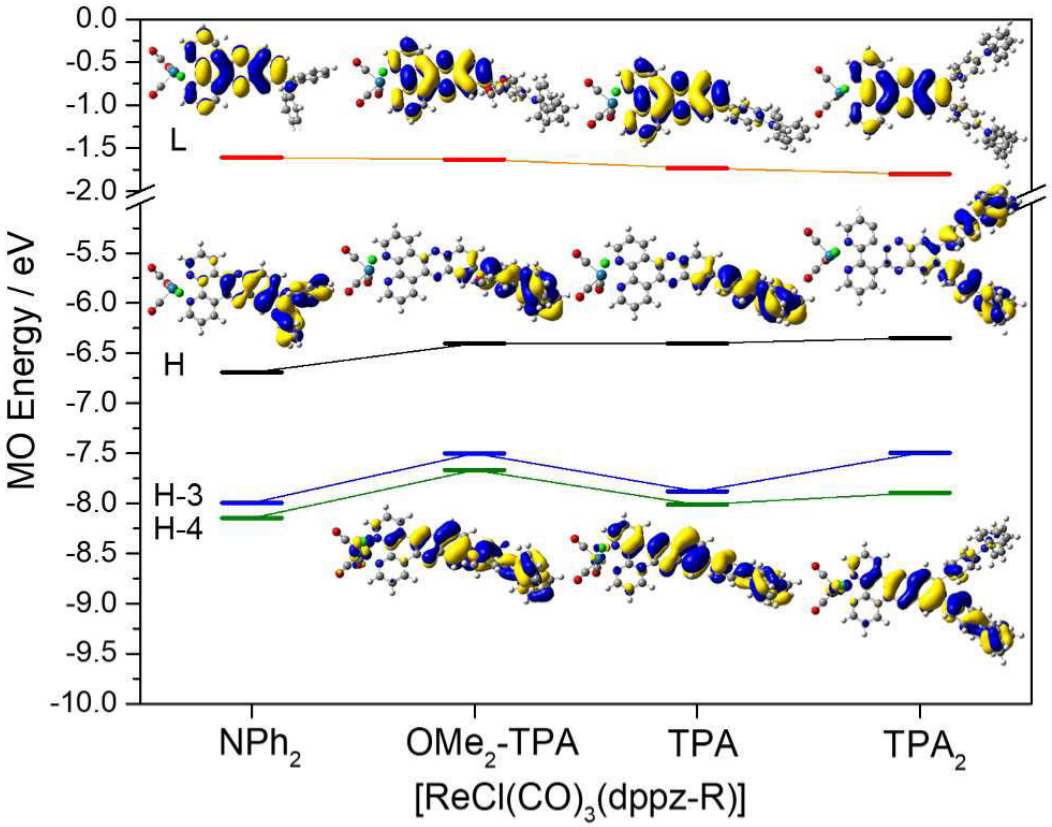


Figure 4.4 *TDDFT calculated frontier molecular orbitals of the complexes of interest (CAM-B3LYP, 6-31g(d), in CH_2Cl_2).*[26]

Nevertheless, the TDDFT calculations also indicate that the lowest energy transition is not completely HOMO→LUMO. As shown in Table 4.1, from dppz-NPh_2 to dppz-$(TPA)_2$, as well as the corresponding complexes, the contribution of HOMO-2, H-3 and H-4 increases with the increasing energy of transitions. The small contribution of H-3 and H-4 indicates the minor involvement of the [$Re(CO)_3Cl$] moiety in the transitions.

2. Resonance Raman (RR) spectroscopy of the complexes has been conducted to investigate the electronic structure of the Frank-Condon state. The RR spectra were measured with various excitation wavelengths across the lowest energy absorption band. The RR spectra of [$Re(CO)_3$(dppz-TPA)Cl] show no apparent changes under different irradiation wavelengths, which is predominated by the TPA and dppz(phz) modes. This indicates that the Frank-Condon state is dominated by the ILCT from TPA to dppz. For [$Re(CO)_3$(dppz-$(OMe)_2$TPA)Cl] and [$Re(CO)_3$(dppz-$(TPA)_2$)Cl], RR spectra show that ILCT is still the dominant and lowest state, and both MLCT and

$\pi\pi^*$ are shown at higher energy levels. For $[Re(CO)_3(phen\text{-}NPh_2)Cl]$, the NPh_2 bands at *ca.* 1608 and 1601 cm^{-1} are observed to be weaker than TPA, reflecting the weaker electron donation ability compared to TPA. The RR data for all complexes suggest a long-lived ILCT state, which is found to be sensitive to oxygen, thus is proposed to be triplet in nature.

3. Transient absorption spectroscopy shows that the spectra of the $[Re(CO)_3(dppz\text{-}L)Cl]$ (L: NPh_2, TPA, TPA_2 $(OMe)_2TPA$) complexes are significantly different to that of $[Re(CO)_3(dppz)Cl]$, which has no electron-donating substituent on the dppz ligand. This further supports the existence of a long lived ^{3}ILCT state.

4. For the same TRIR data, Gordon and co-workers have different interpretations. The most stable excited state with a lifetime of microseconds is assigned to the ^{3}ILCT state. The excited state with a lifetime of tens of picoseconds is assigned to the singlet ^{1}ILCT state, as comparison with previous research.[27] Blanco *et al.* investigated the photophysics of a series of $[Re(CO)_3(3\text{-}R\text{-}1\text{-}(2\text{-}pyridyl)\text{-}imidazo[1,5\text{-}\alpha]pyridine)Cl]$ (R: CH_3, Ph, PhBu, $PhNMe_2$, $PhNO_2$, $PhCF_3$) complexes.[27] A slow singlet $^1IL\ \pi\pi^*_{impy}$ (impy: 1-(2-pyridyl)-imidazo[1,5-α]pyridine) to triplet $^3IL\ \pi\pi^*_{impy}$ spin crossover was observed for all complexes, which was supported by both TRIR and DFT calculations. The spin crossover rate was found to be several tens of ps, which is 200~300 times slower than the ^{1}MLCT to ^{3}MLCT intercrossing rate for analogue complexes with MLCT as the lowest excited states. This phenomenon is ascribed to the spin-orbit interactions.[27] Meanwhile, the excited state with a lifetime of several nanoseconds is assigned to the $\pi\pi^*$ excited state.

Similar investigations have been carried out by Larsen *et al.* on the photophysics of the donor-acceptor (D-A) ligands, dppz-$PhNPh_2$ and dppz-$PhNMe_2$, where dppz is substituted with strong electron-donors $PhNPh_2$ and $PhNMe_2$, together with their Re complexes $[Re(CO)_3(D\text{-}A)L]$ (L: Cl^-, py, dmap).[24] The TRIR of the dmap-complexes has also shown the existence of three excited states, denoted as I, II, III. The TRIR results of the three excited states of $[Re(CO)_3(dppz\text{-}PhNPh_2)(dmap)]^+$ in CH_2Cl_2 is summarized in Table 4.2.

Table 4.2 *TRIR results of $[Re(CO)_3(dppz\text{-}PhNPh_2)dmap]^+$ in CH_2Cl_2 by Larsen et al., reproduced from Ref. 24.*

Carbonyl region frequencies	Fingerprint region frequencies	Lifetime /ns	State
2034, 1930	1634, 1606, 1591, 1558, 1361, 1335, 1317	-	GS
2015, 1875	-	0.020	I
2029, 1906	1600, 1547, 1337, 1307	2800	II
2026, 1898	1594, 1571, 1331, 1319	0.300	III

Similar to the TRIR results of Adams *et al.*,[26] upon UV photolysis, three excited states with different lifetimes have been observed. Also, state I is observed to convert to the relatively stable state II with a lifetime of several μs. Meanwhile, the ν(CO) positions of state II and III are very similar. These states are proposed to be associated with an IL nature. States II and III are assigned to the ILCT states, while the assignment of state I cannot be unambiguously made. The reaction process is similar to what Gordon and co-workers reported.[26]

In this work, we wish to try to resolve the issues of the interpretation of the photophysics and conduct TRIR on $[Re(CO)_3(dppz\text{-}NPh_2)Cl]$ in solvents with different polarities, to understand how solvent can affect the photophysics of the complex, and also in a wish to better understand the reaction mechanism.

4.1.2 Photophysics of Re-phen Complexes

Different to metal-dppz complexes, the metal-phen complexes only have the phen ligand as the electron-acceptor. Previous studies on the photophysics of the $[Re(CO)_3(phen)L]$ complexes have suggested that, for the Re-phen complexes with no substituents on the phen ligand, the Re-to-phen MLCT is the predominant excited state,[17,19] which has been found to have potential applications in many fields, such as cell imaging[28] and protein probe.[29] The Re-phen carbonyl complexes have been the focus of research for decades.[30] The primary work on $[Re(CO)_3(phen)L]$ was conducted by Wrighton and Morse.[31] They investigated the photophysics of a series of $[Re(CO)_3XCl]$ (X: 5-L-1,10-phenanthroline(L: CH_3, H, Cl, Br, NO_2), 4,7-diphenyl-1,10-phenanthroline, 1,10-phenanthroline-5,6-dione) complexes. It was found that the absorption and emission spectra of the $[Re(CO)_3XCl]$ complexes are sensitive to the substituents and solvent polarities. All Re-phen complexes exhibit similar absorptions, while when the phen ligand is substituted by more electron withdrawing groups, the absorption is observed to shift to a lower energy. All evidence points to the $MLCT_{Re\rightarrow X}$ states. Fredericks investigated the photophysics of a series of Re-phen complexes $[Re(CO)_3(phen)L]^+$ (L: CH_3CN, PhCN, pyridine, piperidine) with different axial ligands, using electronic absorption and emission spectroscopy, as well as IR spectroscopy.[32] It was observed that the emissions of all complexes at room temperature are $MLCT_{Re\rightarrow phen}$ in nature, while it is found that the energy of the MLCT state increases when the electron density on the Re decreases, in the order CH_3CN~PhCN > pyridine > piperidine. It is also found that at 77 K, the emission is a mixture of IL $\pi\pi^*$ and MLCT emissions, while the IL $\pi\pi^*$ emission becomes more important when the energy of the MLCT state is higher. This phenomenon has also been observed by Wallace *et al*.[33,34] The investigations of the $[Re(CO)_3(py)(L)]^+$ complexes (L: phen, 2,9-Me_2phen, 4,7-Ph_2phen, 2,9-Me_2-4,7-Ph_2phen, 3,4,7,8-Me_4-phen, 4,7-Me_2phen, 5,6-Me_2phen, 5-Phphen) show that, the multiple-emissions in low temperature glass may be attributed to the fact that in frozen glass, the energy gap between ^{3}IL and ^{3}MLCT is decreased. This is because the MLCT states are more sensitive to the solvent environmental changes, and in solution the MLCT is stabilized by the solvent dipole changes. However, IL states are relatively insensitive as these

transitions involve less electron-density redistribution compared to the MLCT state, and thus are less sensitive to the solvent dipole changes. Therefore, the energy of the MLCT state in frozen glass increases while the IL state is much less influenced. It was also discovered by electrochemical investigations that the energy level of the MLCT is influenced by the substituents on the phen ligands. The energy is observed to increase when phen is substituted with electron donating groups such as methyl, while it is observed to decrease when substituted with phenyl. Meanwhile, it is found that substituents on the N-containing rings is more influential than the 5,6-posisions. The substituent positions of the phen ligand is shown in Figure 4.5.

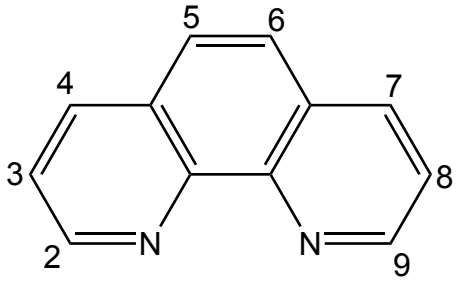


Figure 4.5 *The substituent positions of the phen ligand.*

It is also found that the emission lifetime of these Re-phen complexes is highly dependent on the temperature. It is found the emission lifetime decreases with increasing temperature in fluid phase from 150-315 K, except for $[Re(CO)_3(3,4,7,8\text{-}Me_4\text{-phen})(py)]^+$, of which the emission lifetime first increases with increasing temperature, then reaches a maximum at *ca.* 230 K, and then decreases with further temperature increasing. This is explained by the author in the following way. The energy levels of $[Re(CO)_3(3,4,7,8\text{-}Me_4\text{-phen})(py)]^+$ are different from the other Re-phen complexes, as shown in Figure 4.6.

The multiple-emission of most Re-phen complexes studied in low-temperature glasses indicates that, in frozen glasses, the ^{3}MLCT state may be very close-lying to the ^{3}IL state. The decreased lifetime with increasing temperature in fluid solution may reflect the thermal population of a higher-lying state that has a shorter lifetime than the ^{3}MLCT state in fluid solution, which is not the ^{3}IL state that has a longer lifetime than the ^{3}MLCT state, and the ^{3}IL state in the fluid solution is proposed to

lie at even higher energy level than the unknown upper state as shown in Figure 4.6, except for $[Re(CO)_3(3,4,7,8\text{-}Me_4\text{-}phen)(py)]^+$, with the most electron rich substituents on the phen ligand among all complexes. The lifetime of which, is prolonged with the population of the ^{3}IL state, and then decays with further thermal population of the higher unknown upper state.

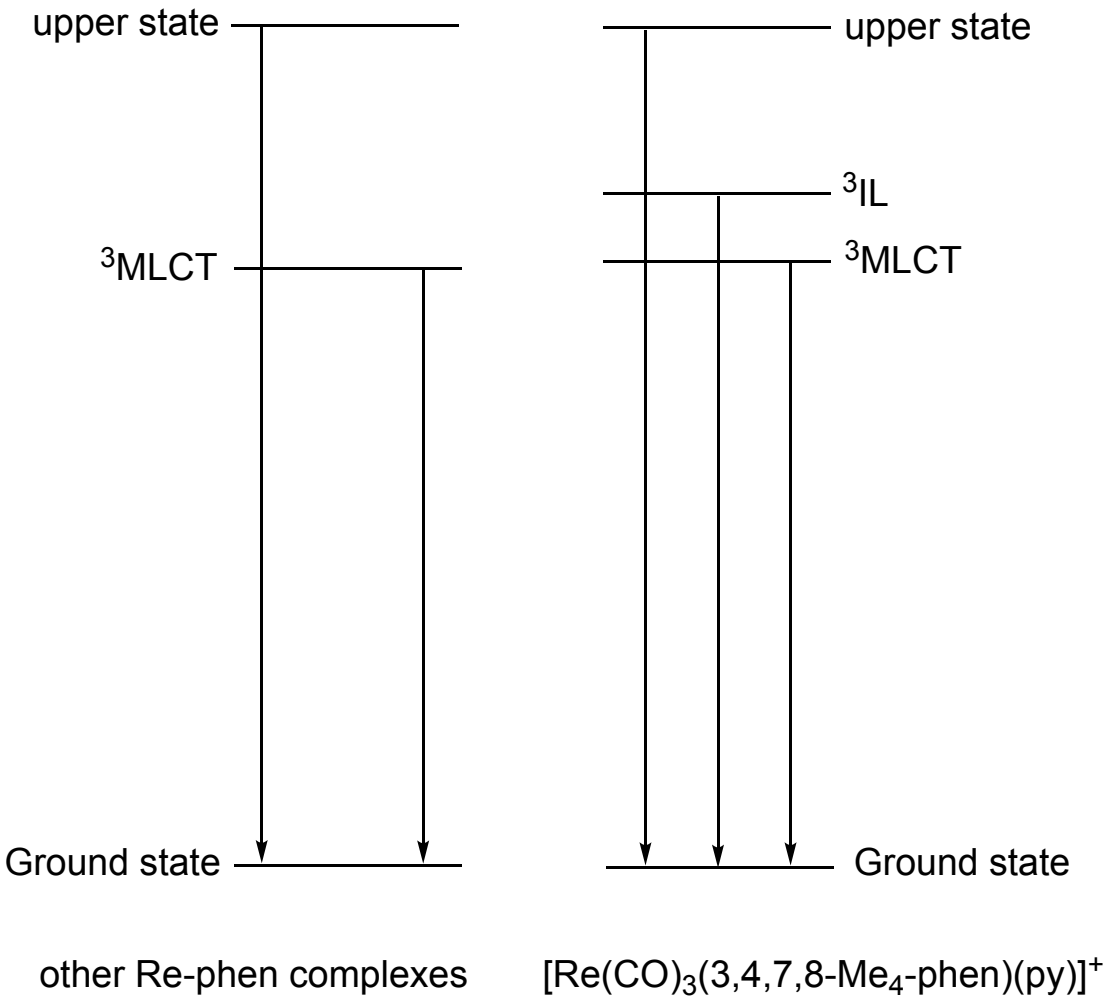


Figure 4.6 *Energy scheme of the $[Re(CO)_3(L)(py)]^+$ (L: phen, 2,9-Me_2phen, 4,7-Ph_2phen, 2,9-Me_2-4,7-Ph_2phen, 3,4,7,8-Me_4-phen, 4,7-Me_2phen, 5,6-Me_2phen, 5-Phphen) complexes in fluid solutions.*

The photophysics of the $[Re(CO)_3(3,4,7,8\text{-}Me_4\text{-}phen)(L)]^+$ complexes has been further investigated,[35,36,37,38] and is found to have potential application in photo-induced molecular machines due to the relatively high energy level of the MLCT states.[37,38] Murakami and co-workers investigated the photo-induced *trans*↔*cis* isomerization of $[Re(CO)_3(3,4,7,8\text{-}Me_4phen)(\textit{trans}\text{-}L)]^+$ [L=stpy (4-styrylpyridine);

bpe (1,2-bis(4-pyridyl)ethylene)]. It was found that under the irradiation of a series of wavelengths 313, 334, 365, 404 nm, the *trans*-[$Re(CO)_3$(3,4,7,8-Me_4phen)(*trans*-L)]$^+$ (L=stpy; bpe) successfully underwent the *trans*→*cis* isomerization. The initiation of the isomerization upon complexed with the [$Re(CO)_3$(3,4,7,8-Me_4phen)]$^+$ fragment is evidenced by the fact that the *trans*→*cis* isomerization of the complex can be initiated by 404 nm, which cannot be absorbed by the free L ligand (L=stpy; bpe). The isomerization process is basically based on three triplet excited states: $^3MLCT_{Re\rightarrow Me_4phen}$, ^3IL_L, and $^3IL_{Me_4phen}$. The *trans*→*cis* isomerization is directly associated with $^3IL_{trans\text{-}L}$. For the *trans*-complexes, the lowest excited state is $^3IL_{trans\text{-}L}$, therefore *trans*→*cis* isomerization can be induced by photolysis. The reverse *cis*→*trans* isomerization has also been observed upon 254 nm irradiation. After the *trans*→*cis* isomerization, the lowest lying excited state turns to $^3MLCT_{Re\rightarrow Me_4phen}$ for the *cis*-complexes, while the reverse *cis*→*trans* isomerization observed for the *cis*-complexes is attributed to the close-lying of states $^3IL_{cis\text{-}L}$ with $^3MLCT_{Re\rightarrow Me_4phen}$. The *trans*-complexes are non-emissive while the *cis*-isomers are emissive, thus this photo-induced reversible *trans*↔*cis* isomerization can be applied in photo-induced molecular devices.

The photophysics of the Re-phen complexes with strong electron donating substituents on the phen ligand has been extensively investigated.[39,40] As previously discussed in Section 4.1.1, the lowest-lying state of the Re-diimine complexes can be changed to a IL state with the addition of a strong electron donating group on the diimine ligand. Pomestchenko *et al.*[39] investigated the photophysics of the [$Re(CO)_3$(phenC≡C$AuPPh_3$)Cl] complex, where -C≡C$AuPPh_3$ is a strong electron donating ligand. It is found that the excited state of [$Re(CO)_3$(phenC≡C$AuPPh_3$)Cl] is a mixture of the ^{3}MLCT and ^{3}IL states, and ^{3}MLCT and ^{3}IL are in equilibrium. Qin *et al.* investigated a series of [$Re(CO)_3$(L)Cl] complexes where L is the phen ligand with different strong electron donating substituents (L_1: 4',5'-dimethyldithiotetrathia-fulvenyl[4,5-f]phen; L_2: 4',5'-ethylenedithio-tetrathia-fulvenyl[4,5-f]phen; L_3: 4',5'-bis(methyloxycarbonyl)-dithiotetrathiafulvenyl[4,5-f]phen).[40] For these Re-phen complexes with strong electron donating groups on the phen ligand, intense ^{3}IL $\pi\pi^*$ excited state has been observed while no typical ^{3}MLCT has been found.

In this work, we wish to investigate the electron donor-acceptor system on a phen ligand. TRIR investigations on a series of $[Re(CO)_3(Phen\text{-}TPA)X]^{n=0,1}$ complexes (TPA: triphenylamine; X: Cl^-, Br^-, n=0; py, dmap, n=1) in CH_2Cl_2 have been conducted. The structure of the $[Re(CO)_3(Phen\text{-}TPA)X]^{n=0,1}$ complexes is shown in Figure 4.7.

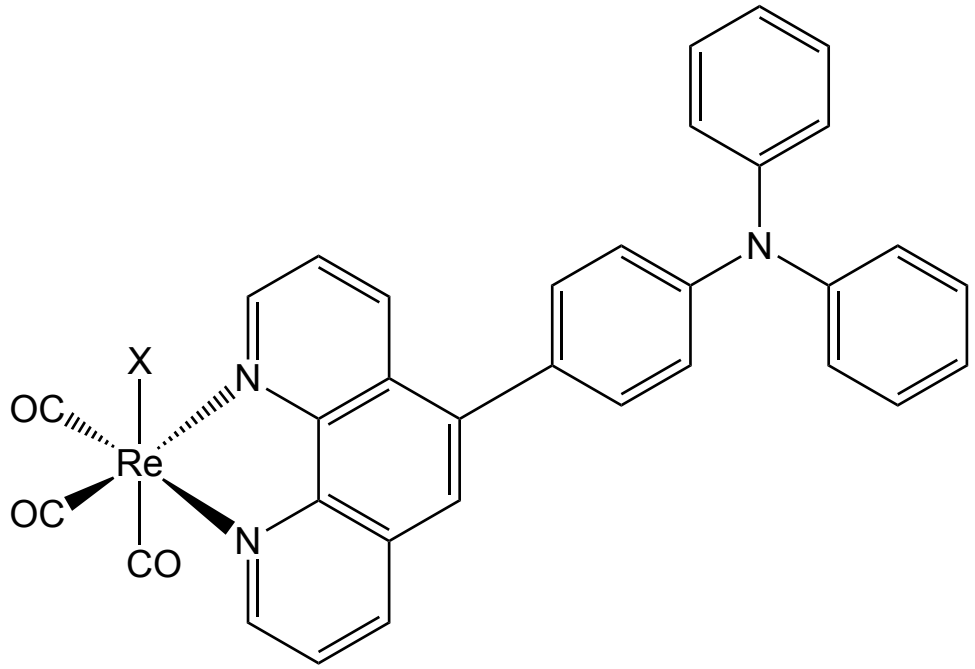


Figure 4.7 *Strucure of the $[Re(CO)_3(Phen\text{-}TPA)X]^{n=0,1}$ complexes (TPA: triphenylamine; X: Cl^-, Br^-, n=0; py, dmap, n=1).*

The phen ligand is a well-recognized electron-accepting ligand, while TPA is a strong electron-donating ligand, thus it is expected that upon UV irradiation, strong ILCT (Intraligand-Charge-Transfer) from TPA to phen will occur. Here we are especially interested in how the change of the axial ligand (Cl^-, Br^-, py, damp) would influence the photophysics of the $[Re(CO)_3(Phen\text{-}TPA)X]^{n=0,1}$ (TPA: triphenylamine; X: Cl^-, Br^-, n=0; py, dmap, n=1) complexes. CH_2Cl_2 has been used as the solvent. As discussed before, for $[Re(CO)_3(3,4,7,8\text{-}Me_4phen)(\textit{trans}\text{-}L)]^+$ (L=stpy; bpe), where the ancillary ligand is a large conjugated ligand stpy and bpe, the $^3IL_{\textit{trans}\text{-}L}$ is found to lie at lower energy level than the $^3MLCT_{Re\rightarrow Me_4phen}$ state. However, the ancillary ligands we used here (py, dmap, Cl^-, Br^-) are less conjugated, while the effects on the electron density of the Re centre which may have an influence on the phtophysics is more interesting for investigation. The electron density of the Re centre is expected to increase with the ancillary ligands of anions Cl^- and Br^-

compared to the py and dmap ligands, which may affect the relative energy levels of different states. For the $[Re(CO)_3(3,4,7,8\text{-}Me_4phen)(\textit{trans}\text{-}L)]^+$ (L=stpy; bpe) complexes, the absorption λ_{max} of MLCT is observed to blue-shift compared to the neutral chloro-complex $[Re(CO)_3(3,4,7,8\text{-}Me_4phen)Cl]$, which reflects that the energy of the MLCT state may be reduced when the Re-phen fragment is complexed with the electron rich anion Cl^-. Here in this work, TRIR investigations in both the carbonyl and fingerprint regions have been conducted for detailed studies, in cooperation with our collaborators from the University of Otago and the Friedrich Schiller University Jena, who performed the transient absorption spectroscopy, Raman spectroscopy and DFT calculations as part of the work described in the end of the Chapter.[41]

4.2 Result and Discussion

4.2.1 TRIR Investigations of $[Re(CO)_3(dppz\text{-}NPh_2)Cl]$ in Toluene

Three excited states have been observed as expected, according to TRIR of $[Re(CO)_3(dppz\text{-}NPh_2)Cl]$ in toluene, as shown in Figure 4.8.

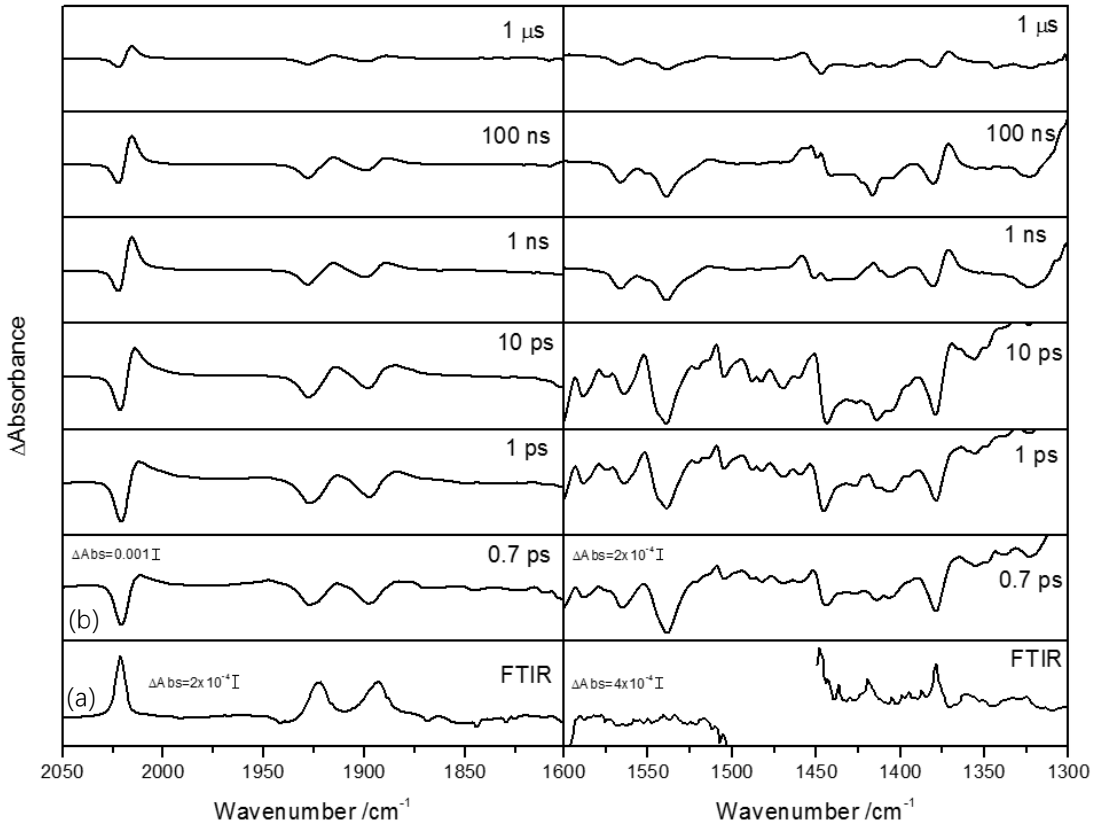


Figure 4.8 *(a) FTIR spectrum and (b) TRIR spectra obtained following photolysis (355 nm) of $[Re(CO)_3(dppz\text{-}NPh_2)Cl]$ in toluene for both carbonyl (left) and fingerprint (right) IR regions.*

Upon UV photolysis, in the carbonyl region, it can be observed that along with the parent bleaches (2021, 1923 and 1895 cm^{-1}), three bands at *ca.* 2013, 1914 and 1885 cm^{-1} are formed, and are also observed to blue-shift to *ca.* 2016, 1916 and 1890 cm^{-1} at later timedelays. Along with the formation of the three early bands at *ca.* 2013, 1914 and 1885 cm^{-1}, the bands at *ca.* 2035, 2006 and 1947 cm^{-1} are also observed to form initially after irradiation, more clearly shown in Figure 4.9. The bands at 2035 and 1947 cm^{-1} are assigned to the MLCT state due to the large $\Delta\nu$(CO) compared to the parent bleach to higher wavenumbers.

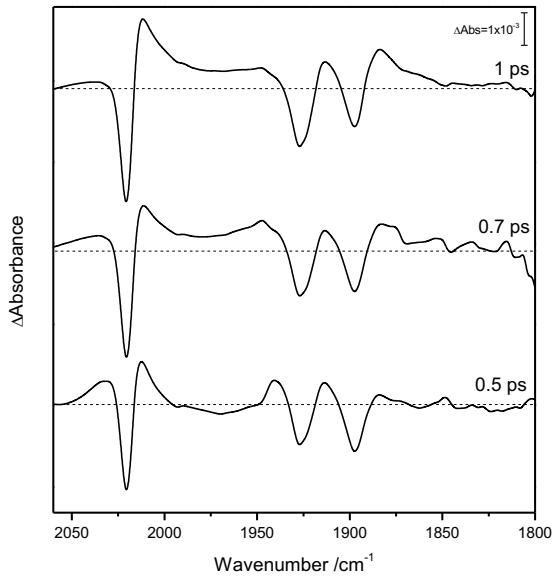


Figure 4.9 *Early ps-TRIR spectra obtained following photolysis (355 nm) of $Re(CO)_3(dppz\text{-}NPh_2)Cl$ in toluene.*

Similar to Adams' work, a shoulder band at *ca.* 2006 cm^{-1} is also observed to decay within 30 ps (21 ±0.7 ps), which is similar to the formation rates of the bands at 2016 (1.9 ±0.4 ps, 23 ±3 ps) and 1890 cm^{-1} (0.3 ±0.05 ps, 16 ±2 ps), and this may indicate a conversion between these two species, as shown in Figure 4.10.

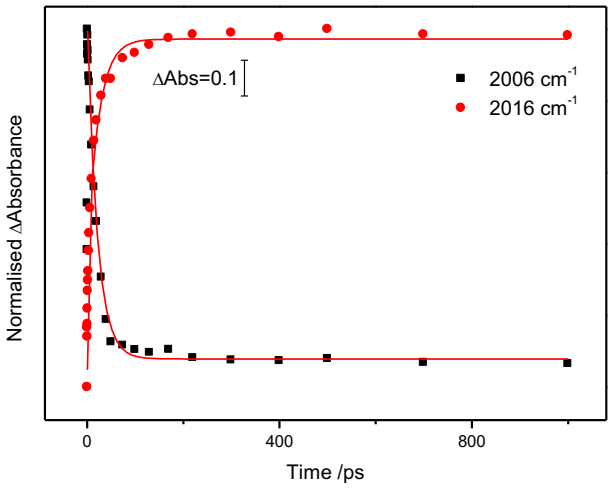


Figure 4.10 *TRIR kinetic traces obtained at 2016 and 2006 cm^{-1} corresponding to State II and State I.*

On the ns-timescale, kinetic analysis shows that the decay rate of the bands at 2016, 1916 and 1890 cm^{-1} (300 ±30 ns, 2.3 ±0.3 μs) is consistent with the recovery rate of the parent bands (300 ±40 ns, 2.4 ±0.4 μs), as shown in Figure 4.11.

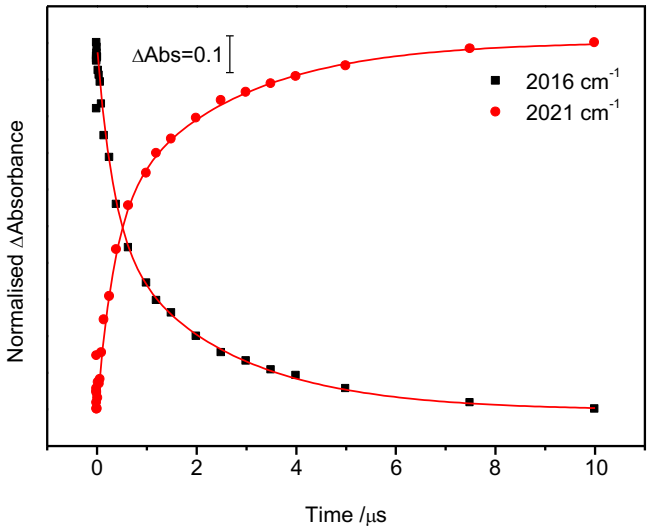


Figure 4.11 *TRIR kinetic traces obtained at 2021 and 2016 cm^{-1} corresponding to the parent band and State II.*

Therefore, the band at 2006 cm^{-1} is assigned to state I, while the bands at 2016, 1916 and 1890 cm^{-1} are assigned to state II, and the band at 2013 cm^{-1} is assigned to state III, which is found to decay in *ca.* 300 ns to the ground state (Table 4.3). In the fingerprint region as shown in Figure 4.8, three bands at *ca.* 1508, 1420 and 1369 cm^{-1} show similar growth and decay rates as the bands at 2016 and 1890 cm^{-1}, thus are assigned as the state II. The overall results are summarized in Table 4.3.

Table 4.3 *Summary of the TRIR results of [Re(CO)$_3$(dppz-NPh$_2$)Cl] in toluene.*

ν(CO) /cm^{-1}	ν(fingerprint) /cm^{-1}	growth	decay	assignment
2021, 1928, 1897	-	400±70 ns, 2.7±0.5 μs	-	parent
2021, 1923, 1894	-	-	-	GS FTIR
2035, 1947	-	-	-	MLCT
2006, 1885	-	-	25±2 ps	State I
2016, 1916, 1890	1508, 1478, 1420, 1369	1.1±0.2 ps, 20±2 ps	2.0±0.5 μs	State II
2013, 1914, 1885	-	-	25±4 ps, 300±80 ns	State III

Therefore, the mechanism of [Re(CO)$_3$(dppz-NPh$_2$)Cl] in toluene can be shown in Figure 4.12.

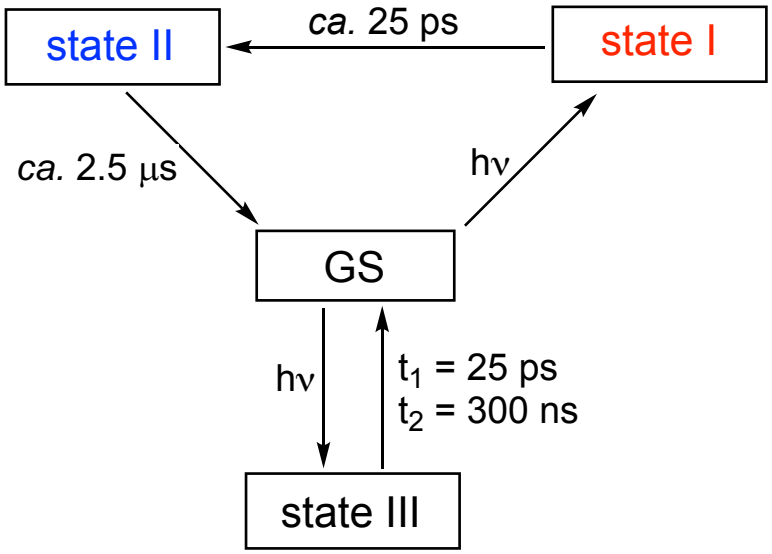


Figure 4.12 *The proposed reaction scheme of [Re(CO)$_3$(dppz-NPh$_2$)Cl] in toluene.*

4.2.2 Photophysics of $[Re(CO)_3(dppz\text{-}NPh_2)Cl]$ in Acetone

The TRIR spectra of $[Re(CO)_3(dppz\text{-}NPh_2)Cl]$ in acetone is shown in Figure 4.13.

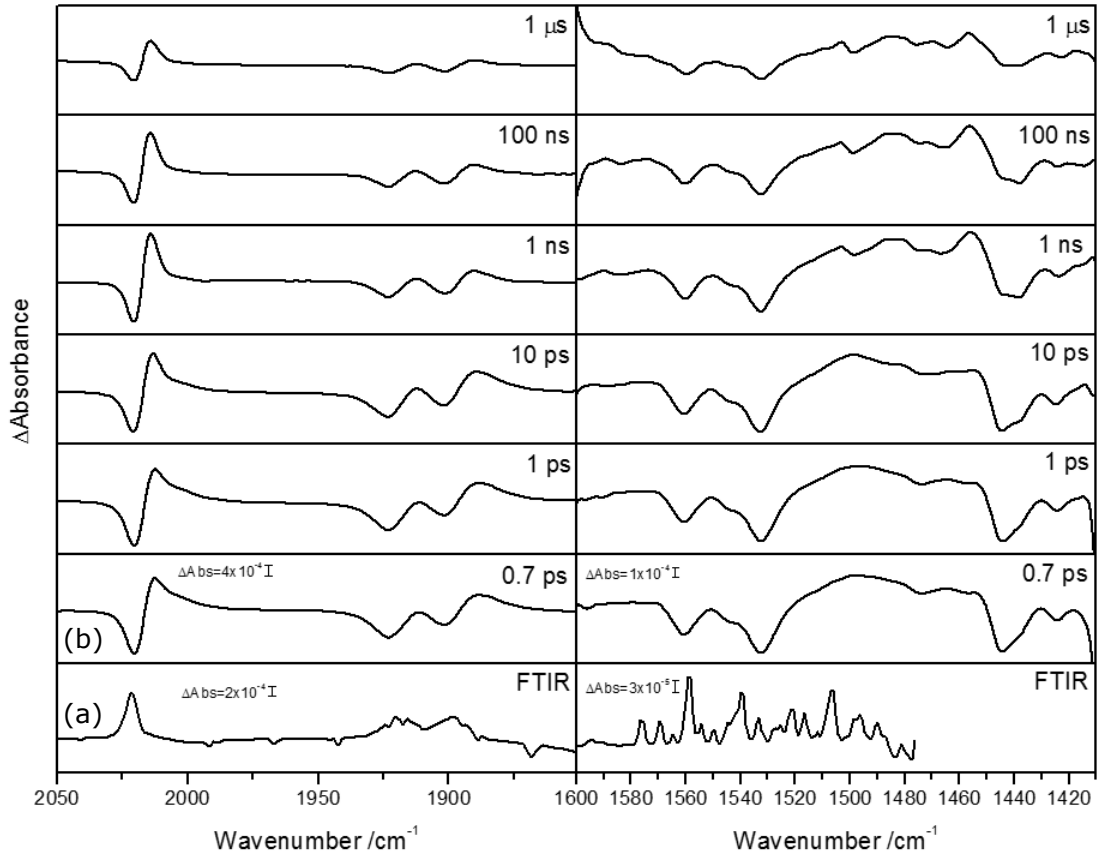


Figure 4.13 *(a) FTIR spectrum and (b) TRIR spectra obtained following photolysis (355 nm) of $[Re(CO)_3(dppz\text{-}NPh_2)Cl]$ in acetone for both carbonyl (left) and fingerprint (right) IR regions.*

Upon UV photolysis, similar to that in toluene, parent bands were bleached (2021, 1923, 1902 cm^{-1}) and three bands at slightly lower wavenumber at *ca.* 2013, 1912 and 1887 cm^{-1} were formed. The formation of the shoulder band at *ca.* 2006 cm^{-1} is also observed. However, unlike that observed in toluene, the MLCT state was not observed in acetone. The more detailed early time ps-TRIR is shown in Figure 4.14. Compared to Figure 4.9, it can be clearly seen that no MLCT state was observed. This may be due to the hydrogen-bonding interactions between acetone and the dppz-ligand which may cause the quench of the MLCT state in acetone.

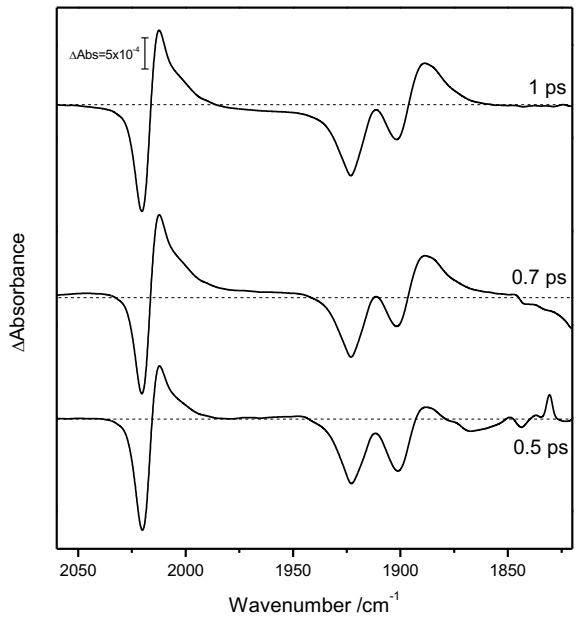


Figure 4.14 *Early ps-TRIR spectra of [Re(CO)$_3$(dppz-NPh$_2$)Cl] in acetone, irradiated by 355 nm.*

Similar to that in toluene, a band at 2013 cm^{-1} is observed to have slightly blue-shifted to *ca.* 2016 cm^{-1}. The decay of the band at 2013 cm^{-1} (166 ±19 ps) is consistent with the parent bands recovery (9 ±3 ps, 172 ±36 ps) on the ps-timescale, as shown in Figure 4.15.

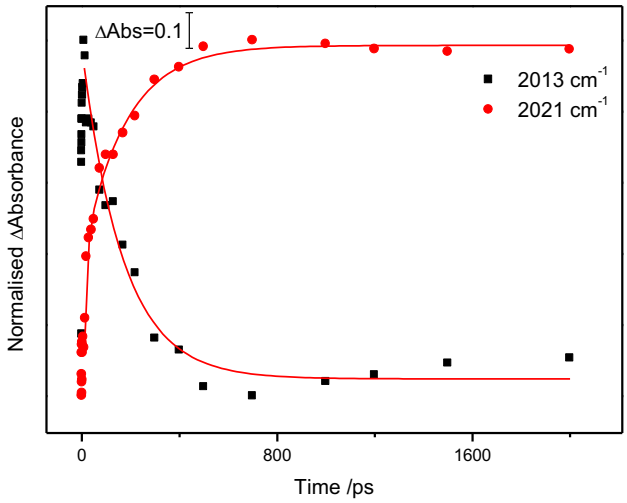


Figure 4.15 *TRIR kinetic traces obtained at 2021 and 2013 cm^{-1} corresponding to the parent band and state III.*

Similar to that in toluene, the band at 2016 cm^{-1} is assigned to state II, the band at 2006 cm^{-1} is assigned to state I, while the band at 2013 cm^{-1} is assigned to state III. Bands sharing similar kinetics with state II and the ground state are also observed in the fingerprint region, which are summarized in Table 4.4.

Table 4.4 *TRIR data summary of [Re(CO)$_3$(dppz-NPh$_2$)Cl] in acetone.*

ν(CO) /cm^{-1}	ν(fingerprint region) /cm^{-1}	growth	decay	assignment
2021, 1923, 1902	1564, 1535, 1443, 1427	172±36 ps, 2.3±0.3 μs	-	Parent
2021, 1920, 1898	-	-	-	GS FTIR
2006	-	-	23±1 ps	State I
2016, 1914, 1890	1502, 1479, 1468, 1458	14±2 ps	243±85 ps, 0.3±0.1 μs, 2.5±0.3 μs	State II
2013, 1912, 1887		-	166±19 ps, 600±140 ns	State III

Therefore, the reaction process is similar to that in toluene as well as the work reported by Adams *et al.*,[26] as shown in Figure 4.16.

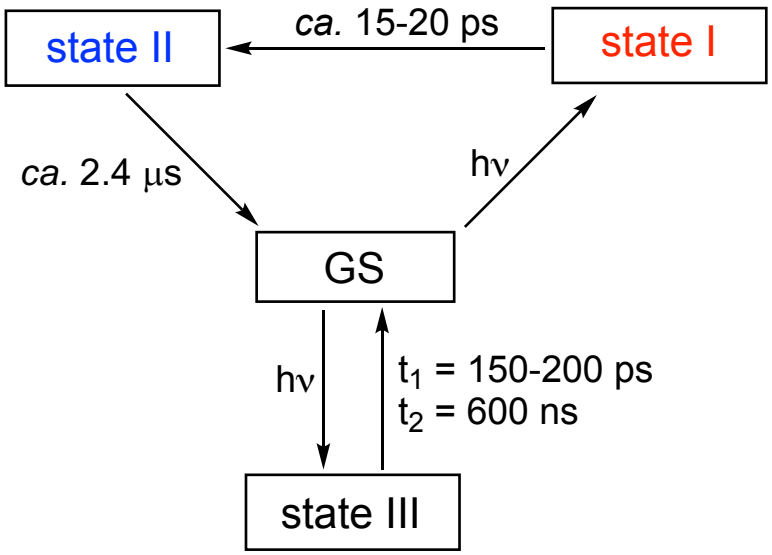


Figure 4.16 *The assumed reaction scheme of [Re(CO)$_3$(dppz-NPh$_2$)Cl] in acetone.*

It can be noted that, changing of solvent polarity has little effect on state I and state II, while the lifetime of state III is prolonged in acetone compared to that in toluene.

Interestingly, the lifetimes of both state II and III are observed to be prolonged (state II: *ca.* 5.3 μs, state III: *ca.* 950 ns) when the concentration of Re(dppz-NPh_2)$(CO)_3Cl$ is halved in acetone, while the lifetime of state I is almost unaffected (*ca.* 25 ps). This could be explained by the fact that the decay of state I is faster than the diffusion rate, thus decreasing the concentration of [$Re(CO)_3$(dppz-NPh_2)Cl] will have little effect on its lifetime. Whereas for state II and III, decreasing the concentration lowers the rate of collision, therefore the lifetimes are prolonged. The quenching of the electronically excited state is normally recognized as a diffusion-controlled reaction. For the diffusion-controlled reactions, the reaction constant can be given by the following equation:

$$\kappa = 16\kappa_B T/\beta\eta \qquad (2)$$

κ_B: Boltzmann constant; T: temperature; β: a numerical constant, in solvent when r_s >> radius of the solvent molecules, β is given 6, while for molecular diffusion, β is given 4; η: viscosity of the solvent. κ is often converted into the more normal units, L/(mol^{-1} s^{-1}) by multiplying $1000N_A$. N_A: Avogadro constant.

The viscosity of acetone is 3.16 $x10^{-4}$ (N s/m^2, Pa s), for toluene is 5.6 $x10^{-4}$ (N s/m^2, Pa s). At room temperature, using equation (2), in acetone the κ is *ca.* 2.1 $x10^9$ L/(mol^{-1} s^{-1}), while in toluene κ is *ca.* 1.2 $x10^9$ L/(mol^{-1} s^{-1}). Therefore, the diffusion rate for [$Re(CO)_3$(dppz-NPh_2)Cl] in both solvents are on the ns-timescale, hence the concentration change will have little effect on state I.

It should be noted that compared to previous work in CH_2Cl_2 (*ca.* 2 ns),[26] the lifetime of state III is extremely prolonged. So far, several observations have been made as following:

1. The lifetime of state I appears to be unaffected by the change of solvent as well as the concentration of [$Re(CO)_3$(dppz-NPh_2)Cl].

2. Lifetimes of states II and III are affected by the concentration of [$Re(CO)_3$(dppz-NPh_2)Cl].

Therefore, if state I is ^{1}IL$\pi\pi$*, state II is ^{3}IL$\pi\pi$*, state III is ILCT, then state I is unaffected by both concentration and solvent polarity changes, while state II is expected to be only affected by the concentration of [$Re(CO)_3$(dppz-NPh_2)Cl], and it should be almost unaffected by the solvent polarity changes, and state III is expected to be significantly affected by the solvent polarity changes. This is actually consistent with the experimental results observed. According to our results, supported by previous work by Adams *et al.*,[26] the lifetime of state I is *ca.* 20-40 ps in three solvents, toluene (ε: 2.38), CH_2Cl_2 (ε: 8.93) and acetone (ε: 20.7), while for state II, the lifetime in the three solvents is *ca.* 2-3 μs, which may also indicates the concentration of [$Re(CO)_3$(dppz-NPh_2)Cl] in three solvents is similar. For the ILCT state III, the more polar solvent is expected to stabilize the charge-separated state. Therefore, in acetone the lifetime (*ca.* 600 ns) is longer than that observed in CH_2Cl_2 (*ca.* 2 ns). However, why in toluene the lifetime of state III (*ca.* 300 ns) is longer-lived than that observed in CH_2Cl_2 is still unclear, this may be the result of the phenyl ring π-stacking that may stabilize the ILCT state in toluene.

If state I is ^{1}ILCT, state II is ^{3}ILCT, state III is IL$\pi\pi$*, then state III is only expected to be affected by the concentration of [$Re(CO)_3$(dppz-NPh_2)Cl], while unaffected by the solvent polarity changes. Both state I and II are expected to be affected by the solvent polarity changes, while state II is also expected to be affected by the concentration of [$Re(CO)_3$(dppz-NPh_2)Cl]. But the behavior of state I may disprove this assumption. However, when looking at state III, the lifetime indicates that the concentration of [$Re(CO)_3$(dppz-NPh_2)Cl] in the three solvents follows: CH_2Cl_2 > toluene > acetone, while the polarity of the three solvents is acetone > CH_2Cl_2 > toluene, therefore the lifetime of state II in acetone should be the longest, which is consistent with the results.

4.2.3 Photophysics of $[Re(CO)_3(Phen\text{-}TPA)L]$ (L: Cl^-, Br^-)

TRIR of a series of $[Re(CO)_3(Phen\text{-}TPA)L]^{n=0,+1}$ [L: Cl^-, Br^- (n=0), py, dmap (4-(dimethylamino)pyridine) (n=+1)] complexes were conducted in CH_2Cl_2, in order to understand how the ancillary ligand L as well as the electron donor substituent TPA on the phen ligand can affect the photophysics of the $[Re(CO)_3(Phen\text{-}TPA)L]$ complexes. The halide (L: Cl^-, Br^-) and non-halide (L: py, dmap) complexes are discussed in two sections. In this section, results of the halide complexes are first displayed, while the detailed discussion is in Section 4.2.4 together with the non-halide complexes.

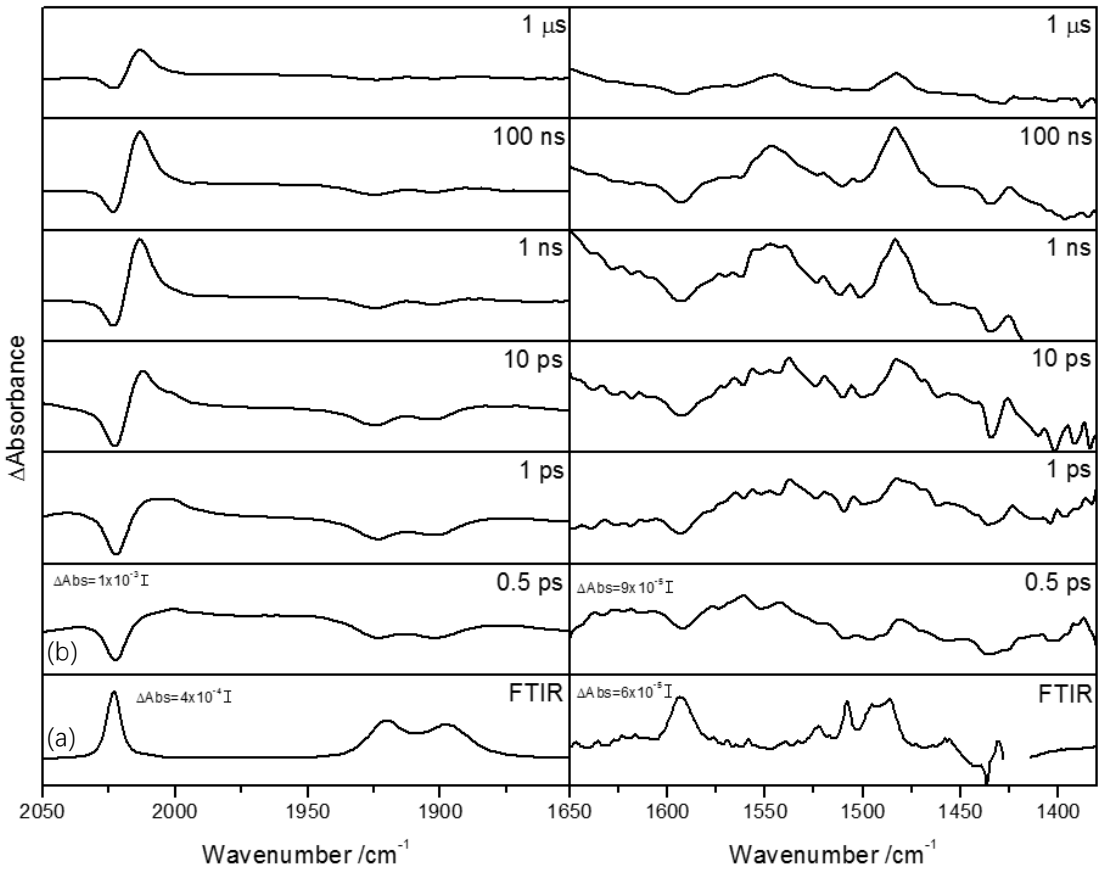


Figure 4.17 *(a) FTIR spectrum and (b) TRIR spectra obtained following photolysis (355 nm) of $[Re(CO)_3(Phen\text{-}TPA)Cl]$ in CH_2Cl_2 for both carbonyl (left) and fingerprint (right) IR regions.*

As shown in Figure 4.17, upon UV photolysis, two broad features centered at *ca.* 2001 and 1876 cm^{-1} are formed along with the parent bleaches (2023, 1921, 1898 cm^{-1}), which then narrow and blue-shift to *ca.* 2014 and 1891 cm^{-1}. Meanwhile, it

can be observed that a band at higher wavenumber than the parent bleach (2023 cm^{-1}) has also formed on early ps-timescale, which is more clearly shown in Figure 4.18.

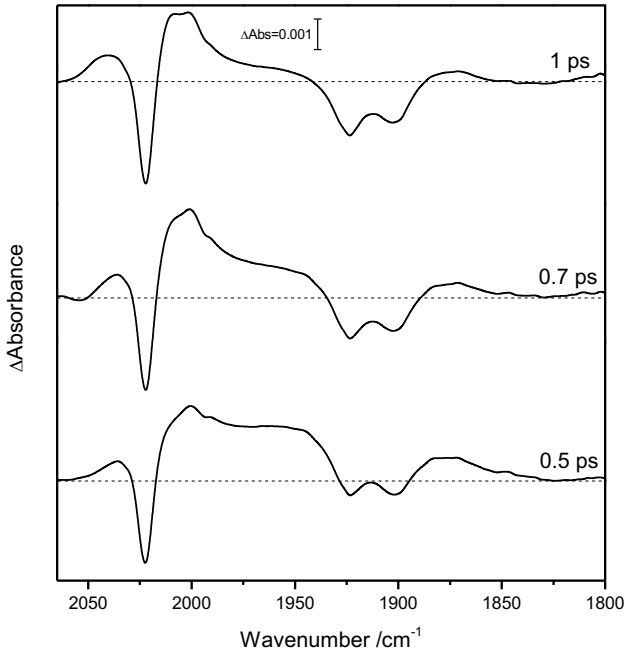


Figure 4.18 *Early ps-TRIR spectra of [Re(CO)$_3$(Phen-TPA)Cl] in CH_2Cl_2, irradiated by 355 nm.*

A band at higher wavenumber than the parent bleach 2023 cm^{-1} at *ca*. 2035 cm^{-1} is observed in timedelay 0.5 ps, which then blue-shifts to *ca.* 2050 cm^{-1} within 10 ps, which may be attributed to the vibrational cooling. Considering the blue-shift compared to the parent bleach, the band at 2050 cm^{-1} is assigned to a MLCT state. The MLCT state is relatively short-lived, with a lifetime of *ca.* 18 ps. Kinetic analysis shows that the decay of the MLCT state (18 ±2 ps) is consistent with the early formation of the band at 2014 cm^{-1} (16 ±1 ps, 279 ± 41 ps), as shown in Figure 4.19.

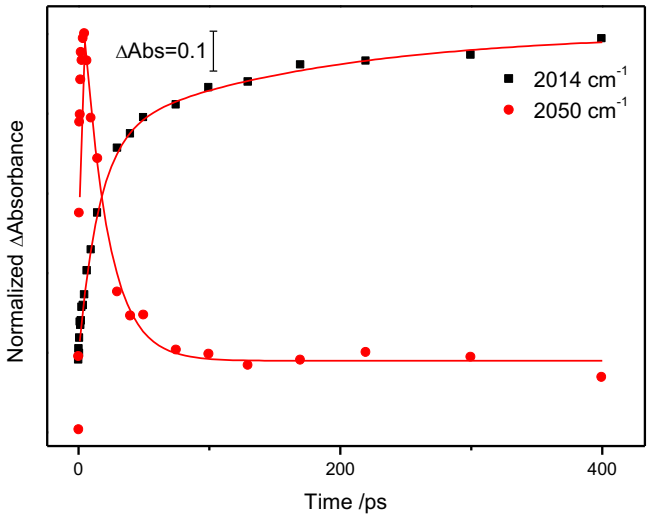


Figure 4.19 *TRIR kinetic traces obtained at 2050 and 2014 cm^{-1} corresponding to the MLCT state and the ILCT 2 state.*

The kinetics indicate that there is also a conversion relationship between the band at 2001 cm^{-1} (4 ±2 ps, 203 ±146 ps) and the band at 2014 cm^{-1} (16 ±1 ps, 279 ±41 ps), as shown in Figure 4.20.

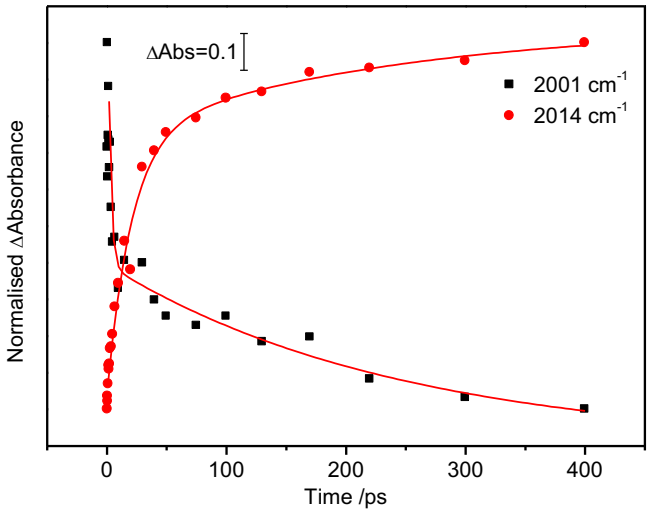


Figure 4.20 *TRIR kinetic traces obtained at 2014 and 2001 cm^{-1} corresponding to the ILCT 2 state and the ILCT 1 state, respectively.*

While at later timedelays, the bands at 2014, 1913 and 1891 cm^{-1} are observed to decay at a similar rate (2.1 ±0.6 μs) with the recovery of the parent bands (1.6

±0.1 μs), as shown in Figure 4.21.

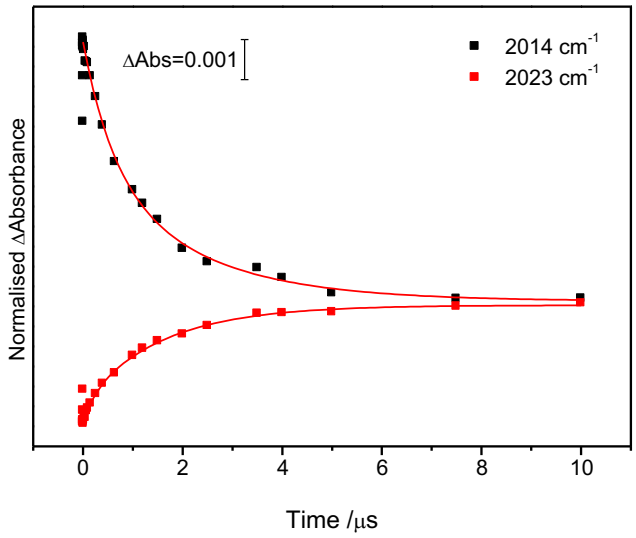


Figure 4.21 *TRIR kinetic traces obtained at 2023 and 2014 cm^{-1} corresponding to the parent band and the ILCT 2 state.*

Considering the relatively small red-shift of Δν(CO) compared to the parent bleaches, as well as the TPA-phen electron donor-acceptor structure, the bands at 2001, 1876 cm^{-1} are tentatively assigned to ILCT state 1, denoted as ILCT 1, while the bands at 2014, 1913 and 1891 cm^{-1} are denoted as ILCT 2. In the fingerprint region, bands sharing similar kinetics with the ground state, the ILCT 1 state and the ILCT 2 state have been observed. The overall results are summarized in Table 4.5.

Table 4.5 *TRIR data summary of $[Re(CO)_3(Phen\text{-}TPA)Cl]$ in CH_2Cl_2.*

ν(CO) /cm^{-1}	ν(fingerprint) /cm^{-1}	growth	decay	assignment
2023, 1921, 1898	1593	1.6 ±0.1 μs	-	Parent
2023, 1921, 1897	-	-	-	GS FTIR
2050	-	-	18 ±2 ps	MLCT
2001, 1876	1538	-	4 ±2 ps, 203 ±146 ps	ILCT 1
2014, 1913, 1891	1548, 1484	16 ±1 ps, 279 ±41 ps	2.1 ±0.6 μs	ILCT 2

Therefore, the overall mechanism and kinetics can be shown in Figure 4.22.

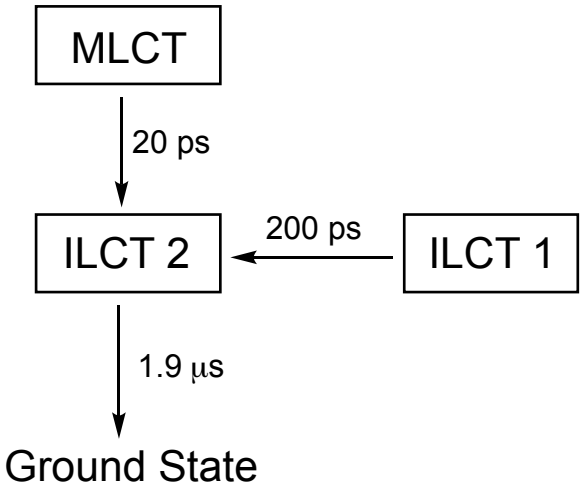


Figure 4.22 *Mechanism scheme of [Re(CO)$_3$(Phen-TPA)Cl] in CH_2Cl_2 according to the TRIR results.*

TRIR investigations of the Br-analogue [Re(CO)$_3$(Phen-TPA)Br] have also been conducted. It was found that the halide ligand change has little impact on the photophysics of the [Re(CO)$_3$(Phen-TPA)X] (X: Cl, Br) complexes. Figure 4.23 shows the TRIR spectra of [Re(CO)$_3$(Phen-TPA)Br] in CH_2Cl_2.

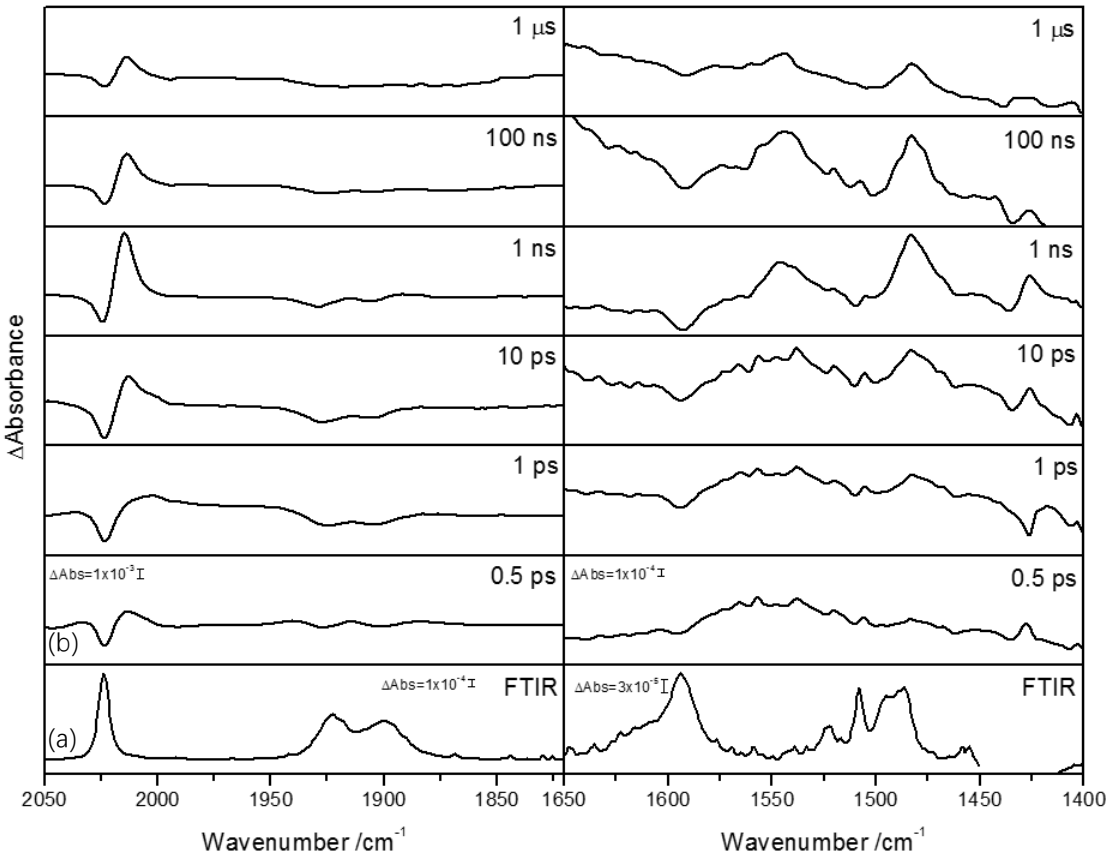


Figure 4.23 *(a) FTIR spectrum and (b) TRIR spectra obtained following photolysis (355 nm) of [Re(CO)$_3$(Phen-TPA)Br] in CH_2Cl_2 for both carbonyl (left) and fingerprint (right) IR regions.*

Similar to [Re(CO)$_3$(Phen-TPA)Cl], upon UV photolysis, the MLCT state is observed at higher wavenumber at *ca.* 2049 cm^{-1}, as well as the initial formation of the bands at 2001 and 1876 cm^{-1}. The bands at 2014, 1916 and 1892 cm^{-1} were also observed at later timedelays, similar to that for [Re(CO)$_3$(Phen-TPA)Cl]. Compared to [Re(CO)$_3$(Phen-TPA)Cl], here the bands observed at 2001 and 1876 cm^{-1} are assigned to the ILCT 1 state, while the bands at 2014, 1916 and 1892 cm^{-1} are assigned to the ILCT 2 state. Kinetic analysis shows that the ILCT 2 state is formed bi-exponentially in 11±1 ps, 174±41 ps, similar to that of [Re(CO)$_3$(Phen-TPA)Cl]. Also, the formation rate of the ILCT 2 state fits the decay rate of the MLCT state (*ca.* 15 ps) as well as the decay rate of the ILCT 1 state (*ca.* 250 ps), similar to [Re(CO)$_3$(Phen-TPA)Cl] as discussed before. The lifetime of the ILCT 2 state is *ca.* 3 μs. The reaction mechanism can be described in Figure 4.24.

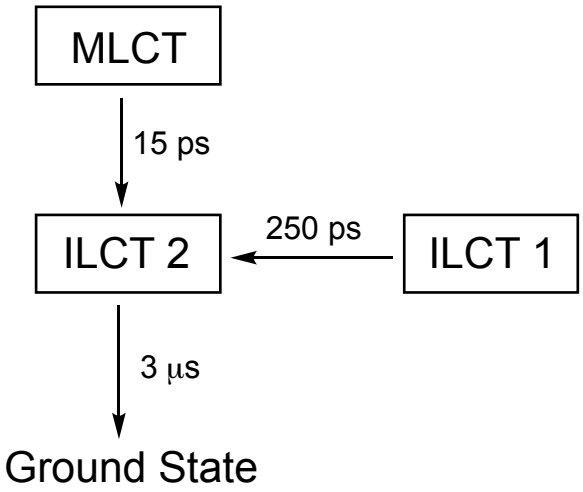


Figure 4.24 *Mechanism scheme of [Re(CO)$_3$(Phen-TPA)Br] in CH_2Cl_2 according to the TRIR results.*

4.2.4 Photophysics of $[Re(CO)_3(Phen\text{-}TPA)L]^+$ (L: py, dmap)

TRIR investigations of the $[Re(CO)_3(Phen\text{-}TPA)L]^+$ complexes with py (pyridine) and dmap (4-(dimethylamino)pyridine) ligands as the axial ligand L have also been carried out. Interestingly, it is found that the lifetimes of the excited states have been significantly reduced compared to the halide complexes $[Re(CO)_3(Phen\text{-}TPA)X]$ (X: Cl^-, Br^-). Figure 4.25 shows the TRIR spectra of $[Re(CO)_3(Phen\text{-}TPA)(py)]^+$ in CH_2Cl_2.

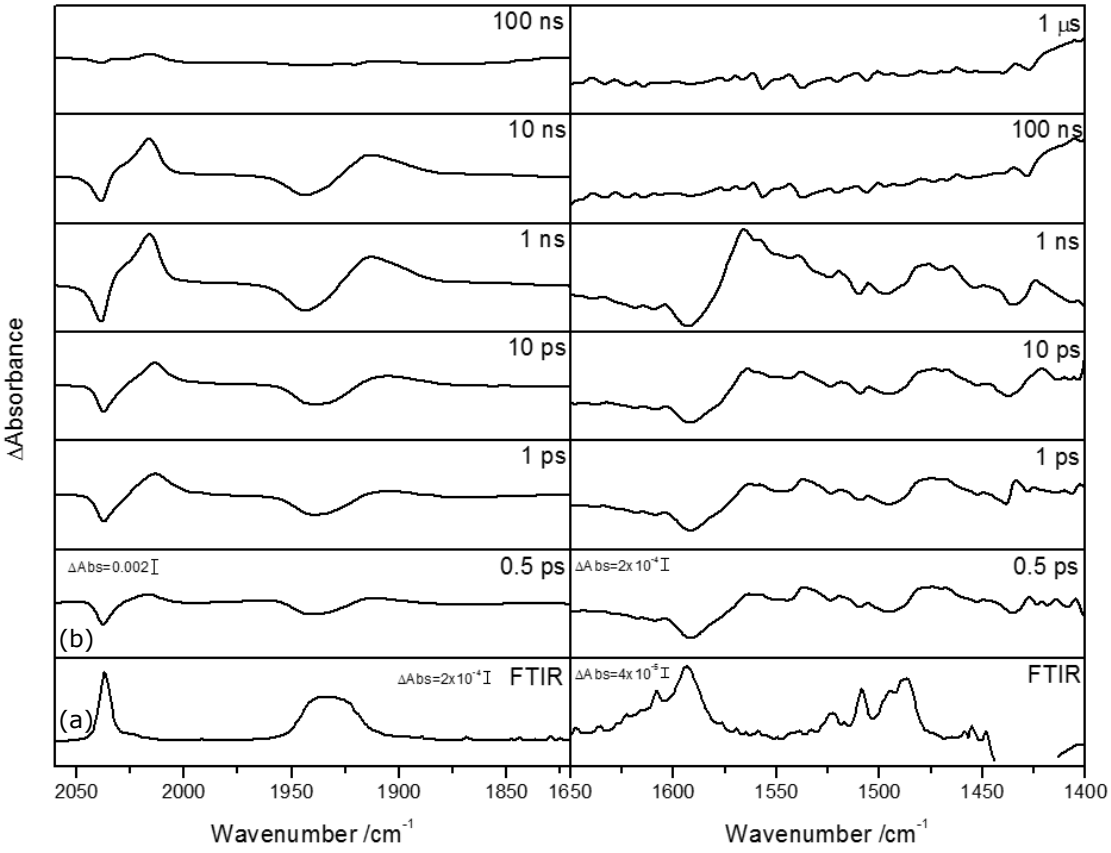


Figure 4.25 *(a) FTIR spectrum and (b) TRIR spectra obtained following photolysis (355 nm) of $[Re(CO)_3(Phen\text{-}TPA)(py)]^+$ in CH_2Cl_2 for both carbonyl (left) and fingerprint (right) IR regions.*

Compared to the halide $[Re(CO)_3(Phen\text{-}TPA)X]$ (X: Cl^-, Br^-) complexes, no apparent MLCT state has been observed for $[Re(CO)_3(Phen\text{-}TPA)(py)]^+$, as shown more clearly in Figure 4.26. At 0.5 ps, a weak band at *ca.* 2048 cm^{-1} is observed, unlike the $Re(Phen\text{-}TPA)(CO)_3X$ (X: Cl^-, Br^-) complexes, where the MLCT state was still observable at 10 ps. The MLCT band diminishes completely after 0.7 ps. However, the timedelay at 0.5 ps is not completely reliable as the first positive time-point of

the experiment due to possible baseline fluctuation.

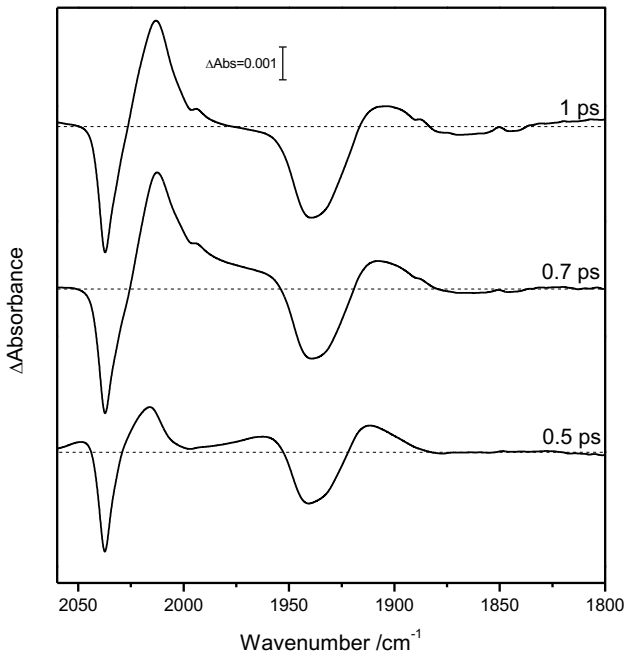


Figure 4.26 *Early ps-TRIR spectra of* $[Re(CO)_3(Phen\text{-}TPA)(py)]^+$ *in* CH_2Cl_2*, irradiated by 355 nm.*

Similar to $[Re(CO)_3(Phen\text{-}TPA)Cl]$ and $[Re(CO)_3(Phen\text{-}TPA)Br]$, upon UV photolysis, several bands were observed at lower wavenumber to the parent bleaches. Kinetics show that the formation rate of the band at 2014 cm^{-1} and the broad feature centred at *ca.* 1907 cm^{-1} is 17 (± 2) ps, consistent with the decay rate of the weak shoulder band at 1994 cm^{-1} (14 ± 4 ps). Here, the bands at 2014 and 1907 cm^{-1} are assigned to the ILCT 2 state, while the band at 1994 cm^{-1} is assigned as the ILCT 1 state. The lifetime of the ILCT 2 state is *ca.* 25 ns, which fits the recovery rate of the parent bands (23 ±0.4 ns), as shown in Figure 4.27. The lifetime of the ILCT 2 state is significantly shorter than that of the halide $[Re(CO)_3(Phen\text{-}TPA)X]$ (X: Cl^-, Br^-) complexes as discussed before.

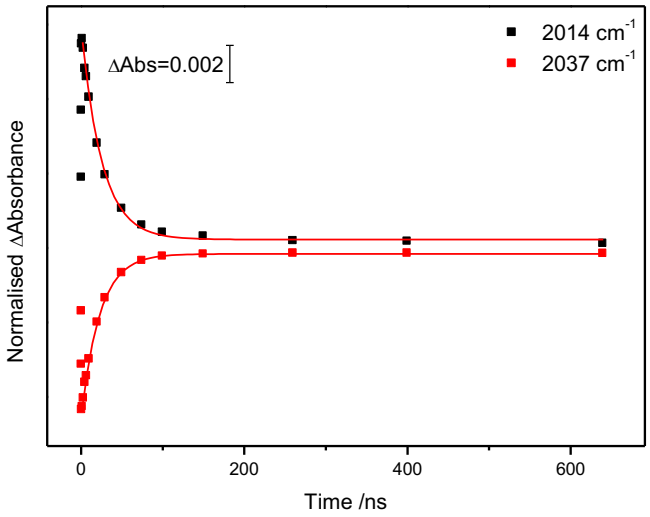


Figure 4.27 *TRIR kinetic traces obtained at 2037 and 2014 cm^{-1} corresponding to the parent band and the ILCT 2 state.*

In the fingerprint region, bands sharing similar kinetics with the ground state and the ILCT 2 state have also been observed. The overall results are summarized in Table 4.6.

Table 4.6 *TRIR data summary of $[Re(CO)_3(Phen\text{-}TPA)(py)]^+$ in CH_2Cl_2.*

ν(CO) /cm^{-1}	ν(fingerprint) /cm^{-1}	growth	decay	assignment
2037, 1939	1594, 1510	23 ±0.4 ns	-	Parent
2037, 1934	-	-	-	GS FTIR
1994	-	-	14 ±4 ps	ILCT 1
2014, 1907	1566, 1557, 1538, 1520, 1506, 1475, 1465	17 ±2 ps	25 ±0.7 ns	ILCT 2

Therefore, the reaction mechanism of $[Re(CO)_3(Phen\text{-}TPA)(py)]^+$ in CH_2Cl_2 can be shown in Figure 4.28.

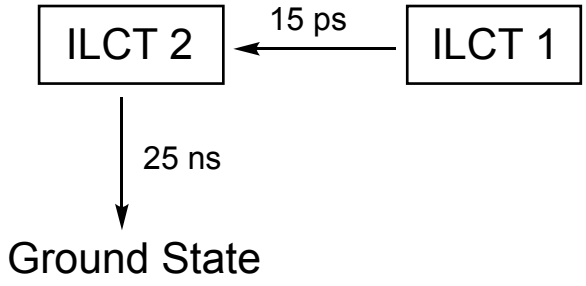


Figure 4.28 *Mechanism scheme of $[Re(CO)_3(Phen\text{-}TPA)(py)]^+$ in CH_2Cl_2 according to the TRIR results.*

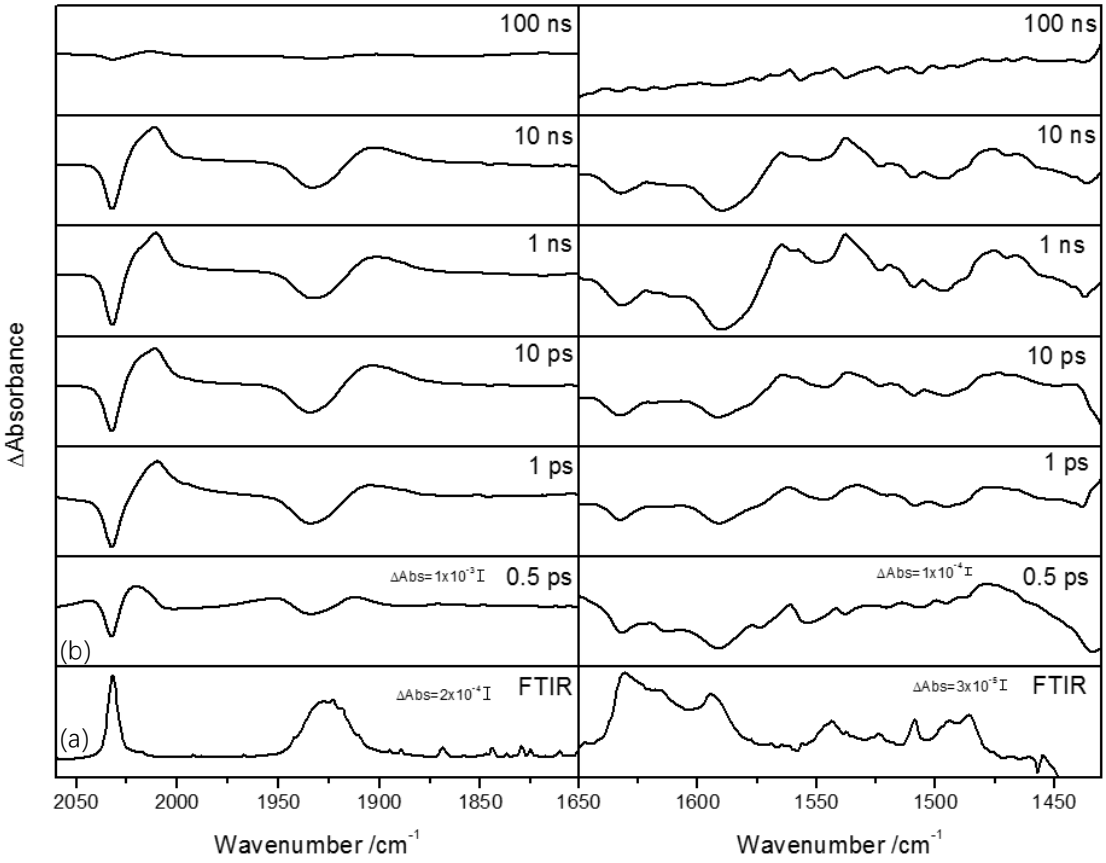


Figure 4.29 *(a) FTIR spectrum and (b) TRIR spectra obtained following photolysis (355 nm) of $[Re(CO)_3(Phen\text{-}TPA)(dmap)]^+$ in CH_2Cl_2 for both carbonyl (left) and fingerprint (right) IR regions.*

Figure 4.29 shows the TRIR of $[Re(CO)_3(Phen\text{-}TPA)(dmap)]^+$ in CH_2Cl_2. Similar to $[Re(CO)_3(Phen\text{-}TPA)(py)]^+$, after UV photolysis, no MLCT state has been observed. The conversion from the ILCT 1 state (1994 cm^{-1}) to the ILCT 2 state (2010, 1907 cm^{-1}) has also been observed at similar rate to $[Re(CO)_3(Phen\text{-}TPA)(py)]^+$, while

the lifetime of the ILCT 2 state is also similar to that of $[Re(CO)_3(Phen\text{-}TPA)(py)]^+$, which finally recovers to the ground state. The reaction mechanism is shown in Figure 4.30.

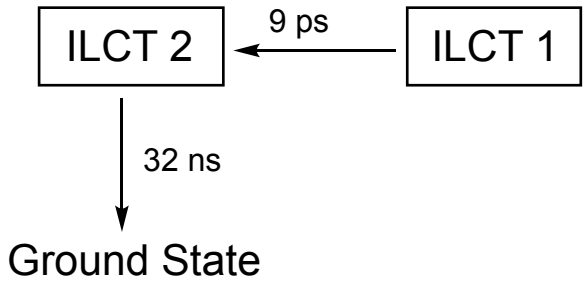


Figure 4.30 *Mechanism scheme of $[Re(CO)_3(Phen\text{-}TPA)(dmap)]^+$ in CH_2Cl_2 according to the TRIR results.*

Our collaborators from the University of Otago and Friedrich Schiller University Jena have done related research work and in the following, the results will be borrowed as a complement for the discussion of the TRIR results.

Figure 4.31 shows the Electronic Absorption spectra of the $[Re(CO)_3(phen\text{-}TPA)L]$ (L: Cl^-, Br^-, py, dmap) complexes as well as the individual Phen-TPA ligand. This is done by our collaborators from University of Otago. It is found that all four complexes have very distinct spectra compared to the discrete ligand Phen-TPA, while they can be divided into two types: the $[Re(CO)_3(Phen\text{-}TPA)X]$ (X: Cl^-, Br^-) complexes have similar spectra, and the $[Re(CO)_3(Phen\text{-}TPA)L]^+$ (L: py, dmap) complexes share similar spectra, as shown in Figure 4.31.

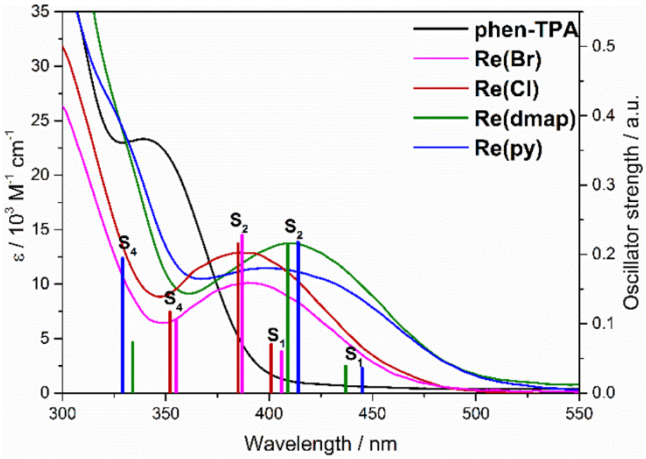


Figure 4.31 *Electronic Absorption spectra of [Re(CO)$_3$(phen-TPA)L] (L: Cl$^-$, Br$^-$, py, dmap) complexes as well as the individual Phen-TPA ligand. Reproduced from Ref. 41.*

As can be observed from Figure 4.31, complexation of the phen-TPA ligand to the [Re(CO)$_3$L] moiety leads to the formation of a band around 400 nm. As shown in the spectra, increasing the electron withdrawing ability of the ancillary ligand L (py≈dmap>Cl$^-$≈Br$^-$) causes the red-shift of the band at *ca.* 400 nm. This is contrary to the MLCT state for many Re-diimine complexes, as more electron withdrawing ancillary ligand L will stabilize the dπ(Re) orbital, thus will cause the blue-shift of the lowest-lying MLCT band. This result may indicate that the MLCT state may not be the lowest-lying energy state for the four [Re(CO)$_3$(phen-TPA)L] (L: Cl$^-$, Br$^-$, py, dmap) complexes. Instead, for the ILCT (TPA-phen) state where the electron transfers from the electron rich TPA group to the phen moiety, more electron withdrawing ancillary ligand L will stabilize the π*(phen) orbital, which will cause the red-shift of the band of the lowest-lying energy state. Meanwhile, the assumption is consistent with the TDDFT results. The calculation results suggest that the broad absorption bands between *ca.* 350 and 500 nm is mainly due to the excitation into two singlet ILCT states, denoted as S_1 and S_2, as shown in Figure 4.31. Both ILCT states are associated with a charge transfer from the electron-donor moiety TPA (π(TPA) orbital, HOMO) to the electron-acceptor phen ligand (π*(phen) orbital LUMO, LUMO+1). The oscillator strength of S_1 is significantly weaker than S_2, which is attributed to the poor overlap between orbitals involved

in the CT process. The MLCT state is proposed to be at higher energy, denoted as S_4 (Figure 4.31). Also as shown in the spectra, the MLCT states for [$Re(CO)_3$(phen-TPA)Cl] and [$Re(CO)_3$(phen-TPA)Br] are lower than that of [$Re(CO)_3$(phen-TPA)(py)]$^+$ and [$Re(CO)_3$(phen-TPA)(dmap)]$^+$. This is consistent with our TRIR results, as the MLCT state has only been observed for the halide complexes. This may indicate that the MLCT state of the non-halide [$Re(CO)_3$(phen-TPA)(py)]$^+$ and [$Re(CO)_3$(phen-TPA)(dmap)]$^+$ complexes may not be populated by 355 nm excitation wavelength.

In order to better understand the electron transitions, Resonance Raman (RR) Spectroscopy has been conducted. Figure 4.32 is the RR spectra of [$Re(CO)_3$(phen-TPA)Cl].

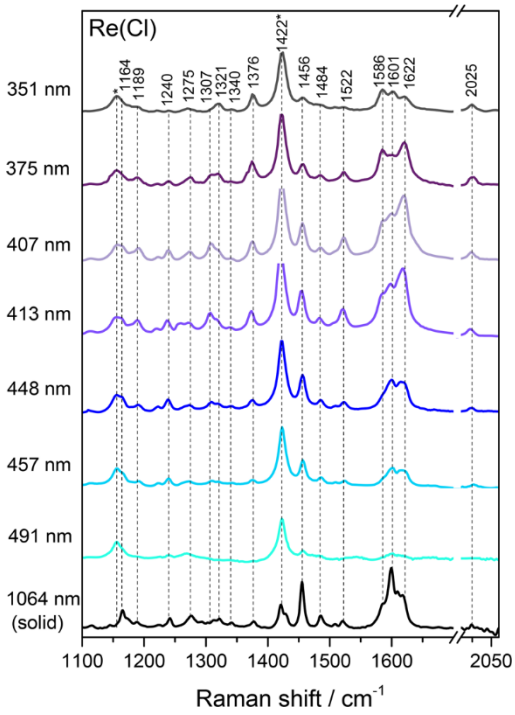


Figure 4.32 *Resonance Raman Spectroscopy of [Re(CO)$_3$(phen-TPA)Cl]. *: solvent band. Reproduced from Ref. 41.*

The bands at 1586 and 1622 cm^{-1} are typical features of TPA, and the bands at 1376, 1422, 1522 cm^{-1} are phen-based. As shown in Figure 4.32, when the energy of λ_{ex} decreases from 351 to 407 nm, these bands are enhanced. As shown in Figure 4.31, the energy of the S_2 band of [$Re(CO)_3$(phen-TPA)Cl] is around 390 nm. Therefore, this state is attributed to the more intense S_2 state (TPA→phen). When

the energy of λ_{ex} decreases further, the intensity of TPA and phen-based bands decreases. This weak state is attributed to the S_1 state.

The existence of the MLCT state is also evidenced by the RR spectra. When λ_{ex} is 351 nm, compared to the 1064 (solid) nm non-resonant spectrum, the CO band at 2025 cm^{-1} is enhanced while the TPA bands at 1586 and 1622 cm^{-1} are much weaker, suggesting a MLCT state. Also, the RR spectra suggest there may be an overlap between the MLCT state and the ILCT 2 state, as when λ_{ex} drops from 351 to 375 nm, the TPA bands at 1586 and 1622 cm^{-1} are enhanced, while the band at 2025 cm^{-1} shows no apparent decay.

The RR spectra of $[Re(CO)_3(phen\text{-}TPA)Br]$, $[Re(CO)_3(phen\text{-}TPA)(py)]^+$ and $[Re(CO)_3(phen\text{-}TPA)(dmap)]^+$ are similar to that of $[Re(CO)_3(phen\text{-}TPA)Cl]$, only except that the MLCT states are higher than that of $[Re(CO)_3(phen\text{-}TPA)Cl]$, and the ILCT states of $[Re(CO)_3(phen\text{-}TPA)(py)]^+$ and $[Re(CO)_3(phen\text{-}TPA)(dmap)]^+$ are at lower energy compared to $[Re(CO)_3(phen\text{-}TPA)Cl]$ and $[Re(CO)_3(phen\text{-}TPA)Br]$, consistent with the electronic absorption spectra (Figure 4.31), as well as our TRIR results, and is also supported by the TDDFT calculations.

Steady state emission spectroscopy has also been conducted. The results are summarized in Table 4.7. All four complexes are emissive, and the λ_{em} is observed to be highly influenced by the ancillary ligand. When the ancillary ligand changes from Br^-, Cl^- to py and dmap, the λ_{em} is red-shifted, similar to that observed in the absorption spectra (Figure 4.31). Therefore, the results indicate that the excited states involved in absorption and emission spectra are both ILCT states. This is also supported by quantum chemical calculations.

Transient absorption and emission spectroscopy has also been conducted by our collaborators to obtain kinetic information. It is observed that the emitting lifetimes are sensitive to $^3O_2$, indicating that the emitting states are triplet states. The excited state lifetimes of all four complexes obtained from both absorption and emission spectroscopy are similar, and the results show that the excited state lifetime is significantly influenced by the ancillary ligand, from 6 μs for

[$Re(CO)_3$(phen-TPA)Br] to 27 ns for [$Re(CO)_3$(phen-TPA)(py)]$^+$. The lifetimes are summarized in Table 4.7. The relatively shorter lifetimes obtained by TRIR is ascribed to the deactivation of self-quenching effect due to higher concentration of solution used in TRIR experiments. The overall absorption and emission data is summarized in Table 4.7.

Table 4.7 *Summary of the absorption and emission data. Reproduced from Ref. 41.*

species	λ_{abs} (nm)	λ_{em} (nm)	E_{em} (eV)	τ (ns)	k_r (s^{-1})	k_{nr} (s^{-1})
Re(Br)	389	605	2.05	6000	$2.7x10^3$	$1.6x10^5$
Re(Cl)	386	607	2.04	3900	$1.3x10^3$	$2.5x10^5$
Re(dmap)	410	678	1.83	44	$3.5x10^4$	$2.3x10^7$
Re(py)	401	689	1.80	27	$3.7x10^4$	$3.8x10^7$

The significant influence of the ancillary ligand on the excited state lifetimes is explained by the energy gap law assumption. Akin to many other Re complexes, $\tau \approx 1/\kappa_{nr}$ (nr: nonradiative decay). And according to the energy gap law, when the energy gap between the emissive state (T_1) and the ground state (S_0) increases, the rate of κ_{nr} will decrease as the result of the reduced overlap between the wavefunctions of the two states, as well as a reduction in the Franck-Condon factor. The emission energy and the $\ln(\kappa_{nr})$ value are found to follow a linear relationship, as shown in Figure 4.33.

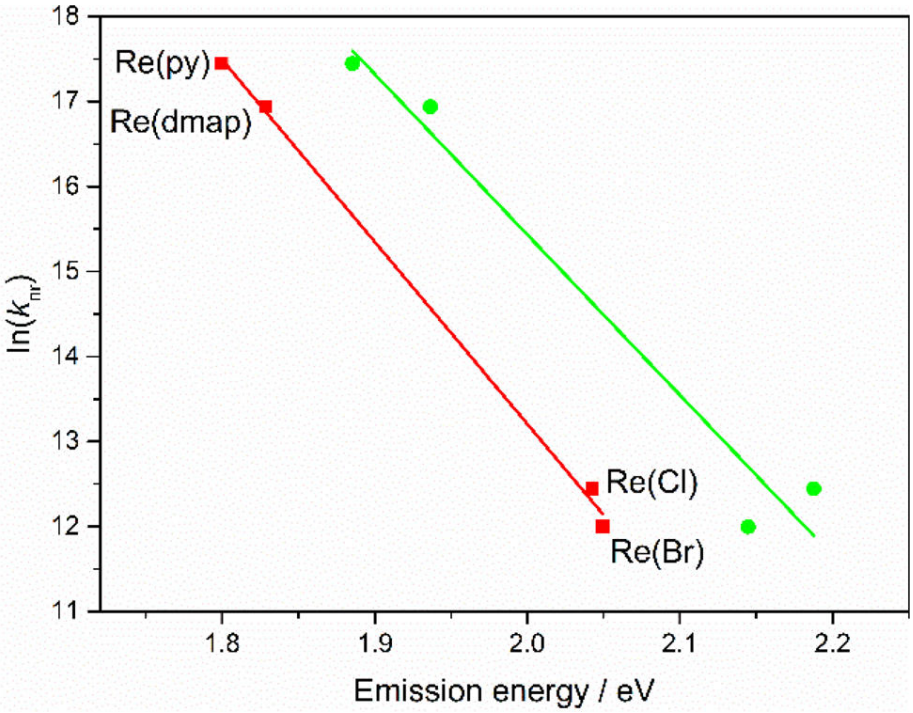


Figure 4.33 *Plots of emission energy versus ln(κ_{nr}) for the ILCT states of [Re(CO)$_3$(phen-TPA)Cl], [Re(CO)$_3$(phen-TPA)Br], [Re(CO)$_3$(phen-TPA)(py)]$^+$ and [Re(CO)$_3$(phen-TPA)(dmap)]$^+$ complexes. The gradient of the red line is -21.4 eV^{-1}. The green line is the calculated emission energy vs. ln(κ_{nr}) with similar gradient value.*

Transient resonance Raman (TR^2) spectroscopy has also been conducted to explore the electronic structure of the thermally equilibrated excited (THEXI) state, as shown in Figure 4.34.

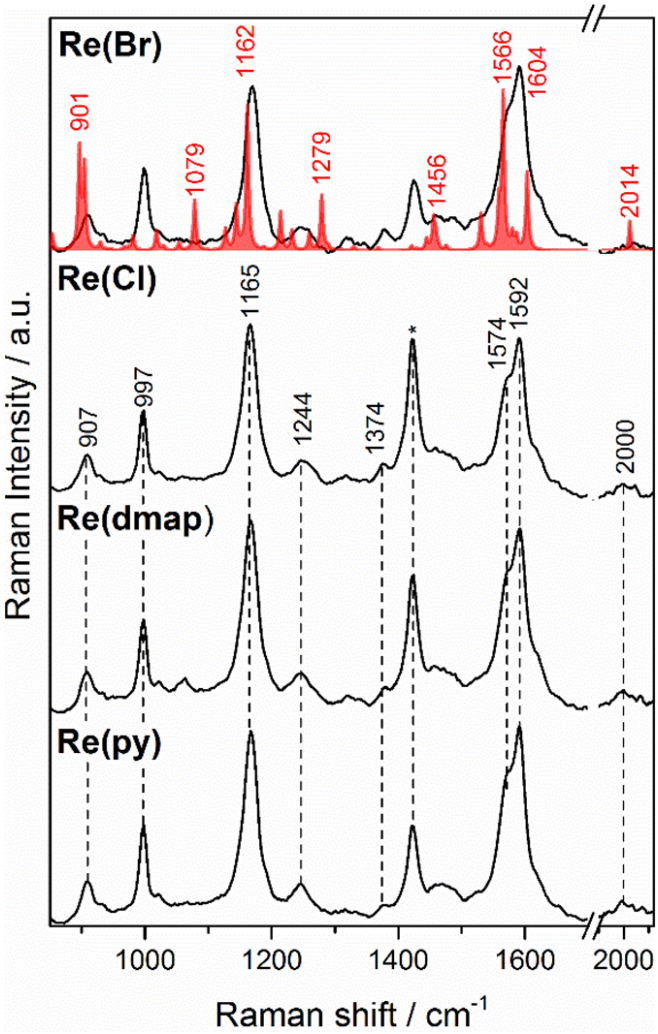


Figure 4.34 *Transient resonance Raman spectra of [Re(CO)$_3$(phen-TPA)L] (L: Cl$^-$, Br$^-$, py, dmap) complexes in CH_2Cl_2 with 355 nm excitation. The red spectrum is the simulated spectrum for [Re(CO)$_3$(phen-TPA)Br], Reproduced from Ref. 41.*

For all [Re(CO)$_3$(phen-TPA)L] (L: Cl$^-$, Br$^-$, py, dmap) complexes, the bands at 907, 997, 1165, 1574 and 1592 cm^{-1} were observed, which are typical bands for the TPA cation. As shown in Figure 4.34, the red spectrum is the simulated lowest ^{3}ILCT state of [Re(CO)$_3$(phen-TPA)Br] by quantum chemical calculations, and is in good agreement with the experimental results. This applies to all four complexes. Therefore, the lowest-lying excited state for all complexes can be assigned to ^{3}ILCT.

Therefore, in conclusion, for all four complexes, the conversion between two ILCT states has been observed, which is completed in 10-20 ps. The more stable ILCT state, denoted as ILCT 2, is suggested to be a triplet state, thus is denoted as ^{3}ILCT.

While the initially formed ILCT state is thought to be a singlet ILCT state. For the halide complexes, a MLCT state has been observed, which also decays to the ^{3}ILCT state, as shown in Figure 4.35.

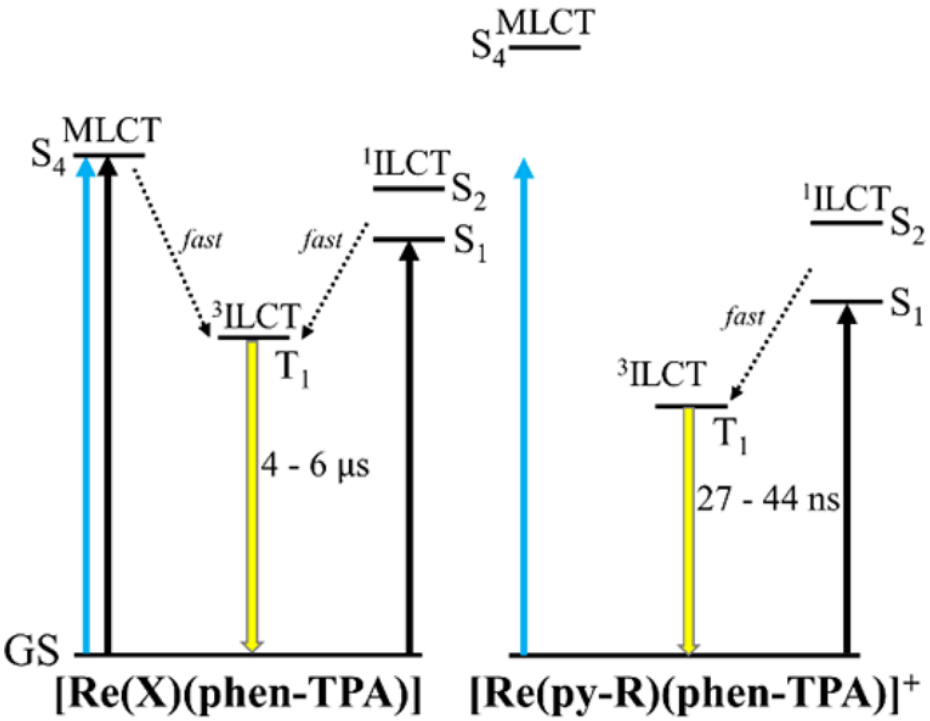


Figure 4.35 *Energy level scheme of left: [Re(CO)$_3$(phen-TPA)X] (X: Cl$^-$, Br$^-$); right: [Re(CO)$_3$(phen-TPA)L]$^+$ (L: py, dmap). Irradiation by 355 nm. Reproduced from Ref. 41.*

4.3 Conclusion

For $[Re(CO)_3(dppz\text{-}NPh_2)Cl]$ in both toluene and acetone, three dppz-NPh_2 ligand-based excited states have been observed, denoted as state I, II and III. In toluene, a weak and short-lived MLCT state was observed, however this was not seen in acetone. In both solvents, similar reaction process has been observed, that upon UV irradiation, both state I and III are generated initially, while state I converts to state II in tens of ps, and state III decays in few ns to the ground state. State II is stable with a lifetime of several μs.

It is interesting to find that changing the solvent has little effect on the lifetime of state I and II, while state III is prolonged in acetone compared to in toluene. However, it is found that the lifetime of state II and III is highly dependent on the concentration of $[Re(CO)_3(dppz\text{-}NPh_2)Cl]$, while the lifetime of state I is almost unaffected, which could be explained by a diffusion-controlled reaction rate.

For the Re-phen complexes $[Re(CO)_3(Phen\text{-}TPA)X]^{n=0,1}$ (X: Cl^-, Br^- n=0; py, dmap n=1), using TRIR, it is observed that for all four complexes, there exists the conversion between two ILCT states (TPA→phen). For the halide complexes, short-lived MLCT state has been observed, which is not observed for the non-halide complexes. With the assistance of our collaborators, the more stable ILCT state is attributed to a triplet state, while the initially formed unstable ILCT state is a singlet state, which undergoes fast decay to the ^{3}ILCT state. The energy level of the MLCT state of the non-halide complexes is proposed to be much higher than that of the halide complexes, thus under irradiation of 355 nm, MLCT state is not observed for the non-halide complexes. Kinetic analysis of the TRIR data shows that the lifetime of the ^{3}ILCT state for $[Re(CO)_3(Phen\text{-}TPA)L]^+$ (L: py, dmap) is on the ns-timescale, for 20-30 ns, while the lifetime for the halide analogue $[Re(CO)_3(Phen\text{-}TPA)X]$ (X: Cl^-, Br^-) is much prolonged with a lifetime of *ca.* 2.0-3.0 μs. The lifetimes obtained by TRIR are shorter compared to that obtained by transient absorption and emission spectroscopy by our collaborators, which has been attributed to the self-quenching effect due to the higher concentration used in TRIR experiments. However, both TRIR and transient absorption and emission spectroscopy reveal that

the lifetime of the lowest-lying ^{3}ILCT state is highly influenced by the ancillary ligand. The reason is still unclear, although it might be explained by the energy gap law.

References

1 J. Fees, W. Kaim, M. Moscherosch, W. Matheis, J. Klima, M. Krejcik and S. Zalis, *Inorg. Chem.*, 1993, **32**, 166–174.

2 J. Fees, M. Ketterle, A. Klein, J. Fiedler and W. Kaim, *J. Chem. Soc. Dalton Trans.*, 1999, 2595–2600.

3 J. Dyer, W. J. Blau, C. G. Coates, C. M. Creely, J. D. Gavey, M. W. George, D. C. Grills, S. Hudson, J. M. Kelly, P. Matousek, J. J. McGarvey, J. McMaster, A. W. Parker, M. Towrie and J. A. Weinstein, *Photochem. Photobiol. Sci.*, 2003, **2**, 542–554.

4 E. J. C. Olson, D. Hu, A. Hörmann, A. M. Jonkman, M. R. Arkin, E. D. A. Stemp, J. K. Barton and P. F. Barbara, *J. Am. Chem. Soc.*, 1997, **119**, 11458–11467.

5 A. E. Friedman, J. C. Chambron, J. P. Sauvage, N. J. Turro and J. K. Barton, *J. Am. Chem. Soc.*, 1990, **112**, 4960–4962.

6 M. K. Brennaman, J. H. Alstrum-Acevedo, C. N. Fleming, P. Jang, T. J. Meyer and J. M. Papanikolas, *J. Am. Chem. Soc.*, 2002, **124**, 15094–15098.

7 M. K. Brennaman, T. J. Meyer and J. M. Papanikolas, *J. Phys. Chem. A*, 2004, **108**, 9938–9944.

8 M. R. Waterland, K. C. Gordon, J. J. McGarvey and P. M. Jayaweera, *J. Chem. Soc. Dalton Trans.*, 1998, 609–616.

9 E. Amouyal, A. Homsi, J.-C. Chambron and J.-P. Sauvage, *J. Chem. Soc. Dalton Trans.*, 1990, 1841–1845.

10 M. K. Kuimova, W. Z. Alsindi, A. J. Blake, E. S. Davies, D. J. Lampus, P. Matousek, J. McMaster, A. W. Parker, M. Towrie, X.-Z. Sun, C. Wilson and M. W. George, *Inorg. Chem.*, 2008, **47**, 9857–9869.

11 H. van der Salm, M. G. Fraser, R. Horvath, S. A. Cameron, J. E. Barnsley, X.-Z. Sun, M. W. George and K. C. Gordon, *Inorg. Chem.*, 2014, **53**, 3126–3140.

12 G. E. Shillito, C. B. Larsen, J. R. W. McLay, N. T. Lucas and K. C. Gordon, *Inorg. Chem.*, 2016, **55**, 11170–11184.

13 H. van der Salm, M. G. Fraser, R. Horvath, J. O. Turner, G. M. Greetham, I. P. Clark, M. Towrie, N. T. Lucas, M. W. George and K. C. Gordon, *Inorg. Chem.*, 2014, **53**, 13049–13060.

14 M. G. Fraser, A. G. Blackman, G. I. S. Irwin, C. P. Easton and K. C. Gordon, *Inorg. Chem.*, 2010, **49**, 5180–5189.

15 C. Goze, C. Leiggener, S.-X. Liu, L. Sanguinet, E. Levillain, A. Hauser and S. Decurtins, *ChemPhysChem*, **8**, 1504–1512.

16 C. Jia, S.-X. Liu, C. Tanner, C. Leiggener, A. Neels, L. Sanguinet, E. Levillain, S. Leutwyler, A. Hauser and S. Decurtins, *Chem. – Eur. J.*, **13**, 3804–3812.

17 J. R. Schoonover, G. F. Strouse, R. B. Dyer, W. D. Bates, P. Chen and T. J. Meyer, *Inorg. Chem.*, 1996, **35**, 273–274.

18 D. M. Dattelbaum, K. M. Omberg, P. J. Hay, N. L. Gebhart, R. L. Martin, J. R. Schoonover and T. J. Meyer, *J. Phys. Chem. A*, 2004, **108**, 3527–3536.

19 H. D. Stoeffler, N. B. Thornton, S. L. Temkin and K. S. Schanze, *J. Am. Chem. Soc.*, 1995, **117**, 7119–7128.

20 M. K. Kuimova, D. C. Grills, P. Matousek, A. W. Parker, X.-Z. Sun, M. Towrie and M. W. George, *Vib. Spectrosc.*, 2004, **35**, 219–223.

21 M. K. Kuimova, X. Z. Sun, P. Matousek, D. C. Grills, A. W. Parker, M. Towrie and M. W. George, *Photochem. Photobiol. Sci.*, 2007, **6**, 1158–1163.

22 J. Dyer, C. M. Creely, J. C. Penedo, D. C. Grills, S. Hudson, P. Matousek, A. W. Parker, M. Towrie, J. M. Kelly and M. W. George, *Photochem. Photobiol. Sci.*, 2007, **6**, 741–748.

23 M. K. Kuimova, W. Z. Alsindi, J. Dyer, D. C. Grills, O. S. Jina, P. Matousek, A. W. Parker, P. Portius, X. Z. Sun, M. Towrie, C. Wilson, J. Yang and M. W. George, *Dalton Trans.*, 2003, 3996–4006.

24 C. B. Larsen, H. van der Salm, C. A. Clark, A. B. S. Elliott, M. G. Fraser, R. Horvath, N. T. Lucas, X.-Z. Sun, M. W. George and K. C. Gordon, *Inorg. Chem.*, 2014, **53**, 1339–1354.

25 P. A. Summers, J. A. Calladine, N. Ibrahim, K. P. Kusumo, C. A. Clark, X.-Z. Sun, M. L. Hamilton, M. Towrie, J. McMaster, M. Schröder and M. W. George, *Polyhedron*, 2017, **123**, 259–264.

26 B. S. Adams, G. E. Shillito, H. van der Salm, R. Horvath, C. B. Larsen, X.-Z. Sun, N. T. Lucas, M. W. George and K. C. Gordon, *Inorg. Chem.*, 2017, **56**, 12967–12977.

27 A. M. Blanco-Rodríguez, H. Kvapilová, J. Sýkora, M. Towrie, C. Nervi, G. Volpi, S. Záliš and A. Vlček, *J. Am. Chem. Soc.*, 2014, **136**, 5963–5973.

28 A. J. Amoroso, M. P. Coogan, J. E. Dunne, V. Fernández-Moreira, J. B. Hess, A. J. Hayes, D. Lloyd, C. Millet, S. J. A. Pope and C. Williams, *Chem. Commun.*, 2007, 3066–3068.

29 K. K.-W. Lo, K.-S. Sze, K. H.-K. Tsang and N. Zhu, *Organometallics*, 2007, **26**, 3440–3447.

30 A. A. Martí, G. Mezei, L. Maldonado, G. Paralitici, R. G. Raptis and J. L. Colón, *Eur. J. Inorg. Chem.*, 2005, **2005**, 118–124.

31 M. Wrighton and D. L. Morse, *J. Am. Chem. Soc.*, 1974, **96**, 998–1003.

32 S. M. Fredericks, J. C. Luong and M. S. Wrighton, *J. Am. Chem. Soc.*, 1979, **101**, 7415–7417.

33 L. Wallace and D. P. Rillema, *Inorg. Chem.*, 1993, **32**, 3836–3843.

34 L. Wallace, D. C. Jackman, D. P. Rillema and J. W. Merkert, *Inorg. Chem.*, 1995, **34**, 5210–5214.

35 D. R. Striplin and G. A. Crosby, *Chem. Phys. Lett.*, 1994, **221**, 426–430.

36 D. R. Striplin and G. A. Crosby, *Coord. Chem. Rev.*, 2001, **211**, 163–175.

37 A. O. T. Patrocínio and N. Y. Murakami Iha, *Inorg. Chem.*, 2008, **47**, 10851–10857.

38 A. O. T. Patrocinio, M. K. Brennaman, T. J. Meyer and N. Y. Murakami Iha, *J. Phys. Chem. A*, 2010, **114**, 12129–12137.

39 I. E. Pomestchenko, D. E. Polyansky and F. N. Castellano, *Inorg. Chem.*, 2005, **44**, 3412–3421.

40 J. Qin, L. Hu, G.-N. Li, X.-S. Wang, Y. Xu, J.-L. Zuo and X.-Z. You, *Organometallics*, 2011, **30**, 2173–2179.

41 G. E. Shillito, T. B. J. Hall, D. Preston, P. Traber, L. Wu, K. E. A. Reynolds, R. Horvath, X. Z. Sun, N. T. Lucas, J. D. Crowley, M. W. George, S. Kupfer and K. C. Gordon, *J. Am. Chem. Soc.*, 2018, **140**, 4534–4542.

Chapter 5 TRIR Investigations on the Photoproperties of MOF Materials

5.1 Introduction

Metal-Organic-Framework (MOF) materials, consist of metal ions which act as nodes and organic ligands as linkers, hold the structure together.[1,2,3] They have attracted considerable attention in recent decades, due to their various applications in many fields, such as gas storage,[4,5] catalysis,[6,7] magnetism material,[8] and more recently, stabilization of transient intermediates during reactions.[9,10]

Coordination networks, including MOFs and supermolecular cages, are found to be capable of stabilising transient intermediates that are normally undetectable in solvents at ambient temperatures. The cavities of a MOF,[11] supermolecule capsule[12,13] and even enzyme pockets[14] can act as "cages" to isolate intermediates. Haneda *et al.* reported a single-crystal-to-single-crystal (SCSC) reaction of acetaldehyde with amines forming acetaldehydeimines in the pores of a porous coordination network.[15] In the network, the amines are first incorporated into the rectangular pores of the coordination network during the synthesis of the single crystal of the network. The crystal was then immersed in solvent with certain concentration of acetaldehyde. The pore size of the network is quite large (with the rectangular pores 10x15 Å; the triangular pores are equilateral, with a side 12 Å long). This creates a pseudo-solution phase within the network, in which the reagents can easily diffuse as in solution, while the morphology of the network is retained and can be analyzed by XRD. It is found that a 100% conversion of amines to imines can occur, evidenced by X-ray crystallographic analysis, microscopic IR analysis and elemental analysis, as shown in Figure 5.1.

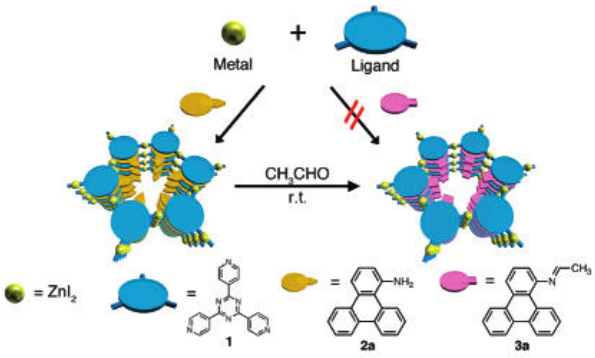


Figure 5.1 *Reaction of amines in the pores of the coordination network with acetaldehyde to form imines in a SCSC manner.*[15]

In the network, 100% of the amines can be converted into imines, while in solvents, the unstable imines can be easily hydrolyzed or isomerized into enamines. Thus, the structure of the coordination network can not only create a pseudo-solution phase for the reaction, but also stabilize the short-lived unstable imine species. This allows XRD analysis, which is normally difficult for many conventional solvent and solid-state reactions.

Even extremely unstable intermediates such as hemiaminal can be detected using XRD *via* this method.[10] Hemiaminal is an extremely unstable intermediate, and is only observed by spectroscopic methods in low-temperature matrices.[12,13,16] Using a MOF scaffold as matrix, the usually short-lived intermediate hemiaminal is kinetically trapped in the pores of the MOF framework, which allows XRD analysis. Therefore, it is argued that the pores of these networks can provide kinetic stabilization for transient intermediates.

Studies on photo-induced reactions within coordination networks have also attracted much attention recently. Kawano *et al.* succeeded in *in situ* observation of the unsaturated Cp'$Mn(CO)_2$ species (Cp': methylcyclopentadienyl) using X-ray diffraction.[17] This was achieved by encapsuling Cp'$Mn(CO)_3$ within the cavity of a supermolecular cage, using UV irradiation to initiate the CO-ejection. Unsaturated metal carbonyl species is very unstable, normally with a lifetime less than 1 ps in solvent. Detection of it often requires low-temperature inert matrix. MOF networks are also found to be able to act as matrix for investigating photo-reactions. Blake

et al. have used TRIR to investigate the photoproperties of the linker complex $Re(CO)_3$(diimine)Cl within the MOF scaffold with the formula $\{Mn(DMF)_2$-$[C_{12}H_6N_2O_4Re(CO)_3Cl]\}_\infty$[18] (denoted as ReMn MOF, the structure is shown in Figure 5.2. DMF: dimethylformamide). It was found that upon irradiation, the $Re(CO)_3$(diimine)Cl complex forms both ^{3}MLCT and IL $\pi\pi^*$ excited states, while ^{3}MLCT is unstable and quickly decays and converts into an IL $\pi\pi^*$ state.

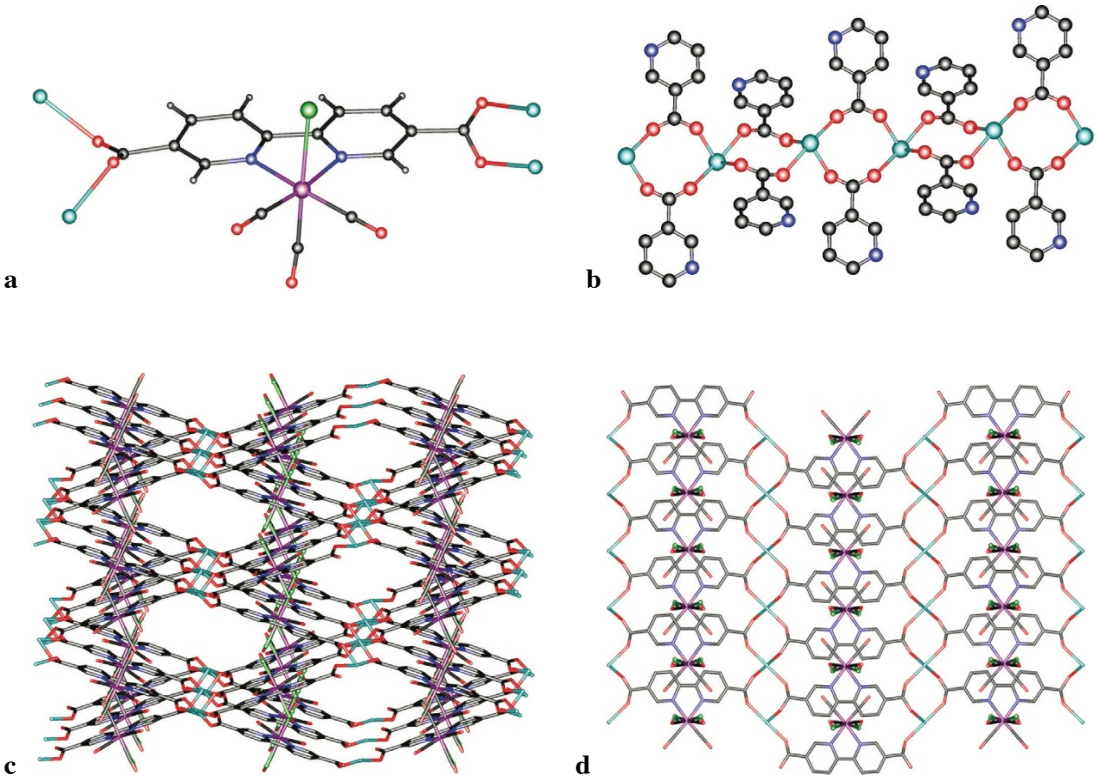


Figure 5.2 *Views of the single-crystal structure of the ReMn MOF. a: $Re(CO)_3$(diimine)Cl in fac-configuration; b: view of the $[Mn(carboxylate)]_\infty$ alone the a axis; c: view of the 3D structure of the ReMn MOF; d: view of the ReMn MOF along the c axis. Light blue: Mn, purple: Re, grey: C, red: O, blue: N, green: halide (Cl or Br). H atoms and DMF molecules coordinated to Mn(II) cations are ignored.*[18]

This is unusual for the $Re(CO)_3$(dimine)Cl complex, as it is well known for an intense photo-initiated ^{3}MLCT state in solution after photo irradiation, according to many studies.[19,20,21,22] Similar phenomena has been observed before for discrete Re-diimine complexes in the solid state at low temperature, and is denoted as

"rigidochromism", which was first discovered by Clark *et al.*[23] They found that when the PrCN-EtCN solvent in the presence of $Re(CO)_3(bpy)Cl$ undergoes transformation from fluid to glass, the $\Delta\nu(CO)$ of the MLCT excited state compared to the parent bleaches decreased sharply (*ca.* 20 cm^{-1}). The decrease of $\Delta\nu(CO)$ of the MLCT state compared to the parent bleaches is ascribed to the mixing with the $\pi\pi^*$ excited state at higher energy level when in solid state. Meyer and co-workers have conducted IR measurements of fac-$[Re^{I}(CO)_3(4,4'\text{-}X_2bpy)(4\text{-}Etpy)]^+$ (X= H, CH_3 and CO_2Et; 4Etpy is 4-ethylpyridine) in both CH_3CN and poly(methyl methacrylate) (PMMA) films at room temperature.[24] It is found that the $\Delta\nu(CO)$ shift between the MLCT state and the ground state in PMMA is much less than in CH_3CN solution. They attributed this phenomenon to the result of orbital mixing of π^*-(4,4'-X2bpy$^{\cdot-}$) with π^*-(CO) in PMMA solid-state matrix, instead of MLCT-$\pi\pi^*$ mixing proposed by Clark *et al*. However, according to Blake *et al.*, the unusual phenomenon is attributed to the fact that in the MOF scaffold, the $\pi\pi^*$ excited state is lower in energy than the MLCT state, rather than mixing of different excited states. The co-existence of MLCT and $\pi\pi^*$ excited states in solid state has also been observed by Towrie *et al*.[25]

It is also found that on the later timescales, MOFs with a $M(CO)_3(diimine)X$ (M: Re, Mn; X: Br (for Mn only), Cl) moiety, exhibit isomerization from *fac*- to *mer*- after photo-initiated CO-loss. For ReMn MOF, only 10% of the *fac*-complex has transformed into the *mer*-isomer, while for the analogue MOF with $Mn(CO)_3(diimine)X$ as the linker (denoted as MnMn MOF), 25% is reached. This is also unusual for the $Re(CO)_3(diimine)Cl$ complex, as although the *fac*- to *mer*-isomerization has been observed for the $Mn(CO)_3(diimine)X$ (X: halide) complexes,[26] such isomerization for the analogue Re complexes are rare, as in most cases the MLCT excited state is observed to generate after irradiation, and the MLCT state is proven to be unreactive in most conditions. While for the analogue Mn-complexes, although the MLCT state is also considered to be the lowest excited state, Mn-diimine carbonyl complexes are more photo-reactive, and the photo-induced CO-loss is often observed.[27,28] According to Oskam and co-workers, the high photo-reactivity of Mn-diimine complexes is attributed to the low LF state close in energy to the lowest MLCT state, due to the small ligand-field splitting of Mn(I).

Oskam and co-workers reported that the *fac*-$Mn(CO)_3$(a-dimine)X complex (X: halide) can dimerize into $Mn_2(CO)_6$(a-diimine)$_2$ *via* the *mer*-isomer *mer*-$Mn(CO)_3$(a-dimine)X,[29] as shown in Figure 5.3.

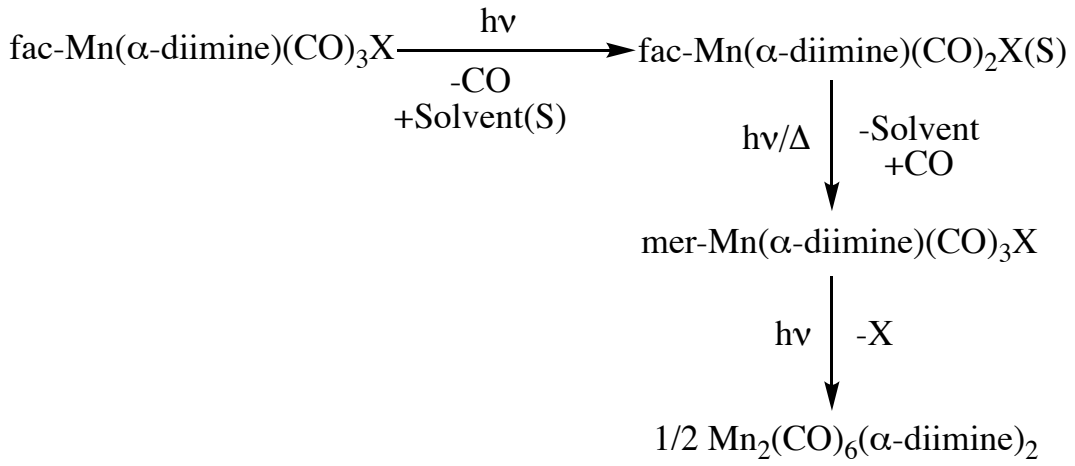


Figure 5.3 *Dimerization of fac-Mn(CO)$_3$(α-dimine)X via the mer-isomer. Reproduced from Ref. 29.*[29]

DFT calculations on the *fac*-$Mn(CO)_3$(diimine)Cl complexes proposed that, upon irradiation, CO dissociation from the equatorial position will lead to the Cl rearrangement from the axial position to the equatorial position, which then re-combines with CO to form an isomer, while CO-loss from axial position does not lead to this position rearrangement of Cl.[30]

The *fac*- to *mer*-isomerization of the $Re(CO)_3$(diimine)Cl complex incorporated in the MOF structure has been further investigated using FTIR, Raman mapping, DFT and TRIR by Easun *et. al.*[31] It is found that upon UV photolysis, both *fac*- and *mer*-dicarbonyls have been formed, which then recombine with CO trapped in the MOF channel to form the *fac*- and *mer*-isomers. Similar $Re(CO)_3$(dnb)Cl complex in alkane solvents has been investigated as a comparison to the MOF. Results show that after UV photolysis, a dicarbonyl species is formed and then decays and recombines with CO to form both the *fac*- and *mer*-isomers, similar to the *fac* to *mer* isomerization of Re(diimine)$(CO)_3$Cl in the MOF structure.

Apart from investigations of the *fac* to *mer* isomerization of the MnMn MOF on the

late timescales, research on the early timescale of the photoreaction has also been conducted.[32] The ps-TRIR of the MnMn MOF is shown in Figure 5.4.

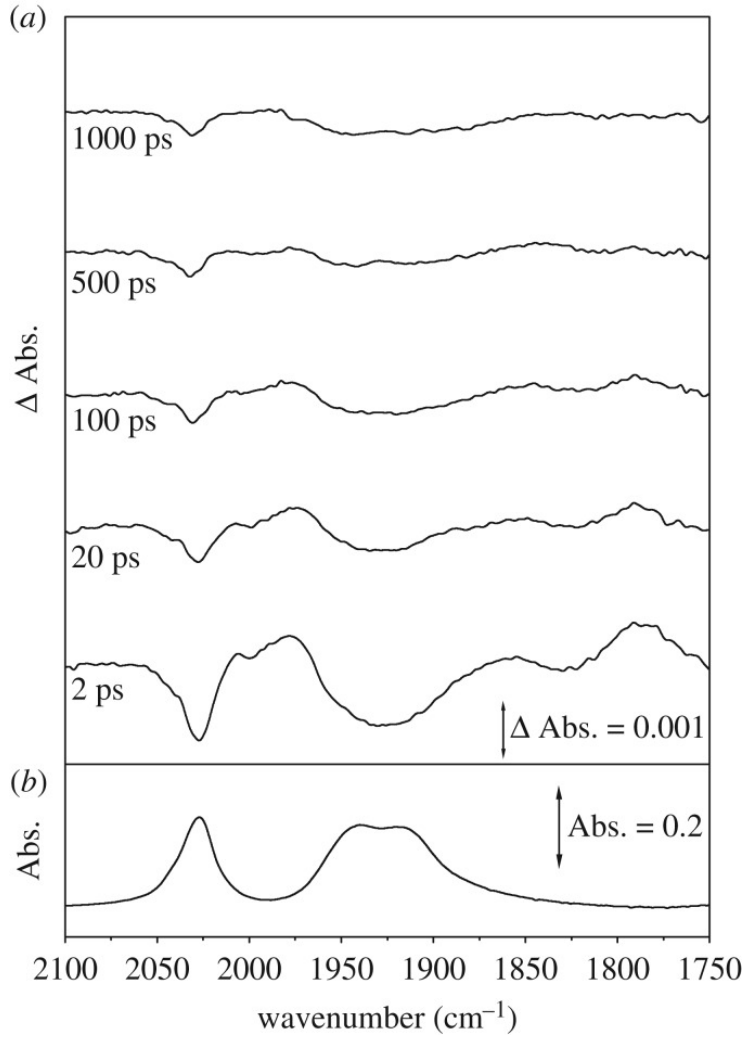


Figure 5.4 *(a) Ps-TRIR of MnMn MOF in a KBr disc, irradiated by 400 nm UV pump; (b) FTIR of MnMn MOF in a KBr disc.*[32]

According to the author, the two bands at 1975 and 1790 cm^{-1} are assigned to the dicarbonyl moiety, $Mn(CO)_2$(diimine)Cl in the MOF framework. Thus, in contrast to the ReMn MOF, for the MnMn MOF, the photo-induced excited state, such as MLCT or IL-$\pi\pi^*$, was not observed. CO-loss dicarbonyl species has been observed to form directly after photolysis, and coordination to the remaining DMF in the MOF channel is suggested.

Apart from investigations on the MnMn MOF, Reade *et al.* has also synthesized MOF materials with similar frameworks to the MnMn MOF, denoted as ReLi MOF (formula: $\{Li_2(DMF)_2[(2,2'\text{-bipy-}5,5'\text{-dicarboxylate})Re(CO)_3Cl]\}_n$) and MnLi MOF (formula: $\{Li_2(DMF)_2\text{-}[(2,2'\text{-bipy-}5,5'\text{-dicarboxylate})Re(CO)_3Cl]\}_n$). For the ReLi MOF, the transformation from ^{3}MLCT to IL $\pi\pi^*$ excited state has been observed after photolysis, similar to the analogue ReMn MOF. However, only a small portion of the ^{3}MLCT has been transformed into the IL $\pi\pi^*$ excited state, and the transformation rate is significantly decreased compared to the ReMn MOF, which may indicate a decreased driving force for the transformation from ^{3}MLCT to IL $\pi\pi^*$ for the ReLi MOF. The properties of the ReLi MOF are more like the discrete complex $Re(CO)_3$(diimine)Cl which often exhibit strong and long-lasting ^{3}MLCT excited state in solvent.

For the MnLi MOF, TRIR shows that after UV irradiation, a dicarbonyl species has been formed, similar to the MnMn MOF. The dicarbonyl species quickly recombines with CO which is unable to escape from the MOF channel. Concurrently, an unknown species has been observed to form along with the decay of the dicarbonyl species and is very stable. The species doesn't decay and remains for the rest of the experimental timescale.

Apart from the MLCT excited states, irreversible charge transfer has also been observed in MOF with similar structure using TRIR.[33] MOFs with the formula $[\{Cu(DMF)(H_2O)[(2,2'\text{-bipyridine-}5,5'\text{-dicarboxylate})\text{-}Re(CO)_3Cl]\}\cdot DMF]_\infty$ synthesised from $Re(CO)_3$(2,2'-bipyridine-5,5'-dicarboxylate)Cl as bridging ligands and Cu(II) as nodes. It is found that using UV irradiation, electron transfer from Re(I) to Cu(II) can occur, leaving Re(II) and Cu(I), and the electron transfer process is irreversible.

M-(poly-pyrazol) complexes, with structure similar to the M-diimine complexes, however have very different properties. Compared to the M-diimine complexes, research on transition-metal complexes coordinate to the poly-pyrazol ligands (TM-(poly-pyrazol) complexes) is relatively rare. Nevertheless, M-(poly-pyrazol) complexes have still attracted plenty of attention since the first synthesis of

poly(pyrazol-1-yl)borate ligands by Trofimenko *et al.* in 1960s.[34] Poly(pyrazol-1-yl)alkane ligands are isoelectronic and isosteric with the poly(pyrazol-1-yl)borate ligands which have also drawn much attention. Specifically, TM-bis(pyrazol-1-yl)methane complexes have been the focus of much research recently. They have potential applications in many fields. For example, electrochemical devices,[35] catalysis,[36] medical application.[37] The structure is shown in Figure 5.5.

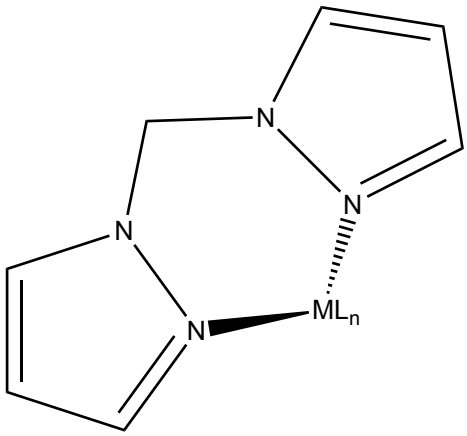


Figure 5.5 *Structure of the M-bis(pyrazol-1-yl)methane complex.*

Transition metal complexes with bis(pyrazol-1-yl)methane ligands are very different from the well-known similar TM-diimine complexes due to the structural differences. When diimine ligands such as bi-pyridine or phen ligands coordinate to a metal centre, a planar five-membered -M-N-C-C-N ring is formed, while for the bis(pyrazol-1-yl)methane ligands, usually a six-membered -M-N-N-C-N-N ring of a boat configuration is formed. Nevertheless, many studies suggest that the derivative ligands are flexible and are not necessarily in the boat configurations. Many other configurations such as the chair configuration or even the planar configuration for derivatives M-(N-N)$_2$-E (E is not carbon) have been discovered.[38,39]

Bis(pyrazol-1-yl)methane ligands are proved to be capable of binding to both early and late transition metals.[40,41] However, research on bis(pyrazol-1-yl)methane ligands coordinating to group seven metals are rare. Reger *et al*. has synthesized a series of derivatives of (1-pyrenyl)pyrazol ligands and complex Re(CO)$_3${1,1'-

bis[3-(1-pyrenyl)pyrazolyl]butane}Br, and analysed their structures and photophysical properties using X-ray, NMR, Electronic Spectroscopy, *etc*.[42] In the absorption spectra of the (1-pyrenyl)pyrazol ligand, an absorption band has been found centred near 280 nm, and is assigned to a pyrazol-based $\pi-\pi*$ transition, which is typical for the N-heterocyle ligands.[43] While for the Re-complexes with the bis-(1-pyrenyl)pyrazol ligands, absorption spectra show that, similar to the individual (1-pyrenyl)pyrazol ligands, pyrenyl-based and pyrazol-based $\pi-\pi*$ transition have been observed, while no MLCT absorption has been observed. This is different to most of the Re-diimine complexes, of which the MLCT state is the most typical excited state upon UV photolysis. And many other TM-(bis-pyrazol) complexes have also been found to generate non-MLCT states upon irradiation.[44,45] This might be the result of the structural difference. As for the Re-(bis-(1-pyrenyl)pyrazol) complexes, the N-heterocycle ring may not be in a planar configuration, thus may cause difficulty for electron flow from the Re centre to the pyrazol ligand. It is also interesting to note that, unlike most of the Re-diimine complexes, the Re-bis(1-pyrenyl)pyrazol complexes are non-emitting (Figure 5.6).

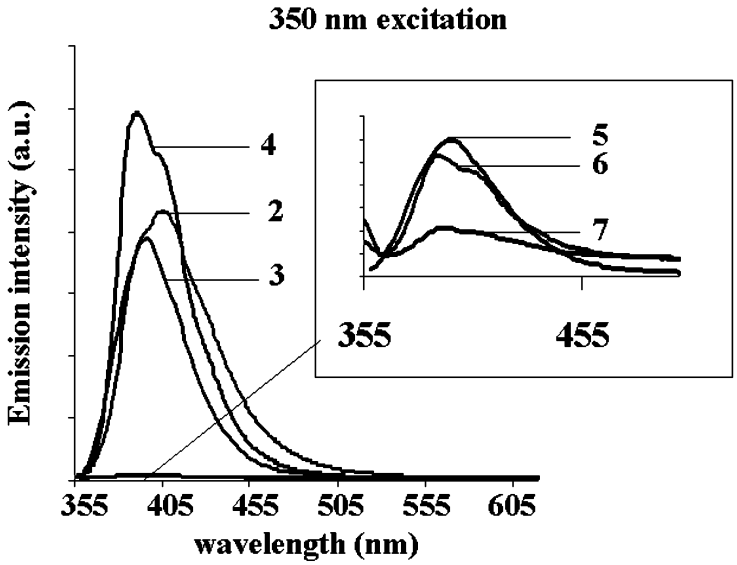


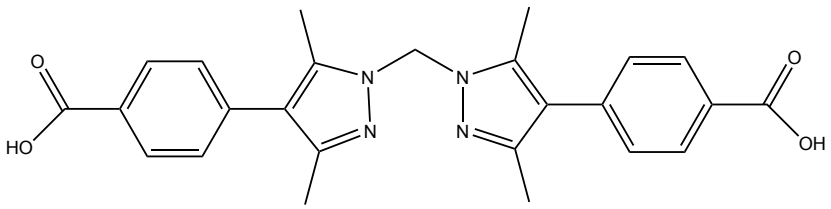
Figure 5.6 *Emission Spectra of a series of (1-pyrenyl)pyrazol ligand derivatives 2-4 and Re-bis(1-pyrenyl)pyrazol complexes 5-7. (2: 3(5)-(1-pyrenyl)pyrazole; 3: α-α'-bis[(1-pyrenyl)pyrazol-1-yl]butane; 4: 1,1'-bis[3-(1-pyrenyl)pyrazol-1-yl]butane; 5: $Re(CO)_3${α-α'-bis[3-(1-pyrenyl)pyrazol-1-yl]methane}Br; 6: $Re(CO)_3${1-1'-bis[3-(1-pyrenyl)pyrazol-1-yl]butane}Br; 7: $Re(CO)_3${2-2'-bis[3-(1-pyrenyl) pyrazol-1-yl]propane}Br).*[42]

As shown in Figure 5.6, compared to the (1-pyrenyl)pyrazol derivatives 2-4, the emissions of the Re-bis(1-pyrenyl)pyrazol complexes are nearly zero. NMR results indicate that, in tetrachloroethane, the Re-bis(1-pyrenyl)pyrazol complexes 5-7 are monomeric, thus the quenching is *via* an intramolecular pathway. Also, the recovery of the fluorescence cannot be achieved *via* the removal of the Br^- ligand. Thus, the quenching may be caused by coordination to the Re centre.

Similar phenomenon has been observed by Machura *et al.*[46] Machura and co-workers have synthesized the $Re(CO)_3$[bis(3,5-dimethyl-pyrazol-1-yl)methane]Cl (denoted as $Re(CO)_3$(bdmpzm)Cl) and the $Re(CO)_3$-[(pyrazol-1-yl)methane]Cl (denoted as $Re(CO)_3$(bpzm)Cl) complexes, and have analyzed their structures and properties using X-Ray, Spectroscopic techniques, DFT calculations, *etc*. Interestingly, they found that $Re(CO)_3$(bdmpzm)Cl is non-emitting, similar to the Re-bis(1-pyrenyl)pyrazol complexes discussed before. However, most Re-diimine complexes are luminescent, most of which has typical MLCT states. Machura *et al.* also predicted that a CO-loss species $Re(CO)_2$(bdmpzm)Cl is expected to form upon UV irradiation for the $Re(CO)_3$(bdmpzm)Cl complex, based on the DFT calculations.

In this work, we wish to use MOF frameworks as scaffolds to investigate the photoproperties of M-(bis-pyrazol) complexes, $M(CO)_3$(bdmpzm)X (M: Mn, Re; X: Cl, Br) within MOF structures. The MOFs have been synthesized by our collaborators from University of Adelaide. The details of the MOF frameworks will be discussed in the following section.

Bloch *et al.* successfully synthesized a MOF framework with bis(4-(4-carboxyphenyl)-1*H*-3,5-dimethylpyrazolyl)methane) as the linker ligand (denoted as LH_2 ligand),[47] the structure is shown in Figure 5.7.



LH_2

Figure 5.7 *Structure of the bis(4-(4-carboxyphenyl)-1H-3,5-dimethylpyrazolyl)-methane) ligand, denoted as LH_2, reproduced from Ref. 47.*

It is found that the vacant MOF structure without metalation is highly flexible, evidenced by gas absorption and XRD, as shown in Figure 5.8. The LH_2 ligand can bend when the MOF structure is dehydrated or degassed.

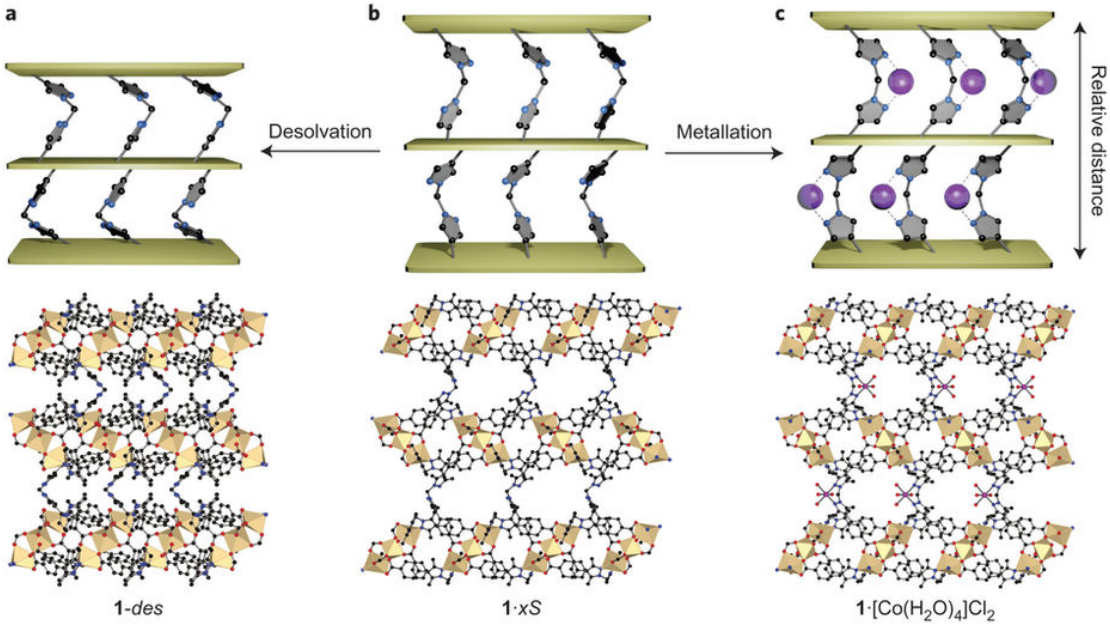


Figure 5.8 *The flexibility of the MOF structure synthesized by Sumby et. al. upon desolvation, and the post-synthesis metalation. 1 represents the un-metalized MOF scaffold.*[47]

XRD result reveals that upon desolvation, the pillaring ligand LH_2 undergoes a dramatic torsional rotation, which results in a significant acute bridging angle of 97.5° compared to 105.1° before desolvation. Thus, the two-dimensional planes are contracted (Figure 5.8). This is ascribed by Bloch *et al.* to the inherent flexibility of the non-coordinated LH_2 ligand between the two-dimensional planes in the MOF structure.

The flexibility of the LH_2 ligand is also supported by the N_2 absorption isotherm experiment, as shown in Figure 5.9.

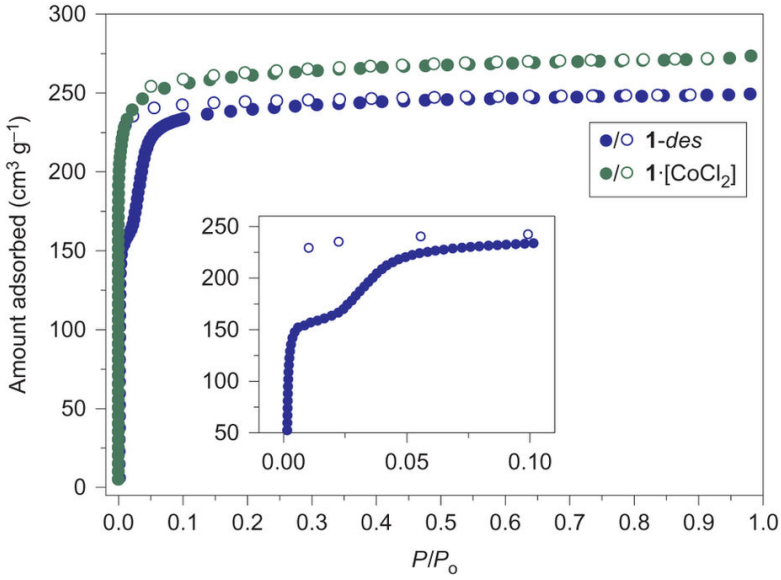


Figure 5.9 *N_2 absorption isotherm of 1-des (desolvated) and 1·[$CoCl_2$] (metalised by $CoCl_2$). 1 represents the un-metalized MOF scaffold.*[47]

The step of absorption between P/P_0 of *ca.* 0.005-0.06 of the un-metalised MOF 1-des (1 represents the un-metalised MOF scaffold; des: desolvated) indicates an enlargement of the pore size, which is consistent with the expanding of the MOF with the intrusion of N_2. This also reflects the flexibility of the un-metalised MOF structure. For the CoMOF 1·[$CoCl_2$], in which the MOF structure 1 is coordinated to the Co ions, the step in the low P/P_0 region is not observed. This indicates the transformation from a flexible structure to a rigid structure after metalation.

Metalation of the MOF structure 1 has been completed using post-synthesis method. Several metal ions have been used, Cu, Co, Zn, Rh and Cd. PXRD indicates that the crystallinity of the MOF structure is remained, and the metalation yield is quantitative for all metalation reactions.

Interestingly, it is found that the crystal of the CoMOF 1·[$Co(H_2O)_4$]Cl_2 at room temperature is pink, while after heating or being immersed in neat MeCN, the crystal turns into blue. This colour transformation is well known in Co(II) chemistry

and is associated with the ligand field geometry change from O_h to T_d. SCXRD reveals that in the pink crystal, Co is coordinated to 4 H_2O molecules as well as the LH_2 ligand, and is denoted as $1{\cdot}[Co(H_2O)_4]Cl_2$, where 2 Cl^- anions are in the outside pores of the MOF. While in the blue crystal, Co is coordinated to 2 Cl^- which migrate from the pores to the Co centre. The blue crystal turns into pink when exposed in the air at room temperature after few minutes. Elemental analysis confirmed the coordination of 4 H_2O molecules in the pink crystal transformed from the blue crystal. The transformation process is shown in Figure 5.10.

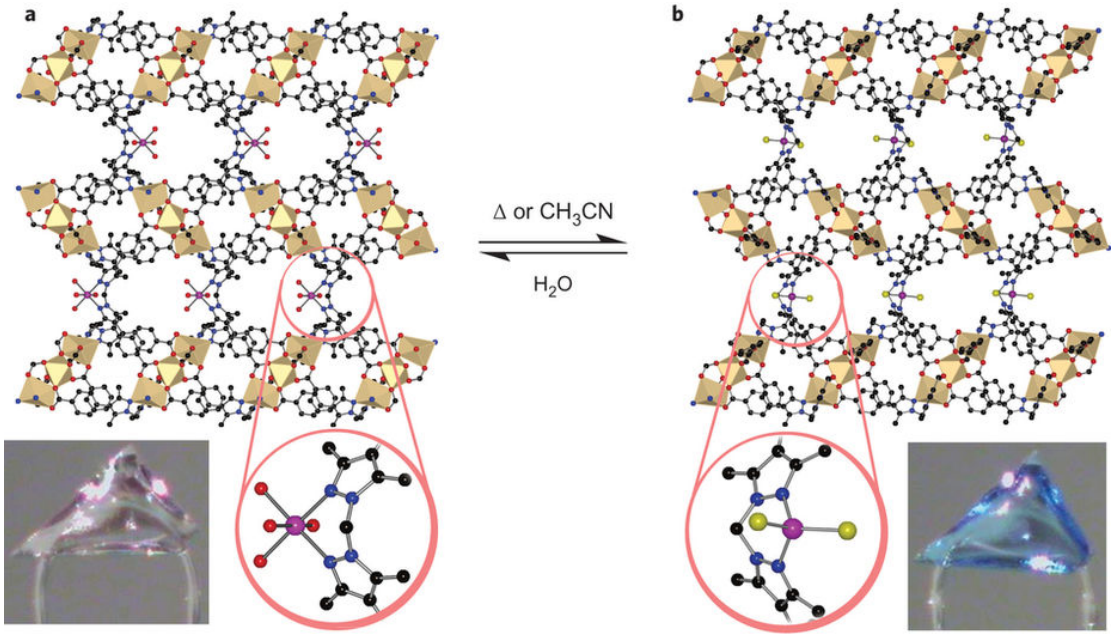


Figure 5.10 *The reversible transformation process from a: Co-MOF with Co(bdmpzm)(H₂O)₄Cl₂ as the linker, to b: the dried Co-MOF with Co(bdmpzm)Cl₂ as the linker when immersed in MeCN or by heating. The wet Co-MOF crystal at room temperature is observed as a pink crystal which turns into blue when immersed in MeCN or upon heating, and the color transformation is observed to reverse when the MOF crystal is exposed to air or cooled down to room temperature. The transformation process is also evidenced by spectroscopy results.*[47]

This may also indicate that the pores of the MOF structure are not large enough for intrusion of molecules bigger than H_2O such as MeCN. As if the MeCN can successfully intrude the MOF channels, it is expected that MeCN could bind to the un-coordinated Co centre after photolysis.

In our work, the same MOF framework is metalized using post-synthesis method with Re and Mn ions, with $M(CO)_3$(bdmpzm)X (M: Re, Mn; X: Cl (Re only), Br) as the target complexes for investigation. We wish to investigate both the photophysical and photochemical properties of these target complexes as linkers within the MOF scaffolds, and also whether the size of the MOF channels will have an effect on the photoreactions.

5.2 Result and Discussion

5.2.1 TRIR of the Re Linker Complex

In order to better understand the photoproperties of the Re-MOF, TRIR of the photosensitive linker complex – $Re(CO)_3(bdmpzm)Cl$ has been conducted (bdmpzm: bis(3,5-dimethyl-pyrazol-1-yl)methane). Two solvents with different polarities– DCM (ε : 8.93) and MeCN (ε : 37.5) have been used in order to investigate the coordination abilities of the solvents and polarity effects on the photoproperties of the $Re(CO)_3(bdmpzm)Cl$ linker complex. The TRIR spectra obtained in CH_2Cl_2 are shown in Figure 5.11.

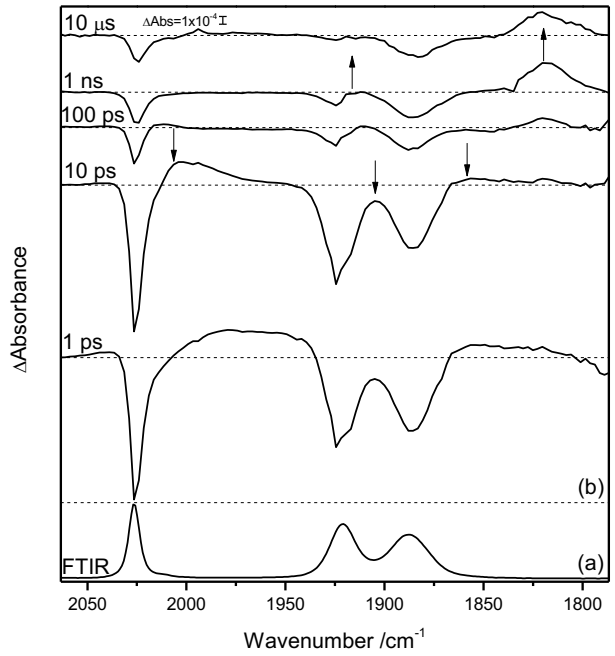


Figure 5.11 *(a) FTIR spectrum and (b) TRIR spectra obtained following photolysis (266 nm) of $Re(CO)_3(bdmpzm)Cl$ in CH_2Cl_2.*

As shown in Figure 5.11, after UV photolysis, the parent bands are instantly bleached within a few ps, two broad features at *ca.* 1980 and 1850 cm^{-1} are also formed. These bands then narrow and blue-shift to higher wavenumbers within 15 ps. It is also observed that a band at *ca.* 1905 cm^{-1} is appearing simultaneously for 11 (±2) ps. The band positions are obscure either due to weak intensity or overlap

with the parent bleaches. Thus, Lorentzian curve fitting are conducted for the time delay of 50 ps, as shown in Figure 5.12.

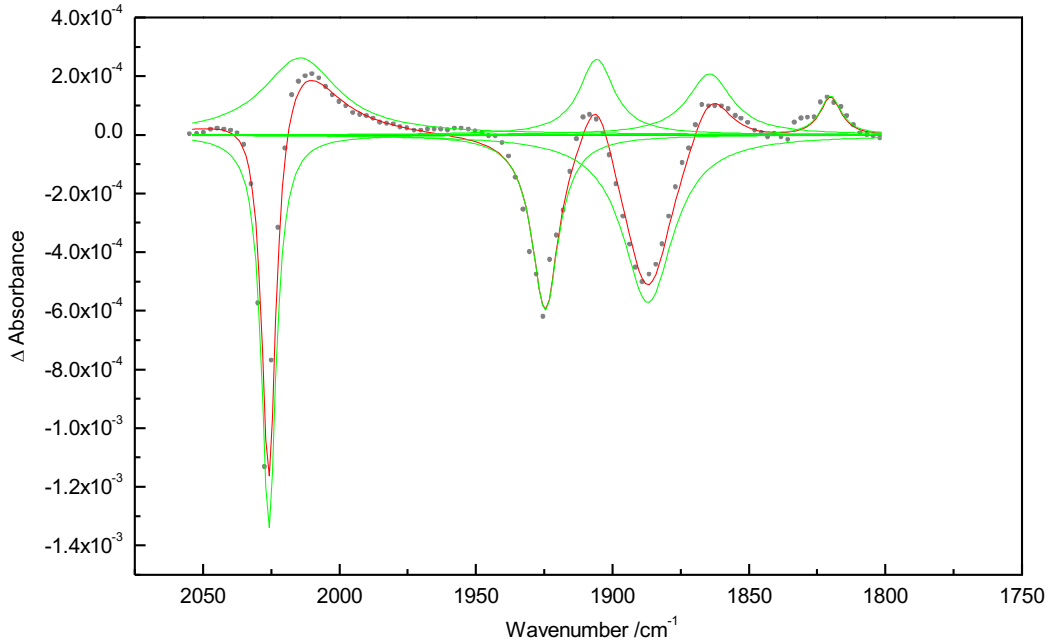


Figure 5.12 *Lorentzian curve fitting of 50 ps time delay in CH_2Cl_2.*

From Figure 5.12 it can be clearly observed that, in 50 ps, three bands at slightly lower wavenumber compared to the parent bands (2026, 1925, 1887 cm^{-1}) at *ca.* 2014, 1906 and 1864 cm^{-1} are formed. Kinetic analysis reveals the formation rate of this species to be 14 (±2) ps, consistent with the decay rate of the vibrational hot bands (*ca.* 1980 and 1850 cm^{-1}) for 13 (±2) ps. Together with the formation of these three bands, another band at *ca.* 1820 cm^{-1} can also be observed. Lifetime of the bands at 2014, 1906 and 1864 cm^{-1} is *ca.* 60 ps, which is consistent with the recovery rate of the parent bands (57 ±4 ps, 90% recovery), as shown in Figure 5.13.

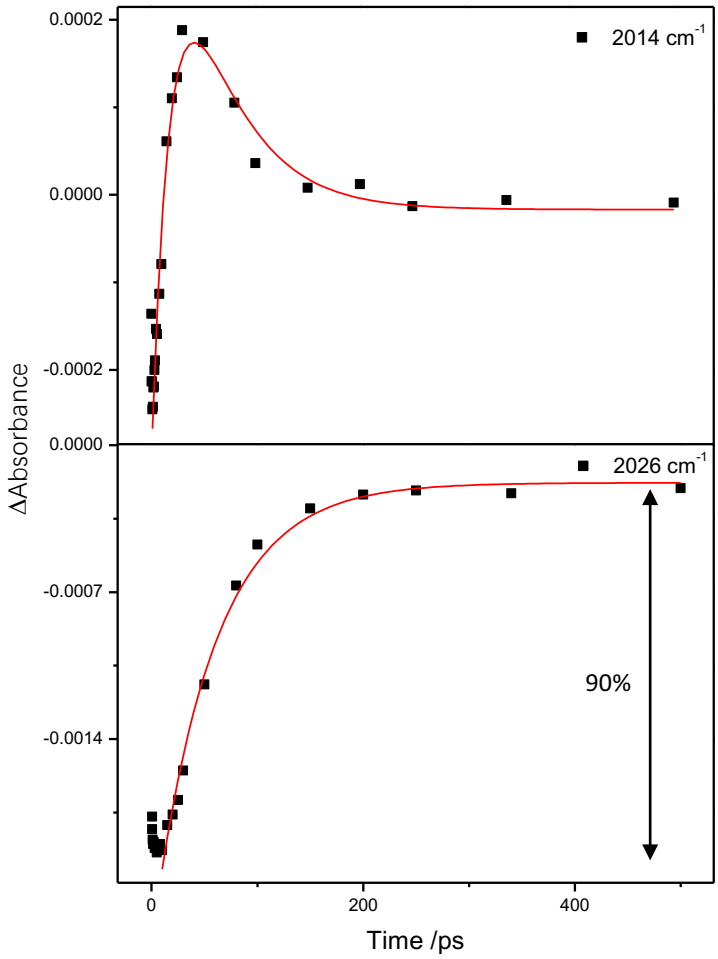


Figure 5.13 *TRIR kinetic traces obtained at 2026 and 2014 cm^{-1} corresponding to the parent band and the π–π* excited state.*

The slight red-shift of the bands at 2014, 1906 and 1864 cm^{-1} compared to the parent bands, and the fact that the lifetimes of these bands are within 100 ps are all typical features of a π–π* excited state. Thus, here the bands at 2014, 1906 and 1864 cm^{-1} are assigned to the π–π* excited state. The 90% recovery of the parent bleach indicates that 90% of the activated parent complex has turned to the π–π* excited state upon photolysis.

Also, it can be observed from Figure 5.11 that two other bands at *ca.* 1820 cm^{-1} and another one between the parent bleaches (1925 and 1887 cm^{-1}) are formed, and the band at 1820 cm^{-1} is also shown in the Lorentzian fitting curve in Figure 5.12. As can be observed from Figure 5.11, the band between the two parent

bleaches (1925, 1887 cm^{-1}) is obscured due to overlap with the two parent bleaches as well as the π–π^* excited state on the early ps-timescale. Thus, Lorentzian curve fitting are also conducted for the later time delay of 10 ns, as shown in Figure 5.14.

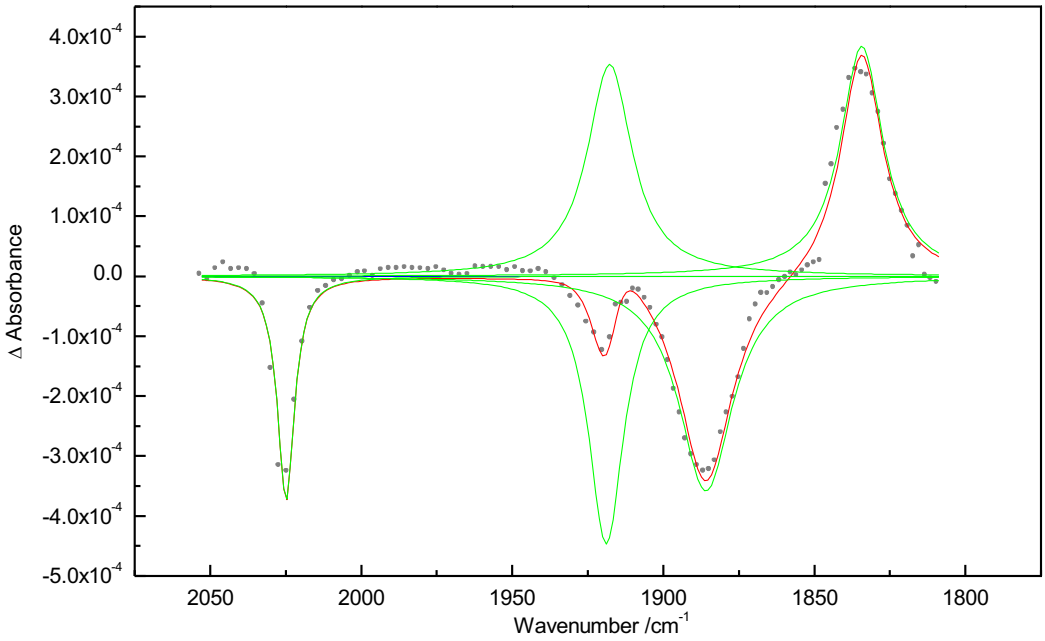


Figure 5.14 *Lorentzian curve fitting of 10 ns time delay in CH_2Cl_2.*

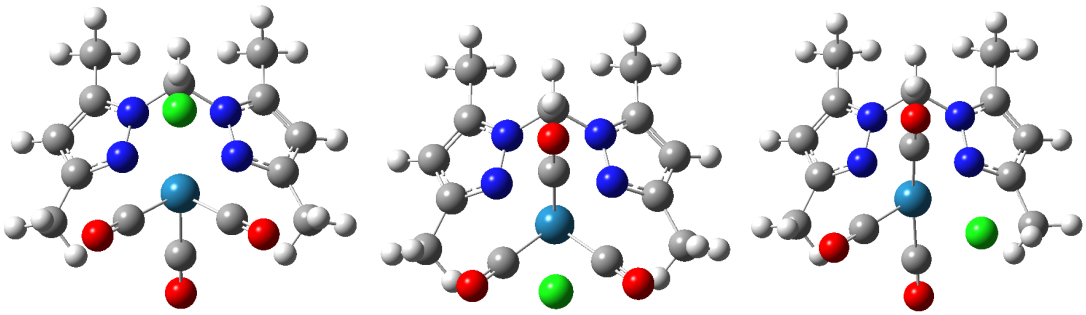
As shown in Figure 5.14, the original TRIR spectrum (red line) shows that the parent band at *ca.* 1925 cm^{-1} is relatively weak, which is different from the FTIR shown in Figure 5.11. Therefore it is proposed that there may be a band overlapped at this position, as revealed by the Lorentzian curve fitting shown in Figure 5.14 at *ca.* 1918 cm^{-1}.

Machura *et. al.* has performed DFT calculations on $Re(CO)_3(bdmpzm)Cl$[46] and suggested that $Re(CO)_3(bdmpzm)Cl$ is expected to lose CO upon UV irradiation, and undergo ligand substitution reaction in solvents. DFT calculations have also been conducted for assisting the assignment, the results are summarized in Table 5.1.

Table 5.1 *DFT calculations for the $Re(CO)_3$(bdmpzm)Cl species with and without solvation of DCM (B3LYP, 6-31G(d), gas phase).*

Species	DFT IR frequency	IR intensity /x10^3 Km mol^{-1}	Energy /a.u.
*fac*1	2108, 2032, 1993	0.689, 0.972, 0.944	-1527.2582
*fac*1 loss CO at axial	2026, 1951	0.990, 0.938	-1413.8662
*fac*1 loss CO at axial (DCM)	2020, 1952	0.768, 0.951	-2373.5707
*fac*1 loss CO at equatorial	2026, 1951	0.990, 0.938	-1413.8662
*fac*1 loss CO at equatorial (DCM)	2020, 1952	0.768, 0.952	-2373.5707
*fac*2	2107, 2032, 1989	0.742, 0.949, 0.941	-1527.2566
*fac*2 loss CO at axial	2025, 1945	0.983, 0.947	-1413.8623
*fac*2 loss CO at axial (DCM)	2024, 1957	0.996, 0.942	-2373.5540
*fac*2 loss CO at equatorial	2025, 1945	0.983, 0.947	-1413.8623
*fac*2 loss CO at equatorial (DCM)	2027, 1921	0.829, 0.869	-2373.5620
mer	2117, 2019, 2013	0.202, 1.74, 0.835	-1527.2218
mer loss CO at axial 1	2026, 1951	0.990, 0.938	-1413.8662
mer loss CO at axial 1 (DCM)	2020, 1952	0.768, 0.951	-2373.5707
mer loss CO at axial 2	2025, 1945	0.983, 0.947	-1413.8623
mer loss CO at axial 2 (DCM)	2023, 1923	0.918, 0.856	-2373.5636
mer loss CO at equatorial	2074, 1971	0.071, 2.00	-1413.8237
mer loss CO at equatorial (DCM)	2073, 1970	0.076, 1.86	-2373.5241

For the $Re(CO)_3$(bdmpzm)Cl complex, three configurations have been calculated, denoted as the *fac*1, *fac*2 and *mer*-isomers, as shown in Figure 5.15.



(a) (b) (c)

Figure 5.15 *Structure scheme of (a) fac1- (b) fac2- and (c) mer-isomers of* $Re(CO)_3(bdmpzm)Cl$.

As shown in Figure 5.15, as the bdmpzm ligand is not planar, based on the position of Cl^-, (a) is denoted as the *fac*1-isomer and (b) is denoted as the *fac*2-isomer. When Cl^- is located at the equatorial position, it is denoted as the *mer*-isomer as shown in (c).

IR frequency calculations on the CO-loss dicarbonyl species have been conducted (Table 5.1). All species are named based on the position of the lost CO. For example, *fac*1 loss CO at axial means this dicarbonyl species is formed from the *fac*1-isomer which lose one CO at the axial position. Considering that in DCM, the unsaturated dicarbonyl species should coordinate to solvent, thus DFT calculations on the solvated species have also been conducted (Table 5.1). The overall calculated spectra are shown in Figure 5.16.

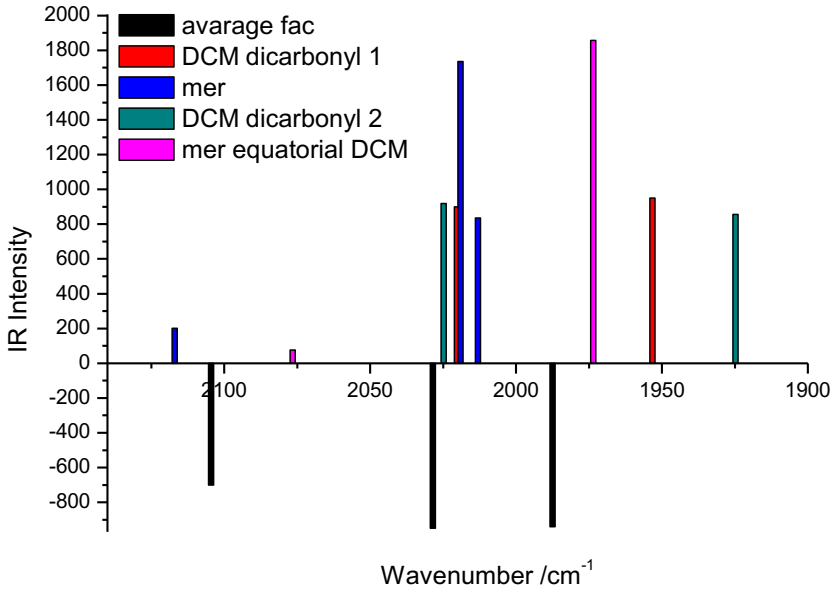


Figure 5.16 *Spectra calculated by DFT (B3LYP, 6-31G(d)) of $Re(CO)_3(bdmpzm)Cl$ in DCM. Average fac represents the average ν(CO) of fac1 and fac2; DCM dicarbonyl 1 represents the average ν(CO) of the DCM-bound dicarbonyls at ca. 2022, 1955 cm^{-1}; DCM dicarbonyl 2 represents the average ν(CO) of the DCM-bound dicarbonyls at ca. 2025, 1922 cm^{-1}; mer equatorial DCM represents the DCM-bound mer-dicarbonyl species which loses one CO at the equatorial position.*

As shown in Figure 5.16, the ν(CO) positions of the solvated species *fac*-$Re(CO)_2(bdmpzm)Cl(DCM)$ is consistent with the TRIR spectra shown in Figure 5.11 and 5.14. Thus, the bands at 1918 and 1820 cm^{-1} are tentatively assigned to the solvated species $Re(CO)_2(bdmpzm)Cl(CH_2Cl_2)$. The *mer*-isomers are not expected to form according to the DFT calculations (Figure 5.16). The solvated species $Re(CO)_2(bdmpzm)Cl(CH_2Cl_2)$ may be transformed directly from the cooling of the vibrationally hot $Re(CO)_2(bdmpzm)Cl(CH_2Cl_2)$*, evidenced by the kinetic plots (Figure 5.17). As shown in Figure 5.17, the bands at 1918 and 1820 cm^{-1} are observed to form at similar rate to the decay of the vibrational hot bands at 12 (± 2) ps. Furthermore, no decay of $Re(CO)_2(bdmpzm)Cl(CH_2Cl_2)$ is observed during the experimental timescale (up to 500 μs).

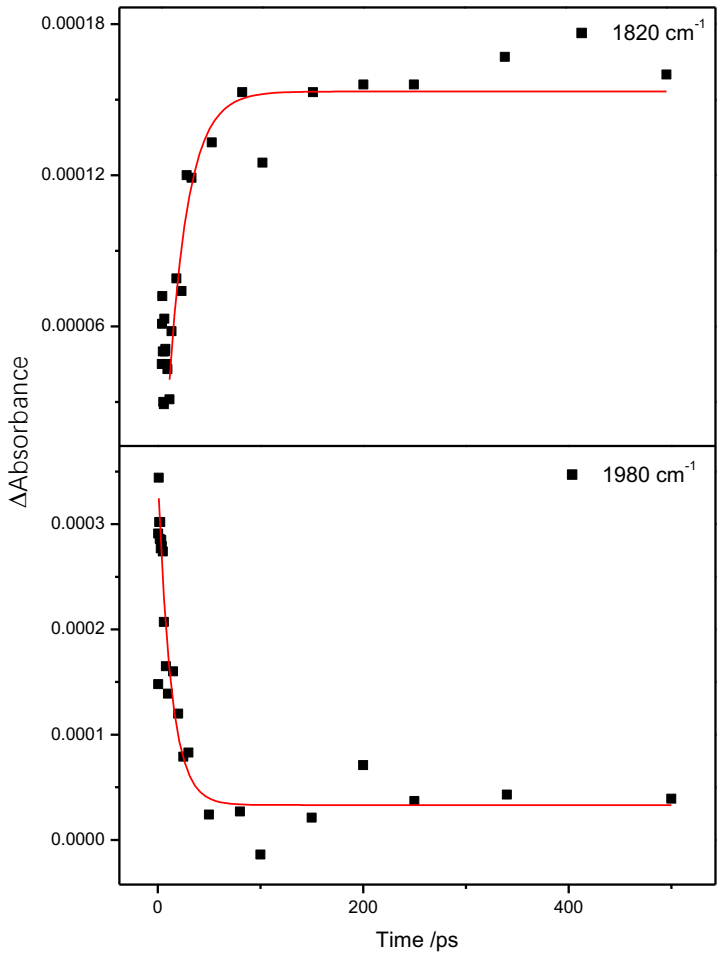


Figure 5.17 *TRIR kinetic traces obtained at 1980 and 1820 cm^{-1} corresponding to the vibrational hot state and the solvated species $Re(CO)_2(bdmpzm)Cl(CH_2Cl_2)$.*

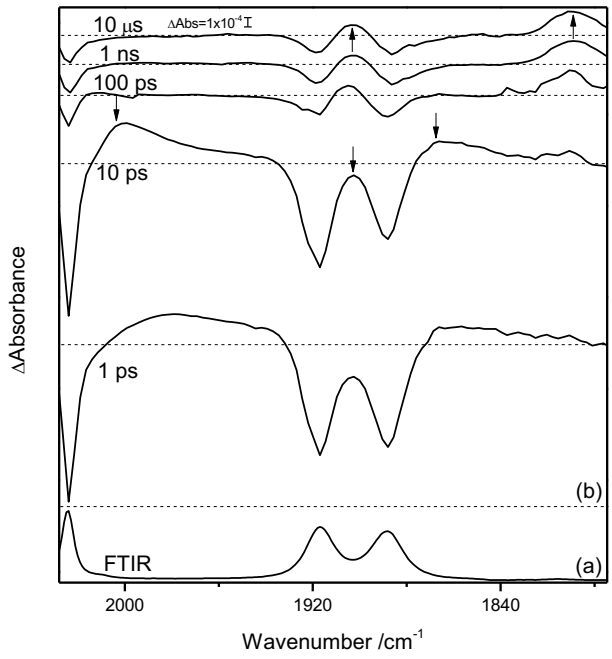


Figure 5.18 *(a) FTIR spectrum and (b) TRIR spectra obtained following photolysis (266 nm) of $Re(CO)_3(bdmpzm)Cl$ in CH_3CN.*

Similar to TRIR in CH_2Cl_2, in CH_3CN after UV photolysis, the formation of two broad hot features at *ca.* 1980 and 1860 cm^{-1} is also observed (Figure 5.18), which then narrow and blue-shift to four bands at *ca.* 2013, 1904, 1874 and 1810 cm^{-1}, as shown more clearly in the Lorentzian curve fitting in Figure 5.19.

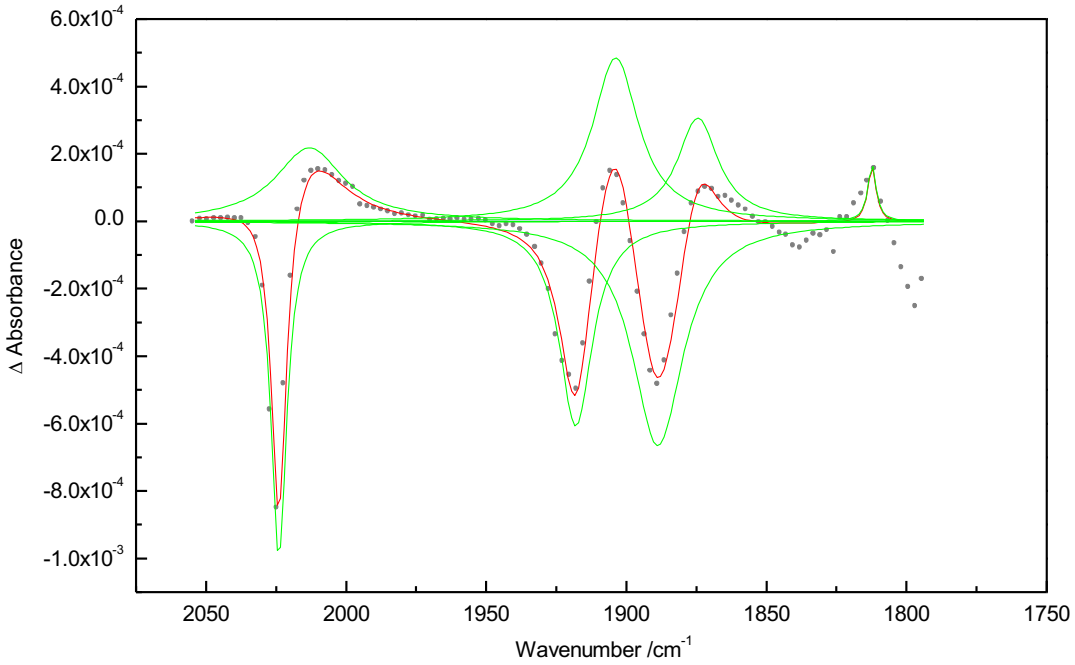


Figure 5.19 *Lorentzian curve fitting of 50 ps time delay in MeCN.*

Similar to that observed in CH_2Cl_2, as the Lorentzian fitting indicates, upon UV photolysis, three bands are found at slightly lower wavenumber than the parent bleaches. These bands are assigned to the π–π^* excited state. Meanwhile, the formation of a band at *ca.* 1810 cm^{-1} is observed.

Kinetic analysis suggests that the formation of the π–π^* excited state is consistent with the decay of the vibrational hot bands at 16 (± 2) ps, similar to that observed in CH_2Cl_2. The decay rate of the π–π^* excited state is also observed to be consistent with the recovery rate of the parent bands (90% recovery) at similar rate to that observed in CH_2Cl_2 (*ca.* 60 ps), as shown in Figure 5.20.

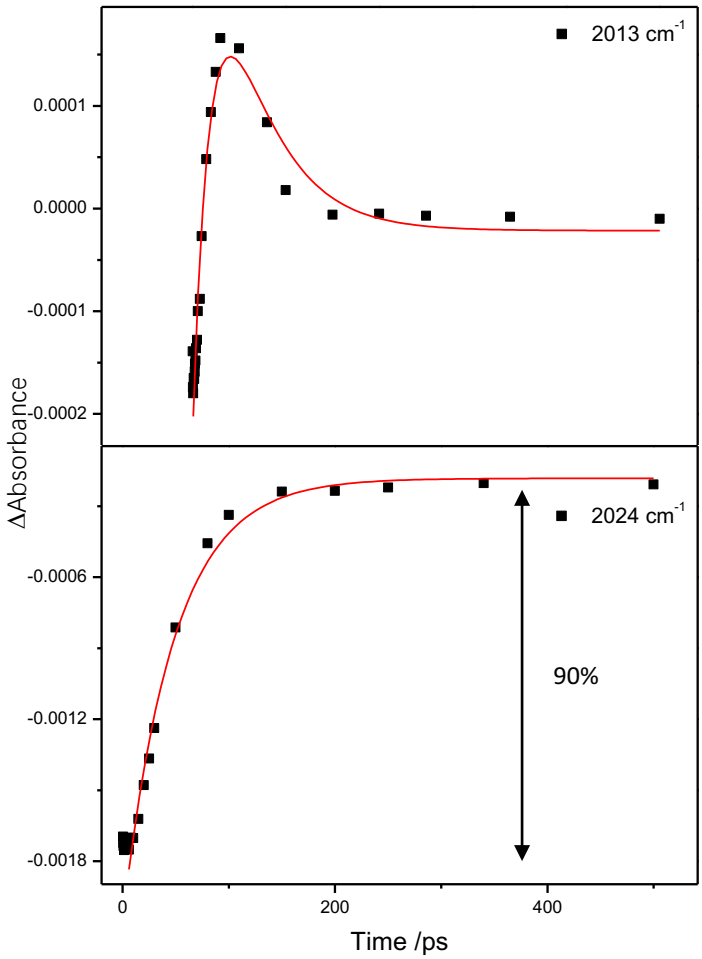


Figure 5.20 *TRIR kinetic traces obtained at 2024 and 2013 cm^{-1} corresponding to the parent band and the* π–π* *excited state.*

Similar to the experiment in CH_2Cl_2, as can be observed in Figure 5.18, two other bands at *ca.* 1903 and 1810 cm^{-1} are also observed to form, and the band at 1810 cm^{-1} is also shown in the Lorentzian fitting curve in Figure 5.19. Considering that the band at 1903 cm^{-1} may have overlapped with the parent band bleaches as well as the π–π* excited state on the ps-timescale, therefore, Lorentzian curve fitting of 10 ns time delay has also been conducted, as shown in Figure 5.21.

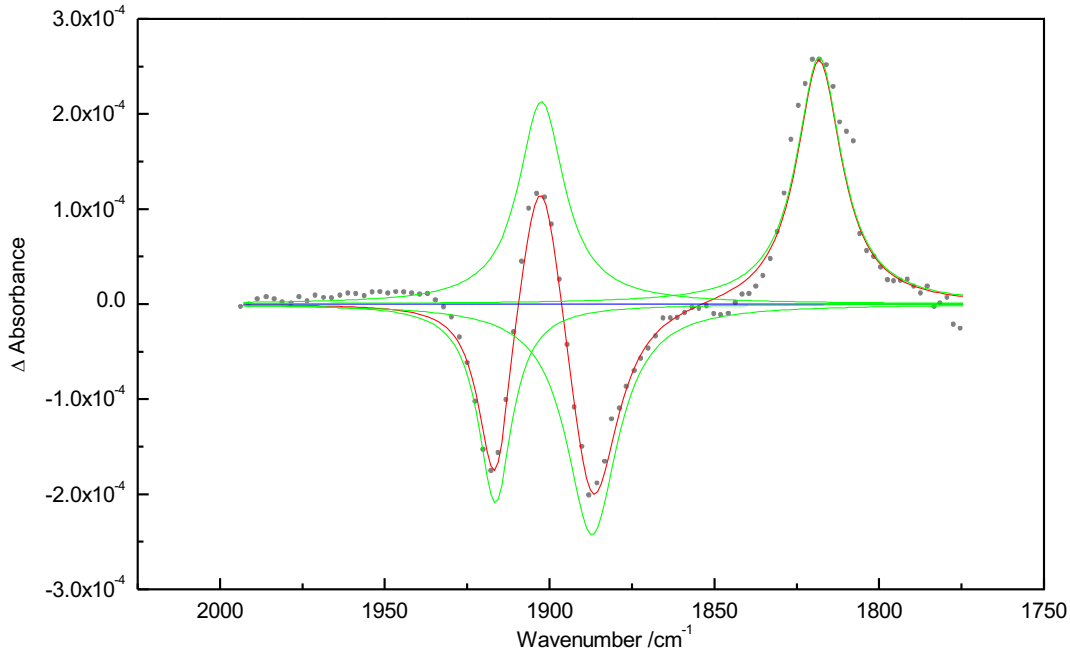


Figure 5.21 *Lorentzian curve fitting of 10 ns time delay in MeCN.*

Similar to that observed in CH_2Cl_2, here the bands at 1903 and 1810 cm^{-1} are assigned to the solvated species $Re(CO)_2$(bdmpzm)Cl(MeCN). The DFT calculations are shown in Table 5.2. The $\Delta\nu$(CO) of *fac*-$Re(CO)_2$(bdmpzm)Cl(MeCN) compared to the parent bands by DFT is consistent with the TRIR spectra (Figure 5.18). It is interesting to note that, the ν(CO) band positions of *fac*-$Re(CO)_2$(bdmpzm)Cl(MeCN) are slightly blue-shifted compared to *fac*-$Re(CO)_2$(bdmpzm)Cl(DCM) (Table 5.1), which is in contrast to the TRIR spectra.

Kinetic analysis shows that, the formation rate of $Re(CO)_2$(bdmpzm)Cl(MeCN) is consistent with the decay rate of the vibrational hot bands at 16 (± 4) ps, as shown in Figure 5.22.

Table 5.2 *DFT calculations for the $Re(CO)_3(bdmpzm)Cl$ species with solvation of MeCN (B3LYP, 6-31G(d), gas phase).*

Species	DFT IR frequency	IR intensity /x10^3 Km mol^{-1}	Energy /a.u.
fac1 loss CO at axial (MeCN)	2028, 1952	0.870, 0.952	-1546.6615
fac1 loss CO at equatorial (MeCN)	2028, 1952	0.870, 0.953	-1546.6615
fac2 loss CO at axial (MeCN)	2019, 1966	1.14, 1.04	-1546.6424
fac2 loss CO at equatorial (MeCN)	2026, 1947	0.902, 0.954	-1546.6597
mer loss CO at axial 1 (MeCN)	2028, 1952	0.870, 0.953	-1546.6615
mer loss CO at axial 2 (MeCN)	2026, 1947	0.902, 0.954	-1546.6597
mer loss CO at equatorial (MeCN)	2074, 1978	0.058, 1.91	-1546.6155

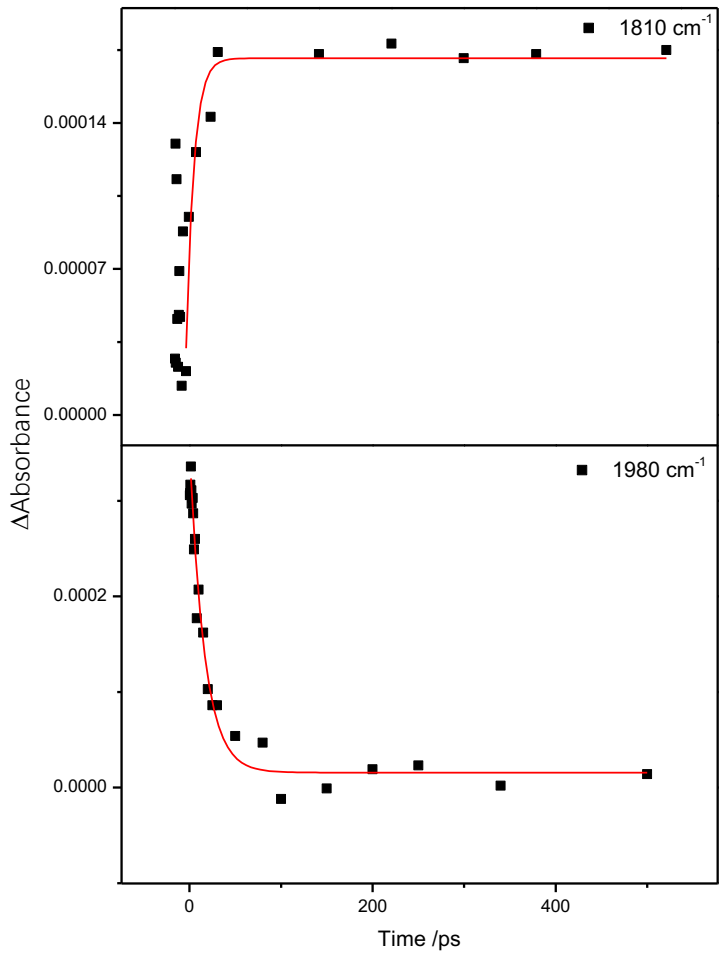


Figure 5.22 *TRIR kinetic traces obtained at 1980 and 1810 cm^{-1} corresponding to the vibrational hot state and the solvated species $Re(CO)_2(bdmpzm)Cl(MeCN)$.*

Based on the discussion, the mechanism of $Re(CO)_3(bdmpzm)Cl$ in both solvents, CH_2Cl_2 and MeCN, can be described in the following scheme (Figure 5.23).

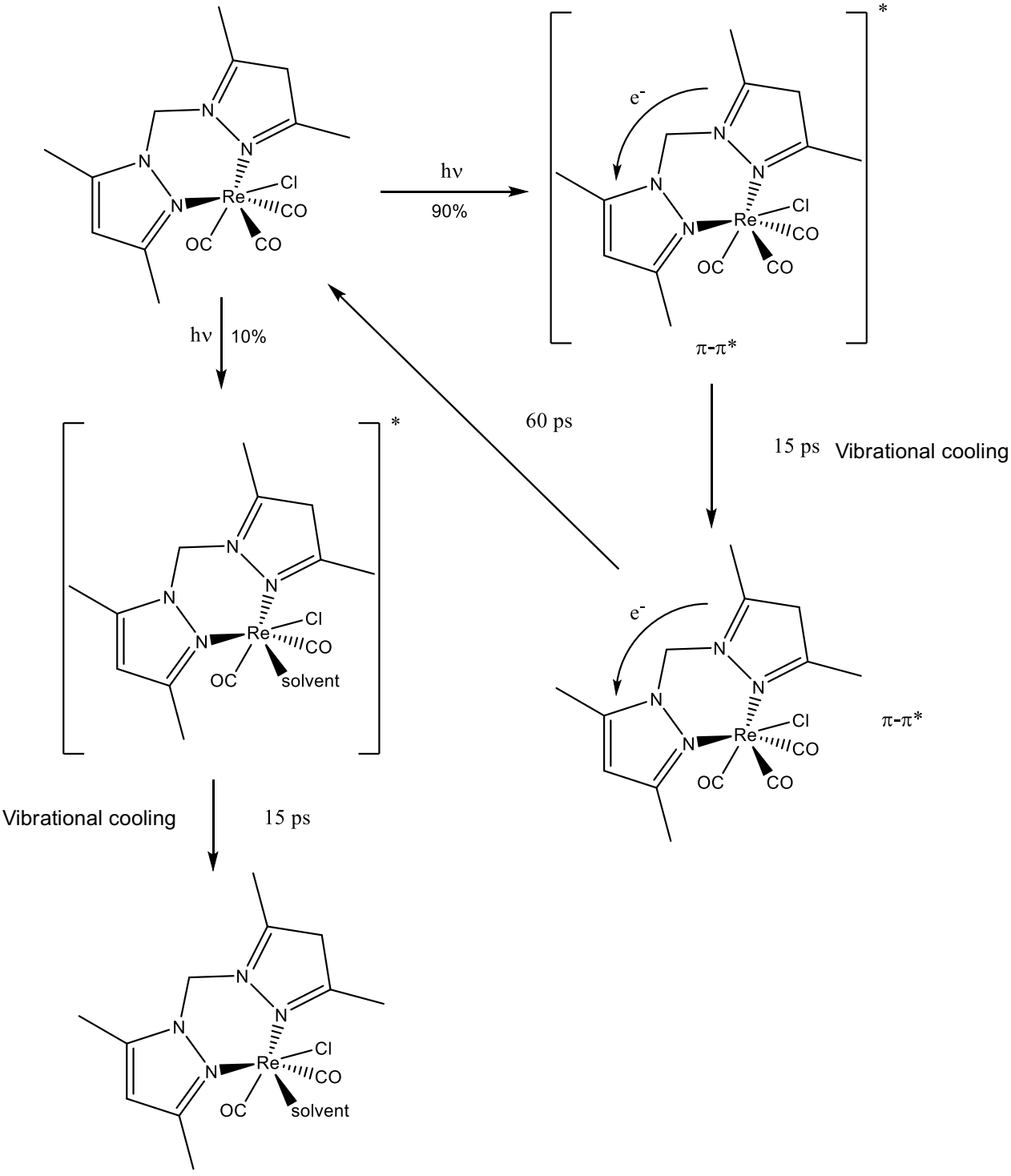


Figure 5.23 *Reaction mechanism of $Re(CO)_3(bdmpzm)Cl$ in both solvents, CH_2Cl_2 and MeCN. * indicates the vibrational hot state.*

The overall data is summarized in Table 5.3. As the data suggests, the lifetime of

the π–π* excited state does not seem to be significantly affected by the different polarities of solvents, which is consistent with previous research.[48] Lifetimes of the solvated species in both solvents are long-lived. The solvated species show no decay on the experimental timescale (up to 500 μs).

Table 5.3 *Summary of the TRIR data of $Re(CO)_3(bdmpzm)Cl$ in two solvents, CH_2Cl_2 and MeCN.*

Solvent	Peaks /cm^{-1}	Formation rate /ps	Lifetime /ps	Assignment
CH_2Cl_2	2014, 1906, 1864	14	60	π–π*
	2026, 1925, 1887	57 (recovery)	--	ground state
	1980, 1850 (br)	--	13	vibrational hot state
	1918, 1820	12	--	CO loss
MeCN	2013, 1904, 1874	16	57	π–π*
	2024, 1918, 1889	58 (recovery)	--	ground state
	1980, 1860 (br)	--	16	vibrational hot state
	1903, 1810	15	--	CO loss

Previous work on Re-(diimine) complexes have suggested that the MLCT excited state is the most common excited state upon UV photolysis, as the diimine ligands can act as electron acceptors and the HOMO orbitals in most Re-diimine complexes are proposed to be centred on the metal centre. However, our TRIR investigations on the $Re(CO)_3(bdmpzm)Cl$ complex may suggest a different story. As shown in the TRIR spectra in Figure 5.11 and 5.18, upon UV photolysis, in both solvents, CH_2Cl_2 and MeCN, a π–π* excited state is formed instead of a MLCT state. This may be due to the different configurations between M-diimine and M-bdmpzm complexes. For most M-diimine complexes, the –M-N-C-C-N ring is normally in a planar configuration, while for the M-bipyrazol complexes, the –M-N-N-C-N-N ring is normally in a "boat" configuration. Thus, the electron flow from the metal centre to the organic ligand may be much more difficult for bdmpzm compared to bipyridine ligands.

5.2.2 TRIR of Re-MOF

As discussed before, the $Re(CO)_3(bdmpzm)Cl$ complex is the linker in the Re-MOF provided by our collaborators from University of Adelaide. The Re MOF is synthesized using a post-synthesis method. The detailed method is described elsewhere[47].

The photoproperties of $Re(CO)_3(bdmpzm)Cl$ have been discussed in Section 5.2.1. It will also be interesting to see if incorporation of $Re(CO)_3(bdmpzm)Cl$ into a MOF structure will have any impact on the photoproperties of this Re-dipyrazol complex.

Bis(3,5-dimethylpyrazol)methane is a very flexible ligand, and according to the research by our collaborator, desolvation of the MOF skeleton will change the internal dihedral angle of the bis(3,5-dimethyl-pyrazol)methane ligands, thus can change the channel of the MOF, as shown in Figure 5.24.

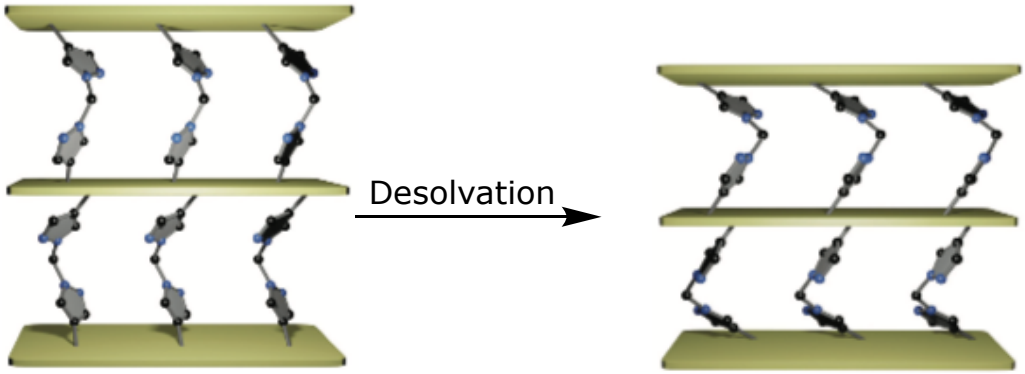


Figure 5.24 *Scheme of the desolvation process of the MOF skeleton.*[47]

Therefore, we also would like to investigate whether solvent molecules in the MOF channel would have any influence on the photoproperties of the Re MOF. Therefore, the Re-MOF samples were first immersed in two solvents, ethanol (ε: 24.5) and toluene (ε: 2.38), and then were pressed into NaCl discs for TRIR detection. Figure 5.25 shows the TRIR spectra of Re-MOF in ethanol.

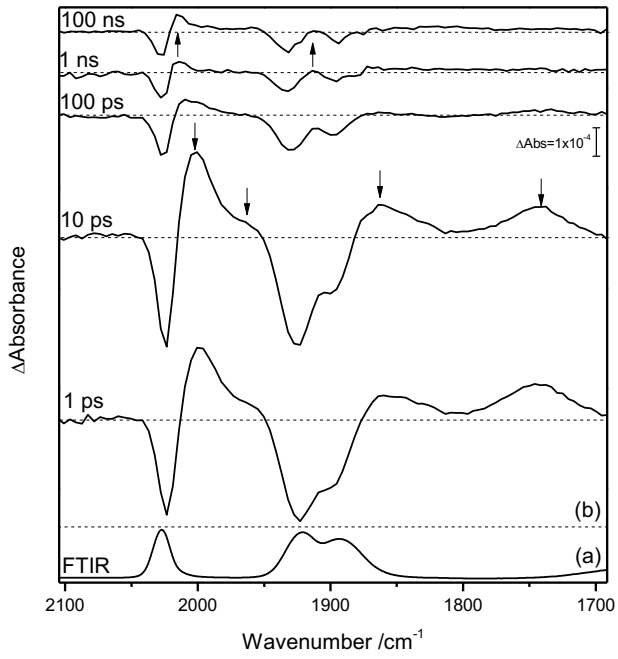


Figure 5.25 *(a) FTIR spectrum and (b) TRIR spectra obtained following photolysis (266 nm) of Re-MOF in ethanol in a NaCl disc.*

From the TRIR spectra, it can be observed that, upon UV photolysis, along with the depletion of the parent bands (2028, 1923, 1894 cm^{-1}), three bands at lower wavenumber at *ca.* 2000, 1862 and 1743 cm^{-1} and a shoulder band at *ca.* 1963 cm^{-1} are formed. At later timescales, these bands are observed to decay and two bands at *ca.* 2015 and 1913 cm^{-1} are formed.

Kinetic analysis shows that the three bands at *ca.* 2000, 1862 and 1743 cm^{-1} and the shoulder band at 1963 cm^{-1} decay at similar rate at 41 (± 3) ps, which is consistent with the early time recovery rate of the parent bleaches (49 ± 5 ps, 74% recovery), as shown in Figure 5.26.

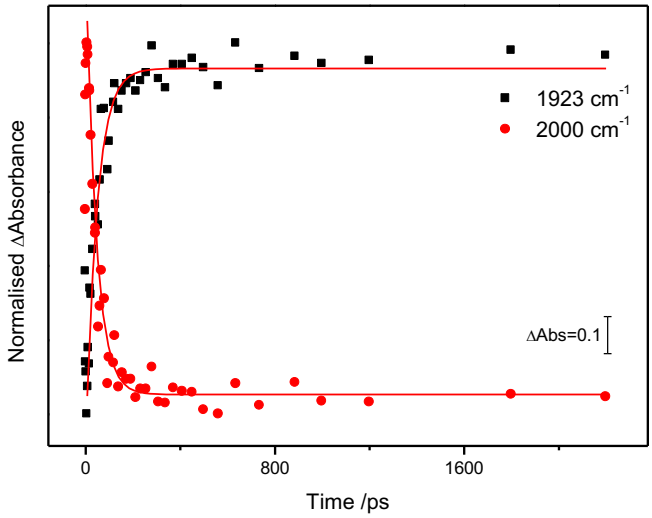


Figure 5.26 *TRIR kinetic traces obtained at 2000 and 1923 cm^{-1} corresponding to the ππ* excited state and the parent band.*

Considering the TRIR of the individual $Re(CO)_3(bdmpzm)Cl$ complex in solvents (Section 5.2.1), which shows that for $Re(CO)_3(bdmpzm)Cl$, the ππ* state as well as the CO-loss solvated dicarbonyl species are formed at the same time upon UV photolysis. Therefore, here the bands at 2000 and 1862 cm^{-1} are tentatively assigned to the ππ* state, while the bands at 1963 and 1743 cm^{-1} are assigned to the CO-loss dicarbonyl species which recombines with the CO trapped in MOF to reform the parent complex.

Global analysis has been carried out to assist the data analysis, the results are shown in Figure 5.27.

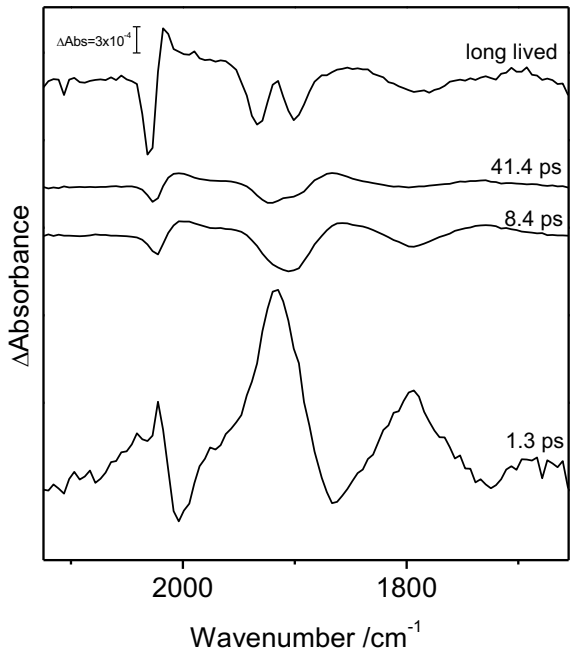


Figure 5.27 *Global analysis results of the TRIR spectra of Re-MOF in ethanol.*

As shown in Figure 5.27, the kinetics revealed by global analysis is consistent with our TRIR results. The initial species with a lifetime of *ca.* 1.3 ps is considered to be inconvincible, as 1 ps is the first time point of the experiment, and abnormal baseline fluctuation often occurs. The global analysis reveals the lifetime of the four bands (2000, 1963, 1862 and 1743 cm^{-1}) to be *ca.* 41.4 ps, similar to our TRIR results (41 ± 3 ps). Besides, the global analysis results reveal that there is a vibrational cooling of the $\pi\pi^*$ state and the solvated CO-loss dicarbonyl species at *ca.* 8.4 ps, similar to that observed for the linker complex in solvents (*ca.* 15 ps) as discussed in Section 5.2.1.

The observation of the short-lived CO-loss dicarbonyl species has been reported in recent studies, which suggested that the photo-ejected CO is trapped in the MOF channel, therefore the CO-loss dicarbonyl species can quickly recombines with CO to reform parent complexes. Reade *et al.* reported the TRIR investigations on MnMn MOF (formula: $\{Mn(DMF)_2[Mn(2,2'\text{-bipyridine-}5,5'\text{-dicarboxylate})(CO)_3X]\}_n$; X: Cl, Br), in which the linker complex $Mn(CO)_3$(diimine)X was investigated.[32] It was observed that after UV photolysis, along with the bleach of the parent bands (2028,

1940 cm^{-1}), a new species at 1975 and 1790 cm^{-1} was formed and was assigned to the DMF-bound dicarbonyl species Mn(diimine)$(CO)_2$(DMF)X, as the large red-shift of the ν(CO) position of this species compared to the parent bleaches indicates the coordination to a strongly binding ligand. The Mn(diimine)$(CO)_2$(DMF)X species is observed to decay for *ca.* 23 ps and recovers to the parent complex Mn$(CO)_3$(diimine)X (80% recovery). For the MnLi MOF (formula: $\{Li_2(DMF)_2[(2,2'$-bipyridine-5,5'-dicarboxylate)Mn$(CO)_3Br]\}_n$), in which the linker complex Mn(diimine)$(CO)_3$Br was investigated, TRIR reveals that upon UV photolysis, similar to the MnMn MOF, along with the bleach of the parent bands (2022, 1936 and 1909 cm^{-1}), two new bands were observed to form at lower wavenumbers (1967, 1802 cm^{-1}) and are also assigned to a CO-loss dicarbonyl species with a short lifetime of *ca.* 75 ps. This dicarbonyl species then recombines with CO to form the parent complex in 80%. Also, the decay of the dicarbonyl species is accompanied by the formation of a band at *ca.* 2016 cm^{-1}. Therefore, compared to previous analogous studies, it is reasonable to consider that we may have also formed short-lived CO-loss dicarbonyls upon photolysis (1963 and 1743 cm^{-1}). The large red-shift of the ν(CO) positions compared to the parent complex may indicate that the dicarbonyl species may have coordinated to a strong binding ligand.

As the Re-MOF sample was once immersed in ethanol, therefore it is expected that the CO-loss dicarbonyl species may have coordinated to ethanol in the channel. However, as DMF may also remain in the channel as residue of the synthesis process, and water may also exist in the channel. Hence DFT calculations are conducted to assist the assignment, as shown in Table 5.4, 5.5 and 5.6.

Table 5.4 *DFT calculations for the $Re(CO)_3$(bdmpzm)Cl species with solvation of ethanol (B3LYP, 6-31G(d), gas phase).*

Species	DFT IR frequency	IR intensity /x10^3 Km mol^{-1}	Energy /a.u.
*fac*1	2108, 2032, 1993	0.689, 0.972, 0.944	-1527.2582
*fac*2	2107, 2032, 1989	0.742, 0.949, 0.941	-1527.2566
mer	2117, 2019, 2013	0.202, 1.74, 0.835	-1527.2218
*fac*1 loss CO at axial (EtOH)	2008, 1929	0.833, 0.939	-1568.9301
*fac*1 loss CO at equatorial (EtOH)	2008, 1929	0.833, 0.939	-1568.9301
*fac*2 loss CO at axial (EtOH)	2002, 1928	0.833, 0.927	-1568.9353
*fac*2 loss CO at equatorial (EtOH)	2005, 1923	0.899, 0.935	-1568.9297
mer loss CO at axial 1 (EtOH)	2008, 1929	0.833, 0.939	-1568.9301
mer loss CO at axial 2 (EtOH)	2005, 1923	0.899, 0.935	-1568.9297
mer loss CO at equatorial (EtOH)	2066, 1957	0.101, 1.97	-1568.8839

Table 5.5 *DFT calculations for the $Re(CO)_3$(bdmpzm)Cl species with solvation of DMF (B3LYP, 6-31G(d), gas phase).*

Species	DFT IR frequency	IR intensity /x10^3 Km mol^{-1}	Energy /a.u.
*fac*1 loss CO at axial (DMF)	2005, 1935	0.848, 0.963	-1662.4109
*fac*1 loss CO at equatorial (DMF)	2005, 1935	0.848, 0.963	-1662.4109
*fac*2 loss CO at axial (DMF)	2002, 1914	0.907, 0.921	-1662.4051
*fac*2 loss CO at equatorial (DMF)	2002, 1929	0.925, 0.963	-1662.4095
mer loss CO at axial 1 (DMF)	2005, 1935	0.848, 0.963	-1662.4109
mer loss CO at axial 2 (DMF)	2003, 1929	0.925, 0.963	-1662.4095
mer loss CO at equatorial (DMF)	2058, 1954	0.175, 1.93	-1662.3614

Table 5.6 *DFT calculations for the $Re(CO)_3$(bdmpzm)Cl species with solvation of water (B3LYP, 6-31G(d), gas phase).*

Species	DFT IR frequency	IR intensity /x10^3 Km mol^{-1}	Energy /a.u.
*fac*1 loss CO at axial (H_2O)	2014, 1944	0.885, 0.984	-1490.3170
*fac*1 loss CO at equatorial (H_2O)	2014, 1944	0.885, 0.984	-1490.3170
*fac*2 loss CO at axial (H_2O)	2022, 1939	1.02, 0.941	-1490.3094
*fac*2 loss CO at equatorial (H_2O)	2011, 1937	0.943, 0.982	-1490.3140
mer loss CO at axial 1 (H_2O)	2025, 1946	0.966, 0.939	-1490.3118
mer loss CO at axial 2 (H_2O)	2011, 1937	0.943, 0.982	-1490.3140
mer loss CO at equatorial (H_2O)	2070, 1959	0.149, 2.00	-1490.2666

The calculated values of all solvated species are similar as the DFT calculations indicate. One band of the solvated dicarbonyl shifts significantly to lower wavenumber compared to the parent bands, while another band is between the two lower bands of the parent complex. For the DMF-bound species, the ν(CO) band positions are similar compared to the analogue ethanol-bound species. While for the water species, the ν(CO) band positions are at higher wavenumber, and the energy of each species is also at higher level compared to the DMF- and ethanol-bound species. Therefore, the CO-dicarbonyl species could have coordinated to ethanol or DMF, while coordination to water cannot be excluded. The *mer*-isomer *mer*-$Re(CO)_3$(bdmpzm)Cl may also have formed. However, as suggested by the DFT calculation, for the *mer*-isomer, two bands are expected between the two lower bands of the *fac*-parent complex, while another weak band is expected at slightly higher wavenumber than the highest band of the *fac*-parent complex, both of which are difficult to observe in the TRIR spectra (Figure 5.25).

As shown in the TRIR spectra, after the decay of the $\pi\pi^*$ excited state and the CO-loss dicarbonyl species, two bands at *ca.* 2015 and 1913 cm^{-1} are formed. The formation of these two bands are obscured due to overlap with the band at 2000 cm^{-1} and the parent bleaches. However, the small red-shift of ν(CO) positions compared to the parent bands (2028, 1923, 1894 cm^{-1}) leads to the assumption that, the bands at 2015 and 1913 cm^{-1} indicate small electron density increase on

the Re centre, similar to the ππ* excited state. The small electron density increase is thought to be possibly caused by the MOF scaffold. The initial ππ* excited state formed upon UV photolysis may decay and transfer parts of the energy to the MOF scaffold. The recombination of the CO-loss dicarbonyl species with CO may also transfer energy to the scaffold, therefore the excited state in the scaffold may in turn increase the electron density on the Re centre. As described in the Introduction Section 5.1, the MOF scaffold is composed of Mn ions and bdmpzm organic linkers, therefore the possibility of the excitation of the MOF scaffold cannot be excluded out.

Lifetime of the excited state in the MOF scaffold is extremely long for 389 (± 86) ns, and is consistent with the recovery of the parent bands (345 (± 88) ns), as shown in Figure 5.28. This is also consistent with the global analysis result (Figure 5.27), which suggests a long-lived species at *ca.* 2015 cm^{-1}.

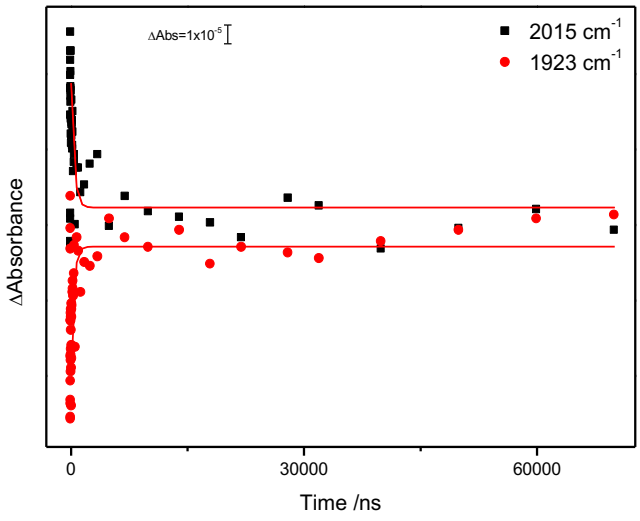


Figure 5.28 *TRIR kinetic traces obtained at 2015 and 1923 cm^{-1} corresponding to the scaffold excited state and the parent band.*

The extraordinarily long lifetime of the excited state in the MOF scaffold might be due to the stability effect of the rigid MOF structure, thus structural changes within the MOF structure are more difficult than in solvent. Also, in the MOF, the complexes in the scaffold are not as much surrounded by solvent molecules as in condensed solution. Therefore, energy diffusion may become more difficult in MOF than in

condensed phase, which may also be the cause of the extremely long lifetime of the excited state.

Similar TRIR spectra have been observed for Re-MOF samples from toluene, as shown in Figure 5.29.

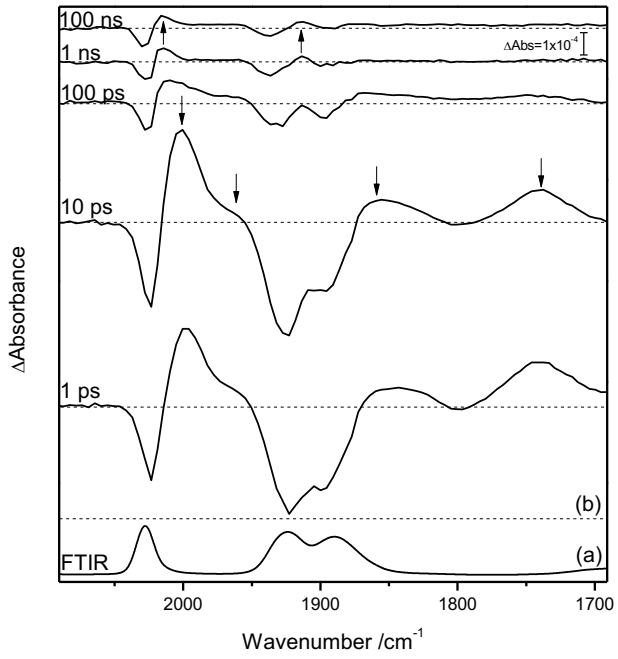


Figure 5.29 *(a) FTIR spectrum and (b) TRIR spectra obtained following photolysis (266 nm) of Re-MOF in toluene in a NaCl disc.*

Similar to Re-MOF in ethanol, upon UV photolysis, along with the depletion of the parent bands (2027, 1923, 1895 cm^{-1}), three bands at lower wavenumber at *ca.* 2000, 1860, 1741 cm^{-1} and a shoulder band at *ca.* 1962 cm^{-1} are formed. Kinetic analysis shows similar lifetimes for the bands at 2000, 1962, 1860 and 1741 cm^{-1} to that observed for Re-MOF in ethanol, at *ca.* 40 ps. This is consistent with the early time recovery rate of the parent bands (40 ±2 ps, 75% recovery), as shown in Figure 5.30.

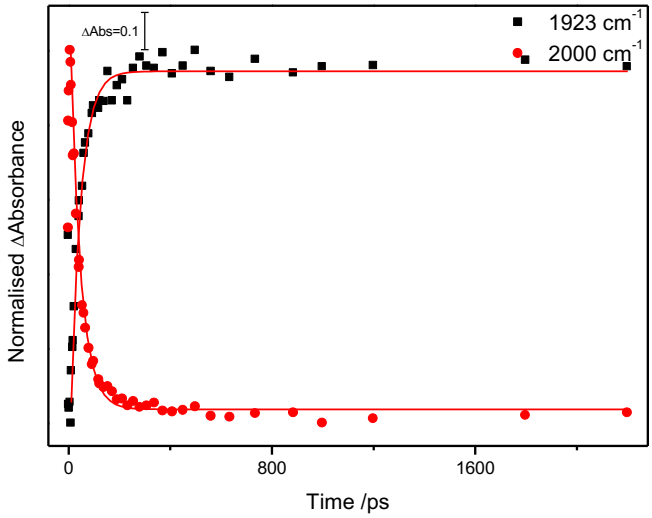


Figure 5.30 *TRIR kinetic traces obtained at 2000 and 1923 cm^{-1} corresponding to the $\pi\pi^*$ excited state and the parent band.*

Similar to the experiment of Re-MOF in ethanol, the bands at 2000 and 1860 cm^{-1} are assigned to the $\pi\pi^*$ excited state, while the bands at 1962 and 1741 cm^{-1} are assigned to the CO-loss dicarbonyl species. The lifetimes of these two species are not affected by the presence of different solvents in the MOF channel.

Global analysis has been carried out to assist the data analysis, the results are shown in Figure 5.31.

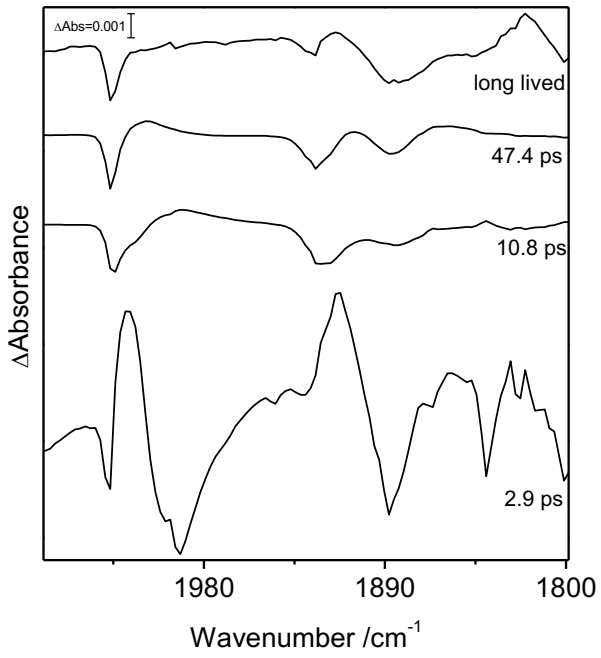


Figure 5.31 *Global analysis results of the TRIR spectra of Re-MOF in toluene.*

As shown in Figure 5.31, the kinetics revealed by global analysis is consistent with the TRIR results. The initial species with a lifetime of *ca.* 2.9 ps is considered to be inconvincible, as discussed before. The global analysis reveals the lifetime of the four bands (2000, 1962, 1860 and 1741 cm^{-1}) to be *ca.* 47.4 ps, consistent with the TRIR results (*ca.* 40 ps). Similar to the Re-MOF in ethanol, the global analysis results reveal the vibrational cooling of the $\pi\pi^*$ state and the solvated CO-loss dicarbonyl species at *ca.* 10.8 ps, similar to that observed for the Re-MOF in ethanol (8.4 ps).

Meanwhile, as the ν(CO) band positions of the CO-loss dicarbonyl species at 1962 and 1741 cm^{-1} are similar to that observed in Re-MOF in ethanol (1963 and 1743 cm^{-1}), this may raise the question as whether the coordination to toluene was successful. Therefore, DFT calculations of toluene-solvated dicarbonyl species has been conducted, the results are summarized in Table 5.7.

Table 5.7 *DFT calculations for the $Re(CO)_3$(bdmpzm)Cl species with solvation of toluene (B3LYP, 6-31G(d), gas phase).*

Species	DFT IR frequency	IR intensity /x10^3 Km mol^{-1}	Energy /a.u.
*fac*1 loss CO at axial (tol)	2025, 1941	0.977, 0.989	-1685.4304
*fac*1 loss CO at equatorial (tol)	2025, 1941	0.977, 0.989	-1685.4304
*fac*2 loss CO at axial (tol)	2026, 1938	0.923, 0.848	-1685.4273
*fac*2 loss CO at equatorial (tol)	2026, 1938	0.923, 0.848	-1685.4263
mer loss CO at axial 1 (tol)	2025, 1941	0.977, 0.988	-1685.4304
mer loss CO at axial 2 (tol)	2026, 1938	0.923, 0.848	-1685.4273
mer loss CO at equatorial (tol)	2072, 1966	0.091, 1.93	-1685.3880

As the DFT results in Table 5.7 suggest, compared to ethanol, DMF or water (Table 5.4, 5.5, 5.6), the ν(CO) positions of the toluene species are at much higher wavenumbers. Therefore, considering the similar ν(CO) positions compared to the sample in ethanol in the TRIR spectra, the coordination to toluene may not be successful. Similar coordination to the sample in ethanol may have occurred. Therefore, in both samples in ethanol and toluene, coordination to DMF or water may have occurred. However, considering the similarity of ethanol and DMF as suggested by Table 5.4 and 5.5, for the sample in ethanol, the coordination to ethanol may be successful, while for the sample in toluene, the dicarbonyl species may have coordinated to DMF (or water) in the channel.

Similarly, the bands formed at later timescales at *ca.* 2015 and 1913 cm^{-1} are assigned to the excited state of the MOF scaffold, which forms after the energy transferred from the decayed ππ* excited state, as well as from the CO-loss dicarbonyl species which recombines with CO. However, it is found that the lifetime of the scaffold excited state is prolonged to *ca.* 1 μs (Re-MOF from ethanol: *ca.* 400 ns). This has also been revealed by global analysis (Figure 5.31) which suggests a long-lived species at ca. 2015 cm^{-1}. The decay rate of the scaffold excited state fits the recovery rate of the parent bands (1.2 ±0.2 μs), as shown in Figure 5.32.

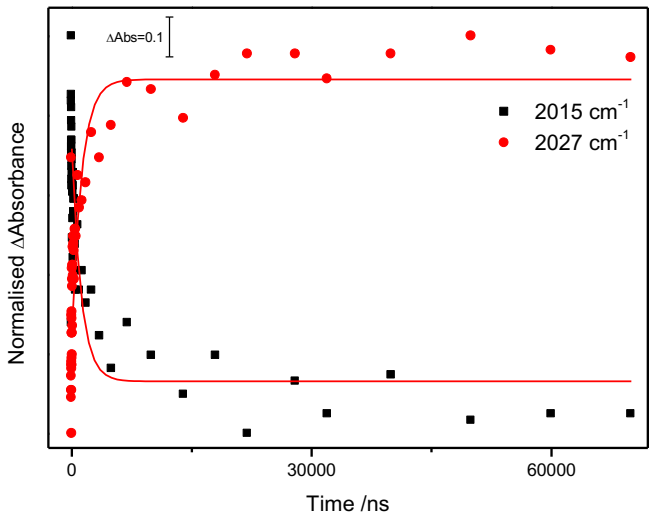


Figure 5.32 *TRIR kinetic traces obtained at 2027 and 2015 cm^{-1} corresponding to the parent band and the scaffold excited state.*

The reason for this prolonged lifetime can be explained by the fact that as the polarity of toluene (ε: 2.38) is much smaller than ethanol (ε: 24.5), the excited state of the MOF scaffold is quenched more easily in ethanol than in toluene. Also, the larger size of toluene may make the intrusion of the toluene molecules into the MOF channel more difficult, thus creating a more vacuum-like environment for the scaffold excited state.

For comparison, TRIR investigations of dried samples have also been conducted.

Two methods have been used to obtain dry samples. The first method is to dry the Re-MOF powder first in the oven for 15 mins at 110 °C, then press it into a NaCl disc. The second method is to first press the NaCl disc with the Re-MOF powder, then dry the disc in the oven for 15 mins at 110 °C. TRIR investigations of these two methods have been conducted to see if different methods will result in different drying efficiencies, and whether will have an impact on the photoproperties of Re-MOF.

Figure 5.33 shows the ps-TRIR spectra of Re-MOF in ethanol dried as powder.

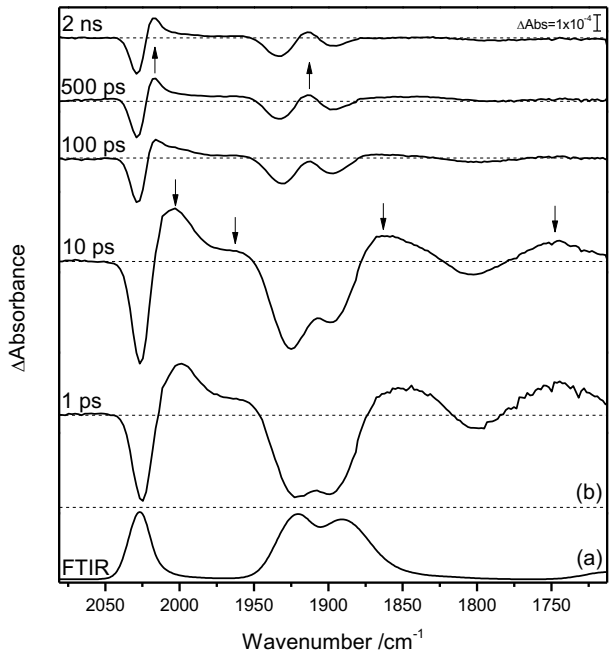


Figure 5.33 *(a) FTIR spectrum and (b) ps-TRIR spectra obtained following photolysis (266 nm) of Re-MOF in ethanol dried as powder, in a NaCl disc.*

The TRIR spectra for the Re-MOF sample dried as powder is similar to the wet sample. Upon UV photolysis, along with the bleach of the parent bands (2027, 1921, 1890 cm^{-1}), four bands at *ca.* 2003, 1962, 1866 and 1745 cm^{-1} are formed. At later time delays, two bands at *ca.* 2017 and 1913 cm^{-1} are formed. Based on the previous results, the bands at 2003 and 1866 cm^{-1} are assigned to the π–π* excited state, while the bands at 1963 and 1745 cm^{-1} are assigned to the CO-loss dicarbonyl species, and the bands at 2017 and 1913 cm^{-1} are assigned to the excited state of the MOF scaffold.

Kinetic analysis also shows similar results to wet samples. Lifetime of the π–π* excited state is 45 (±1) ps, and lifetime of the CO-loss dicarbonyl species is 43 (±2) ps, consistent with the early time recovery rate of the parent bands (45 ±1 ps, 67% recovery), as shown in Figure 5.34.

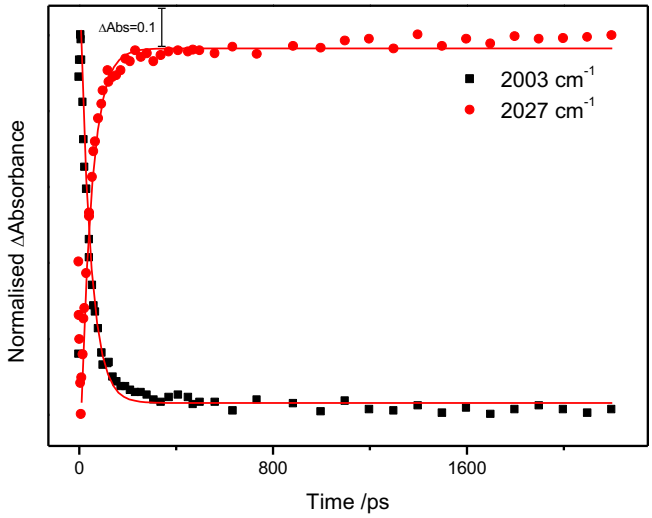


Figure 5.34 *TRIR kinetic traces obtained at 2027 and 2003 cm^{-1} corresponding to the parent band and the ππ* excited state.*

As discussed before, the formation rate of the bands at 2017 and 1913 cm^{-1} (the scaffold excited state) at early time cannot be obtained accurately due to the overlap with other bands or parent bleaches. However, as shown in Figure 5.35, the TRIR data here is satisfying. Kinetic analysis of the band at 2017 cm^{-1} shows a bi-exponential growth (9 ± 1 ps, 46 ± 4 ps). The first component (9 ± 1 ps) reflects the decay of the vibrational hot state for *ca.* 9 ps, as indicated by the global analysis as discussed before. The second component (46 ± 4 ps) fits the decay of the ππ* excited state and the CO-loss dicarbonyl species (Figure 5.35).

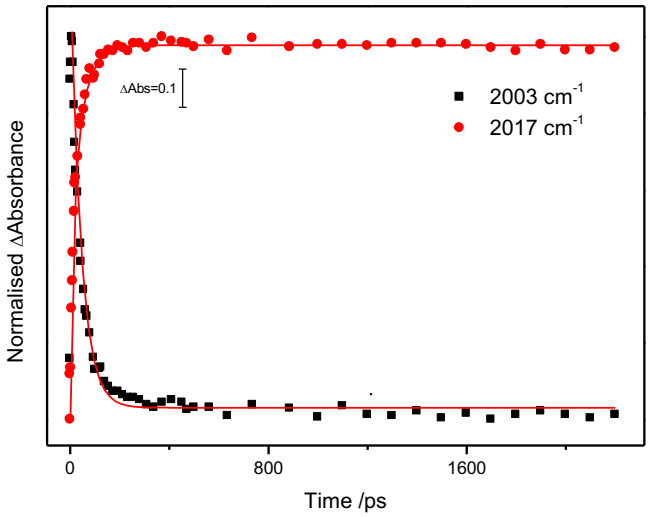


Figure 5.35 *TRIR kinetic traces obtained at 2017 and 2003 cm^{-1} corresponding to the scaffold excited state and the $\pi\pi^*$ excited state.*

Thus, the kinetic result evidences the energy transfer from the vibrational hot state of $\pi\pi^*$ and the CO-loss dicarbonyls, as well as the cooled-down $\pi\pi^*$ excited state and the CO-loss dicarbonyls, to the excited state of the MOF scaffold.

From the results, it can be noted that, the lifetimes of the $\pi\pi^*$ excited state and the CO-loss dicarbonyls seem not to have been affected by the desolvation process. However, the drying efficiency of this method is still in question, as the Re-MOF powder will still be hydrophilic to the water in the atmosphere in the disc making process after cooling to room temperature. So TRIR of Re-MOF sample using another method – pressing Re-MOF into a NaCl disc then dry it in the oven, as discussed before, has also been conducted. It is expected that in this method, although the disc will still be exposed to the atmosphere, however, as the MOF is surrounded by large amount of dry NaCl crystals, the NaCl crystals would absorb water from the air, and thus can hinder the water absorption by the MOF, which may bring better desolvation and dehydration effects, compared to the method drying as powder. Following are the discussion.

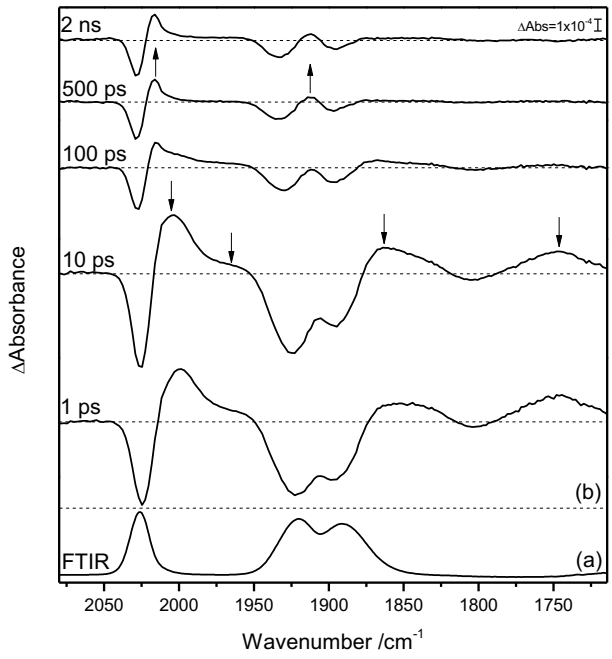


Figure 5.36 *(a) FTIR spectrum and (b) ps-TRIR spectra obtained following photolysis (266 nm) of Re-MOF in ethanol dried as disc, in a NaCl disc.*

As shown in the TRIR spectra, the reaction process is similar to the wet sample and the dry sample prepared by another method (Re-MOF dried as powder). The CO-loss dicarbonyl species (1964, 1746 cm^{-1}), the $\pi-\pi^*$ excited state (2004, 1864 cm^{-1}) and the excited state of the MOF scaffold (2016, 1912 cm^{-1}) have all been observed. Kinetic analysis shows similar kinetic behaviors compared to other samples. Lifetime of the CO-loss dicarbonyl species is 50 (± 2) ps, and lifetime of the $\pi-\pi^*$ excited state is 49 (± 3) ps, consistent with the recovery rate of the parent bands (50 ± 2 ps) and the formation rate of the scaffold excited state (9 ± 6 ps, 45 ± 5 ps). Thus, the lifetimes of the CO-loss dicarbonyl species as well as the $\pi-\pi^*$ excited state seem to be unaffected by the desolvation and dehydration process.

TRIR on dry Re-MOF sample from toluene has also been conducted, in order to check if desolvation from different solvents will have any impact on the reaction process.

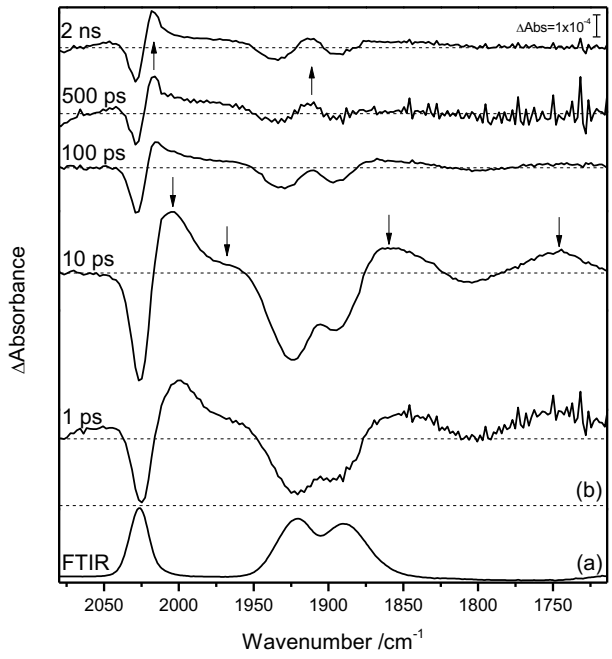


Figure 5.37 *(a) FTIR spectrum and (b) ps-TRIR spectra obtained following photolysis (266 nm) of Re-MOF in toluene dried as disc, in a NaCl disc.*

Similar to the previous results, upon UV photolysis, along with the bleach of the parent bands (2027, 1921, 1889 cm^{-1}), the π–π* excited state (2004 and 1864 cm^{-1}) as well as the CO-loss dicarbonyl species (1966 and 1744 cm^{-1}) are formed instantly, and at later time delays, the excited state of the MOF scaffold is formed at *ca.* 2017 and 1912 cm^{-1}. Kinetic analysis shows similar lifetimes of the π–π* excited state (47 ± 3 ps) and the CO-loss dicarbonyl species (48 ± 3 ps) to dried Re-MOF samples from ethanol, and is consistent with the recovery rate of the parent bands (50 ± 2 ps), and the formation rate of the scaffold excited state (47 ± 2 ps).

Based on the results, it can be noted that, changing of drying methods or changing samples from different solvents have little influence on the early reaction process. The lifetimes of the π–π* excited state and the CO-loss dicarbonyl species are nearly unaffected. Also, the ν(CO) positions of the CO-loss dicarbonyl species are similar for all samples. Therefore, it is very likely that in all samples, perhaps except for the wet sample from ethanol, the CO-loss dicarbonyl species are coordinated to

water.

As mentioned earlier, the MOF channel may allow the intrusion of ethanol while toluene may be excluded due to larger molecular size. Thus, the intrusion of water which possesses small molecular size and strong polarity, becomes very likely and aroused our interests.

Therefore, TRIR of Re-MOF immersed in water has also been conducted. The spectra are shown in Figure 5.38.

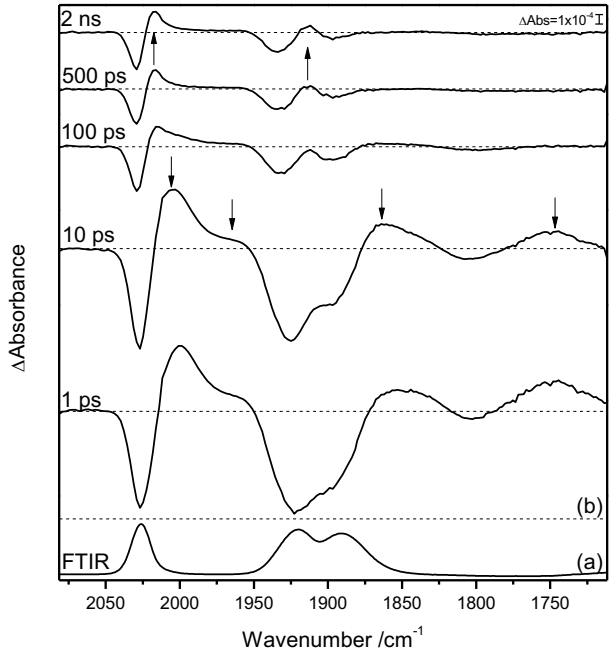


Figure 5.38 *(a) FTIR spectrum and (b) ps-TRIR spectra obtained following photolysis (266 nm) of Re-MOF from ethanol, first blow-dried (using argon) then immersed in water, in a NaCl disc.*

As expected, the reaction process is similar to previous results. The $\pi\pi^*$ excited state is observed at *ca.* 2003 and 1864 cm^{-1}, with a lifetime of 40 (± 1) ps, while the CO-loss dicarbonyl species is observed at *ca.* 1963 and 1746 cm^{-1}, which then decays and recovers to the parent complex (43 ±2 ps). The lifetime of the scaffold excited state is observed to be 5 (±1) ps, 48 (±5) ps.

Therefore, based on the results, it can be concluded that although these two drying methods may have different drying efficiencies, Re-MOF dried using both methods would still introduce certain amount of water from the air. This also applies to the wet samples from solvents, as the solvents could also contain certain amount of water, and this may be the cause of the similarity of reaction processes and kinetic behaviors among all samples.

We also wish to see if changing the environment in the MOF channel will have any impact on the lifetime of the scaffold excited state. Therefore $TR^{M}PS$-TRIR ($TR^{M}PS$: time-resolved multiple probe spectroscopy) experiments on dried samples have been conducted.

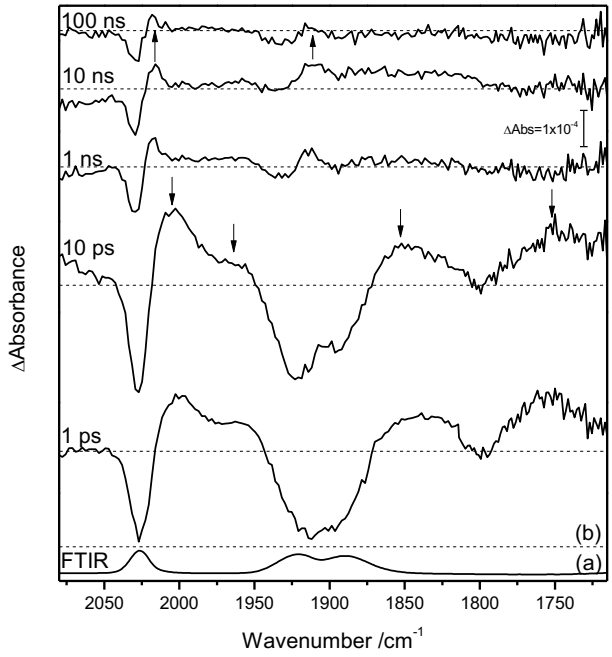


Figure 5.39 *(a) FTIR spectrum and (b) $TR^{M}PS$-TRIR spectra obtained following photolysis (266 nm) of Re-MOF in toluene dried as disc, in a NaCl disc.*

Kinetic analysis shows that, the lifetime of the scaffold excited state is 156 (±32) ns, similar to the recovery rate of the parent bands (81 ±18 ns). Thus, the decay rate of the scaffold excited state has been significantly shortened compared to the wet samples (*ca.* 400 ns for the sample in ethanol and *ca.* 1000 ns for the sample in toluene).

Therefore, desolvation of Re-MOF will result in shortening of the lifetime of the scaffold excited state, while has little influence on the lifetimes of the π–π* excited state and the CO-loss dicarbonyl species. The shortening of the lifetime of the scaffold excited state could be explained by the fact that desolvation would introduce more water from the air into the MOF channels, which was once occupied or covered by solvent molecules. And the introduce of water will result in the faster quench of the scaffold excited state.

$TR^{M}PS$-TRIR of Re-MOF dried as powder has also been carried out. It is found that as expected, lifetime of the π–π* excited state (*ca.* 43 ps) and the CO-loss dicarbonyl species (*ca.* 45 ps) is not affected. For the scaffold excited state, similar lifetime to Re-MOF dried as disc has been observed (187 ± 79 ns). The TRIR spectra is shown in Figure 5.40.

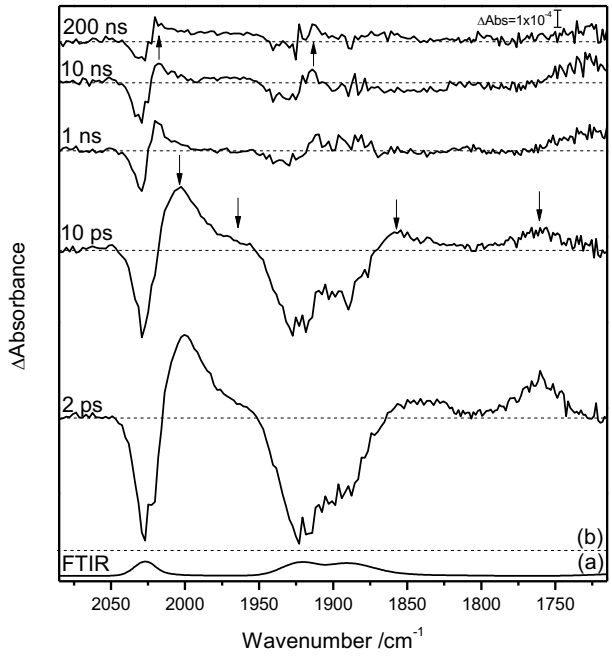


Figure 5.40 *(a) FTIR spectrum and (b) $TR^{M}PS$-TRIR spectra obtained following photolysis (266 nm) of Re-MOF in ethanol dried as powder, in a NaCl disc.*

As discussed before, the sample dried as disc is considered to be dehydrated more efficiently than sample dried as powder. However, the results show that the lifetimes of the scaffold excited state are quite similar for both samples. Therefore,

two assumptions are proposed: first, the water contamination of both samples is similar; second, although the sample dried as disc contains less water, but the water contamination is enough for quick quench of the scaffold excited state.

5.2.3 TRIR of the Mn Linker Complex

By incorporation of the Mn(I) ions into the MOF scaffold, using the post-synthesis method, another MOF was synthesized by our collaborators, denoted as the Mn-MOF. TRIR studies of the Mn-MOF have been undertaken and are described later in this Chapter. Meanwhile, TRIR investigations on the Mn linker complex [$Mn(CO)_3$(bdmpzm)Br] have been conducted, in order to understand the photoproperties of the Mn linker complex and to help with understanding the photophysical and photochemical behaviours of the Mn-MOF.

The TRIR spectra of $Mn(CO)_3$(bdmpzm)Br in toluene is shown in Figure 5.41.

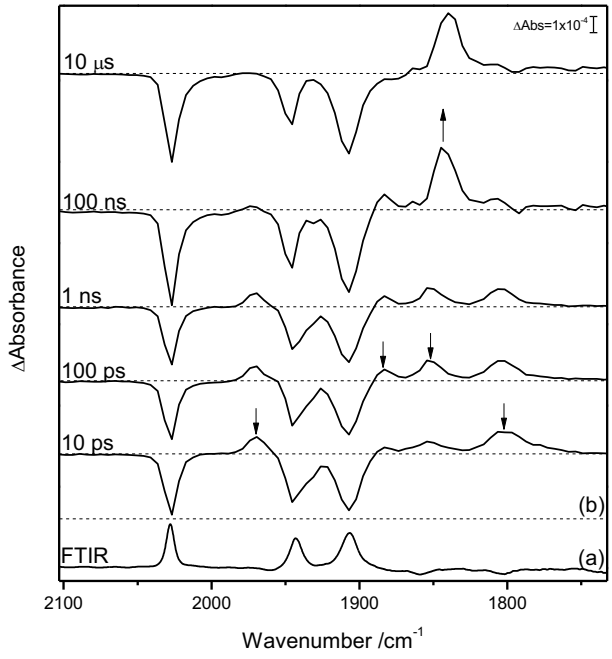


Figure 5.41 *(a) FTIR spectrum and (b) TRIR spectra obtained following photolysis (355 nm) of $Mn(CO)_3$(bdmpzm)Br in toluene.*

Upon UV photolysis, four bands are formed at *ca.* 1969, 1883, 1854 and 1803 cm^{-1}. To aid in analysis, global analysis has been conducted, and the results are shown in Figure 5.42.

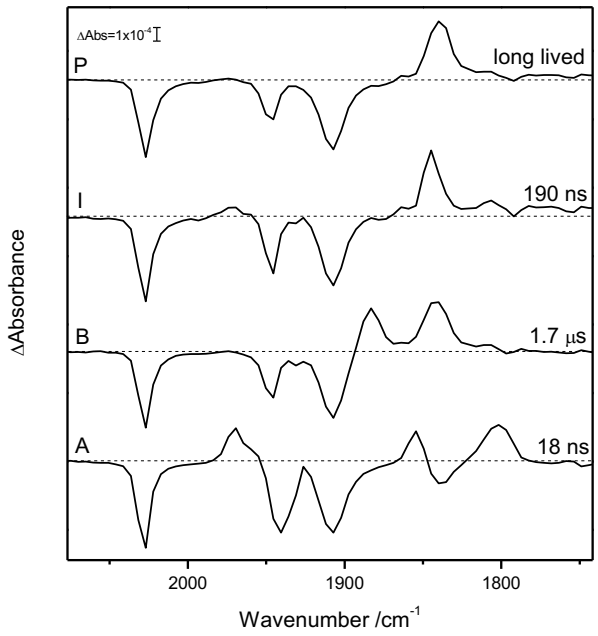


Figure 5.42 *Global analysis results of the TRIR spectra of $Mn(CO)_3$(bdmpzm)Br in toluene.*

The global analysis results indicate that two species, A (1969, 1854, 1802 cm^{-1}) and B (1883, 1842 cm^{-1}) are formed upon UV photolysis. Species A was found to have a lifetime of *ca.* 18 ns, while species B has a lifetime of *ca.* 1.7 μs. Species A was found to convert to an intermediate I (1845 cm^{-1}) with a lifetime of *ca*. 190 ns, and both species I and B were found to convert to a stable final product, named as P (1840 cm^{-1}).

DFT calculations using a B3LYP method and 6-31G(d) basis set in gas phase have been conducted in order to assist with the assignment of these bands. The results are shown in Table 5.8.

Table 5.8 *Summary of DFT calculations of Mn(bdmpzm)(CO)$_3$Br and the solvated species in toluene (B3LYP, 6-31G(d), gas phase).*

Species	IR frequency/ cm^{-1}	IR intensity /x10^3 Km mol^{-1}	Energy/ a.u.
*fac*1	2111, 2050, 2016	0.643, 0.780, 0.826	-4710.5443
*fac*1 loss CO at axial	2061, 1983	0.828, 0.851	-4597.1802
*fac*1 loss CO at axial (tol)	2061, 1985	0.764, 0.802	-4868.7543
*fac*1 loss CO at equatorial	2061, 1983	0.828, 0.851	-4597.1802
*fac*1 loss CO at equatorial (tol)	2061, 1985	0.764, 0.802	-4868.7543
*fac*2	2112, 2052, 2010	0.709, 0.745, 0.819	-4710.5420
*fac*2 loss CO at axial	2059, 1980	0.893, 0.849	-4597.1739
fac2 loss CO at axial (tol)	2051, 1972	0.864, 0.739	-4868.7478
*fac*2 loss CO at equatorial	2059, 1980	0.893, 0.849	-4597.1739
*fac*2 loss CO at equatorial (tol)	2051, 1972	0.865, 0.739	-4868.7478
mer	2116, 2039, 2034	0.698, 1.39, 0.163	-4710.5216
mer loss CO at axial 1	2061, 1983	0.828, 0.851	-4597.1802
mer loss CO at axial 1 (tol)	2061, 1985	0.764, 0.802	-4868.7543
mer loss CO at axial 2	2059, 1980	0.893, 0.849	-4597.1739
mer loss CO at axial 2 (tol)	2051, 1972	0.864, 0.739	-4868.7478
mer loss CO at equatorial	2002	1.74	-4597.1536
mer loss CO at equatorial (tol)	1997	1.68	-4868.7278

Based on the IR frequencies predicted by DFT, the calculated ν(CO) band positions of toluene-bound species can be shown in Figure 5.43.

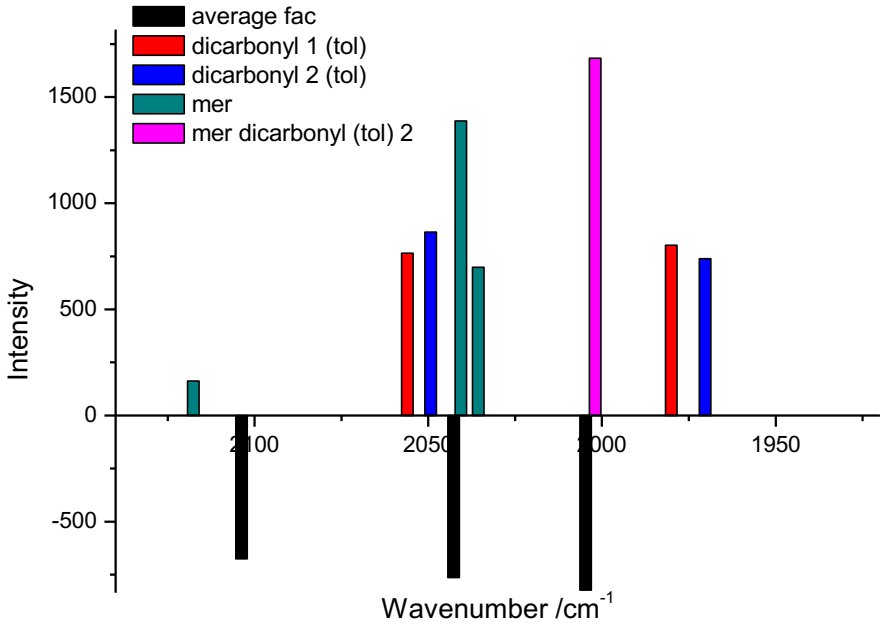


Figure 5.43 *Predicted ν(CO) band positions from DFT calculations of $Mn(CO)_3(bdmpzm)Br$ in toluene (B3LYP 6-31G(d)). Average fac represents the average ν(CO) of fac1 and fac2; dicarbonyl 1 (tol) represents dicarbonyl species with ν(CO) at 2061 and 1985 cm^{-1}; dicarbonyl 2 (tol) represents dicarbonyl species with ν(CO) at 2051 and 1972 cm^{-1}; mer dicarbonyl (tol) 2 represents the mer dicarbonyl species with ν(CO) at 1997 cm^{-1}.*

From these results, it can be shown that the unsaturated dicarbonyl species shift to higher energies compared to the dicarbonyls in which toluene is bound. Comparing the DFT to the experimental results, both *fac*- and *mer*-dicarbonyls may have been formed upon UV photolysis. Species A at 1969 and 1803 cm^{-1} could be assigned to the unsaturated dicarbonyls consisting of both *fac*- and *mer*-configurations. as DFT suggests, the band positions of the *fac*- and *mer*-dicarbonyls in many instances occur at similar positions. And the band at 1854 cm^{-1} might be one of the unsaturated *mer*-dicarbonyls as suggested by DFT at 2002 cm^{-1}. Species B is tentatively assigned as the C-H-bound species, which is not stable and undergoes structural change in *ca.* 1.7 μs to the final stable ring-edge-bound

structure. Species I is assigned as possibly another ring-edge-bound structure, but slightly higher in energy than the final product, and undergoes structural isomerization to form the final product P in *ca.* 190 ns.

TRIR studies in DMF have also been conducted, as we wish to explore if the changes of solvent properties will have any impact on the photoproperties of $Mn(CO)_3$(bdmpzm)Br. Following are the discussions of these investigations.

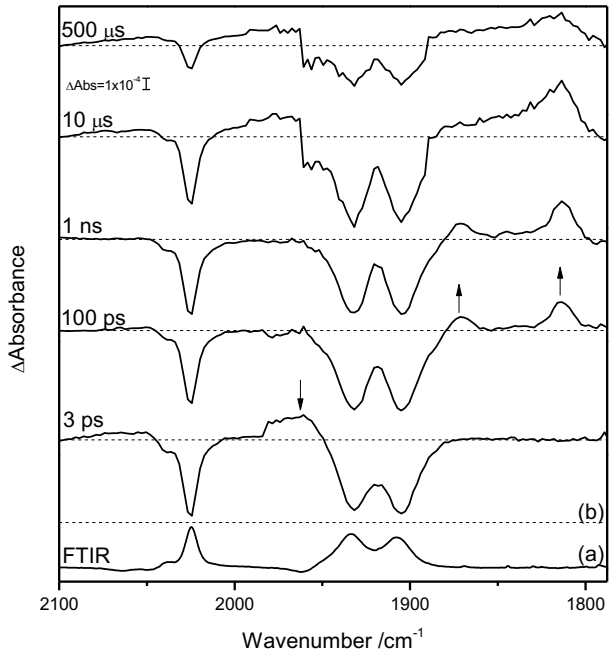


Figure 5.44 *(a) FTIR spectrum and (b) TRIR spectra obtained following photolysis (266 nm) of $Mn(CO)_3$(bdmpzm)Br in DMF.*

As shown in Figure 5.44, similar to the experiments in toluene, upon UV photolysis a band at *ca.* 1963 cm^{-1} was formed. It can be noted that a band between the parent bleaches (1935 and 1908 cm^{-1}) at *ca.* 1919 cm^{-1} was also formed. Two bands at *ca.* 1871 and 1815 cm^{-1} were formed at later time delays, and showed no decay for the rest of the experimental timescale (up to 1 ms).

Global analysis of the data has also been conducted (Figure 5.45).

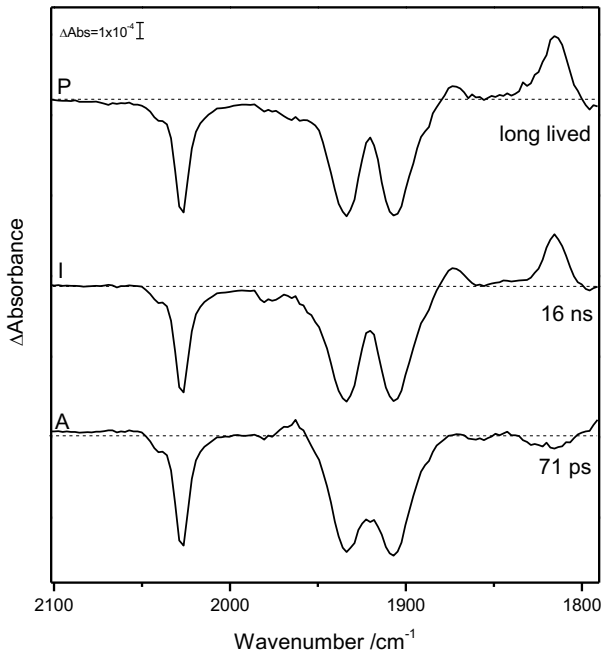


Figure 5.45 *Global analysis results of the TRIR spectra of Mn(bdmpzm)(CO)$_3$Br in DMF.*

The global analysis of the data indicates that species A (1963 cm^{-1}) is formed upon UV photolysis, and decays to form an intermediate, I (1919, 1871, 1815 cm^{-1}), in 71 ps. Species I has a lifetime of *ca*. 16 ns, and converts to the final stable product, P (1918, 1870, 1814 cm^{-1}). Considering the stability of the final product P, it is assigned to the DMF-bound species Mn(CO)$_2$(bdmpzm)Br(DMF). Considering the similarities of the ν(CO) band positions between species I and the final product P [Mn(CO)$_2$(bdmpzm)Br(DMF)], species I is tentatively assigned to Mn(CO)$_2$(bdmpzm)Br(DMF) but of a slightly different structure of higher energy compared to the final product P. Species A is assigned to an uncoordinated dicarbonyl species Mn(CO)$_2$(bdmpzm)Br which solvates with DMF to form I.

The lifetime of the dicarbonyl species Mn(CO)$_2$(bdmpzm)Br in DMF is significantly shortened compared to that observed in toluene (*ca.* 18 ns), which is expected as the polarity of DMF (ε= 36.7) is much larger than toluene (ε= 2.38), also that DMF is more coordinating.

DFT calculations have been conducted in order to assist with the band assignments. The results are summarized in Table 5.9.

Table 5.9 *Results from DFT calculations on $Mn(CO)_2$(bdmpzm)Br(DMF) (method: B3LYP; basis set: 6-31G(d); gas phase).*

Species	ν(CO)/ cm^{-1}	IR intensity /x10^3 Km mol^{-1}	Energy/ a.u.
*fac*1 loss CO at axial(DMF)	2040, 1967	0.868, 0.715	-4845.7187
*fac*1 loss CO at equatorial(DMF)	2040, 1967	0.868, 0.715	-4845.7187
*fac*2 loss CO at axial(DMF)	2032, 1949	0.846, 0.759	-4845.7121
*fac*2 loss CO at equatorial(DMF)	2036, 1963	0.859, 0.774	-4845.7178
mer loss CO at axial 1(DMF)	2040, 1967	0.868, 0.715	-4845.7187
mer loss CO at axial 2(DMF)	2036, 1963	0.859, 0.774	-4845.7178
mer loss CO at equatorial(DMF)	2063, 1981	0.109, 1.63	-4845.6903

According to the DFT results (Tables 5.8, 5.9), the ν(CO) positions of the DMF-bound species shift to lower wavenumbers compared to the nonsolvated species and the toluene-bound species, which is consistent with the assignments ($Mn(CO)_2$(bdmpzm)Br(toluene): 1840 cm^{-1}; $Mn(CO)_2$(bdmpzm)Br(DMF): 1814 cm^{-1}). This is expected as DMF is thought to donate more electron density to the metal centre than toluene.

5.2.4 TRIR of Mn-MOF

The Mn-MOF has the same scaffold as the Re-MOF discussed in Section 5.2.2. The Mn-MOF is provided by our collaborators from University of Adelaide, also synthesized using the post-synthesis method. The Mn (I) ion is incorporated into the MOF scaffold, in which $Mn(CO)_3(bdmpzm)X$ (X: Cl, Br) is the linker complex.

Two Mn-MOFs containing the linker complexes $Mn(CO)_3(bdmpzm)X$ (X: Cl, Br) have been investigated using TRIR, and are denoted as Mn-MOF (Cl) and Mn-MOF (Br), based on the halogen ligand.

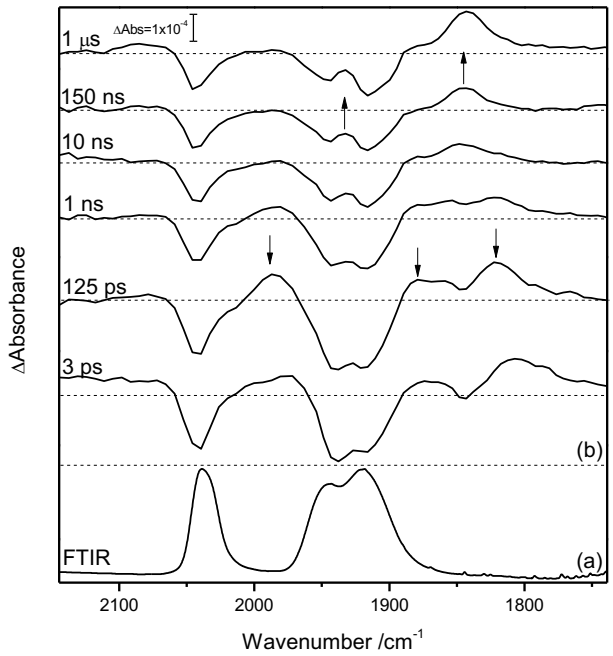


Figure 5.46 *(a) FTIR spectrum and (b) TRIR spectra obtained following photolysis (355 nm) of Mn-MOF (Cl) in a NaCl disc.*

As shown in Figure 5.46, upon UV photolysis, three bands at lower wavenumbers to the parent bleaches are formed at *ca.* 1973, 1860 and 1805 cm^{-1}, which then narrow and blue-shift to *ca.* 1983, 1870 and 1821 cm^{-1}. At later time delays, the three bands (*ca.* 1983, 1870 and 1821 cm^{-1}) decay and two bands at *ca.* 1932 and 1843 cm^{-1} are formed, which are stable during the experimental timescale (up to 50 μs).

The results of kinetic analysis from this experiment are summarized in Table 5.10.

Table 5.10 *Summary of TRIR results and kinetics of the Mn-MOF (Cl).*

band position/ cm^{-1}	growth /ns	decay /ns
1805		0.025 ± 0.006
1843	t_1= 0.02 ± 0.008; t_2= 6.9 ± 2.6	
1916 (parent)	t_1= 0.03 ± 0.01; t_2= 0.9 ± 0.4	
1932	t_1= 0.03 ± 0.008; t_2= 1.0 ± 0.2	
1943 (parent)	t_1= 0.03 ± 0.01; t_2= 1 ± 0.5	
1983		t_1= 0.3 ± 0.09; t_2= 4.2 ± 2.7
2039 (parent)	t_1= 0.03 ± 0.007; t_2= 0.9 ± 0.3	

As the data shows, the band at 1983 cm^{-1} decays bi-exponentially (t_1= 0.3 ± 0.09 ns; t_2= 4.2 ± 2.7 ns). The short-lived component t_1 is similar to the t_2 component of the parent bands recovery (*ca.* 1 ns), while t_2 is similar to the growth rate of the band at 1843 cm^{-1} (6.9 ± 2.6 ns). The t_1 of the parent bands recovery, and the t_1 growth of the band at 1843 cm^{-1} also fit the decay rate of the assigned vibrational hot band at 1805 cm^{-1}.

Comparing to the similar TRIR spectra of the linker complex $Mn(CO)_3$(bdmpzm)Br, the bands at 1983 and 1822 cm^{-1} are tentatively assigned to the unsaturated dicarbonyl species $Mn(CO)_2$(bdmpzm)Cl. The band at *ca.* 1870 cm^{-1} may be one of the *mer* dicarbonyl species. These assignments are supported by DFT calculations, see Table 5.11 (From the calculated IR spectra, the *mer*-dicarbonyl species which loses CO at the equatorial position was found to have ν(CO) different to the other *mer*-dicarbonyls. It possesses two ν(CO) band positions of significantly different intensities. Thus, in real IR spectra, the weak absorption band expected at higher wavenumber may not be observed. Other *mer*-dicarbonyls may overlap with the *fac*-dicarbonyls, as suggested by the DFT results in Table 5.11).

The stability of the final product at *ca.* 1932 and 1843 cm^{-1} leads to the question that whether the linker complex $Mn(CO)_3$(bdmpzm)Cl in the MOF structure is in a vacuum environment or is it surrounded by molecules in the MOF channel. These

molecules could be residue of solvents or reagents from the synthesis process or from the ambient air. The final product (1932 and 1843 cm^{-1}) shows no decay during the experimental timescale (up to 50 μs), indicating that the final dicarbonyl species has coordinated to the surrounding molecules.

According to the synthesis method undertaken by our collaborators,[47] water and DMF could all be trapped in the MOF channel. Also, as the MOF sample was sealed in ethanol when sent from our collaborators, which means ethanol could also be in the MOF channel even when the sample is dried prior to measurement. Therefore, DFT calculations on the solvated dicarbonyls by H_2O, ethanol and DMF were undertaken, and the results are summarized in Table 5.11.

Table 5.11 *Summary of the DFT calculations of $Mn(CO)_3$(bdmpzm)Cl and the solvated dicarbonyl species with H_2O, ethanol and DMF (method: B3LYP, 6-31G(d), gas phase).*

Species	ν(CO)/ cm^{-1}	IR intensity /x10^3 Km mol^{-1}	Energy/ a.u.
*fac*1	2117, 2057, 2015	0.819, 0.813, 0.819	-2599.0209
*fac*1 loss CO at axial	2065, 1984	0.836, 0.865	-2485.6567
*fac*1 loss CO at axial(H_2O)	2048, 1973	0.748, 0.901	-2562.0984
*fac*1 loss CO at axial(EtOH)	2046, 1960	0.710, 0.843	-2195.4459
*fac*1 loss CO at axial(DMF)	2043, 1966	0.709, 0.867	-2734.1947
*fac*1 loss CO at equatorial	2065, 1984	0.826, 0.865	-2485. 6567
*fac*1 loss CO at equatorial(H_2O)	2048, 1973	0.748, 0.902	-2562.0984
*fac*1 loss CO at equatorial(EtOH)	2046, 1960	0.709, 0.844	-2195.4459
*fac*1 loss CO at equatorial(DMF)	2043, 1967	0.709, 0.867	-2734.1947

*fac*2	2116, 2055, 2009	0.687, 0.781, 0.802	-2599.0173
*fac*2 loss CO at axial	2062, 1979	0.896, 0.844	-2485. 6521
*fac*2 loss CO at axial(H_2O)	2057, 1968	0.837, 0.854	-2562.0901
*fac*2 loss CO at axial(EtOH)	2040, 1960	0.743, 0.803	-2195.4511
*fac*2 loss CO at axial(DMF)	2038, 1944	0.772, 0.812	-2734.1861
*fac*2 loss CO at equatorial	2062, 1979	0.896, 0.844	-2485. 6521
*fac*2 loss CO at equatorial(H_2O)	2044, 1968	0.799, 0.885	-2562.0935
*fac*2 loss CO at equatorial(EtOH)	2042, 1953	0.759, 0.819	-2195.4440
*fac*2 loss CO at equatorial(DMF)	2038, 1962	0.769, 0.849	-2734.1920
mer	2123, 2045, 2037	0.170, 1.46, 0.704	-2598.9968
mer loss CO at axial 1	2065, 1984	0.826, 0.865	-2485. 6567
mer loss CO at axial 1(H_2O)	2059, 1976	0.804, 0.856	-2562.0942
mer loss CO at axial 1(EtOH)	2047, 1963	0.714, 0.862	-2195.4460
mer loss CO at axial 1(DMF)	2043, 1967	0.709, 0.867	-2734.1947
mer loss CO at axial 2	2062, 1979	0.896, 0.844	-2485. 6521
mer loss CO at axial 2(H_2O)	2044, 1968	0.799, 0.885	-2562.0935
mer loss CO at axial 2(EtOH)	2042, 1953	0.759, 0.819	-2195.4440

mer loss CO at axial 2(DMF)	2038, 1962	0.768, 0.849	-2734.1920
mer loss CO at equatorial	2006	1.80	-2485.6284
mer loss CO at equatorial(H_2O)	2082, 1989	0.148, 1.75	-2562.0653
mer loss CO at equatorial(EtOH)	1992	1.74	-2195.4179
mer loss CO at equatorial(DMF)	2070, 1986	0.126, 1.70	-2734.1646

Comparing the data in Table 5.11, it was apparent that solvation causes the ν(CO) band positions to shift to lower wavenumbers. The ν(CO) band positions of the ethanol and the DMF-bound species are at lower positions than that of the water-bound species. Considering the relative energies, the DMF species is proposed to be the most stable. Therefore, in the presence of DMF, it is likely that the CO-loss dicarbonyls may coordinate to DMF.

Based on the experimental results and DFT calculations, a proposed reaction mechanism for Mn-MOF but localized on the $Mn(CO)_3$(bdmpzm)Cl linker complex can be described as shown in Figure 5.47.

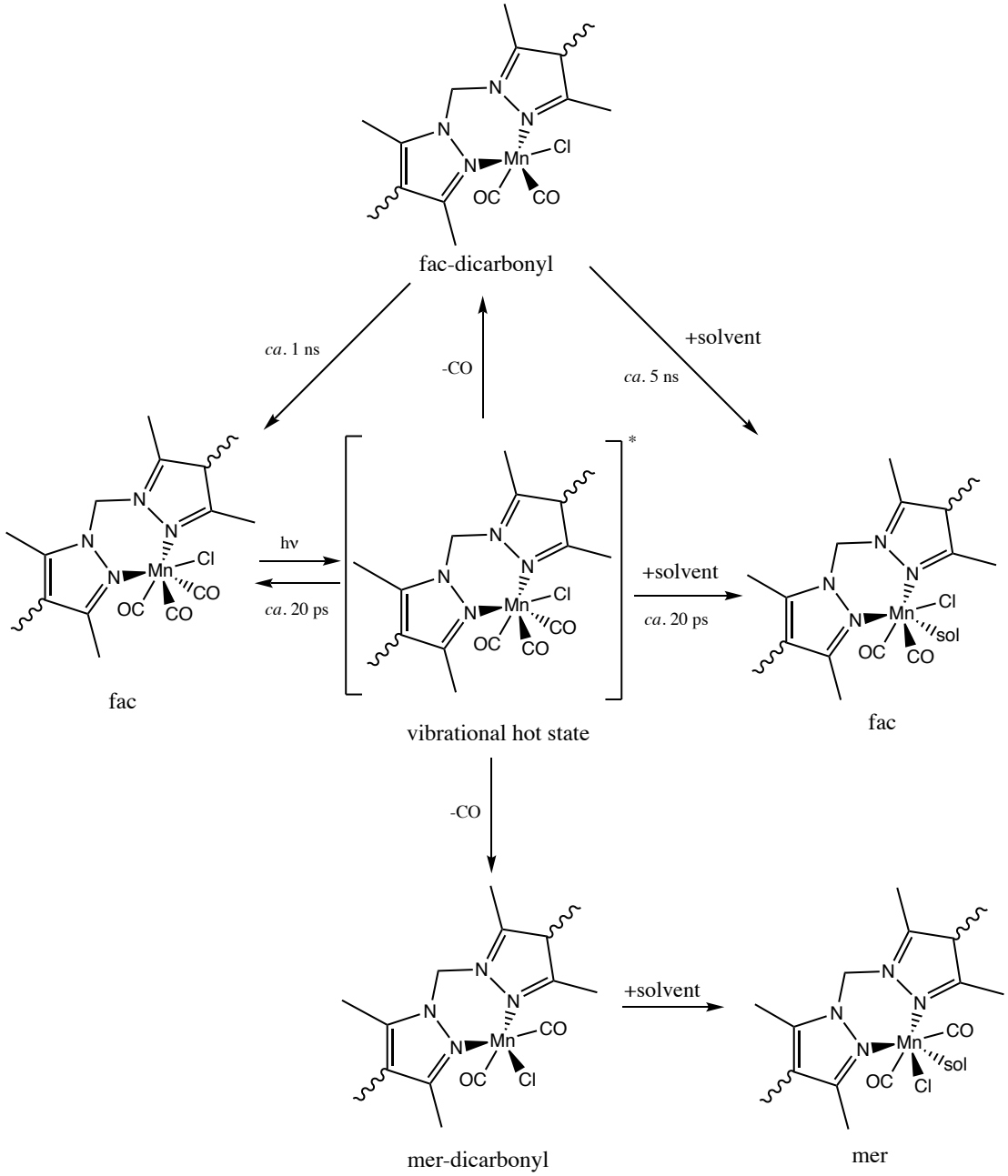


Figure 5.47 *Assumed photo-reaction mechanism of the linker complex $Mn(CO)_3(bdmpzm)Cl$ within the MOF structure. Sol corresponds to substance present in the MOF channel.*

We also explored the effect of changing the halide of the linker complex to Br using TRIR. The results are almost identical to those obtained for Mn-MOF (Cl). The TRIR spectra are shown in Figure 5.48.

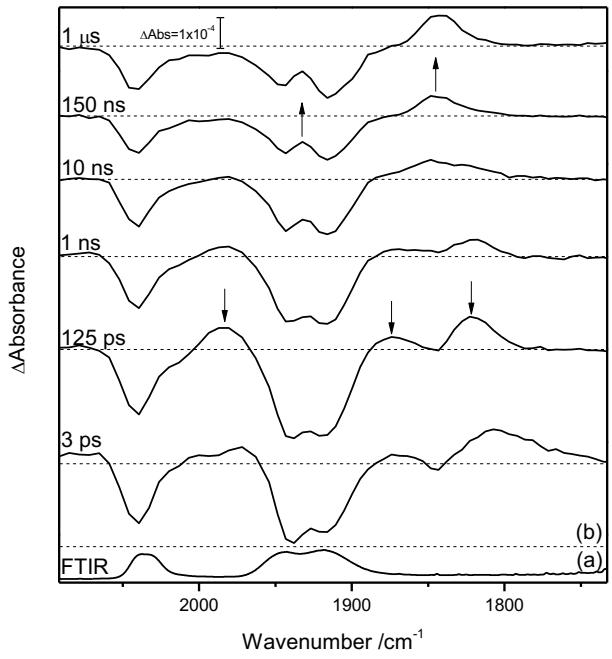


Figure 5.48 *(a) FTIR spectrum and (b) TRIR spectra obtained following photolysis (355 nm) of Mn-MOF (Br) in a NaCl disc.*

Almost identical to Mn-MOF (Cl), upon UV photolysis three bands are formed at *ca.* 1981, 1874 and 1822 cm^{-1}, along with the bleach of the parent bands (2039, 1943 and 1916 cm^{-1}). Two bands at *ca.* 1932 and 1843 cm^{-1} are formed at later time delays.

Kinetic analysis revealed similar reaction kinetics to those obtained for Mn-MOF (Cl). It is concluded that the halogen ligands Cl^- and Br^- are similar in nature and appear to have no significant influence on the photoreaction of the linker complex $Mn(CO)_3(bdmpzm)X$ (X: Cl, Br) within the MOF. It is also possible that rather than coordination of Cl^- or Br^- as the axial ligand, instead, DMF, ethanol or water may have coordinated.

To investigate the influence of these different axial ligands, DFT calculations on the complexes $Mn(CO)_3(bdmpzm)(H_2O)$, $Mn(CO)_3(bdmpzm)(EtOH)$ and $Mn(CO)_3$-(bdmpzm)(DMF) were conducted. The results are shown in Tables 5.12, 5.13 and 5.14.

Table 5.12 *Summary of the DFT calculations (B3LYP, 6-31G(d), gas phase) of* $Mn(CO)_3(bdmpzm)(H_2O)$.

Species	ν(CO)/ cm^{-1}	IR intensity /x10^3 Km mol^{-1}	Energy/ a.u.
*fac*1	2139, 2071, 2064	0.462, 0.839, 0.766	-2214. 9208
*fac*1 loss CO at axial	2089, 2026	0.653, 0.856	-2101.5974
*fac*1 loss CO at equatorial	2089, 2026	0.653, 0.856	-2101.5606
*fac*2	2143, 2077, 2064	0.557, 0.756, 0.722	-2214. 7751
*fac*2 loss CO at axial	2084, 2018	0.684, 0.829	-2101.4995
*fac*2 loss CO at equatorial	2096, 2035	0.733, 0.837	-2101.5134
mer	2158, 2078, 2058	0.168, 1.28, 0.767	-2214.9403
mer loss CO at axial 1	2089, 2026	0.653, 0.856	-2101.5389
mer loss CO at axial 2	2096, 2035	0.733, 0.837	-2101.4429
mer loss CO at equatorial	2128, 2040	0.060, 1.71	-2101.5902

The IR spectra generated from these calculations are shown in Figure 5.49. For ease of viewing, the spectra are presented as difference spectra, such as the ν(CO) bands of the parent complex is negative in intensity and the bands of all transient species are positive.

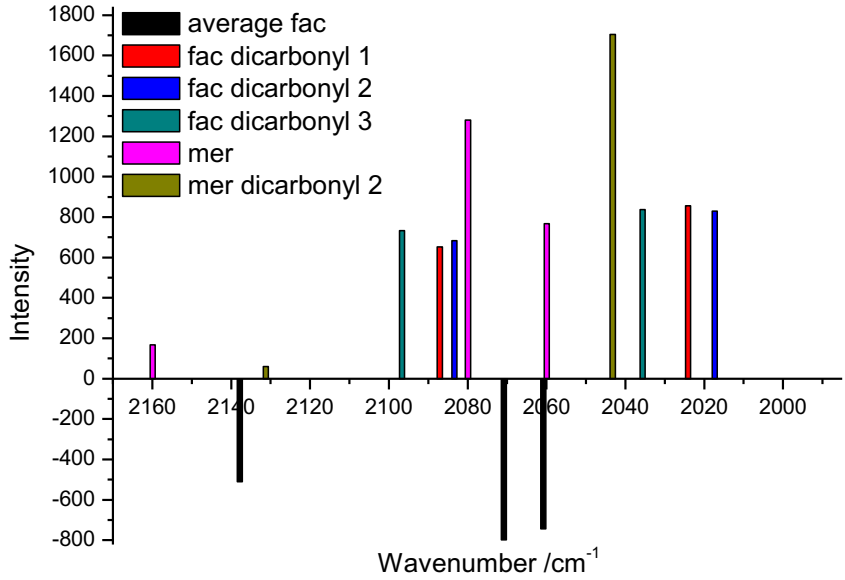


Figure 5.49 *ν(CO) band positions from calculations ran on the $Mn(CO)_3(bdmpzm)(H_2O)$ species (B3LYP, 6-31G(d), gas phase). Average fac: average ν(CO) of fac 1 and fac 2; fac dicarbonyl 1: 2089, 2026 cm^{-1}; fac dicarbonyl 2: 2084, 2018 cm^{-1}; fac dicarbonyl 3: 2096, 2035 cm^{-1}; mer dicarbonyl 2: 2128, 2040 cm^{-1}.*

Table 5.13 *Summary of the results of the DFT calculations (B3LYP, 6-31G(d), gas phase) of Mn(bdmpzm)(CO)$_3$(EtOH) and Mn(bdmpzm)(CO)$_2$(EtOH).*

Species	IR frequency/ cm^{-1}	IR intensity /x10^3 Km mol^{-1}	Energy/ a.u.
*fac*1	2137, 2068, 2062	0.452, 0.854, 0.725	-2293.5286
*fac*1 loss CO at axial	2083, 2020	0.608, 0.840	-2180.2189
*fac*1 loss CO at equatorial	2082, 2021	0.578, 0.893	-2179.9437
*fac*2	2140, 2072, 2061	0.536, 0.726, 0.737	-2292.8342
*fac*2 loss CO at axial	2091, 2030	0.749, 0.882	-2180.2242
*fac*2 loss CO at equatorial	2089, 2029	0.711, 0.856	-2180.2486
mer	2151, 2070, 2057	0.139, 1.21, 0.759	-2293.5470
mer loss CO at axial 1	2084, 2023	0.642, 0.840	-2180.1621
mer loss CO at axial 2	2090, 2030	0.703, 0.862	-2180.2387
mer loss CO at equatorial	2123, 2034	0.040, 1.64	-2180.2173

The calculated IR spectra is shown in Figure 5.50

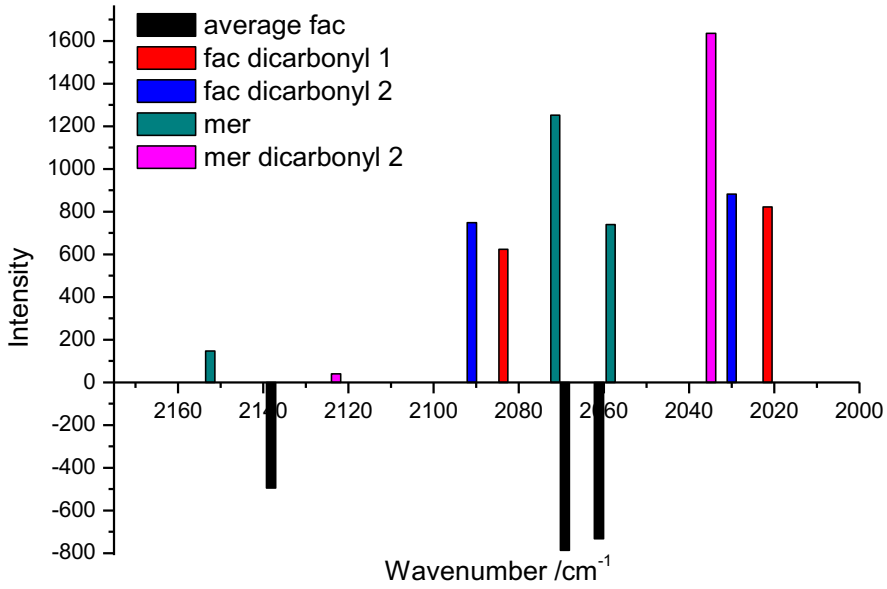


Figure 5.50 *DFT calculations of Mn(bdmpzm)(CO)$_3$(EtOH) species (B3LYP, 6-31G(d), gas phase). Average fac: average ν(CO) of fac 1 and fac 2; fac dicarbonyl 1: 2083, 2020 cm^{-1}; fac dicarbonyl 2: 2091, 2030 cm^{-1}; mer dicarbonyl 2: 2123, 2034 cm^{-1}.*

Table 5.14 *Summary of the results of the DFT calculations (B3LYP, 6-31G(d), gas phase) of the Mn(bdmpzm)(CO)$_3$(DMF) species.*

Species	IR frequency/ cm^{-1}	IR intensity /x10^3 Km mol^{-1}	Energy/ a.u.
*fac*1	2133, 2066, 2051	0.471, 0.817, 0.804	-2387.1352
*fac*1 loss CO at axial	2077, 2011	0.580, 0.823	-2273.7671
*fac*1 loss CO at equatorial	2077, 2011	0.579, 0.823	-2273.7671
*fac*2	2135, 2068, 2051	0.452, 0.834, 0.887	-2387.1231
*fac*2 loss CO at axial	2076, 2001	0.653, 0.759	-2273.7699
*fac*2 loss CO at equatorial	2076, 2002	0.653, 0.759	-2273.7699
mer	2151, 2069, 2047	0.160, 1.09, 0.879	-2387.1167
mer loss CO at axial 1	2077, 2011	0.579, 0.823	-2273.7671
mer loss CO at axial 2	2076, 2002	0.653, 0.759	-2273.7699
mer loss CO at equatorial	2122, 2033	0.044, 1.65	-2273.7406

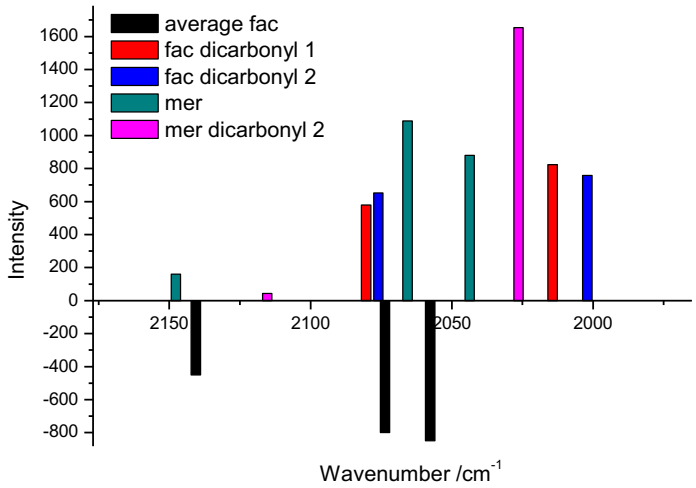


Figure 5.51 *DFT calculations of Mn(bdmpzm)(CO)$_2$(DMF) (B3LYP, 6-31G(d), gas phase). Average fac: average ν(CO) of fac 1 and fac 2; fac dicarbonyl 1: 2077, 2011 cm^{-1}; fac dicarbonyl 2: 2076, 2002 cm^{-1}; mer dicarbonyl 2: 2122, 2033 cm^{-1}.*

Comparing the DFT results of Mn(bdmpzm)(CO)$_3$Cl (Table 5.11), Mn(bdmpzm)(CO)$_3$Br (Table 5.8), Mn(bdmpzm)(CO)$_3$(H$_2$O) (Table 5.12), Mn(bdmpzm)(CO)$_3$(EtOH) (Table 5.13) and Mn(bdmpzm)(CO)$_3$(DMF) (Table 5.14), it can be noted that, the Δν(CO) between the two lower ν(CO) bands is smaller for Mn(bdmpzm)(CO)$_3$(H$_2$O), Mn(bdmpzm)(CO)$_3$(EtOH) and Mn(bdmpzm)(CO)$_3$(DMF) being of *ca.* 10, 8 and 15 cm^{-1}, respectively. This is in distinct difference with that of Mn(bdmpzm)(CO)$_3$Cl for *ca.* 44 cm^{-1}, and Mn(bdmpzm)(CO)$_3$Br for *ca.* 38 cm^{-1}. The experimental Δν(CO) for the Mn-linker in Mn-MOF (Cl) and Mn-MOF (Br) is *ca.* 27 cm^{-1}. The Δν(CO) of Mn(bdmpzm)(CO)$_3$Br in toluene is *ca.* 36 cm^{-1}, in DMF is *ca.* 25 cm^{-1} (Section 5.2.3). Meanwhile, the much higher energies of Mn(bdmpzm)(CO)$_3$(H$_2$O) (*ca.* -2215 a.u.), Mn(bdmpzm)(CO)$_3$(C$_2$H$_5$OH) (*ca.* -2294 a.u.) and Mn(bdmpzm)(CO)$_3$(DMF) (*ca.* -2387 a.u.), compared to Mn(bdmpzm)(CO)$_3$Cl (*ca.* -2599 a.u.) and Mn(bdmpzm)(CO)$_3$Br (*ca*. -4711 a.u.), leads to the conclusion that in the presence of the halogen ligands, coordination of H$_2$O, C$_2$H$_5$OH and DMF is of low probability. From this, the identical IR spectra and kinetic behaviors of Mn-MOF (Cl) and Mn-MOF (Br) is attributed to the changing of halogen ligands has little influence on the photoproperties of the Mn-MOF. Previous

research has shown that changing of halide ligands from Cl to Br alters the electronic excited state of the Re-diimine complexes, from a MLCT to XLCT state.[21] However, the results here suggest that for the Mn-(bis-pyrazol) complexes, the halide ligands have little influence on its photophysical properties, which is more evidence for the difference in the photophysical behaviors of the metal-diimine and metal-(bis-pyrazol) complexes.

In order to better understand the reaction mechanism, the effects of temperature have also been investigated using TRIR. The results are discussed in the following section.

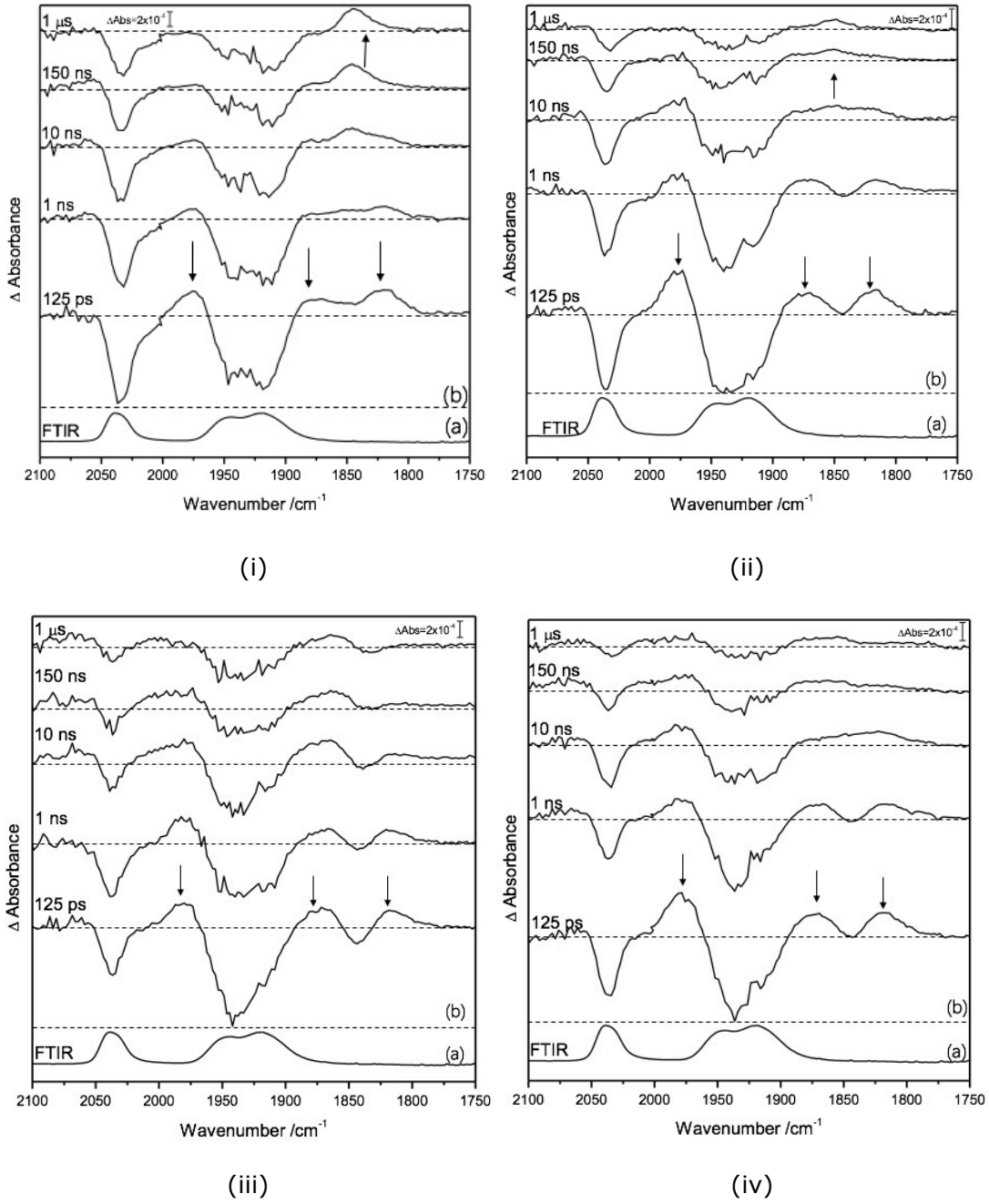


Figure 5.52 *(a) FTIR spectrum and (b) TRIR spectra obtained following photolysis (355 nm) of Mn-MOF (Cl) in a NaCl disc at different temperatures of (i) room temperature; (ii) 180 K; (iii) 150 K; (iv) 120K.*

By comparing the spectra at different temperatures (Figure 5.52), it can be noted that, the band intensity of the final product at *ca.* 1845 cm^{-1} was found to decrease with decreasing temperature. At 120K it is difficult to resolve the presence of any band near 1845 cm^{-1}, while the bands at *ca.* 1975, 1820 and 1870 cm^{-1} were stable at low temperatures. Kinetic analysis shows that the lifetime of the bands at *ca.*

1820 and 1975 cm^{-1} (*ca.* 2-4 ns) did not change with temperature. Kinetic links between ν(CO) bands at 1820 cm^{-1} (80 ±20 ps, 3.9 ±1.8 ns), 1845 cm^{-1} (20 ±9 ps, 4.8 ±2 ns) and one of the parent bands at 2034 cm^{-1} (30 ±4 ps, 6 ±2 ns) are observed at room temperature.

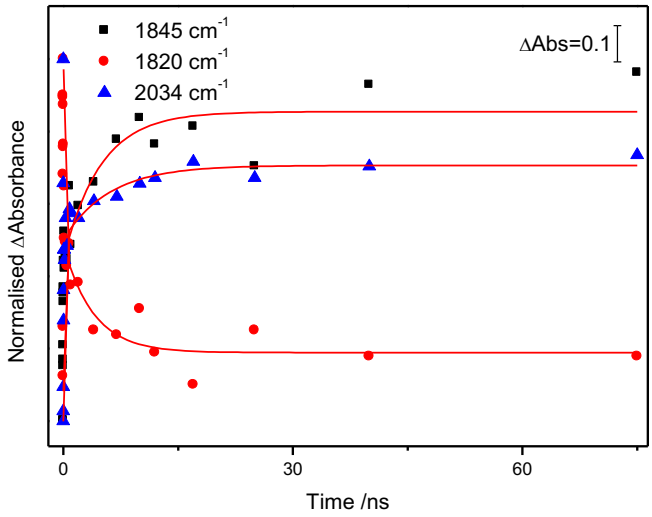


Figure 5.53 *TRIR kinetic traces of bands corresponding to different species observed following photolysis of Mn-MOF (Cl) in a NaCl disc at room temperature.*

The low temperature appears to hinder the formation of the final product at *ca.* 1845 cm^{-1} assigned to a solvated dicarbonyl species coordinated to molecules in the MOF channel, such as water, ethanol and DMF. The species at 1870 cm^{-1} is assumed to be the unsaturated mer-dicarbonyl, while the bands at *ca.* 1975 and 1820 cm^{-1} are attributed to the unsaturated dicarbonyl $Mn(CO)_2$(bdmpzm)Cl. The results from the low temperature study imply that low temperature may slow down the coordination of water, ethanol or DMF to the unsaturated dicarbonyl species.

TRIR investigations on Mn-MOF (Br) under different temperatures was also undertaken, similar results were obtained and are not presented here.

As discussed above, it is proposed that the linker complex $Mn(CO)_3$(bdmpzm)X (X: Cl, Br) coordinates to molecules in the MOF channel after photo-induced CO-loss. From this we chose to investigate how the nature of the molecules in the MOF channel affect the photoreactivity of the MOF. For these studies, our collaborators

sent another batch of Mn-MOF. As the photoproperties of the MOFs discussed in this Chapter to date [Mn-MOF (Cl) and Mn-MOF (Br)] have been found to be identical, they are denoted from this point on as Mn-MOF (2015), and the new batch of Mn-MOF denoted as Mn-MOF (2016). From our collaborators, we were informed that Mn-MOF (2016) has $Mn(bdmpzm)(CO)_3Br$ as the linker complex.

Five solvents were investigated in these studies, ethanol, toluene, hexane, perfluorohexane (PFH) and perfluorotriethylamine (PFTEA). For each solvent, a sample of Mn-MOF was first immersed, and then pressed into a NaCl disc. TRIR spectra obtained for each of the solvents are shown in Figure 5.54. It was found that different solvents have no apparent influence on the photoreaction of Mn-MOF (2016), except ethanol.

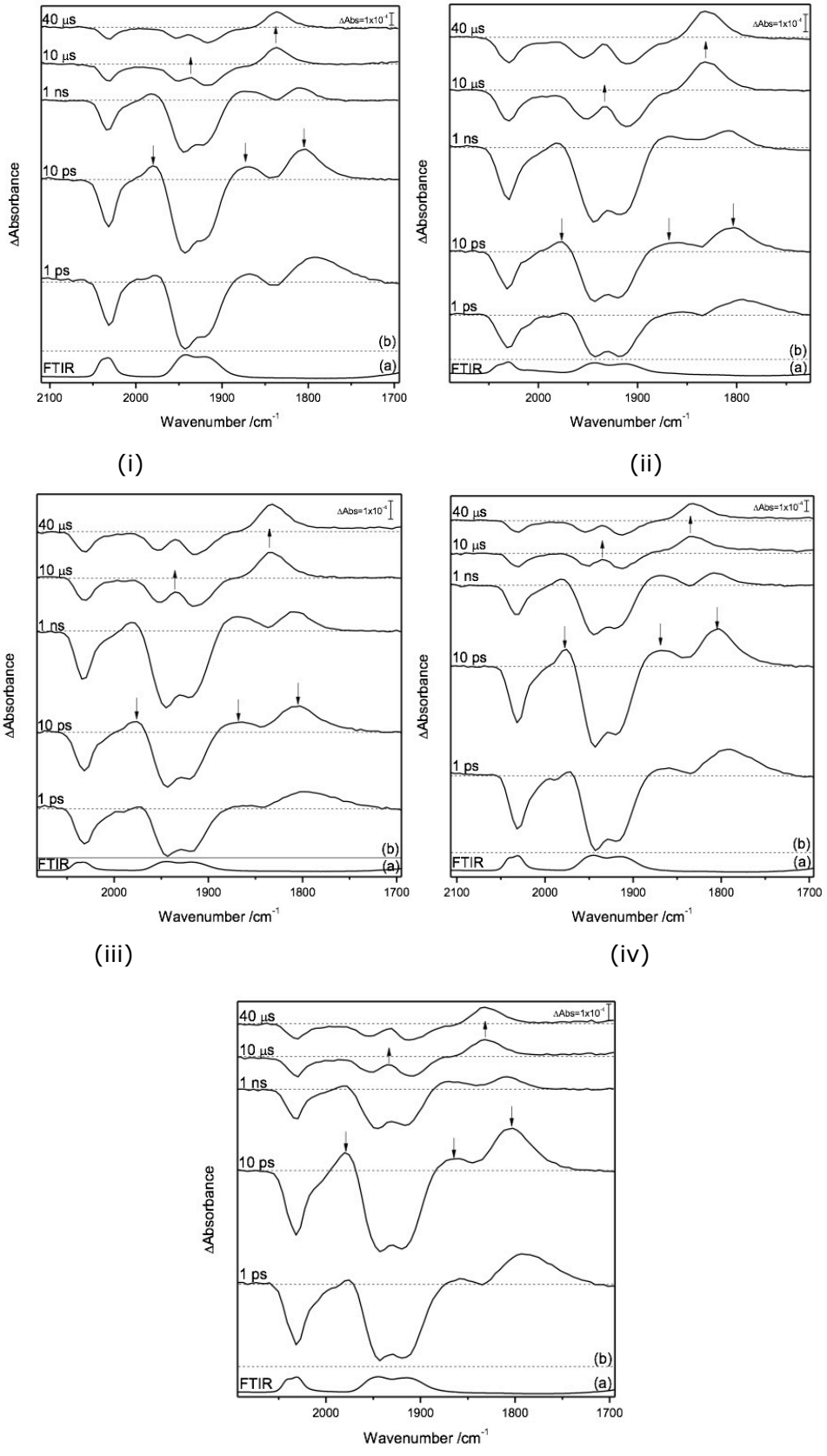


Figure 5.54 *(a) FTIR spectrum and (b) TRIR spectra obtained following photolysis (355 nm) of Mn-MOF (2016) in a NaCl disc following immersion in (i) ethanol; (ii)*

toluene; (iii) hexane; (iv) PFH (perfluorohexane); (v) PFTEA (perfluorotriethylamine).

It was observed from the TRIR spectra that, upon UV photolysis, three transient ν(CO) bands at *ca.* 1980, 1872 and 1809 cm^{-1} are formed. At later time delays, these bands decay and two bands at *ca.* 1933 and 1832 cm^{-1} are generated. However, in ethanol the ν(CO) of the final dicarbonyl product was observed to blue-shift to *ca.* 1836 cm^{-1}. Kinetic analysis reveals similar kinetics for samples in different solvents except ethanol on the early ps-timescale. The bands at 1980 and 1809 cm^{-1} were observed to decay in *ca.* 5 ns for all samples except ethanol. While for the sample in ethanol, the lifetime of these two bands is *ca.* 0.5 ns, as shown in Figure 5.55.

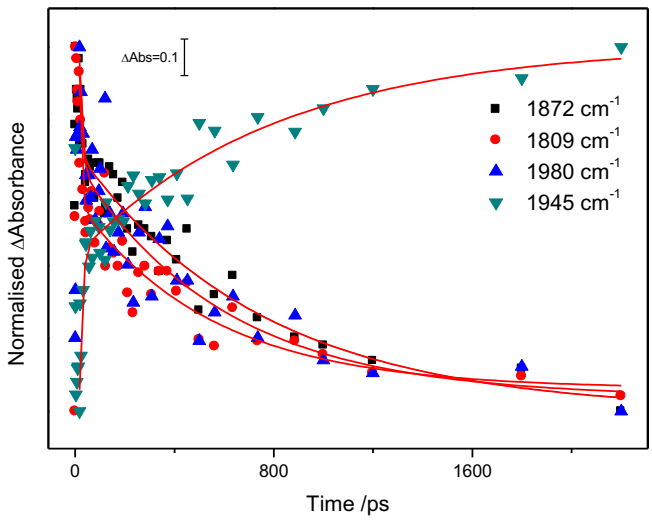


Figure 5.55 *Kinetic traces obtained at 1980, 1945 (parent band), 1872 and 1809 cm^{-1} of Mn-MOF (2016) in ethanol on the ps-timescale. 1872 cm^{-1}: t_1= 8 ± 3 ps; t_2= 0.7 ± 0.1 ns; 1809 cm^{-1}: t_1= 8 ± 3.5 ps; t_2= 0.5 ± 0.1 ns; 1980 cm^{-1}: t_1= 11 ± 7 ps; t_2= 0.6 ± 0.2 ns; 1945 cm^{-1}: t_1= 11 ± 3 ps; t_2= 0.8 ± 0.2 ns.*

The results of Mn-MOF (2016) are similar to Mn-MOF (2015) as discussed before. Thus, the bands at 1980 and 1809 cm^{-1} are assigned to the unsaturated dicarbonyl species. The band at 1872 cm^{-1} is assigned to the unsaturated *mer*-dicarbonyl species.

On the ns-timescale, kinetic analysis suggests that the final product at *ca.* 1933 and 1832 cm^{-1} is formed from the species at 1872 cm^{-1} (Figure 5.56).

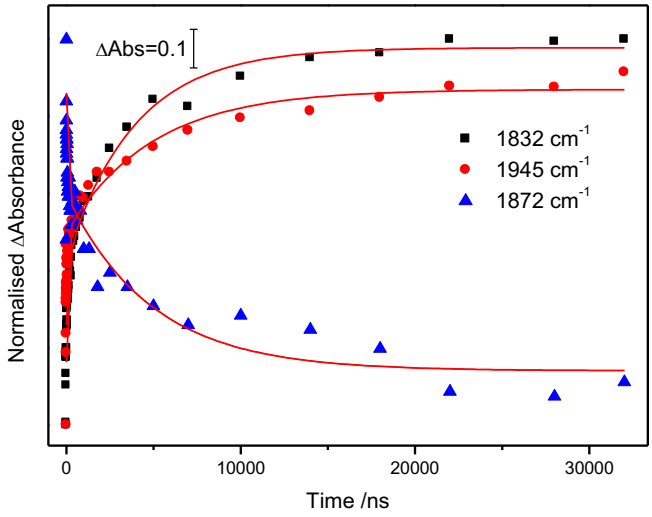


Figure 5.56 *TRIR kinetic traces obtained at 1945 (parent band), 1872 and 1832 cm^{-1} of Mn-MOF (2016) in ethanol on the ns-timescale. 1832 cm^{-1}: t_1= 128 ± 20 ns; t_2= 3.9 ± 0.4 μs; 1945 cm^{-1}: t_1= 56 ± 10 ns; t_2= 4.9 ± 0.7 μs; 1872 cm^{-1}: t_1= 41 ± 10 ns; t_2= 4.9 ± 0.9 μs.*

It is proposed that the band at 1872 cm^{-1} is the unsaturated *mer*-dicarbonyl species, which slowly coordinates to the surrounding molecules, and forms the *mer*-solvated species. Kinetic analysis shows that for samples in toluene, hexane, PFH and PFTEA, the lifetime of the decay of the band at 1872 cm^{-1} and formation of the band at 1832 cm^{-1} is *ca.* 2~3 μs, while for the sample in ethanol, the measured lifetime is *ca.* 4.5 μs. The band position of the final product also blue-shifted to 1836 cm^{-1} for the sample in ethanol. This is attributed to the fact that for the solvents toluene, hexane, PFH and PFTEA, which are considered to be larger in size compared to ethanol, may be unable to successfully penetrate into the MOF channel, unlike EtOH. Water (ε: 80.1) or DMF (ε: 36.7) may exist in the MOF channel. Both of these molecules are more polar than ethanol (ε: 24.5), and may exist due to residues from synthesis or from water absorbed from the atmosphere. This explains the red-shift of ν(CO) compared to ethanol, as well as the faster solvation rate.

As the DFT calculations of $Mn(bdmpzm)(CO)_3Br$ and the DMF-bound dicarbonyl

species Mn(bdmpzm)$(CO)_2$Br(DMF) have been already conducted, as shown in Tables 5.8 and 5.9. Therefore, here only the DFT calculations of the water-bound species Mn(bdmpzm)$(CO)_2$Br(H_2O) is presented, as shown in Table 5.15.

Table 5.15 *DFT calculation (method: B3LYP; basis set: 6-31G(d), gas phase) on the Mn(bdmpzm)$(CO)_2$Br(H_2O) species.*

Species	IR frequency/ cm^{-1}	IR intensity /x10^3 Km mol^{-1}	Energy/ a.u.
*fac*1 loss CO at axial(H_2O)	2044, 1973	0.745, 0.903	-4673.6219
*fac*1 loss CO at equatorial(H_2O)	2044, 1973	0.745, 0.903	-4673.6219
*fac*2 loss CO at axial(H_2O)	2054, 1970	0.846, 0.860	-4673.6146
*fac*2 loss CO at equatorial(H_2O)	2041, 1968	0.803, 0.892	-4673.6182
mer loss CO at axial 1(H_2O)	2055, 1976	0.799, 0.860	-4673.6175
mer loss CO at axial 2(H_2O)	2041, 1968	0.803, 0.892	-4673.6182
mer loss CO at equatorial(H_2O)	2077, 1984	0.136, 1.67	-4673.5907

Based on this data, the calculated IR spectra can be plotted and are shown in Figure 5.57.

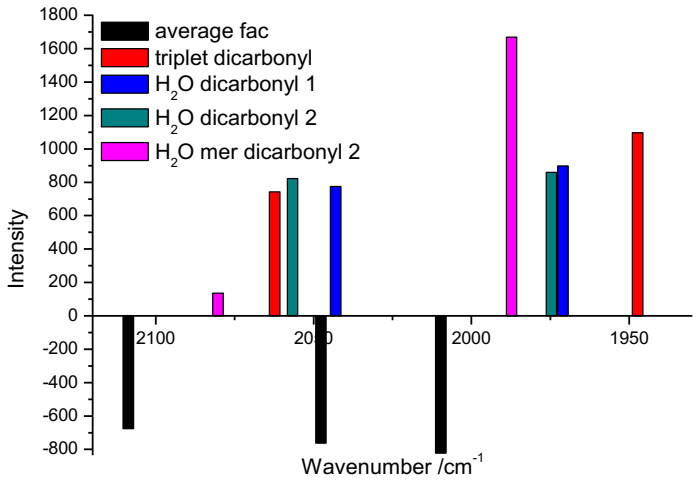


Figure 5.57 *Calculated ν(CO) bands from DFT calculations of $Mn(CO)_2$(bdmpzm)Br dicarbonyls coordinated with H_2O. (B3LYP, 6-31G(d), gas phase). H_2O dicarbonyl 1: 2043, 1971 cm^{-1}; H_2O dicarbonyl 2: 2055, 1973 cm^{-1}; H_2O mer dicarbonyl 2: 2077, 1984 cm^{-1}.*

Thus, in MOF structure, the final product is considered to have transformed from both the unsaturated *fac*-dicarbonyl and *mer*-dicarbonyl, similar to the results of the linker complex in solvents as discussed in Section 5.2.3 and Mn-MOF (2015). Therefore, based on the data and discussions, the photochemistry of the linker complex in MOF structure is proposed to be as shown in Figure 5.58.

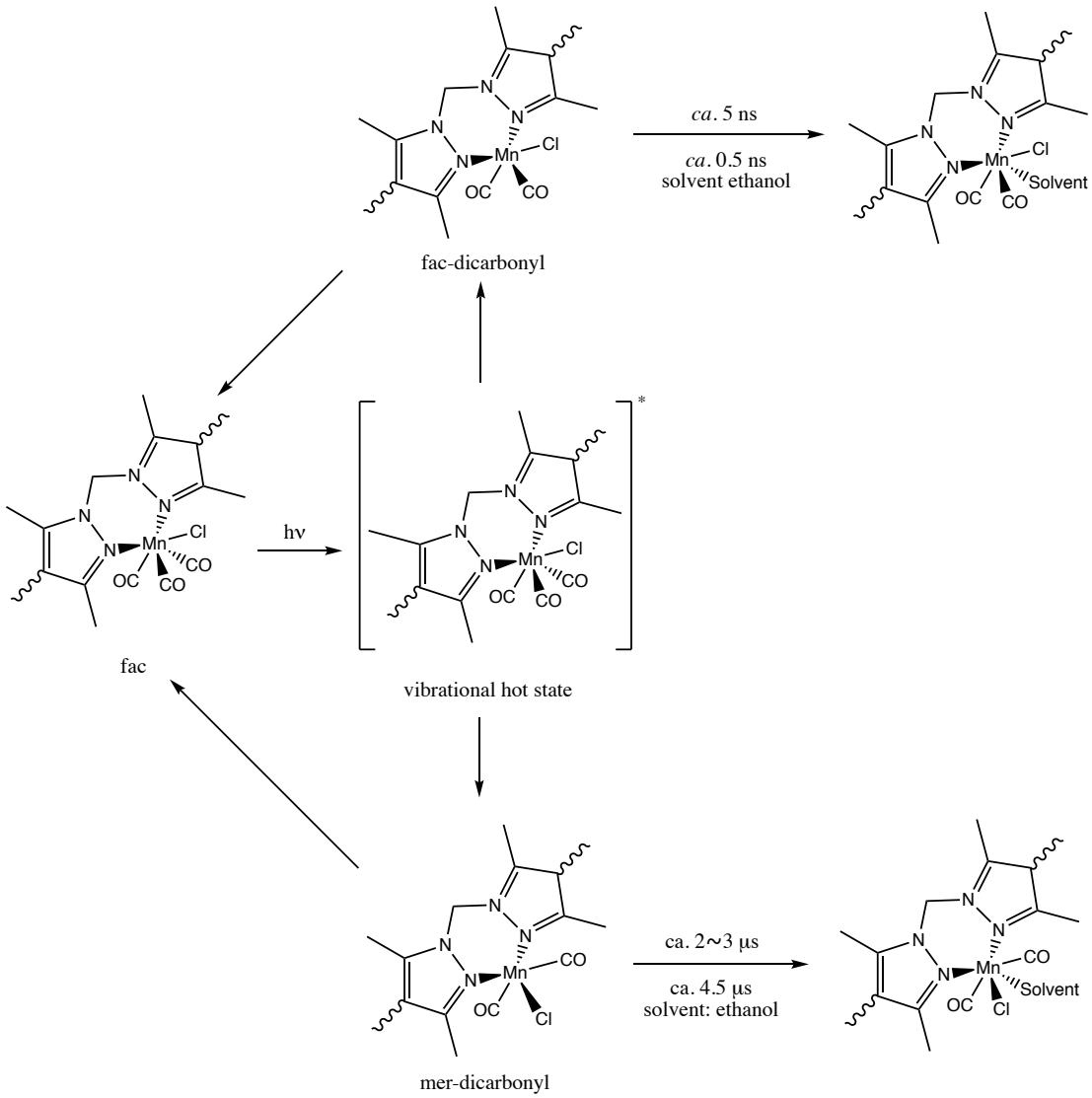


Figure 5.58 *Assumed reaction mechanism of the linker complex $Mn(CO)_3(bdmpzm)Br$ within the Mn-MOF (2016) structure.*

The recorded FTIR spectra support the existence of water within the Mn-MOF (2016) structure (Figure 5.59). FTIR of both wet and dried samples are collected. Two methods were used to dry the Mn-MOF (2016) sample. Drying the sample as powder and drying the disc once it has been made.

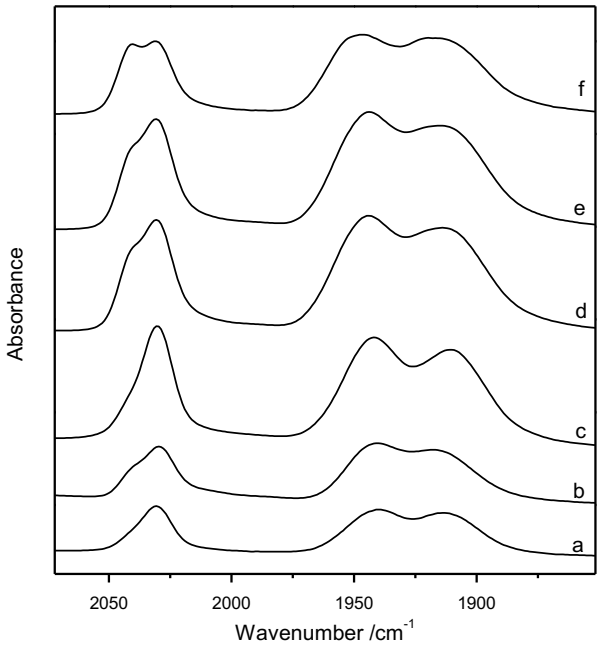


Figure 5.59 *FTIR spectra of Mn-MOF (2016) samples prepared using different methods. a: Mn-MOF was suspended in ethanol and dried as a disc; b: Mn-MOF is from ethanol and dried from the powder; c: Mn-MOF is from toluene and dried as a disc; d: Mn-MOF is from toluene and dried from the powder; e: Mn-MOF was suspended in toluene, blow-dried using argon and then immersed in water, undried; f: Mn-MOF was suspended in toluene and undried. All disc samples were prepared in a NaCl disc and dried samples are processed by heating in an oven at 110 °C for 15 min.*

From the FTIR spectra (Figure 5.59) it can clearly be observed that, for samples f and e, which are regarded as containing water in the MOF channel, there is a shoulder band at *ca.* 2039 cm^{-1}. This was also observed for samples dried as powders from both solvents. For the samples dried as discs, this shoulder band at *ca.* 2039 cm^{-1} is diminished, as shown for samples a and c, indicating that this dehydration process is much more complete than drying the powder. In the disc, the Mn-MOF is surrounded by NaCl crystals, which may be capable of slowing down the intrusion of water from the air. While for the samples dried as powder, although dehydration of the sample was completed to some extent in the oven, when the powder is exposed to the air, it can readily absorb moisture.

Following on from this, TRIR studies on the dried samples were also conducted, and similar reaction processes to the wet samples were observed. However, the kinetics of these processes were different compared to the wet solvated samples. Figure 5.60 shows the TRIR spectra of the dried sample of Mn-MOF (2016) which is dried as a disc.

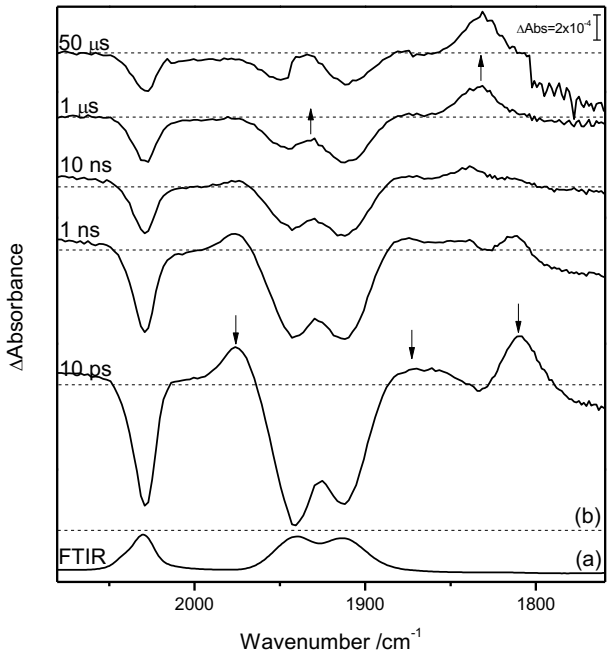


Figure 5.60 *(a) FTIR spectrum and (b) TRIR spectra obtained following photolysis (355 nm) of dried Mn-MOF (2016) dried as disc, sample originally from an ethanol suspension.*

Similar to the wet solvated samples, upon UV photolysis, three features are formed at *ca.* 1976, 1871 and 1810 cm^{-1}. On the later timescale, these bands decay and two bands at *ca.* 1929 and 1831 cm^{-1} are formed. However, kinetic analysis shows that the decay of the initial three features and formation of the bands at 1831 and 1929 cm^{-1} are accelerated for the dried sample compared to the wet sample. The bands at 1976 and 1810 cm^{-1} decays quickly at a similar rate (t_1= 40 ± 9 ps; t_2= 3 ± 0.5 ns and t_1= 50 ± 20 ps; t_2= 2 ± 0.6 ns). The growth rate of the band at 1831 cm^{-1} is similar to the recovery of the parent band at 2029 cm^{-1} (t_1= 17 ± 6 ns; t_2= 1052 ± 325 ns and t_1= 2 ± 0.9 ns; t_2= 1147 ± 820 ns, respectively). Kinetic analysis of the broad feature at *ca.* 1872 cm^{-1} was unsuccessful due to the intense

noise in this region. Nevertheless, the formation of the bands at 1831 and 1929 cm^{-1}, as well as the parent band recovery are still considered to be related to the decay of the bands at 1976, 1810 cm^{-1}, and the broad feature at *ca.* 1872 cm^{-1}. As this compares well with previous results.

The acceleration of the transformation rate of the dicarbonyl species to the final product and the parent bands recovery has also been observed for dried Mn-MOF suspended in toluene. Similar spectra were observed to those in EtOH and as such are not shown here.

The bands for the dried samples are assigned based on former discussions and mechanism as shown in Figure 5.58. The bands at *ca.* 1976 and 1810 cm^{-1} are assigned to the unsaturated dicarbonyl species, while the broad feature at *ca.* 1872 cm^{-1} is assigned to the unsaturated *mer*-dicarbonyl species. The ν(CO) bands at *ca.* 1929 and 1831 cm^{-1} are assigned to the solvated dicarbonyl species, most likely coordinated to water or DMF. However, if the final solvated dicarbonyl species is coordinated to H_2O, then it is expected that by drying the sample, the unsaturated dicarbonyl species can be stabilized and thus the transformation into the final solvated species will be slowed down. However, the kinetics show the opposite result. Meanwhile, the FTIR spectra (Figure 5.59) suggest that the samples dried as discs contain less water than the solvated wet samples or samples dried as powders. These observations may be explained by the fact that, as discussed before, the large molecule sizes of the solvents, such as toluene, hexane, PFH and PFTEA, may make it difficult for these solvent molecules to penetrate into the MOF channel. However, instead, they may cover the cavities, and other molecules such as water cannot enter easily into the channel. The high water contamination of the solvated samples as shown in the FTIR spectra, might be the result of the water molecules being blocked by large solvent molecules outside the cavities, therefore the water molecules cannot easily intrude into the pore to coordinate with the Mn centre. After the drying process, the solvent molecules outside are removed, and the coordination to the unsaturated photo-generated dicarbonyls by other molecules such as water in the air will be more facile. For the sample from the suspension in ethanol, removal of ethanol in the MOF channel might introduce

water into the cavities (the difference of the band position of the final product at 1831 cm^{-1} for the dried sample compared to the solvated sample at 1836 cm^{-1} also supports this assumption).

For the reasons above, the generation of the final solvated product is expected to be faster for samples dried as powder compared to the wet samples and samples dried as discs if this is the case. As samples dried as powder have been shown to contain more water in the scaffold by FTIR (Figure 5.59). This is supported by TRIR results of samples that have been dried as powders and is summarized in Table 5.16.

Table 5.16 *Summary of kinetics of Mn-MOF (2016) samples dried as powder.*

solvent	band positions /cm^{-1}	growth /ns	decay /ns
ethanol	1811		t_1= 0.1 ± 0.04;
			t_2= 7 ± 2
	1832	t_1= 0.7 ± 0.2;	
		t_2= 249 ± 62	
	1870		t_1= 0.3 ± 0.08;
			t_2= 2537 ± 414
	1916 (parent)	t_1= 7 ± 3;	
		t_2= 1874 ± 957	
	1976		t_1= 0.1 ± 0.05;
			t_2= 22 ± 11
	1942 (parent)	t_1= 2 ± 0.6;	
		t_2= 1727 ± 633	
	2029 (parent)	t_1= 2 ± 1;	
		t_2= 1381 ± 698	
toluene	1811		t_1= 0.9 ± 0.4;
			t_2= 29 ± 16
	1832	t_1= 1.5 ± 0.5;	
		t_2= 214 ± 49	
	1870		t_1= 0.9 ± 0.2;
			t_2= 2320 ± 821
	1914 (parent)	t_1= 9 ± 4;	
		t_2= 2558 ± 1289	
	1976		t_1= 1 ± 0.4;
			t_2= 31 ± 23
	1943 (parent)	t_1= 6 ± 2;	
		t_2= 2283 ± 814	
	2030 (parent)	t_1= 4 ± 2;	
		t_2= 2000 ± 1378	

It was observed that the formation of the final product was accelerated for the samples that had been dried as powders from both solvents. This is expected as

the samples dried as powder are desolvated, thus the solvent molecules outside the cavities will be removed. The high content of water is revealed in the FTIR spectra (Figure 5.59). Hence, there is no wonder why the formation of the water-coordinated dicarbonyls $Mn(CO)_2(bdmpzm)Cl(H_2O)$ is accelerated (*ca.* 200 ns) compared to the wet solvated samples (*ca.* 2-4 μs) and samples dried as disc (*ca.* 1 μs).

5.3 Conclusion

In this Chapter, photoproperties of MOF with bis(4-(4-carboxyphenyl)-1*H*-3,5-dimethylpyrazolyl)methane) (3,5-dimethyl-pyrazolylmethane : bdmpzm) as bridging ligands and Mn (II) as nodes, which has been metallized using post-synthesis method with Re (I) (denoted as Re-MOF) and Mn (I) (denoted as Mn-MOF) ions, and also the discrete linker complexes $M(CO)_3$(bdmpzm)X [M: Mn, Re; X: Br (Mn only), Cl (Re only)] have been investigated using both TRIR and DFT calculations.

TRIR on the linker complex of the Re-MOF, $Re(CO)_3$(bdmpzm)Cl has been conducted in two solvents, MeCN and CH_2Cl_2. Result shows that in both solvents, after UV irradiation, the vibrational hot state is formed, which then decays and forms the $\pi\pi^*$ excited state as well as the solvated dicarbonyl species $Re(CO)_2$(bdmpzm)Cl(solvent) (solvent: CH_2Cl_2, MeCN). The $\pi\pi^*$ excited state quickly decays (lifetime: *ca.* 60 ps) to the ground state, while the solvated species is stable and remains for the rest of the experimental timescale. Polarity difference of the solvents CH_2Cl_2 (ε: 8.93) and MeCN (ε: 37.5) has little influence on the lifetime of the $\pi\pi^*$ excited state. However, ν(CO) of $Re(CO)_2$(bdmpzm)Cl(MeCN) (1810, 1903 cm^{-1}) is lower than $Re(CO)_2$(bdmpzm)Cl(CH_2Cl_2) (1820, 1918 cm^{-1}), which may suggest better electron donation of MeCN compared to CH_2Cl_2. The observation of the $\pi\pi^*$ excited state is unusual for the Re-diimine complexes in solvent, where the ^{3}MLCT excited state is more commonly recognised as the characteristic electronic transition. Thus, the results may indicate that the bi-pyrazolyl ligands may have very different properties compared to the diimine ligands, and cannot be simply considered as analogues.

Based on the work of the linker complex, TRIR investigations on the Re-MOF has also been conducted. The Re-MOF are immersed first in two suspensions of ethanol and toluene, and are then pressed into a NaCl disc for TRIR measurement. For both Re-MOF, upon UV photolysis, similar to the linker complex $Re(CO)_3$(bdmpzm)Cl, both the $\pi\pi^*$ excited state and the CO-loss dicarbonyl species are observed. The CO-loss dicarbonyl species is proposed to have coordinated to the surrounding

molecules, such as water and DMF, or ethanol for the sample from the ethanol suspension. After the decay of the ππ* excited state and the CO-loss dicarbonyl species, an excited state of the MOF scaffold is formed with extremely long lifetime of *ca.* 400 ns for Re-MOF from ethanol, and *ca.* 1 μs for Re-MOF from toluene. This excited state is proposed to form due to the energy transfer from the decay of the ππ* excited state and the CO-loss dicarbonyl species. The extremely long lifetime for the excited sate of the MOF scaffold is attributed to the rigidity of the MOF structure, in which the scaffold excited state may not be quenched as easily as in condensed solvent, as the rigidity of the MOF scaffold and gas-phase like environment (the MOF cavities are not as condense as in solvent and is expected to be more gas-phase like) may hinder the quick energy diffusion which can be easily completed in condensed solvent. The prolonged lifetime of the scaffold excited state of Re-MOF from toluene compared to Re-MOF from ethanol can be explained by the fact that although the environment in the MOF channel is not as condensed as in solvent, small molecules such as ethanol could still intrude into the cavities. Besides, the polarity of toluene (ε: 2.38) is much weaker than ethanol (ε: 24.5), thus the quenching of the scaffold excited state is more facile when surrounded by ethanol molecules. Moreover, as the molecule size of toluene is much larger compared to ethanol, it would be more difficult for toluene molecules to intrude into the MOF channels compared to ethanol, thus can create a more vacuum-like environment, which would also slow down the quench of the scaffold excited state.

TRIR on the dried samples have also been conducted as comparison. Two methods have been used to desolvate and dehydrate the Re-MOF sample, denoted as sample dried as powder, and sample dried as disc. Sample dried as powder is considered to be well desolvated but may still contain water, while sample dried as disc is considered to have been desolvated and dehydrated more completely.

The similarities of the ps-TRIR spectra of the dried samples with different drying methods, as well as the Re-MOF immersed in water reveals that the desolvation and dehydration of the MOF has little impact on the early ps-timescale reaction process.

TR^{M}PS-TRIR on Re-MOF dried as disc and powder have been conducted, and the result reveals that the lifetime of the scaffold excited state has been significantly shortened to *ca.* 150 ns for both samples, comparing to the wet samples from ethanol (*ca.* 400 ns) and toluene (*ca.* 1 μs). This may support the existence of water in the dry samples using either drying methods, as the existence of strong polarized water in the MOF channel could accelerate the quenching of the scaffold excited state, even in low water contamination.

Apart from TRIR studies on Re-MOF and its linker complex, TRIR investigations on the analogue Mn-MOF and its linker complex $Mn(CO)_3$(bdmpzm)Br have also been conducted.

Firstly, TRIR of the linker complex $Mn(CO)_3$(bdmpzm)Br has been investigated in two solvents, toluene and DMF. In toluene, based on the TRIR and the global analysis results, it is found that upon UV photolysis, one species with a lifetime of *ca.* 18 ns is formed, which is assigned to the unsaturated CO-loss dicarbonyl species in both *fac*- and *mer*-configurations. Another stable species is also formed at the same time, with a lifetime of *ca.* 1.7 μs, and is assigned to the C-H-bound species, in which the Mn centre is coordinated to the C-H of toluene. The unsaturated dicarbonyl species is observed to convert to an intermediate with a lifetime of *ca.* 190 ns, and this intermediate is observed to decay and convert to the final product. The final product is found to be stable during the experimental timescale, proposed to be the "ring-edge"-bound toluene species. The intermediate with a lifetime of *ca.* 190 ns is also proposed to be a "ring-edge"-bound species, but its configuration is at slightly higher energy level. The C-H-bound species is also observed to convert to the final product.

TRIR in DMF has also been conducted. Similar to that in toluene, the unsaturated dicarbonyl species is observed upon UV photolysis, but with much shorter lifetime (*ca.* 71 ps). This is attributed to the larger polarity and better coordinating ability of DMF compared to toluene. The unsaturated dicarbonyl species is observed to get solvated and convert to an intermediate with a lifetime of *ca.* 16 ns. This intermediate is observed to convert to the final stable product, the DMF-bound

species. The intermediate with a lifetime of 16 ns is also proposed to be a DMF-bound species, but with slightly higher energy.

For the Mn-MOF, TRIR investigations on two batches of MOF provided by our collaborators have been conducted, denoted as Mn-MOF (2015) and Mn-MOF (2016). All the Mn-MOF shares the same scaffold with the Re-MOF, and have $Mn(CO)_3$(bdmpzm)X [X: Br, Cl (MnMOF (2015) only)] as the linker complex.

TRIR shows that, For Mn-MOF(Cl) (2015), similar to its linker complex in solvents, upon UV photolysis, unsaturated dicarbonyl species in both *fac*- and *mer*-configurations are observed. The solvated species are observed at later time delays, where solvent might be water or DMF as residue after synthesis, also supported by DFT calculations. TRIR investigations on Mn-MOF (Br) (2015) reveals similar behavior to Mn-MOF (Cl) (2015), which is ascribed to the similar properties between the Br-complex and the Cl-complex, supported by DFT.

TRIR investigations on the influence of temperature has also been conducted. The result shows that the formation of the solvated species may be hindered under low temperatures.

For the Mn-MOF (2016), TRIR investigations on how solvents in the MOF channel could influence the photo-reaction of the MOF have been conducted. Five solvents have been chosen, ethanol, toluene, hexane, perfluorohexane (PFH) and perfluorotriethylamine (PFTEA). Mn-MOF (2016) samples were first immersed in these solvents and then pressed into NaCl discs for TRIR measurement. However, the TRIR result reveals that, apart from the sample from ethanol, the TRIR spectra for the samples in other solvents (toluene, hexane, PFH, PFTEA) are identical. For all samples, upon UV photolysis, similar to Mn-MOF (2015), the unsaturated dicarbonyl species in both *fac*- and *mer*-configurations are observed. The solvated species is observed at later timescales. TRIR spectra for all samples are almost identical, except that for the sample in ethanol, the ν(CO) of the solvated dicarbonyl species moves slightly to higher wavenumber (1836 cm^{-1}) compared to the samples in other solvents (1832 cm^{-1}). Also, kinetic analysis shows that the transformation

from the unsaturated *mer*-dicarbonyl species to the solvated species for the sample from ethanol is *ca.* 4.5 μs, while for all the other solvents, toluene, hexane, PFH and PFTEA, which are considered to have larger molecular sizes, the rate is faster for *ca.* 2~3 μs. This is explained by the fact that only ethanol may have successfully penetrated into the MOF channel. While for the samples in solvents with larger molecular sizes (toluene, hexane, PFH, PFTEA), the diffusion of solvent is unsuccessful, and what is inside the MOF channel might be DMF or water. Either DMF or water is more polar than ethanol, thus the coordination rate is faster than ethanol, and ν(CO) of the solvated species is relatively red-shifted.

FTIR of Mn-MOF (2016) has evidenced the existence of water in the wet Mn-MOF samples and samples dried as powder. For the samples dried as disc, it is observed that the transformation from the unsaturated dicarbonyl species to the solvated species is accelerated compared to the wet samples, which is explained by the fact that for the wet samples from solvents with large molecular sizes, toluene, hexane, PFH and PFTEA, the solvent molecule may not have diffused into the MOF channel, instead, they may cover the cavities of the MOF, thus water cannot easily penetrate into the MOF channel.

For the samples dried as powder, a further acceleration of the formation of the solvated species is observed. This is expected as FTIR suggests higher water contamination of the sample dried as powder.

References

1 H.C. Joe Zhou and S. Kitagawa, *Chem. Soc. Rev.*, 2014, **43**, 5415–5418.

2 K. K. Gangu, S. Maddila, S. B. Mukkamala and S. B. Jonnalagadda, *Inorganica Chim. Acta*, 2016, **446**, 61–74.

3 I. Ahmed and S. H. Jhung, *Mater. Today*, 2014, **17**, 136–146.

4 B. Liu, S. Yao, X. Liu, X. Li, R. Krishna, G. Li, Q. Huo and Y. Liu, *ACS Appl. Mater. Interfaces*, 2017, **9**, 32820–32828.

5 X. Lin, I. Telepeni, A. J. Blake, A. Dailly, C. M. Brown, J. M. Simmons, M. Zoppi, G. S. Walker, K. M. Thomas, T. J. Mays, P. Hubberstey, N. R. Champness and M. Schröder, *J. Am. Chem. Soc.*, 2009, **131**, 2159–2171.

6 W. Jiang, J. Yang, Y. Y. Liu, S. Y. Song and J. F. Ma, *Inorg. Chem.*, 2017, **56**, 3036–3043.

7 B. B. Lu, J. Yang, G. B. Che, W. Y. Pei and J. F. Ma, *ACS Appl. Mater. Interfaces*, 2018, **10**, 2628-2636.

8 W. Ouellette, A. V. Prosvirin, K. Whitenack, K. R. Dunbar and J. Zubieta, *Angew. Chem. Int. Ed.*, 2009, **48**, 2140–2143.

9 T. Haneda, M. Kawano, T. Kawamichi and M. Fujita, *J. Am. Chem. Soc.*, 2008, **130**, 1578–1579.

10 T. Kawamichi, T. Haneda, M. Kawano and M. Fujita, *Nature*, 2009, **461**, 633.

11 S. S. Kaye and J. R. Long, *J. Am. Chem. Soc.*, 2008, **130**, 806–807.

12 T. Iwasawa, R. J. Hooley and J. Rebek, *Science*, 2007, **317**, 493–496.

13 R. J. Hooley, T. Iwasawa and J. Rebek, *J. Am. Chem. Soc.*, 2007, **129**, 15330–15339.

14 A. Heine, G. DeSantis, J. G. Luz, M. Mitchell, C. H. Wong and I. A. Wilson, *Science*, 2001, **294**, 369–374.

15 T. Haneda, M. Kawano, T. Kawamichi and M. Fujita, *J. Am. Chem. Soc.*, 2008, **130**, 1578–1579.

16 D. A. Evans, G. Borg and K. A. Scheidt, *Angew. Chem.*, 2002, **114**, 3320–3323.

17 M. Kawano, Y. Kobayashi, T. Ozeki and M. Fujita, *J. Am. Chem. Soc.*, 2006, **128**, 6558–6559.

18 A. J. Blake, N. R. Champness, T. L. Easun, D. R. Allan, H. Nowell, M. W.

George, J. Jia and X. Z. Sun, *Nat. Chem.*, 2010, **2**, 688.

19 M. W. George, F. P. A. Johnson, J. R. Westwell, P. M. Hodges and J. J. Turner, *J. Chem. Soc. Dalton Trans.*, 1993, 2977–2979.

20 D. J. Stufkens and A. Vlček, *Coord. Chem. Rev.*, 1998, **177**, 127–179.

21 B. D. Rossenaar, D. J. Stufkens and A. Vlček, *Inorg. Chem.*, 1996, **35**, 2902–2909.

22 D. R. Gamelin, M. W. George, P. Glyn, F. W. Grevels, F. P. A. Johnson, W. Klotzbuecher, S. L. Morrison, G. Russell, K. Schaffner and J. J. Turner, *Inorg. Chem.*, 1994, **33**, 3246–3250.

23 I. P. Clark, M. W. George, F. P. A. Johnson and J. J. Turner, *Chem. Commun.*, 1996, 1587–1588.

24 D. M. Dattelbaum and T. J. Meyer, *J. Phys. Chem. A*, 2002, **106**, 4519–4524.

25 M. Towrie, A. W. Parker, K. L. Ronayne, K. F. Bowes, J. M. Cole, P. R. Raithby and J. E. Warren, *Appl. Spectrosc.*, 2009, **63**, 57–65.

26 S. Sato, T. Morimoto and O. Ishitani, *Inorg. Chem.*, 2007, **46**, 9051–9053.

27 R. R. Andrea, W. G. J. De Lange, D. J. Stufkens and A. Oskam, *Inorg. Chem.*, 1989, **28**, 318–323.

28 B. D. Rossenaar, D. J. Stufkens, A. Oskam, J. Fraanje and K. Goubitz, *Inorganica Chim. Acta*, 1996, **247**, 215–229.

29 G. J. Stor, S. L. Morrison, D. J. Stufkens and A. Oskam, *Organometallics*, 1994, **13**, 2641–2650.

30 A. Rosa, G. Ricciardi, E. J. Baerends and D. J. Stufkens, *J. Phys. Chem.*, 1996, **100**, 15346–15357.

31 T. L. Easun, J. Jia, J. A. Calladine, D. L. Blackmore, C. S. Stapleton, K. Q. Vuong, N. R. Champness and M. W. George, *Inorg. Chem.*, 2014, **53**, 2606–2612.

32 T. J. Reade, T. S. Murphy, J. A. Calladine, R. Horvath, I. P. Clark, G. M. Greetham, M. Towrie, W. Lewis, M. W. George and N. R. Champness, *Phil Trans R Soc A*, 2017, **375**, 20160033.

33 T. L. Easun, J. Jia, T. J. Reade, X. Z. Sun, E. Stephen Davies, A. J. Blake, M. W. George and N. R. Champness, *Chem. Sci.*, 2014, **5**, 539–544.

34 S. Trofimenko, *J. Am. Chem. Soc.*, 1967, **89**, 6288–6294.

35 S. Ranjan, S. Y. Lin, K. C. Hwang, Y. Chi, W. L. Ching, C. S. Liu, Y. T. Tao, C.

H. Chien, S. M. Peng and G. H. Lee, *Inorg. Chem.*, 2003, **42**, 1248–1255.

36 J. Hurtado, L. Ibarra, D. Yepes, P. García-Huertas, M. A. Macías, O. Triana-Chavez, E. Nagles, L. Suescun and A. Muñoz-Castro, *J. Mol. Struct.*, 2017, **1146**, 365–372.

37 E. Nagles, L. Ibarra, J. P. Llanos, J. Hurtado and O. Garcia-Beltrán, *J. Electroanal. Chem.*, 2017, **788**, 38–43.

38 B. F. Fieselmann and G. D. Stucky, *Inorg. Chem.*, 1978, **17**, 2074–2077.

39 C. A. Kosky, P. Ganis and G. Avitabile, *Acta Crystallogr. B*, 1971, **27**, 1859–1864.

40 S. Trofimenko, *J. Am. Chem. Soc.*, 1970, **92**, 5118–5126.

41 C. Pettinari and R. Pettinari, *Coord. Chem. Rev.*, 2005, **249**, 663–691.

42 D. L. Reger, J. R. Gardinier, P. J. Pellechia, M. D. Smith and K. J. Brown, *Inorg. Chem.*, 2003, **42**, 7635–7643.

43 J. A. Simon, S. L. Curry, R. H. Schmehl, T. R. Schatz, P. Piotrowiak, X. Jin and R. P. Thummel, *J. Am. Chem. Soc.*, 1997, **119**, 11012–11022.

44 B. Machura, J. Palion, M. Penkala, T. Groń, H. Duda and R. Kruszynski, *Polyhedron*, 2013, **56**, 189–199.

45 C. Feng, D. Zhang, G. Y. Gao, Y. Peng and H. Zhao, *J. Inorg. Organomet. Polym. Mater.*, 2016, **26**, 431–438.

46 B. Machura, R. Kruszynski, M. Jaworska, P. Lodowski, R. Penczek and J. Kusz, *Polyhedron*, 2008, **27**, 1767–1778.

47 W. M. Bloch, A. Burgun, C. J. Coghlan, R. Lee, M. L. Coote, C. J. Doonan and C. J. Sumby, *Nat. Chem.*, 2014, **6**, 906.

48 M. W. George and J. J. Turner, *Coord. Chem. Rev.*, 1998, **177**, 201–217.

Chapter 6 Experimental

6.1 Apparatus Information

6.1.1 Nottingham Ultrafast TRIR Apparatus

Some of the ps-TRIR and ns-TRIR in this work was done using the ultrafast TRIR apparatus in Nottingham in collaboration with Dr Xue-Zhong Sun. More detailed description of the apparatus can be found elsewhere.[1] In the Nottingham ultrafast TRIR apparatus, first laser pulses (800 nm, 2.3 mJ, 1kHz, 140 fs) are generated by a tunable Ti: sapphire oscillator (MaiTai, Spectra Physics) and a regenerative amplifier (Spitfire Pro, Spectra Physics). Then the pulses are split into two parts using a beam splitter.

One part pumps the TOPAS-C optical parametric amplifier (Light Conversion), which is then followed by a difference frequency generator, producing a tunable mid-IR pulse (180 cm^{-1}, 2 μJ at 2000 cm^{-1}). The IR pulse is further split into two parts using a beam splitter. One part is used as a reference for detecting signal fluctuation using a single element MCT (mercury cadmium telluride) detector (Kolmar Technology). The other part is used to probe the sample. After passing through the sample, the IR probe pulse passes through a 250 nm IR monochromator, which is then followed by a 128-element MCT detector. The MCT detector is followed by a 144-channel amplifier, and the electric signals are finally turned into digital signals which can be processed using a computer by a 16-bit analog to digital converter.

The other part of the original laser pulse is used to generate the UV pump, utilizing harmonic generator (TimePlate Tripler, Minioptic Technology Inc.). This allows for UV pump pulses of 400 nm and 267 nm to be generated. Alternatively, UV pump pulses in the range of 300~700 nm can be generated by first pumping a TOPAS-C optical parametric amplifier, followed by a harmonic generation and frequency mixing. Different time delays under ns-timescale are achieved by using a translation stage (LMA Actuator, Aerotech). The UV pump is then used to initiate

the reaction.

For time delays in the range of ns-to-μs timescale, the optical delay-line can no longer be used as this may require distance that will be too long in the apparatus. Therefore, a pulse generator (DG535 Stanford Research Systems) is used for achieving large time delays. Q-switched Nd: YVO laser (1064 nm, 600 ps, Advanced Optical Technology) is used to generate the UV pump. The trigger-time between the electric current and the electronic pulses which are used to generate the UV laser can be tuned using the pulse generator. The UV pump and IR probe are synchronized, therefore different time delays can be obtained, in the range of 0.5 ns to 100 μs.

The change in absorbance (ΔAbs) is measured by the pump-on and pump-off signals using an optical chopper. To avoid sample decomposition, the sample is rastered in the x and y planes. And to ensure the complete probe of the initiated samples, the IR probe is focused onto a spot with diameter of *ca.* 80 μm while the UV pump is focused onto the spot sharing the same centre with diameter of *ca.* 100 μm.

6.1.2 Ultrafast TRIR Apparatus in Rutherford Appleton Laboratory (RAL)

Some of the ps-TRIR and ns-TRIR in this work was done using the ultrafast TRIR apparatus in Rutherford Appleton Laboratory (RAL). The ultrafast TRIR apparatus in RAL is similar to that in Nottingham. Detailed description can be found elsewhere thus only a brief introduction is given here.[2] The original pulse (50 fs, 0.8 mJ, 10kHz, 800 nm) is generated using a Ti:sapphire dual output amplifier (Thales Laser), and is then split into two using a beam splitter. The first part is used to generate a UV pump (266 nm) *via* a third harmonic generation. The time delays are achieved using optical delay-line. The other part of the original pulse is used to generate the tunable mid-IR beam, utilizing optical parametric amplifiers (TOPAS, Light Conversion). The IR beam is further split into two parts, one acts as the reference and is followed by a 64-element MCT detector (Infrared Associates),

while the other part is used as the IR probe which passes through the sample and then is followed by two 128-element MCT detectors (Infrared Associates).

6.1.3 Time-Resolved Multiple Probe Spectroscopy (TR^MPS) Apparatus in Rutherford Appleton Laboratory (RAL)

Some of the data in this work was obtained by using the TR^MPS apparatus in RAL. The detailed description can be found elsewhere thus only a brief introduction is given here.[3]

In the TR^MPS apparatus, two laser amplifiers (Thales Laser and Spectra Physics) are used as the UV pump and IR probe with different repetition rates, at 1 and 10 kHz respectively. The UV pump and IR probe are synchronized, therefore for each UV pump, multiple IR probes follow with time delays from ps to μs-timescales.

6.1.4 FTIR Spectroscopy

All FTIR (Fourier Transform Infrared) spectra were recorded on a Thermo Nicolet FTIR Spectrometer with a resolution of 2 cm^{-1}. Samples are measured using a Harrick's IR solution cell (Harrick Corp.) with calcium fluoride windows (25 x 2 mm, Crystran).

6.2 Materials

6.2.1 Materials Used in Chapter 2

$CpMn(CO)_3$ (Strem), $Cp'Mn(CO)_3$ (Aldrich), $CpRe(CO)_3$ (Strem), $Cp^*Re(CO)_3$ (Strem), tributylsilane (99%, Aldrich), tributylgermane (99%, Aldrich), tributylstannane (97%, Aldrich) were used as received, without further purification. Solvents perfluoro(methylcyclohexane) (94%, Alfa Aesar) and *n*-heptane (Aldrich, spectrophotometric grade) were refluxed under atmosphere of argon in the presence of CaH_2 for 48 h before use, and were later stored under argon.

6.2.2 Materials Used in Chapter 3

$W(CO)_6$ (Aldrich), xenon (>99.99% Aldrich), benzene (99.8%, Aldrich), fluorobenzene (99%, Aldrich), chlorobenzene (99.8%, Aldrich), bromobenzene (99%, Aldrich), iodobenzene (98 %, Aldrich), chlorocyclohexane (99%, Aldrich), bromocyclohexane (98%, Aldrich), tributylsilane (99%, Aldrich), tributylgermane (99%, Aldrich), tributylstannane (97%, Aldrich) were used as received and without further purification. Solvents perfluoro(methylcyclohexane) (94%, Alfa Aesar) and *n*-heptane (Aldrich, spectrophotometric grade) were refluxed under atmosphere of argon in the presence of CaH_2 for 48 h before use, and were later stored under argon. $W(CO)_5$(pyridine), $W(CO)_5$(piperidine) and $W(CO)_5$(4-acetylpyridine) were synthesized by the former group members.

6.2.3 Materials Used in Chapter 4

$Re(dppz\text{-}NPh_2)(CO)_3Cl$, $Re(phen\text{-}TPA)(CO)_3$(pyridine), $Re(phen\text{-}TPA)(CO)_3$(4-(dimethylamino)pyridne), $Re(phen\text{-}TPA)(CO)_3Cl$, $Re(phen\text{-}TPA)(CO)_3Br$ were prepared and offered by our collaborators from University of Otago. Toluene (99.8%, Aldrich), acetone (99.5%, Aldrich), dichloromethane (99.8%, Aldrich) were refluxed under atmosphere of argon in the presence of CaH_2 for 48 h before use, and were then stored under argon.

6.2.4 Materials Used in Chapter 5

The Re-MOF and Mn-MOF were prepared and provided by our collaborators from University of Adelaide. NaCl (Aldrich) crystal was dried in oven (130 °C) for over 24 h before use.

6.3 Sample Preparations

6.3.1 Sample in Solution Phase

As the TRIR measurement uses powerful laser of high repetition rate, and also as that many samples are highly air and water sensitive, therefore to avoid sample decomposing and degradation as well as unwanted by-reactions, a flow system is build, which consists of a Harrick cell with CaF_2 windows, a high-pressure glass sample reservoir and Teflon tubes. The whole flow system is connected to a standard Schlenk line, and is in an air-free environment under an atmosphere of argon. The solvent is injected into the flow system as well as the solid sample is added to the system under atmosphere of argon. Usually a volume of 16~20 ml of solution is required for the TRIR measurement. The concentration of the solution can be tuned by either the amount of compound adding into the solution or by using Teflon spacer of different thickness which is placed between the two CaF_2 windows (thickness: 2 mm, diameter: 25 mm) of the Harrick cell. The concentration of solution is first tested using FTIR, and is ideal in the range of IR absorption between 0.1~0.8. The solution is then degassed for several times. For experiments involving gas, a gas filling station constructed by Dr. Ian Clark at Rutherford Appleton Laboratory is used, and 1.5 bar of the gas is introduced into the flow system connected to the Schlenk line which has been degassed in advance. During the TRIR measurement, the prepared solution is flowed constantly between the Harrick cell and the high-pressure glass reservoir by using a peristaltic pump.

6.3.2 Sample in Solid Phase

The MOF samples in Chapter 5 is prepared using NaCl disc. Small amount of MOF is mixed with dried NaCl crystal and ground evenly. Then the mixed powder is pressed using the press under weight of 10 tons for 15 mins. Then a transparent NaCl disc of 1~2 mm thickness can be obtained. The disc then is fixed in a clamp which has been 3D-printed designed for the TRIR apparatus in RAL.

6.4 Data Analysis

Kinetic fittings were performed using OriginPro 9.0. Band fittings were performed using Origin Pro 7.5. Maxima Values of bands were used to fit exponential fitting models of kinetic traces. Program Ultraview (developed at the Rutherford Appleton Laboratory) has been utilized in TRIR data processing.

6.5 DFT Calculations

All calculations were conducted using the Gaussview interface and Gaussian 03. The functional used is B3LYP, the basis-set used is 6-31G(d), while for Re, W, Br and I, the LANL2DZ basis set was implemented. All calculations were performed in gas phase.

References

1 M. Towrie, D. C. Grills, J. Dyer, J. A. Weinstein, P. Matousek, R. Barton, P. D. Bailey, N. Subramaniam, W. M. Kwok, C. Ma, D. Phillips, A. W. Parker and M. W. George, *Appl. Spectrosc.*, 2003, **57**, 367–380.

2 G. M. Greetham, P. Burgos, Q. Cao, I. P. Clark, P. S. Codd, R. C. Farrow, M. W. George, M. Kogimtzis, P. Matousek, A. W. Parker, M. R. Pollard, D. A. Robinson, Z. J. Xin and M. Towrie, *Appl. Spectrosc.*, 2010, **64**, 1311–1319.

3 G. M. Greetham, D. Sole, I. P. Clark, A. W. Parker, M. R. Pollard and M. Towrie, *Rev. Sci. Instrum.*, 2012, **83**, 103107.